

H. Sezer Atamturktur · Babak Moaveni  
Costas Papadimitriou · Tyler Schoenherr *Editors*

# Model Validation and Uncertainty Quantification, Volume 3

Proceedings of the 33rd IMAC, A Conference  
and Exposition on Structural Dynamics, 2015



# Conference Proceedings of the Society for Experimental Mechanics Series

*Series Editor*

Tom Proulx

Society for Experimental Mechanics, Inc.

Bethel, CT, USA

More information about this series at <http://www.springer.com/series/8922>



H. Sezer Atamturktur • Babak Moaveni • Costas Papadimitriou  
Tyler Schoenherr  
Editors

# Model Validation and Uncertainty Quantification, Volume 3

Proceedings of the 33rd IMAC, A Conference and Exposition  
on Structural Dynamics, 2015

*Editors*

H. Sezer Atamturktur  
Civil Engineering Department  
Clemson University  
Clemson, SC, USA

Costas Papadimitriou  
Department of Mechanical Engineering  
University of Thessaly  
Volos, Greece

Babak Moaveni  
Department of Civil and Environmental Engineering  
Tufts University  
Medford, MA, USA

Tyler Schoenherr  
Sandia National Laboratories  
Albuquerque, NM, USA

ISSN 2191-5644                      ISSN 2191-5652 (electronic)  
Conference Proceedings of the Society for Experimental Mechanics Series  
ISBN 978-3-319-15223-3              ISBN 978-3-319-15224-0 (eBook)  
DOI 10.1007/978-3-319-15224-0

Library of Congress Control Number: 2015937350

Springer Cham Heidelberg New York Dordrecht London  
© The Society for Experimental Mechanics, Inc. 2015

This work is subject to copyright. All rights are reserved by the Publisher, whether the whole or part of the material is concerned, specifically the rights of translation, reprinting, reuse of illustrations, recitation, broadcasting, reproduction on microfilms or in any other physical way, and transmission or information storage and retrieval, electronic adaptation, computer software, or by similar or dissimilar methodology now known or hereafter developed.

The use of general descriptive names, registered names, trademarks, service marks, etc. in this publication does not imply, even in the absence of a specific statement, that such names are exempt from the relevant protective laws and regulations and therefore free for general use.

The publisher, the authors and the editors are safe to assume that the advice and information in this book are believed to be true and accurate at the date of publication. Neither the publisher nor the authors or the editors give a warranty, express or implied, with respect to the material contained herein or for any errors or omissions that may have been made.

Printed on acid-free paper

Springer International Publishing AG Switzerland is part of Springer Science+Business Media ([www.springer.com](http://www.springer.com))

# Preface

*Model Validation and Uncertainty Quantification* represents one of ten volumes of technical papers presented at the 33rd IMAC, A Conference and Exposition on Balancing Simulation and Testing, 2015, organized by the Society for Experimental Mechanics, and held in Orlando, Florida, February 2–5, 2015. The full proceedings also include volumes on Nonlinear Dynamics; Dynamics of Civil Structures; Sensors and Instrumentation; Special Topics in Structural Dynamics; Structural Health Monitoring & Damage Detection; Experimental Techniques, Rotating Machinery & Acoustics; Shock & Vibration Aircraft/Aerospace, Energy Harvesting; and Topics in Modal Analysis.

Each collection presents early findings from experimental and computational investigations on an important area within Structural Dynamics. Model Validation and Uncertainty Quantification (MVUQ) is one of these areas.

Modeling and simulation are routinely implemented to predict the behavior of complex dynamical systems. These tools powerfully unite theoretical foundations, numerical models and experimental data which include associated uncertainties and errors. The field of MVUQ research entails the development of methods, with associated metrics, for the rigorous test of model prediction accuracy and robustness considering all relevant sources of uncertainties and errors through systematic comparisons against experimental observations.

The organizers would like to thank the authors, presenters, session organizers, and session chairs for their participation in this track.

Clemson, SC, USA  
Medford, MA, USA  
Volos, Greece  
Albuquerque, NM, USA

H. Sezer Atamturktur  
Babak Moaveni  
Costas Papadimitriou  
Tyler Schoenherr



# Contents

<b>1</b>	<b>Experimental Validation of the Dual Kalman Filter for Online and Real-Time State and Input Estimation</b> .....	<b>1</b>
	Saeed Eftekhar Azam, Eleni Chatzi, Costas Papadimitriou, and Andrew Smyth	
<b>2</b>	<b>Comparison of Uncertainty in Passive and Active Vibration Isolation</b> .....	<b>15</b>
	Roland Platz and Georg C. Enss	
<b>3</b>	<b>Observation DOF's Optimization for Structural Forces Identification</b> .....	<b>27</b>
	Silvia Milana, Annalisa Fregolent, and Antonio Culla	
<b>4</b>	<b>Nonlinear Structural Finite Element Model Updating Using Batch Bayesian Estimation</b> .....	<b>35</b>
	Hamed Ebrahimian, Rodrigo Astroza, and Joel P. Conte	
<b>5</b>	<b>A Comparative Assessment of Nonlinear State Estimation Methods for Structural Health Monitoring</b> .....	<b>45</b>
	Majdi Mansouri, Onur Avci, Hazem Nounou, and Mohamed Nounou	
<b>6</b>	<b>Hierarchical Bayesian Model Updating for Probabilistic Damage Identification</b> .....	<b>55</b>
	Iman Behmanesh, Babak Moaveni, Geert Lombaert, and Costas Papadimitriou	
<b>7</b>	<b>Nonlinear Structural Finite Element Model Updating Using Stochastic Filtering</b> .....	<b>67</b>
	Rodrigo Astroza, Hamed Ebrahimian, and Joel P. Conte	
<b>8</b>	<b>Dispersion–Corrected, Operationally Normalized Stabilization Diagrams for Robust Structural Identification</b> .....	<b>75</b>
	Vasilis K. Dertimanis, Minas D. Spiridonakos, and Eleni N. Chatzi	
<b>9</b>	<b>Online Damage Detection in Plates via Vibration Measurements</b> .....	<b>85</b>
	Giovanni Capellari, Saeed Eftekhar Azam, and Stefano Mariani	
<b>10</b>	<b>Advanced Modal Analysis of Geometry Consistent Experimental Space-Time Databases in Nonlinear Structural Dynamics</b> .....	<b>93</b>
	Ioannis T. Georgiou	
<b>11</b>	<b>Comparison of Damage Classification Between Recursive Bayesian Model Selection and Support Vector Machine</b> .....	<b>105</b>
	Zhu Mao and Michael Todd	
<b>12</b>	<b>A Comparative Study of Mode Decomposition to Relate Next-ERA, PCA, and ICA Modes</b> .....	<b>113</b>
	Ayad Al-Rumaithi, Hae-Bum Yun, and Sami F. Masri	
<b>13</b>	<b>Comparison of Different Approaches for the Model-Based Design of Experiments</b> .....	<b>135</b>
	Ina Reichert, Peter Olney, Tom Lahmer, and Volkmar Zabel	
<b>14</b>	<b>Sensitivity Analysis for Test Resource Allocation</b> .....	<b>143</b>
	Chenzhao Li and Sankaran Mahadevan	
<b>15</b>	<b>Predictive Validation of Dispersion Models Using a Data Partitioning Methodology</b> .....	<b>151</b>
	Gabriel Terejanu	



<b>16</b>	<b>SICODYN Research Project: Variability and Uncertainty in Structural Dynamics</b> .....	157
	Sylvie Audebert	
<b>17</b>	<b>Experimental Variability on Modal Characteristics of an In-Situ Pump</b> .....	163
	Sylvie Audebert, Anne Coulon, Marie-Ange Andrianoely, Stéphane Muller, and Emmanuel Foltête	
<b>18</b>	<b>Variability of a Bolted Assembly Through an Experimental Modal Analysis</b> .....	171
	Sami Daouk, François Louf, Christophe Cluzel, Olivier Dorival, and Laurent Champaney	
<b>19</b>	<b>Bottom-Up Calibration of an Industrial Pump Model: Toward a Robust Calibration Paradigm</b> .....	179
	A. Kuczkowiak, S. Huang, S. Cogan, and M. Ouisse	
<b>20</b>	<b>Model Validation in Scientific Computing: Considering Robustness to Non-probabilistic Uncertainty in the Input Parameters</b> .....	189
	Greg Roche, Saurabh Prabhu, Parker Shields, and Sez Atamturktur	
<b>21</b>	<b>Robust-Optimal Design Using Multifidelity Models</b> .....	199
	Kendra Van Buren and François Hemez	
<b>22</b>	<b>Robust Modal Test Design Under Epistemic Model Uncertainties</b> .....	207
	Fabien Maugan, Scott Cogan, Emmanuel Foltête, and Aurélien Hot	
<b>23</b>	<b>Clustered Parameters of Calibrated Models When Considering Both Fidelity and Robustness</b> .....	215
	Sez Atamturktur, Garrison Stevens, and Yuting Cheng	
<b>24</b>	<b>Uncertainty Propagation Combining Robust Condensation and Generalized Polynomial Chaos Expansion</b> .....	225
	K. Chikhaoui, N. Kacem, N. Bouhaddi, and M. Guedri	
<b>25</b>	<b>Robust Updating of Operational Boundary Conditions for a Grinding Machine</b> .....	235
	Elvio Bonisoli and Marco Brino	
<b>26</b>	<b>Impact of Numerical Model Verification and Validation Within FAA Certification</b> .....	249
	David M. Moorcroft and Joseph Pelletiere	
<b>27</b>	<b>The Role of Model V&amp;V in the Defining of Specifications</b> .....	257
	Todd Simmermacher, Greg Tipton, Jerry Cap, and Randy Mayes	
<b>28</b>	<b>A Perspective on the Integration of Verification and Validation into the Decision Making Process</b> .....	265
	Kenneth T. Hu, Angel Urbina, and Joshua Mullins	
<b>29</b>	<b>A MCMC Method for Bayesian System Identification from Large Data Sets</b> .....	275
	P.L. Green	
<b>30</b>	<b>Bayesian Inference for Damage Detection in Unsupervised Structural Health Monitoring</b> .....	283
	Reza Mohammadi-Ghazi and Oral Buyukozturk	
<b>31</b>	<b>Reducing MCMC Computational Cost with a Two Layered Bayesian Approach</b> .....	291
	Ramin Madarshahian and Juan M. Caicedo	
<b>32</b>	<b>Comparison of FRF Correlation Techniques</b> .....	299
	Timothy Marinone and Adam Moya	
<b>33</b>	<b>Improved Estimation of Frequency Response Covariance</b> .....	311
	Daniel C. Kammer and Matthew Bonney	
<b>34</b>	<b>Cross Orthogonality Check for Structures with Closely Spaced Modes</b> .....	321
	Anders Skaftø, Manuel L. Aenlle, and Rune Brincker	
<b>35</b>	<b>Modeling of an Instrumented Building Subjected to Different Ground Motions</b> .....	329
	Amaia Martinez and Carlos E. Ventura	
<b>36</b>	<b>Calibration and Cross-Validation of a Car Component Model Using Repeated Testing</b> .....	339
	Karl-Johan Larsson, Snævar Leó Grétarsson, Majid K. Vakilzadeh, and Thomas Abrahamsson	

<b>37</b>	<b>Structural Dynamics Model Calibration and Validation of a Rectangular Steel Plate Structure</b> .....	351
	Hasan G. Pasha, Karan Kohli, Randall J. Allemang, Allyn W. Phillips, and David L. Brown	
<b>38</b>	<b>Human Activity Recognition Using Multinomial Logistic Regression</b> .....	363
	Ramin Madarshahian and Juan M. Caicedo	

# Chapter 1

## Experimental Validation of the Dual Kalman Filter for Online and Real-Time State and Input Estimation

Saeed Eftekhar Azam, Eleni Chatzi, Costas Papadimitriou, and Andrew Smyth

**Abstract** In this study, a novel dual implementation of the Kalman filter is proposed for simultaneous estimation of the states and input of structures via acceleration measurements. In practice, the uncertainties stemming from the absence of information on the input force, model inaccuracy and measurement errors render the state estimation a challenging task and the research to achieve a robust solution is still in progress. Via the use of numerical simulation, it was shown that the proposed method outperforms the existing techniques in terms of robustness and accuracy of displacement and velocity estimations [8]. The efficacy of the proposed method is validated using the data obtained from a shake table experiment on a laboratory test structure. The measured accelerations of the floors of the structure are fed into the filter, and the estimated time histories of the displacement estimates are cross-compared to the true time histories obtained from the displacement sensors.

**Keywords** Dual Kalman filter • Unknown input • State estimation • Modal identification • TSSID • Experimental validation • Laboratory test

### 1.1 Introduction

This paper contributes to the procedure of fatigue damage prediction in the entire body of large-scale structures via sparse vibration measurements. An accurate prediction of the fatigue damage demands reliable estimations of the strain time histories in points of interest and their vicinity. Accurate prediction of the strain time histories in turn requires accurate estimates of the states at corresponding degrees-of-freedom of the system [1]. This may be casted as a problem of reliable state estimation under the premise of unknown input measurements. When dealing with a stochastic linear time invariant system, with a known input, state estimates can be calculated in a straightforward fashion. However, in the problem discussed herein the input is unknown. In the last few decades, a number of methods and techniques have been developed to account for the lack of information on the input. Bernal and Ussia present a comprehensive study of sequential deconvolution of inputs from measured outputs [2]. They pose the problem in a deterministic setup, and prove that when there are less inputs than measured outputs the input to the system can be accurately reconstructed. They have shown that the proposed procedure is conditionally stable and the stability criteria is established. However, in practical cases the conditions that must be satisfied to make the deconvolution work are highly likely to be violated.

One of the most recent methods for joint state and input estimation of linear time invariant systems, attempting to incorporate uncertainties, has been developed by Gillijn and De Moore [3]. The method requires a state space model of the system and the second order statistics of the state of the system to recursively furnish the estimates of the input and state. However, when the number of the outputs exceed the order of the model the method suffers from rank deficiency. Lourens et al. [4] have suggested an alteration of the method developed in [3] to alleviate the above-mentioned numerical instabilities. The effectiveness of the proposed adjustment was studied via the joint input force and acceleration estimation of a simulated steel beam, a laboratory test beam and a large-scale steel bridge. It was observed that, even though the method delivers a reasonable estimate of the accelerations, the displacement estimates are affected by spurious low frequency components,

---

S. Eftekhar Azam • C. Papadimitriou (✉)  
Department of Mechanical Engineering, University of Thessaly, Volos, Greece  
e-mail: [eftekhar@uth.gr](mailto:eftekhar@uth.gr); [costasp@uth.gr](mailto:costasp@uth.gr)

E. Chatzi  
Institute of Structural Engineering, ETH Zürich, Zürich, Switzerland

A. Smyth  
School of Engineering and Applied Science, Columbia University, New York, NY, USA

which were filtered out by using band pass filters. It is noteworthy that in dealing with joint state and parameter estimation, Chatzi and Fuggini [5] have proposed a method to resolve the issues related to the spurious low frequency components in the displacement estimates by including artificial displacement measurements into the observation vector.

Lourens et al. [6] have for the first time applied an augmented Kalman filter (AKF) for unknown force identification in structural systems. It was concluded that the AKF is prone to numerical instabilities due to un-observability issues of the augmented system matrix. Naets et al. proposed an analytical investigation of the stability of the augmented Kalman filter when applied to unknown input and state estimation and demonstrate that the exclusive use of acceleration measurements can lead to unreliable results [7]. In order to alleviate this problem, dummy displacement measurements on a position level are added. The proposed technique is ascertained through numerical investigation and experimental campaign; in both cases it is observed that the AKF based on solely acceleration measurements can lead to unstable results.

To address the shortcomings of the existing methods for state estimation of the structural systems with unknown general inputs, Eftekhar Azam et al. proposed a novel dual Kalman filter (DKF) for state and unknown input estimation via sparse acceleration measurements [8]. It is demonstrated that the successive structure of DKF resolves numerical issues attributed to un-observability and rank deficiency of the AKF. Furthermore, through numerical investigations it is shown that the expert guess on the covariance of the unknown input provides a tool for filtering out the so-called drift effect in the estimated input force and states by GDF. In this paper, an experimental validation of the DKF is pursued; the results of a laboratory experiment are utilized in order to assess the performance of the DKF when real experimental data is used. Moreover, the results obtained by GDF are confronted by those furnished by AKF and GDF.

The paper starts with a section devoted to a brief formulation of the state-space equations for linear time invariant dynamical systems. The next section overviews the DKF, AKF and GDF algorithms and highlights the salient features of each of these approaches in an effort to bring forth their similarities and distinctions. The following section describes the model identification methods used in the current study, and finally the results of the experimental validation of the DKF and its cross-comparison to other filters are recounted.

## 1.2 Formulation of the Dynamic State Space Equations

The methods and techniques used in this work require existence of an underlying mathematical model of the system which serves as the open-loop estimator of the state of the system. To this end, the linear second order differential equation in continuous time is introduced herein:

$$\mathbf{M}\ddot{\mathbf{u}}(t) + \mathbf{C}\dot{\mathbf{u}}(t) + \mathbf{K}\mathbf{u}(t) = \mathbf{f}(t) = \mathbf{S}_p\mathbf{p}(t) \quad (1.1)$$

where  $\mathbf{u}(t) \in \mathbb{R}^n$  denotes the displacement vector and  $\mathbf{K}$ ,  $\mathbf{C}$  and  $\mathbf{M} \in \mathbb{R}^{n \times n}$  stand for the stiffness, damping and mass matrix, respectively.  $\mathbf{f}(t) \in \mathbb{R}^n$  is the excitation force, which herein is presented as a superposition of time histories  $\mathbf{p}(t) \in \mathbb{R}^m$  that are influencing some degrees-of-freedom of the structure as indicated via the influence matrix  $\mathbf{S}_p \in \mathbb{R}^{n \times m}$ .

Time discretization should be implemented on the aforementioned equations in order to facilitate their use with the data coming from the sensors. In doing so, first the state space form of the equations are derived, where the state vector encompasses displacement and velocity. The latter allows one to write Eq. (1.1) in the following form and to define the so-called process equation:

$$\dot{\mathbf{x}}(t) = \mathbf{A}_c\mathbf{x}(t) + \mathbf{B}_c\mathbf{p}(t) \quad (1.2)$$

where the system matrices are:

$$\mathbf{A}_c = \begin{bmatrix} 0 & \mathbf{I} \\ -\mathbf{M}^{-1}\mathbf{K} & -\mathbf{M}^{-1}\mathbf{C} \end{bmatrix}$$

$$\mathbf{B}_c = \begin{bmatrix} 0 \\ \mathbf{M}^{-1}\mathbf{S}_p \end{bmatrix}$$

Regarding the measurement equation, the most general case for the observation process is considered where a combination of the displacements, velocities and accelerations are supposed to form the measurement vector:

$$\mathbf{d}(t) = \begin{bmatrix} \mathbf{S}_d & 0 & 0 \\ 0 & \mathbf{S}_v & 0 \\ 0 & 0 & \mathbf{S}_a \end{bmatrix} \begin{bmatrix} \mathbf{u}(t) \\ \dot{\mathbf{u}}(t) \\ \ddot{\mathbf{u}}(t) \end{bmatrix} \quad (1.3)$$

where  $\mathbf{S}_d$ ,  $\mathbf{S}_v$  and  $\mathbf{S}_a$  denote the selection matrices of appropriate dimension for the displacements, velocities and accelerations, respectively. By using equation of motion, Eq. (1.3) could be transformed so that it forms the observation equation:

$$\mathbf{d}(t) = \mathbf{G}_c \mathbf{x}(t) + \mathbf{J}_c \mathbf{p}(t) \quad (1.4)$$

where the output influence matrix and the direct transmission matrix are:

$$\mathbf{G}_c = \begin{bmatrix} \mathbf{S}_d & 0 \\ 0 & \mathbf{S}_v \\ -\mathbf{S}_a \mathbf{M}^{-1} \mathbf{K} & -\mathbf{S}_a \mathbf{M}^{-1} \mathbf{C} \end{bmatrix}$$

$$\mathbf{J}_c = \begin{bmatrix} 0 \\ 0 \\ \mathbf{S}_a \mathbf{M}^{-1} \mathbf{S}_p \end{bmatrix}$$

In this study, the main focus lies in the seismic excitations applied to the base of a structure, hence the excitation term assumes the following form:

$$\mathbf{f}(t) = -\mathbf{M} \ddot{\mathbf{u}}_g(t) \mathbf{S}_p$$

In Eq. (1.1), it is noteworthy that the coordinate system is relative to the ground displacement, moreover, the subscript  $\mathbf{g}$  refers to the coordinate system, which moves according to seismic ground motions. The matrix  $\mathbf{S}_p$  in this case applies the ground accelerations to all floors of the structure.

In practical situations we might use an identified modal model of the structure, hence the equivalent of Eq. (1.1) in modal coordinates is introduced herein. To derive a modal model of the system, Eq. (1.1) is projected to the subspace spanned by the undamped eigenmodes of the system. In this regard, consider the eigenvalue problem corresponding to Eq. (1.1):

$$\mathbf{K} \Phi = \mathbf{M} \Phi \Omega^2 \quad (1.5)$$

Transforming the coordinate system of Eq. (1.1) via the following mapping:

$$\mathbf{u}(t) = \Phi \mathbf{z}(t) \quad (1.6)$$

where  $\mathbf{z}(t) \in \mathbb{R}^m$ ,  $\Phi \in \mathbb{R}^{n \times m}$ , and then pre multiplying it by  $\Phi^T$  and dividing the right hand side and left hand side by  $\Phi^T \mathbf{M} \Phi$ , considering  $\Phi^T \mathbf{K} \Phi / \Phi^T \mathbf{M} \Phi = \Omega^2$  and assuming the damping is proportional, the Eq. (1.6) can be rewritten:

$$\ddot{\mathbf{z}}(t) + \mathbf{\Gamma} \dot{\mathbf{z}}(t) + \Omega^2 \mathbf{z}(t) = -\mathbf{P} \ddot{\mathbf{u}}_g(t) \quad (1.7)$$

where the components of  $j$ th entry of the diagonal damping matrix  $\mathbf{\Gamma}$  are of the form  $2\xi_j \omega_j$ , in which  $\xi_j$  stands for the relevant modal damping ratio. Additionally,  $\mathbf{P}$  denotes the modal participation factor  $\mathbf{P} = \Phi^T \mathbf{M} \mathbf{S}_p / \Phi^T \mathbf{M} \Phi$ . Note that, a truncated modal space could be substituted in Eq. (1.7)

The recombination of Eqs. (1.3) and (1.4) through use of the relevant matrices, results into the full order state-space equations that are required to implement the input and state estimation algorithm. To derive the modal state-space equations, an eigenvector space must be substituted in Eq. (1.4) hence the following variable transformation would be necessary:

$$\mathbf{x}(t) = \begin{bmatrix} \Phi & 0 \\ 0 & \Phi \end{bmatrix} \boldsymbol{\zeta}(t)$$

where  $\zeta(t)$  is the reduced modal state vector:

$$\zeta(t) = \begin{bmatrix} \mathbf{z}(t) \\ \dot{\mathbf{z}}(t) \end{bmatrix}$$

The reduced modal state-space equation in continuous time will have the following form:

$$\dot{\zeta}(t) = \mathbf{A}_c \zeta(t) + \mathbf{B}_c \ddot{\mathbf{u}}_g(t) \quad (1.8)$$

$$\mathbf{d}(t) = \mathbf{G}_c \zeta(t) + \mathbf{J}_c \ddot{\mathbf{u}}_g(t) \quad (1.9)$$

while the relevant system matrices read:

$$\mathbf{A}_c = \begin{bmatrix} 0 & \mathbf{I} \\ -\boldsymbol{\Omega}^2 & -\boldsymbol{\Gamma} \end{bmatrix}, \mathbf{B}_c = \begin{bmatrix} 0 \\ -\mathbf{P} \end{bmatrix}, \mathbf{G}_c = \begin{bmatrix} \mathbf{S}_d \boldsymbol{\Phi} & 0 \\ 0 & \mathbf{S}_v \boldsymbol{\Phi} \\ -\mathbf{S}_a \boldsymbol{\Phi} \boldsymbol{\Omega}^2 & -\mathbf{S}_a \boldsymbol{\Phi} \boldsymbol{\Gamma} \end{bmatrix}, \mathbf{J}_c = \begin{bmatrix} 0 \\ 0 \\ -\mathbf{S}_a \mathbf{P} \end{bmatrix}$$

To discretize Eqs. (1.8) and (1.9), the sampling rate is denoted by  $1/\Delta t$  and the discrete time instants are defined at  $t_k = k \Delta t$ , for  $k = 1, \dots, N$ . The discrete state-space equation can be expressed by the following notation:

$$\zeta_{k+1} = \mathbf{A} \zeta_k + \mathbf{B} \ddot{\mathbf{u}}_{g,k} \quad (1.10)$$

$$\mathbf{d}_k = \mathbf{G} \zeta_k + \mathbf{J} \ddot{\mathbf{u}}_{g,k} \quad (1.11)$$

where  $\mathbf{A} = e^{\mathbf{A}_c \Delta t}$ ,  $\mathbf{B} = [\mathbf{A} - \mathbf{I}] \mathbf{A}_c^{-1} \mathbf{B}_c$ ,  $\mathbf{G} = \mathbf{G}_c$  and  $\mathbf{J} = \mathbf{J}_c$ .

### 1.3 Dual Kalman Filter for Joint Input and State Estimation

In this article, three methods and techniques for the purpose of input and state estimation are cross-compared. First, the main features of each are outlined so that their similarities and distinctions can be summarized. The first algorithm assessed herein is the filter developed by Gillijn and De Moor (GDF) for input and state estimation of linear time invariant systems [3]. The method belongs to the family of recursive Bayesian filters, as such, Bayes' theorem is incorporated into the filter to render the extraction of information on the states from the latest observations possible. To initialize the procedure, the GDF requires an expert guess on the expected value and the covariance of the state at the beginning, then, it recursively estimates the input and state at discrete time instants. First, an estimate of the mean and covariance of the input force is obtained by updating the guess on the input via the GDF input gain, which is similar, but not identical to the Kalman gain. Once the input is estimated, the state vector is subsequently calculated by applying the GDF state gain to the observation novelty. Then, a time update stage follows the procedure which boils down to a mere transition of the state and input through the state-space equations.

Another existing method to achieve recursive state and input estimation is the augmented Kalman filter (AKF). The notion of the augmented state is extensively used in automatic control in order to concurrently estimate the parameters and state of the system. To mitigate some issues attributed to the GDF, this paper also considers the application of the AKF. The AKF turns out liable to numerical instabilities when pure acceleration measurements are fed into it.

Within the frame of state and parameter estimation, an alternative to the augmented formulation is the dual formulation [9]. In dealing with state and parameter estimation of the laminated composites it was shown that the dual formulation outperforms the augmented formulation at the cost of a more complicated implementation [10]. Dealing with the dual estimation and reduced order modelling of linear time varying systems, the dual estimation concept is used to update the reduced subspace constructed by proper orthogonal decomposition [11]. However, in dealing with joint input and state estimation of linear time invariant systems neither the augmented nor the dual formulation lead to nonlinear state space models. The latter motivates the application of the dual formulation of the input-state estimation with coupled use of the

**Table 1.1** The general scheme of the DKF algorithm for input and state estimation

Initialization at time $t_0$ :
$\hat{\mathbf{p}}_0 = \mathbb{E}[\mathbf{p}_0]$
$\mathbf{P}_0^p = \mathbb{E}[(\mathbf{p}_0 - \hat{\mathbf{p}}_0)(\mathbf{p}_0 - \hat{\mathbf{p}}_0)^T]$
$\hat{\mathbf{x}}_0 = \mathbb{E}[\mathbf{x}_0]$
$\mathbf{P}_0 = \mathbb{E}[(\mathbf{x}_0 - \hat{\mathbf{x}}_0)(\mathbf{x}_0 - \hat{\mathbf{x}}_0)^T]$
At time $t_k$ , for $k = 1, \dots, N_t$ :
Prediction stage for the input:
1. Evolution of the input and prediction of covariance input:
$\mathbf{p}_k^- = \mathbf{p}_{k-1}$
$\mathbf{P}_k^{p^-} = \mathbf{P}_{k-1}^p + \mathbf{Q}^p$
Update stage for the input:
2. Calculation of Kalman gain for input:
$\mathbf{G}_k^p = \mathbf{P}_k^{p^-} \mathbf{J}^T (\mathbf{J} \mathbf{P}_k^{p^-} \mathbf{J}^T + \mathbf{R})^{-1}$
3. Improve predictions of input using latest observation:
$\hat{\mathbf{p}}_k = \mathbf{p}_k^- + \mathbf{G}_k^p (\mathbf{d}_k - \mathbf{G} \hat{\mathbf{x}}_{k-1} - \mathbf{J} \mathbf{p}_k^-)$
$\mathbf{P}_k^p = \mathbf{P}_k^{p^-} - \mathbf{G}_k^p \mathbf{J} \mathbf{P}_k^{p^-}$
Prediction stage for the state:
4. Evolution of state and prediction of covariance of state:
$\mathbf{x}_k^- = \mathbf{A} \hat{\mathbf{x}}_{k-1} + \mathbf{B} \hat{\mathbf{p}}_k$
$\mathbf{P}_k^- = \mathbf{A} \mathbf{P}_{k-1} \mathbf{A}^T + \mathbf{Q}^x$
Update stage for the state:
5. Calculation of Kalman gain for state:
$\mathbf{G}_k^x = \mathbf{P}_k^- \mathbf{G}^T (\mathbf{G} \mathbf{P}_k^- \mathbf{G}^T + \mathbf{R})^{-1}$
6. Improve predictions of state using latest observation:
$\hat{\mathbf{x}}_k = \mathbf{x}_k^- + \mathbf{G}_k^x (\mathbf{d}_k - \mathbf{G} \mathbf{x}_k^- - \mathbf{J} \hat{\mathbf{p}}_k)$
$\mathbf{P}_k = \mathbf{P}_k^- - \mathbf{G}_k^x \mathbf{G} \mathbf{P}_k^-$

Kalman filter. Within the dual estimation scheme, similar to the augmented formulation, the concept of the fictitious transition equation for unknown input is used. Hence, similar to the AKF, in dealing with the DKF the covariance of the fictitious noise must be additionally adjusted to obtain accurate estimates of the state. However, unlike the AKF, the DKF estimates the input and state in two different stages. After initialization, at a first stage the input and the covariance of the input are estimated by applying the Kalman gain to the innovation. At a second stage, the estimated input is fed into a standard Kalman filter which uses the dynamic state-space model to furnish the estimate of the state (Table 1.1).

## 1.4 Experimental Validation

To assess the performance of the DKF, AKF and GDF in the joint state-input estimation task, the data available from a laboratory structure, shown in Fig. 1.1 has been used. The test is carried out on a three dimensional structure that is comprised of four floors which are stacked onto each other via single span frames. The frame is laterally braced along its strong axis to prevent rotational movements. The structure is subjected to seismic excitations by means of the hydraulic uniaxial shacking table, of the Carleton lab facility in Columbia University, and the response of the structure in terms of the displacements and accelerations is measured on all floor levels by means of laser and MEMS accelerometer sensors, respectively. The methods and techniques that are described and introduced in the previous section require a physical description of the structure, represented in state-space form. In order to obtain the aforementioned numerical model, in this study two approaches are followed; first a modal model of the structure; the second model is established via a recently developed transformation strategy applied on a numerical model obtained by a subspace identification method [12]. Next, a general scheme of each model identification procedure is outlined. The motivation for utilizing both the TSSID and modal model of the structure lies in the numerical divergence of GDF estimates for some sparse sensor setups when the TSSID is used. It is noteworthy that the TSSID model does not make any restrictive assumption on the system matrices; however, the modal model presumes a proportional damping. It is shown that inherent differences between two models can lead to different performances when the state and input estimation is dealt with.

**Fig. 1.1** The four storey shear frame setup on the Carleton laboratory uniaxial shake table

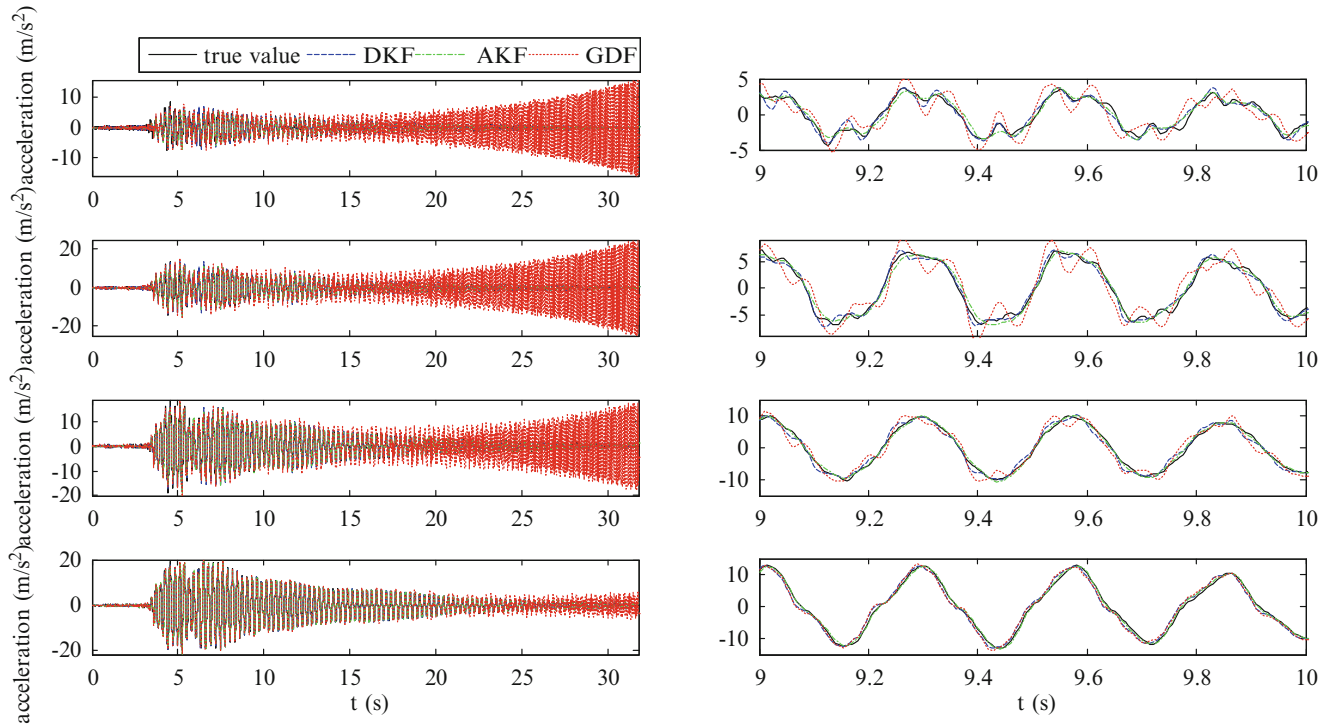


In this paper, the modal characteristics of the structure are estimated using vibration data induced by a measured seismic force applied to its base. The adopted method is based on a least squares minimization of the measure of fit between the Frequency Response Function (FRF) matrix estimated from the measured output acceleration time histories and the FRF matrix predicted by a modal model. In a procedure that can be divided in three main steps, the number of contributing modes and the values of the modal properties are estimated through the FRF estimated from the measured input-output response time histories. In a first step, conventional least squares complex frequency algorithms using the right matrix fraction polynomial model [13, 14] are adopted to acquire estimates of the modal frequencies modal damping ratios and participation factors, and stabilization diagrams furnish a tool to distinguish between the physical and the mathematical modes. In a second step, given that the aforementioned error function is quadratic with respect to the complex mode shapes and the so-called upper and lower residual terms [15], the mode shapes and damping ratios are obtained. These values in most cases are very close to the optimal values. In a third step, the values obtained in the first and second stage are used to efficiently perform the minimization of the objective function. Hence, the computational cost is significantly reduced, when considering that the abovementioned objective function is quadratic with respect to the complex mode shapes.

As a second alternative, a transformed subspace identification technique is used to construct a state-space model for its use with the recursive Bayesian filters. Specifically, the underlying SSI technique is the n4sid algorithm which fits in the class of subspace identification methods [12]. This constitutes an input-output identification method, consisting of QR decomposition of the past and future block Hankel matrices of input and output in order to calculate the main projection matrices. Subsequently, a singular value decomposition (SVD) is executed for extracting the rank of the system and to cast the problem in a standard least-square form. The solution of the latter least squares yields the numerical state space model that fits the input-output data. The disadvantage of Stochastic Subspace Identification methods lies in that the derived state space models are not in their canonical form, i.e. they are not formulated with a minimal parameterization. More importantly, the identified models are not represented in physical coordinates. However, in this study it is necessary to be able to estimate the physical states of the system in the form of displacement, since these are to be subsequently used for fatigue estimation. In this regard, a transformation procedure for achieving such a transformation for structural systems developed by Chatzis et al. [16], hereinafter referred to as the TSSID.

In what follows, the results of the state and input identification by using the DKF, AKF and GDF are presented. First the identified modal properties of the structure are introduced to the filters for deriving the model of the structure.



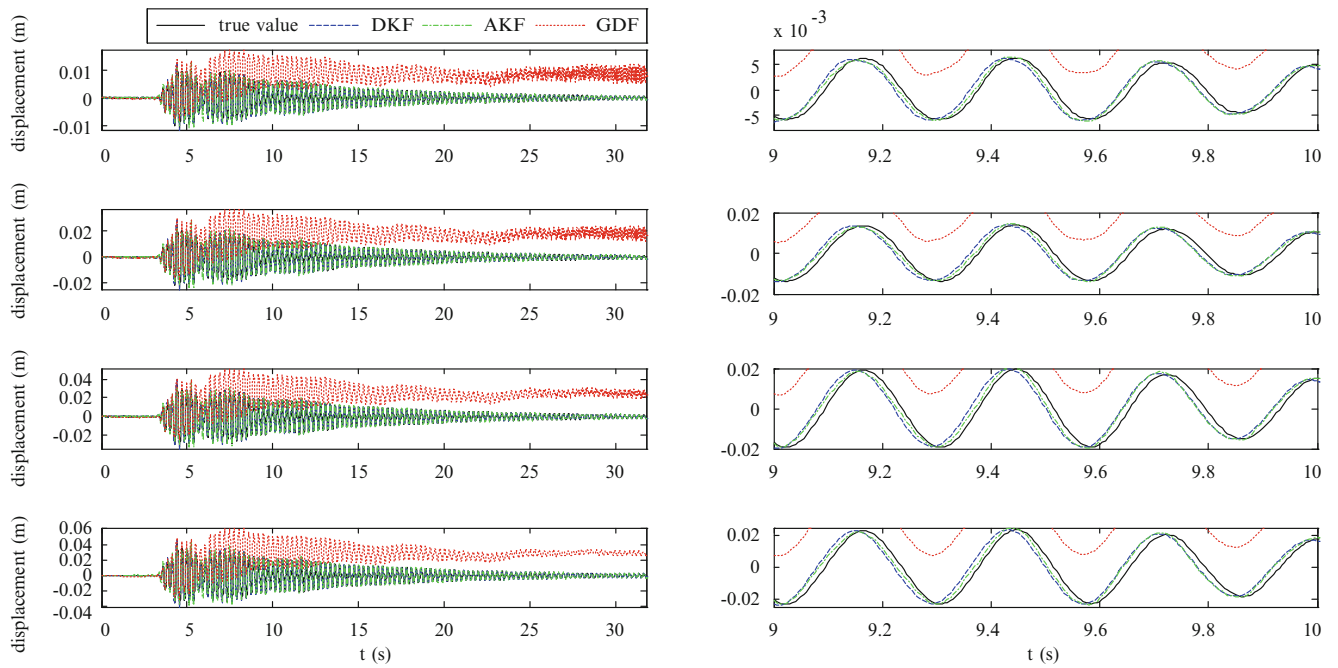


**Fig. 1.2** Acceleration time histories estimated by DKF, AKF and GDF of the floors 1, 2, ..., 4 from top to bottom, respectively

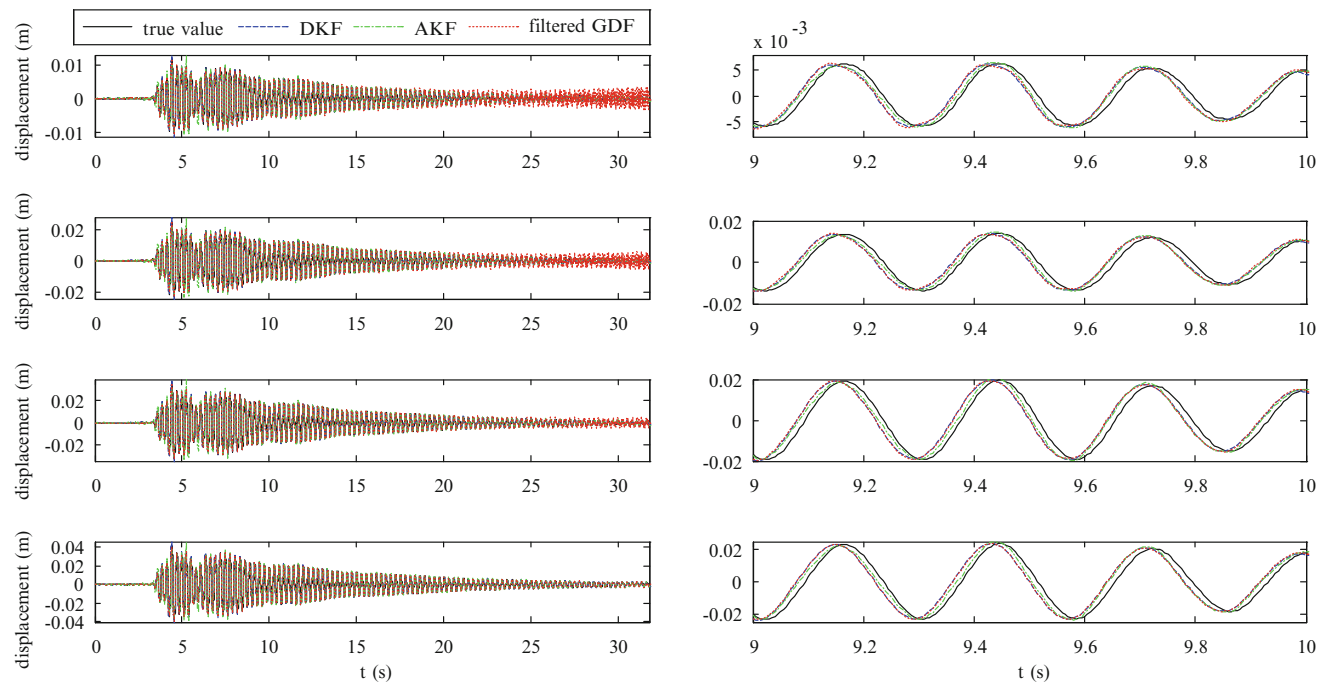
For the joint state and input estimation for systems with unknown input, the GDF does not require any a-priori assumption on the statistics of the input to the system; on the contrary, the AKF and DKF need the initial value of the mean and covariance of input force to deliver the estimates of the input and states of the system. The value of the covariance of the input force, which plays the role of the regularization parameter, strongly influences the quality of the estimates furnished by the Bayesian filters. In this work, we make use of the L-curve approach in order to adjust the values of the process noise for the state and input estimation [6]. In this way, it turns out that  $\mathbf{Q}^p = 10^{-6} \times \mathbf{I}$  and  $\mathbf{Q}^s = 1 \times \mathbf{I}$  should be selected for the AKF and DKF respectively when only the measured acceleration time history of the last floor is regarded as observation process. Henceforward  $\mathbf{I}$  is an identity matrix of appropriate dimension. The diagonal values of the covariance matrix of the observation noise for acceleration measurement are set to  $10^{-3} m/s^2$ . The process noise  $\mathbf{Q}^s$  and initial covariance of the state of  $\mathbf{P}_0$  are both set to  $10^{-20} \times \mathbf{I}$ . Figures 1.2 and 1.3 show the acceleration and displacement estimation results provided by the DKF, AKF and GDF for the case where only the acceleration time history of the last DOF is observed. In Fig. 1.2, it is evident that the DKF and AKF provide a reasonable estimate of the observed acceleration time histories; however, the GDF results are affected by numerical instabilities. By increasing the number of the observations the numerical instability can be mitigated, however the emphasis of the current study is on cross-comparison of the three methods when sparse measurements are dealt with. Figure 1.3 shows the results of the displacement estimates provided by the DKF, AKF and GDF. The displacement time history estimated by the GDF is affected by the low frequency components and the same instability trend as in the acceleration estimation. It is observed that the DKF and AKF both provide reasonable estimates of the displacement time history of the test structure.

In what preceded, it was seen that the results of displacement time history estimate furnished by GDF have been affected by low frequency components. In order to get insights on the performance of the GDF filter apart from the drift in the estimates, the modal displacements estimated by GDF have been filtered by using a band pass filter. Figure 1.4 presents the results of such analysis, and confronts the obtained result by DKF and AKF estimates. It is observed that, after implementing the filtering procedure in the estimation results the GDF estimates become more accurate; and match the results furnished by DKF in terms of accuracy and agreement to the target values, nonetheless, the numerical instability caused by low density of the observation sensors still persists.

Next, a model obtained by stochastic subspace identification procedures [5] is incorporated into the filters to investigate the performance of the different schemes when a more realistic model is incorporated into the filters. In this regard, the model obtained through TSSID method, which is described in previous section is introduced into the DKF, AKF and GDF.



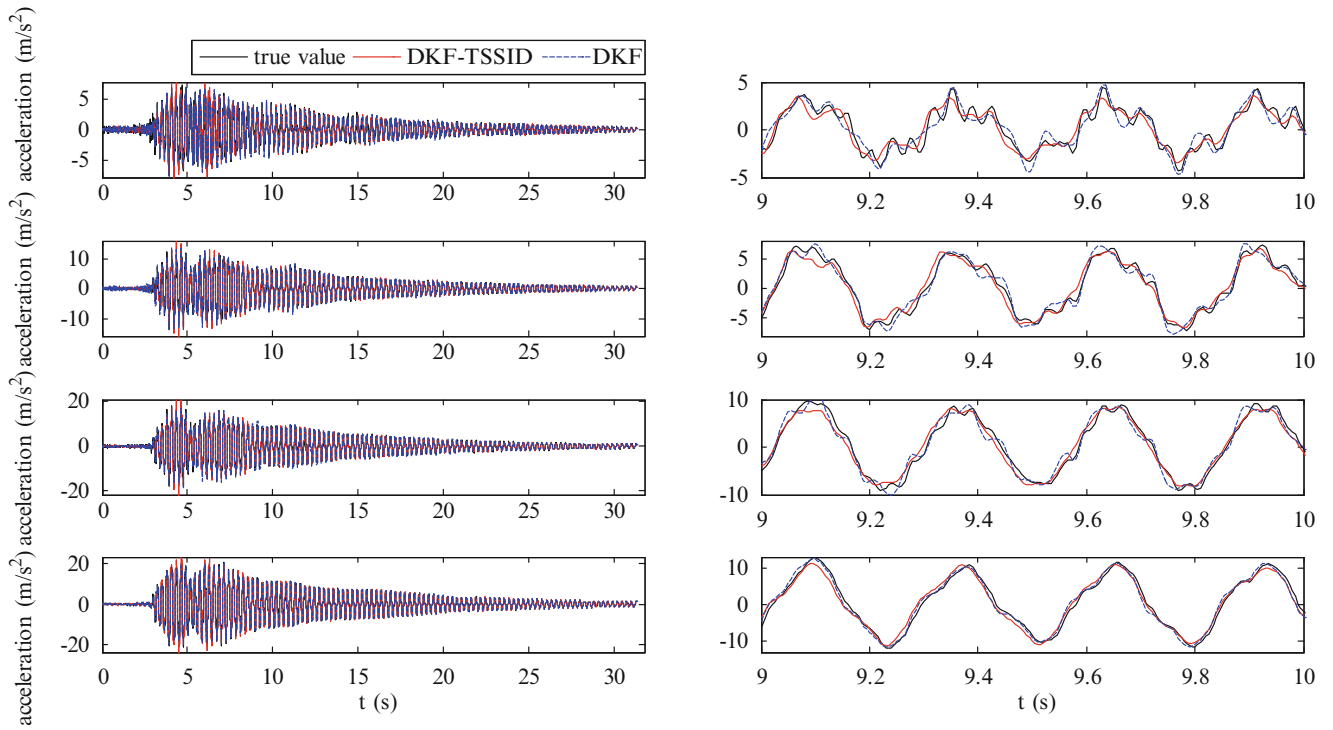
**Fig. 1.3** Displacement time histories estimated by DKF, AKF and GDF of the floors 1, 2, ..., 4 from top to bottom, respectively



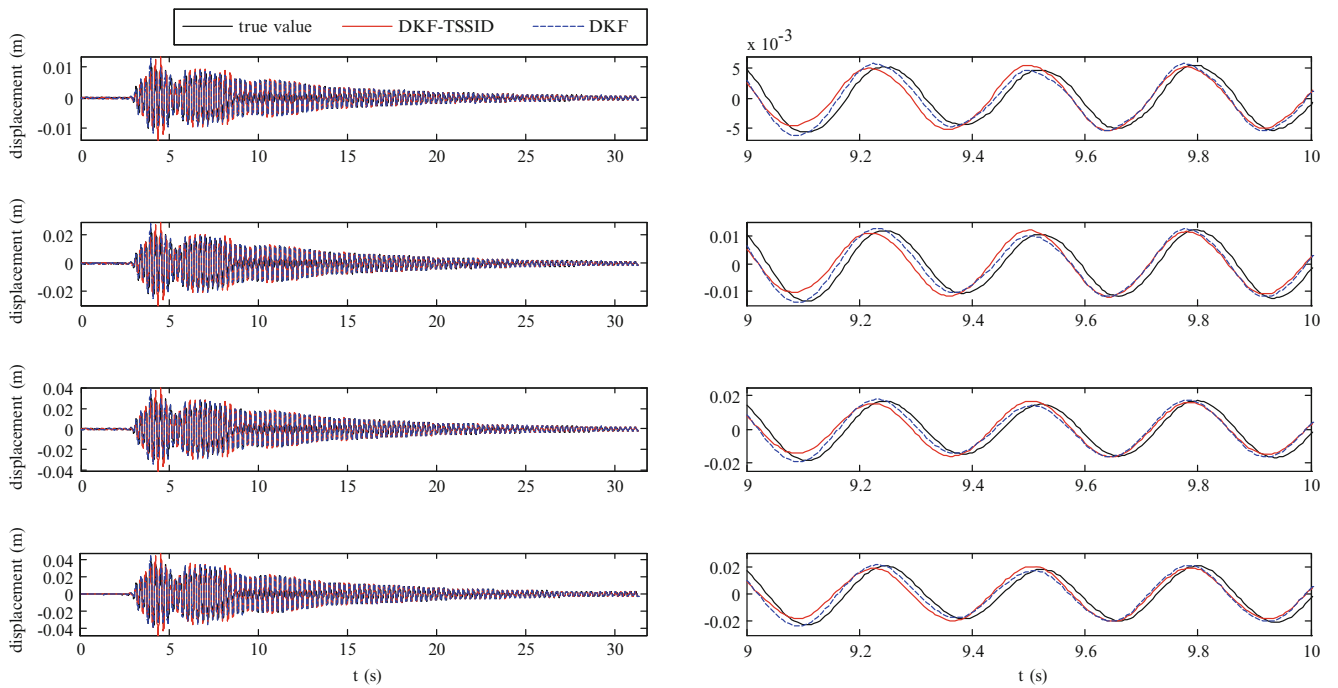
**Fig. 1.4** Displacement time histories estimated by DKF, AKF and band pass-filtered GDF for the floors 1, 2, ..., 4 from top to bottom, respectively

It was observed that, the GDF fails to provide a solution to the problem when sparse measurements are made. Once again, by increasing the number of the observation DOFs the GDF results can be improved.

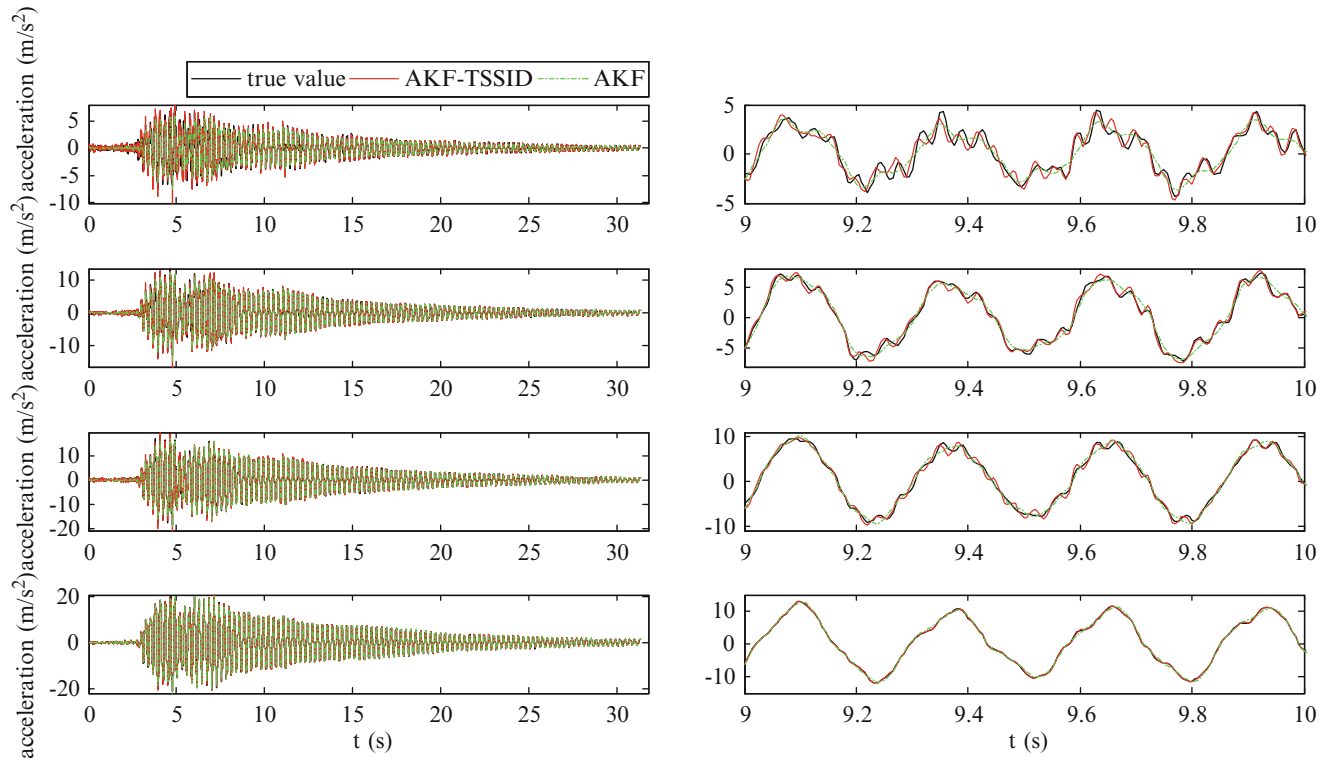
Next the capability of the AKF and DKF when sparse acceleration measurements are available is investigated. It is assumed that only the acceleration time history of the last floor is observed, thereafter the performances of the two filter when using modal model and TSSID model are cross-compared. In Figures 1.5 and 1.6 the results of acceleration and displacement estimation furnished by DKF are shown. In Fig. 1.5 it is observed that the acceleration estimations in non-measured DOFs is less accurate than the observed one, additionally, moving from last floor to first floor as the noise to signal



**Fig. 1.5** Acceleration time histories estimated by DKF when modal model and TSSID model are used for the floors 1, 2, ..., 4 from top to bottom, respectively



**Fig. 1.6** Displacement time histories estimated by DKF when modal model and TSSID model are used for the floors 1, 2, ..., 4 from top to bottom, respectively

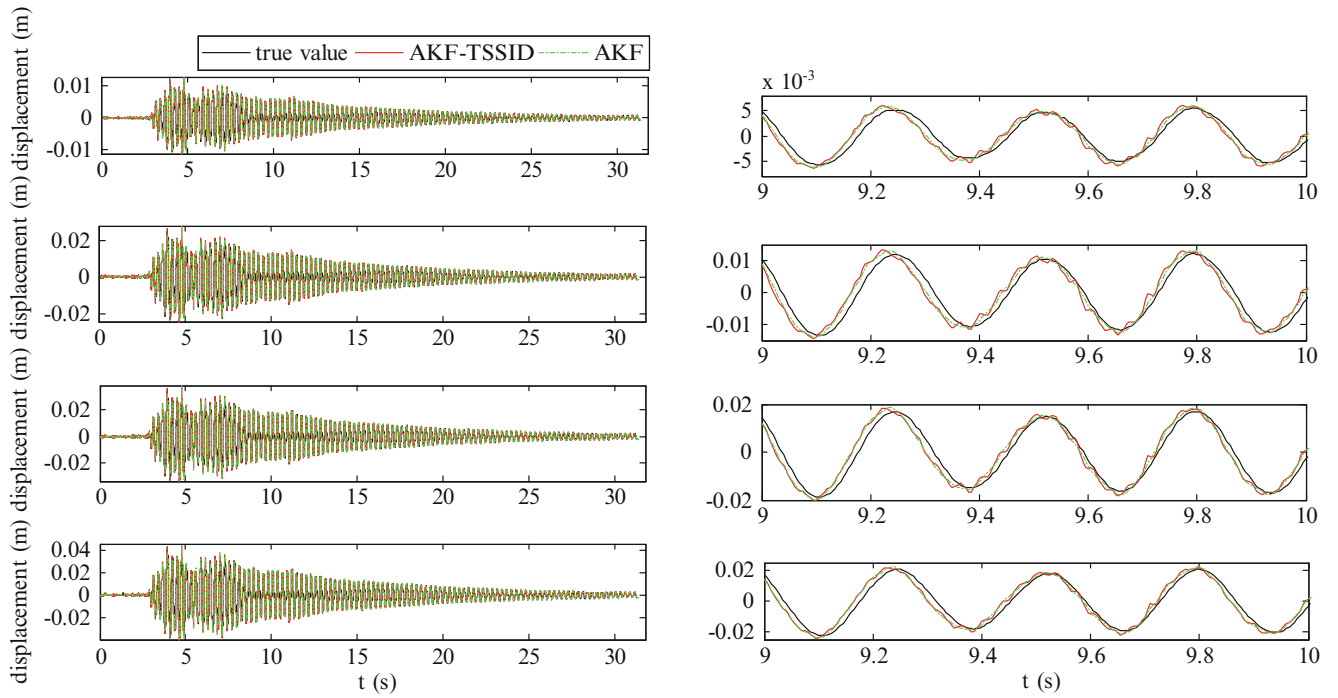


**Fig. 1.7** Acceleration time histories estimated by AKF when modal model and TSSID model are used for the floors 1, 2, ..., 4 from top to bottom, respectively

ration increases the accuracy of the estimations decrease. Concerning the displacement time histories, it is observed that use of both models lead to the same level of accuracy of displacement estimates.

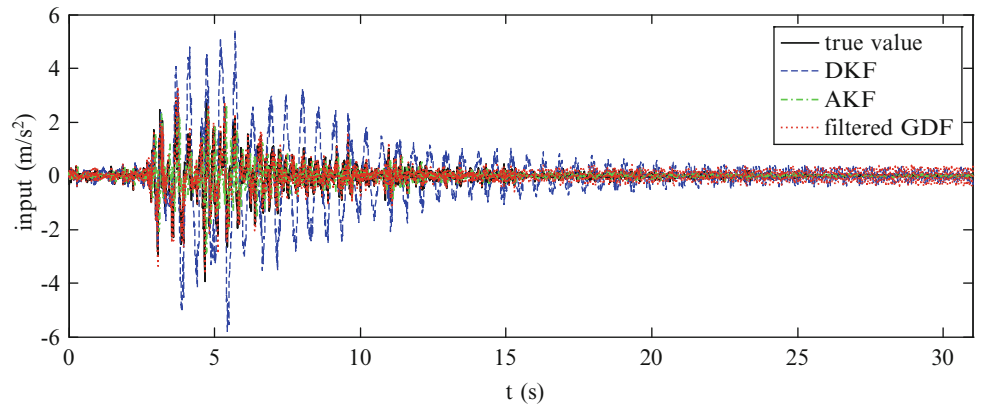
Dealing with the performance of the AKF when the TSSID model is used Figs. 1.7 and 1.8 present the relevant estimates when the sensor configuration used in the last example is considered. It is observed that use of the TSSID model leads to a more accurate acceleration estimation for un-observed DOFs. Similar to the acceleration estimates obtained by the DKF, the lower the floor the less the accuracy becomes due to the higher signal to noise ratio. Regarding the displacement time histories, both models deliver a similar accuracy.

Finally, the input estimation capability of the three methods is discussed. In Figures 1.9 and 1.10 show the time histories of input and displacement, when DKF, AKD and a band-pass filtered GDF are used. In the latter case, the accelerations of the floor #2 and #4 are assumed as the observation process, due to divergence of the GDF results in the case of a single observation. Moreover, the low frequency drift in the displacement estimates is removed, in a post-processing phase, i.e., not in an online manner, by applying a band pass filter on the modal coordinates. In doing so, first the displacement time histories are projected onto the modal basis, thereafter a band pass filter is used to remove spurious frequencies, which for its lower and upper bounds features the  $0.1 \omega_j$ ,  $j = 1, 2, \dots, 4$  and Nyquist frequency, respectively. Concerning the band pass filter applied to the input, the lower bound is set  $0.1 \omega_1$ . In Figure 1.9, it is observed that the filtered GDF provides a close match between estimated and true input; however, the DKF and AKF fail to provide a reasonable agreement between estimated values and their target ones. However, it is noteworthy that the amplitude of the AKF input estimates is closer to the target value than the DKF. In Figure 1.10 the displacement time histories associated with the inputs are shown. It is observed that the AKF does not provide accurate estimates when tuned so that the amplitude of the identified input is close to target values. Concerning the GDF, it is observed that once the spurious low frequency components are removed by the aforementioned band pass filter (off-line), accurate estimates of the displacement time histories are indeed obtained. When dealing with the DKF, it is observed that the accuracy of the displacement estimates is slightly lower than that of the filtered GDF, however these are delivered on an online manner. It is important to note that the DKF as well could be tuned, via calibration of the fictitious process noise, to better approximate the unknown input, at the cost of reduced accuracy for the state estimates. However in the fatigues estimation problem discussed herein, the main objective is the estimate of the displacement states in particular and not of the unknown input itself. Therefore, the DKF is the preferred solution herein, given that is also operates in an online manner.



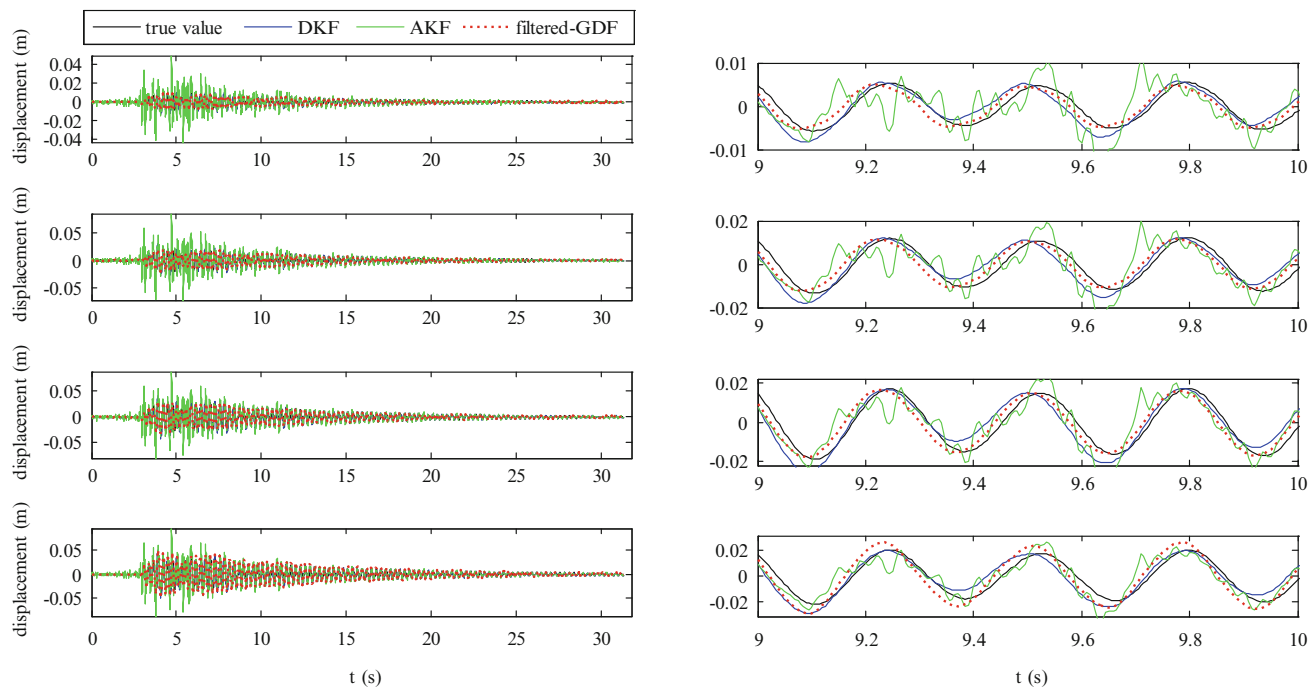
**Fig. 1.8** Displacement time histories estimated by AKF when modal model and TSSID model are used for the floors 1, 2, ..., 4 from top to bottom, respectively

**Fig. 1.9** Input time histories estimated by DKF, AKF and band pass filtered GDF when TSSID model is used for floors 1, 2, ..., 4 from top to bottom, respectively. The DKF and AKF are tuned for input estimation rather than the displacement, i.e.  $\mathbf{Q}^p = 10^{-3} \times \mathbf{I}$



## 1.5 Conclusion

In this work the AKF, GDF and a novel dual Kalman filter are applied for calculating the input and displacement time histories of a laboratory test structure tested on a uniaxial shake-table. Concerning the GDF, it is known that the accumulation of the errors arising from integration of noisy accelerations leads to low frequency components in the displacement and input force estimation which must be filtered out. Consequently, in this work the accuracy of the aforementioned estimates after low-pass filtering have been evaluated, which for online purposes is not an optimal consideration. Next, the augmented Kalman filter (AKF), which has been proposed by Lourens et al. [6] for solution of the input and state estimation is considered. The AKF requires introducing the observation process vector into the state transition matrix; it has been shown through theoretical studies that in case of pure accelerations measurements this method suffers from un-observability issues [7]. To address abovementioned issues, a dual formulation of the Kalman filter is considered herein. Numerical investigations have shown that the DKF not only solves the issues stemming from un-observability of the system matrices in the AKF, but also mitigates issues arising from the accumulation of the measurement errors including the drift in displacement and input force estimates [8]. To evaluate the performance of the proposed method a laboratory test structure has served as the examined test case. The measured accelerations of the floors of the structure are fed into the filter, and the estimated time histories of the displacement are confronted by the true time histories obtained from the displacement sensors. In



**Fig. 1.10** Displacement time histories estimated by DKF, AKF and band pass filtered GDF when TSSID model is used for the floors 1, 2, ..., 4 from top to bottom, respectively. The DKF and AKF are tuned for input estimation rather than the displacement, i.e.  $\mathbf{Q}^p = 10^{-3} \times \mathbf{I}$

the latter experimental campaign it is witnessed that when dealing with noisy acceleration measurements the GDF always features spurious low frequency components. Moreover, it is observed that limited DOF observations render the GDF prone to numerical instability and divergence. Concerning the AKF, it is shown that when fed with limited DOF acceleration measurements, the filter becomes sensitive to the tuning of the covariance of the fictitious noise process, in contrast to the proposed DKF algorithm.

**Acknowledgement** This research has been implemented under the “ARISTEIA” Action of the “Operational Programme Education and Lifelong Learning” and was co-funded by the European Social Fund (ESF) and Greek National Resources. The authors would also like to thank Associate Professor Manolis Chatzis for his help in the acquisition and processing of the experimental data.

## References

1. Papadimitriou C, Fritzen CP, Kraemer P, Ntotsios E (2011) Fatigue predictions in entire body of metallic structures from a limited number of vibration sensors using Kalman filtering. *Struct Control Health Monit* 18:554–573
2. Bernal D, Ussia A (2015) Sequential deconvolution input reconstruction. *Mech Syst Signal Process* 50–51:41–55
3. Gillijns S, De Moor B (2007) Unbiased minimum-variance input and state estimation for linear discrete-time systems with direct feedthrough. *Automatica* 43:934–937
4. Lourens E, Papadimitriou C, Gillijns S, Reynders E, De Roeck G, Lombaert G (2012) Joint input-response estimation for structural systems based on reduced-order models and vibration data from a limited number of sensors. *Mech Syst Signal Process* 29:310–327
5. Chatzi E, Fuggini C (2014) Online correction of drift in structural identification using artificial white noise observations and an unscented Kalman filter. *Special Volume of Smart Structures and Systems on Errors / uncertainties in sensors for Structural Health Monitoring*, (in press)
6. Lourens E, Reynders E, De Roeck G, Degrande G, Lombaert G (2012) An augmented Kalman filter for force identification in structural dynamics. *Mech Syst Signal Process* 27:446–460
7. Naets F, Cuadrado J, Desmet W (2015) Stable force identification in structural dynamics using Kalman filtering and dummy-measurements. *Mech Syst Signal Process* 50–51:235–248
8. Eftekhar Azam S, Papadimitriou C, Chatzi EN (2014) Recursive Bayesian filtering for displacement estimation via output-only vibration measurements. In: *Proceedings of the 2014 world congress on advances in civil, environmental, and materials research, presented at the ACEM’14, Busan*
9. Wenzel TA, Burnham K, Blundell M, Williams R (2006) Dual extended Kalman filter for vehicle state and parameter estimation. *Veh Syst Dyn* 44:153–171

10. Mariani S, Corigliano A (2005) Impact induced composite delamination: state and parameter identification via joint and dual extended Kalman filters. *Comput Methods Appl Mech Eng* 194:5242–5272
11. Eftekhari Azam S (2014) Online damage detection in structural systems. Springer, Cham, Switzerland
12. Van Overschee P, De Moor B (1994) N4SID: subspace algorithms for the identification of combined deterministic-stochastic systems. *Automatica* 30:75–93
13. Verboven P (2002) Frequency domain system identification for modal analysis. Ph.D. thesis, Department of Mechanical Engineering, Vrije Universiteit, Brussels
14. Cauberghe B (2004) Applied frequency-domain system identification in the field of experimental and operational modal analysis. Ph.D. thesis, Department of Mechanical Engineering, Vrije Universiteit, Brussels
15. Heylen W, Lammens S, Sas P (1997) Modal analysis theory and testing. Department of Mechanical Engineering, Katholieke Universiteit, Leuven
16. Chatzis MN, Chatzi EN, Smyth AW (2014) An experimental validation of time domain system identification methods with fusion of heterogeneous data. *Earthq Eng Struct Dyn*, doi: 10.1002/eqe.2528

# Chapter 2

## Comparison of Uncertainty in Passive and Active Vibration Isolation

Roland Platz and Georg C. Enss

**Abstract** In this contribution, the authors discuss a clear and comprehensive way to deepen the understanding about the comparison of parametric uncertainty for early passive and active vibration isolation design in an adequate probabilistic way. A simple mathematical one degree of freedom linear model of an automobile's suspension leg, excited by harmonic base point stroke and subject to passive and active vibration isolation purpose is used as an example study for uncertainty comparison. The model's parameters are chassis mass, suspensions leg's damping and stiffness for passive vibration isolation, and an additional gain factor for velocity feedback control when active vibration isolation is assumed. Assuming the parameters to be normally distributed, they are non-deterministic input for MONTE CARLO-Simulations to investigate the dynamic vibrational response due the deterministic excitation.

The model parameters are assumed to vary according plausible assumptions from literature and own works. Taking into account three different damping levels for each passive and active vibration isolation approach, the authors investigate the numerically simulated varying dynamical output from the model's dynamic transfer function in six case studies in frequency and time domain. The cases for the output in frequency domain are (i) varying maximum vibration amplitudes at damped resonance frequencies for different passive and active damping levels, (ii) varying vibration amplitudes at the undamped resonance frequency, (iii) varying isolation frequency, (iv) varying amplitudes at the excitation frequency beyond the passive system's fixed isolation frequency, and (v) vibration amplitudes for  $-15$  dB isolation attenuation. In time domain, case (vi) takes a closer look at the varying decaying time until steady state vibration is reached.

**Keywords** Vibration isolation • Velocity feedback control • Parametric uncertainty • Monte Carlo-simulation •  $\chi^2$ -Test

### 2.1 Introduction

The evaluation of uncertainty becomes predominant in early design phases when it comes to early decision making when defining the product's properties. If a decision has to be made between passive, active or semi-active designs today, the authors observe that the active approach often wins because of its increasing manifoldness and popularity using smart materials and systems that are used in active systems. However, increasing possibility and popularity may overlook advantages of the more conventional, and often less expensive passive alternatives with similar good performance, for example for vibration attenuation with energy absorbing material or compensators [1]. Systems become more complex, e.g. additional electric energy for actuators, sensors, and control is needed, if active vibration reduction technology is selected, [2]. The active system's functionality is versatile, however, it depends on these additional features with additionally functional uncertainty compared to the, in most cases, more simple passive approach. Favoring active over passive solutions should be built on solid ground, taking into account the evaluation and comparison of uncertainty for both approaches. It is the general desire that uncertainty decreases when going active. However, the increasing call backs for complex active systems for example in the automotive industry tell another story [3].

In [4], the authors showed analytically that active control may lead to a vibration isolation ability with less deviation in amplitude and phase responses than with passive control. This was seen throughout the frequency range of interest when sweeping through the undamped resonance frequency  $\omega_0$  until angular excitation frequencies are way beyond the angular isolation frequency  $\omega_{iso} = \sqrt{2}\omega_0$ . However, this was only a first and rough analytical approach that did not go deeper into

---

R. Platz (✉)

Fraunhofer Institute for Structural Durability and System Reliability LBF, Bartningstraße 47, 64289 Darmstadt, Germany  
e-mail: [roland.platz@lbf.fraunhofer.de](mailto:roland.platz@lbf.fraunhofer.de)

G.C. Enss

Technische Universität Darmstadt, System Reliability and Machine Acoustics SzM, Magdalenenstraße 4, 64289 Darmstadt, Germany



the comparison between passive and active vibration attenuation potential under parametric uncertainty at various significant dynamic properties such as the damped angular eigenfrequency  $\omega_D$ , at the angular isolation frequency  $\omega_{iso}$ , at an amplitude attenuation of  $-15$  dB or at the ability for fast decaying time to reach damped steady state vibrations after initial excitation. What is more, the authors did not look closely to the quality of MONTE CARLO-Simulations in terms of confidence levels when using assumed sample trails. In this current contribution, the authors use the  $\chi^2$ -Test to validate normal distribution assumptions of the model's input parameters and evaluate the computational adequacy when using 100 samples and 10,000 sample trials.

In this contribution, first the model input parameters are randomly generated with 100 samples. Second, 10,000 samples are taken into account. Using a random generator with different sampling rates to approximate normal distribution of the input model parameters, the authors evaluate the MONTE CARLO-Simulation's quality and validity based on the  $\chi^2$ -test as well as the simulation's practicability with respect to computational cost in time. Variations of characteristic properties in frequency and in time domain of vibration isolation caused by the varying model input parameters are studied for six different cases that cover significant cornerstones for passive and active vibration isolation:

- (i) varying maximum vibration amplitude  $|\underline{V}_{max}|$  for different passive and active damping levels
- (ii) varying vibration amplitudes  $|\underline{V}_0|$  at the undamped resonance frequency  $\omega_0$
- (iii) varying isolation frequency  $\omega_{iso}$
- (iv) varying amplitudes  $|\underline{V}_{100}|$  at the excitation frequency beyond the passive system's fixed isolation frequency,  $\Omega = 100 \text{ 1/s} > \omega_{iso}$
- (v) varying excitation frequency  $\omega_{15}$  for  $-15$  dB isolation attenuation
- (vi) varying decaying time  $t_{0,01}$  until steady state vibration is reached or, respectively, initial transient vibrations are damped, so only 1% is left.

This investigation is part of German Collaborative Research Center SFB 805 "Control of uncertainty in load-carrying mechanical systems", [5]. This present contribution gives an example to compare passive and active solutions in case of vibration reduction with a basic mathematical dynamic model of a vehicle's chassis with a suspension leg in an early step of product development.

## 2.2 Numerical Example for Mathematical Evaluation of Uncertainty in Passive and Active Vibration Reduction Design

### 2.2.1 Linear Mathematical Dynamic Model of a Simple Mass-Damper-Spring System for Passive and Active Vibration Isolation

As introduced in [4], a suspension leg supporting a vehicle's chassis, Fig. 2.1a, is used as a simple example for a mass-damper-spring system to generally compare passive and active vibration isolation capability with respect to uncertainty in the system's model parameters. In a linear mathematical model, Fig. 2.1b, the chassis is represented by the mass  $m$ . The mechanical properties of the suspension leg, which is assumed to be free of mass, result from the damping coefficient  $b$ , stiffness  $k$  and the velocity feedback gain  $g$ . Passive damping is used when  $g = 0$ , active damping is present when  $g \neq 0$ . The mass oscillates in  $z$ -direction with the angular excitation frequency  $\Omega$  when excited by harmonic base point stroke

$$w(t) = \hat{w} \cos(\Omega t + \delta) \quad (2.1)$$

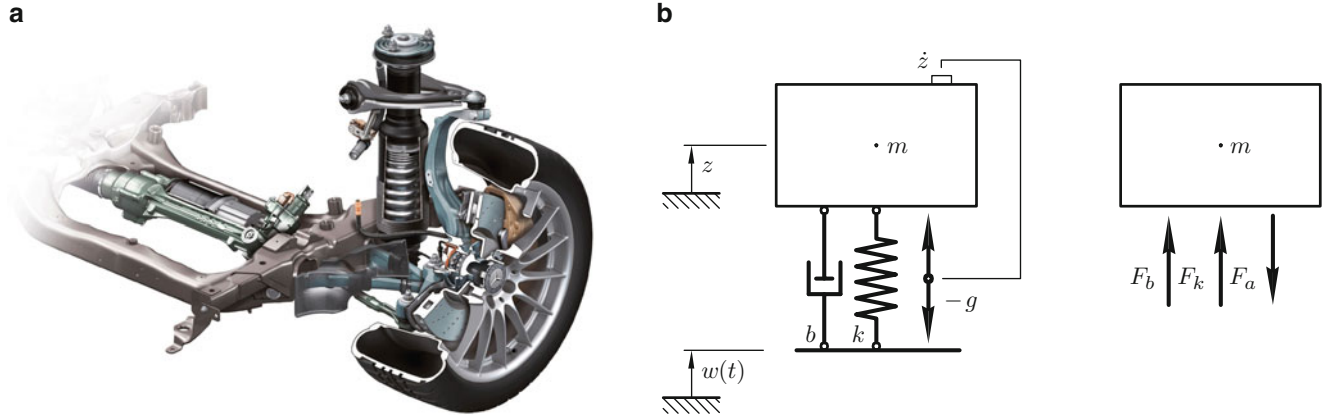
with the excitation amplitude  $\hat{w}$ , time  $t$  and phase shift  $\delta$ , with  $\delta = 0$  in the following.

When linearity is assumed, the forces in Fig. 2.1b, are

$$F_b = b(\dot{z} - \dot{w}(t)), F_a = -g\dot{z} \text{ and } F_k = k(z - w(t)) \quad (2.2)$$

due to passive and active damping as well as due to stiffness, leading to the linear equation of motion for absolute vibration in  $z$ -direction

$$m\ddot{z} + (b + g)\dot{z} + kz = b\dot{w}(t) + kw(t). \quad (2.3)$$



**Fig. 2.1** Mass-damper-spring system, (a) suspension leg (DAIMLERBENZ), (b) simple mechanical model (left) and cut free forces (right), [4]

For active damping, the feedback gain  $g$  is, different from [4], proportional to the mass vibration velocity  $\dot{z}$  only. Practically,  $\dot{z}$  can be measured by inductive sensors for the active velocity feedback control, Fig. 2.1b, left. With

$$2D\omega_0 = \frac{b}{m} \quad \text{and} \quad \omega_0^2 = \frac{k}{m}, \quad (2.4)$$

referring to the damping ratio  $D$  and the angular eigenfrequency  $\omega_0$ , Eq.(2.3) is transferred into complex form with the particulate integral approach

$$\underline{z}_p(t) = \hat{z}_p e^{i\Omega t} \quad \text{and} \quad \underline{w}(t) = \hat{w} e^{i\Omega t} \quad (2.5)$$

to become

$$\left\{ -\Omega^2 + i\Omega \left( 2D\omega_0 + \frac{g}{m} \right) + \omega_0^2 \right\} \hat{z}_p e^{i\Omega t} = \left\{ i\Omega 2D\omega_0 + \omega_0^2 \right\} \hat{w} e^{i\Omega t}. \quad (2.6)$$

Using the frequency relation  $\eta = \Omega/\omega_0$  and the factor  $\zeta = \Omega/(m\omega_0^2)$ , the complex amplification function for the mass displacement in  $z$ -direction in frequency domain is

$$\underline{V}(\eta) = \frac{\hat{z}_p}{\hat{w}} = \frac{1 + i2D\eta}{(1 - \eta^2) + i(2D\eta + g\zeta)} \quad (2.7)$$

with its amplitude

$$|\underline{V}(\eta)| = \sqrt{\frac{1 + (2D\eta)^2}{(1 - \eta^2)^2 + (2D\eta + g\zeta)^2}} \quad (2.8)$$

and its phase

$$\psi(\eta) = \arctan \frac{-2D\eta^3 - g\zeta}{1 - \eta^2 + (2D\eta)^2 + 2D\eta g\zeta}. \quad (2.9)$$

**Table 2.1** Deterministic input parameter and modal parameter

Input parameter				Modal parameter							
Property	Variable	Value	Unit	Property	Variable	Value	Unit	Property	Variable	Value	Unit
Mass	$m$	1	kg	Eigenfrequency	$\omega_0$	31.62	1/s	–			
Stiffness	$k$	1,000	N/m								
Damping Coefficient	$b_1$	0.095	Ns/m	Damped Eigenfrequency	$\omega_{D1}$	31.62	1/s	Damping Ratio	$D_1$	0.15	%
	$b_2$	9.487	Ns/m		$\omega_{D2}$	31.27	1/s		$D_2$	15	%
	$b_3$	18.974	Ns/m		$\omega_{D3}$	30.17	1/s		$D_3$	30	%
Gain	$g_1$	16	Ns/m	–							
	$g_2$	25	Ns/m								
	$g_3$	35	Ns/m								

### 2.2.2 Deterministic Amplitude and Phase Progression of the Simple Mass-Damper-Spring System for Passive and Active Vibration Isolation

Significant deterministic dynamic characteristics of passive and active vibration isolation are explained in the following before non-deterministic parameters are taken into account. So, any uncertainty will be neglected in this section. Table 2.1 specifies the assumed deterministic model parameters mass  $m$ , stiffness  $k$  as well as three different damping coefficient  $b_1 < b_2 < b_3$  and three different velocity feedback gains  $g_1 < g_2 < g_3$ .

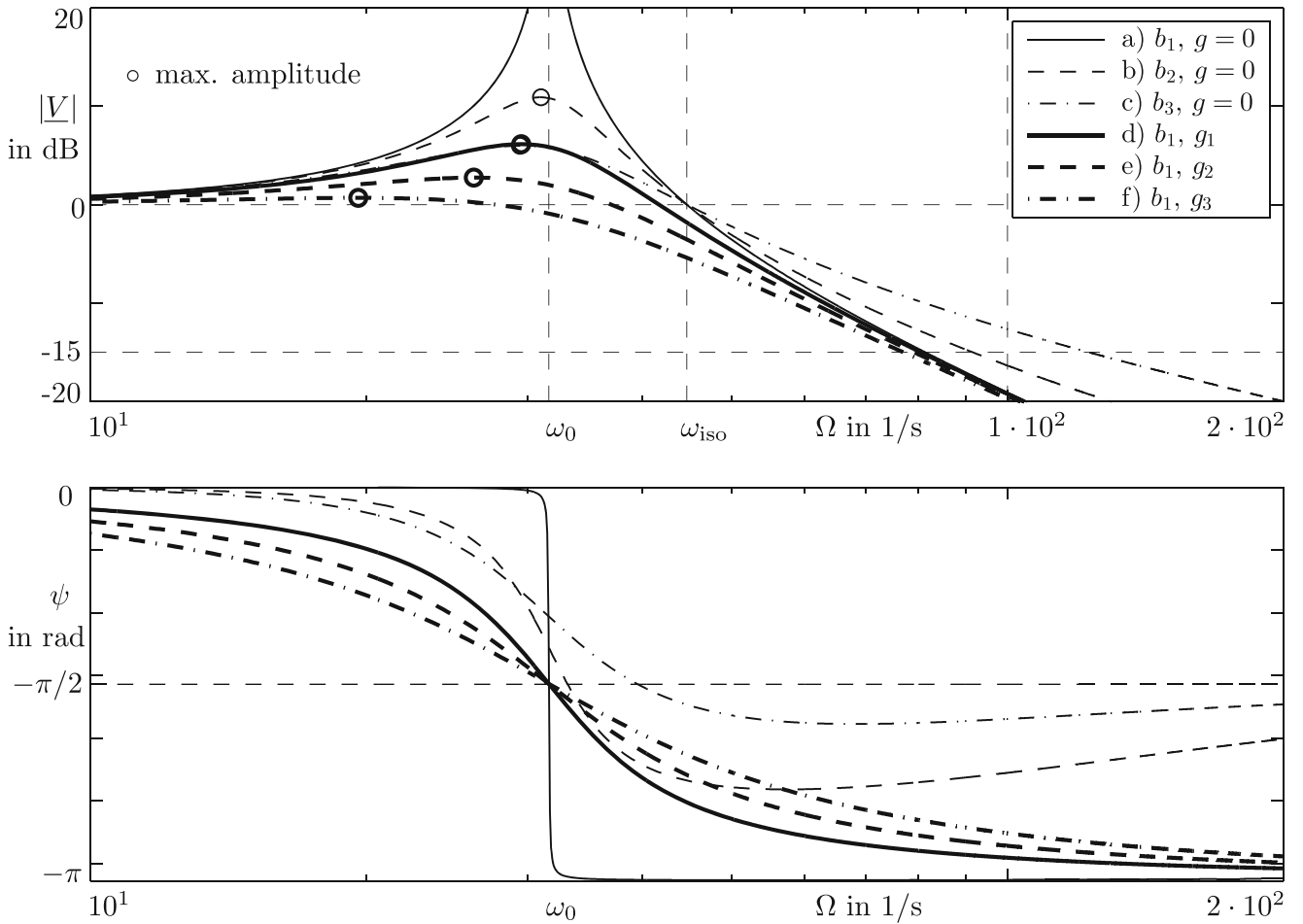
Figure 2.2 shows the typical amplitude  $|\underline{V}(\Omega)|$  and phase  $\psi(\Omega)$  progression in a BODE-Diagram according to (2.8) and (2.9) after transforming back  $\Omega = \eta \omega_0$  within the frequency range  $10^1 \leq \Omega \leq 2 \cdot 10^2$  1/s and according to the model's input parameters in Table 2.1. In case of passive vibration isolation, the three different and increasing damping coefficients  $b = b_1 < b_2 < b_3$  are taken into account. As usual, isolation  $|\underline{V}(\omega_{\text{iso}})| = 0$  begins at the isolation frequency  $\Omega = \omega_{\text{iso}} = \sqrt{2} \omega_0$  for all passive damping levels with  $g = 0$  for cases (a), (b) and (c) in Fig. 2.2. The higher the damping, the less decrease of amplitudes beyond  $\Omega > \omega_{\text{iso}}$  is expected. In case of active vibration isolation in cases (d)–(f), three different and increasing gains  $g = g_1 < g_2 < g_3$  with  $b = b_1$  for all gains are assumed. In case of active vibration isolation, the isolation effect  $|\underline{V}(\Omega)| = 0$  starts earlier at  $\Omega < \omega_{\text{iso}}$  with increasing gain.

For the two particular cases (c) and (d) in Fig. 2.2, damping and gain are selected to be  $b = b_3$  with  $g = 0$  for passive vibration isolation and  $b = b_1$  with  $g = g_1$  for active vibration isolation, Table 2.1. As a result, similar amplitudes occur until approximately the undamped angular eigenfrequency  $\Omega = \omega_0$  is reached. With further increasing  $\Omega$ , though, the amplitude due to active vibration isolation in (d) decreases faster than in (c), isolation begins earlier at  $\Omega < \omega_{\text{iso}}$ .

Typical for passive vibration isolation, normally the same phase shift  $\psi(\omega_0) = -\pi/2$  for different passive damping for cases (a)–(c) at the undamped angular eigenfrequency  $\omega_0$  does not exist, Fig. 2.2. For high angular excitation frequencies, the phases tend towards  $\psi(\Omega \gg \omega_0) = -\pi/2$  for all cases (a)–(f). For passive vibration isolation, the phase shift  $-\pi/2$  is reached much earlier for passive vibration isolation with  $b \gg b_1$  and  $g = 0$  in cases (b) and (c) than for active vibration isolation with  $b = b_1$  and  $g \neq 0$  in cases (d)–(f). Additionally and in case of an active approach in cases (d)–(f), Fig. 2.2 shows that for different damping at the undamped angular eigenfrequency  $\omega_0$ , same phase shift  $\psi(\omega_0) = -\pi/2$  does occur. Eventually, for high angular excitation frequencies, the phases also tend towards  $\psi(\Omega \gg \omega_0) = -\pi/2$ . As a result, cases (c) and (d) lead to same amplitudes until resonance, however, no similarities in phase shift are seen.

### 2.2.3 Variation and Probability Measures of Mathematical Model's Parameters

The analytical model of the complex amplification function  $\underline{V}(\eta)$  in frequency domain (2.7) is mathematically exact and is not uncertain. Therefore, model uncertainty does not exist in this example, even though the model simplifies real world condition. The deterministic assumptions for the parameters mass  $m$ , damping coefficient  $b$ , stiffness  $k$  and gain  $g$  in Table 2.1 are appropriate to clarify the adequate characteristic dynamic behavior of vibration isolation with respect to harmonic base point stroke in Fig. 2.2. In many cases, a simple linear mathematical model is used as first estimation of a chassis' dynamic behavior mounted on a suspension leg, [6]. The authors are aware of making errors due to the chassis and suspension leg model's simplicity. Although, they are acknowledged errors, referring to [7]. For example, further parameters are missing that exist in real application, like parameters to describe connections and joints between damping, stiffness and actuating devices, parameters that represent electrical contacts or fatigue processes that cause changes in geometric and



**Fig. 2.2** BODE-diagram, amplitude  $|V(\Omega)|$  and phase  $\psi(\Omega)$  with  $m, k, b$  and  $g$  as shown in Table 2.1 according cases (a)  $b = b_1, g = 0$ , (b)  $b_2, g = 0$ , (c)  $b_3, g = 0$  for the PASSIVE system (—); and according cases (d)  $b = b_1, g = g_1$ , (e)  $b_1, g_2$ , (f)  $b_1, g_3$  for the ACTIVE system (—)

material properties as well as tolerances due to manufacturing variations. These errors are acknowledged and accepted by the authors for simplification reasons. Yet, if these errors would have been taken into account in the mathematical model, it is in most cases impractical to retrieve adequate information about the error's real variation or, respectively, probabilistic or possibilistic nature of the errors. For the most part, adequate data that covers all possible variations of either additional parameters, non-linear behavior and other errors is not available in early design phases. There is hardly a representative amount of similar products that can be compared with each other and that can be studied and evaluated in a reasonable time. Even if there was a representative amount, there is uncertainty in the way to measure the parameter's actual real world values and the dynamic system's non-linear behavior in a trustworthy way.

In this contribution and for the adequate comparison of passive and active vibration isolation, the authors assume a variation of the predominant parameters mass  $m$  damping coefficient  $b$ , stiffness  $k$  and feedback gain  $g$  only. The variations are assumed in such a way that they are legitimate by experience and literature [7]. What is more, only parametric and stochastic uncertainty are considered when applying passive or active vibration isolation within small amplitudes in the linear mathematical model (2.7). The variation of parameters is assumed to be normally distributed around an assumed nominal value and within lower and upper ranges that are known by experience and literature, [8]. The lower and upper ranges in % of each model parameter in Table 2.2 quantify the interval of variation of the model's parameters shown in Table 2.1.

**Table 2.2** Varying input parameter assumptions

Input parameter				
Property	Variable	Nominal value	Unit	Variation
Mass	$m$	1	kg	$\pm 3\%$
Stiffness	$k$	1,000	N/m	$\pm 10\%$
Damping Coefficient	$b_1$	0.095	Ns/m	
	$b_2$	9.487	Ns/m	$\pm 30\%$
	$b_3$	18.974	Ns/m	
Gain	$g_1$	16	Ns/m	
	$g_2$	25	Ns/m	$\pm 15\%$
	$g_3$	35	Ns/m	

According to the authors general experimental experience in [9], and according to the experimental affirmation in similar structural dynamic works like in [8], the mass  $m$  may vary between  $\pm 3\%$ , damping  $b$  varies between  $\pm 30\%$  and the stiffness  $k$  between  $\pm 10\%$  around their nominal values, Table 2.2. Prior investigations by the authors in [9] show that according to active approaches to enhance buckling stability in axially loaded beams, the gain to control actuators based on piezoelectric material may vary between  $\pm 15\%$  around its mean or nominal value.

The lower and upper ranges are expected to represent  $\pm 3\sigma$  with 99.7% probability, which is an accepted approach to derive a standard deviation for assuming normal distribution, [8]. With this assumption,  $N$  samples of independently varying mass  $m_n$ , stiffness  $k_n$ , damping  $b_{1,n}$ ,  $b_{2,n}$  and  $b_{3,n}$  as well as gain  $g_{1,n}$ ,  $g_{2,n}$  and  $g_{3,n}$  with  $n = 1, \dots, N$  are randomly generated by a numerical random generator via MATLAB. The complex amplification function (2.7) is calculated  $N$  times via MONTE CARLO-Simulation for each case (a)–(f) in Fig. 2.2 by independently varying the model's parameters in Table 2.2 assuming normal distribution.

Figure 2.3 shows the histograms of the relative frequency  $M_{nb}(x)/n$  in the  $n_b$ th bin or class, with varying amounts of bins  $N_b$  and constant bin-width  $\Delta$  per parameter quantity sample  $x_n$ , for  $n_b = 1, \dots, N_b$  bins and for  $n = 1, \dots, N = 100$  samples. The samples are randomly generated according to assumed normal distribution. As an example, the first row of histograms presents the relative mass frequencies  $M_n(m)/n$  with up to  $N_b = 13$  bins and with equal bin-width  $\Delta = 0.005$  kg, and sampled as quantities  $m_n$  via MATLAB random generator for cases (a)–(f). For each varying damping and gain value in cases (a)–(f), each sample quantity of mass  $m_n$  is generated newly and randomly for  $N = 100$  times. In Fig. 2.3, each histogram also shows the empirical mean value  $\bar{x}$  and the standard variation  $s_x$ , calculated with

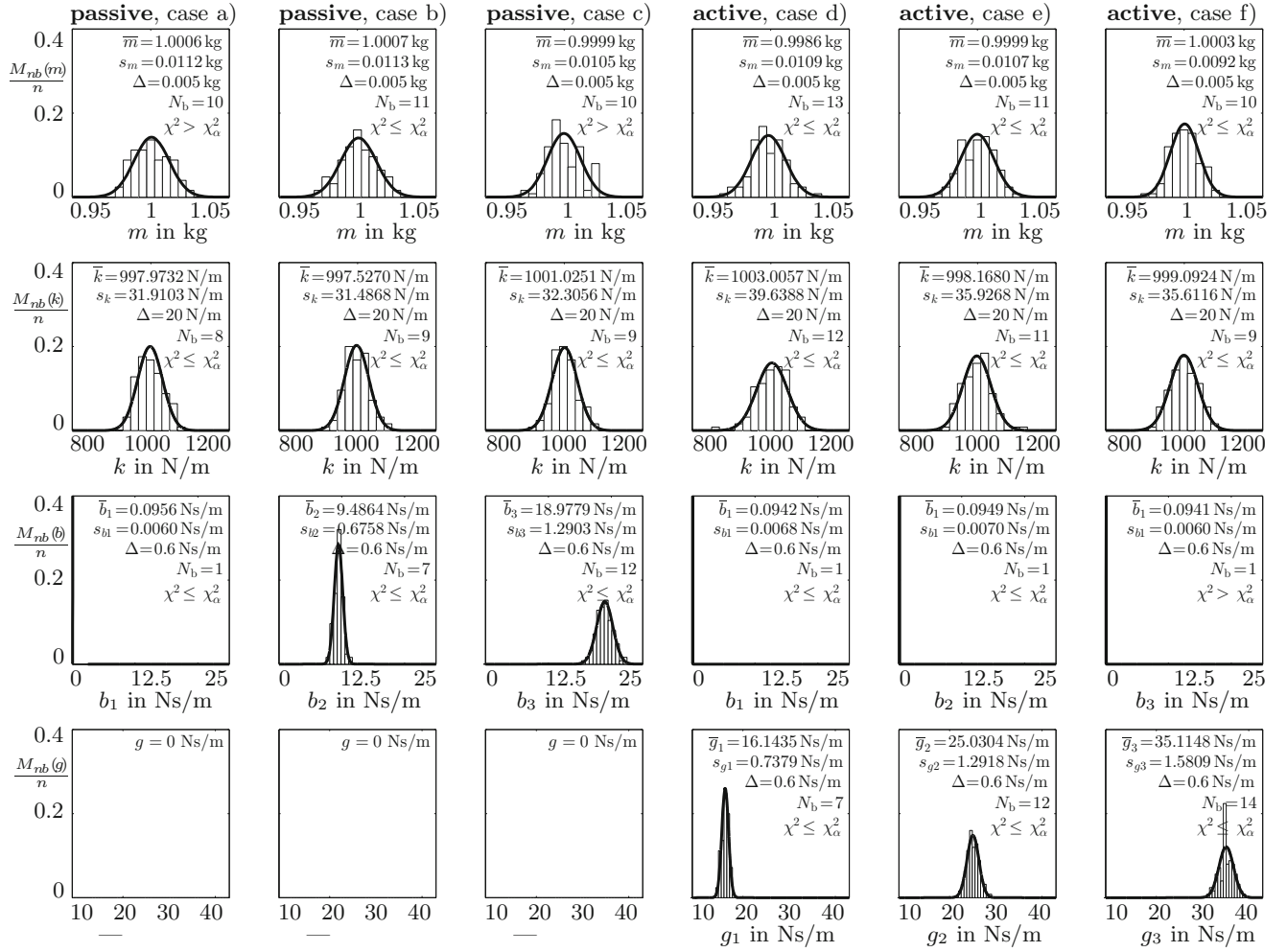
$$\bar{x} = \frac{1}{N} \sum_{n=1}^N x_n \quad \text{and the variance} \quad s_x^2 = \frac{1}{n-1} \sum_{n=1}^N (x_n - \bar{x})^2 \quad (2.10)$$

for each randomly generated quantity  $x_n$  from  $N = 100$  samples. In addition, the histograms displays the bin-width  $\Delta$  and amount of bins  $N_b$ , and the fitted continuous normal frequency distribution density function

$$p_0(x) = \frac{1}{s_x \sqrt{2\pi}} e^{-\frac{1}{2} \left( \frac{x - \bar{x}}{s_x} \right)^2} \quad (2.11)$$

due to the empirical mean value  $\bar{x}$  and the standard deviation  $s_x$  according to (2.10). Each histogram in the first row in Fig. 2.3 quantifies the empirical mean values  $\bar{m}$  and standard deviation  $s_m$  of mass  $m$  and the fitted continuous frequency distribution density function  $p_0(m)$  according to (2.11) for each case (a)–(f). In the same manner, the following rows 2–4 show histograms of the relative frequency, empirical mean values and standard deviation width and amount of bins, the fitted continuous frequency distribution density function for the input model parameter stiffness  $k$ , damping  $b_1$ ,  $b_2$  and  $b_3$  as well as  $g_1$ ,  $g_2$  and  $g_3$  for cases (a)–(f). Finally, the  $\chi^2$ -test of goodness of fit (g.o.f.) is conducted to evaluate the adequacy of assuming normal distributed  $N = 100$  model parameter samples and indicated in the histograms, [10]. The Null-hypothesis

$$H_0 \implies p(x) \equiv p_0(x) \quad (2.12)$$



**Fig. 2.3** Histograms of the relative frequency  $M_{nb}(x)/n$  for constant bin-width  $\Delta$  and varying amounts  $n_b = 1, \dots, N_b$  of bins per input model parameter  $x = m, k, b_{1-3}$ , and  $g_{1-3}$  according to Table 2.2 for cases (a)–(f) in Fig. 2.2, assuming normal distribution, with the empirical mean values  $\bar{x}$ , standard deviation  $s_x$ , curve progression of the hypothetical continuous frequency distribution density function  $p_0(x)$  (—) and  $\chi^2$ -test results for  $N = 100$  samples

is accepted when equivalence occurs between an actual measured distribution function  $P(x)$  via sample trials and a hypothetical assumed distribution function  $P_0(x)$  or, respectively, their distribution density functions  $p(x) = dP(x)/dx$  and  $p_0(x) = dP_0(x)/dx$ . Practically, the g.o.f. is conducted to verify the equivalency via

$$\chi^2 = \sum_{n_b=1}^{N_b} \frac{(M_{nb} - n p_{nb})^2}{n p_{nb}} = \sum_{n_b=1}^{N_b} \frac{M_{nb}^2}{n p_{nb}} - n, \quad (2.13)$$

with the absolute amount  $M_{nb}$  of samples in the  $n_b$ th bin and the corresponding probability  $p_{nb}$ , satisfying

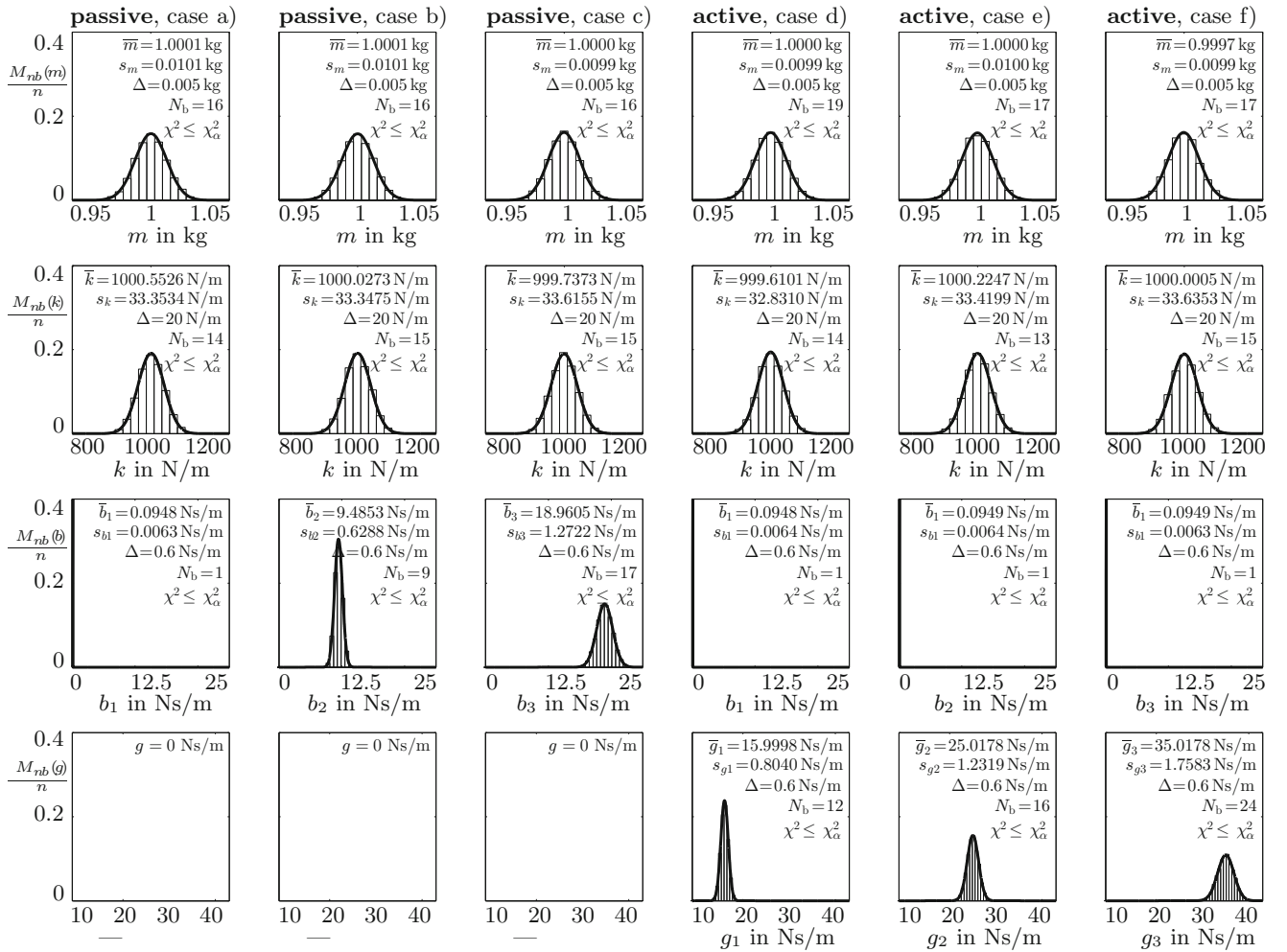
$$\sum_{n_b=1}^{N_b} p_{nb} = 1 \quad \text{and} \quad \sum_{n_b=1}^{N_b} M_{nb} = N. \quad (2.14)$$

As a result,

$$\begin{aligned} \chi^2 \leq \chi_\alpha^2 &\implies \text{accept } H_0 \\ \chi^2 > \chi_\alpha^2 &\implies \text{refuse } H_0, \end{aligned}$$

with the critical value  $\chi^2_\alpha$  due to the level of significance  $\alpha = 0,05$ , when satisfying the condition  $n p_{nb} > 1$  at bounding bins and  $n p_{nb} \geq 1$  for the other bins, [10]. The very low damping values  $b_1$  in cases (a) and (d)–(f) in Fig. 2.3 for passive and active vibration isolation lead to small standard deviations  $s_b$  with practically only one bin, yet fulfilling the requirements in (2.14).

In Fig. 2.4, the amount of samples is increased from  $N = 100$  to  $N = 10,000$ , the results for  $M_{nb}(x)/n$ ,  $p_0(x)$ ,  $\bar{x}$ ,  $s_x$ ,  $\Delta$ ,  $N_b$ , and  $\chi^2$  for cases (a)–(f) are shown again. Comparing Fig. 2.3 with Fig. 2.4, it is seen that using only  $N = 100$  samples, the g.o.f. becomes adequate in most cases, compared to the increased amount  $N = 10,000$  of samples. Even for the less absolute damping and gain values  $b$  and  $g$  in the third and fourth row, the g.o.f. for  $N = 100$  samples is adequate in most cases. In this example, the Null-hypothesis is refused only for the first and third histogram in the first row, cases (a) and (c), and in the sixth histogram in the third row, case (f). Using  $N = 10,000$  samples, Null-hypothesis is accepted throughout all rows which can be verified also by simply looking at the smooth histograms that comply with the continuous hypothetical distribution density functions  $p_0(x)$ .



**Fig. 2.4** Histograms of the relative frequency  $M_{nb}(x)/n$  for constant bin-width  $\Delta$  and varying amounts  $n_b = 1, \dots, N_b$  of bins per input model parameter  $x = m, k, b_{1-3}$ , and  $g_{1-3}$  according to Table 2.2 for cases (a) to (f) in Fig. 2.2, assuming normal distribution, with the empirical mean values  $\bar{x}$ , standard deviation  $s_x$ , curve progression of the hypothetical continuous frequency distribution density function  $p_0(x)$  (—) and  $\chi^2$ -test results for  $N = 10,000$  samples

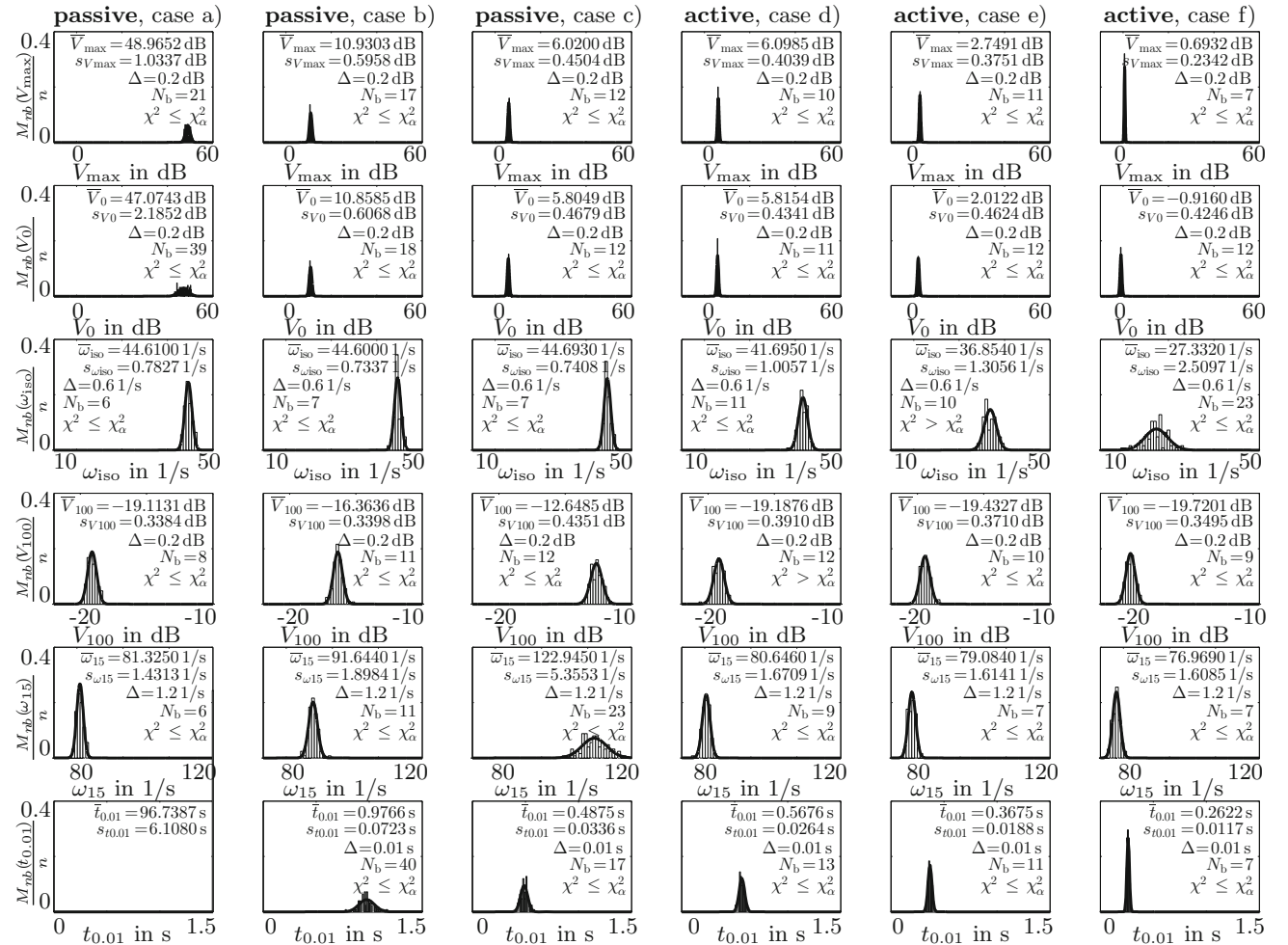
## 2.2.4 Comparison of Uncertainty in Passive and Active Vibration Isolation for Various Characteristic Isolation Properties by MONTE CARLO-Simulation

The varying model parameters in Figs. 2.3 and 2.4 are the input model parameters to calculate the varying amplification of the mass displacement's amplitude  $|V(\eta)|$  in (2.8) via MONTE CARLO-Simulation, with respect to the cases (i)–(vi) from Sect. 2.1 and according to the cases (a)–(f) in Fig. 2.2. The decaying time

$$t_{0.01} = \frac{-2 \ln \left( \frac{z_d(t)}{\hat{z}} \right)}{2 D \omega_0 + g/m} \quad (2.15)$$

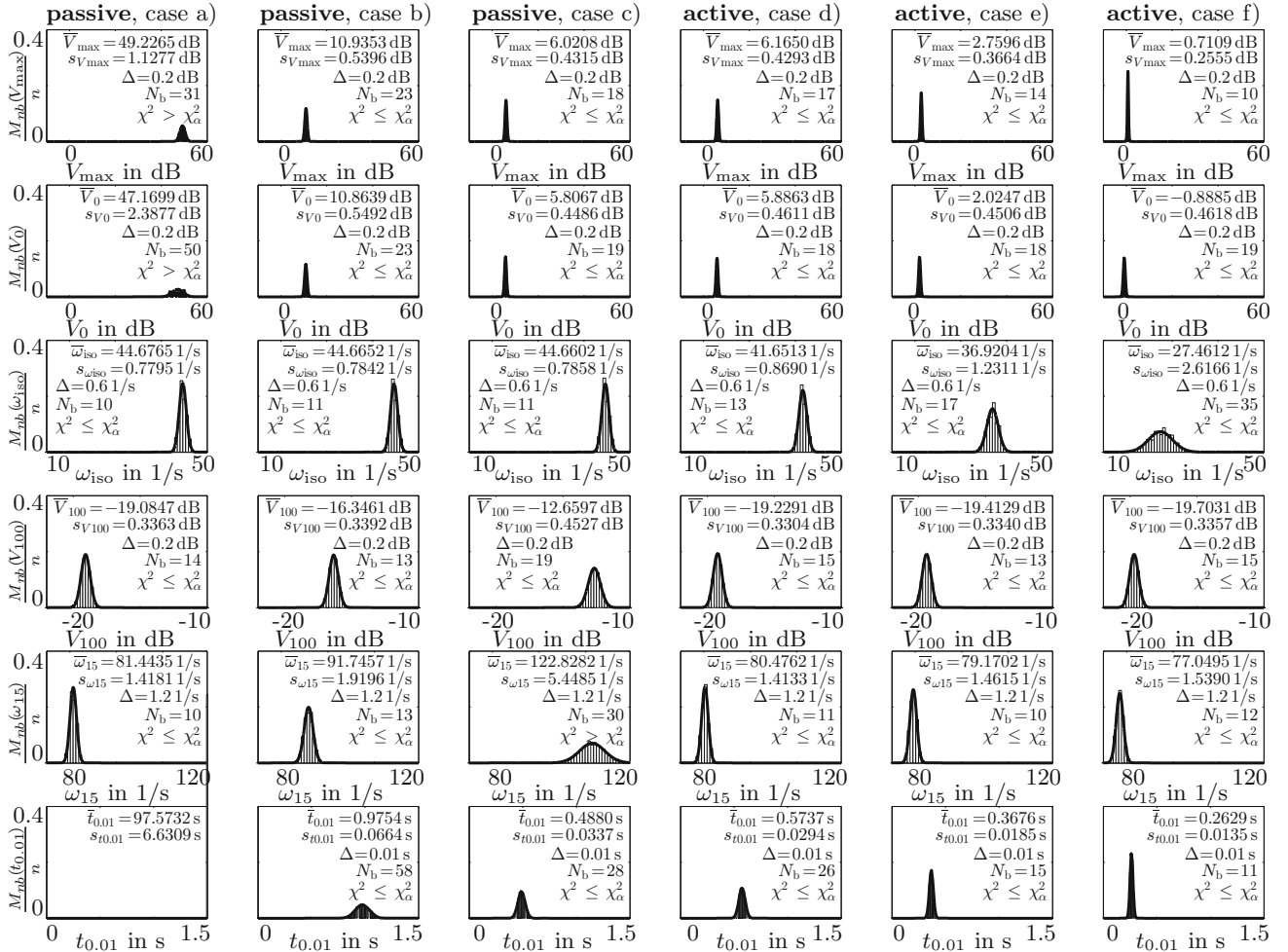
for case (vi) is derived from the homogeneous solution of (2.3) in time domain, with the decaying curve  $z_d(t)$  and the initial amplitude  $\hat{z}$ . The authors assume steady state vibration when the decaying amplitude is down to 1% of its initial amplitude,  $z_d(t)/\hat{z} = 0.01$ .

Figures 2.5 and 2.6 show the histograms of the relative frequency  $M_{nb}(x)/n$  for varying amounts of bins  $N_b$  and constant bin-width  $\Delta$  per varying dynamic output property  $x = V_{\max}, V_0, \omega_{\text{iso}}, V_{100}, \omega_{15}$ , and  $t_{0.01}$  along with the empirical mean values  $\bar{x}$ , the standard deviation  $s_x$ , the curve progression of the hypothetical continuous frequency distribution density



**Fig. 2.5** Histograms of the relative frequency  $M_{nb}(x)/n$  for constant bin-width  $\Delta$  and varying amounts  $n_b = 1, \dots, N_b$  of bins per dynamic output property  $x = V_{\max}, V_0, \omega_{\text{iso}}, V_{100}, \omega_{15}$ , and  $t_{0.01}$  after calculating (2.8) with varying model input parameters from Fig. 2.3 via MONTE CARLO-Simulation, with the empirical mean values  $\bar{x}$ , standard deviation  $s_x$ , curve progression of the hypothetical continuous frequency distribution density function  $p_0(x)$  (—) and  $\chi^2$ -test results for  $N = 100$  samples





**Fig. 2.6** Histograms of the relative frequency  $M_{nb}(x)/n$  for constant bin-width  $\Delta$  and varying amounts  $n_b = 1, \dots, N_b$  of bins per dynamic output property  $x = V_{\max}, V_0, \omega_{\text{iso}}, V_{100}, \omega_{15}$ , and  $t_{0.01}$  after calculating (2.8) with varying model input parameters from Fig. 2.3 via MONTE CARLO-Simulation, with the empirical mean values  $\bar{x}$ , standard deviation  $s_x$ , curve progression of the hypothetical continuous frequency distribution density function  $p_0(x)$  (—) and  $\chi^2$ -test results for  $N = 10,000$  samples

function  $p_0(x)$  and the result of the  $\chi^2$ -test due to  $N = 100$  and  $N = 10,000$  samples. The output properties are calculated via (2.8) with varying model input parameters from Figs. 2.3 and 2.4 running a MONTE CARLO-Simulation. Each row in Figs. 2.5 and 2.6 shows the varying output properties according cases (i)–(vi), and cases (a)–(f).

It is seen that for

- (i) the relative frequency  $M_{nb}(V_{\max})/n$  of the maximum amplitude  $V_{\max}$  is relatively narrow around the empirical mean value  $\bar{V}_{\max}$  with relatively small standard deviation  $s_{V_{\max}}$  for passive and active vibration control, except for low passive damping  $b_1$ , case (a). In this example, g.o.f. is not satisfied in case (a) for the increased sample size with  $N = 10,000$ . However, the same high scatter tendency as for  $N = 100$  samples is obvious.
- (ii) the relative frequency  $M_{nb}(V_0)/n$  of the amplitude  $V_0$  at angular resonance frequency  $\omega_0$  shows the same tendency as for  $V_{\max}$  in scatter and g.o.f.
- (iii) the relative frequency  $M_{nb}(\omega_{\text{iso}})/n$  of the angular isolation frequency  $\omega_{\text{iso}}$  becomes relatively less narrow around the empirical mean  $\bar{\omega}_{\text{iso}}$  with relatively high standard deviation  $s_{\omega_{\text{iso}}}$  due to higher gain  $g$  for active vibration isolation approach, cases (e) and (f). This tendency is seen in both low and high sampling rates with  $N = 100$  and  $N = 10,000$  samples.
- (iv) the relative frequency  $M_{nb}(V_{100})/n$  of the amplitude  $V_{100}$  at the angular excitation frequency beyond the passive system's fixed angular isolation frequency  $\Omega = 100 \text{ 1/s} > \omega_{\text{iso}}$  becomes relatively less narrow around the empirical mean  $\bar{V}_{100}$  and with relatively small standard deviation  $s_{V_{100}}$  due to high damping  $b_3$  for the passive approach, case (c). With high active damping  $g_1$  to  $g_3$  in cases (d)–(f), the relative frequency becomes narrow around the empirical mean

again. As far as the passive and active approach with the same amplitudes in Fig. 2.2 until the maximum at  $\Omega \approx \omega_0$  is concerned, cases (c) and (d), also less scatter is observed for the active approach for  $\Omega = 100 \text{ 1/s} > \omega_{\text{iso}}$ . The same trend is seen with low and high sampling rates.

- (v) the relative frequency  $M_{nb}(\omega_{15})/n$  of the angular frequency  $\omega_{15}$  at  $-15$  dB vibration attenuation becomes relatively less narrow around the empirical mean  $\bar{\omega}_{15}$  with relatively small standard deviation  $s_{\omega_{15}}$  at higher passive damping  $b_3$ , case (c). For gains  $g_1$  to  $g_3$  in cases (d)–(f), scatter is always less in both low and high sampling rates. The same trend is seen with low and high sampling rates.
- (vi) the relative frequency  $M_{nb}(t_{0.01})/n$  of the varying decaying time  $t_{0.01}$  until steady state vibration is reached becomes relatively more narrow around the empirical mean  $\bar{t}_{0.01}$  with relatively small standard deviation  $s_{t_{0.01}}$  at high passive damping  $b_3$  in case (c) and even more narrow with smaller standard deviation at higher gains  $g_2$  and  $g_3$  by the active approach, cases (d)–(f). The same trend is seen with low and high sampling rates.

The computing time for all results in Figs. 2.5 and 2.6 is 4.7 s for  $N = 100$  and 485.2 s for  $N = 10,000$ . With respect to the discussion above and for the comprehensive example in this contribution, less computing time for less sample rates is sufficient for adequate evaluation of uncertainty in passive and active vibration isolation numerically for this study.

## 2.3 Conclusion

The observations described in this contribution show that, generally, the tendency of varying standard deviations for passive and active vibration isolation approaches with respect to characteristic amplitudes and angular frequencies due to the damping properties is not affected by using low and high sampling rates, leading to low and high cost in computation time, in numerical simulation. What is more, high active damping results in high scatter at the angular isolation frequency, but results in less scatter at angular frequencies beyond the isolation point compared to the passive approach. Also, the scatter of the amplitude attenuation beyond the angular isolation frequency is less with the active approach. So for the comparison of uncertainty in passive and active vibration isolation, the active approach is not necessarily accompanied with less uncertainty throughout a wide angular frequency range even beyond the isolation starts. Especially right at the angular frequency where vibration isolation starts, the active approach appears to be more uncertain with increasing active damping. Preparations are under way to validate the numerical comparison of uncertainty in passive and active vibration isolation with an experimental example.

**Acknowledgements** The authors like to thank the German Research Foundation DFG for funding this research within the SFB 805.

## References

1. VDI 2062 (2007) Vibration insulation – insulation elements, part 2, Verein Deutscher Ingenieure. Beuth Verlag, Berlin
2. VDI 2064 (2010) Aktive Schwingungsisolierung – active vibration isolation Verein Deutscher Ingenieure. Beuth Verlag, Berlin
3. Otterbach B (2012) Rückrufe auf Rekordniveau (engl.: Recalls on record level). Online edition Automobil Industrie. <http://www.automobil-industrie.vogel.de/mixed/articles/352299/>, last cited 25 Oct 2013
4. Platz R, Ondoua S, Enss GC, Melz T (2014) Approach to evaluate uncertainty in passive and active vibration reduction. In: Atamturktur HS et al (eds) Model validation and uncertainty quantification, volume 3: proceedings of the 32nd IMAC, a conference and exposition on structural dynamics, 2014, conference proceedings of the society for experimental mechanics series. Springer International Publishing, Cham, Switzerland, pp 345–352
5. Hanselka H, Platz R (2010) Ansätze und Maßnahmen zur Beherrschung von Unsicherheit in lasttragenden Systemen des Maschinenbaus (engl. Controlling uncertainties in load carrying systems). Konstruktion 11/12:55–62
6. Vöth S (2006) Dynamik schwingungsfähiger Systeme (engl. Dynamics of vibrations systems). Vieweg & Sohn Verlag, Wiesbaden
7. Oberkampf WL, DeLand SM, Rutherford BM, Diegert KV, Alvin KF (2002) Error and uncertainty in modeling and simulation. Reliab Eng Syst Saf 75:333–357
8. Schuëller GI (2007) On the treatment of uncertainties in structural mechanics and analysis. Comput Struct 85:235–243
9. Platz R, Enss GC, Ondoua S, Melz T (2014) Active stabilization of a slender beam-column under static axial loading and estimated uncertainty in actuator properties. In: Second International Conference on Vulnerability and Risk Analysis and Management (ICVRAM) and the sixth International Symposium on Uncertainty Modeling and Analysis (ISUMA), July 13–16 2014, Liverpool, pp 235–245
10. Bronstein IN, Semendjajew KA (1991) Taschenbuch der Mathematik (engl. Handbook of mathematics), 25 edn. Verlag Harri Deutsch, Frankfurt am Main

# Chapter 3

## Observation DOF's Optimization for Structural Forces Identification

Silvia Milana, Annalisa Fregolent, and Antonio Culla

**Abstract** Frequently, in industrial application, the knowledge of the force distribution acting on complex structures is required. Generally, the direct measurement of these force fields is impossible to perform, mainly due to the difficulties associated with the transducers placement. Therefore, the development of force identification techniques is a very important topic in applied mechanics. Unfortunately, this inverse problem is typically ill-conditioned. In recent decades, some force identification procedures has been developed, but it is difficult to enforce these techniques in operating condition. In this paper, a procedure to design the operative setup is proposed in order to determine the best configuration of sensors position. To this aim, two indices are used and, through a Finite Element Model of the structure, they are calculated. The procedure allows to reach the best configuration of the measurement points in order to minimize the ill-conditioning of the problem. To validate the procedure, the results of an experimental test on a complex structure are compared with the numerical results.

**Keywords** Force identification • Sensor placement • Ill-conditioned problem • Regularization technique • Finite element model

### 3.1 Introduction

Identification of external forces acting on structural systems is fundamental in many structural dynamic problems. Since the identification problems are ill-conditioned, regularization techniques are necessary to obtain meaningful results. In recent decades, several techniques have been developed to solve this problem. Among these, two approaches are of particular interest: Force Analysis Technique [1, 2] that use a finite difference scheme and wavenumber approach [3]. These techniques, although effective, need the knowledge of the analytical model of the studied system. On the contrary, the techniques based on modal expansion or on the use of frequency response function [4] can be used with more complex systems through numerical techniques as finite elements method. The accuracy of the identification technique is strongly affected by the position of the measurement points. In this paper a frequency domain technique is considered and an operative procedure to design an optimal measurement setup for a complex structure is described. A wide set of points on the considered structure is selected, the method allows to recognize a subset of them where the sensors can be positioned to reach the best results in force identification. Two indices are defined allowing to minimize the error of the identification procedure. The first one take into account the norm of the relative difference between the amplitude of the identified forces and of the real force, the second one gives the relative difference between the identified force in the correct position and the mean of the identified forces on the whole set of points. This technique is tested on a complex structure. A numerical simulation is performed using a FE Model of the studied system in order to identify numerically the force acting on the structure. The identified forces allow to calculate the indices and to select the best configuration of points. This result is validated by comparing the indices obtained by a set of measurements performed on a experimental setup at the location identified by the numerical procedure and those calculated by the numerical results.

---

S. Milana (✉) • A. Fregolent • A. Culla  
Dipartimento di Ingegneria Meccanica e Aerospaziale, Università di Roma La Sapienza, Via Eudossiana 18, 00184 Rome, Italy  
e-mail: [silvia.milana@uniroma1.it](mailto:silvia.milana@uniroma1.it)

## 3.2 Theoretical Background

The forces identification problem in frequency domain is defined as follows:

$$\mathbf{f}(\omega) = \mathbf{H}^+(\omega)\mathbf{a}(\omega) \quad (3.1)$$

where  $\mathbf{f}(\omega)$  is a  $(n \times 1)$  vector of unknown forces,  $\mathbf{a}(\omega)$  is a  $(m \times 1)$  of measured responses and  $\mathbf{H}(\omega)$  is the  $(m \times n)$  Frequency Response Function (FRF) matrix. An accurate choice of the response measurement points is one of the key factors to obtain the actual applied forces. Since in operational condition it is impossible to test a large number of measurement point sets (setup), it is convenient to evaluate the best setup through a numerical procedure. The first step of the analysis is the choice of a set of  $N_t$  points where the measurements can be performed. This set of points are depending on the considered frequency range [5]. The  $N_p$  points that belong to the optimal setup are chosen by comparing  $N_c$  configurations of  $N_p$  points selected among the  $N_t$  points. In order to establish the best configuration, two indices are used. They require the identified forces in each configuration calculated through a numerical model.

### 3.2.1 Numerical Model

The procedure needs the knowledge of the numerical frequency response function of the structure  $H_n$  for the whole set of  $N_t$  points. These FRFs are computed through the following relationship:

$$H_{n \ i,j}(\omega) = \sum_{h=1}^n \frac{\phi_h(x_i)\phi_h(x_j)}{M_h(\omega_h^2 - \omega^2 + j\eta_h\omega_h^2)} \quad (3.2)$$

where the eigenvalues  $\omega_h$  and the eigenvectors  $\phi_h$  are obtained by a FE model. The acceleration of the selected points is given by:

$$\mathbf{a}(\omega) = \mathbf{H}(\omega)\mathbf{f}(\omega) \quad (3.3)$$

The numerical force reconstruction is performed using the computed acceleration polluted adding a random error proportional to the mean value of the signal for each frequency and for each point.

### 3.2.2 Reconstruction of the Force Field

The reconstruction of force field for each configuration needs the inversion of the matrix  $\mathbf{H}$ . Due to the ill-conditioning of the problem, errors in the data can highly perturb the solution. Therefore to reconstruct the force field the employ of regularization techniques is required. In this work, two regularisation techniques both based on Singular Values Decomposition (SVD) of the matrix  $\mathbf{H}$  are considered: Truncated Singular Values Decomposition (TSVD) [6] and Tikhonov regularisation [7]. Using SVD, the force can be expressed as:

$$\mathbf{f}(\omega) = \sum_{i=1}^n \frac{\mathbf{u}_i^* \mathbf{a}(\omega) \mathbf{v}_i}{\sigma_i} \quad (3.4)$$

where  $\mathbf{u}_i$  are the left eigenvectors,  $\mathbf{v}_i$  are the right eigenvectors and  $\sigma_i$  are the singular values. Regularisation introduces a filter  $\xi$  in the sum of previous equation:

$$\mathbf{f}(\omega) = \sum_{i=1}^n \xi_i \frac{\mathbf{u}_i^* \mathbf{a}(\omega) \mathbf{v}_i}{\sigma_i} \quad (3.5)$$

The form of the filter  $\xi$  depends on the regularisation technique. In TSVD it assume the following discrete values

$$\xi_i = \begin{cases} 1 & \text{if } n < k \\ 0 & \text{if } n > k \end{cases} \quad (3.6)$$

where  $k$  is the index correspondent to the number of singular values considered in the sum of Eq. (3.5) The regularised solution becomes:

$$\mathbf{f}(\omega) = \sum_{i=1}^k \frac{\mathbf{u}_i^* \mathbf{a}(\omega)_i \mathbf{v}_i}{\sigma_i} \quad (3.7)$$

In Tikhonov regularisation the values of  $\xi$  is obtained through the minimisation of the following function:

$$R_\lambda = \|\mathbf{H}\mathbf{f} - \mathbf{x}\|_2^2 + \lambda^2 \|\mathbf{I}\mathbf{f}\|_2^2 \quad (3.8)$$

where the first term is the residual and the second term is the value of the solution. In this case using SVD the filter  $\xi$  has the following expression:

$$\xi_i = \frac{\sigma_i^2}{\sigma_i^2 + \lambda_i^2} \quad (3.9)$$

and the regularised solution becomes:

$$\mathbf{f}(\omega) = \sum_{i=1}^n \frac{\sigma_i^2}{\sigma_i^2 + \lambda_i^2} \frac{\mathbf{u}_i^* \mathbf{a}_i(\omega) \mathbf{v}_i}{\sigma_i} \quad (3.10)$$

Note that, the solution  $\mathbf{f}(\omega)$  depends on the value assumed by the parameter  $\lambda$ . The optimal value of the regularization parameter  $\lambda$  is obtained through Generalised Cross Validation (GCV) [8].

### 3.2.3 Successful Indices

In order to analyze the large number of results obtained from numerical identification, two indices are used. The first index  $I_{NORM}$  takes into account the norm of the relative difference between the magnitude of the reconstructed force and the value of the actual force

$$I_{NORM} = \left[ 1 - \frac{\| |\mathbf{f}_{actual}| - |\mathbf{f}_{identified}| \|}{\| \mathbf{f}_{actual} \|} \right] \cdot 100 \quad (3.11)$$

The second index  $I_{AVG}$  is the relative difference between the identified force in the correct position and the mean of the identified forces on the whole set of points.

$$I_{AVG} = \frac{|f_{identified}| - \sum_{i=1, \neq dp}^n \frac{|f_{identified}_i|}{n-1}}{f_{actual}} \cdot 100 \quad (3.12)$$

The proposed procedure is performed on  $N_c$  configurations of  $N_p$  points chosen among the  $N_t$  points set. Therefore the two indices have dimensions ( $N_c \times N_p \times N_f$ ), where  $N_f$  are the number of considered frequencies.

The use of these indices allows to analyze the results obtained from numerical simulation performed considering each point  $N_p$  of each configuration  $N_c$  as a drive point. Therefore, it is possible to obtain the values of these indices for each frequency, each drive point, and each configuration considered.

### 3.3 Test Structure

The proposed technique is tested on an aluminium structure (Fig. 3.1). The structure consists of a cantilever column with two staggered short arms and a horizontal beam. The horizontal beam is bolted at the top of the column, involving both translational and rotational DoFs. The geometrical dimensions are reported in Table 3.1. The cross section is  $40 \times 8$  mm for all beams, with the short side along the  $z$ -direction.

The experimental frequency response function  $\mathbf{H}_e$  is obtained up to 600 Hz by exciting the structure and measuring the accelerations along  $z$ -direction at seven locations.

#### 3.3.1 Result

The Finite Element Model of the structure (Fig. 3.1) is built using beam element and  $\mathbf{H}_n$  is calculated by the procedure described in Sect. 3.2.1.

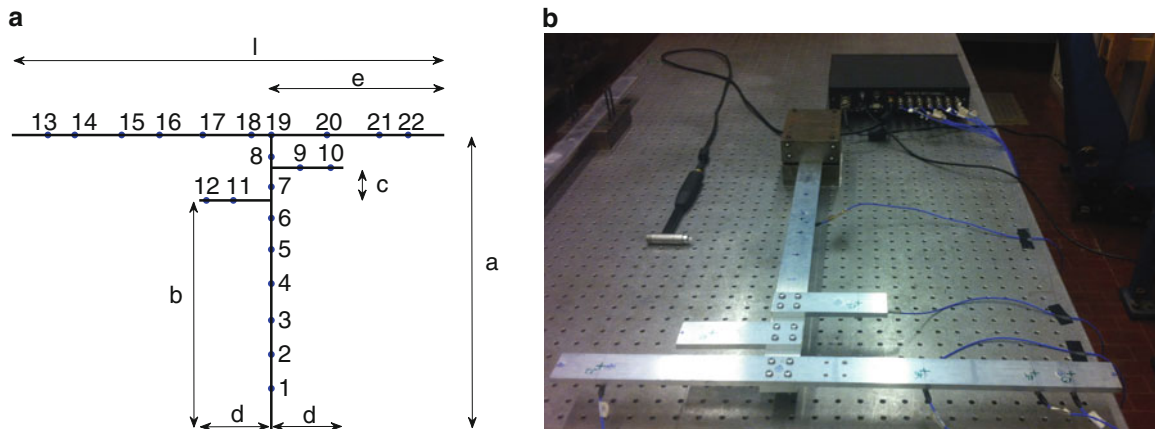
The procedure described in Sect. 3.2 is performed for all considered points of the structure ( $N_t$ ). The points position is shown in Fig. 3.1. The force identification is performed on  $N_c$  configurations of  $N_p$  points changing the drive point position on each point of each configuration. The results are analyzed at the seven frequencies shown in Table 3.2.

The considered configurations are shown in Table 3.3.

A matrix of dimension ( $N_c \times N_p \times N_f$ ) is obtained for each index. The choice of optimal setup corresponds to the maximization of the two indices. This choice can be obtained by averaging the index matrices over all the  $N_p$  points or over all the  $N_f$  frequencies. The average is performed over the parameter chosen according to the operational condition. For instance, if the force location is roughly known, it could be more interesting to average over the frequencies. On the contrary, if the force location is completely unknown, but the force is band limited, it could be more interesting to average over the  $N_p$  points. Here, for seek of generality, the analysis is performed by averaging both over  $N_p$  and over  $N_f$ .

In Fig. 3.2 the comparison between the indices averaged over all drive points for some of the considered configuration are shown.

The indices corresponding to configuration number 1 assume the greatest value. In Table 3.4 are shown the indices averaged all  $N_p$  points or over all the  $N_f$  frequencies. These results show again that the first configuration is the best one. Consequently, the points of the first configuration (shown in Fig. 3.3 together with their coordinates) are selected to perform the experimental measurements.



**Fig. 3.1** Model of considered structure. (a) Finite element model. (b) Experimental setup

**Table 3.1** Geometrical dimensions [mm]

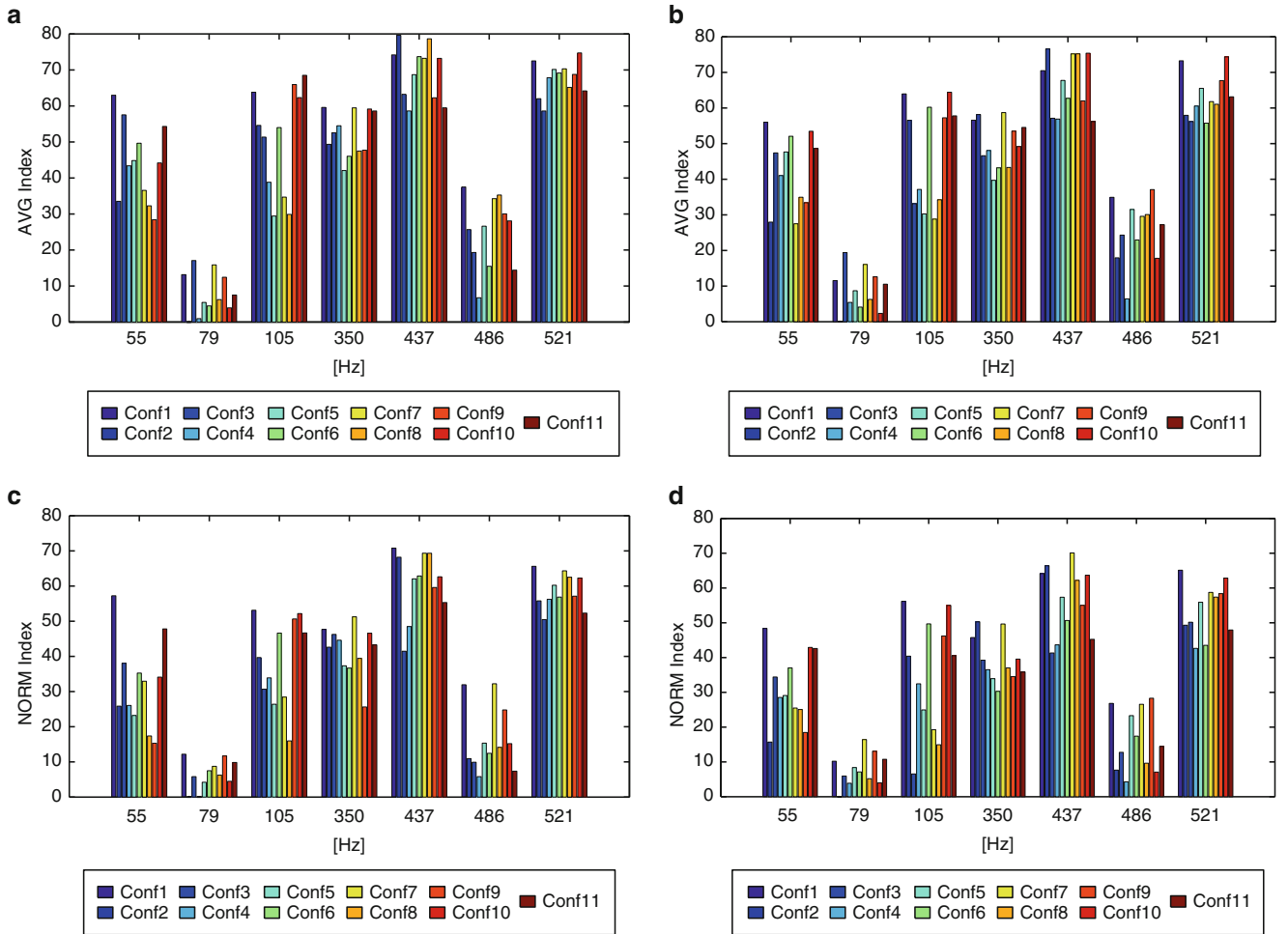
$a$	$b$	$c$	$d$	$e$	$l$
540	420	60	100	240	600

**Table 3.2** Selected frequencies

Frequency number	1	2	3	4	5	6	7
Value [Hz]	55	79	105	350	437	486	521

**Table 3.3** Displayed configuration

Configuration	Points						
Conf 1	3	10	12	13	14	16	22
Conf 2	5	9	11	14	17	18	20
Conf 3	1	5	10	13	17	19	21
Conf 4	1	5	7	9	17	19	21
Conf 5	1	7	8	11	17	19	20
Conf 6	3	4	6	8	12	14	20
Conf 7	4	5	7	9	11	13	16
Conf 8	3	4	6	8	17	20	22
Conf 9	3	6	8	12	13	16	21
Conf 10	2	7	10	11	14	20	21
Conf 11	5	10	11	12	14	17	20

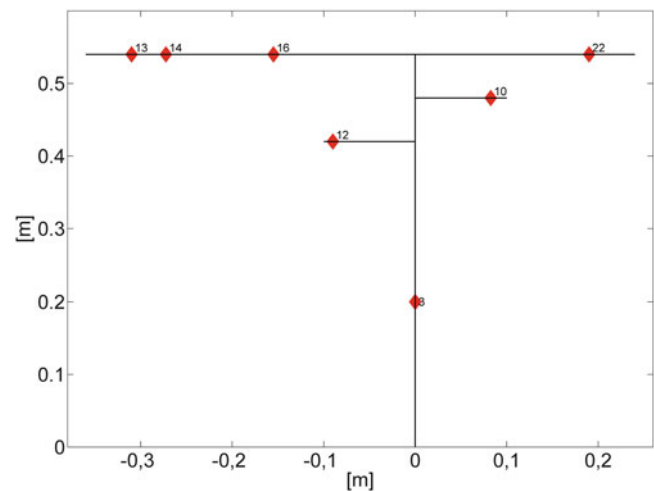
**Fig. 3.2** Comparison between index obtained from numerical simulation with different configurations. (a)  $I_{AVG}$  Tikhonov regularisation. (b)  $I_{AVG}$  TSVD regularisation. (c)  $I_{NORM}$  Tikhonov regularisation. (d)  $I_{NORM}$  TSVD regularisation (Color figure online)

The same procedure, performed for the numerical results, is followed using the experimental data in order to obtain  $I_{NORM}$  and  $I_{AVG}$ . Note that  $H_e$  is obtained through experimental data. In Fig. 3.4  $H_n$  and  $H_e$  for the drive point 14 are compared. It is possible to notice a good agreement between these frequency response functions, by considering that the numerical model is not updated on the experimental results. However, the values of some resonances do not perfectly agree. In particular, in correspondence of the 4th considered frequency (350 Hz), there is a difference of the 3.5 %, as highlighted in Fig. 3.4. Note that this frequency corresponds to a resonance only in the experimental case. Figure 3.5 shows the comparison between the average over all points  $N_p$  of numerical and experimental indices in correspondence of the selected frequencies

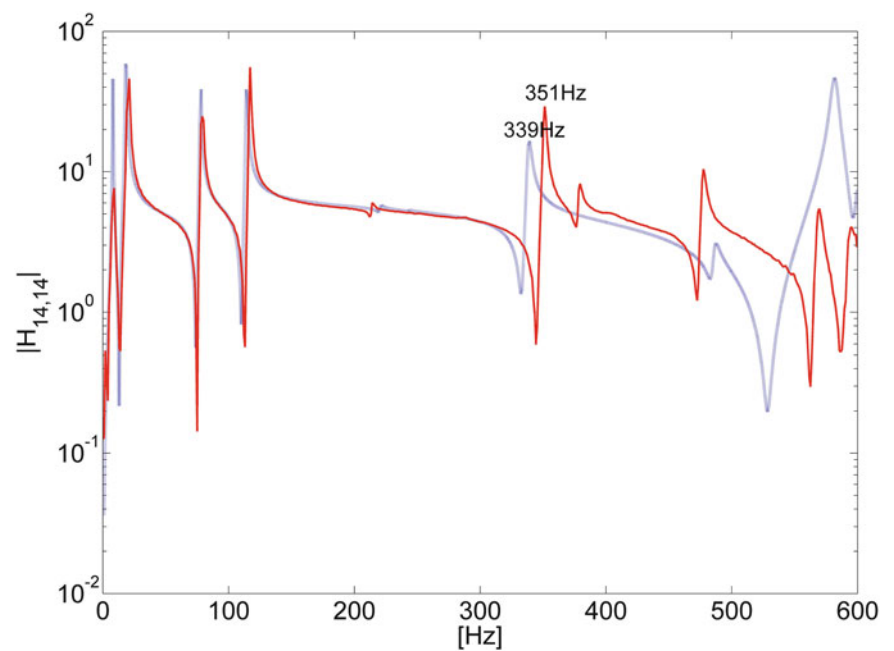
**Table 3.4** Average over all drive points of indices

Conf	$I_{NORM}$ TSVD	$I_{AVG}$ TSVD	$I_{NORM}$ TIKH	$I_{AVG}$ TIKH
1	45	52	42	46
2	33	42	34	36
3	27	41	34	34
4	27	37	33	32
5	33	42	38	38
6	34	43	36	37
7	38	43	39	40
8	30	41	37	36
9	36	46	39	40
10	39	48	44	44
11	34	45	40	40

**Fig. 3.3** Configuration of experimental setup

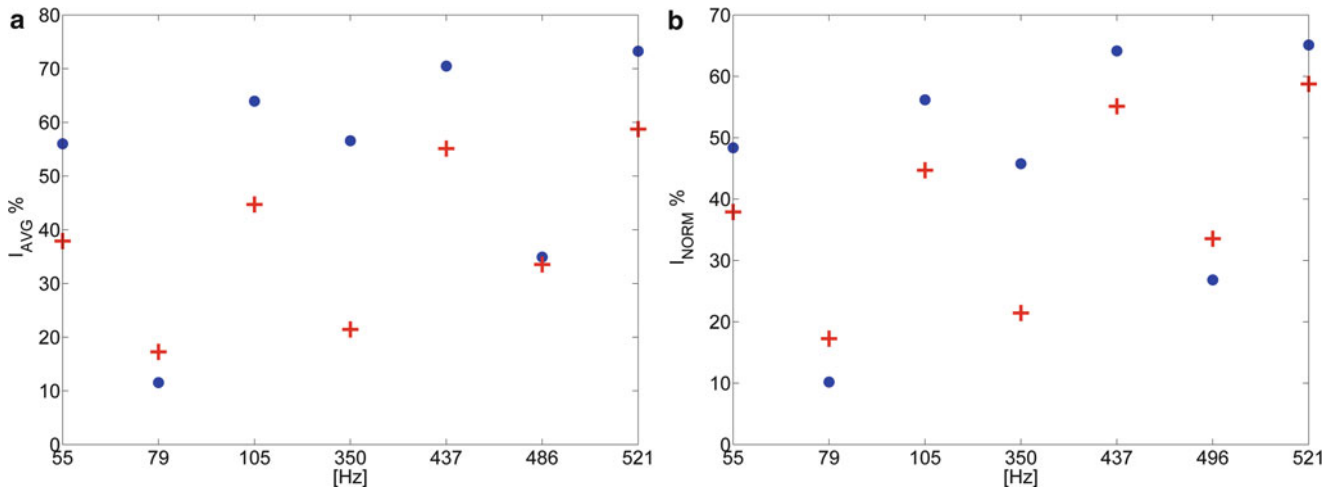


**Fig. 3.4** Comparison between frequency response functions  $H_{14,14}$ : numerical (---), experimental (---)



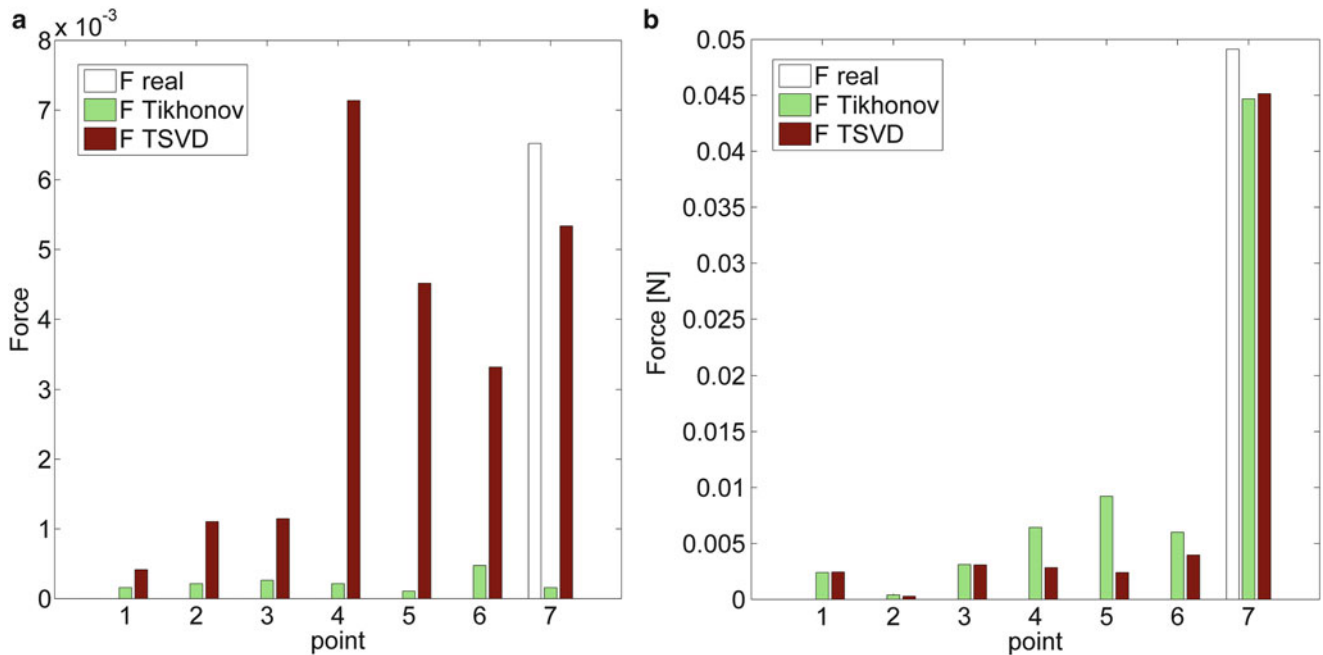
(see table in Fig. 3.3). As expected, the experimental results have a smaller value than the numerical results. However, the trend is similar almost everywhere except for the 4th frequency where the gap between the simulated and experimental resonance is reflected on the indices values.





**Fig. 3.5** Comparison between numerical simulation and experimental data in best configuration (numerical o), (experimental +). (a)  $I_{AVG}$  TSVD regularisation. (b)  $I_{NORM}$  TSVD regularisation

Figure 3.6 shows the comparison between the forces identified with numerical and experimental procedures in correspondence of 4<sup>th</sup> frequency (350 Hz). In the experimental case the force is bad identified because 350 Hz corresponds to a resonance of the experimental FRFs. The analysis of the full set of figures allows to establish that the obtained values of the indices ensure the possibility of identify the forces field, although the values could seem small.



**Fig. 3.6** Force at 4<sup>th</sup> frequency 350 Hz. (a) Experimental. (b) Numerical

### 3.4 Conclusions

In this paper a procedure to design the best operative setup to perform forces identification is presented. A FEM of a complex structure is developed and a numerical force identification is performed. Two indices are employed that allow to select the

best configuration of points. In order to validate the numerical procedure, experimental measurements of acceleration are performed on the selected set of points. The results show that the selected configuration is the best in the set of considered points.

**Acknowledgements** This research is supported by University of Rome La Sapienza. The authors thank Paolo Donello for his contribution to this research during his master thesis.

## References

1. Pézerat C, Guyader J-L (2000) Force analysis technique: reconstruction of force distribution on plates. *Acta Acustica United Acustica* 86(2):322–332
2. Leclère Q, Pézerat C (2012) Vibration source identification using corrected finite difference schemes. *J Sound Vib, Acta Acustica United Acustica* 331(6):1366–1377
3. Fregolent A, Sestieri A (1996) Force identification from vibration measurements in the wavenumber domain. *Proc ISMA* 21:517–526
4. Ibrahim SR, Fregolent A, Sestieri A (1996) Structural force identification at unmeasured locations. In: *Proceedings-spie the international society for optical engineering*. Spie international society for optical, pp 927–933
5. Fabumni JA (1968) Effects of structural modes on vibratory force determination by the pseudoinverse technique. *AIAA J* 24(3):504–509
6. Hansen PC (1994) Regularization tools: a Matlab package for analysis and solution of discrete ill-posed problems. *Numer Algorithms* 6(1):1–35
7. Tikhonov AN, Arsenin VY (1977) *Solution of ill-posed problems*. Winston/Wiley, Washington
8. Golub GH, Heath M, Wahba G (1979) Generalized cross-validation as a method for choosing a good ridge parameter. *Technometrics* 21: 215–223

# Chapter 4

## Nonlinear Structural Finite Element Model Updating Using Batch Bayesian Estimation

Hamed Ebrahimián, Rodrigo Astroza, and Joel P. Conte

**Abstract** This paper proposes framework for nonlinear finite element (FE) model updating, in which state-of-the-art nonlinear structural FE modeling and analysis techniques are combined with the maximum likelihood estimation (MLE) method to estimate time-invariant parameters governing the nonlinear hysteretic material constitutive models used in the FE model of the structure. Using the MLE as a parameter estimation tool results in a nonlinear optimization problem, which can be efficiently solved using gradient-based optimization algorithms such as the interior-point method. Gradient-based optimization algorithms require the FE response sensitivities with respect to the material parameters to be identified, which are computed accurately and efficiently using the direct differentiation method (DDM). The estimation uncertainties are evaluated based on the Cramer-Rao lower bound (CRLB) theorem by computing the exact Fisher Information matrix using the FE response sensitivities. A proof-of-concept example, consisting of a cantilever steel column representing a bridge pier, is provided to validate the proposed nonlinear FE model updating framework. The simulated responses of this bridge pier to an earthquake ground motion is polluted with artificial output measurement noise and used to estimate the unknown parameters of the material constitutive model. The example illustrates the excellent performance of the proposed parameter estimation framework even in the presence of high measurement noise.

**Keywords** Nonlinear finite element model • Model updating • Bayesian estimation • Nonlinear system identification • Damage identification

### 4.1 Introduction

Structural modal identification (MID) methods use the measured response of the structure under low-amplitude forced or ambient vibrations to extract the modal properties of an equivalent linear elastic dynamic system [1]. When a structure suffers damage or when its material and/or geometric properties change, the identified modal properties of the structure deviate from its initial undamaged modal properties. The variations in the identified modal parameters or features extracted from them can be used to detect the occurrence of damage in the structure. Finite element (FE) model updating [2] is another approach that has been used for system and damage identification (DID) of structures. Various methods have been proposed and employed for FE model updating and estimating the modeling parameters in the literature such as methods based on least-square estimation (e.g., [3–5]) and methods based on stochastic filters (e.g., [6–10] to name only a few). However, the studies reported in the literature typically use simplistic structural models, which are unable to predict the response of a large and complex structure in a real world application.

The structural engineering community has benefited from well-established, experimentally validated, mechanics-based FE modeling and analysis techniques that play an increasingly important role in analysis and design of structures. Relying on realistic and physical nonlinear material constitutive models, nonlinear structural FE modeling and analysis techniques can be combined with nonlinear parameter estimation approaches to yield nonlinear FE model updating methods. Authors have been recently pursued this objective by incorporating nonlinear Kalman filter as a recursive parameter estimation tool to update nonlinear FE structural models [11, 12]. This paper presents a batch estimation method based on the maximum

---

H. Ebrahimián (✉) • J.P. Conte  
University of California, San Diego, 9500 Gilman Drive, La Jolla, CA 92093, USA  
e-mail: [hebrahim@ucsd.edu](mailto:hebrahim@ucsd.edu)

R. Astroza  
University of California, San Diego, 9500 Gilman Drive, La Jolla, CA 92093, USA  
Universidad de Los Andes, Monseñor Álvaro del Portillo, Santiago 12455, Chile  
e-mail: [rastroza@ucsd.edu](mailto:rastroza@ucsd.edu)

likelihood estimation (MLE) approach to estimate the unknown modeling parameters of a nonlinear structural FE model using the measured dynamic input and output response of the structure during an earthquake event. Estimation of both the expected values and the covariance matrix of the modeling parameters is the objective of the parameter estimation framework presented here. In a real world application, the updated nonlinear FE model can be interrogated to reconstruct the nonlinear response process experienced by the structure during the damaging event, thus providing detailed information about the location, type, and extent of damage in the structure.

## 4.2 Nonlinear Finite Element Model Updating and Parameter Estimation

The time-discretized equation of motion of a nonlinear FE model at  $k$ th time step is expressed as

$$\mathbf{M}(\boldsymbol{\theta}) \ddot{\mathbf{q}}_k(\boldsymbol{\theta}) + \mathbf{C}(\boldsymbol{\theta}) \dot{\mathbf{q}}_k(\boldsymbol{\theta}) + \mathbf{r}_k(\mathbf{q}_k(\boldsymbol{\theta}), \boldsymbol{\theta}) = \mathbf{f}_k \quad (4.1)$$

where  $\mathbf{M}$  = mass matrix,  $\mathbf{C}$  = damping matrix,  $\mathbf{r}_k(\mathbf{q}_k(\boldsymbol{\theta}), \boldsymbol{\theta})$  = history-dependent (or path-dependent) internal resisting force vector,  $\mathbf{q}_k$ ,  $\dot{\mathbf{q}}_k$ ,  $\ddot{\mathbf{q}}_k$  = nodal displacement, velocity, and acceleration vectors,  $\boldsymbol{\theta}$  is the modeling parameter vector,  $\mathbf{f}_k$  = dynamic load vector, and the subscripts indicate the time step. In the case of earthquake base excitation,  $\mathbf{f}_k = -\mathbf{M}\mathbf{L}\ddot{\mathbf{u}}_{gk}$ , where  $\mathbf{L}$  is the base acceleration influence matrix and  $\ddot{\mathbf{u}}_{gk}$  denotes the input ground acceleration vector. In the most general case, the response of a nonlinear FE structural model at  $k$ th time step can be expressed as a (nonlinear) function of the nodal displacement, velocity, and acceleration vectors at that time step, i.e.,

$$\widehat{\mathbf{y}}_k = \mathbf{g}(\mathbf{q}_k, \dot{\mathbf{q}}_k, \ddot{\mathbf{q}}_k) \quad (4.2)$$

where  $\widehat{\mathbf{y}}_k$  = predicted response vector at  $k$ th time step, and  $\mathbf{g}(\dots)$  is the (nonlinear) output function. By combining Eqs. (4.1) and (4.2), the response of a nonlinear FE structural model to an earthquake ground motion at each time step is expressed as a nonlinear function of the modeling parameters, the input ground acceleration time history from the beginning until that time step, and initial conditions of the FE model, i.e.,

$$\widehat{\mathbf{y}}_k = \mathbf{h}_k(\boldsymbol{\theta}, \ddot{\mathbf{u}}_{g1 \rightarrow k}, \mathbf{q}_0, \dot{\mathbf{q}}_0) \quad (4.3)$$

In Eq. (4.3),  $\ddot{\mathbf{u}}_{g1 \rightarrow k} = [\ddot{\mathbf{u}}_{g1}^T, \ddot{\mathbf{u}}_{g2}^T, \dots, \ddot{\mathbf{u}}_{gk}^T]^T$  where  $\ddot{\mathbf{u}}_{gk}$  = vector of measured input ground acceleration at  $k$ th time step,  $\mathbf{q}_0$  = initial nodal displacement vector,  $\dot{\mathbf{q}}_0$  = initial nodal velocity vector, and  $\mathbf{h}_k(\dots)$  is the nonlinear response function of the FE model at  $k$ th time step. The measured response vector of the structure,  $\mathbf{y}_k$ , is related to the model predicted response vector,  $\widehat{\mathbf{y}}_k$ , through the prediction error framework [13].

$$\mathbf{y}_k = \widehat{\mathbf{y}}_k + \mathbf{v}_k \quad (4.4)$$

in which  $\mathbf{v}_k$ , the prediction error vector, accounts for output measurement noise and modeling error. The prediction error is modeled as a stationary zero-mean Gaussian white noise process [14], i.e.,  $\mathbf{v}_k \sim N(\mathbf{0}, \mathbf{R})$ , where the covariance matrix  $\mathbf{R}$  is assumed to be time invariant and diagonal, i.e.,  $\mathbf{R} = [r_j]$ ,  $j = 1 \rightarrow n_y$ .

To estimate the unknown modeling parameters, they are modeled as random variables according to Bayesian approach for parameters estimation. The Bayes' rule is employed to infer the *a posteriori* probability density function (PDF) of the modeling parameters from the time histories of noisy input and output measurements and the *a priori* PDF of the modeling parameters. Assuming that the components of input ground acceleration are known and deterministic, the *a posteriori* PDF of the modeling parameters can be written as:

$$p(\boldsymbol{\theta} | \mathbf{y}_{1 \rightarrow k}) = \frac{1}{c} p(\mathbf{y}_{1 \rightarrow k} | \boldsymbol{\theta}) p(\boldsymbol{\theta}) \quad (4.5)$$

in which  $\mathbf{y}_{1 \rightarrow k} = [\mathbf{y}_1^T, \mathbf{y}_2^T, \dots, \mathbf{y}_k^T]^T$  and  $c = \int p(\mathbf{y}_{1 \rightarrow k} | \boldsymbol{\theta}) p(\boldsymbol{\theta}) d\boldsymbol{\theta}$  is a constant called evidence.  $p(\mathbf{y}_{1 \rightarrow k} | \boldsymbol{\theta}) = l(\boldsymbol{\theta}, \mathbf{y}_{1 \rightarrow k})$  is the likelihood function. Considering minimum prior knowledge about the modeling parameters, the *a priori* PDF is modeled using uniform distribution. This means that when there is a little prior knowledge on  $\boldsymbol{\theta}$  or the prior knowledge

associates with high uncertainty, the *a posteriori* PDF will be maximized, in the limiting case, at value of  $\boldsymbol{\theta}$  that minimizes the negative log-likelihood function, which is called the maximum likelihood (ML) estimate of  $\boldsymbol{\theta}$  [15]:

$$\hat{\boldsymbol{\theta}}_{ML} = \arg \min_{\boldsymbol{\theta}} - [\Lambda(\boldsymbol{\theta}, \mathbf{y}_{1 \rightarrow k})] \quad (4.6)$$

where  $\Lambda(\boldsymbol{\theta}, \mathbf{y}_{1 \rightarrow k}) = \ln(l(\boldsymbol{\theta}, \mathbf{y}_{1 \rightarrow k}))$  is the log-likelihood function. According to Eq. (4.4), it is clear that  $l(\boldsymbol{\theta}, \mathbf{y}_{1 \rightarrow k}) = p(\mathbf{y}_{1 \rightarrow k} | \boldsymbol{\theta}) = p(\mathbf{v}_{1 \rightarrow k})$  and since  $\mathbf{v}$  is assumed to be a Gaussian white noise process, it is independent and identically distributed (i.i.d) in time; therefore [16],

$$\hat{\boldsymbol{\theta}}_{ML} = \arg \min_{\boldsymbol{\theta}} \left( \frac{k}{2} \ln(|\mathbf{R}|) + \frac{1}{2} \sum_{i=1}^k (\mathbf{y}_i - \mathbf{h}_i(\boldsymbol{\theta}, \ddot{\mathbf{u}}_{g1 \rightarrow i}, \mathbf{q}_0, \dot{\mathbf{q}}_0))^T \mathbf{R}^{-1} (\mathbf{y}_i - \mathbf{h}_i(\boldsymbol{\theta}, \ddot{\mathbf{u}}_{g1 \rightarrow i}, \mathbf{q}_0, \dot{\mathbf{q}}_0)) \right) \quad (4.7)$$

in which  $|\mathbf{R}|$  is the determinant of  $\mathbf{R}$  matrix. Assuming equal variances for the prediction error at different measurement channels results in identical diagonal entries for  $\mathbf{R}$  (i.e.,  $\mathbf{R} = r \mathbf{I}_{n_y \times n_y}$ ), where  $r$  is the prediction error. Therefore, the MLE problem reduces to a least squares problem, as proposed and used by many researchers in the field of structural model updating (e.g., [17–19]).

$$\hat{\boldsymbol{\theta}} = \arg \min_{\boldsymbol{\theta}} \left( \sum_{i=1}^k \|\mathbf{y}_i - \mathbf{h}_i(\boldsymbol{\theta}, \ddot{\mathbf{u}}_{g1 \rightarrow i}, \mathbf{q}_0, \dot{\mathbf{q}}_0)\|^2 \right) \quad (4.8)$$

Nevertheless, assuming equal variances for the prediction error at different measurement channels is a restrictive and often invalid assumption. For example, the equal variance assumption is incorrect in the case of heterogeneous sensor array, where the measured signals from different sensor types have different unit scale and amplitude. This invalid assumption makes the least squares estimation procedure to give a relatively higher weight to the measurement data with higher amplitude. To allow the use of heterogeneous sensor array in nonlinear FE model updating procedure and enhance the robustness of the parameter estimation process, an extended estimation procedure is suggested in this paper, in which not only the modeling parameters but also the variances of the prediction error, which are the diagonal entries of the covariance matrix  $\mathbf{R}$  and are shown by the vector  $\mathbf{r} = [r_j]$  ( $j = 1 \rightarrow n_y$ ), are estimated. Following Eq. (4.7), the extended estimation problem can be formulated as a general optimization problem:

$$(\hat{\boldsymbol{\theta}}, \hat{\mathbf{r}})_{ML} = \arg \min_{(\boldsymbol{\theta}, \mathbf{r})} J(\mathbf{r}, \boldsymbol{\theta}, \mathbf{y}_{1 \rightarrow k}, \ddot{\mathbf{u}}_{g1 \rightarrow k}) \quad (4.9)$$

$$J(\mathbf{r}, \boldsymbol{\theta}, \mathbf{y}_{1 \rightarrow k}, \ddot{\mathbf{u}}_{g1 \rightarrow k}) = \left( \frac{k}{2} \sum_{j=1}^{n_y} \ln(r_j) + \frac{1}{2} \sum_{i=1}^k (\mathbf{y}_i - \mathbf{h}_i(\boldsymbol{\theta}, \ddot{\mathbf{u}}_{g1 \rightarrow i}))^T \mathbf{R}^{-1} (\mathbf{y}_i - \mathbf{h}_i(\boldsymbol{\theta}, \ddot{\mathbf{u}}_{g1 \rightarrow i})) \right) \quad (4.10)$$

in which  $J(\dots)$  is the objective function of the optimization problem and the dependence of  $J$  on  $\mathbf{q}_0$  and  $\dot{\mathbf{q}}_0$  is dropped for notational convenience. By defining a feasible range for the modeling parameters and the variance components (i.e.,  $\boldsymbol{\theta}_{\min} \leq \boldsymbol{\theta} \leq \boldsymbol{\theta}_{\max}$  and  $r_{j,\min} \leq r_j \leq r_{j,\max}$ ) the parameter estimation problem is transformed into a constrained nonlinear optimization problem, which is solved using an interior-point method [20, 21] in this paper. The utilized numerical algorithm is implemented and available as a part of MATLAB optimization toolbox [22]. The algorithm requires the computation of the gradients of the objective function with respect to the modeling parameter vector,  $\boldsymbol{\theta}$ , and the variance vector,  $\mathbf{r}$ , which can be respectively computed as:

$$\frac{\partial J}{\partial \boldsymbol{\theta}} = - \sum_{i=1}^k \left( \frac{\partial \mathbf{h}_i(\boldsymbol{\theta}, \ddot{\mathbf{u}}_{g1 \rightarrow i})}{\partial \boldsymbol{\theta}^T} \right)^T \mathbf{R}^{-1} (\mathbf{y}_i - \mathbf{h}_i(\boldsymbol{\theta}, \ddot{\mathbf{u}}_{g1 \rightarrow i})) \quad (4.11)$$

$$\frac{\partial J}{\partial r_j} = \frac{k}{2r_j} - \frac{1}{2} \sum_{i=1}^k \frac{(y_{ij} - h_{ij}(\boldsymbol{\theta}, \ddot{\mathbf{u}}_{g1 \rightarrow i}))^2}{r_j^2} \quad (4.12)$$

in which  $y_{ij}$  is the  $j$ th component of the response vector at  $i$ th time step. The term  $\frac{\partial \mathbf{h}_i(\boldsymbol{\theta}, \ddot{\mathbf{u}}_{g1 \rightarrow i})}{\partial \boldsymbol{\theta}^T}$  in Eq. (4.11) is the sensitivity (or rate of variation) of the FE response at  $i$ th time step with respect to the modeling parameters,  $\boldsymbol{\theta}$ , and is referred to as the FE response sensitivity matrix. FE response sensitivity analysis is a well-developed subject with a variety of applications including structural optimization, probabilistic analysis, and reliability analysis of structural and geotechnical systems (e.g., [23–26]). The FE response sensitivities can be computed approximately using the finite difference method (FDM), which requires at least  $n_{\boldsymbol{\theta}} + 1$  evaluations of the nonlinear FE model, where  $n_{\boldsymbol{\theta}}$  is the number of parameters with respect to which the sensitivities are computed. Alternatively, the FE response sensitivities can be exactly evaluated using the computationally more efficient direct differentiation method (DDM) [27]. The DDM is based on the exact (consistent) differentiation of the FE numerical scheme with respect to the FE model parameters of interest. The use of DDM in the current nonlinear FE model updating framework significantly improves the computational efficiency of the parameter estimation procedure especially for large scale FE models. The fundamentals of DDM-based FE response sensitivity computation are briefly described in the next section.

### 4.3 DDM Method for Finite Element Response Sensitivity Analysis

The time discretized equation of motion shown in Eq. (4.1) is solved using recursive numerical integration in time. Using an implicit single-step time integration scheme, such as the Newmark-beta method [28], the acceleration and velocity at time step  $(k + 1)$  are interpolated as

$$\ddot{\mathbf{q}}_k = a_1 \mathbf{q}_k + a_2 \mathbf{q}_{k-1} + a_3 \dot{\mathbf{q}}_{k-1} + a_4 \ddot{\mathbf{q}}_{k-1} \quad (4.13)$$

$$\dot{\mathbf{q}}_k = b_1 \mathbf{q}_k + b_2 \mathbf{q}_{k-1} + b_3 \dot{\mathbf{q}}_{k-1} + b_4 \ddot{\mathbf{q}}_{k-1} \quad (4.14)$$

where  $a_1$  to  $a_4$  and  $b_1$  to  $b_4$  are constant integration coefficients. Substitution of these equations into Eq. (4.1) yields the following nonlinear vector-valued algebraic equation, which can be solved using incremental iterative procedures such as Newton-Raphson method [29].

$$a_1 \mathbf{M}(\boldsymbol{\theta}) \mathbf{q}_k(\boldsymbol{\theta}) + b_1 \mathbf{C}(\boldsymbol{\theta}) \mathbf{q}_k(\boldsymbol{\theta}) + \mathbf{r}_k(\mathbf{q}_k(\boldsymbol{\theta}), \boldsymbol{\theta}) = \tilde{\mathbf{f}}_k \quad (4.15)$$

in which

$$\tilde{\mathbf{f}}_k = \mathbf{f}_k - \mathbf{M}(\boldsymbol{\theta}) [a_2 \mathbf{q}_{k-1}(\boldsymbol{\theta}) + a_3 \dot{\mathbf{q}}_{k-1}(\boldsymbol{\theta}) + a_4 \ddot{\mathbf{q}}_{k-1}(\boldsymbol{\theta})] - \mathbf{C}(\boldsymbol{\theta}) [b_2 \mathbf{q}_{k-1}(\boldsymbol{\theta}) + b_3 \dot{\mathbf{q}}_{k-1}(\boldsymbol{\theta}) + b_4 \ddot{\mathbf{q}}_{k-1}(\boldsymbol{\theta})] \quad (4.16)$$

and  $\boldsymbol{\theta} = [\theta_1, \theta_2, \dots]^T$  is the vector of time-invariant material parameters. Now, Eq. (4.15) is separately differentiated with respect to each material parameter,  $\theta_i$  ( $i = 1 \rightarrow n_{\boldsymbol{\theta}}$ ), to obtain the response sensitivity with respect to this parameter, i.e.,

$$\underbrace{\left[ a_1 \mathbf{M}(\boldsymbol{\theta}) + b_1 \mathbf{C}(\boldsymbol{\theta}) + \frac{\partial \mathbf{r}_k(\mathbf{q}_k, \boldsymbol{\theta})}{\partial \mathbf{q}_k^T} \right]}_{=(\mathbf{K}_T^{dyn})_k} \frac{\partial \mathbf{q}_k}{\partial \theta_i} = - \left. \frac{\partial \mathbf{r}_k(\mathbf{q}, \boldsymbol{\theta})}{\partial \theta_i} \right|_{\mathbf{q}=\mathbf{q}_k} - \left( a_1 \frac{\partial \mathbf{M}(\boldsymbol{\theta})}{\partial \theta_i} + b_1 \frac{\partial \mathbf{C}(\boldsymbol{\theta})}{\partial \theta_i} \right) \mathbf{q}_k + \frac{\partial \tilde{\mathbf{f}}_k}{\partial \theta_i} \quad (4.17)$$

in which  $\frac{\partial \mathbf{r}_k(\mathbf{q}_k, \boldsymbol{\theta})}{\partial \mathbf{q}_k^T} = (\mathbf{K}_T^{stat})_k$  is the static (consistent) tangent stiffness matrix and is readily available from the FE solution if a Newton-Raphson iterative scheme is used (at least in the last iteration) to solve Eq. (4.15). Moreover, the matrix in the left hand side of Eq. (4.17) is called the dynamic tangent stiffness matrix,  $(\mathbf{K}_T^{dyn})_k$ , which is also available from the FE solution. Using Eq. (4.16), the last term in the right hand side of Eq. (4.17) is obtained as

$$\begin{aligned} \frac{\partial \tilde{\mathbf{f}}_k}{\partial \theta_i} &= \frac{\partial \mathbf{f}_k}{\partial \theta_i} - \frac{\partial \mathbf{M}(\boldsymbol{\theta})}{\partial \theta_i} [a_2 \mathbf{q}_{k-1}(\boldsymbol{\theta}) + a_3 \dot{\mathbf{q}}_{k-1}(\boldsymbol{\theta}) + a_4 \ddot{\mathbf{q}}_{k-1}(\boldsymbol{\theta})] - \mathbf{M}(\boldsymbol{\theta}) \left[ a_2 \frac{\partial \mathbf{q}_{k-1}}{\partial \theta_i} + a_3 \frac{\partial \dot{\mathbf{q}}_{k-1}}{\partial \theta_i} + a_4 \frac{\partial \ddot{\mathbf{q}}_{k-1}}{\partial \theta_i} \right] \\ &\quad - \frac{\partial \mathbf{C}(\boldsymbol{\theta})}{\partial \theta_i} [b_2 \mathbf{q}_{k-1}(\boldsymbol{\theta}) + b_3 \dot{\mathbf{q}}_{k-1}(\boldsymbol{\theta}) + b_4 \ddot{\mathbf{q}}_{k-1}(\boldsymbol{\theta})] - \mathbf{C}(\boldsymbol{\theta}) \left[ b_2 \frac{\partial \mathbf{q}_{k-1}}{\partial \theta_i} + b_3 \frac{\partial \dot{\mathbf{q}}_{k-1}}{\partial \theta_i} + b_4 \frac{\partial \ddot{\mathbf{q}}_{k-1}}{\partial \theta_i} \right] \end{aligned} \quad (4.18)$$

Depending on the type of material parameter,  $\frac{\partial \mathbf{f}_k}{\partial \theta_i}$ ,  $\frac{\partial \mathbf{M}(\boldsymbol{\theta})}{\partial \theta_i}$ , and  $\frac{\partial \mathbf{C}(\boldsymbol{\theta})}{\partial \theta_i}$  are usually easy to derive at the element level [25]. Furthermore, the vectors  $\frac{\partial \mathbf{q}_{k-1}}{\partial \theta_i}$ ,  $\frac{\partial \dot{\mathbf{q}}_{k-1}}{\partial \theta_i}$ , and  $\frac{\partial \ddot{\mathbf{q}}_{k-1}}{\partial \theta_i}$  are available from the last time step sensitivity computation. Thus,  $\frac{\partial \mathbf{f}_k}{\partial \theta_i}$  can be computed without any complication. The first term in the right-hand-side of Eq. (4.17) represents the partial derivative of the internal resisting force vector with respect to the material parameter,  $\theta_i$ , conditional on the displacement vector,  $\mathbf{q}_k$ , remaining fixed. To compute this conditional partial derivative, the structure's internal resisting force vector at time step  $k$  needs to be explicitly derived. In a displacement-based FE model of frame-type structures, the structure's internal resisting force vector is derived by assembling the element nodal resisting force vectors as

$$\mathbf{r}_k(\mathbf{q}_k(\boldsymbol{\theta}), \boldsymbol{\theta}) = \mathbf{A}_{ele=1}^{\#ele} \{ \mathbf{r}_k^{ele}(\mathbf{q}_k^{ele}(\boldsymbol{\theta}), \boldsymbol{\theta}) \} \quad (4.19)$$

in which  $\mathbf{A}_{ele=1}^{\#ele} \{ \dots \}$  denotes the direct stiffness assembly process including the transformation from the element local coordinate system to the structure global coordinate system,  $\mathbf{r}_k^{ele}(\mathbf{q}_k^{ele}, \boldsymbol{\theta}) =$  element nodal resisting force vector, and  $\mathbf{q}_k^{ele} =$  element nodal displacement vector in the element local coordinate system. The element nodal resisting force vector is obtained, through the principle of virtual displacements, as the following weighted integral of the section stress vector,  $\boldsymbol{\sigma}_k^{sec}$ , [30]

$$\mathbf{r}_k^{ele}(\mathbf{q}_k^{ele}(\boldsymbol{\theta}), \boldsymbol{\theta}) = \int_{L_{ele}} \mathbf{B}^T \boldsymbol{\sigma}_k^{sec}(\boldsymbol{\varepsilon}_k^{sec}(\boldsymbol{\theta}), \boldsymbol{\theta}) dL \quad (4.20)$$

where  $\mathbf{B} =$  strain-displacement transformation matrix,  $\boldsymbol{\sigma}_k^{sec}(\boldsymbol{\varepsilon}_k^{sec}, \boldsymbol{\theta}) =$  section stress resultant vector, and  $\boldsymbol{\varepsilon}_k^{sec} =$  section strain (or deformation) vector. Finally, the section stress vector is obtained by integrating the fiber stresses over the cross-section as

$$\boldsymbol{\sigma}_k^{sec}(\boldsymbol{\varepsilon}_k^{sec}(\boldsymbol{\theta}), \boldsymbol{\theta}) = \int_{A_{sec}} \mathbf{a} \sigma_k^{fib}(\boldsymbol{\varepsilon}_k^{fib}(\boldsymbol{\theta}), \boldsymbol{\theta}) dA \quad (4.21)$$

in which  $\mathbf{a} =$  section kinematic (compatibility) vector,  $\sigma_k^{fib}(\boldsymbol{\varepsilon}_k^{fib}, \boldsymbol{\theta}) =$  fiber stress (uniaxial), and  $\boldsymbol{\varepsilon}_k^{fib} =$  fiber strain (uniaxial). Now, the conditional partial derivative of the structure's internal resisting force vector with respect to the material parameter,  $\theta_i$ , can be computed as

$$\left. \frac{\partial \mathbf{r}_k(\mathbf{q}, \boldsymbol{\theta})}{\partial \theta_i} \right|_{\mathbf{q}=\mathbf{q}_k} = \mathbf{A}_{ele=1}^{\#ele} \left\{ \int_{L_{ele}} \mathbf{B}^T \int_{A_{sec}} \mathbf{a} \left. \frac{\partial \sigma_k^{fib}(\boldsymbol{\varepsilon}_k^{fib}, \boldsymbol{\theta})}{\partial \theta_i} \right|_{\boldsymbol{\varepsilon}_k^{fib}=\boldsymbol{\varepsilon}_k^{fib}} dAdL \right\} \quad (4.22)$$

where  $\left. \frac{\partial \sigma_k^{fib}(\boldsymbol{\varepsilon}_k^{fib}, \boldsymbol{\theta})}{\partial \theta_i} \right|_{\boldsymbol{\varepsilon}_k^{fib}=\boldsymbol{\varepsilon}_k^{fib}}$  is the history-dependent variation of fiber stress with respect to the material parameter  $\theta_i$  conditional on the fiber strain remaining fixed. This conditional partial derivative can be computed by analytically differentiating the material constitutive law of the fiber with respect to  $\theta_i$  [24–27].

#### 4.4 Uncertainty Quantification

A ML estimator has some general asymptotic properties that can be used to evaluate the estimation uncertainties. The covariance of a ML estimator can be asymptotically evaluated using the Cramér-Rao lower bound (CRLB) [15]. In general, CRLB provides a lower bound for the estimation covariance for any unbiased estimator. It can be shown that a ML estimator is asymptotically unbiased and its estimation covariance asymptotically converges to the CRLB [15, 31, 32].

#### 4.4.1 Derivation of CRLB Based on the Exact Fisher Information Matrix

The Fisher Information matrix (FIM) for the MLE problem shown by Eq. (4.9) can be exactly computed as [33]:

$$\mathbf{I}(\boldsymbol{\theta}, \mathbf{r}) = \begin{bmatrix} (\mathbf{I}_{\theta\theta})_{n_\theta \times n_\theta} & \mathbf{0}_{n_\theta \times n_y} \\ \mathbf{0}_{n_y \times n_\theta} & (\mathbf{I}_{\mathbf{r}\mathbf{r}})_{n_y \times n_y} \end{bmatrix} \quad (4.23)$$

Following the Cramér-Rao theorem [15, 31, 32]:

$$\begin{bmatrix} E \left[ (\hat{\boldsymbol{\theta}} - E(\hat{\boldsymbol{\theta}})) (\hat{\boldsymbol{\theta}} - E(\hat{\boldsymbol{\theta}}))^T \right] & E \left[ (\hat{\boldsymbol{\theta}} - E(\hat{\boldsymbol{\theta}})) (\hat{\mathbf{r}} - E(\hat{\mathbf{r}}))^T \right] \\ E \left[ (\hat{\mathbf{r}} - E(\hat{\mathbf{r}})) (\hat{\boldsymbol{\theta}} - E(\hat{\boldsymbol{\theta}}))^T \right] & E \left[ (\hat{\mathbf{r}} - E(\hat{\mathbf{r}})) (\hat{\mathbf{r}} - E(\hat{\mathbf{r}}))^T \right] \end{bmatrix} \geq \begin{bmatrix} \mathbf{I}_{\theta\theta}^{-1} & \mathbf{0} \\ \mathbf{0} & \mathbf{I}_{\mathbf{r}\mathbf{r}}^{-1} \end{bmatrix} \quad (4.24)$$

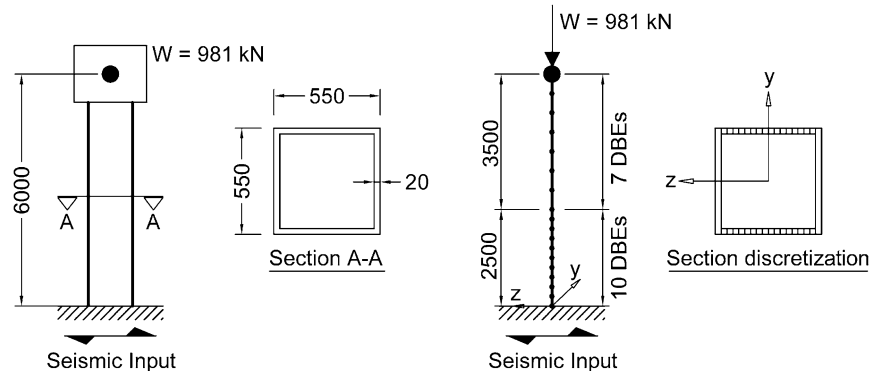
in which  $E[X] = E_{\mathbf{Y}|\boldsymbol{\theta}}[X] = \int X p(\mathbf{y}_{1 \rightarrow k} | \boldsymbol{\theta}) d\mathbf{y}$  and  $\mathbf{Y}$  is the stochastic response of the structure to a specific earthquake input motion. Therefore, the lower bound for the covariance matrix of the modeling parameter can be computed as:

$$COV(\hat{\boldsymbol{\theta}}) \geq \mathbf{I}_{\theta\theta}^{-1}, \quad \mathbf{I}_{\theta\theta} = \sum_{i=1}^k \left[ \left( \frac{\partial \mathbf{h}_i(\boldsymbol{\theta}, \ddot{\mathbf{u}}_{g1 \rightarrow i})}{\partial \boldsymbol{\theta}^T} \right)^T \mathbf{R}^{-1} \frac{\partial \mathbf{h}_i(\boldsymbol{\theta}, \ddot{\mathbf{u}}_{g1 \rightarrow i})}{\partial \boldsymbol{\theta}^T} \right]_{at \boldsymbol{\theta}, \mathbf{r}} \quad (4.25)$$

where  $\frac{\partial \mathbf{h}_i(\boldsymbol{\theta}, \ddot{\mathbf{u}}_{g1 \rightarrow i})}{\partial \boldsymbol{\theta}^T}$  is the response sensitivity matrix and  $\mathbf{I}_{\theta\theta}$  is evaluated for the true modeling parameter and noise variance vectors,  $\boldsymbol{\theta}$  and  $\mathbf{r}$  respectively, which can be approximated by the ML estimates  $\hat{\boldsymbol{\theta}}$  and  $\hat{\mathbf{r}}$ . Based on the asymptotic properties of MLE,  $\hat{\boldsymbol{\theta}}$  and  $\hat{\mathbf{r}}$  asymptotically merge  $\boldsymbol{\theta}$  and  $\mathbf{r}$ , respectively, and therefore, the estimation covariance asymptotically merges the FIM computed at  $\hat{\boldsymbol{\theta}}$  and  $\hat{\mathbf{r}}$ .

#### 4.5 Validation Study

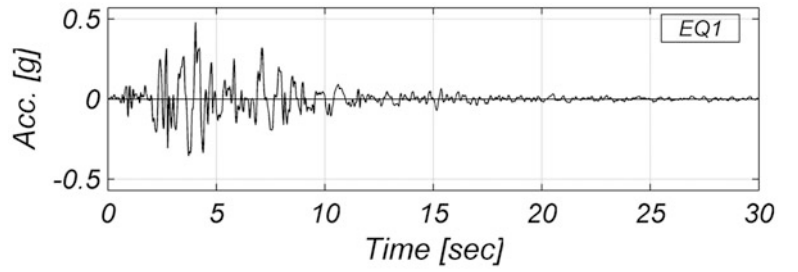
The benchmark structure used for this validation study is a 6.0 m cantilever steel column representing a small bridge pier [11]. The column has a built-up box section with dimension  $550 \times 550 \times 20$  mm (built from ASTM A36 steel) and carries a lumped dead load of 981 kN as shown in Fig. 4.1. It is assumed that the section can attain its full plastic capacity without any significant local buckling, strength degradation, or softening behavior. Using fiber-section displacement-based beam-column elements, a 2D model of the structure is developed in OpenSees [34] as shown in Fig. 4.1. The steel fibers are modeled using the modified Giuffr -Menegotto-Pinto material constitutive model [35], in which the stress-strain relation is defined using smooth curved shaped hysteretic loading and unloading branches. In general, this material model is governed by eight time-invariant parameters, five of which are empirical parameters controlling the curvature of the hysteretic loops



**Fig. 4.1** Left: cantilever steel column with box section, Right: details of the developed FE model (DBE: displacement-based element, length unit: mm)



**Fig. 4.2** 1989 Loma Prieta earthquake, Corralitos – Eureka Canyon Road station, 90° component



and the stress shift (to mimic the isotropic hardening). While these five parameters are assumed as known constants in this problem, the other three material parameters are treated as unknown modeling parameters to be identified. These parameters are  $\sigma_y$  = initial yield strength,  $E$  = elastic modulus, and  $b$  = strain hardening ratio. The true (exact) values of these material parameters are taken as  $\sigma_y^{true} = 250 \text{ MPa}$ ,  $E^{true} = 200 \text{ GPa}$ , and  $b^{true} = 0.1$ .

One ground acceleration record from 1989 Loma Prieta earthquake is selected for the nonlinear time history analyses (Fig. 4.2) [36]. The nonlinear analysis is started by first applying the gravity loads quasi-statically. Then, the nonlinear time history analysis is performed using the Newmark average acceleration method [28] to integrate the equations of motion using a time step of  $\Delta t = 0.02 \text{ s}$ . The Newton-Raphson method is employed to solve iteratively the nonlinear dynamic equilibrium equations at each time step. Tangent stiffness-proportional Rayleigh damping [28] is used to model the damping characteristics by defining a damping ratio of 2 % for the first elastic mode ( $T_1 = 0.76 \text{ s}$ ).

To simulate the response of the structure, the FE model is analyzed and the acceleration response time history of the column top in the direction of the seismic input is obtained and artificially polluted by measurement noise, which is modeled as a zero-mean Gaussian white noise, to provide the measured response of the structure. The measured response of the structure is used in the proposed parameter estimation framework to evaluate the point estimate of the modeling parameters ( $\hat{\theta} = [\hat{\sigma}_y, \hat{E}, \hat{b}]^T$ ) and the error variance  $\hat{\mathbf{r}}$  (which is a one dimensional vector in this case). The uncertainties associated with the estimated modeling parameters are evaluated by computing the CRLB based on the exact FIM. Although the estimation of the prediction error variance would have no influence on the point estimate of the modeling parameters in the case of single output measurement or multiple output measurements with similar signal amplitude and noise characteristics, the estimated error variance is essential for computing the estimation uncertainties as shown in Eq. (4.25).

To investigate the robustness of the parameter estimation framework and its sensitivity to the output measurement noise level, three different amplitudes for output measurement noise are considered, namely 0.5 %g, 2 %g, and 5 %g RMS. The 2 %g and 5 %g RMS noise levels are unrealistically high; nevertheless, they are considered to examine the performance of the estimation framework using extreme noisy measurements. The true values of noise variance for the three considered noise levels (0.5 %g, 2 %g, and 5 %g RMS) are  $r^{true} = 0.24 \times 10^{-2}$ ,  $3.85 \times 10^{-2}$ , and  $24.06 \times 10^{-2}$ , respectively. These true values are used later to evaluate the accuracy of the estimation results. The initial estimates for the modeling parameters and noise variance are selected as  $\sigma_{y_0} = 0.75\sigma_y^{true}$ ,  $E_0 = 1.30E^{true}$ ,  $b_0 = 1.35b^{true}$ , and  $r_0 = 0.62 \times 10^{-2} \left[ \frac{m}{s^2} \right]^2$ . The feasible search domain for the modeling parameters are set as  $0.4 \theta_0 \leq \theta \leq 2.5 \theta_0$ , where  $\theta_0$  = vector of initial estimates of the modeling parameters, and for noise variance are set as  $0.025 r_0 \leq r \leq 40 r_0$ . Figure 4.3 shows the convergence history of the three modeling parameters and the noise variance for the three considered levels of measurement noise. Table 4.1 shows the estimated modeling parameters and noise variance, normalized with respect to the true parameter values, for all the cases considered. The table also lists the coefficient of variation ( $COV = \sigma_{\theta_i} / \hat{\theta}_i$ ) of the modeling parameters computed using the proposed method for evaluating the CRLB. Figure 4.3 and Table 4.1 confirm the successful performance of the proposed parameter estimation framework. As can be seen for the case of 5 %g RMS noise level in Table 4.1, the excessive level of measurement noise results in biased estimation of the modelling parameters. The detrimental effects of high amplitude measurement noise become more dominant in the estimation of strain hardening ratio,  $b$ . Listed in Table 4.1, the estimated COVs have an excellent qualitative agreement with the estimation accuracy: the COVs are higher when the estimations are more biased. For all the considered cases, the modulus of elasticity  $E$  has the smallest COV, followed by the yield strength,  $\sigma_y$ , and the strain hardening ratio,  $b$ , has the largest COV. Moreover, the COVs consistently increase as the level of measurement noise increases.

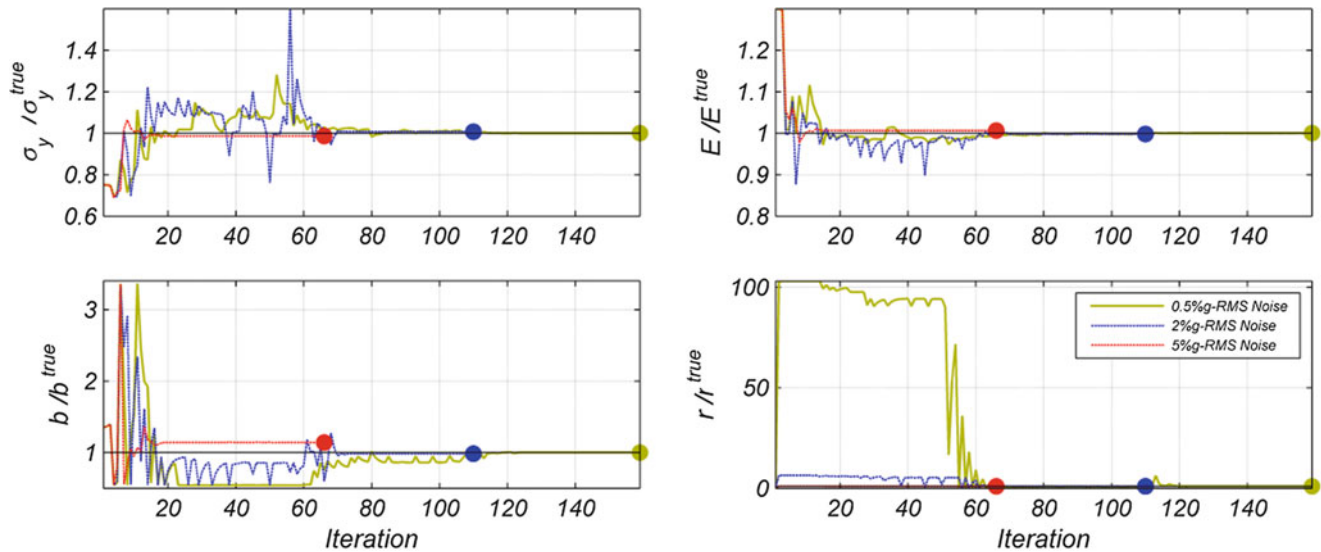


Fig. 4.3 Convergence history of the modeling parameters and noise variance for the three levels of measurement noise considered

Table 4.1 Estimation results for three measurement noise levels considered

Motion name	Noise level (%g RMS)	Modeling parameters			Noise variance	COV (%)		
		$\sigma_y / \sigma_y^{true}$	$E/E^{true}$	$b/b^{true}$	$r/r^{true}$	$\sigma_y$	$E$	$b$
Loma Prieta EQ., Eureka Canyon Road station	0.5	1.00	1.00	1.00	1.02	0.14	0.03	1.05
	2	1.01	1.00	0.98	1.01	0.55	0.12	4.26
	5	0.99	1.01	1.14	1.00	1.45	0.32	9.49

## 4.6 Conclusions

This paper proposed a framework for nonlinear finite element (FE) model updating of civil structures using measured dynamic input and output data. The proposed extended batch estimation method is based on the maximum likelihood estimation (MLE) approach to estimate the unknown modeling parameters, the measurement noise amplitude, and the covariance matrix of the modeling parameters. Using the MLE as a parameter estimation tool resulted in a nonlinear optimization problem, which was efficiently solved using interior-point method, a gradient-based optimization procedure. The FE response sensitivities were accurately and efficiently computed using the direct differentiation method (DDM). The covariance matrix of the modeling parameters were evaluated based on the Cramer-Rao lower bound (CRLB) theorem by computing the exact Fisher Information matrix (FIM). The computation of the FIM required the knowledge of measurement noise variance, which was estimated through the extended estimation framework. A proof-of-concept example, consisting of a cantilever steel column representing a bridge pier, was provided to validate the proposed framework. Different levels of measurement noise were considered to evaluate the performance and robustness to output measurement noise of the proposed framework. The results proved the excellent performance of the estimation framework even in presence of extremely high measurement noise levels.

## References

- Juang J (1994) Applied system identification. Prentice Hall PTR, Upper Saddle River
- Friswell MI, Mottershead JE (1995) Finite element model updating in structural dynamics. Kluwer Academic Publishers, Dordrecht
- Sues RH, Mau ST, Wen Y-K (1988) Systems identification of degrading hysteretic restoring forces. ASCE J Eng Mech 114(5):833–846
- Smyth AW, Masri SF, Chassiakos AG, Caughey TK (1999) On-line parametric identification of MDOF nonlinear hysteretic systems. ASCE J Eng Mech 125(2):133–142
- Lin J, Betti R, Smyth AW, Longman RW (2001) On-line identification of non-linear hysteretic structural systems using a variable trace approach. Earthq Eng Struct Dyn 30(9):1279–1303
- Hoshiya M, Saito E (1984) Structural identification by extended Kalman filter. ASCE J Eng Mech 110(12):1757–1770

7. Loh C, Tsaur Y (1988) Time domain estimation of structural parameters. *Eng Struct* 10(2):95–105
8. Wu M, Smyth AW (2007) Application of the unscented Kalman filter for real-time nonlinear structural system identification. *Struct Control Health Monit* 14(7):971–990
9. Chatzi EN, Smyth AW, Masri SF (2010) Experimental application of on-line parametric identification for nonlinear hysteretic systems with model uncertainty. *Struct Saf* 32(5):326–337
10. Ching J, Beck JL, Porter KA (2006) Bayesian state and parameter estimation of uncertain dynamical systems. *Probabilistic Eng Mech* 21: 81–96
11. Ebrahimian H, Astroza R, Conte JP (2014) Extended Kalman filter for material parameter estimation in nonlinear structural finite element models using direct differentiation method. *Earthq Eng Struct Dynam* (in review)
12. Astroza R, Ebrahimian H, Conte JP (2014) Material parameter identification in distributed plasticity FE models of frame-type structures using nonlinear stochastic filtering. *ASCE J Eng Mech* 04014149. doi:10.1061/(ASCE)EM.1943-7889.0000851
13. Ljung L (1999) *System identification: theory for the user*, 2nd edn. PTR Prentice Hall, Upper Saddle River
14. Beck JL (2010) Bayesian system identification based on probability logic. *Struct Control Health Monit* 17(7):825–847
15. Moon TK, Stirling WC (2000) *Mathematical methods and algorithms for signal processing*. Prentice-Hall, Upper Saddle River
16. Yuen K-V, Kuok S-C (2011) Bayesian methods for updating dynamic models *ASME Appl Mech Rev* 64(1)
17. Beck JL, Katafygiotis LS (1998) Updating models and their uncertainties. Part I: Bayesian statistical framework. *ASCE J Eng Mech* 124(4):455–461
18. Yuen K-V, Beck JL, Katafygiotis LS (2006) Unified probabilistic approach for model updating and damage detection. *ASME J Appl Mech* 73(4):555–564
19. Liu P, Au S-K (2013) Bayesian parameter identification of hysteretic behavior of composite walls. *Probabilistic Eng Mech* 34:101–109
20. Byrd RH, Hribar ME, Nocedal J (1999) An interior point algorithm for large-scale nonlinear programming. *SIAM J Optim* 9(4):877–900
21. Byrd RH, Gilbert JC, Nocedal J (2000) A trust region method based on interior point techniques for nonlinear programming. *Math Program* 89(1):149–185
22. MathWorks T (2014) *MATLAB optimization toolbox, user's guide*, R2014a. The MathWorks Inc., Natick
23. Tsay JJ, Arora JS (1990) Nonlinear structural design sensitivity analysis for path dependent problems. Part 1: general theory. *Comput Methods Appl Mech Eng* 81(2):183–208
24. Kleiber M, Antunez H, Hien TD, Kowalczyk P (1997) *Parameter sensitivity in nonlinear mechanics: theory and finite element computations*. Wiley, New York
25. Zhang Y, Der Kiureghian A (1993) Dynamic response sensitivity of inelastic structures. *Comput Methods Appl Mech Eng* 108(1–2):23–36
26. Conte JP (2001) Finite element response sensitivity analysis in earthquake engineering. In *Earthquake engineering frontiers in the New Millennium*, Lisse
27. Conte JP, Vijalapura PK, Meghella M (2003) Consistent finite-element response sensitivity analysis. *ASCE J Eng Mech* 129(12):1380–1393
28. Chopra AK (2012) *Dynamics of structures: theory and applications to earthquake engineering*, 4th edn. Prentice-Hall, Inc, Englewood Cliffs
29. Bathe KJ (1996) *Finite element procedures*. Prentice-Hall, Inc, Upper Saddle River
30. Filippou FC, Fenves GL (2004) Methods of analysis for earthquake-resistant structures. In *Earthquake engineering: from engineering seismology to performance-based engineering*, CRC Press LLC, Chapter 6
31. Goodwin GC, Payne RL (1977) *Dynamic system identification: experiment design and data analysis*. Academic Press, New York
32. Kay SM (1993) *Fundamentals of statistical signal processing, vol 1, Estimation theory*. Upper Saddle River, Prentice Hall
33. Ebrahimian H, Astroza R, Conte JP (2014) Nonlinear structural parameter estimation and uncertainty quantification using Bayesian inference method. SSRP 14/12, Department of Structural Engineering, University of California, San Diego/La Jolla
34. OpenSees (2014) Open system for earthquake engineering simulation [Online]. <http://opensees.berkeley.edu/>. Accessed 10 2014
35. Filippou FC, Popov EP, Bertero VV (1983) Effects of bond deterioration on hysteretic behavior of reinforced concrete joints, EERC report 83–19, Earthquake Engineering Research Center, Berkeley
36. Center for Engineering Strong Motion Data, CESMD – a cooperative effort [Online]. <http://strongmotioncenter.org/>. Accessed September 2013

## Chapter 5

# A Comparative Assessment of Nonlinear State Estimation Methods for Structural Health Monitoring

Majdi Mansouri, Onur Avci, Hazem Nounou, and Mohamed Nounou

**Abstract** Researchers have been studying the uncertainties unique to civil infrastructure such as redundancy; nonlinearity; interaction with surrounding; heterogeneity; boundaries and support conditions; structural continuity, stability, integrity; life cycle performance expectations and so on. For incorporating such uncertainties, filtering techniques accounting for stochasticity can be implemented employing collected data from the structures. In this paper, an Iterated Square Root Unscented Kalman Filter (ISRUKF) method is proposed for the estimation of the nonlinear state variables of nonlinear structural systems, idealized herein for simplified spring-mass-dashpot. Various conventional and state-of-the-art state estimation methods are compared for the estimation performance, namely the Unscented Kalman Filter (UKF), the Square-Root Unscented Kalman Filter (SRUKF), the Iterated Unscented Kalman Filter (IUKF) and the Iterated Square Root Unscented Kalman Filter (ISRUKF) methods. The comparison reveals that the ISRUKF method provides a better estimation accuracy than the IUKF method; while both methods provide improved accuracy over the UKF and SRUKF methods. The benefit of the ISRUKF method lies in its ability to provide accuracy related advantages over other estimation methods since it re-linearizes the measurement equation by iterating an approximate maximum a posteriori (MAP) estimate around the updated state, instead of relying on the predicted state.

**Keywords** Iterated square root • Unscented Kalman filter • State estimation • Structural health monitoring

## 5.1 Introduction

It has been discussed in the SHM literature that the structural identification methods proven for manufactured (mechanical) systems were unsuccessfully used for constructed (civil) systems over the years. Many characteristic attributes of the civil structures were ignored in the process since the developed methods were more applicable to manufactured systems. Even very refined three dimensional models of civil structures cannot mitigate the influences of bias sources of uncertainty. Uncertainties unique to civil structures are; local and global redundancy; material, dynamic and geometric nonlinearity; interaction with surrounding forces; heterogeneity of the members and materials; boundaries and support conditions; structural continuity, stability and integrity; life cycle performance expectations. In accounting for these for the uncertainties, there is a need for improvement of the model predictions using data collected from structures. In the widely established approach of modal parameter estimation, the system can be ill-conditioned due to uncertainties in the measurements. The potential errors in structural model updating combined with aleatory uncertainty in modal parameter estimation often results in inconsistencies between the real structural behavior and the finite element model predictions. However, in most of the published research in SHM, the ill-conditioned state and the presence of uncertainty are not considered. For nonlinear state estimations, various state estimation techniques (the Extended Kalman filter (EKF) [1–3], Unscented Kalman Filter (UKF) [4, 5], Central Difference Kalman Filter (CDKF) [6], and Square-Root Unscented Kalman Filter (SRUKF) [7]) have been developed and used by researchers. In the extended Kalman filter method, in order to approximate the covariance matrix of the state vector, the model describing the system is linearized at every time sample. However, for highly nonlinear or complex models, the EKF results are not always successful. Instead of linearizing the model, the UKF method utilizes the unscented

---

M. Mansouri • H. Nounou  
Electrical and Computer Engineering Program, Texas A&M University at Qatar, Doha, Qatar

O. Avci (✉)  
Civil & Architectural Engineering Department, Qatar University, Doha, Qatar

M. Nounou  
Chemical Engineering Program, Texas A&M University at Qatar, Doha, Qatar

transformation to approximate the mean and the covariance matrix of the state vector. In the unscented transformation process, a set of samples (sigma points) are selected and propagated through the nonlinear model, providing more accurate approximations of the mean and covariance matrix of the state vector. One drawback of the UKF method is that the number of sigma points is often not very large and may not adequately represent relatively complicated distributions. As an alternative to these methods, the square-root unscented Kalman filter, and the central difference Kalman filter have been developed. The advantage of these filters is that evaluating the quasi log-likelihood distribution only takes a fraction of a second. The iterated square-root unscented Kalman filter has been recently suggested by Wu et al. [8] for target tracking using TDOA measurements. The ISRUKF employs an iterative procedure within a single measurement update step by resampling the sigma points till a termination criterion, based on the minimization of the maximum likelihood estimate, is satisfied. Furthermore, the ISRUKF method propagates and updates the square root of the state covariance iteratively and directly in Cholesky factored form. In addition to providing reduction in the computational complexity, ISRUKF has as increased numerical stability and better (or at least equal) performance when compared to the other algorithms.

The organization of the paper is as follows. In Sect. 5.2, the state estimation problem is presented. Then, in Sect. 5.3, the developed iterated square-root unscented Kalman filter is described. After that, in Sect. 5.4, the performance of various state estimation methods are compared for the state variables of a three degree of freedom spring-mass-dashpot system. Conclusions are presented in Sect. 5.5.

## 5.2 State Estimation Problem

The formulation of the state estimation problem is presented here in this section.

### 5.2.1 Problem Formulation

The state estimation problem is formulated for a general system model, in this section. Consider a nonlinear state space model to be described as follows [9]:

$$\begin{aligned}\dot{x} &= g(x, u, \theta, w), \\ y &= l(x, u, \theta, v),\end{aligned}\tag{5.1}$$

where  $x \in \mathbb{R}^n$  is a vector of the state variables,  $u \in \mathbb{R}^p$  is a vector of the input variables,  $\theta \in \mathbb{R}^q$  is a known parameter vector,  $y \in \mathbb{R}^m$  is a vector of the measured variables,  $w \in \mathbb{R}^n$  and  $v \in \mathbb{R}^m$  are process and measurement noise vectors, respectively, and  $g$  and  $l$  are nonlinear differentiable functions. Discretizing the state space model (5.1), the discrete model can be written as follows:

$$\begin{aligned}x_k &= f(x_{k-1}, u_{k-1}, \theta_{k-1}, w_{k-1}), \\ y_k &= h(x_k, u_k, \theta_k, v_k),\end{aligned}\tag{5.2}$$

which describes the state variables at some time step ( $k$ ) in terms of their values at a previous time step ( $k-1$ ). Let the process and measurement noise vectors have the following properties:  $\mathbf{E}[w_k] = 0$ ,  $\mathbf{E}[w_k w_k^T] = \mathbf{Q}_k$ ,  $\mathbf{E}[v_k] = 0$  and  $\mathbf{E}[v_k v_k^T] = \mathbf{R}_k$ . Let's assume that the parameter vector is described by the following model:

$$\theta_k = \theta_{k-1} + \gamma_{k-1}.\tag{5.3}$$

which means that it corresponds to a stationary process, with an identity transition matrix, driven by white noise. In order to include the parameter vector  $\theta_k$  into the state estimation problem, let's define a new state vector  $z_k$  that augments the state vector  $x_k$  and the parameter vector  $\theta_k$  as follows:

$$z_k = \begin{bmatrix} x_k \\ \theta_k \end{bmatrix} = \begin{bmatrix} f(x_{k-1}, u_{k-1}, w_{k-1}, \theta_{k-1}) \\ \theta_{k-1} + \gamma_{k-1} \end{bmatrix},\tag{5.4}$$

where  $z_k \in \mathbb{R}^{n+q}$ . Also, defining the augmented noise vector as:

$$\epsilon_{k-1} = \begin{bmatrix} w_{k-1} \\ \gamma_{k-1} \end{bmatrix}, \quad (5.5)$$

the model (5.2) can be written as,

$$z_k = \mathfrak{F}(z_{k-1}, u_{k-1}, \epsilon_{k-1}), \quad (5.6)$$

$$y_k = \mathfrak{R}(z_k, u_k, v_k), \quad (5.7)$$

where  $\mathfrak{F}$  and  $\mathfrak{R}$  are differentiable nonlinear functions. In this work, the objective is to estimate the state variables vector  $z_k$  given the measurements vector  $y_k$ , where the model parameter vector  $\theta_k$  is assumed to be known.

## 5.3 Description of State Estimation Methods

### 5.3.1 Unscented Kalman Filter Method

The EKF approximates the mean and covariance of the state vector by linearizing the nonlinear process and observation equations, which may not provide a satisfactory approximation of these moments. For better estimates of these moments, the unscented Kalman filter takes advantage of the unscented transformation. It must be noted that the unscented transformation is a method for calculating the statistics of a random variable that undergoes a nonlinear mapping. Assume that a random variable  $z \in \mathbb{R}^L$  with mean  $\bar{z}$  and covariance  $\mathbf{P}_z$  is transformed by a nonlinear function,  $y = f(z)$ . In order to find the statistics of  $y$ , define  $2L + 1$  sigma vectors as follows:

$$\begin{aligned} Z_0 &= \bar{z} \\ Z_i &= \bar{z} + (\sqrt{(L + \lambda)\mathbf{P}_z})_i \quad i = 1, \dots, L \\ Z_i &= \bar{z} - (\sqrt{(L + \lambda)\mathbf{P}_z})_i \quad i = L + 1, \dots, 2L \end{aligned} \quad (5.8)$$

where  $\lambda = e^2(L + k) - L$  is a scaling parameter and  $(\sqrt{(L + \lambda)\mathbf{P}_z})_i$  denotes the  $i^{\text{th}}$  column of the matrix square root. The constant  $10^{-4} < e < 1$  determines the spread of the sigma points around  $\bar{z}$ . The constant  $k$  is a secondary scaling parameter which is usually set to zero or  $3 - L$  [3].

Then, these sigma points are propagated through the nonlinear function, i.e.,

$$Y_i = f(Z_i) \quad i = 0, \dots, 2L \quad (5.9)$$

and the mean and covariance matrix of  $y$  can be approximated as weighted sample mean and covariance of the transformed sigma points of  $Y_i$  as follows:

$$\begin{aligned} \bar{y} &\approx \sum_{i=0}^{2L} W_i^{(m)} Y_i, \\ \text{and } \mathbf{P}_z &\approx \sum_{i=0}^{2L} W_i^{(c)} (Y_i - \bar{y})(Y_i - \bar{y})^T, \end{aligned} \quad (5.10)$$

where the weights are given by:

$$\begin{aligned} W_i^{(m)} &= \frac{\lambda}{\lambda + r}, \\ W_0^{(c)} &= \frac{\lambda}{\lambda + r} + (1 - e^2 + \xi), \\ \text{and } W_i^{(m)} &= W_i^{(c)} = \frac{1}{2(\lambda + r)}, \quad i = 0, \dots, 2L. \end{aligned} \quad (5.11)$$

The parameter  $\xi$  is used to incorporate prior knowledge about the distribution of  $z$ . It has been shown that for a Gaussian and non-Gaussian variables, the unscented transformation results in approximations that are accurate up to the third and second order, respectively.

The prediction update equations are as follows:

$$\begin{aligned}
\hat{z}_k^- &= \mathfrak{F}(\hat{z}_{k-1}^-, u_{k-1}), \\
P_{z_k}^- &= P_{z_{k-1}} + R_{k-1}^\delta, \\
R_{k-1}^\delta &= (\lambda_{RLS}^{-1} - 1) P_{z_{k-1}}, \\
Z_{k|k-1} &= \left[ \hat{z}_k^- \quad \hat{z}_k^- + \sqrt{r + \lambda} \sqrt{P_{z_k}^-} \quad \hat{z}_k^- - \sqrt{r + \lambda} \sqrt{P_{z_k}^-} \right], \\
Y_{k|k-1} &= \mathfrak{F}(Z_{k|k-1}, u_{k-1}), \\
\hat{y}_k &= \sum_{i=0}^{2r} W_i^{(m)} Y_{i,k|k-1}.
\end{aligned} \tag{5.12}$$

The prediction update equations are as follows:

$$\begin{aligned}
P_{y_k} &= \sum_{i=0}^{2r} W_i^{(c)} [Y_{i,k|k-1} - \hat{y}_k] [Y_{i,k|k-1} - \hat{y}_k]^T + R_k^\xi, \\
P_{z_k, y_k} &= \sum_{i=0}^{2r} W_i^{(c)} [Z_{i,k|k-1} - \hat{y}_k] [Z_{i,k|k-1} - \hat{y}_k]^T, \\
K_k &= P_{z_k, y_k} P_{y_k}^{-1}, \\
\hat{z}_k &= \hat{z}_k^- + K_k (y_k - \hat{y}_k), \\
P_{z_k} &= P_{z_k}^- - K_k P_{y_k} K_k^T.
\end{aligned} \tag{5.13}$$

### 5.3.2 Square-Root Unscented Kalman Filter Method

In the EKF, the covariance  $\mathbf{P}_k$  itself is recursively calculated, while, the UKF requires instead calculation of the matrix square-root  $\mathbf{S}_k \mathbf{S}_k^T = \mathbf{P}_k$ , at each time step. In the SRUKF,  $\mathbf{S}_k$  will be propagated directly, avoiding the computational complexity to refactorize at each time step [7]. The SRUKF is initialized with a state mean vector and the square root of a covariance.

$$\hat{z}_0 = E[z_0] \tag{5.14}$$

and,

$$\mathbf{S}_0 = \text{chol} \{E[(z_0 - \hat{z}_0)(z_0 - \hat{z}_0)']\} \tag{5.15}$$

$$\Psi_{k-1} = [\hat{z}_{k-1} \quad \hat{z}_{k-1} + h\mathbf{S}_{k-1} \quad \hat{z}_{k-1} - h\mathbf{S}_{k-1}] \tag{5.16}$$

The Cholesky factorization decomposes a symmetric, positive-definite matrix into the product of a lower-triangular matrix and its transpose. This matrix is used directly to obtain the sigma points:

The scaling constant  $h$  is expressed as,

$$h = \sqrt{L\alpha^2} \tag{5.17}$$

where  $\alpha$  is a tunable parameter less than one. The sigma points are then passed through the nonlinear process system, which predicts the current attitude based on each sigma point.

$$\Psi_{k|k-1} = f[\Psi_{k-1}] \tag{5.18}$$

The estimated state mean and square root covariance are calculated from the transformed sigma points using,

$$\hat{z}_k^- = \sum_{i=0}^{2L} W_i^{(m)} \Psi_{i,k|k-1} \quad (5.19)$$

$$S_k^- = qr \left\{ \left[ \sqrt{W_1^{(c)}} (\Psi_{1:2L,k|k-1} - \hat{z}_k^-) \sqrt{\mathbf{R}^w} \right] \right\} \quad (5.20)$$

$$S_k^- = cholupdate \left\{ S_k^-, \Psi_{0,k} - \hat{z}_k^-, W_0^{(c)} \right\} \quad (5.21)$$

where,  $W_0^{(c)} = 2(1 - \alpha^2 + \frac{1}{2}\beta)$ ,  $W_0^{(m)} = 1 - \alpha^2$ ,  $W_i^{(m)} = W_i^{(c)} = \frac{1}{2L\alpha^2}\beta$ ,  $\beta$  is a tunable parameter used to incorporate prior distribution. The transformed sigma points are then used to predict the measurements using the measurement model:

$$Y_{k|k-1} = h[\Psi_{k|k-1}] \quad (5.22)$$

The expected measurement  $\hat{y}_k^-$  and square root covariance of  $\tilde{y}_k = y_k - \hat{y}_k^-$  (called the innovation) are given by the unscented transform expressions just as for the process model:

$$\hat{y}_k^- = \sum_{i=0}^{2L} W_i^{(m)} y_{i,k|k-1} \quad (5.23)$$

$$S_{\tilde{y}_k} = qr \left\{ \left[ \sqrt{W_1^{(c)}} (Y_{1:2L,k|k-1} - \hat{y}_k^-) \sqrt{\mathbf{R}^v} \right] \right\} \quad (5.24)$$

$$S_{\tilde{y}_k} = cholupdate \left\{ S_{\tilde{y}_k}, Y_{0,k} - \hat{y}_k^-, W_0^{(c)} \right\} \quad (5.25)$$

To determine how much to adjust the predicted state mean and covariance based on the actual measurement, the Kalman gain matrix  $\mathbf{K}_k$  is calculated as follows:

$$\mathbf{P}_{z_k y_k} = \sum_{i=0}^{2L} W_i^{(c)} [\Psi_{i,k|k-1} - \hat{z}_k^-] [Y_{i,k|k-1} - \hat{y}_k^-]^T \quad (5.26)$$

$$\mathbf{K}_k = \mathbf{P}_{z_k y_k} / S_{\tilde{y}_k}^T / S_{\tilde{y}_k} \quad (5.27)$$

Finally, the state mean and covariance are updated using the actual measurement and the Kalman gain matrix:

$$\hat{z}_k = \hat{z}_k^- + \mathbf{K}_k (y_k - \hat{y}_k^-) \quad (5.28)$$

$$\mathbf{U} = \mathbf{K}_k S_{\tilde{y}_k} \quad (5.29)$$

$$S_k = cholupdate \{ S_k^-, \mathbf{U}, -1 \} \quad (5.30)$$

where,  $\mathbf{R}^w$  is the process noise covariance,  $\mathbf{R}^v$  is the measurement noise covariance, *chol*—is Cholesky method of matrix factorization, *qr* is QR matrix decomposition and *cholupdate* is a Cholesky factor updating.

### 5.3.3 Iterated Square-Root Unscented Kalman Filter Method

With the success of IUKF development [10] and the superiority of SRUKF, an improved performance would be expected if the iterates are implemented in SRUKF. Yet, with the potential problems experienced with the IUKF method, precaution should be taken for effective performance of the iterated filter [8]. The development of the ISRUKF method is due to the need to overcome this problem, using a different iteration strategy. The pseudo-code for the ISRUKF method can be summarized as follows.



- Step 1:  
For each instant  $k (k \geq 1)$ , evaluate the state estimate  $\hat{z}_k$  and corresponding square root covariance matrix  $\mathbf{S}_k$  through (5.13) to (5.29).
- Step 2:  
Let  $\hat{z}_{k,0} = \hat{z}_k^-$ ,  $\mathbf{S}_{k,0} = \mathbf{S}_k^-$  and  $\hat{z}_{k,1} = \hat{z}_k$ .  $\mathbf{S}_{k,1} = \mathbf{S}_k$ . Also let  $j = 2$
- Step 3  
Generate new sigma points in the same way as (5.17):

$$\Psi_{k,j} = [\hat{z}_{k,j-1} \quad \hat{z}_{k,j-1} + h\mathbf{S}_{k,j-1} \quad \hat{z}_{k-1,j-1} - h\mathbf{S}_{k,j-1}] \quad (5.31)$$

- Step 4  
Recalculate (5.17) to (5.29) as follows

$$\Psi_{i,j} = f[\Psi_{i,j}] \quad (5.32)$$

$$\hat{z}_{i,j}^- = \sum_{i=0}^{2L} W_i^{(m)} \Psi_{i,j} \quad (5.33)$$

$$\mathbf{S}_{k,j}^- = qr \left\{ \left[ \sqrt{W_1^{(c)}} (\Psi_{1:2L,j} - \hat{z}_{k,j}^-) \right] \right\} \quad (5.34)$$

$$\mathbf{S}_{k,j}^- = cholupdate \left\{ \mathbf{S}_{k,j}^-, \Psi_{i,j} - \hat{z}_{k,j}^-, W_1^{(c)} \right\} \quad (5.35)$$

$$Y_{i,j} = h[\Psi_{i,j}] \quad (5.36)$$

$$\hat{y}_{k,j}^- = \sum_{i=0}^{2L} W_i^{(m)} y_{i,j} \quad (5.37)$$

$$\mathbf{S}_{\tilde{y}_{k,j}} = qr \left\{ \left[ \sqrt{W_1^{(c)}} (Y_{1:2L,j} - \hat{y}_{k,j}^-) \sqrt{\mathbf{R}_k^n} \right] \right\} \quad (5.38)$$

$$\mathbf{S}_{\tilde{y}_{k,j}} = cholupdate \left\{ \mathbf{S}_{\tilde{y}_{k,j}}, Y_{i,j} - \hat{y}_{k,j}^-, W_0^{(c)} \right\} \quad (5.39)$$

$$\mathbf{P}_{z_{k,j} y_{k,j}} = \sum_{i=0}^{2L} W_i^{(c)} [\Psi_{i,j} - \hat{z}_{k,j}^-] [Y_{i,j} - \hat{y}_{k,j}^-]^T \quad (5.40)$$

$$\mathbf{K}_k = \mathbf{P}_{z_{k,j} y_{k,j}} / \mathbf{S}_{\tilde{y}_{k,j}}^T / \mathbf{S}_{\tilde{y}_{k,j}} \quad (5.41)$$

$$\hat{z}_{k,j} = \hat{z}_{k-j}^- + \mathbf{K}_{k,j} (y_{k,j} - \hat{y}_{k,j}^-) \quad (5.42)$$

$$\mathbf{U} = \mathbf{K}_{k-j} \mathbf{S}_{\tilde{y}_{k,j}} \quad (5.43)$$

$$\mathbf{S}_{k,j} = cholupdate \left\{ \mathbf{S}_{k-j}^-, \mathbf{U}, -1 \right\} \quad (5.44)$$

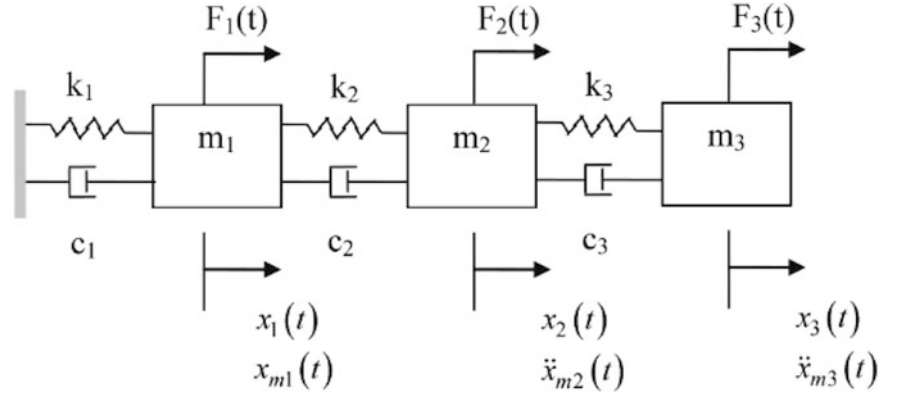
## 5.4 Simulation Results

The results of state estimation methods (UKF, IUKF, SRUKF and ISRUKF) are compared in this section. They are compared through their utilization to estimate the states variables of a three degree of freedom spring-mass-dashpot system.

### 5.4.1 State Estimations for Three Degree of Freedom Spring-Mass-Dashpot System

A three degree of freedom spring-mass-dashpot system is utilized for the performance evaluation of state estimation techniques (shown in Fig. 5.1).

**Fig. 5.1** Three degree of freedom spring-mass-dashpot system. Note that the first degree of freedom is associated with a non-linear hysteretic component [11]



The purpose of this section is to estimate the seven state variables given displacement measurements for  $m_1$  and accelerometer measurements for  $m_2$  and  $m_3$ . The state space equations representing the system can be written as follows:

$$\begin{bmatrix} z_1(k+1) \\ z_2(k+1) \\ z_3(k+1) \\ z_4(k+1) \\ z_5(k+1) \\ z_6(k+1) \\ z_7(k+1) \end{bmatrix} = \begin{bmatrix} z_1(k) + Tz_5(k) \\ z_2(k) + Tz_6(k) \\ z_3(k) + Tz_7(k) \\ z_4(k) + T\tilde{z}_4 \\ z_5(k) + \frac{T}{m_1}\tilde{z}_5 \\ z_6(k) \\ z_7(k) \end{bmatrix} + \begin{bmatrix} 0 \\ 0 \\ 0 \\ 0 \\ T\left(v_1 + \frac{F_1(k)}{m_1}\right) \\ T(\ddot{x}_{m_2} + v_2) \\ T(\ddot{x}_{m_3} + v_3) \end{bmatrix}$$

where,

$$\begin{aligned} \tilde{z}_4 &= z_5(k) - \beta|z_5(k)||z_4(k)|^{n-1} - \gamma z_5(k)|z_4(k)|^n, \\ \tilde{z}_5 &= -k_1 z_4(k) - k_2 z_1(k) + k_2 z_2(k) - (c_1 + c_2)z_5(k) + c_2 z_6(k). \end{aligned}$$

The observation vector in discrete form is given by,

$$y(k) = \begin{bmatrix} x_{m_1}(k) \\ \ddot{x}_{m_2}(k) \\ \ddot{x}_{m_3}(k) \end{bmatrix} = \begin{bmatrix} z_1(k) \\ \frac{1}{m_2}\tilde{z}_2(k) \\ \frac{1}{m_3}\tilde{z}_3(k) \end{bmatrix} + \begin{bmatrix} 0 \\ \frac{F_2(k)}{m_2} \\ \frac{F_3(k)}{m_3} \end{bmatrix} + \begin{bmatrix} v_1 \\ v_2 \\ v_3 \end{bmatrix} \quad (5.45)$$

where,

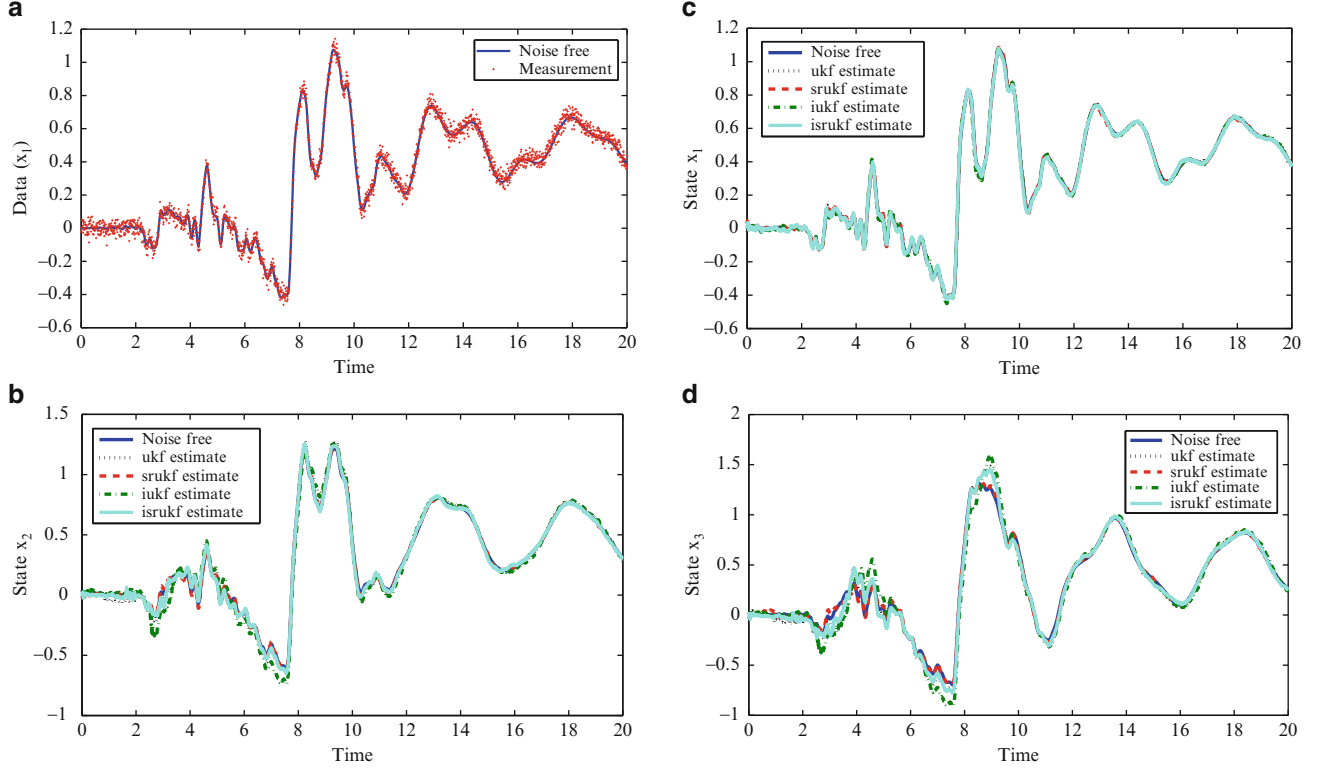
$$\begin{aligned} \tilde{z}_2 &= k_2 z_1(k) - (k_2 + k_3)z_2(k) + k_3 z_3(k) + c_2 z_5(k) - (c_2 + c_3(k)) \\ &\quad + z_6(k) + c_3 z_7(k), \\ \tilde{z}_3 &= k_3 z_2(k) - k_2 + k_3 z_3(k) + c_3 z_6(k) - c_3 z_7(k). \end{aligned}$$

#### 5.4.2 Generation of Dynamic Data

For dynamic data generation from the SHM system the model (5.46) [11] is used to simulate the responses of the state as functions of time by solving the differential equations (5.46) using fourth order Runge Kutta Integration.

**Table 5.1** SHM parameters and physical properties

Parameter	Value	Parameter	Value	Parameter	Value
$m_1$	1	$m_2$	1	$m_3$	1
$c_1$	0.25	$c_2$	0.25	$c_3$	0.25
$k_1$	9	$k_2$	9	$k_3$	9
$\beta$	2	$\gamma$	1	$n$	2

**Fig. 5.2** Estimation of state variables using various state estimation techniques (UKF, IUKF, SRUKF and ISRUKF)

$$\dot{z} = \begin{bmatrix} \dot{x}_1 \\ \dot{x}_2 \\ \dot{x}_3 \\ \dot{r}_1 \\ \ddot{x}_1 \\ \ddot{x}_2 \\ \ddot{x}_3 \end{bmatrix} = \begin{bmatrix} z_5 \\ z_6 \\ z_7 \\ z_5 - 2|z_5||z_4|^{2-1}z_4 - 1z_5|z_4|^2 \\ -9z_4 - 9z_1 + 9z_2 - 0.5z_5 + 0.25z_6 + \ddot{v}_g \\ -9z_1 - 18z_2 + 9z_3 - 0.25z_5 + 0.5z_6 + 0.25z_7 - \ddot{v}_g \\ 9z_2 - 9z_3 + 0.25z_6 - 0.25z_7 - \ddot{v}_g \end{bmatrix} \quad (5.46)$$

where the state variables  $x_1$ ,  $x_2$ ,  $x_3$  are displacements and  $r_1$  is the hysteretic Bouc Wen parameter.

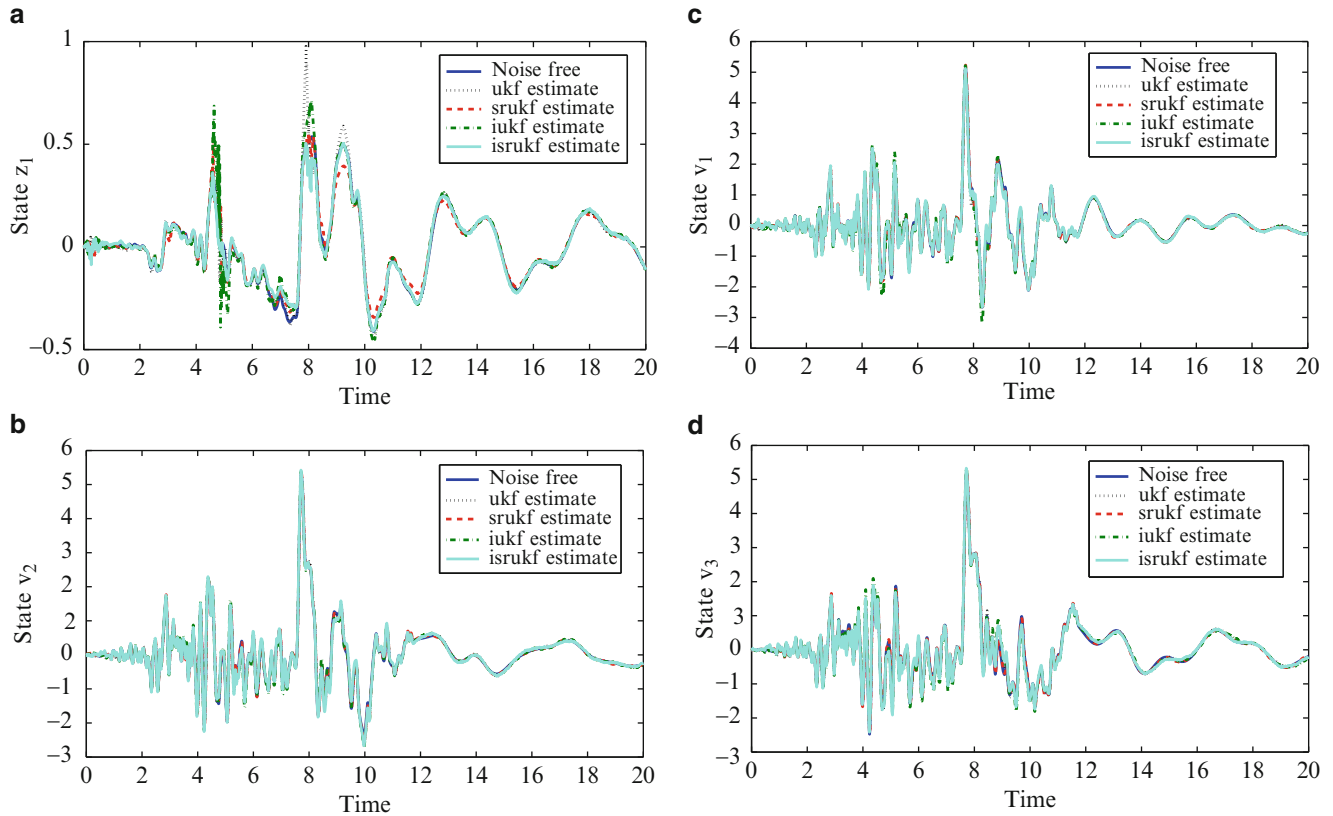
It must be noted that these simulated states are assumed to be noise free. They are contaminated with zero mean Gaussian errors. The SHM parameters as well as other physical properties are shown in Table 5.1. Figure 5.2a shows the changes in the state variable (displacement  $x_1$ ).

For all simulations, the following parameters are used. The sampling frequency of the 1994 Northridge earthquake acceleration data that was used as ground excitation  $\ddot{v}_g$ , is 100 Hz ( $T = 0.01$  s). The Northridge earthquake signal was filtered with a low frequency cutoff of 0.13 Hz and a high frequency cutoff of 30 Hz. A duration of 20 s of the earthquake record was adopted in this example. The number of sigma points is fixed to 33 for all the techniques ( $L = 16$ ). The process noise of 1% RMS noise-to-signal ratio was added. The observation noise level was of 4–7% root mean square (RMS) noise to signal ratio. All the simulations performed in this paper are implemented using MATLAB version 7.1, using an Intel Pentium CPU 3.4 GHz, 1.0 G of RAM PC.

### 5.4.3 Estimation of State Variables from Noisy Measurements

The purpose of this study was to compare the estimation accuracy of UKF, IUKF, SRUKF and ISRUKF when they are utilized to estimate the seven state variables of the three degree of freedom spring-mass-dashpot system model. Hence, we consider the state vector that we wish to estimate,  $z_k = x_k = [x_1 \ x_2 \ x_3 \ z_1 \ v_1 \ v_2 \ v_3]^T$ , and the model parameters,  $k_1, k_2, k_3, c_1, c_2, c_3, \beta, \gamma$ , and  $n$  are assumed to be known.

The simulation results for state estimations of seven state variables  $x_1, x_2, x_3, z_1, v_1, v_2$  and  $v_3$  using UKF, IUKF, SRUKF and ISRUKF are shown in Figs. 5.2a–d and 5.3a–d, respectively. Also, the performance comparison of the state estimation techniques in terms of RMSE are presented in Table 5.2 (Mean RMSE (MRMSE) for UKF = 0.085, MRMSE (SRUKF) = 0.059, MRMSE (IUKF) = 0.051, and MRMSE (ISRUKF) = 0.039 and execution times respectively. It is easily observed from Figs. 5.2 and 5.3 as well as Table 5.2 that UKF is outperformed by the alternative techniques, albeit at the expense of a larger computational time (see Table 5.2). The results also show that the ISRUKF achieves a better accuracy than the IUKF. Both ISRUKF and IUKF can provide improved accuracy over the UKF and SRUKF approaches.



**Fig. 5.3** Estimation of state variables using various state estimation techniques (UKF, IUKF, SRUKF and ISRUKF)

**Table 5.2** Comparison of state estimation techniques

Technique	$x_1$	$x_2$	$x_3$	$z_1$	$v_1$	$v_2$	$v_3$	Execution time
UKF	0.015	0.060	0.106	0.045	0.125	0.099	0.147	0.96 s
SRUKF	0.011	0.029	0.065	0.038	0.088	0.082	0.099	1.12 s
IUKF	0.010	0.028	0.042	0.043	0.085	0.073	0.076	1.44 s
ISRUKF	0.010	0.020	0.023	0.018	0.079	0.060	0.067	1.51 s

## 5.5 Conclusions

In this paper, the problem of nonlinear state estimations were addressed using the developed iterated square-root unscented Kalman filter. The ISRUKF method is compared to the unscented Kalman filter, the square-root unscented Kalman filter and the iterated unscented Kalman filter to estimate the state variables of the SHM. The comparative studies reveal that ISRUKF has better state accuracies than IUKF, and both of the methods can provide improved accuracy over UKF and SRUKF techniques. It must be emphasized that ISRUKF has a very good stability, and also a high state accuracy with low mean square errors.

**Acknowledgements** This work was made possible by NPRP grant NPRP08-148-3-051 from the Qatar National Research Fund (a member of Qatar Foundation). The statements made herein are solely the responsibility of the authors. Special thanks to Dr. Eleni Chatzi for letting use of the model for dynamic data generation for 3-DOF SHM system.

## References

1. Simon D (2006) Optimal state estimation: Kalman,  $H_{\infty}$ , and nonlinear approaches. Wiley, Hoboken
2. Grewal M, Andrews A (2008) Kalman filtering: theory and practice using MATLAB. Wiley, Hoboken
3. Julier S, Uhlmann J (1997) New extension of the kalman filter to nonlinear systems. Proc SPIE 3(1):182–193
4. Mansouri M, Nounou H, Nounou M, Datta AA (2012) Modeling of nonlinear biological phenomena modeled by s-systems using Bayesian method. In: Proceedings of the 2012 IEEE EMBS Conference on Biomedical Engineering and Sciences (IECBES), IEEE, pp 305–310
5. Romanenko A, Castro JA (2004) The unscented filter as an alternative to the ekf for nonlinear state estimation: a simulation case study. Comput Chem Eng 28(3):347–355
6. Zhu J, Zheng N, Yuan Z, Zhang Q, Zhang X, He Y (2009) A slam algorithm based on the central difference kalman filter. In: Proceedings of the 2009 IEEE intelligent vehicles symposium, IEEE, pp 123–128
7. Van Der Merwe R, Wan E (2001) The square-root unscented kalman filter for state and parameter-estimation. In: Proceedings of the IEEE International Conference on Acoustics, Speech, and Signal Processing, 2001 (ICASSP'01), vol 6. IEEE, Salt Lake City, pp 3461–3464
8. Wu P, Li X, Bo Y (2013) Iterated square root unscented kalman filter for maneuvering target tracking using tdoa measurements. Int J Control Automat Syst 11(4):761–767
9. Vajesta A, Schmitz R (1970) An experimental study of steady-state multiplicity and stability in an adiabatic stirred reactor. AIChE J 3:410–419
10. Zhan R, Wan J (2007) Iterated unscented kalman filter for passive target tracking. IEEE Trans Aerosp Electron Syst 43(3):1155–1163
11. Chatzi EN, Smyth AW (2013) Particle filter scheme with mutation for the estimation of time-invariant parameters in structural health monitoring applications. Struct Control Health Monit 20(7):1081–1095

# Chapter 6

## Hierarchical Bayesian Model Updating for Probabilistic Damage Identification

Iman Behmanesh, Babak Moaveni, Geert Lombaert, and Costas Papadimitriou

**Abstract** This paper presents the newly developed Hierarchical Bayesian model updating method for identification of civil structures. The proposed updating method is suitable for uncertainty quantification of model updating parameters, and probabilistic damage identification of the structural systems under changing environmental conditions. The Bayesian model updating frameworks in the literature have been successfully used for predicting the “parameter estimation uncertainty” of model parameters with the assumption that there is no underlying inherent variability in the updating parameters. However, different sources of uncertainty such as changing ambient temperature or wind speed, and loading conditions will introduce variability in structural mass and stiffness of civil structures. The Hierarchical Bayesian model updating is capable of predicting the underlying variability of updating parameters in addition to their estimation uncertainty. This approach is applied for uncertainty quantification and damage identification of a three-story shear building model. The proposed updating framework is finally implemented for uncertainty quantification of model updating results based on experimentally measured data of a footbridge which is exposed to severe environmental conditions. In this application, the stiffness parameter of the model is estimated as a function of measured temperature through the Hierarchical framework.

**Keywords** Hierarchical Bayesian model updating • Uncertainty quantification • Damage identification • Effects of changing ambient temperature on model updating

### 6.1 Introduction

The existence, location, and severity of damage can be potentially predicted from vibration measurements (e.g., modal data) and using Finite Element (FE) model updating techniques [1]. Readers are referred to [2–4] for detailed reviews on vibration-based model updating and damage identification of structural systems. The FE model updating methods can be divided into two broad categories of deterministic and probabilistic approaches. The former is well established in the literature [1, 2, 5], with several successful applications to civil structures [6–11]. However, the quality of structural identification results from the deterministic FE model updating methods can be significantly affected by first, the accuracy and informativeness of measured vibration data and second, the accuracy of the initial FE model. Several studies in the past have revealed the sensitivity of identified modal data to measurement noise, estimation errors, and most importantly changing environmental conditions [12–16]. Also, the structural FE models are usually associated with many idealizations and simplifications due to complexity and size of the civil structures. These modeling errors bring another source of uncertainty into the identification process [4, 17, 18]. Therefore, probabilistic FE model updating methods such as Bayesian methods have become popular to address the underlying structural uncertainties. However, although these Bayesian methods [19–21] can successfully predict the parameter estimation uncertainties, they do not consider the inherent variability of structural parameters (e.g., structural stiffness or mass) due to different sources of uncertainties such as ambient temperature, temperature gradient, rain, snow, wind speed, and traffic load.

---

I. Behmanesh • B. Moaveni (✉)

Department of Civil and Environmental Engineering, Tufts University, Medford, MA, USA  
e-mail: [babak.moaveni@tufts.edu](mailto:babak.moaveni@tufts.edu)

G. Lombaert

Department of Civil Engineering, KU Leuven, Heverlee, Belgium

C. Papadimitriou

Department of Mechanical Engineering, University of Thessaly, Volos, Greece

In the past few years, the Bayesian FE model updating methods have been extended for structural identification and reliability problems [21–30]. There are also a few studies that applied this method on full-scale civil structures [31–33]. Based on the Bayes theorem the posterior (updated) probability distribution function (PDF) of the updating structural parameters  $\boldsymbol{\theta}$ , and the model error parameters  $\boldsymbol{\sigma}^2$ , given a single data set  $\mathbf{D}$  can be expressed as:

$$p(\boldsymbol{\theta}, \boldsymbol{\sigma}^2 | \mathbf{D}) \propto p(\mathbf{D} | \boldsymbol{\theta}, \boldsymbol{\sigma}^2) p(\boldsymbol{\theta}, \boldsymbol{\sigma}^2) \quad (6.1)$$

where  $p(\mathbf{D} | \boldsymbol{\theta}, \boldsymbol{\sigma}^2)$  is the so-called likelihood function and  $p(\boldsymbol{\theta}, \boldsymbol{\sigma}^2)$  is the prior probability. In this study the measured data  $\mathbf{D}$  is composed of identified system eigenvalues (squares of circular natural frequencies) and mode shapes. By assuming zero-mean, uncorrelated Gaussian distributions for eigenvalue and mode shape errors the likelihood function can be written as the following if  $N_t$  number of independent data sets is available:

$$p(\tilde{\boldsymbol{\lambda}}_1 \dots \tilde{\boldsymbol{\lambda}}_{N_t}, \tilde{\boldsymbol{\Phi}}_1 \dots \tilde{\boldsymbol{\Phi}}_{N_t} | \boldsymbol{\theta}, \boldsymbol{\sigma}) = \prod_{t=1}^{N_t} \prod_{m=1}^{N_m} N(\tilde{\boldsymbol{\lambda}}_{tm} | \boldsymbol{\lambda}_m(\boldsymbol{\theta}), \boldsymbol{\sigma}_{\lambda_m}^2) N(\tilde{\boldsymbol{\Phi}}_{tm} | \boldsymbol{\Phi}_m(\boldsymbol{\theta}), \boldsymbol{\Sigma}_{\boldsymbol{\Phi}_m}) \quad (6.2)$$

The identified eigenvalues and mode shapes are represented by  $\tilde{\boldsymbol{\lambda}}$  and  $\tilde{\boldsymbol{\Phi}}$ , respectively. Also  $\boldsymbol{\lambda}(\boldsymbol{\theta})$  and  $\boldsymbol{\Phi}(\boldsymbol{\theta})$  denote the model calculated eigenvalues and unit length mode shapes. Note that the model calculated mode shapes  $\boldsymbol{\Phi}(\boldsymbol{\theta})$  contain only the measured DOFs. In this equation,  $N_m$  is the total number of identified modes,  $N(\tilde{\boldsymbol{\lambda}}_{tm} | \boldsymbol{\lambda}_m(\boldsymbol{\theta}), \boldsymbol{\sigma}_{\lambda_m}^2)$  is the value of a Gaussian PDF with the mean  $\boldsymbol{\lambda}_m(\boldsymbol{\theta})$  and the standard deviation  $\boldsymbol{\sigma}_{\lambda_m}$  at  $\tilde{\boldsymbol{\lambda}}_{tm}$ , and similarly  $N(\tilde{\boldsymbol{\Phi}}_{tm} | \boldsymbol{\Phi}_m(\boldsymbol{\theta}), \boldsymbol{\Sigma}_{\boldsymbol{\Phi}_m})$  is the vector of a multidimensional Gaussian PDF with the mean  $\boldsymbol{\Phi}_m(\boldsymbol{\theta})$  and the covariance matrix  $\boldsymbol{\Sigma}_{\boldsymbol{\Phi}_m}$  at  $\tilde{\boldsymbol{\Phi}}_{tm}$ . The sub-index  $tm$  indicates the identified modal data of mode  $m$  from test  $t$ . The standard deviations  $\boldsymbol{\sigma}_{\lambda}$  and the covariance matrix  $\boldsymbol{\Sigma}_{\boldsymbol{\Phi}}$  can be either updated (as updating parameters) or directly calculated based of the identified  $N_t$  data sets.

The posterior probability distributions of the updating parameters can be estimated either by generating Markov Chain Monte Carlo (MCMC) [22, 23, 26, 33, 34] or by approximating the posterior PDF through asymptotic approximations [21, 24, 25, 27, 31]. If the former is used, the distribution of the generated samples provides a measure of parameter estimation uncertainties, and if the latter is used the covariance matrix of updating parameters can be estimated as the inverse Hessian of  $-\text{Log}(p(\boldsymbol{\theta}, \boldsymbol{\sigma}^2 | \mathbf{D}))$  at the optimum of the updating parameters. However, these estimated uncertainties will decrease with increasing number of data sets [20, 33, 35], referred to as “noise mitigation” in [21]. This reduction will not be observed when the uncertainties of the updating structural parameters are estimated by a frequentist approach; the estimated uncertainties converge with increasing the number of data. In frequentist approach, the distributions of updating parameters are estimated from the deterministically identified parameters corresponding to different test data [15, 36, 37]. This inconsistency is due to the estimation of conceptually different uncertainties in the two approaches. In the Bayesian approach, all uncertainties are assumed to be reducible (epistemic uncertainty [38]), but in the frequentist framework the variations of the modal data are considered to be due to inherent variability of the structural properties (aleatory uncertainty [38]).

It is believed that the variability of the identified modal parameters is mainly due to changes in physical structural properties such as mass, damping, stiffness, or boundary conditions [12–16]. These changes will result in different modal parameters from test to test. Therefore, it is desired to predict both the inherent variability and the parameter estimation uncertainties of the updating parameters. In this paper, we implement the concept of Hierarchical Bayesian modeling [39, 40] to propose a new probabilistic model updating technique for model calibration, uncertainty quantification, and damage identification of structural systems. In the proposed framework, both the parameter estimation uncertainties and the inherent variability of updating structural parameters due to for example changing environmental conditions can be predicted.

## 6.2 Hierarchical Bayesian FE Model Updating

Hierarchical models are powerful and have been used in many disciplines [39, 41], but very few can be found in structural engineering applications [42]. In the proposed Hierarchical Bayesian model updating process, first a probability distribution is assumed for the structural parameters; a truncated Gaussian distribution (no negative stiffness) is assumed in this study, i.e.,  $\boldsymbol{\theta} \propto N(\boldsymbol{\mu}_{\boldsymbol{\theta}}, \boldsymbol{\Sigma}_{\boldsymbol{\theta}})$ . Based on the error functions in Eqs. (6.3) and (6.4), the posterior probability distribution of updating parameters, including  $\boldsymbol{\theta}_t$ ,  $\boldsymbol{\mu}_{\boldsymbol{\theta}}$ ,  $\boldsymbol{\Sigma}_{\boldsymbol{\theta}}$ , and  $\boldsymbol{\sigma}^2 = \{\boldsymbol{\sigma}_{\lambda}^2, \boldsymbol{\Sigma}_{\boldsymbol{\Phi}}\}$  can be expressed as in Eq. (6.5) for a single data set from test  $t$ .

$$\tilde{\lambda}_{tm} - \lambda_m(\theta_t) = e_{\lambda_{tm}} \sim N(0, \sigma_{\lambda_m}^2) \quad (6.3)$$

$$\tilde{\Phi}_{tm} - a_m \Phi_m(\theta_t) = \mathbf{e}_{\Phi_{tm}} \sim N(\mathbf{0}, \Sigma_{\Phi_m}) \quad (6.4)$$

$$p(\boldsymbol{\mu}_\theta, \Sigma_\theta, \theta_t, \sigma^2 | \tilde{\lambda}_t, \tilde{\Phi}_t) \propto \prod_{m=1}^{N_m} p(\tilde{\lambda}_{tm}, \tilde{\Phi}_{tm} | \theta_t, \sigma^2) p(\theta_t | \boldsymbol{\mu}_\theta, \Sigma_\theta) p(\boldsymbol{\mu}_\theta) p(\Sigma_\theta) p(\sigma^2) \quad (6.5)$$

The sub-index  $t$  for the structural parameters and the identified modal data in Eqs. (6.3) and (6.4) specifies the values of updating structural parameter during the collection of data set  $t$ . The prior probabilities are specified in two hierarchical stages of  $p(\theta_t | \boldsymbol{\mu}_\theta, \Sigma_\theta)$  and hyper-prior probability distributions  $p(\boldsymbol{\mu}_\theta)p(\Sigma_\theta)p(\sigma^2)$ . In the case of having  $N_t$  independent data sets, the posterior can be stated as:

$$p(\boldsymbol{\mu}_\theta, \Sigma_\theta, \Theta, \sigma^2 | \tilde{\lambda}, \tilde{\Phi}) \propto \prod_{t=1}^{N_t} \prod_{m=1}^{N_m} p(\tilde{\lambda}_{tm}, \tilde{\Phi}_{tm} | \theta_t, \sigma^2) p(\theta_t | \boldsymbol{\mu}_\theta, \Sigma_\theta) p(\boldsymbol{\mu}_\theta) p(\Sigma_\theta) p(\sigma^2) \quad (6.6)$$

where  $\Theta = \{\theta_1, \dots, \theta_t, \dots, \theta_{N_t}\}$ .

In this approach  $\sigma^2$  reflects a measure of goodness of fit for the updated model, where zero values would indicate a perfect match between the model and the data. Theoretically, all the components of  $\sigma^2$  including  $N_m$  eigenvalue and  $N_m \times N_s$  mode shape errors can be considered as an updating parameter. However, for computational efficiency the following assumption is used in this study:

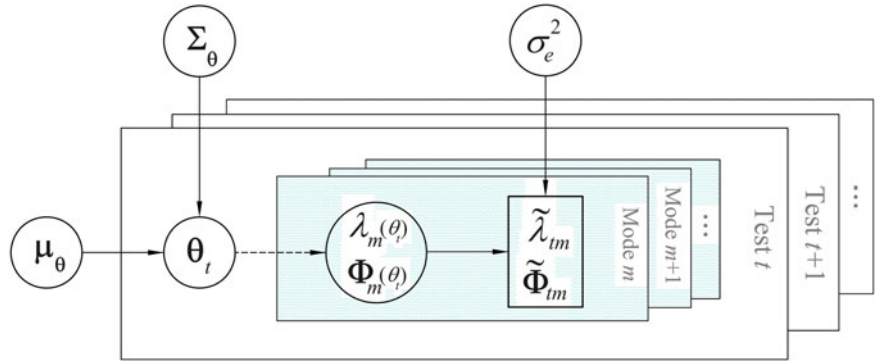
$$\sigma_{\lambda_m} = \bar{\lambda}_m \sigma_e \quad m = 1, 2, \dots, N_m \quad (6.7)$$

$$\Sigma_{\Phi_m} = w \sigma_e^2 \mathbf{I}(N_s) \quad (6.8)$$

where  $N_s$  is number of mode shape components (number of sensors),  $\mathbf{I}$  is the identity matrix, and  $w$  is a weight factor [25]. In Eq. (6.8), no correlation between the mode shape components are considered; more information on the effects of mode shape component correlations can be found in [43]. The graphical representation of the proposed Hierarchical Bayesian modeling is shown in Fig. 6.1.

Depending on the selection of updating structural parameters, it is often reasonable to assume no correlation between these parameters and therefore the covariance matrix can be represented as a diagonal matrix  $\Sigma_\theta = \text{Diag}(\sigma_{\theta_1}^2, \sigma_{\theta_2}^2, \dots, \sigma_{\theta_p}^2, \dots, \sigma_{\theta_{N_p}}^2)$  with  $N_p$  = number of updating structural parameters in  $\theta$ . This method can also be extended for correlated updating structural parameters. A Gamma probability distribution is assumed for the prior probability of the  $\sigma_{\theta_p}^{-2}$ :

$$p(\sigma_{\theta_p}^{-2}) = \text{Gamma}(\alpha, \beta) \quad (6.9)$$



**Fig. 6.1** Graphical representation for the proposed Hierarchical Bayesian modeling



where  $\alpha$  and  $\beta$  can be taken identically for all the updating structural parameters. By assuming uninformative priors for  $\boldsymbol{\mu}_\theta$  and  $\sigma_e^2$ , the joint posterior probability distribution of all the updating parameters can be stated as:

$$p\left(\boldsymbol{\Theta}, \boldsymbol{\mu}_\theta, \boldsymbol{\Sigma}_\theta, \sigma_e^2 \mid \tilde{\boldsymbol{\lambda}}, \tilde{\boldsymbol{\Phi}}\right) \propto \sigma_e^{-N_t N_m (N_s + 1)} \prod_{p=1}^{N_p} \left(\sigma_{\theta_p}^{-2}\right)^{\frac{N_t}{2} + \alpha - 1} \exp\left(-\frac{\sigma_e^{-2}}{2} \sum_{t=1}^{N_t} \left\{J\left(\boldsymbol{\theta}_t, \tilde{\boldsymbol{\lambda}}_t, \tilde{\boldsymbol{\Phi}}_t\right)\right\} - \sum_{p=1}^{N_p} \frac{\sigma_{\theta_p}^{-2}}{2} \left\{\sum_{t=1}^{N_t} \left(\theta_{tp} - \mu_{\theta_p}\right)^2 + 2/\beta\right\}\right) \quad (6.10)$$

where

$$J\left(\boldsymbol{\theta}_t, \tilde{\boldsymbol{\lambda}}_t, \tilde{\boldsymbol{\Phi}}_t\right) = \sum_{m=1}^{N_m} \left\{ \tilde{\lambda}_{tm}^{-2} \left(\tilde{\lambda}_{tm} - \lambda_m\left(\boldsymbol{\theta}_t\right)\right)^2 + w^{-1} \left(\tilde{\boldsymbol{\Phi}}_{tm} - a_{tm} \boldsymbol{\Phi}_m\left(\boldsymbol{\theta}_t\right)\right)^T \left(\tilde{\boldsymbol{\Phi}}_{tm} - a_{tm} \boldsymbol{\Phi}_m\left(\boldsymbol{\theta}_t\right)\right) \right\} \quad (6.11)$$

In Eq. (6.11),  $a_{tm}$  is the mode shape scaling factor. The most common technique to solve Eq. (6.10) is the Gibbs Sampler [39, 40].

In the Gibbs sampling techniques, samples are generated from the full conditional probability distribution of each parameter until convergence is reached. Equations (6.12), (6.13), (6.14) and (6.15) present the full conditional posterior probability distributions of all the updating parameters.

$$p\left(\boldsymbol{\theta}_t \mid \boldsymbol{\mu}_\theta, \boldsymbol{\Sigma}_\theta, \sigma_e^2, \tilde{\boldsymbol{\lambda}}, \tilde{\boldsymbol{\Phi}}\right) \propto \exp\left(-\sigma_e^{-2} J\left(\boldsymbol{\theta}_t, \tilde{\boldsymbol{\lambda}}_t, \tilde{\boldsymbol{\Phi}}_t\right) - \sum_{p=1}^{N_p} \sigma_{\theta_p}^{-2} \left(\theta_{tp} - \mu_{\theta_p}\right)^2\right), \quad t = 1, \dots, N_t \quad (6.12)$$

$$p\left(\boldsymbol{\mu}_\theta \mid \boldsymbol{\Theta}, \boldsymbol{\Sigma}_\theta, \sigma_e^2, \tilde{\boldsymbol{\lambda}}, \tilde{\boldsymbol{\Phi}}\right) \sim N\left(\boldsymbol{\mu}_\theta \mid \bar{\boldsymbol{\theta}}_t, \boldsymbol{\Sigma}_\theta / N_t\right) \quad (6.13)$$

$$p\left(\sigma_e^{-2} \mid \boldsymbol{\Theta}, \boldsymbol{\mu}_\theta, \boldsymbol{\Sigma}_\theta, \tilde{\boldsymbol{\lambda}}, \tilde{\boldsymbol{\Phi}}\right) \sim \text{Gamma}\left(\sigma_e^{-2} \mid \left(N_t N_m (N_s + 1) / 2 + 1\right), 2 \left(\sum_{t=1}^{N_t} J\left(\boldsymbol{\theta}_t, \tilde{\boldsymbol{\lambda}}_t, \tilde{\boldsymbol{\Phi}}_t\right)\right)^{-1}\right) \quad (6.14)$$

$$p\left(\sigma_{\theta_p}^{-2} \mid \boldsymbol{\Theta}, \boldsymbol{\mu}_\theta, \sigma_e^2, \tilde{\boldsymbol{\lambda}}, \tilde{\boldsymbol{\Phi}}\right) \sim \text{Gamma}\left(\sigma_{\theta_p}^{-2} \mid \left(N_t / 2 + \alpha\right), \left(1/\beta + \frac{1}{2} \sigma_{\theta_p}^{-2} \sum_{t=1}^{N_t} \left(\theta_{tp} - \mu_{\theta_p}\right)^2\right)^{-1}\right) \quad (6.15)$$

According to Eqs. (6.12), (6.13), (6.14) and (6.15), the full conditional probability distributions of all the updating parameters except  $\boldsymbol{\theta}_t$  are either Gaussian or Gamma distributions. By generating adequate number of samples, the posterior joint probability distribution of updating parameters can be accurately estimated. Generating samples from Eqs. (6.13), (6.14) and (6.15) is not challenging due to their known distribution functions; however, generating samples for the conditional probability distributions of  $\boldsymbol{\theta}_t$ , Eq. (6.12), requires using advanced sampling techniques such as adaptive Metropolis-Hastings [22, 44], or Translational Markov Chain Monte Carlo algorithm [26, 34]. This step can become very time-consuming; therefore parallel computing can be implemented as the  $\boldsymbol{\theta}_t$  samples can be generated independently for each test data. Alternatively, Laplace asymptotic approximation can be used to approximate the conditional probability distributions of  $\boldsymbol{\theta}_t$  in Eq. (6.12) as a Gaussian distribution to simplify the sampling process. The standard deviations of the generated samples reflect the ‘‘parameter estimation uncertainties’’ which will be reduced by increasing the number of data sets used in the updating process (except for  $\boldsymbol{\theta}_t$  parameters).

The proposed Hierarchical Bayesian updating framework is extended to be used for probabilistic damage identification of civil structures. In Eq. (6.16), Damage Factor (DF) is defined as the relative loss of stiffness in parameter  $p$  from the reference state to the damaged state:

$$DF = 1 - \theta_p^c / \theta_p^r \quad (6.16)$$

where superscript  $r$  refers to the reference state and superscript  $c$  refers to the current state of the structure. The probability of damage exceedance from a given damage factor  $df$  can be expressed as:

$$\begin{aligned}
 P \left[ \theta_p^r - \theta_p^c \geq df \times \theta_p^r \mid \mathbf{D}^r, \mathbf{D}^c \right] &= 1 - CDF \left( df \times \theta_p^r \mid \mu_{\theta_p}^r - \mu_{\theta_p}^c, \sqrt{(\sigma_{\theta_p}^r)^2 + (\sigma_{\theta_p}^c)^2} \right) \\
 &= \frac{1}{2} - \frac{1}{2} \operatorname{erf} \left( \frac{df \times \theta_p^r - (\mu_{\theta_p}^r - \mu_{\theta_p}^c)}{\sqrt{2 \left( (\sigma_{\theta_p}^r)^2 + (\sigma_{\theta_p}^c)^2 \right)}} \right)
 \end{aligned} \tag{6.17}$$

where  $CDF$  is the cumulative Gaussian distribution function, and  $\operatorname{erf}$  is Gauss Error Function.

### 6.3 Application to a Numerical Case Study

The performance of the proposed Hierarchical procedure is numerically evaluated by means of a three-story shear building model. The mass of each story is set to 1.2 metric ton, and the stiffness of stories one to three are considered as random variables with truncated Gaussian distributions of  $N(2,000 \text{ kN/m}, 100^2 \text{ kN}^2/\text{m}^2)$ ,  $N(1,000 \text{ kN/m}, 50^2 \text{ kN}^2/\text{m}^2)$ , and  $N(1,000 \text{ kN/m}, 20^2 \text{ kN}^2/\text{m}^2)$ , respectively. The natural frequencies of the building at the mean values of story stiffnesses are 2.378, 6.498, and 8.876 Hz. In Sect. 6.3.1, the performance of the proposed framework is evaluated for parameter estimation and uncertainty quantification, and the results are compared with those of the classical Bayesian model updating framework. In Sect. 6.3.2, the proposed framework is applied for probabilistic damage identification where the estimated variability/uncertainty of updating structural parameters is propagated in the damage identification results.

For comparison purposes, the posterior distributions of the updating structural parameters are also estimated based on the Bayesian framework of [21, 23] and they are shown in Fig. 6.3. The Adaptive Metropolis-Hastings algorithm of [44] is used to sample the posterior probability distributions of updating parameters. As it can be observed, although the estimated MAP values are in good agreement with the true mean values and those estimated from Hierarchical framework, the estimated uncertainties are significantly underestimated and always decrease with addition of data. Plus, unlike the Hierarchical approach, there is no parameter in classical Bayesian framework to represent the goodness of fit. As discussed in Sect. 6.2, the error standard deviations in classical framework are either directly calculated from the collected measured data or updated. In the former case, this parameter represent the variability of the measured modal data, and in the latter case, the estimated values contain both the modeling errors and the variability of structural parameters. This comparison highlights the benefits of the proposed Hierarchical Bayesian model updating framework.

#### 6.3.1 Performance Evaluation of the Hierarchical Bayesian FE Model Updating

400 sets of natural frequencies and mode shapes are simulated by sampling the story stiffness values from their considered probability distributions. The coefficients of variation (standard deviation divided by the mean) for the generated natural frequencies are 1.53%, 1.08%, and 1.52% for mode 1 to 3 respectively. These generated modal data will be used as the measured data in the model updating processes.

Four different subsets of data with  $n_t = \{5, 20, 50, \text{ and } 400\}$  data set numbers are used for model updating. Table 6.1 provides the updating results which include the MAP estimates of the mean and standard deviation of the three updating

**Table 6.1** MAP estimates from the Hierarchical framework with no modeling errors

	$\theta_1$		$\theta_2$		$\theta_3$		$\operatorname{Log}(\sigma_e)$
	Mean ( $\hat{\mu}_\theta$ )	STD ( $\hat{\sigma}_\theta$ )	Mean ( $\hat{\mu}_\theta$ )	STD ( $\hat{\sigma}_\theta$ )	Mean ( $\hat{\mu}_\theta$ )	STD ( $\hat{\sigma}_\theta$ )	
<i>Exact</i>	2,000	100	1,000	50	1,000	20	–
$n_t = 5$	2,008.6	86.3	1,021.0	44.9	992.0	8.0	–19.8
$n_t = 20$	1,988.6	106.2	1,009.2	47.7	999.9	19.7	–19.8
$n_t = 50$	2,000.0	99.0	1,000.0	49.5	1,000.0	19.8	–19.9
$n_t = 400$	1,999.7	100.1	1,004.1	49.3	999.2	19.5	–19.9

structural parameters and the error standard deviation  $\sigma_e$  for all the four considered data subset numbers. The parameters are accurately estimated except for the case with  $n_t = 5$ , where insufficient number of data sets is used in the updating process. The statistics (means and standard deviations) of the structural parameters are also estimated based on frequentist approach and they match perfectly to the results of Table 6.1. Therefore, in the absence of modeling errors the Hierarchical and frequentist approaches provide identical estimations. In the presence of modeling errors however, the two approaches provide similar, but not identical results (not shown here for brevity). As expected, the estimated standard deviations of updating structural parameters are converged by increasing number of data sets. The standard deviation of error functions is also provided in the last column of Table 6.1, which is very close to zero, indicating a good match between the data and the model. Figure 6.2 shows the *most probable* posterior PDFs of the three stiffness updating parameters. The term most probable is referring to the fact that the posterior PDFs of Fig. 6.2 are based on most probable (MAP estimates) means and standard deviations of the updating parameters and their estimation uncertainties are ignored, i.e.,  $N(\hat{\mu}_{\theta_p}, \hat{\sigma}_{\theta_p}^2)$ .

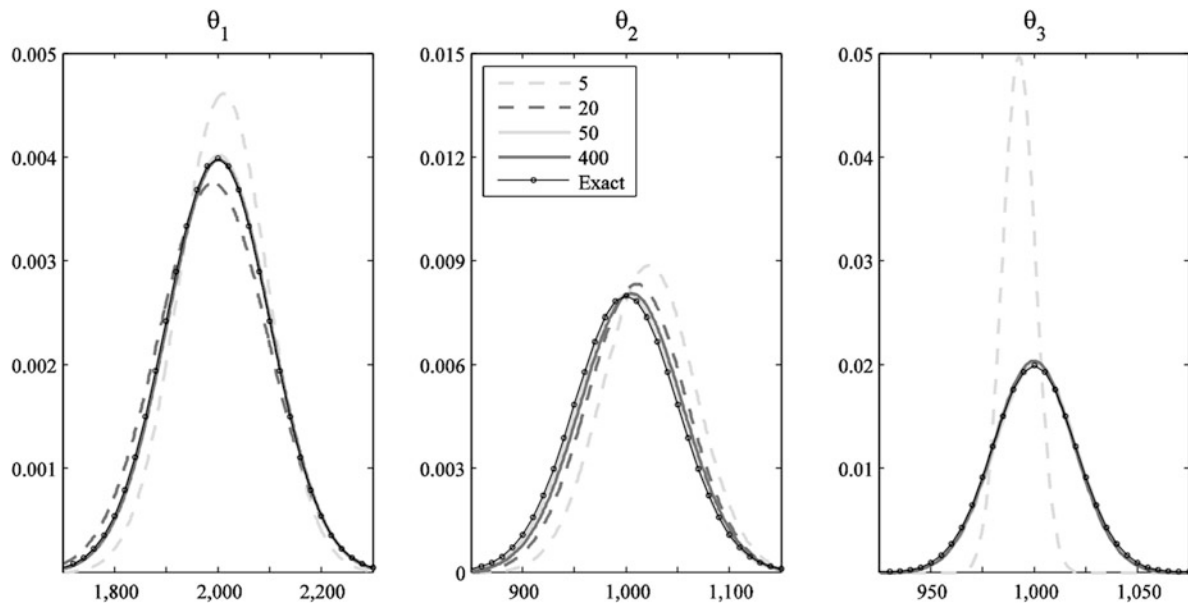


Fig. 6.2 Most probable posterior PDFs using Hierarchical Bayesian framework

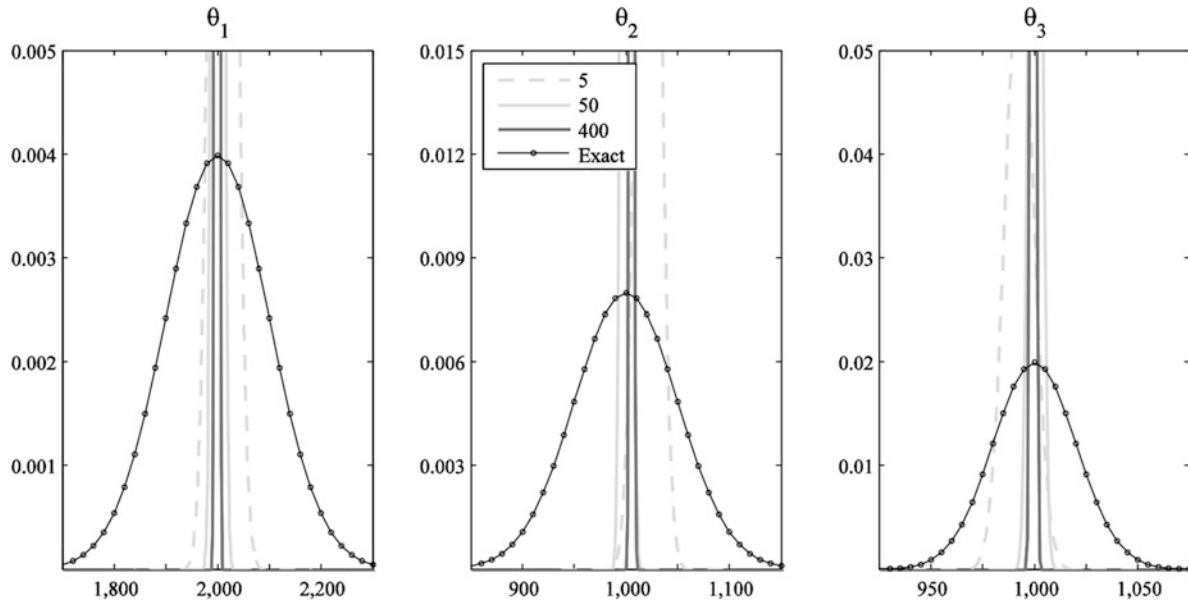


Fig. 6.3 Posterior PDFs from the classical Bayesian framework

### 6.3.2 Hierarchical Bayesian FE Model Updating for Damage Identification

Three collections of measured data are generated with each collection representing a specific damage scenario and including 400 data sets. The first collection is considered as the reference data, the second collection of 400 data sets is generated from the structure in the undamaged state to evaluate the performance of the proposed method in the presence of variability in the modal data at the structural undamaged state. The third collection is generated in the damaged state. Damage is considered to be 5% stiffness loss of the first story, so that the mean of the first story stiffness is reduced to 1,900 [kN/m] while its standard deviation is kept the same as in the undamaged state. At the mean values of story stiffnesses, the natural frequencies of the structure are 2.357, 6.439, and 8.809 Hz. The most reduction in the natural frequencies is observed for mode 1 and found to be only 0.92%. This reduction is within the variation range of natural frequencies in the undamaged state, which makes the damage identification challenging. This scenario is often observed in operational civil structures where the variations of modal data due to damage might be within the variation ranges of the data due to changing ambient/environmental conditions [12–16].

#### 6.3.2.1 Damage Identification from Undamaged State Data (Collection 2)

As discussed previously, the parameter estimation uncertainties can be obtained from the Gibbs samples. As an example case, the posterior probability distributions of the mean and standard deviation of the first story stiffness is shown in Fig. 6.4 for three different cases of  $n_r$ . It can be observed that the estimation uncertainties will be reduced by increasing number of data sets. These estimation uncertainties will propagate to the damage exceedance probabilities of Eq. (6.17). Therefore, the probability of damage exceedance will be associated to estimation uncertainties as well. Damage exceedance probabilities are estimated and shown in Fig. 6.5 for a range of given damage factors  $[-0.10$  to  $0.15]$  and based on 50 data sets. In this plot, darker color shows higher probability density. Vertical lines correspond to probability distribution of damage exceedance probability at a given damage factor, i.e., PDF of  $P[DF > df]$ . The horizontal lines correspond to probability distribution of damage at a given confidence level. In Fig. 6.5, the PDF of damage exceeding 4%,  $P[DF > 0.04]$  and the PDF of damage at a 50% confidence level are shown. As expected, the estimation uncertainties are reduced by increasing the number of data, however, damage is still estimated probabilistically due to inherent variability of structural parameters [38].

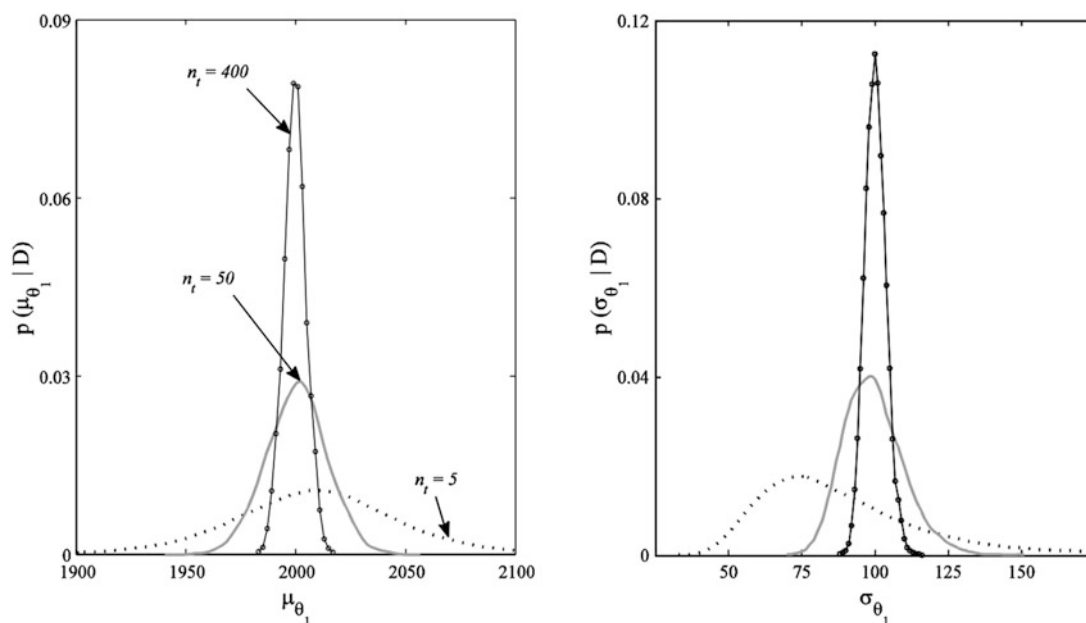
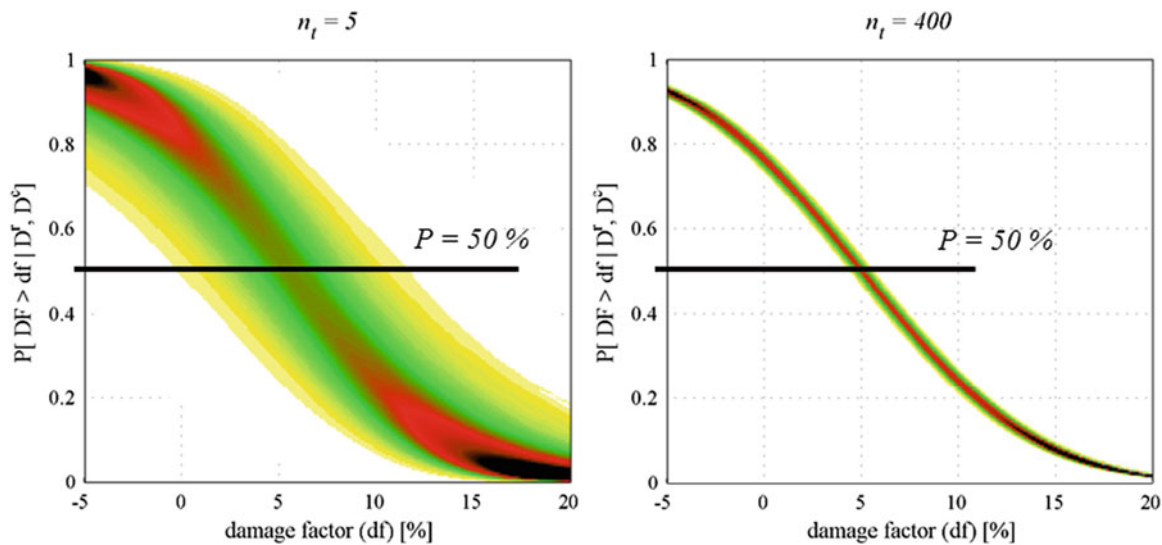
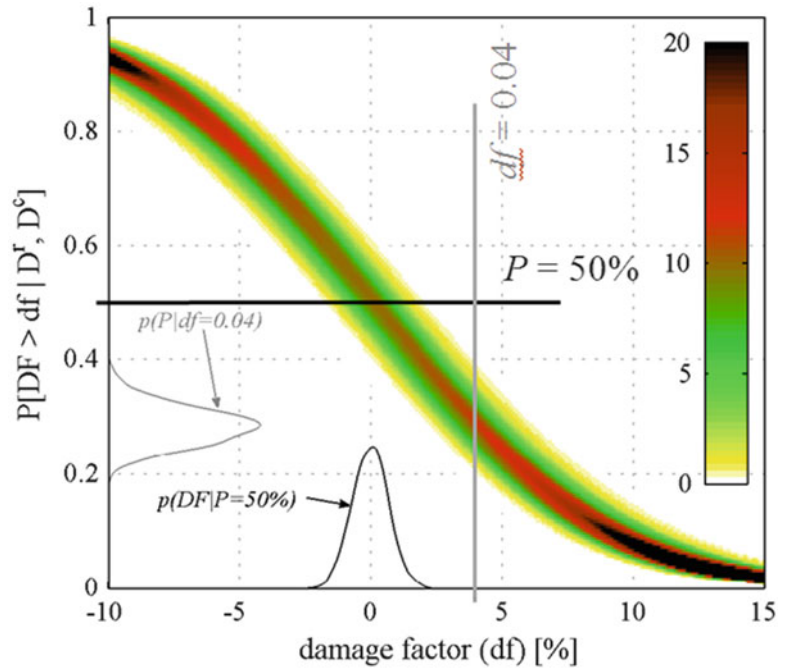


Fig. 6.4 Parameter estimation uncertainties for the mean and standard deviation of  $\theta_1$  in the undamaged state

**Fig. 6.5** PDF of damage exceedance probabilities for damage factor range of  $[-0.10, 0.15]$  in the first story using 50 data sets



**Fig. 6.6** Probability of damage given the baseline data and the data in the damaged state

### 6.3.2.2 Damage Identification from Damaged State Data (Collection 3)

Damage identification is performed based on the damaged state data: the third collection. The PDF of damage exceedance are shown in Fig. 6.6 for two cases of  $n_t = \{5 \text{ and } 400\}$ .

Unlike the results of Fig. 6.5, the most probable damage factor (MAP of  $p(DF | P = 50\%)$ ) is very close to the true damage factor 5%. The predictions become more accurate by adding more data sets. These results highlight the fact the damage can be identified even when the changes of the modal data due to damage are within the variation range of modal data due to environmental/ambient conditions provided that adequate number of measured data sets is available. It should be mentioned that damage identification still can be performed based on few number of data sets; however, the corresponding large estimation uncertainties should be included for any decision making or detection analysis. The proposed framework is well suited for damage assessment of operational civil structures where changing environmental conditions can significantly affect the identified natural frequencies and mode shapes.

## 6.4 Application to the Dowling Hall Footbridge Using Real Measured Data

The Dowling Hall Bridge is a pedestrian bridge located at Tufts University campus and is equipped with a continuous monitoring system [11, 16, 33]. The monitoring system collects 5 min of ambient vibration data every hour, and the modal data (natural frequencies, mode shapes, and damping ratios) are extracted from each collected data set. It has been observed that the identified natural frequencies of the footbridge have a strong correlation with the measured ambient temperature. Figure 6.7 shows the identified natural frequencies of five vibration modes, collected from January 2010 to March 2012, versus the recorded ambient temperature during collection of each data set. The frequencies increase at lower temperatures especially at temperature below freezing point. This can be due to an increase in the elastic Young's modulus of bridge deck after the moist inside concrete freezes. Other than ambient temperature, other factors can affect the identified natural frequencies from test to test such as the live load (weight of the pedestrians on the bridge), rain, wind speed, and identification errors. In this study, only the ambient temperature measurements will be used for model calibration of the Dowling Hall footbridge through the proposed Hierarchical Bayesian updating process. The collected data from the Dowling Hall bridge is a good example of Hierarchical data in structural systems as each data set was collected at a different environmental condition and can correspond to different structural mass and stiffness properties.

The updating structural parameter  $\theta$  is defined as a modification factor for elastic Young's modulus of concrete deck, i.e.,  $E = \theta E_0$  where  $E_0$  is the initial value considered as 26,752 [N/mm<sup>2</sup>]. The probability distribution of  $\theta$  is assumed to follow a truncated Gaussian (no negative value) distribution with temperature dependent mean  $\mu_{\theta}(T_t)$ , and an independent variance  $\sigma_{\theta}^2$ , i.e.,  $\theta(T_t) \sim N(\mu_{\theta}(T_t), \sigma_{\theta}^2)$ . The temperature model is defined as:

$$\mu_{\theta}(T_t) = Q + S \times T_t + R \times \left(1 - \text{erf}\left(\frac{T_t - \hat{T}}{\tau}\right)\right) \quad (6.18)$$

where  $T_t$  is the recorded temperature during test  $t$ ,  $\text{erf}$  denotes the value of Gaussian cumulative distribution function, and  $Q$ ,  $R$ ,  $\hat{T}$ ,  $\tau$ ,  $S$ ,  $\sigma_{\theta}^2$ ,  $\sigma_e^2$  are updating parameters to be estimated. The first two terms in Eq. (6.18) represent the linear trend observed at high temperature ranges. The third term captures the trend at lower temperatures (close or below freezing point) with transition temperatures  $\hat{T}$  and  $\tau$  characterizing the transition range. This temperature model stems from the observed trend of natural frequencies and ambient temperature shown in Fig. 6.7. The inherent uncertainty in the estimated elastic Young's modulus ( $\sigma_{\theta}^2$ ) will then be due to the mentioned sources of uncertainties except ambient temperature which is explicitly considered in this framework. The error functions can be written as in Eqs. (6.3) and (6.4) except that the parameters  $\theta_t$  should be replaced by  $\theta_t(T_t)$ . Assumptions stated in Eqs. (6.7) and (6.8) are also considered in this example. The graphical representation of the probabilistic model is shown in Fig. 6.8.

5000 Gibbs samples are generated and Fig. 6.9 shows the samples for four selected parameters, including  $\theta_1$ ,  $R$ ,  $Q$ , and  $\sigma_{\theta}$ . As it can be seen, the estimated uncertainties in the parameters are negligible since the modeling errors are not significant (relatively low  $\sigma_e$ ) and large number of data sets is available (for this example 6,713 data sets are used;  $N_t = 6,713$ ). Figure 6.10 shows the  $\theta_t(T_t)$  values at the final Gibbs step along with the estimated  $\mu_{\theta}(T_t)$  from Eq. (6.18). The calibrated finite element model that contains temperature dependent stiffness parameters can be used for more accurate damage identification or reliability analysis in the presence of changing environmental conditions.

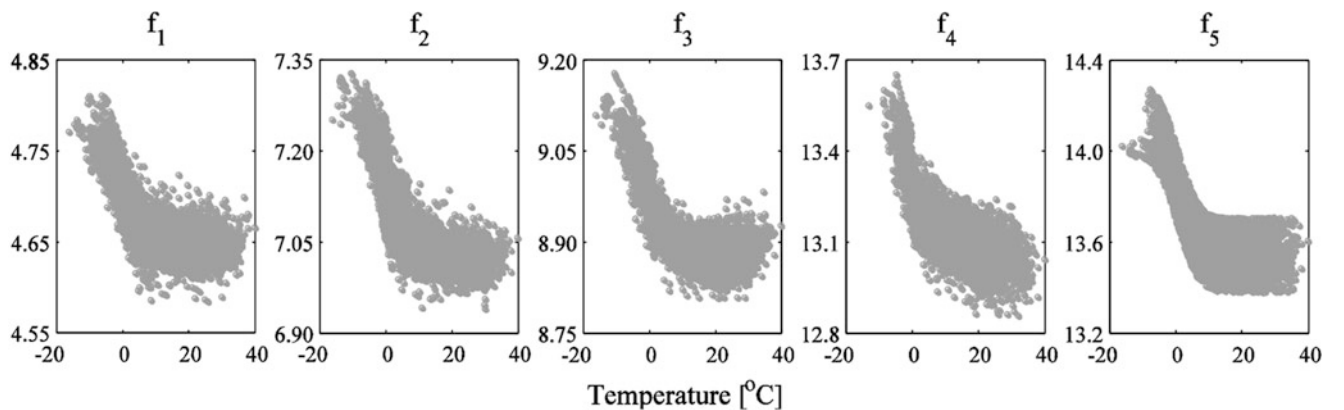
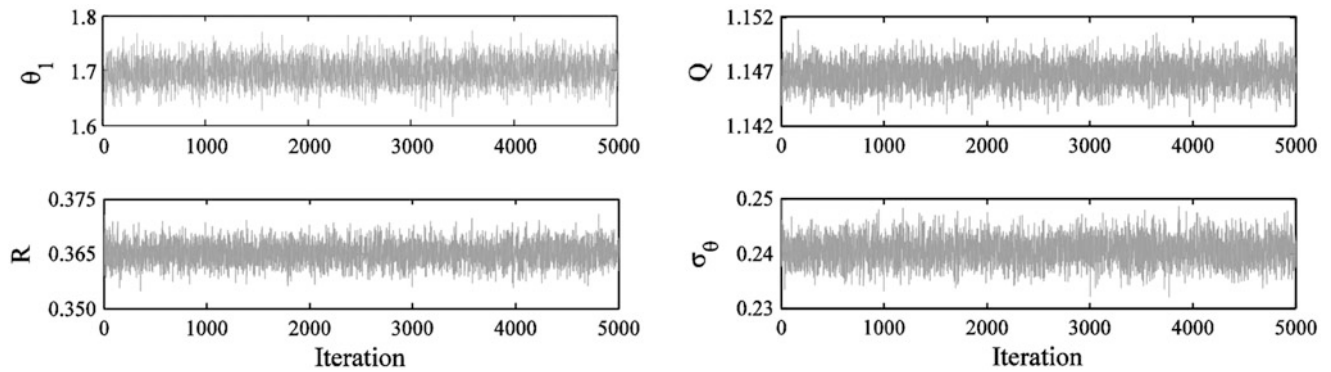
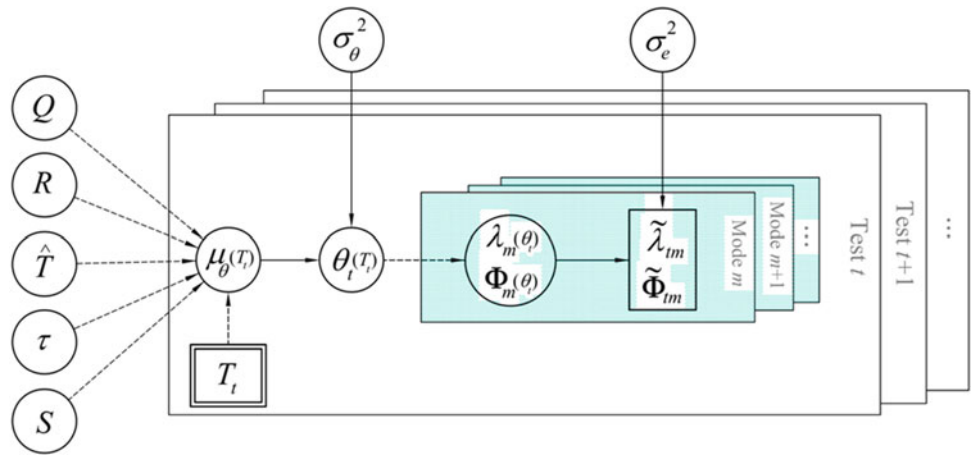


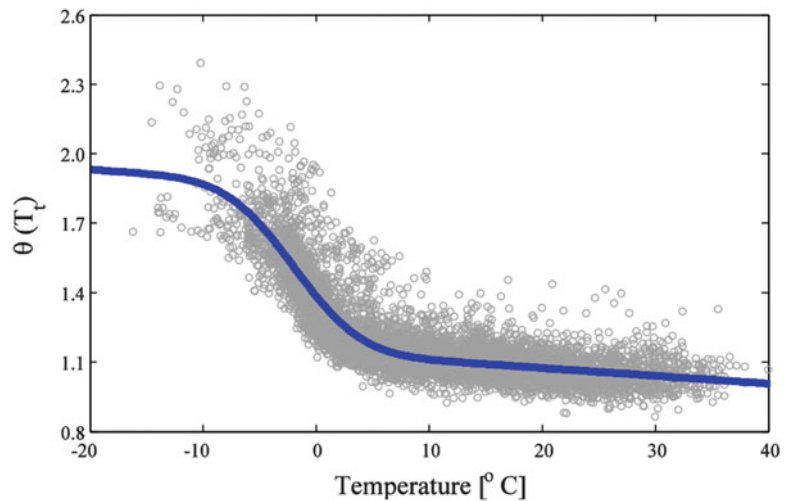
Fig. 6.7 Effect of ambient temperature variations on the identified natural frequencies

**Fig. 6.8** Graphical representation of the Hierarchical Bayesian model calibration including temperature measurements



**Fig. 6.9** The generated Gibbs samples for  $\theta_1$ ,  $Q$ ,  $R$ , and  $\sigma_\theta$

**Fig. 6.10** All the  $\theta_i(T_i)$  values at the final Gibbs samples (gray dots) and the estimated  $\mu_\theta(T_i)$  (solid line)



### 6.5 Summary and Conclusion

A new probabilistic updating process based on Hierarchical Bayesian modeling method is proposed for model calibration, uncertainty quantification, and damage identification of structural systems. This framework can accurately predict the overall uncertainty of updating parameters due to different uncertainty sources including estimation uncertainty and inherent variability of structural properties (mass, stiffness) due to changing environmental effects. These changing environmental effects may include ambient temperature, wind speed, rain, snow, and traffic load.

The performance of the proposed technique is evaluated for model calibration, uncertainty quantification, and damage identification of a three story shear building based on numerically simulated data. In the absence of modeling errors, the estimated updating parameters are found to be identical to the estimation results from the frequentist approach and are very close (with negligible error) to the true values. The proposed technique is also successfully applied for damage identification. The results highlight the fact that damage can be identified even when the change of the modal data due to damage is within the variation range of modal data due to environmental conditions provided that an adequate number of measured data sets is available. The proposed framework is well suited for damage assessment of operational civil structures where changing environmental conditions can significantly affect the identified natural frequencies and/or mode shapes.

Finally, the proposed Hierarchical framework is applied for model calibration of the Dowling Hall footbridge using experimentally collected data over 27 months. The identified natural frequencies of the footbridge show strong correlation with ambient temperature especially for temperatures below freezing point. A nonlinear relation is assumed to model the variation of concrete Elastic Young's modulus with ambient temperature. The parameters of the nonlinear relation and their uncertainties are estimated through the proposed Hierarchical framework. The temperature model provides a very good fit to the data. The temperature-dependent calibrated FE model can then be used for more accurate damage identification and reliability analysis in the presence of changing environmental conditions.

**Acknowledgment** The authors would like to acknowledge partial support of this study by the National Science Foundation Grant No. 1125624 which was awarded under the Broadening Participation Research Initiation Grants in Engineering (BRIGE) program. The authors would also like to acknowledge Mr. Durwood Marshall at the Tufts Technology Services for his help and support in using Tufts High-performance computing research cluster and Ms. Shirin Mardani for preparing the AutoCAD drawings.

## References

1. Friswell MI, Mottershead JE (1995) Finite element model updating in structural dynamics. Kluwer Academic Publishers, Boston/Dordrecht
2. Mottershead JE, Friswell MI (1993) Model updating in structural dynamics – a survey. *J Sound Vib* 167:347–375
3. Sohn H, Farrar CR, Hemez FM, Shunk DD, Stinemates DW, Nadler BR, Czarnecki JJ (2004) A review of structural health monitoring literature: 1996–2001. Los Alamos National Laboratory, Los Alamos
4. Friswell MI (2007) Damage identification using inverse methods. *Philos Trans Roy Soc A Math Phy Eng Sci* 365:393–410
5. Farhat C, Hemez FM (1993) Updating finite element dynamic models using an element-by-element sensitivity methodology. *Aiaa J* 31: 1702–1711
6. Teughels A, De Roeck G (2004) Structural damage identification of the highway bridge Z24 by FE model updating. *J Sound Vib* 278:589–610
7. Huth O, Feltrin G, Maeck J, Kilic N, Motavalli M (2005) Damage identification using modal data: experiences on a prestressed concrete bridge. *J Struct Eng* 131:1898–1910
8. Moaveni B, He X, Conte JP, Restrepo JJ (2010) Damage identification study of a seven-story full-scale building slice tested on the UCSD-NEES shake table. *Struct Saf* 32:347–356
9. Asgari E, Moaveni B, Stavridis A (2014) Nonlinear finite element model updating of an infilled frame based on identified time-varying modal parameters during an earthquake. *J Sound Vib* 333:6057–6073
10. Shahidi SG, Pakzad SN (2013) Generalized response surface model updating using time domain data. *J Struct Eng*
11. Moaveni B, Behmanesh I (2012) Effects of changing ambient temperature on finite element model updating of the Dowling Hall Footbridge. *Eng Struct* 43:58–68
12. Cornwell P, Farrar CR, Doebling SW, Sohn H (1999) Environmental variability of modal properties. *Exp Tech* 23:45–48
13. Peeters B, De Roeck G (2001) One-year monitoring of the Z 24-Bridge: environmental effects versus damage events. *Earthq Eng Struct Dyn* 30:149–171
14. Clinton JF, Bradford SC, Heaton TH, Favela J (2006) The observed wander of the natural frequencies in a structure. *Bull Seismol Soc Am* 96:237–257
15. Moaveni B, Conte JP, Hemez FM (2009) Uncertainty and sensitivity analysis of damage identification results obtained using finite element model updating. *Comput Aid Civi Infrastruct Eng* 24:320–334
16. Moser P, Moaveni B (2011) Environmental effects on the identified natural frequencies of the Dowling Hall Footbridge. *Mech Syst Signal Process* 25:2336–2357
17. Goller B, Schueller G (2011) Investigation of model uncertainties in Bayesian structural model updating. *J Sound Vib* 330:6122–6136
18. Behmanesh I, Moaveni B (2014) Bayesian FE model updating in the presence of modeling errors, model validation and uncertainty quantification, vol 3. Springer, pp 119–133
19. Beck JL, Katafygiotis LS (1998) Updating models and their uncertainties. I: Bayesian statistical framework. *J Eng Mech ASCE* 124:455–461
20. Sohn H, Law KH (1997) A Bayesian probabilistic approach for structure damage detection. *Earthq Eng Struct Dyn* 26:1259–1281
21. Beck JL, Au SK, Vanik MV (2001) Monitoring structural health using a probabilistic measure. *Comput Aid Civ Infrastruct Eng* 16:1–11
22. Beck JL, Au SK (2002) Bayesian updating of structural models and reliability using Markov chain Monte Carlo simulation. *J Eng Mech ASCE* 128:380–391
23. Yuen KV, Beck JL, Au SK (2004) Structural damage detection and assessment by adaptive Markov chain Monte Carlo simulation. *Struct Control Health Monit* 11:327–347



24. Ching J, Beck JL (2004) Bayesian analysis of the Phase II IASC-ASCE structural health monitoring experimental benchmark data. *J Eng Mech ASCE* 130:1233–1244
25. Christodoulou K, Papadimitriou C (2007) Structural identification based on optimally weighted modal residuals. *Mech Syst Signal Process* 21:4–23
26. Ching JY, Chen YC (2007) Transitional Markov chain Monte Carlo method for Bayesian model updating, model class selection, and model averaging. *J Eng Mech ASCE* 133:816–832
27. Christodoulou K, Ntotsios E, Papadimitriou C, Panetsos P (2008) Structural model updating and prediction variability using Pareto optimal models. *Comput Methods Appl Mech Eng* 198:138–149
28. Papadimitriou C, Beck JL, Katafygiotis LS (2001) Updating robust reliability using structural test data. *Probab Eng Mech* 16:103–113
29. Beck JL (2010) Bayesian system identification based on probability logic. *Struct Control Health Monit* 17:825–847
30. Yuen K-V (2010) Bayesian methods for structural dynamics and civil engineering. John Wiley & Sons, Singapore
31. Ntotsios E, Papadimitriou C, Panetsos P, Karaiskos G, Perros K, Perdikaris PC (2009) Bridge health monitoring system based on vibration measurements. *Bull Earthq Eng* 7:469–483
32. Simoen E, Conte JP, Moaveni B, Lombaert G (2013) Uncertainty quantification in the assessment of progressive damage in a 7-story full-scale building slice. *J Eng Mech* 139:1818–1830
33. Behmanesh I, Moaveni B (2014) Probabilistic identification of simulated damage on the Dowling Hall footbridge through Bayesian finite element model updating. *Struct control health monitor*
34. Angelikopoulos P, Papadimitriou C, Koumoutsakos P (2012) Bayesian uncertainty quantification and propagation in molecular dynamics simulations: a high performance computing framework. *J Chem Phys* 137:144103
35. Goulet JA, Smith IFC (2013) Structural identification with systematic errors and unknown uncertainty dependencies. *Comput Struct* 128:251–258
36. Au SK (2012) Connecting Bayesian and frequentist quantification of parameter uncertainty in system identification. *Mech Syst Signal Process* 29:328–342
37. Moaveni B, Barbosa AR, Conte JP, Hemez FM (2014) Uncertainty analysis of system identification results obtained for a seven-story building slice tested on the UCSD-NEES shake table. *Struct Control Health Monit* 21:466–483
38. Kiureghian AD, Ditlevsen O (2009) Aleatory or epistemic? Does it matter? *Struct Saf* 31:105–112
39. Gilks WR, Richardson S, Spiegelhalter DJ (1998) Markov chain Monte Carlo in practice. Chapman & Hall, Boca Raton
40. Gamerman D, Lopes HF (2006) Markov chain Monte Carlo: stochastic simulation for Bayesian inference. Taylor & Francis, Boca Raton
41. Gilks WR (2005) Markov chain Monte Carlo. Wiley Online Library
42. Ballesteros G, Angelikopoulos P, Papadimitriou C, Koumoutsakos P (2014) Bayesian hierarchical models for uncertainty quantification in structural dynamics, vulnerability, uncertainty, and risk: quantification, mitigation, and management, ASCE, pp 1615–1624
43. Simoen E, Papadimitriou C, Lombaert G (2013) On prediction error correlation in Bayesian model updating. *J Sound Vib* 332:4136–4152
44. Andrieu C, Thoms J (2008) A tutorial on adaptive MCMC. *Stat Comput* 18:343–373

# Chapter 7

## Nonlinear Structural Finite Element Model Updating Using Stochastic Filtering

Rodrigo Astroza, Hamed Ebrahimian, and Joel P. Conte

**Abstract** This paper describes a novel framework that combines advanced mechanics-based nonlinear (hysteretic) finite element (FE) models and stochastic filtering techniques to estimate unknown time-invariant parameters of nonlinear inelastic material models used in the FE model. Using input-output data recorded during earthquake events, the proposed framework updates the nonlinear FE model of the structure. The updated FE model can be directly used for damage identification purposes. The unscented Kalman filter (UKF) is used as parameter estimation technique to identify the unknown time-invariant parameters of the FE model. A two-dimensional, 3-bay, 3-story steel moment frame is used to verify the proposed framework. The steel frame is modeled using fiber-section beam-column elements with distributed plasticity and is subjected to a ground motion recorded during the 1989 Loma Prieta earthquake. The results show that the proposed methodology provides accurate estimates of the unknown material parameters of the nonlinear FE model.

**Keywords** Damage identification • Nonlinear finite element model • Model updating • Stochastic filter • Structural health monitoring

### 7.1 Introduction

The fields of system identification (SID) and damage identification (DID) are attracting significant attention from the structural engineering community. With the aim of implementing accurate and robust DID methodologies, research on structural health monitoring (SHM) for civil structures has increased considerably during the last years. Several researchers have studied vibration-based DID methods for civil structures based on changes in identified modal properties (e.g., [1, 2]); however, these methods have been applied to real structures or full-scale structural specimens subjected to damage induced by realistic sources of dynamic excitation only in the last years (e.g., [3–5]). Because modal properties are related to global properties of the structure and because actual response of structures is nonlinear from the onset of loading, some researchers have objected the use of modal parameters for damage identification purposes. Considering the relevance of nonlinearities in the dynamic response of civil structures, SID and DID for nonlinear structures have been the subject of intense research (e.g., [6–9]). Nevertheless, these studies have used highly idealized structural models, localizing the modeling of nonlinear behavior in a few prescribed elements defined by nonlinear hysteretic force-deformation laws not traditionally used in state-of-the-art modeling of civil structures.

Finite element (FE) model updating, which can be defined as the process of calibrating a FE model to minimize the discrepancy between the FE predicted and measured responses of a structure, has emerged as a powerful method [10, 11] that enables the use of more realistic models for SID and DID purposes. Recently, Bayesian techniques have been used for FE model updating of linear and nonlinear structures, for both static and dynamic loading (e.g., [12–15]). In the case of nonlinear response, previous studies employed highly simplified nonlinear models (e.g., lumped plasticity, shear building, empirical-based nonlinear material models) which are not able to properly characterize the behavior of real large and complex civil structures.

---

R. Astroza (✉)

Department of Structural Engineering, University of California, San Diego, 9500 Gilman Drive, La Jolla, CA 92093, USA

Facultad de Ingeniería y Ciencias Aplicadas, Universidad de los Andes, Monseñor Álvaro del Portillo 12455, Las Condes, Santiago, Chile  
e-mail: [rastroza@ucsd.edu](mailto:rastroza@ucsd.edu)

H. Ebrahimian • J.P. Conte

Department of Structural Engineering, University of California, San Diego, 9500 Gilman Drive, La Jolla, CA 92093, USA  
e-mail: [jpcconte@ucsd.edu](mailto:jpcconte@ucsd.edu)

This paper presents a novel framework that combines advanced mechanics-based nonlinear FE models and a nonlinear Bayesian filter, referred to as the unscented Kalman filter (UKF) [16, 17], to estimate unknown time-invariant parameters of nonlinear inelastic material models used in the FE model. In the implementation of the framework, the software *OpenSees* is used to model the structure and simulate its response to earthquake excitation.

## 7.2 Bayesian Approach for State and Parameter Estimation of Dynamic Systems

Consider a nonlinear state-space model with additive zero-mean Gaussian white noises:

$$\mathbf{x}_{k+1} = \mathbf{f}_k(\mathbf{x}_k, \mathbf{u}_k) + \mathbf{w}_k \quad (7.1a)$$

$$\mathbf{y}_{k+1} = \mathbf{h}_{k+1}(\mathbf{x}_{k+1}, \mathbf{u}_{k+1}) + \mathbf{v}_{k+1} \quad (7.1b)$$

where  $\mathbf{x}_k \in \mathbb{R}^{m_x}$ ,  $\mathbf{u}_k \in \mathbb{R}^{m_u}$ , and  $\mathbf{y}_k \in \mathbb{R}^{m_y}$  are the state vector (defined as the smallest subset of variables needed to completely characterize the system at time  $t_k = k\Delta t$ , where  $\Delta t =$  time step), input vector (deterministic and known), and measurement vector at time  $t_k$ , respectively. The components of the process and measurement noises,  $\mathbf{w}_k$  and  $\mathbf{v}_{k+1}$  respectively, are assumed to be statistically independent processes. Noise processes  $\mathbf{w}_k$  and  $\mathbf{v}_{k+1}$  have covariance matrices  $\mathbf{Q}_k$  and  $\mathbf{R}_{k+1}$ , respectively. The terms  $\mathbf{f}_k$  and  $\mathbf{h}_{k+1}$  are deterministic and known nonlinear vector-valued functions. The objective of a filtering technique is to recursively estimate at least the first two statistical moments of the state vector using the measured input and noisy measurement vectors up to the current time [18]. If modeling parameters are unknown, the state vector can be augmented to contain both state variables and unknown parameters ( $\boldsymbol{\theta}_{k+1}$ ). For the special case that all system dynamics are contained in the measurement equation, a parameter-only estimation problem can be set up [19], i.e., only  $\boldsymbol{\theta}_{k+1}$  is present in the state equation [Eq. (7.1a)].

The UKF can be used to solve the nonlinear state-space model in Eq. (7.1a and b). It is based on the assumptions that the posterior *PDF* of the state at time  $t_k$ ,  $p(\mathbf{x}_k | \mathbf{y}_{1:k})$  (where  $\mathbf{y}_{1:k} = [\mathbf{y}_1^T, \mathbf{y}_2^T, \dots, \mathbf{y}_k^T]^T$ ), and the *PDF*  $p(\mathbf{x}_{k+1} | \mathbf{y}_{1:k})$  are approximated by Gaussian distributions. Then, the posterior *PDF* of the state at time  $t_{k+1}$ ,  $p(\mathbf{x}_{k+1} | \mathbf{y}_{1:k+1})$ , can be approximated as Gaussian with mean vector and covariance matrix estimates given by

$$\hat{\mathbf{x}}_{k+1|k+1} = \hat{\mathbf{x}}_{k+1|k} + \mathbf{K}_{k+1}(\mathbf{y}_{k+1} - \hat{\mathbf{y}}_{k+1|k}) \quad (7.2a)$$

$$\hat{\mathbf{P}}_{k+1|k+1}^{\mathbf{xx}} = \hat{\mathbf{P}}_{k+1|k}^{\mathbf{xx}} - \mathbf{K}_{k+1} \hat{\mathbf{P}}_{k+1|k}^{\mathbf{yy}} \mathbf{K}_{k+1}^T \quad (7.2b)$$

where  $\hat{\mathbf{x}}_{k+1|k+1}$  and  $\hat{\mathbf{P}}_{k+1|k+1}^{\mathbf{xx}}$  denote estimates of the mean and covariance matrix of  $\mathbf{x}_{k+1}$  given  $\mathbf{y}_{1:k+1}$ ,  $\hat{\mathbf{y}}_{k+1|k}$  is the estimate of the mean of  $\mathbf{y}_{k+1}$  given  $\mathbf{y}_{1:k}$  and the Kalman gain matrix,  $\mathbf{K}_{k+1}$ , is defined as

$$\mathbf{K}_{k+1} = \hat{\mathbf{P}}_{k+1|k}^{\mathbf{xy}} \left( \hat{\mathbf{P}}_{k+1|k}^{\mathbf{yy}} \right)^{-1} \quad (7.3)$$

Covariance matrices  $\hat{\mathbf{P}}_{k+1|k}^{\mathbf{xx}}$ ,  $\hat{\mathbf{P}}_{k+1|k}^{\mathbf{xy}}$ ,  $\hat{\mathbf{P}}_{k+1|k}^{\mathbf{yy}}$  require the computation of multi-dimensional integrals that seldom can be evaluated in closed-form; therefore, the unscented transformation (UT) can be alternatively used to approximate them. The UT defines a set of deterministically selected sample points (referred as sigma points or SPs) to represent a random vector  $\mathbf{z}$  such that the sample mean and sample covariance matrix obtained from the SPs match exactly the true mean and covariance matrix of the random vector  $\mathbf{z}$ . When the SPs are propagated through a nonlinear function, they capture the true mean and covariance matrix up to the second order of the Taylor series expansion of the nonlinear function. In this paper, the scaled unscented transformation [17] with parameters  $\alpha = 0.01$ ,  $\kappa = 0$ , and  $\beta = 2$  is adopted. More details about the UKF and scaled UT can be found elsewhere [20].

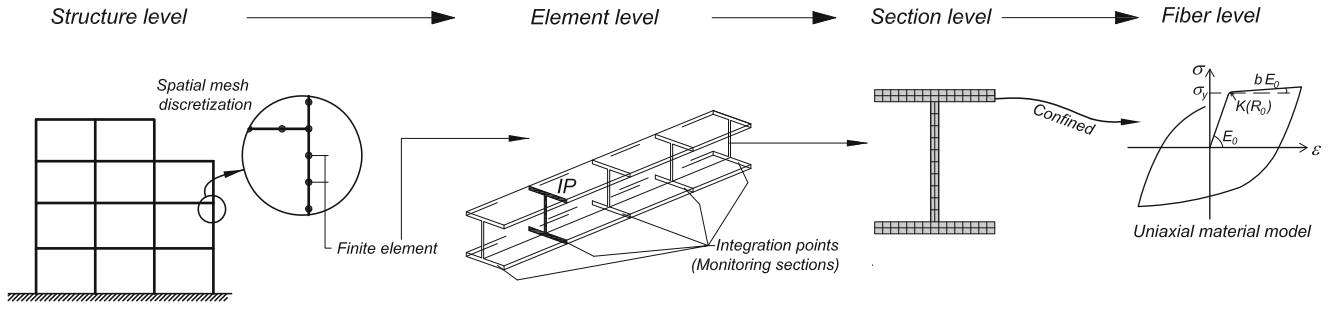


Fig. 7.1 Distributed plasticity FE model of frame-type structures

### 7.3 Mechanics-Based Nonlinear Finite Element Models of Frame-Type Structures

Different approaches have been proposed over the years to model and simulate the nonlinear response of frame-type structures subjected to earthquake loading. Global models, structural FE models, and continuum FE models have been developed for this purpose. The simplest are global models, which concentrate material nonlinearities at global degrees of freedom (DOF), however they lack accuracy and resolution in predicting the nonlinear response of real structures. Structural FE models describe the structure by an assembly of interconnected frame elements. Lumped or concentrated plasticity and distributed plasticity are two categories within structural FE models. Finally, continuum FE models are the most sophisticated but computationally expensive, since they discretize the members of frame-type structures into 3D solid FEs with 3D nonlinear material constitutive models.

Structural FE models with distributed plasticity have been proven to provide accurate results in matching experimental results. In addition, their formulation is simple and computational cost is feasible. Therefore, these types of models have been broadly employed in research and engineering practice. In this type of FE models, material nonlinearity can take place at any numerically monitored cross section (integration point) along the element, and the element behavior is obtained by numerical integration of the section response along the element. Element cross-sections are discretized in longitudinal fibers, which permit to simulate the section nonlinear response using uniaxial material constitutive laws for the fibers (Fig. 7.1). This formulation accounts for the interaction between bending and axial force at the section level, while the interaction with the shear force occurs at the element level. It is noted that a uniaxial material model depends on a set of physical and/or empirical set of parameters. More details about these type structural FE modeling techniques can be found in [21].

### 7.4 Proposed Methodology

The discrete-time equation of motion of a FE model of a structure can be expressed as

$$\mathbf{M}(\boldsymbol{\theta}) \ddot{\mathbf{q}}_{k+1}(\boldsymbol{\theta}) + \mathbf{C}(\boldsymbol{\theta}) \dot{\mathbf{q}}_{k+1}(\boldsymbol{\theta}) + \mathbf{r}_{k+1}[\mathbf{q}_{k+1}(\boldsymbol{\theta}), \boldsymbol{\theta}] = \mathbf{f}_{k+1} \quad (7.4)$$

where  $\boldsymbol{\theta} \in \mathbb{R}^{n_\theta}$  vector of unknown time-invariant modeling parameters,  $\mathbf{q}, \dot{\mathbf{q}}, \ddot{\mathbf{q}} \in \mathbb{R}^n$  = nodal displacement, velocity, and acceleration vectors,  $\mathbf{M} \in \mathbb{R}^{n \times n}$  = mass matrix,  $\mathbf{C} \in \mathbb{R}^{n \times n}$  = damping matrix,  $\mathbf{r}[\mathbf{q}(\boldsymbol{\theta}), \boldsymbol{\theta}] \in \mathbb{R}^n$  = history-dependent internal resisting force vector,  $\mathbf{f} \in \mathbb{R}^n$  = dynamic load vector, and the subscript indicates the time step. For the case of rigid base earthquake excitation the dynamic load vector takes the form  $\mathbf{f}_{k+1} = -\mathbf{M} \mathcal{L} \ddot{\mathbf{u}}_{k+1}^g$ , where  $\mathcal{L} \in \mathbb{R}^{n \times r}$  = influence matrix and  $\ddot{\mathbf{u}}^g \in \mathbb{R}^{r \times 1}$  = input ground acceleration vector with  $r$  = number of base excitation components (in the general case  $r = 6$ , i.e., three rotations and three translations base excitation components)

The structural response can be recorded using different types of sensors (e.g., accelerometers, GPS) and at time  $t_{k+1} = (k+1)\Delta t$ , with  $k = 0, 1, \dots$  and  $\Delta t$  = time step, can be expressed as

$$\mathbf{y}_{k+1} = \mathbf{L}_y \left[ \dot{\mathbf{q}}_{k+1}^T, \dot{\mathbf{q}}_{k+1}^T, \mathbf{q}_{k+1}^T, (\ddot{\mathbf{u}}_{k+1}^g)^T \right]^T + \mathbf{v}_{k+1} = \hat{\mathbf{y}}_{k+1} + \mathbf{v}_{k+1} \quad (7.5)$$

where  $\mathbf{y} \in \mathbb{R}^{n_y}$  = vector of recorded structural response quantities,  $\hat{\mathbf{y}} \in \mathbb{R}^{n_y}$  predicted response of the structure from the FE model,  $\mathbf{L}_y \in \mathbb{R}^{n_y \times 3n+r}$  = output matrix (known), and  $\mathbf{v} \in \mathbb{R}^{n_y}$  = output measurement noise vector assumed to be white Gaussian with zero-mean and covariance matrix  $\mathbf{R}_k$ , i.e.,  $\mathbf{v}_k \sim \mathcal{N}(\mathbf{0}, \mathbf{R}_k)$ .

From Eqs. (7.4) and (7.5), the vector of recorded response quantities at time  $t_{k+1}$ ,  $\mathbf{y}_{k+1}$ , can be expressed as a nonlinear function of the modeling parameters ( $\boldsymbol{\theta}$ ), input ground acceleration time histories ( $\ddot{\mathbf{U}}_{k+1}^g$ ), and initial conditions ( $\mathbf{q}_0, \dot{\mathbf{q}}_0$ ) of the FE model, i.e.,

$$\mathbf{y}_{k+1} = \mathbf{h}_{k+1} \left( \boldsymbol{\theta}, \ddot{\mathbf{U}}_{k+1}^g, \mathbf{q}_0, \dot{\mathbf{q}}_0 \right) + \mathbf{v}_{k+1} \quad (7.6)$$

Here  $\mathbf{h}_{k+1}(\bullet)$  is a nonlinear response function of the nonlinear FE model at time  $t_{k+1}$  and  $\ddot{\mathbf{U}}_{k+1}^g = [(\ddot{\mathbf{u}}_1^g)^T, (\ddot{\mathbf{u}}_2^g)^T, \dots, (\ddot{\mathbf{u}}_{k+1}^g)^T]^T$  is the input ground acceleration time history from time  $t_1$  to  $t_{k+1}$ . At rest initial conditions are assumed henceforth, i.e.,  $\mathbf{q}_0 = \dot{\mathbf{q}}_0 = \mathbf{0}$ .

If the unknown time-invariant modeling parameter vector,  $\boldsymbol{\theta}$ , is modeled as a stationary process according to the Bayesian approach, the evolution of which is characterized by a random walk process, the nonlinear parameter estimation problem at time  $t_{k+1}$  ( $k = 0, 1, 2, \dots$ ) can be formulated as

$$\begin{cases} \boldsymbol{\theta}_{k+1} = \boldsymbol{\theta}_k + \boldsymbol{\gamma}_k \\ \mathbf{y}_{k+1} = \mathbf{h}_{k+1} \left( \boldsymbol{\theta}_{k+1}, \ddot{\mathbf{U}}_{k+1}^g \right) + \mathbf{v}_{k+1} \end{cases} \quad (7.7)$$

where  $\boldsymbol{\gamma}_k$  and  $\mathbf{v}_k$  are called process noise and measurement noise, respectively, and are assumed to be independent Gaussian white noise processes with zero mean vectors and diagonal covariance matrices  $\mathbf{Q}_k$  and  $\mathbf{R}_k$ , respectively, i.e.,  $\boldsymbol{\gamma}_k \sim \mathcal{N}(\mathbf{0}, \mathbf{Q}_k)$  and  $\mathbf{v}_k \sim \mathcal{N}(\mathbf{0}, \mathbf{R}_k)$ . Equation (7.7) represents a nonlinear state-space model like Eq. (7.1), therefore it can be used to estimate the modeling parameter vector,  $\boldsymbol{\theta}$ , using the UKF as summarized in Fig. 7.2. More information about the formulation of the parameter estimation problem for frame-type distributed-plasticity FE models using the UKF is discussed elsewhere [20].

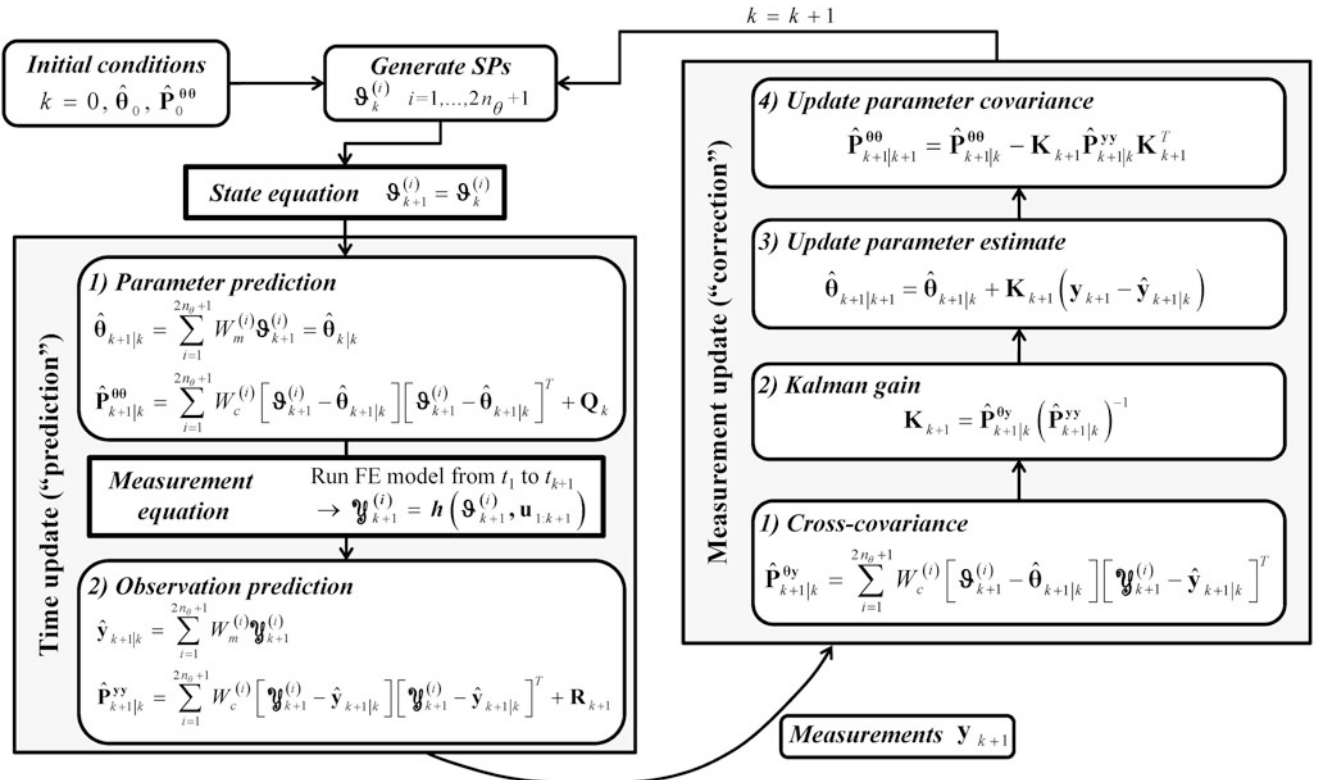


Fig. 7.2 Distributed plasticity FE model of frame-type structures

## 7.5 Application Example

A 2D steel building frame is considered as application example. The steel fibers are modeled using the modified Giuffre-Menegotto-Pinto (G-M-P) material constitutive model [22]. One input earthquake motion is considered to simulate recorded response data, which are then contaminated by measurement noise for the estimation phase. Gravity loads are applied quasi-statically before running the dynamic analysis. The Newmark- $\beta$  average acceleration method is used to integrate the equations of motion in time using a time step  $\Delta t = 1/f_s$ , where  $f_s$  is the sampling rate of the input earthquake motion. The Newton algorithm is used to solve the set of coupled nonlinear algebraic equations resulting from the equations of motion. The framework presented above is used to identify the material parameters and update the nonlinear FE model. The same FE model is used to simulate the response and to estimate the material parameters, i.e., effects of modeling uncertainty are not considered. The ground motion recorded at the station Los Gatos during the 1989 Loma Prieta ( $M_w = 6.9$ ) is selected as input motion (Fig. 7.3). The peak ground acceleration is 0.45 g and the sampling rate is  $f_s = 50$  Hz.

The structure is a 3-story steel moment resisting frame structure studied under the SAC venture, known as the SAC-LA-3 story building [23] (Fig. 7.4a). The modeled 2D frame has 3 stories and 3 bays, with a story height of 3.96 m and a bay width of 9.14 m. Exterior and interior columns are made of A572 steel with  $W14 \times 257$  and  $W14 \times 311$  cross-sections, respectively. Second, third, and roof level beams are made of A36 steel with  $W33 \times 118$ ,  $W30 \times 116$ , and  $W24 \times 68$  cross-sections, respectively. Beam-column joints are assumed to be fully restrained, and rigid end zones are modeled at the ends of beams and columns (Fig. 7.4b). Beams and columns are modeled using one force-based element for each beam and column. Numerical integration over the length of the elements is performed by using Gauss-Lobatto quadrature with 6 and 7 IPs for columns and beams, respectively. Column webs are discretized into 6 fibers along their length and one fiber across their width, while a single fiber is used to represent each flange of the cross-section (Fig. 7.4c). The webs of the second, third, and roof level beams are discretized into 16, 14, and 11 fibers along their length, respectively, and one fiber across their width. A single fiber is used to represent each flange of the cross-section (Fig. 7.4c). A linear elastic section shear force-deformation model is aggregated with the inelastic coupled flexure-axial behavior at the section level and along the element. The flexure-axial behavior is uncoupled from the shear behavior at the section level.

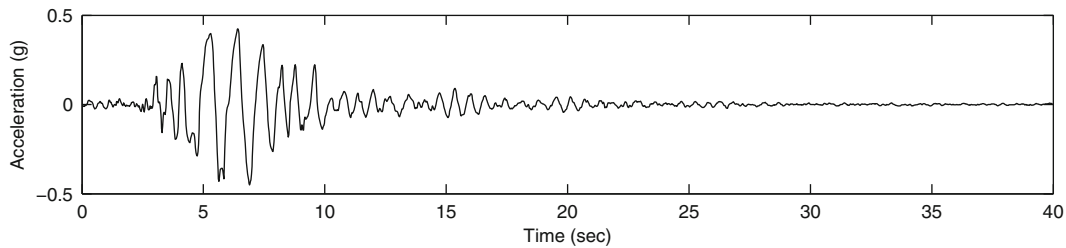


Fig. 7.3 Ground acceleration recorded at the Los Gatos station during the 1989 Loma Prieta earthquake

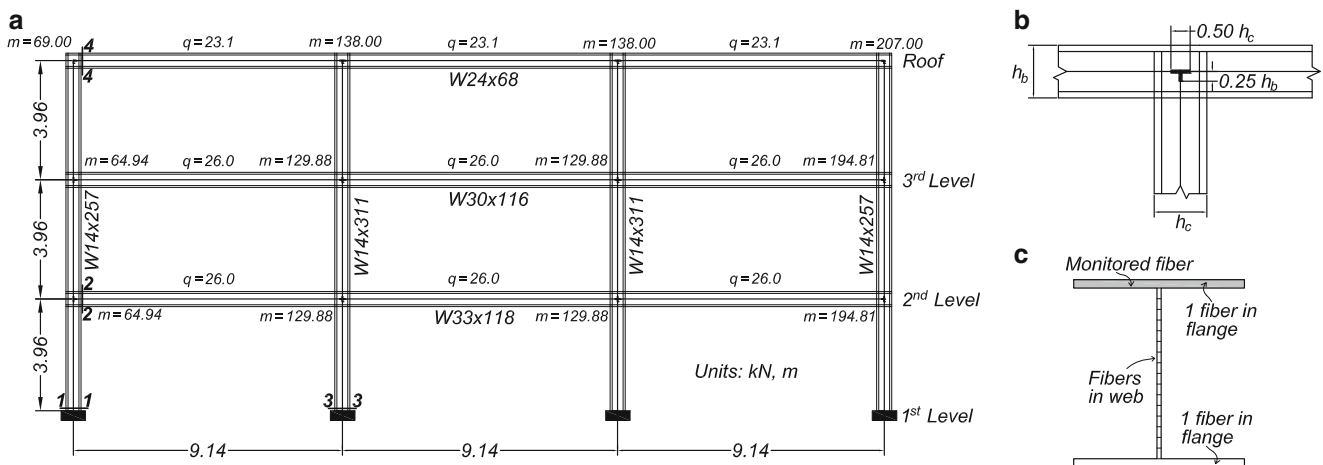


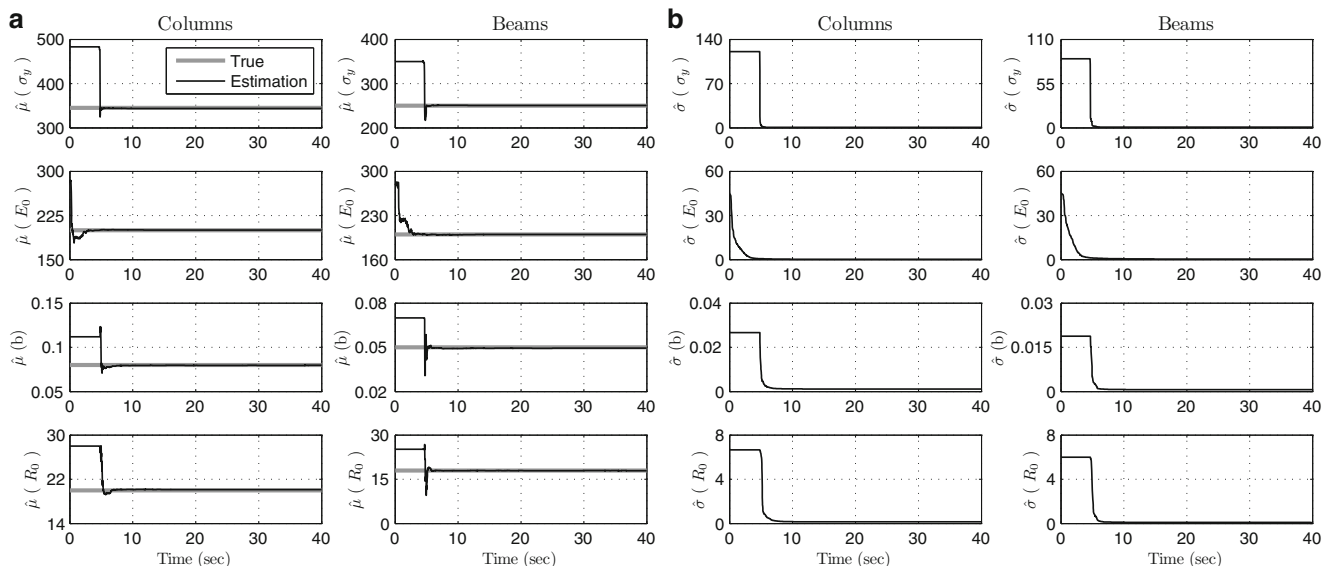
Fig. 7.4 Properties of the 2D frame building model: (a) Geometry, masses, and loads; (b) rigid end zones; (c) cross section discretization

The uniaxial G-M-P material model with primary parameters  $\theta^{true} = [E_0^{col}, \sigma_y^{col}, b^{col}, R_0^{col}, E_0^{beam}, \sigma_y^{beam}, b^{beam}, R_0^{beam}]^T = [200 \text{ GPa}, 345 \text{ MPa}, 0.08, 20, 200 \text{ GPa}, 250 \text{ MPa}, 0.05, 18]^T$  is used to model the axial behavior of the fibers of the cross sections of beams and columns and to simulate the true dynamic response of the frame structure to earthquake excitation. Nodal masses and distributed gravity loads on beams are computed from the design dead and live loads as reported in FEMA-355C and are shown in Fig. 7.4a. The sources of energy dissipation beyond hysteretic energy dissipated through nonlinear material behavior are modeled using mass and tangent stiffness-proportional Rayleigh damping assuming a critical damping ratio of 2 % for the first two initial natural periods (after application of the gravity loads),  $T_1 = 1.06 \text{ s}$  and  $T_2 = 0.35 \text{ s}$ .

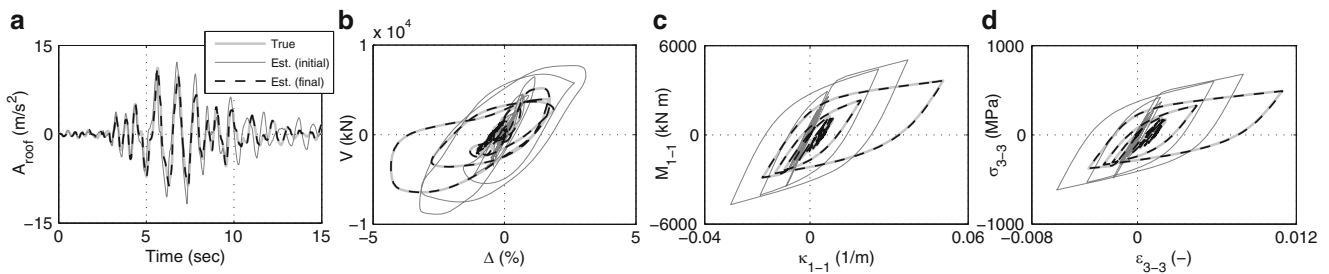
In the material parameter identification process, the UKF algorithm requires 17 SPs ( $=2 \times 8 + 1$ ) and it is assumed that only one horizontal acceleration response is measured at each level (at the left column). The initial estimates of the material parameters to be identified are taken as 140 % of their true values,  $\hat{\theta}_0 = 1.4\theta^{true}$ , and the initial covariance matrix  $\hat{\mathbf{P}}_0^{\theta\theta}$  is assumed diagonal with terms computed assuming a coefficient of variation of the initial parameter estimates (with  $\hat{\theta}_0$  as initial mean) of 15 % for  $E_0^{col}$  and  $E_0^{beam}$  and 25 % for  $\sigma_y^{col}$ ,  $b^{col}$ ,  $R_0^{col}$ ,  $\sigma_y^{beam}$ ,  $b^{beam}$ , and  $R_0^{beam}$ . An output measurement noise with 5 % RMS noise-to-signal-ratio (NSR) is considered. It is assumed that the process noise  $\mathbf{y}_k$  and measurement noise  $\mathbf{v}_k$  are zero-mean Gaussian white noise processes with time-invariant diagonal covariance matrices  $\mathbf{Q}$  and  $\mathbf{R}$ , respectively. A coefficient of variation of  $1 \times 10^{-4}$  is assumed for the initial estimates of the material parameters ( $\theta_0$ ) to construct the process noise covariance matrix  $\mathbf{Q}$ . A standard deviation (or RMS) of the measurement noise  $\mathbf{v}_k$  of  $7 \times 10^{-2}$  of the RMS of the corresponding simulated measurements (horizontal acceleration at the 2nd, 3rd, and roof levels) is assumed in the measurement noise covariance matrix  $\mathbf{R}$ .

Time histories of the mean ( $\hat{\mu}$ ) and standard deviation ( $\hat{\sigma}$ ) estimates of the material parameters for SAC-LA-3 building frame subjected to Los Gatos earthquake motion are shown in Fig. 7.5. The eight parameters are accurately identified and the standard deviation estimates of all these parameters decrease asymptotically to zero. The stiffness related parameters  $E_0^{col}$  and  $E_0^{beam}$  quickly converge to their true values after a few time steps, the strength or yield related parameters  $\sigma_y^{beam}$  and  $\sigma_y^{col}$  converge to their true values soon after the strong motion phase of the earthquake begins and some steel fibers have yielded, and the post-yield related parameters  $b^{beam}$ ,  $b^{col}$ ,  $R_0^{beam}$ , and  $R_0^{col}$  converge to their true values after the strain ductility demand of enough steel fibers has increased sufficiently.

Figure 7.6 compares different global and local responses of the frame obtained using the true material parameter values ( $\theta^{true}$ ), the initial estimate of the parameters ( $\hat{\theta}_0$ ), and the final estimate of the parameters ( $\hat{\theta}_N$ ). The following responses are plotted: absolute horizontal acceleration response history at the roof level ( $A_{roof}$ ), base shear ( $V$ ) versus roof drift ratio ( $\Delta$ ), moment ( $M_{1-1}$ ) versus curvature ( $\kappa_{1-1}$ ) hysteretic response at the base of the left column (section 1–1 in Fig. 7.4a), and stress ( $\sigma_{3-3}$ ) versus strain ( $\epsilon_{3-3}$ ) hysteretic response at one of the extreme fibers at the base of the central-left column (section 3–3 in Fig. 7.4a). All the responses computed using the final estimates of the material parameters are in excellent agreement with the simulated true responses and the correct updating of the nonlinear FE model is clear from the comparison of the true responses with the responses obtained using the initial and final material parameter estimates.



**Fig. 7.5** Estimation results for the material parameters of beams and columns of the frame building: (a) mean values; (b) standard deviations



**Fig. 7.6** Comparison of true and estimated responses of the frame building: (a) absolute horizontal acceleration at the roof, (b) base shear versus roof drift ratio, (c) moment versus curvature at the base of left column section, (d) stress versus strain in extreme fiber at the base of the left-central column

## 7.6 Conclusions

This paper proposes and validates, using numerically simulated data, a novel methodology to estimate unknown time-invariant parameters of nonlinear inelastic material models in frame-type structures subjected to earthquake excitation. The method combines state-of-the-art nonlinear finite element (FE) models and the unscented Kalman filter (UKF) as the estimation tool. The methodology formulates the nonlinear state-space model considering the unknown time-invariant modeling parameters in the state equation and the responses of the nonlinear FE model corresponding to the measured response quantities are used in the measurement equation. A 2D 3-story, 3-bay steel frame subjected to a ground acceleration recorded at the Los Gatos station during the 1989 Loma Prieta earthquake is used to validate the proposed methodology. The simulated responses of the building are contaminated by white noise to analyze the robustness of the identification scheme. The proposed method is able to accurately estimate the unknown time-invariant material parameters of the nonlinear FE model. True and estimated time histories of various global and local response quantities are compared to confirm the effectiveness of the proposed nonlinear FE model updating approach. The proposed framework provides a powerful tool for model updating of advanced mechanics-based nonlinear FE models, even when a limited number of measurement data are available.

**Acknowledgments** Partial support of this research by the UCSD Academic Senate under Research Grant RN091G-CONTE is gratefully acknowledged.

## References

1. Doebling SW, Farrar CR, Prime MB, Shevit DW (1996) Damage identification and health monitoring of structural and mechanical systems from changes in their vibration characteristics: a literature review. Los Alamos National Laboratory Report LA-13070-MS
2. Housner G, Bergman L, Caughey T, Chassiakos A, Claus R, Masri S, Skelton R, Soong T, Spencer B, Yao J (1997) Structural control: past, present, and future. *J Eng Mech ASCE* 123(9):897–971
3. Moaveni B, He X, Conte JP, Restrepo JJ, Panagiotou M (2011) System identification study of a seven-story full-scale building slice tested on the UCSD-NEES shake table. *J Struct Eng* 137(6):705–717
4. Ji X, Fenves G, Kajiwaru K, Nakashima M (2011) Seismic damage detection of a full-scale shaking table test structure. *J Struct Eng* 137(1): 14–21
5. Astroza R, Ebrahimian H, Conte JP, Restrepo JJ, Hutchinson TC (2013) Modal identification of 5-story RC building tested on NEES-UCSD shake table. In: International modal analysis conference, IMAC XXXI, Garden Grove
6. Masri SF, Caughey TK (1979) A nonparametric identification technique for nonlinear dynamic problems. *J Appl Mech* 46(2):433–447
7. Yun CB, Shinozuka M (1980) Identification of nonlinear structural dynamic systems. *J Struct Mech* 8(2):187–203
8. Corigliano A, Mariani S (2004) Parameter identification in explicit structural dynamics: performance of the extended Kalman filter. *Comput Methods Appl Mech Eng* 193(36–38):3807–3835
9. Chatzi EN, Smyth AW (2009) The unscented Kalman filter and particle filter methods for nonlinear structural system identification with non-collocated heterogeneous sensing. *Struct Control Health Monit* 16:99–123
10. Friswell MI, Mottershead JE (1995) Finite element model updating in structural dynamics. Kluwer Academic Publishers, Boston
11. Marwala T (2010) Finite element model updating using computational intelligence techniques: applications to structural dynamics. Springer, London
12. Ching J, Beck JL, Porter KA, Shaikhutdinov R (2006) Bayesian state estimation method for nonlinear systems and its application to recorded seismic response. *J Eng Mech ASCE* 132(4):396–410



13. Huang H, Yang JN, Zhou L (2010) Adaptive quadratic sum-squares error with unknown inputs for damage identification of structures. *Struct Control Health Monit* 17:404–426
14. Nasrellah HA, Manohar CS (2011) Finite element method based Monte Carlo filters for structural system identification. *Prob Eng Mech* 26:294–307
15. Simoen E, Moaveni B, Conte JP, Lombaert G (2013) Uncertainty quantification in the assessment of progressive damage in a seven-story full-scale building slice. *J Eng Mech ASCE* 139(12):1818–1830
16. Julier SJ, Uhlmann JK (1997) A new extension of the Kalman filter to nonlinear systems. In: *The 11th international symposium on aerospace/defense sensing, simulation and controls*, Orlando
17. Wan EA, van der Merwe R (2000) The unscented Kalman filter for nonlinear estimation. In: *IEEE 2000 adaptive systems for signal processing, communications, and control symposium*, Lake Louise
18. Haug AJ (2005) A tutorial on Bayesian estimation and tracking techniques applicable to nonlinear and non-Gaussian processes. MITRE technical report 05 W0000004
19. Haykin S (ed) (2001) *Kalman filtering and neural networks*. Wiley, New York
20. Astroza R, Ebrahimian H, Conte J (2014) Material parameter identification in distributed plasticity FE models of frame-type structures using nonlinear stochastic filtering. *J Eng Mech ASCE* (in-press)
21. Taucer FF, Spacone E, Filippou FC (1991) A fiber beam-column element for seismic response analysis of reinforced concrete structures. Report 91/17, EERC. Earthquake Engineering Research Center (EERC), University of California, Berkeley
22. Filippou FC, Popov EP, Bertero VV (1983) Effects of bond deterioration on hysteretic behavior of reinforced concrete joints. Report EERC 83–19. Earthquake Engineering Research Center, University of California, Berkeley
23. FEMA-355C (2000) State-of-the-art report on systems performance of steel moment frames subjected to earthquake ground shaking. Prepared by the SAC Joint Venture for the Federal Emergency Management Agency, Washington, DC

# Chapter 8

## Dispersion–Corrected, Operationally Normalized Stabilization Diagrams for Robust Structural Identification

Vasilis K. Dertimanis, Minas D. Spiridonakos, and Eleni N. Chatzi

### Nomenclature

DA	Dispersion analysis	MDM	Modal dispersion metric
DOF	Degrees–of–freedom	nMDM	Normalized modal dispersion metric
ERA	Eigensystem realization algorithm	PCE	Polynomial chaos expansion
N/S	Noisetosignal	PDF	Probability density function
LHS	Latin hypercube sampling	SD(s)	Stabilization diagram(s)
LTI	Linear time–invariant		

**Abstract** This study aims at incorporating a certain degree of formalization to stabilization diagrams by integrating two additional features: the former introduces a new quantity, the modal dispersion metric, which expresses a certain part of the total stochastic vibration energy, and it is attributed to each vibration mode. The latter implements a polynomial chaos expansion framework for quantifying the effect of the operational conditions into the modal dispersion index. By combining these two features, a vibration mode is deemed as a structural one when it appears stabilized, i.e., comes with a high modal dispersion index and is operationally normalized. The proposed method is characterized by global applicability, thus also serving as a common measure of effectiveness among diverse parametric identification methods.

**Keywords** Stabilization diagrams • Parametric identification • Dispersion analysis • Operational modal analysis • Polynomial chaos

### 8.1 Introduction

A critical and open research issue in time–domain, model–based structural identification pertains to the estimation of the number of vibration modes [1]. Thus far, among other tools, SDs have proven effective in diverse structural problems [2–4], under the principle that physical eigenmodes tend to appear at a certain frequency, irrespectively of the order of the adopted time–domain model. However, despite the fact that SDs have become a standard measure of model order assessment and are very frequently used in practice, they are still amenable to a number of inconsistencies, including sensitivity to noise, frequency splitting and stabilization of spurious modes.

While certain clearing tools [5, 6] may facilitate the decision process, especially when very large structures are considered, the inherent discrepancies (e.g., the stabilization of spurious modes) may still be present. Furthermore, existing tools that distinguish structural from extraneous modes are, in general, method specific. Among others, the use of modal amplitude

---

V.K. Dertimanis (✉) • M.D. Spiridonakos • E.N. Chatzi  
Institute of Structural engineering, ETH Zürich, Stefano-Francini-Platz 5, 8093 Zürich, Switzerland  
e-mail: [v.derti@ibk.baug.ethz.ch](mailto:v.derti@ibk.baug.ethz.ch)

coherence that is employed within the context of ERA [7] has been reported to be problematic [8], while conventional DA [9] is limited to transfer function representations and it is based on a “sensitive”, residue-based calculation. To enhance the effectiveness of the model order selection process in a more general framework, Reynders and De Roeck [10] propose the modal transfer norm metric, based on the work of Goethals and De Moor [11], while Dertimanis [12] extends the conventional DA scheme to cover state-space models as well [13]. It is noted that the latter two efforts are characterized by global applicability, in the sense that they can be applied to both state-space and transfer function model representations.

The inherent discrepancies of SDs are becoming more severe when structural identification is examined under an operational perspective. There, uncontrollable operational conditions, such as temperature gradients, humidity and others, impose a wide range of uncertainties onto the actual structural performance and, consequently, to its proper identification. As a result, the estimation of modal characteristics becomes a stochastic problem which may only be resolved via the adoption of a probabilistic framework. Generally, two approaches are followed in relative studies, namely, (i) methods which try to discard the influence of environmental factors [14], and (ii) methods which try to model the relationship between the measured vibration data and/or the extracted structural properties with respect to measured environmental quantities [15]. In contrast to the first, the second approach is capable of providing additional insight into the variation mechanisms and may also provide a global structural model, valid for a wide range of operational conditions. The method introduced herein follows the second approach and utilizes conventional modal analysis methods in order to identify the dispersion characteristics of the healthy structure and a PCE model for the projection of these estimates on the probability space of the measured environmental conditions.

The aim of this study is to incorporate a certain degree of sophistication to SDs and to transform them into a more valuable and informative tool when operational identification is considered. This is accomplished by integrating two features in the conventional diagram. The former introduces a new quantity, the MDM, which expresses a certain part of the total stochastic vibration energy, and it is attributed to each vibration mode. The MDM is extracted by applying a novel DA framework [12], which relies on the effective modal decomposition of the vibration output’s zero-lag covariance matrix, and provides further information not only on the presence of a structural mode, but also about its estimated significance. In this respect, a vibration mode is considered structural when it appears stabilized in both frequency and dispersion [16]. The second feature pertains to the expansion of the identified MDMs onto an appropriately selected PC basis. In this way, it is possible to obtain a quantitative description of the manner in which the energy of the structural modes are affected by the varying operational conditions.

The performance of the proposed method is investigated through the structural identification problem of a simulated, three DOF, lumped-mass system, which is considered to operate under varying conditions of mass and temperature. Identification is carried out using excitation and noise-corrupted, structural acceleration response data, and employing the PO-MOESP method [17] for the estimation of state-space models.

## 8.2 Time-Varying Structures

A linear, viscously damped structural system with  $n$  DOF and parameters that vary with time can be represented by a second-order vector differential equation as

$$\mathbf{M}(t)\ddot{\mathbf{q}}(t) + \mathbf{D}(t)\dot{\mathbf{q}}(t) + \mathbf{K}(t)\mathbf{q}(t) = \mathbf{f}(t), \text{ for } t \in [t_0, t_f] \quad (8.1)$$

in which  $\mathbf{M}(t)$ ,  $\mathbf{D}(t)$  and  $\mathbf{K}(t)$  are the real  $[n \times n]$  mass, viscous damping and stiffness matrices,  $\mathbf{q}(t)$  is the  $[n \times 1]$  vibration displacement vector and  $\mathbf{f}(t)$  is the  $[n \times 1]$  vector of excitations.

The variability of structural response may be usually attributed to a number of parameters related with either inherent properties of the structure or exogenous random variables, e.g. environmental and loading conditions, geometry, mass distribution, and so on. Gathering these  $L$  parameters in a single vector  $\boldsymbol{\xi}(t) = [\xi_1(t), \xi_2(t), \dots, \xi_L(t)]$ , Eq. (8.1) may be re-written as

$$\mathbf{M}(\boldsymbol{\xi}(t))\ddot{\mathbf{q}}(t) + \mathbf{D}(\boldsymbol{\xi}(t))\dot{\mathbf{q}}(t) + \mathbf{K}(\boldsymbol{\xi}(t))\mathbf{q}(t) = \mathbf{f}(t), \text{ for } t \in [t_0, t_f] \quad (8.2)$$

If only environmental conditions are considered, and assuming that they are characterized by slow (compared to the structural dynamics) variation, the previous model may be rewritten as

$$\mathbf{M}(\boldsymbol{\xi})\ddot{\mathbf{q}}(t) + \mathbf{D}(\boldsymbol{\xi})\dot{\mathbf{q}}(t) + \mathbf{K}(\boldsymbol{\xi})\mathbf{q}(t) = \mathbf{f}(t), \text{ for } t \in [t_a, t_b] \subset [t_0, t_f] \quad (8.3)$$

The latter may be considered as a local LTI model, which represents the structure when monitored during a small time interval. Within this interval the input parameter vector  $\xi$ , and as a consequence the mechanical properties of the structure, may be considered to be “fixed” to constant values. Then, the input parameter vector  $\xi$  may be considered as a realization of the vector random process  $\Xi$  with joint PDF  $f_{\Xi}(\xi)$ . In this way the initial LTV model of Eq. (8.1) may be written as a LTI model

$$\mathbf{M}(\Xi)\ddot{\mathbf{q}}(t) + \mathbf{D}(\Xi)\dot{\mathbf{q}}(t) + \mathbf{K}(\Xi)\mathbf{q}(t) = \mathbf{f}(t), \quad \text{with } \Xi \in \Omega \quad (8.4)$$

which is however characterized by parameters that are depending on the input variable vector  $\Xi$ . In the equation above,  $\Omega$  designates the event space of the random vector  $\Xi$ .

Under this setting, by defining a  $[2n \times 1]$  state vector as  $\mathbf{x}(t) = [\mathbf{q}^T(t) \ \dot{\mathbf{q}}^T(t)]^T$ , a state-space representation of Eq. (8.4) is given by

$$\dot{\mathbf{x}}(t) = \mathbf{A}_c(\Xi) \cdot \mathbf{x}(t) + \mathbf{B}_c(\Xi) \cdot \mathbf{f}(t) \quad (8.5a)$$

$$\mathbf{y}(t) = \mathbf{C}_c(\Xi) \cdot \mathbf{x}(t) + \mathbf{D}_c(\Xi) \cdot \mathbf{f}(t) \quad (8.5b)$$

with the involved matrices being defined as

$$\mathbf{A}_c(\Xi) = \begin{bmatrix} \mathbf{O}_n & \mathbf{I}_n \\ -\mathbf{M}^{-1}(\Xi) \cdot \mathbf{K}(\Xi) & -\mathbf{M}^{-1}(\Xi) \cdot \mathbf{C}(\Xi) \end{bmatrix} [2n \times 2n], \quad \mathbf{B}_c(\Xi) = \begin{bmatrix} \mathbf{0} \\ \mathbf{M}^{-1}(\Xi) \end{bmatrix} [2n \times n] \quad (8.6)$$

for the state equation and

$$\mathbf{y}(t) = \mathbf{q}(t) \quad (\text{displacement}): \quad \mathbf{C}_c(\Xi) = [\mathbf{I}_n \ \mathbf{O}_n] [n \times 2n], \quad \mathbf{D}_c(\Xi) = \mathbf{0} \quad (8.7a)$$

$$\mathbf{y}(t) = \dot{\mathbf{q}}(t) \quad (\text{velocity}): \quad \mathbf{C}_c(\Xi) = [\mathbf{O}_n \ \mathbf{I}_n] [n \times 2n], \quad \mathbf{D}_c(\Xi) = \mathbf{0} \quad (8.7b)$$

$$\mathbf{y}(t) = \ddot{\mathbf{q}}(t) \quad (\text{acceleration}): \quad \mathbf{C}_c(\Xi) = [-\mathbf{M}^{-1}(\Xi) \cdot \mathbf{K}(\Xi) \ -\mathbf{M}^{-1}(\Xi) \cdot \mathbf{C}(\Xi)] [n \times 2n], \quad \mathbf{D}_c(\Xi) = \mathbf{M}^{-1}(\Xi) \quad (8.7c)$$

for the output equation.

By selecting an appropriate sampling period  $T_s$  and assuming constant intersample behavior of the excitation vector signal [18, Sec. 7.6], the discrete-time equivalent of the system described by Eq. (8.5) is

$$\mathbf{x}[t+1] = \mathbf{A}_d(\Xi) \cdot \mathbf{x}[t] + \mathbf{B}_d(\Xi) \cdot \mathbf{f}[t] \quad (8.8a)$$

$$\mathbf{y}[t] = \mathbf{C}_d(\Xi) \cdot \mathbf{x}[t] + \mathbf{D}_d(\Xi) \cdot \mathbf{f}[t] \quad (8.8b)$$

with  $\mathbf{C}_d(\Xi) = \mathbf{C}_c(\Xi)$ ,  $\mathbf{D}_d(\Xi) = \mathbf{D}_c(\Xi)$  and

$$\mathbf{A}_d(\Xi) = e^{\mathbf{A}_c(\Xi) \cdot T_s}, \quad \mathbf{B}_d(\Xi) = [\mathbf{A}_d(\Xi) - \mathbf{I}] \cdot \mathbf{A}_c^{-1}(\Xi) \cdot \mathbf{B}_c(\Xi) \quad (8.9)$$

### 8.3 Dispersion Analysis

Under the assumption that the structural excitation can be modeled as a zero-mean Gaussian white noise process with covariance matrix

$$\mathbf{\Gamma}_{ff}[h] = \mathbf{\Sigma}_{ff} \delta[h] \quad (8.10)$$

where  $\delta[h]$  denotes Kronecker's Delta function and  $h$  the time lag, it can be proved [12] that a modal decomposition of the state vector's covariance matrix is

$$\mathbf{\Gamma}_{xx}[h, \Xi] \equiv E \left\{ \mathbf{x}[t+h] \mathbf{x}^T[t] \right\} = \sum_{k=1}^{2n} \mathbf{P}_k(\Xi) \lambda_k^h(\Xi) \quad (8.11)$$

where  $\lambda_k(\boldsymbol{\Xi})$  is the  $k$ th eigenvalue of  $\mathbf{A}_d(\boldsymbol{\Xi})$  (distinct eigenvalues have been assumed) and  $\mathbf{P}_k(\boldsymbol{\Xi})$  is given by

$$\mathbf{P}_k(\boldsymbol{\Xi}) = \mathbf{G}_k(\boldsymbol{\Xi}) \boldsymbol{\Sigma} \sum_{m=1}^{2n} \frac{\mathbf{G}_m^T(\boldsymbol{\Xi})}{1 - \lambda_k(\boldsymbol{\Xi})\lambda_m(\boldsymbol{\Xi})} \quad (8.12)$$

In Eq. (8.12),  $\boldsymbol{\Sigma} = \mathbf{B}_d(\boldsymbol{\Xi}) \boldsymbol{\Sigma}_{ff} \mathbf{B}_d^T(\boldsymbol{\Xi})$  and  $\mathbf{G}_k$ 's are the projectors of the spectral decomposition of  $\mathbf{A}_d(\boldsymbol{\Xi})$  [19],

$$f(\mathbf{A}_d(\boldsymbol{\Xi})) = \sum_{k=1}^{2n} \mathbf{G}_k(\boldsymbol{\Xi}) f(\lambda_k(\boldsymbol{\Xi})) \quad (8.13)$$

for which  $\mathbf{G}_k^2(\boldsymbol{\Xi}) = \mathbf{G}_k(\boldsymbol{\Xi})$ ,  $\mathbf{G}_i(\boldsymbol{\Xi})\mathbf{G}_j(\boldsymbol{\Xi}) = \mathbf{O}$ , for  $i \neq j$  and  $\sum_k \mathbf{G}_k(\boldsymbol{\Xi}) = \mathbf{I}$ . In Eq. (8.18),  $f$  denotes a function that is defined for every  $\lambda_k(\boldsymbol{\Xi})$ . Using Eq. (8.11) it is possible to derive a corresponding expression for the output vector  $\mathbf{y}[t]$ , by just exploring the output equation of the state–space representation. It can be deduced that  $\boldsymbol{\Gamma}_{yy}[h, \boldsymbol{\Xi}]$  can be expressed as

$$\boldsymbol{\Gamma}_{yy}[h, \boldsymbol{\Xi}] \equiv E \left\{ \mathbf{y}[t+h] \mathbf{y}^T[t] \right\} = \sum_{k=1}^{2n} \mathbf{Q}_k(\boldsymbol{\Xi}) \lambda_k^h(\boldsymbol{\Xi}) \quad (8.14)$$

where the matrices  $\mathbf{Q}_k(\boldsymbol{\Xi})$  are calculated in respect to the type of the vibration output: in the displacement/velocity case  $\mathbf{Q}_k(\boldsymbol{\Xi}) = \mathbf{C}_d(\boldsymbol{\Xi}) \mathbf{P}_k(\boldsymbol{\Xi}) \mathbf{C}_d^T(\boldsymbol{\Xi})$ , whereas in the acceleration case the expressions are more complicated. Refer to Dertimanis [12] for further details.

Having established a modal decomposition for the covariance matrix of the output vector under broadband stochastic excitation, it follows that at zero lag

$$\boldsymbol{\Gamma}_{yy}[0, \boldsymbol{\Xi}] = \sum_{k=1}^{2n} \mathbf{Q}_k(\boldsymbol{\Xi}) = \sum_{k=1}^n \mathbf{Q}_k(\boldsymbol{\Xi}) + \mathbf{Q}_k^*(\boldsymbol{\Xi}) \quad (8.15)$$

with the asterisk denoting complex conjugate. Taking under consideration that  $\boldsymbol{\Gamma}_{yy}[0, \boldsymbol{\Xi}]$  corresponds to the multivariate equivalent of variance and it can, thus, be associated to the stochastic vibration energy of the output series, a *modal dispersion matrix* can be defined as

$$\mathbf{E}_k(\boldsymbol{\Xi}) = \mathbf{Q}_k(\boldsymbol{\Xi}) + \mathbf{Q}_k^*(\boldsymbol{\Xi}) \quad (8.16)$$

in order to assess the contribution of the  $k$ th mode to the total vibration energy. Correspondingly, the *normalized modal dispersion matrix* is defined as a matrix  $\boldsymbol{\Delta}_k(\boldsymbol{\Xi})$  with elements

$$[\boldsymbol{\Delta}_k]_{ij}(\boldsymbol{\Xi}) = \frac{[\mathbf{E}_k(\boldsymbol{\Xi})]_{ij}}{\left[ \sum_{m=1}^n \mathbf{E}_m(\boldsymbol{\Xi}) \right]_{ij}} 100 \% = \frac{[\mathbf{E}_k(\boldsymbol{\Xi})]_{ij}}{[\boldsymbol{\Gamma}_{yy}[0, \boldsymbol{\Xi}]]_{ij}} 100 \% \quad (8.17)$$

Essentially, the DA framework attributes a quantitative index to each vibration mode. To see that this is indeed the case, a *modal dispersion metric* (MDM) can be defined from the modal dispersion matrices as

$$\delta_{\Delta,k,2}(\boldsymbol{\Xi}) = \|\boldsymbol{\Delta}_k\|_2 \quad (8.18)$$

using the  $L_2$  norm, where  $k = 1, 2, \dots, n$ . Equation (8.18) implies that every vibration mode can now be characterized by four quantities: the natural frequency, the damping ratio, the mode shape and the MDM. This feature can be used in both forward (e.g., for model reduction) and inverse setting. In the latter case, the MDM can be very easily incorporated into SDs. While several alternatives can be potentially examined, two implementations are currently discussed and assessed in the following. The first implementation simply refers to modify the SD in a way that renders the estimated dispersion of each mode. This can be done by either introducing a third dimension to the original two–dimensional format of the SDs, or by attributing a certain color range to the modal dispersion band and, accordingly, coloring each identified mode. In this way, mode stabilization can not only refer to the value of a specific frequency, but also to its attributed color.

Since the MDM that accompanies a specific mode may be expanded over a wide range of numerical values, a second implementation can be accomplished by introducing a *normalized modal dispersion metric* (nMDM) as

$$\bar{\delta}_{\mathfrak{q},k,2}(\Xi) = \frac{\delta_{\mathfrak{q},k,2}}{\max_k(\delta_{\mathfrak{q},k,2})} \quad (8.19)$$

for  $\mathfrak{q} = E, \Delta$ . This metric is always a number between 0 and 1, with the latter value corresponding to the mode of the highest contribution to the stochastic vibration energy of the structure. The use of this normalization to the SDs enables direct extraction of the most important vibration modes. In addition, a threshold can be further employed so as to prevent modes with negligible nMDM, compared to the one of the most important mode, to appear to a SD. It is emphasized that, while the process described herein stems from the original state-space representation, it can be extended to cover transfer function representations as well [12].

## 8.4 Polynomial Chaos Expansion

PCE concerns the expansion of a random output variable on polynomial chaos basis functions which are orthonormal to the probability space of the system's random inputs. More specifically, let us consider the general system  $S$  described by Eq. (8.4), with  $L$  random input parameters represented by independent random variables  $\Xi_1, \dots, \Xi_L$ , e.g. temperatures measured at different locations of the structure, gathered in a random vector  $\Xi$  of prescribed joint PDF  $p_{\Xi}(\xi)$  [20]. The system output, in our case the MDM denoted by  $Y = \delta_{\Delta,k,2}(\Xi)$  will also be random. Provided that  $Y$  has finite variance, it can be expressed as follows:

$$Y = S(\Xi) = \sum_{d \in \mathbb{N}^L} \theta_d \phi_d(\Xi), \quad (8.20)$$

where  $\theta_d$  are unknown deterministic coefficients of projection,  $d$  is the vector of multi-indices of the multivariate polynomial basis, and  $\phi_d(\Xi)$  are the polynomial basis (PC) functions orthonormal to  $p_{\Xi}(\xi)$ . These basis functions may be constructed through tensor products of the corresponding univariate functions.

Each probability density function may be associated with a well-known family of orthogonal polynomials. For instance, normal distribution is associated with Hermite polynomials while uniform distribution with Legendre. A list of the most common probability density functions along with the corresponding orthogonal polynomials and the relations for their construction may be found in [21].

For purposes of practicality the basis functions series must be truncated to a finite number of terms, with the usual approach being the selection of the multivariate polynomial basis with total maximum degree  $|\mathbf{d}_j| = \sum_{m=1}^L d_{(j,m)} \leq P$  for every  $j$ . In this case the dimensionality of the functional subspace is equal to

$$p = \frac{(L + P)!}{L!P!} \quad (8.21)$$

where  $L$  is the number of random variables and  $P$  the maximum basis degree. Therefore, when truncating the infinite series of expansion of Eq. (8.20) to the first  $p$  terms, the resulting PCE model is fully parametrized in terms of a finite number of deterministic coefficients of projection  $\theta_d$ . Parameter vector  $\theta_d$  may be estimated by solving Eq. (8.20) in a least squares sense. Toward this end, the data of the output variables and the PDFs of the input variables have to be employed. The PDFs of the input variables may be obtained by fitting known statistical distributions to the observed input variables values.

By expanding the identified MDMs onto an appropriately selected PC basis, a description of the way that the energy of the structural modes is affected by the changing environmental and/or operational conditions.

## 8.5 Case Study

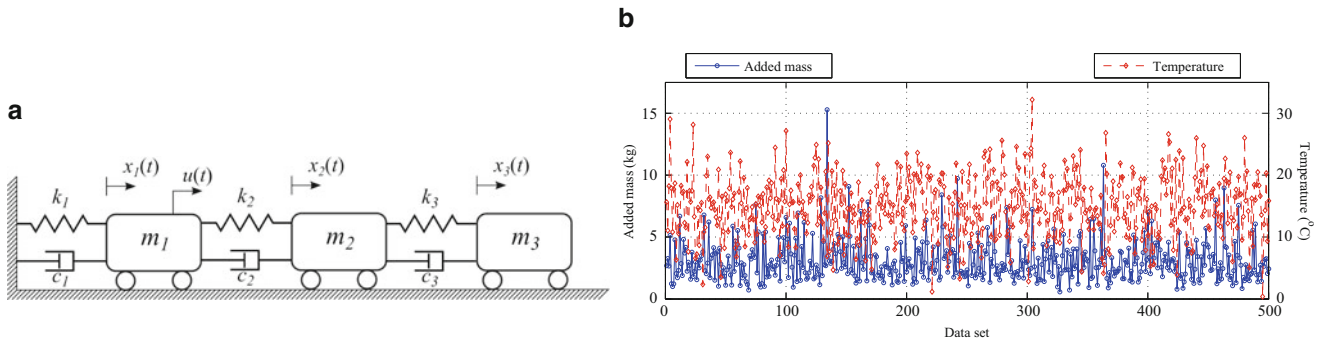
The proposed framework is now applied to the structural identification problem of a single-input, three-output structural system illustrated in Fig. 8.1a. The structure is assumed to operate under varying conditions of mass and temperature. In specific, regarding the former, mass increments are added to  $m_1$ ,  $m_2$  and  $m_3$  (see Fig. 8.1a), in accordance to the log-normal distribution with mean value equal to 1 and variance equal to 0.25, that is,  $\Xi_1 \sim \ln N(1, 0.25)$ . For the latter, the stiffness coefficients are considered to be linearly depended on the temperature according to  $k'_i = k_i [1 - (T - T_{ref})k_T]$ , where  $k_T = 5 \times 10^{-3}$  is the thermal coefficient and  $T_{ref} = 20^\circ\text{C}$  is the reference temperature. The PDF of the temperature corresponds to a normal distribution with mean value equal to 15 and variance equal to 25, i.e.,  $\Xi_2 \sim N(15, 25)$ .

For the identification experiments, 500 samples of the added mass and temperature variables are drawn, by means of the Latin Hypercube Sampling (LHS) method, from their theoretical PDFs and the corresponding data are shown in Fig. 8.1b. For each mass-temperature pair, the structure is brought into the state-space format for acceleration output. Accordingly, discretization is performed using the zero order hold at  $T_s = 0.015625$  s (corresponding to sampling frequency  $F_s = 64$  Hz) and the discrete-time state-space model is excited by a  $u(t) \sim N(0, 10^4)$ . The resulting structural acceleration responses are zero-mean subtracted and noise-corrupted at 5% N/S ratio, forming a final single input-three output data set of  $N = 3,000$  data per channel. Identification is performed by the PO-MOESP [17] method (Hankel matrix with 100 block rows is chosen), for even state orders between 2 and 30.

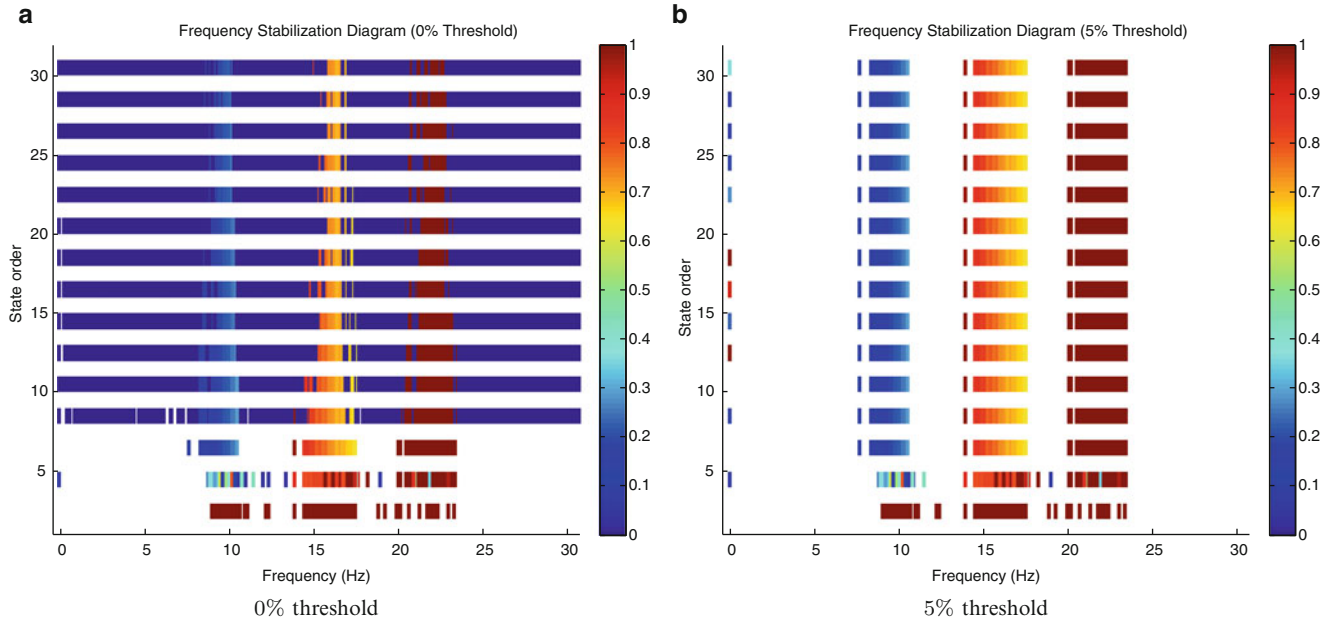
Figure 8.2 shows the results of the identification process, where two instants of the SDs are presented. The modified SDs convey significantly enriched in comparison to the conventional ones. Focusing on the left SD (Fig. 8.2a), one can distinguish three areas that exhibit stabilization in both the frequency and the nMDM. As no threshold is activated, numerous frequencies appear naturally, many of which tend to stabilize. These are however attributed by negligible nMDMs and can safely be discarded as extraneous. This is clearly indicated in Fig. 8.2b, where a 5% threshold has been applied to the SD.

One can distinguish three modes that appear stabilized in both the frequency and the MDM, while it seems that the third mode can be considered as the most significant one, based on its relative contribution to the total stochastic vibration energy. A fourth mode that appears around zero on Fig. 8.2b is accompanied by destabilized dispersion and can safely discarded. Even if the ordering of the modes with respect to their dispersion seems invariant over the change of operational conditions, the calculated dispersions are highly affected by these conditions. This dependency is identified by the dispersion expansion onto PC bases described in the previous section.

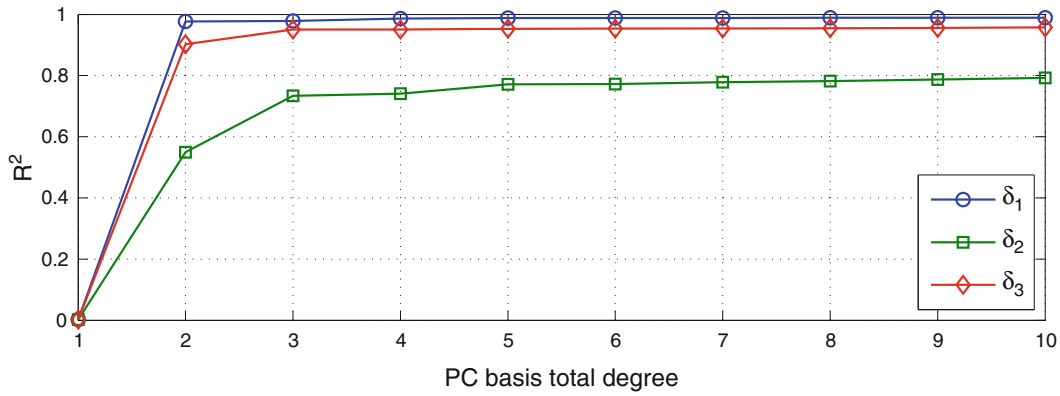
The induced SDs promote a 6th order state-space model for the description of the structural system over the whole range of environmental conditions. This implies the extraction of three structural vibration modes, the MDMs of which are reflected to the corresponding entry of the SD of Fig. 8.2b, that is, the color bars along state order 6. In order to obtain a quantitative description of their performance, a corresponding set of MDMs ( $100 \times 3$ ) are then expanded on the probability space of the latent input variables through PCE. Toward this end, and after transforming the PDF of the mass load into a normal distribution by using the natural logarithm, the Hermite polynomials may be selected for the construction of the multivariate PC basis functions. The total polynomial degree of the PC basis is selected based on the  $R^2$  criterion, that is:



**Fig. 8.1** The numerical case study considered. (a) Three DOF structural system with  $m_1 = 10^2$  kg,  $m_2 = 10^{1.5}$  kg,  $m_3 = 10$  kg,  $k_1 = 10^6$  N/m,  $k_2 = 10^{5.5}$  N/m,  $k_3 = 10^5$  N/m,  $c_1 = 100$  N/m/s,  $c_2 = 10$  N/m/s,  $c_3 = 1$  N/m/s and  $\mathbf{f}(t) = (1, 0, 0)^T u(t)$ . (b) Mass and temperature values for the 500 simulations



**Fig. 8.2** The induced SDs. (a) 0 % threshold (b) 5 % threshold



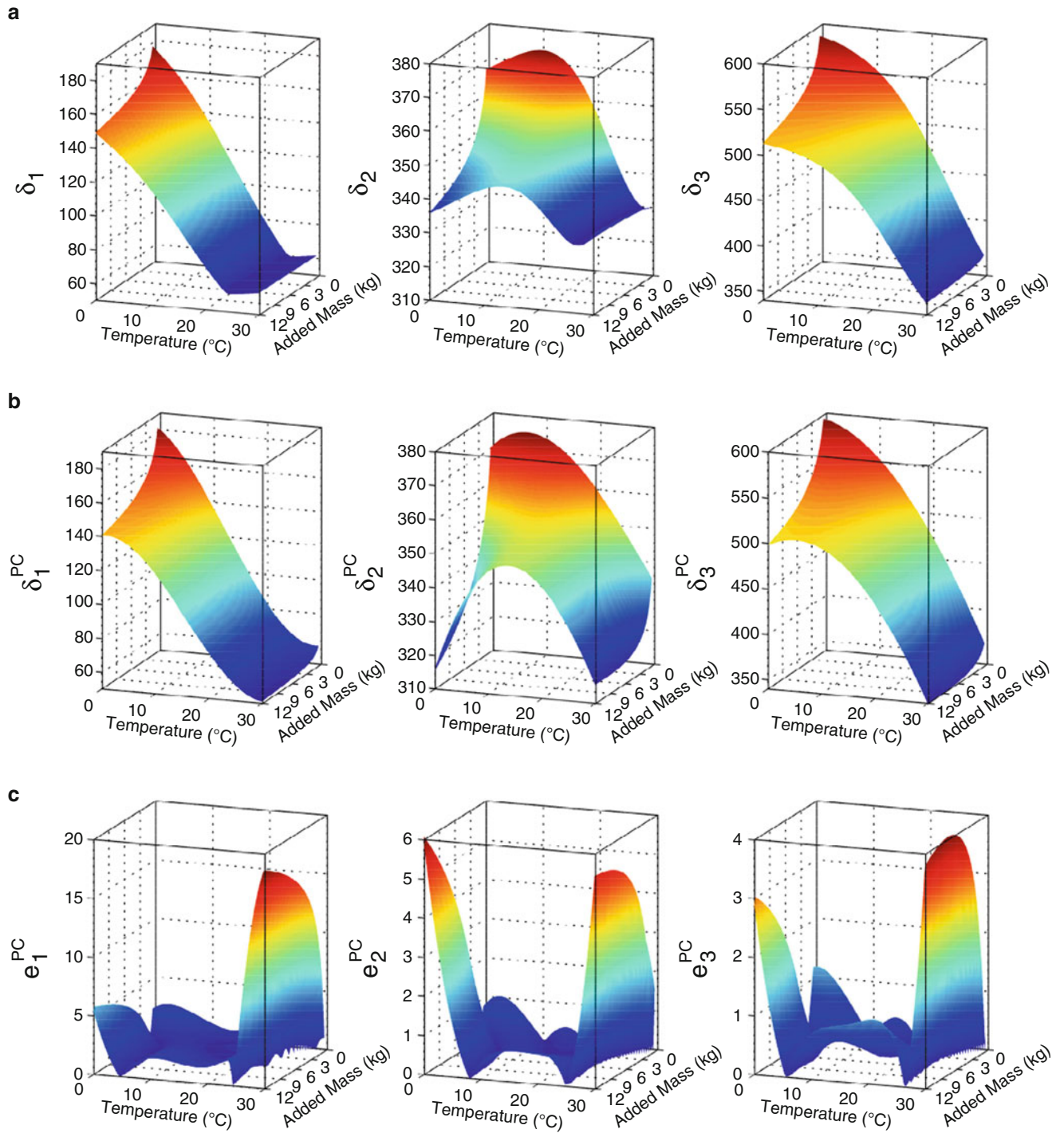
**Fig. 8.3**  $R^2$  criterion values for the expanded MDM estimated values for various total polynomial degrees  $P = 0, \dots, 10$

$$R^2 = 1 - \frac{\sum_{k=1}^{100} (Y_k - Y_k^{PC})^2}{\sum_{k=1}^{100} Y_k^2} \quad (8.22)$$

by searching the maximum total degree within the range between 0 and 10, and the resulting  $R^2$  values are plotted in Fig. 8.3. Based on these results the total polynomial degree is selected equal to three  $P = 3$  for all dispersions. Thus, using Eq. (8.21) with  $P = 3$  and  $L = 2$  gives a total number of 10 candidate basis functions.

The estimated PC coefficients of projection may be used for calculating the PCE based estimates of the MDM values, and thus for constructing a surface that shows the dependence of the dispersion of the 3-DOF system on the two input random variables. The results are plotted against the theoretical curves in Fig. 8.4. It may be observed that there is a good agreement between the theoretical and the estimated dispersions, with the highest errors occurring at extreme values of the input variables.





**Fig. 8.4** (a) Actual dispersion values compared to (b) the PC based dispersion estimates and (c) the corresponding normalized errors. The dispersion are plotted versus the input variables, that is added mass and temperature

## 8.6 Conclusion

A novel framework for the application of SDs to structural systems subject to changing environmental and operational conditions was presented through the integration of additional information to their conventional form. To this end, a newly introduced index, the MDM, that quantifies the modal contribution to the stochastic structural response was attributed to each vibration mode, under the assumption of broadband random excitation.

Accordingly, PCE was utilized for the expansion of the MDM on polynomial chaos basis functions that are orthonormal to the probability space of the systems random inputs, which for the case study considered were limited to mass and temperature. In this respect, it was made possible to track the stochastic vibration energy of each mode over a wide range of varying conditions.

The promising results suggest further research towards this framework, especially with respect to output-only identification and implementation on the operational modelling of real-world structures.

## References

1. Reynders E (2012) System Identification methods for (Operational) modal analysis: review and comparison. *Arch Comput Meth Eng* 19(1):51–124
2. Antonacci E, De Stefano A, Gattulli V, Lepidi M, Matta E (2012) Comparative study of vibration-based parametric identification techniques for a three-dimensional frame structure. *Struct Control Health Monit* 19(5):579–608
3. Bayraktar A, Altunışık AC, Sevim B, Türker T (2011) Seismic response of a historical masonry minaret using a finite element model updated with operational modal testing. *J Vib Control* 17(1):129–149
4. Lau J, Lanslots J, Peeters B, Van der Auweraer H (2007) Automatic modal analysis: reality or myth? In: Proceedings of the 25th international modal analysis conference, IMAC-XXV, Orlando
5. Giraldo D, Caicedo JM, Song W, Mogan B, Dyke SJ (2009) Modal identification through ambient vibration: A comparative study. In: Proceedings of the 24th International modal analysis conference, IMAC-XXIV, St Louis
6. Van Der Auweraer H, Peeters B (2004) Discriminating physical poles from mathematical poles in high order systems: Use and automation of the stabilization diagram. In: Proceedings of the 21st IEEE instrumentation and measurement technology conference, Como
7. Juang JN, Pappa RS (1985) An eigensystem realization algorithm for modal parameter identification and model reduction. *J Guid Control Dyn* 8(5):620–627
8. Florakis A, Fassois SD, Hemez FM (2001) MIMO LMS-ARMAX identification of vibrating structures-Part II: A critical assessment. *Mech Syst Sig Process* 15(4):737–758
9. Fassois SD (2001) MIMO LMS-ARMAX identification of vibrating structures-Part I: The method. *Mech Syst Sig Process* 15(4):723–735
10. Reynders E, De Roeck G (2008) Reference-based combined deterministic-stochastic subspace identification for experimental and operational modal analysis. *Mech Syst Sig Process* 22(3):617–637
11. Goethals I, De Moor B (2002) Model reduction and energy analysis as a tool to detect spurious modes. In: Proceedings of the 2002 International conference on noise and vibration engineering, ISMA, Leuven, Belgium
12. Dertimanis VK (2013) On the use of dispersion analysis for model assessment in structural identification. *J Vib Control* 19(15):2270–2284
13. Dertimanis VK, Koulocheris DV (2011) VAR based state-space structures: realization, statistics and spectral analysis. *Lecture Notes in Electrical Engineering*, vol 85. Springer, New York, pp 301–315
14. Kullaa J (2011) Vibration-based structural health monitoring under variable environmental or operational conditions. *CISM courses and lectures*, chapter 4, vol. 520. Springer, New York, pp 107–181
15. Peeters B, Roeck GD (2001) One-year monitoring of the z24-bridge: environmental effects versus damage events. *Earthq Eng Struct Dyn* 30(2):149–171
16. Dertimanis VK, Chatzi EN (2014) Dispersion-corrected stabilization diagrams for model order assessment in structural identification. In: 7th European workshop on structural health monitoring 2012, EWSHM 2012, Nantes
17. Verhaegen M (1994) Identification of the deterministic part of MIMO state space models given in innovations form from input-output data. *Automatica* 30(1):61–74
18. Fadali MS (2009) *Digital control engineering: analysis and design*. Academic Press, Massachusetts
19. Meyer CD (2000) *Matrix analysis and applied linear algebra*. Society for industrial and applied mathematics, Philadelphia, USA
20. Blatman G, Sudret B (2010) An adaptive algorithm to build up sparse polynomial chaos expansions for stochastic finite element analysis. *Prob Eng Mech* 25(2):183–197
21. Xiu D, Karniadakis G (2002) The wiener-asky polynomial chaos for stochastic differential equations. *SIAM J Sci Comput* 24(2):619–644

# Chapter 9

## Online Damage Detection in Plates via Vibration Measurements

Giovanni Capellari, Saeed Eftekhar Azam, and Stefano Mariani

**Abstract** In this work, we propose a new framework for the online detection of damage in plates via vibration measurements. To this end, a finite element model of the plate is handled by a recursive Bayesian filter for simultaneous state and parameter estimation. To drastically reduce the computational costs and enhance the robustness of the filter, such model is projected onto a (sub-) space spanned by a few vibration modes only, which are provided by a snapshot-based proper orthogonal decomposition (POD) method. A challenge in using such approach for damaging structures stems from the fact that vibration modes can be adjusted only during the training stage of the analysis; if damage occurs or grows when the reduced-order model is at work, the training stage has to be re-started. Here, an alternate method is proposed to concurrently update the sub-space spanned by the modes and to provide estimates of damage location and amplitude. The robustness and accuracy of the proposed approach are ascertained through an ad-hoc pseudo-experimental campaign.

**Keywords** Structural health monitoring • Damage detection • Reduced-order modeling • Proper orthogonal decomposition • Extended Kalman-particle filtering • Thin plates • Finite element

### 9.1 Introduction

The objective of this article is to propose a damage identification scheme for time-continuous structural health monitoring schemes. In doing so, recursive Bayesian filters are coupled with a model order reduction method. The developed methodology furnishes estimates of the local damage parameters associated to a set of purposely defined sub-structures; the mentioned damage indexes are defined in standard fashion, as scalar variables linearly degrading the local virgin stiffness. The effective order reduction technique used herein guarantees a limited computational cost, and a coupling of the procedure with a commercial finite element (FE) code to permit the strategy to be applied to a large variety of problems. The identification method obviously requires that measurements, such as rotations or accelerations at characteristic points on the surface of the structure, are to be gathered during health monitoring.

One of the main disadvantages of any identification technique based on recursive Bayesian filters is the entailed high computational burden. To render the objective of fast, robust and unbiased estimation of damage indexes associated with the sub-structures, two remedies have been adopted: a model order reduction based on the POD, and a modified particle filter. The model order reduction is achieved by adopting a Galerkin-based projection of the original full model into a sub-space spanned by the so-called proper orthogonal modes (POMs), computed with the POD in its snapshot-based version [1–3]. The method is established such that it can be applied to structures independently of the FE model used to discretize them. Henceforth, the damage indexes that define the degradation of the original stiffness of the structure need to be handled.

The reduced bases furnished by POD cannot depend on changes of the stiffness parameters of the system; hence, the reduced-order models established by POMs cannot provide the same level of accuracy for different values of the damage index. As the estimation of the damage indexes is pursued concurrently to the tracking of the state of the structure, an online

---

G. Capellari • S. Mariani

Dipartimento di Ingegneria Civile e Ambientale, Politecnico di Milano, Piazza L. da Vinci 32, Milan 20133, Italy

S. Eftekhar Azam (✉)

Department of Mechanical Engineering, University of Thessaly, Leoforos Athinon, Pedion Areos, Volos 38334, Greece

e-mail: [eftekhar@uth.gr](mailto:eftekhar@uth.gr)

update of the sub-space is proposed to maintain the accuracy of the reduced-order model in case damage gets incepted. The dual estimation of state and damage indexes is based on a particle filter enhanced through the use of a further (extended) Kalman filter, to move the particles before the resampling stage [3, 4]. This intricate formulation allows the tracking of both the dynamic evolution of the partially observed or hidden state of the system, and of the possible growth of the damage indexes.

In order to test the capability of the proposed damage identification technique, a thin plate case is considered. It is demonstrated that the procedure successfully identifies and locates the damage, even when using a reduced-order model of the system consisting in a few (two or three) degrees-of-freedom.

The recent developments in smart embedded data acquisition systems and MEMS (micro electro-mechanical systems) type accelerometers, promise feasibility of the presented method via establishing a way to collect vibration data for lightweight and small structures without varying their response to the external excitations [5].

A method for dual estimation and reduced-order modelling of damaging structures, similar to that adopted herein for dual estimation and sub-space update, was recently developed and successfully applied to shear-type buildings in [1, 3]. In this article, the approach is evolved in such a way that it is now able to locate and estimate (almost) in real-time a structural damage through a few vibration measurements only.

## 9.2 Theory

Let us consider a space-discretized (e.g., through finite elements) structural system. Its time evolution in a dynamic frame is provided by the equations of motion:

$$\mathbf{M}\ddot{\mathbf{u}} + \mathbf{D}\dot{\mathbf{u}} + \mathbf{K}\mathbf{u} = \mathbf{F} \quad (9.1)$$

where:  $\mathbf{M}$  is the mass matrix;  $\mathbf{D}$  is the viscous damping matrix;  $\mathbf{K}$  is the stiffness matrix;  $\mathbf{F}$  is the external force vector;  $\ddot{\mathbf{u}}$ ,  $\dot{\mathbf{u}}$  and  $\mathbf{u}$  are the vectors of system (nodal) accelerations, velocities and displacements, respectively.

In Eq. (9.1) it has been assumed that the system behaves linearly, hence any inelastic response to the loading looks prevented. By discretizing now the time interval of interest according to  $[t_0 \ t_N] = \cup_{i=0}^{N-1} [t_i \ t_{i+1}]$ ,  $N$  being the number of time steps of constant size  $\Delta t = t_{i+1} - t_i$ , within  $[t_i \ t_{i+1}]$  the time update of the structural configuration is given by the Newmark algorithm [6] as:

- prediction stage:

$$\begin{aligned} \tilde{\mathbf{u}}_{i+1} &= \mathbf{u}_i + \Delta t \dot{\mathbf{u}}_i + \Delta t^2 \left(\frac{1}{2} - \beta\right) \ddot{\mathbf{u}}_i \\ \tilde{\dot{\mathbf{u}}}_{i+1} &= \dot{\mathbf{u}}_i + \Delta t (1 - \gamma) \ddot{\mathbf{u}}_i \end{aligned} \quad (9.2)$$

- explicit integration stage:

$$\ddot{\mathbf{u}}_{i+1} = \mathbf{M}^{-1} (\mathbf{F}_{i+1} - \mathbf{D}\tilde{\dot{\mathbf{u}}}_{i+1} - \mathbf{K}\tilde{\mathbf{u}}_{i+1}) \quad (9.3)$$

- correction stage:

$$\begin{aligned} \mathbf{u}_{i+1} &= \tilde{\mathbf{u}}_{i+1} + \Delta t^2 \beta \ddot{\mathbf{u}}_{i+1} \\ \dot{\mathbf{u}}_{i+1} &= \tilde{\dot{\mathbf{u}}}_{i+1} + \Delta t \gamma \ddot{\mathbf{u}}_{i+1} \end{aligned} \quad (9.4)$$

where  $\beta$  and  $\gamma$  are algorithmic parameters. Equation (9.3) shows that the structural stiffness comes into play only in the integration stage and, once it is locally scaled proportionally to a damage (or integrity) scalar coefficient, it can be potentially assumed as time-varying, and tuned by a filtering procedure. In other words, the stiffness matrix can be expressed as a linear combination of  $N_p$  reference stiffness matrices ( $N_p$  being the number of regions, or sub-structures), each one scaled by the corresponding damage index  $d_j$ , with  $j = 1, \dots, N_p$ , so as:

$$\mathbf{K} = \mathbf{K}(d_j) \quad (9.5)$$

Each damage index is here assumed to affect the local Young's modulus of the structural material according to:

$$E_j = (1 - d_j) E \quad (9.6)$$

It thus follows that a step-wise constant assumption for the structural health is proposed, with the integrity possibly changing in time due to the external actions. We do not provide here evolution laws for the local damage, as the filter itself can be shown to be able to tune it through the collected measurements of the system responses.

For later use, Eqs. (9.2) (9.3) and (9.4) are formally written as:

$$z_{i+1} = f_i(z_i) \quad (9.7)$$

once the full state vector  $z_i = \{u_i \dot{u}_i \ddot{u}_i\}^T$  is defined.

Focusing on the displacement vector  $u$  (without explicitly mentioning now the time instant  $t_i$ ), in a linear regime we can write:

$$u = \Phi \zeta \quad (9.8)$$

where  $\Phi$  is a matrix gathering the  $m$  orthonormal bases of the space within which the vector evolves, and  $\zeta$  is the relevant vector of time-varying coefficients combining the time-invariant bases. To reduce the computational burden of the identification procedure, we define a reduced-order displacement vector  $u_r$  as:

$$u_r = \Phi_r \alpha \quad (9.9)$$

where  $\Phi_r$  is a matrix gathering only the most important  $\ell$  bases (or POMs) for the specific problem at hand, and  $\alpha$  is the vector of combination coefficients relevant to such sub-space model. To reduce the norm  $\|u - u_r\|$  as well as the dimension  $\ell$  of the sub-space, POD is here adopted in its snapshot version [7]. We refer the readers to, e.g., [2, 3], where a notation consistent with the present one was adopted, to get insights into all the relevant details of such procedure. It suffices to mention that, once a so-called snapshot matrix is assembled by joining the response of the structure to the considered loading at a specified number of time instants, and after computing a singular value decomposition of this matrix, the resulting left singular vectors represent the sought basis set  $\Phi_r$ , and the singular values allow to define the (energetic) accuracy  $p \in (0, 1]$  of the reduced-order model.

As the bases do not change in time, a reduced-order representation for the velocity and acceleration vectors can be accordingly obtained as  $\dot{u}_r = \Phi_r \dot{\alpha}$  and  $\ddot{u}_r = \Phi_r \ddot{\alpha}$ , respectively. Through a Galerkin projection, the reduced-order equations of motion are obtained as:

$$M_r \ddot{\alpha} + D_r \dot{\alpha} + K_r \alpha = F_r \quad (9.10)$$

where:  $M_r = \Phi_r^T M \Phi_r$ ,  $D_r = \Phi_r^T D \Phi_r$ ,  $K_r = \Phi_r^T K \Phi_r$  and  $F_r = \Phi_r^T F$ .

To allow also for model parameters and, specifically, for the aforementioned scalar damage indexes  $d_j$  in all the regions of the structure (possibly in each finite element), according to a standard procedure adopted for dual identification of partially observed systems, we build an enhanced (or extended) state vector by joining the structural state  $z$  and the parameters ( $\theta$ ) themselves [4]. At time  $t_i$  this reads:

$$x_i = \begin{Bmatrix} z_i \\ \theta_i \end{Bmatrix} \quad (9.11)$$

Considering next an observation equation to link the measurable  $y$  to the full state of the system, in a stochastic frame where noises are also accounted for we can write the reduced-order state estimation and damage identification problem as:

$$\begin{aligned} x_{r,i+1} &= f_{r,i}(x_{r,i}) + v_i \\ y_i &= H \begin{bmatrix} \Phi_{r,i} & & & \\ & \Phi_{r,i} & & \\ & & \Phi_{r,i} & \\ & & & 0 \end{bmatrix} x_{r,i} + w_i \end{aligned} \quad (9.12)$$

**Table 9.1** General scheme of the proposed dual damage identification procedure

Initialization at time $t_0$
At time $t_i$ , for $i = 1, \dots, N$
<i>Prediction stage:</i>
Draw particles
Push the particles toward the region of high probability through an EKF
<i>Update stage:</i>
Evolve weights
Resampling
Compute expected value and other required statistics
Predict subspace and associated covariance
Calculate KF gain for updating subspace
Update subspace and associated covariance

where:  $v_i$  and  $w_i$  are additive, zero mean, white Gaussian noises that respectively represent the uncertainties in the process and measurement equations;  $H$  is a Boolean matrix that links the observation vector to the current state of the system.

To handle the possible evolution of the sub-space onto which the full system is projected, the matrix  $\Phi_r$  has to be continuously tuned during the analysis; we have therefore adopted in Eq. (9.12) the index  $i$  to state that it can evolve in time, and it requires an estimation to be provided by the filtering procedure. To summarize, at each time instant the proposed procedure has to: track the state  $z$  of the system; identify the location and magnitude of damage through vector  $\theta$ ; tune the sub-space projector  $\Phi_r$  if damage grows and a deviation from linearity arises. The whole procedure is reported in Table 9.1.

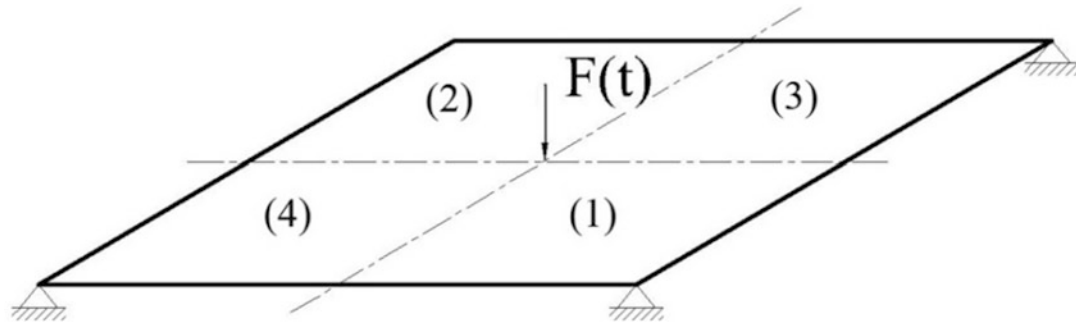
To possibly allow for multivariate probability distributions of state vector components, in [1, 3] we started adopting a particle filtering approach to the aforementioned dual estimation problem. As the relevant costs of identification can get extremely increased in comparison to, e.g., unscented Kalman filtering [4], a Rao-Blackwellized version of the filter was then considered: this explains the second action in the prediction stage of Table 9.1. To also permit the mentioned online evolution of the sub-space projector, a further Kalman filter was shown to be effective in [3]: this is carried out as the fourth and sixth actions in the update stage still mentioned in Table 9.1. All the algorithmic details are here dropped, and interested readers are referred to [1].

### 9.3 Results

The performance of the proposed approach, in terms of state tracking and identification of the structural health (i.e., of the damage indexes), is evaluated through a simple benchmark test. A square plate, whose side length is 200 mm and thickness is 5 mm, is assumed to be simply supported at the four corners and subjected to a concentrated load applied at the central point, see Fig. 9.1. The material is considered to be Aluminum 6061-T6, whose Young's modulus is  $E = 68.9$  MPa, and density is  $\rho = 2.5 \cdot 10^3$  kg/m<sup>3</sup>. In Fig. 9.1, it is also shown that the plate has been subdivided into four sub-structures, each one featuring its own damage index to be estimated.

Two different plate configurations have been considered:

1. a first one characterized by damage indexes  $d_2 = 0.5$  and  $d_1 = d_3 = d_4 = 0$ , constant throughout the whole time interval of the analysis. The goal of this analysis is to show the capability of the reduced-order model to provide accurate estimates of the damage indexes, given the measurements of rotations at the mid-span points along the edges of the plate.
2. a second one characterized by the same damage indexes of the first case up to  $t = 0.25$  s, then featuring a sudden stiffness reduction in region 2 so as  $d_2 = 0.5 \rightarrow 0.7$ . With this analysis, we evaluate the ability of the method of tracking and updating the estimation even in a time-varying environment. In this case, since we want the estimation error associated with the order reduction to be negligible with respect to the error due to the POMs updating process, the number of retained POMs is  $\ell = 3$ .



**Fig. 9.1** Benchmark test: boundary and loading conditions, and region numbering

Results relevant to the first configuration, in terms of damage index estimations at varying number of POMs retained in the reduced-order model, are reported in Fig. 9.2. Considering the 1-POM case, the filter is able to detect that there is a damage in the right region, as the estimate of  $d_2$  is higher than all the others, see Fig. 9.2a; nevertheless, the accuracy of the reduced-order model is too low, and the estimated parameters are not close enough to the target. The estimation obtained with the 2-POMs case gets better, but still the damage indexes of the undamaged regions are only fluctuating around the zero value, see Fig. 9.2b. The 3-POMs case provides instead the damage parameters almost perfectly estimated after an initial transient stage, see Fig. 9.2c.

Moving now to the time-varying health problem, results are collected in Fig. 9.3 once again in terms of damage estimates provided by the filtering approach. Figure 9.3a shows what would happen if the POMs were not updated and kept instead constant over time. As expected, a fast variation of damage parameters is provided, but the parameters are not well estimated after the growth of  $d_2$ . This is due to the fact that in the late stage of the analysis the wrong bases are projecting the matrices on a sub-space that is not coherent with the original full-order one. As the bases are not the optimal ones, the error is not optimally minimized and biases in the estimates show up. Despite the fact the filter cannot identify the right values of the damage indexes, still the method can detect a variation of the structural health and can therefore be used as a sort of damage alert, warning the user that something unexpected is occurring to the system. On the other hand, by plugging in the POMs update stage, after an expected transient phase the damage parameters are correctly identified, see Fig. 9.3b.

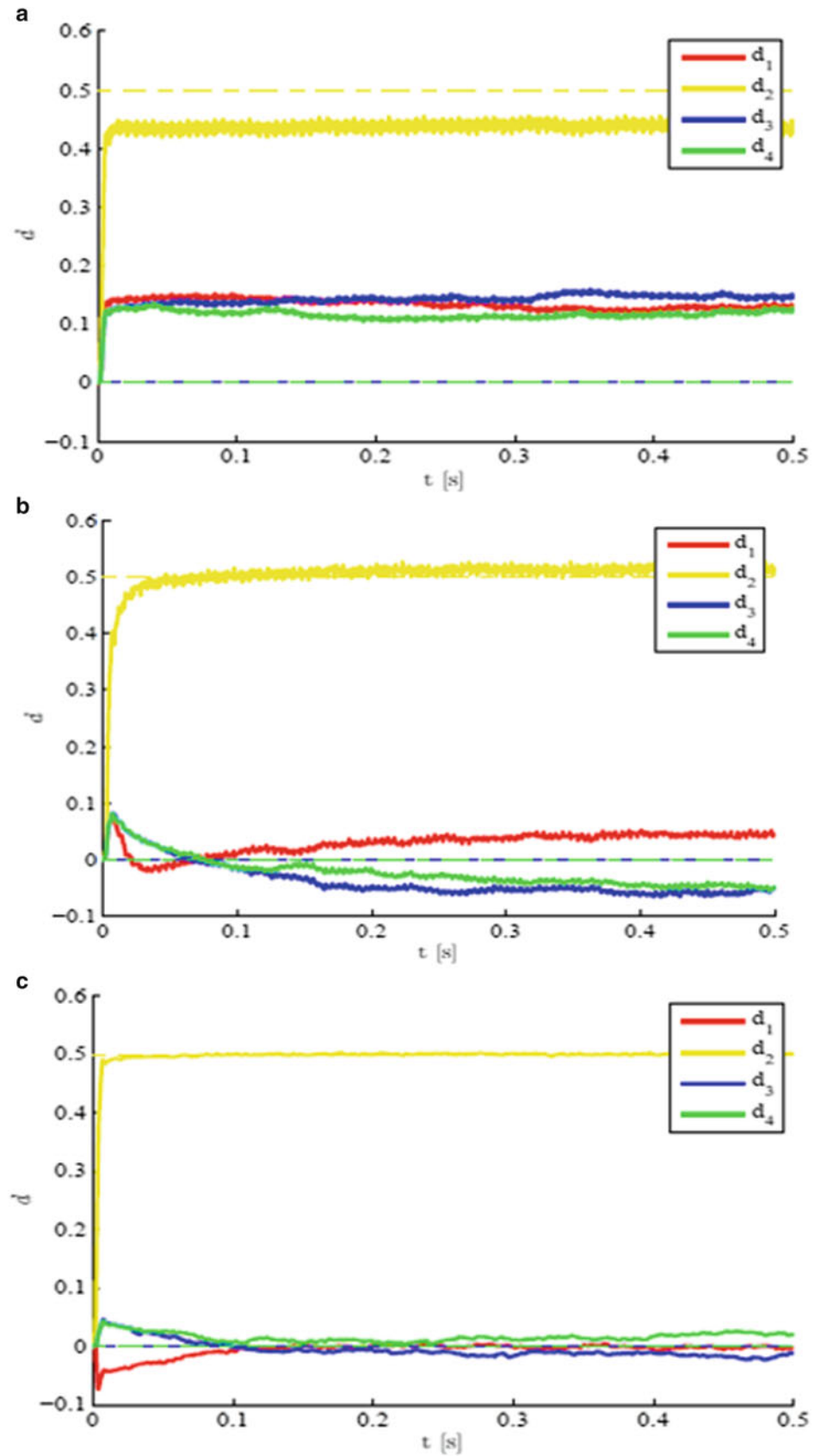
## 9.4 Conclusions

A new online damage identification method based on recursive Bayesian filters has been presented, and adopted to track the health state of a thin plate. The method is based on a Rao-Blackwellized particle filtering strategy, and on a proper orthogonal decomposition-based order reduction of the numerical model used to track the structural behavior.

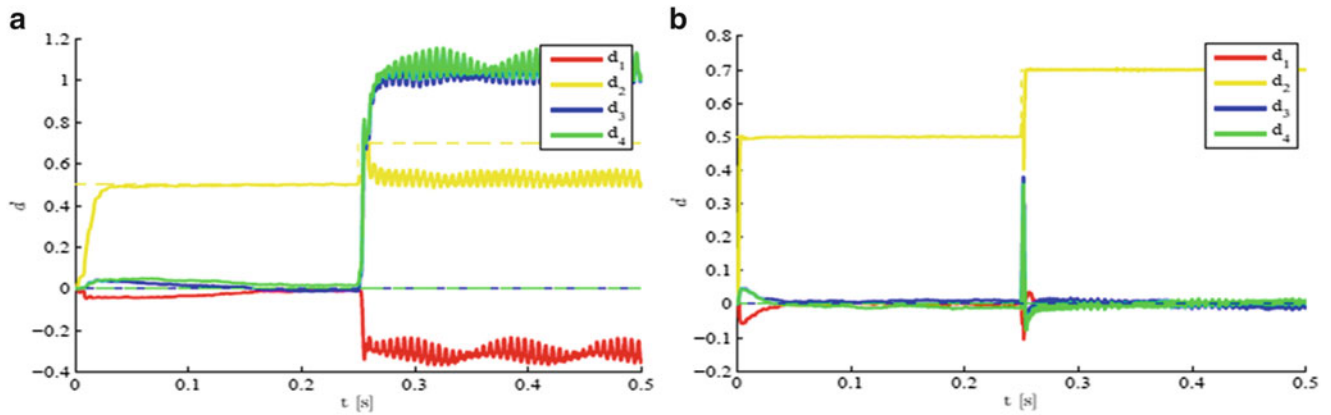
It has been shown that such hybrid approach can locate and accurately estimate the damage parameters associated to the local reduction of the plate stiffness when only two or three degrees-of-freedom are retained in the reduced-order model, thus speeding up the whole identification procedure and possibly allowing real-time structural health monitoring procedures.

**Acknowledgements** The research by S.E.A. has been implemented under the “ARISTEIA” Action of the “Operational Programme Education and Lifelong Learning” and was co-funded by the European Social Fund (ESF) and Greek National Resources. G.C. and S.M. wish to acknowledge a financial support from Fondazione Cariplo through project “Safer Helmets”.

**Fig. 9.2** Time-invariant damage state: damage indexes  $d_j$  identified with (a) one POM, (b) two POMs, and (c) three POMs retained in the reduced-order model







**Fig. 9.3** Time-evolving damage state: damage indexes  $d_j$  identified (a) without, and (b) with POMs update

## References

1. Eftekhar AS (2014) Online damage detection in structural systems. Springer, Cham, Switzerland
2. Eftekhar Azam S, Mariani S (2013) Investigation of computational and accuracy issues in POD-based reduced order modeling of dynamic structural systems. *Eng Struct* 54:150–167
3. Eftekhar Azam S (2012) Dual estimation and reduced order modelling of damaging structures. Ph.D. Politecnico di Milano
4. Eftekhar Azam S, Mariani S (2012) Dual estimation of partially observed nonlinear structural systems: a particle filter approach. *Mech Res Commun* 46:54–61
5. Mariani S, Corigliano A, Caimmi F, Bruggi M, Bendiscioli P, De Fazio M (2013) MEMS-based surface mounted health monitoring system for composite laminates. *Microelectron J* 44:598–605
6. Newmark NM (1959) A method of computation for structural dynamics. *J Eng Mech* 85:67–94
7. Sirovich L (1987) Turbulence and the dynamics of coherent structures. I – coherent structures. II – symmetries and transformations. III – dynamics and scaling. *Q Appl Math* 45:573–590

# Chapter 10

## Advanced Modal Analysis of Geometry Consistent Experimental Space-Time Databases in Nonlinear Structural Dynamics

Ioannis T. Georgiou

**Abstract** We present a study focusing on mining-processing of geometry consistent space-time databases of acceleration fields developed in freely vibrating long aluminum alloy beams. Vibration data mining is conducted by single triad of accelerometers: one fixed and the other two being relocated to cover the structure. The mined space-time databases are evaluated by an advanced modal analysis technique based on proper orthogonal decomposition tools to determine whether they qualify as a genuine measurement of the acceleration vector field resolved along space and time varying local coordinates furnished naturally by the deforming surface of the beam structure. Despite the fact that the dynamics are coupled three-dimensional and evolving in interacting slow-fast time scales, the shapes of the extracted proper orthogonal modes of the transverse component of the acceleration vector field sampled by the single triad of accelerometers are found to be qualitatively close to shapes of normal modes predicted by the Euler-Bernoulli linear beam model. The quantitative differences stem from the influence on vibration dynamics that the static deformation infers to. The sensing-measuring of the acceleration vector field with limited sensor resources exploits the geometric mechanics concepts of slow and fast invariant manifolds thus contributing to low cost practical structural dynamics experimental data.

**Keywords** Vibrations • Modes • Signal processing • Sensing • Accelerations

### 10.1 Introduction

Test and evaluation methodologies targeted for model identification and structural health monitoring of physical one-dimensional solid continua are interesting topics of basic research-both at the theoretical and experiment levels-with measurable economic and societal impacts in cross disciplinary applications in engineering and biology. For example, some core elementary structures in structural engineering and biology structures are essentially one-dimensional continua; and their designed or assigned functions may depend on reliable monitoring of their response to stimuli from the environment and with the system itself. Regarding structural health monitoring to sustain desired performance, one challenge is spatial measurements of flexible rod dynamics with embedded sensors in such a way as to record the interactions of the slow bending motions and fast torsion and extension motions. One-dimensional structures exhibit continuum level multi-scale dynamics manifesting themselves as very slow and fast vibrations in free spatial motions. It would be useful for system identification and damage detection to be able to extract the bending normal modes of vibration of a beam structure from experimental data of arbitrary spatial motions. This depends on reliable distributed dynamics sensing and subsequent processing of space-time distributed signals. Vibration-based damage detection is one of the very promising approaches to structural health monitoring [1]. It can be enhanced further if one learns how to mine and process geometry consistent space-time matrix information on dynamics. For example, a fiber optic sensor is motion conforming by design and function and thus it furnishes information on dynamics variables with respect to local coordinates. This information is geometry consistent. It is mentioned in reference [2] how rich is this information in natural time scales.

Here we shall deal with acceleration measurements furnished by surface accelerometers, being naturally geometry consistent due to the local motion conforming feature. As the rod structure is the paradigm of the structure used to establish the modern geometric mechanics framework, here it is used as a prototypical structural system to cultivate novel ideas for distributed sensing of continuum system slow-fast dynamics in a geometrically exact manner. We exploit the geometric concepts of the Slow Invariant Manifold (SIM) and the transversal fiber of Fast Invariant Manifolds (FIM) to conduct geometry consistent measurements in space using limited resources of sensors: here a triad of light weight acceleration

---

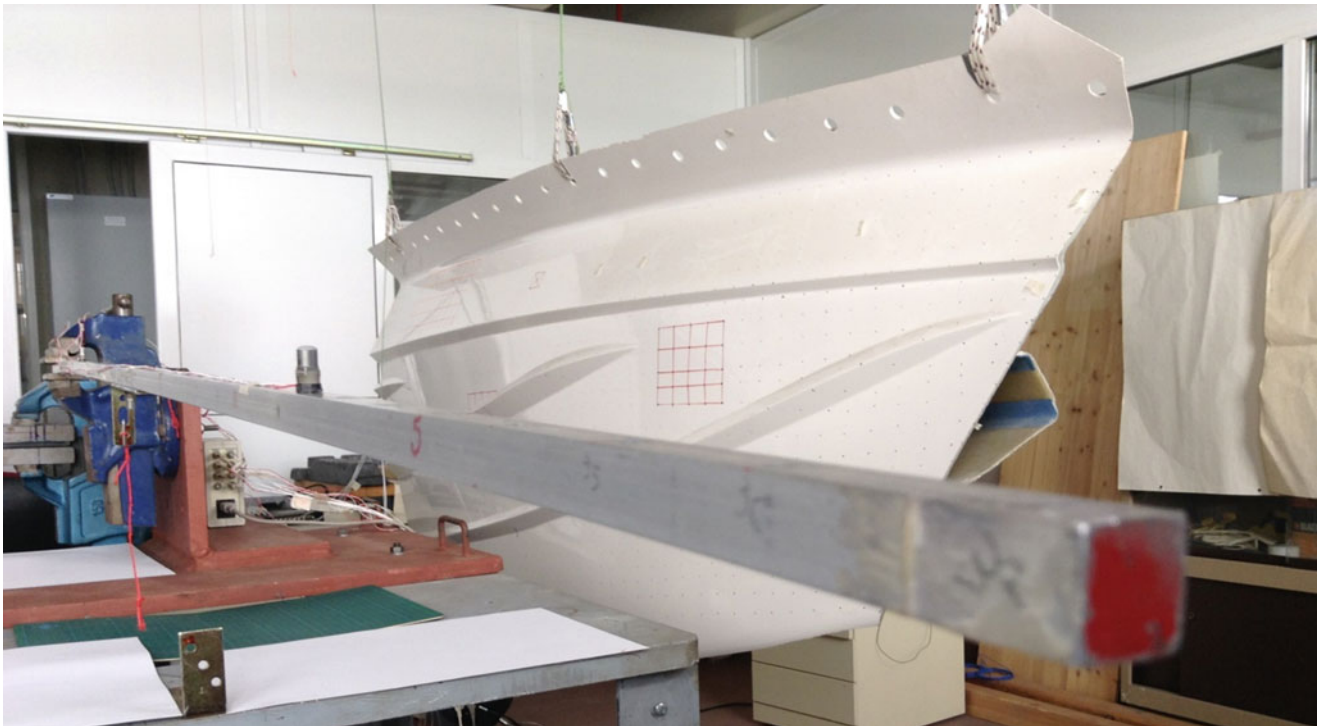
I.T. Georgiou (✉)  
National Technical University of Athens, Zografos Campus, Athens 1578, Greece  
e-mail: [georgiou@central.ntua.gr](mailto:georgiou@central.ntua.gr)

sensors. They follow the local geometry of the deforming beam and thus they sense naturally the acceleration with reference to a local time varying coordinate system. The geometrically exact measurements of the acceleration vector field are interpreted in physics terms by examining their proper orthogonal decomposition modes. The mathematical POD modal structure of the measured geometrically exact acceleration vector field provides a sound basis to identify the modes of coupled dynamics and detect local damage. This work brings in useful concepts of geometric mechanics to enhance experimental nonlinear dynamics. These are the so called Slow Invariant Manifold and its transversal continuum of Fast manifolds. These are well-established geometric concepts of nonlinear dynamical systems. These concepts have been used systematically for broad scope qualitative analysis of structural and mechanical nonlinear dynamical systems [3–5].

## 10.2 Mining Geometry Consistent Structural Dynamics Databases

Distributed sensing-measurement of structural dynamics is essential in engineering applications and basic research endeavors. One area where it is a necessity is the identification of normal modes of vibration as part of system identification and another area, where it is becoming quite important, is damage detection for structural health monitoring. Depending on the size of the system, distributed sensing may come across annoying problems. One such problem is the instrumentation complexity stemming from installing a dense network of sensors. Here we avoid this problem by using a single triad of accelerometers to mine a space-time sample of the acceleration vector field. In a recent work [6], we used a single pair of accelerometers to mine a space-time matrix sample of the acceleration vectors field in physical aluminum alloy beams.

Here we shall use a triad of accelerometers to mine space-time matrix databases of acceleration vector fields developed in physical relatively long beam structures. Figure 10.1 shows the experimental set-up for such a long aluminum alloy beam of uniform square section. The beam crosses perpendicularly the gravitational force field. By using a single triad of accelerometers we shall measure at  $N = 37$  equally spaced points the transverse component of the surface acceleration vector field. The beam is set into a free spatial vibration by releasing it from a well-defined static deformed configuration. The experiment is repeated  $N/2 + 1$  times. Two of the sensors are relocated and thus they span the whole beam and thus furnishing  $N = 37$  measurements distributed in space. The relocated sensors are triggered by the fixed sensor and thus



**Fig. 10.1** Aluminum alloy beam instrumented with three light piezoelectric accelerometers to measure the transverse convected component of the acceleration vector field. Two of the sensors are relocated at the same time to cover the beam from the free tip to the fixed root. The sensors are conforming to the local geometry of the deformed beam

rendering the measurements simultaneous. We beam motion that the beam motion is not planar and that the initial conditions have uncertainties.

So we have a geometry consistent space-time matrix sample of the major transverse acceleration components with does not have a fixed direction but it follows the normal to the surface. *Is this database close to the one obtained by  $N$  distributed sensors?* This is the question that we shall answer. Here the sensing direction of the sensor intersects with the direction of the gravitational field. So the sensor in addition to the inertial force generated at its base is influenced by the gravitational force vector field. In a recent work [6], we investigated a similar problem using a relocated sensor triggered by a fixed one. The sensors were not interacting with the gravitational force field. We have found that the single-pair-of sensors measure the acceleration vector field for a beam whose major bending axis is parallel to the direction of the gravitational field. Here the sensing direction of the accelerometer intersects the gravitational force field. Thus the sensors feel both an inertial force caused by the acceleration itself and a portion of the gravitational force field which becomes quite complicated due to the motion of the sensor.

The typical database of time series mined by the two relocated sensors is represented mathematically by an  $M \times N$  matrix:

$$\mathbb{A} \equiv [\mathbf{a}_1, \mathbf{a}_2, \dots, \mathbf{a}_{n-1}, \mathbf{a}_n, \mathbf{a}_{n+1}, \dots, \mathbf{a}_{N-1}, \mathbf{a}_N] \quad (10.1)$$

Column vector  $\mathbf{a}_n$  represents the  $M$ -points time history recorded at the location  $n$  by the relocated sensor. The question that shall be addressed here is whether the matrix defined above represents a spatially distributed time history sample of the projection of the acceleration vector field in the direction of the axis field formed by the local normal to the beam surface. This is not obvious for several reasons, the most important one stemming from the fact that the accelerometer sensing direction intersects the gravitational field direction.

The typical space-time database is structure geometry consistent due to the way excitation and measurement are conducted. It is not at all certain that it is a genuine sample of the local component of the acceleration vector field. This component is associated with the normal to the deformed beam. This normal is not a constant but it varies with time. The sensing direction of the accelerometer coincides with this time varying direction. In addition, the accelerometer sensing direction intersects the gravitational field direction.

### 10.3 Advanced Modal Analysis by the POD Transform

The space-time database  $\mathbb{A}$  forms a geometric object in a linear space of configurations. The continuum can occupy several configurations. The configuration is determined by the displacement vector field. The configuration of the acceleration vector field is determined by differentiation. This brings in Differential Geometry concepts. Here we have experimental data for the acceleration vector field. And the challenge is to turn them into useful information. The geometric object is formed by the wandering in a finite portion of the space by the trajectory which itself is a curve parameterized by time. We have not restricted the motions to be neither linear nor planar. So the other challenge is to turn this collected space-time data into useful information by keeping in mind that we are not restricted to the classical areas of linear or weakly linear behavior and decoupled dynamics. We allow for fully coupled dynamics and uncertainties.

We introduced the following way of data analysis. The initial database  $\mathbb{A}$  is referred to as the global one. It traces a global trajectory and thus forming a global data cloud with characteristic geometric features just as any physical material object in the physical three-dimensional space [6]. An advanced modal analysis should result in the identification of these features. Viewed as a geometric object, we approached it for analysis purposes by forming a sample of nested sub databases as follows:

$$\mathbb{A}_1 \supset \mathbb{A}_2 \supset \mathbb{A}_3 \supset \mathbb{A}_4 \equiv \mathbb{A} \quad (10.2)$$

Symbol  $\supset$  denotes the set inclusion operation. Table 10.1, column 2, presents the time interval of the sub databases in relation to the time interval of the global database which is  $M = 192,500$  time points long. We evaluate each database, or data cloud, by subjecting it to an advanced decomposition analysis. This analysis is furnished by the discrete time POD transform. It decomposes the raw space-time database into a set of space-time patterns. According to the time discrete POD Transform, the database admits a unique additive modal-like expansion representation:

**Table 10.1** Time interval of the nested databases and head of POD normalized energy spectra

Nested database	Time interval	Normalized POD modal energy
$\mathbf{A}_1$ (black)	[1–17500]	0.614621332, 0.16777836, 0.08646576, 0.056671907
$\mathbf{A}_2$ (red)	[1–47500]	0.605747563, 0.24148926, 0.06996467, 0.034368394
$\mathbf{A}_3$ (blue)	[1–97500]	0.553086419, 0.32528820, 0.05560197, 0.024151623
$\mathbf{A}_4$ (green) global	[1–192500]	0.489160832, 0.40784174, 0.04252305, 0.019629541

$$\mathbb{A} \xrightarrow{\text{POD transform}} \tilde{\mathbb{A}} \equiv \sqrt{\frac{M-1}{2}} \sqrt{\frac{N-1}{2}} \sum_{k=1}^{K^*} \sqrt{\lambda_k} \hat{\mathbf{Q}}_k \hat{\mathbf{\Phi}}_k^T, \quad K^* < N < M; \quad (10.3)$$

$$\hat{\mathbf{Q}}_n \hat{\mathbf{Q}}_m^T = \delta_{mn}, \quad \hat{\mathbf{\Phi}}_m \hat{\mathbf{\Phi}}_n^T = \delta_{mn} : \quad \delta_{mn} = 1, m = n, \quad \delta_{mn} = 0, m \neq n.$$

Symbol T denotes the matrix trace operation. Integer  $K^*$  denotes the number of intrinsic proper orthogonal decomposition (POD) modes. A POD mode in bi-orthogonal is space and time and is characterized by nodal energy content  $\lambda_n$ , unit time modulation (amplitude)  $\hat{\mathbf{Q}}_n \in \mathbb{R}^M$ , and unit space modulation (shape)  $\hat{\mathbf{\Phi}}_n \in \mathbb{R}^N$ .

Set  $\{\hat{\mathbf{Q}}_n\}$  is referred to as the Principal Coordinates. Set  $\{\hat{\mathbf{\Phi}}_n\}$  is referred to as the POD modal shapes. Set  $\{\lambda_n\}$  is referred to as the POD energy spectrum. It is a descending sequence of strictly positive numbers.

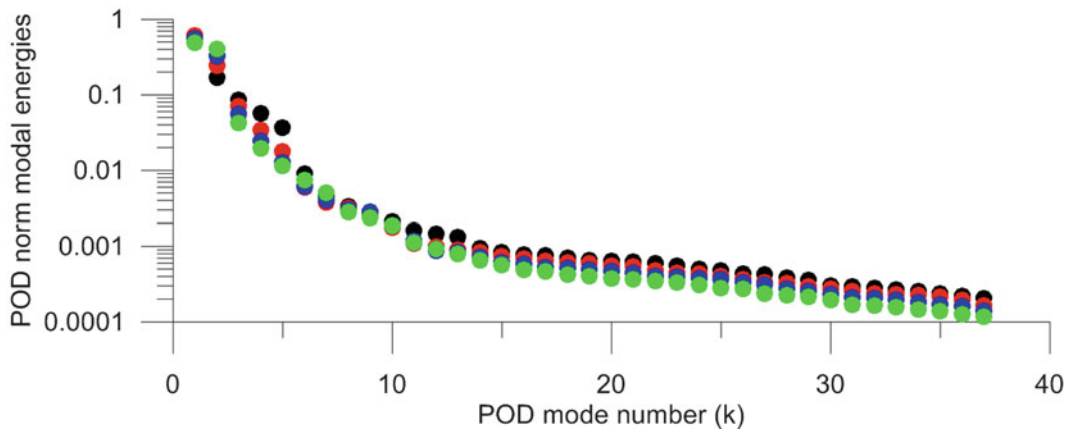
From an energy point of view, the POD transform is characterized by the following energy spectrum property:

$$\sum_{n=1}^{K^*} \lambda_n = \|\mathbb{A}\|^2 \equiv \frac{2}{M-1} \times \frac{2}{N-1} \text{tr}(\mathbb{A}^T \mathbb{A}). \quad (10.4)$$

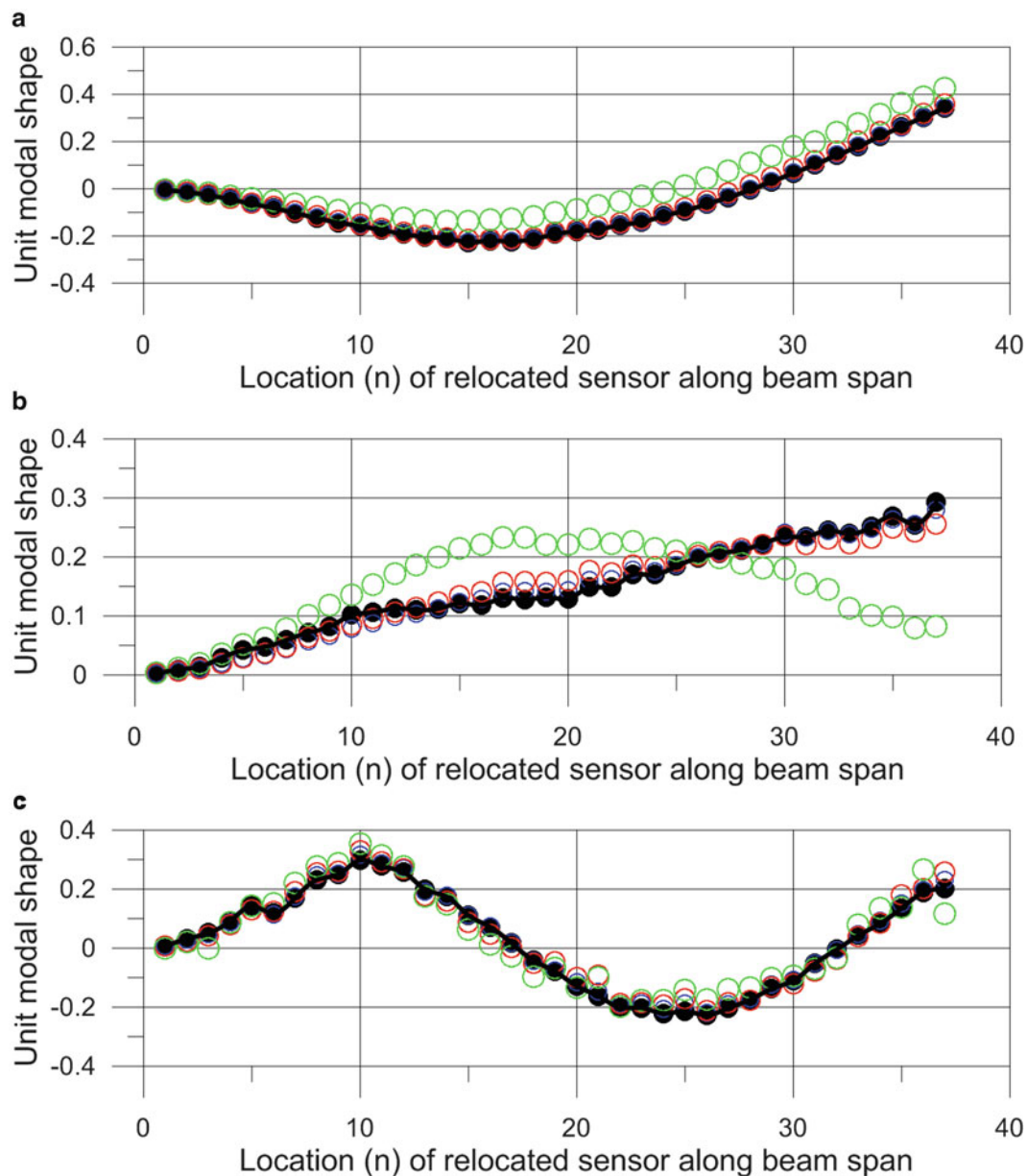
The essence of the POD transform is the fact is that the energy of the database is distributed over the smallest possible number of bi-orthogonal modes. These modes describe the linear geometry of the cloud formed by the database in the space of configurations. The set of numbers  $\{\hat{\lambda}_n \equiv \lambda_n / \|\mathbb{A}\|^2\}$  forms the normalized POD modal energy spectrum. Its distribution over the wave number of POD modes characterizes the database.

The POD analysis of the transverse component of the geometry consistent database of the acceleration vector field justifies the term advanced modal analysis as this shall become evident in the analysis that will follow below. The POD transform has been used in fluid mechanics [7, 8] and structural dynamics [3, 6, 9–11] and complex Machinery elements [12].

All four nested sub databases have been reduced to their intrinsic POD modes by means of the POD transform. Figure 10.2 presents the POD modal distribution of the normalized energy at unity of the database, the normalized POD energy spectrum. The four nested segments of the database of the transverse component of the acceleration vector field are dominated by two POD modes. Table 10.1, column 3, lists these energy fractions. On the average the modal distribution of the database energy is very similar for all databases. The fact that a considerable amount of energy is contained in the first two-to-four modes is



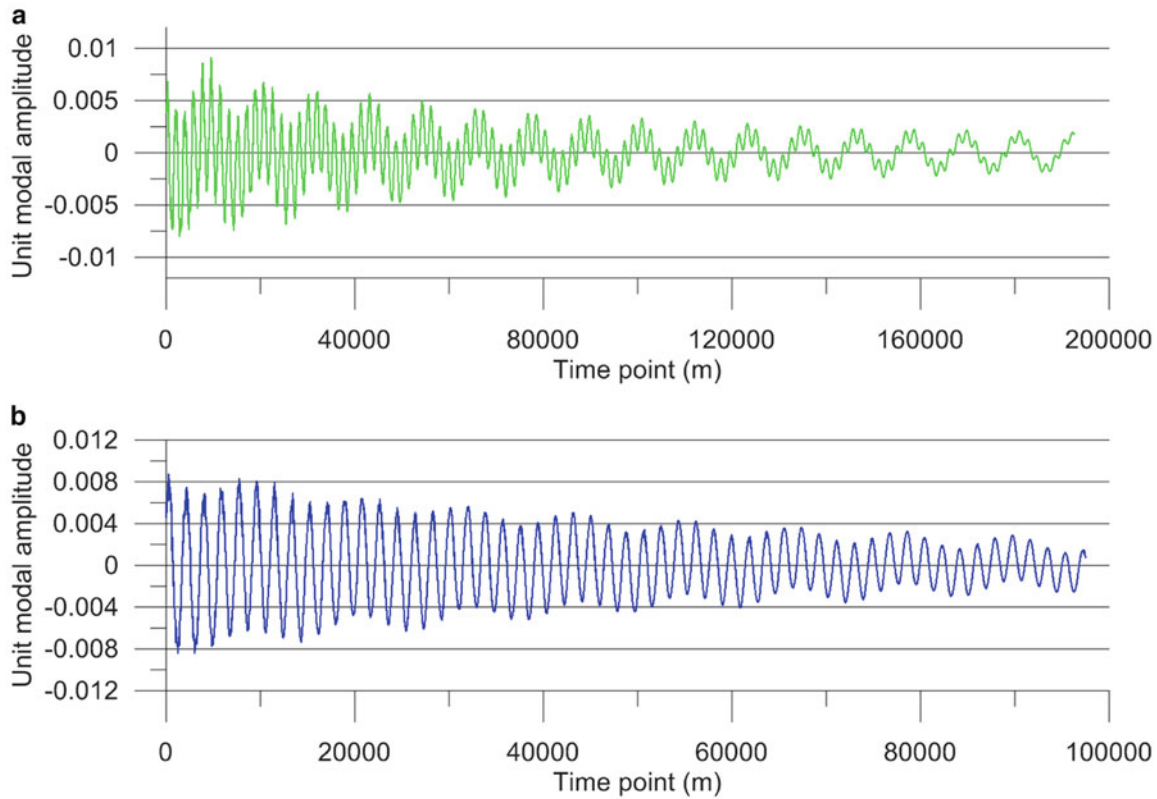
**Fig. 10.2** The POD normalized energy spectra for a sample of nested sub databases of the space-time database mined by two relocated accelerometers triggered by a fixed one



**Fig. 10.3** The unit shapes of the first three POD modes of the four nested databases ( $A_1, A_2, A_3, A_4$ ): (a) 1st mode, (b) 2nd mode, (c) 3rd mode

the feature that determines that the geometry consistent database mined by the single triad of relocated sensor is coherent. From a physics and theoretical standpoints, it is expected that the acceleration vector is coherent. The smaller the number of dominant modes the easier is to estimate the level of coherence. Here it is very clear that we have this case. It turns out that the whole energy spectrum is described quite well by a power law.

Figures 10.3a, b reveal that the 1st and 2nd POD modes of the global database  $A_4 \equiv A$  differ from those of the local databases  $A_1, A_2$ , and  $A_3$ . We see that this difference is reflected clearly in the companion time modulations, Fig. 10.4a vs b. The result above justifies the nested POD analysis to contrast the POD modal structure of local segments of the trajectory to that of the whole trajectory, forming the global geometry. In the literature, it is claimed that for beam structures the POD modes coincide with the normal modes [13, 14]. As the experiment reveals this should hold only under appropriate conditions.

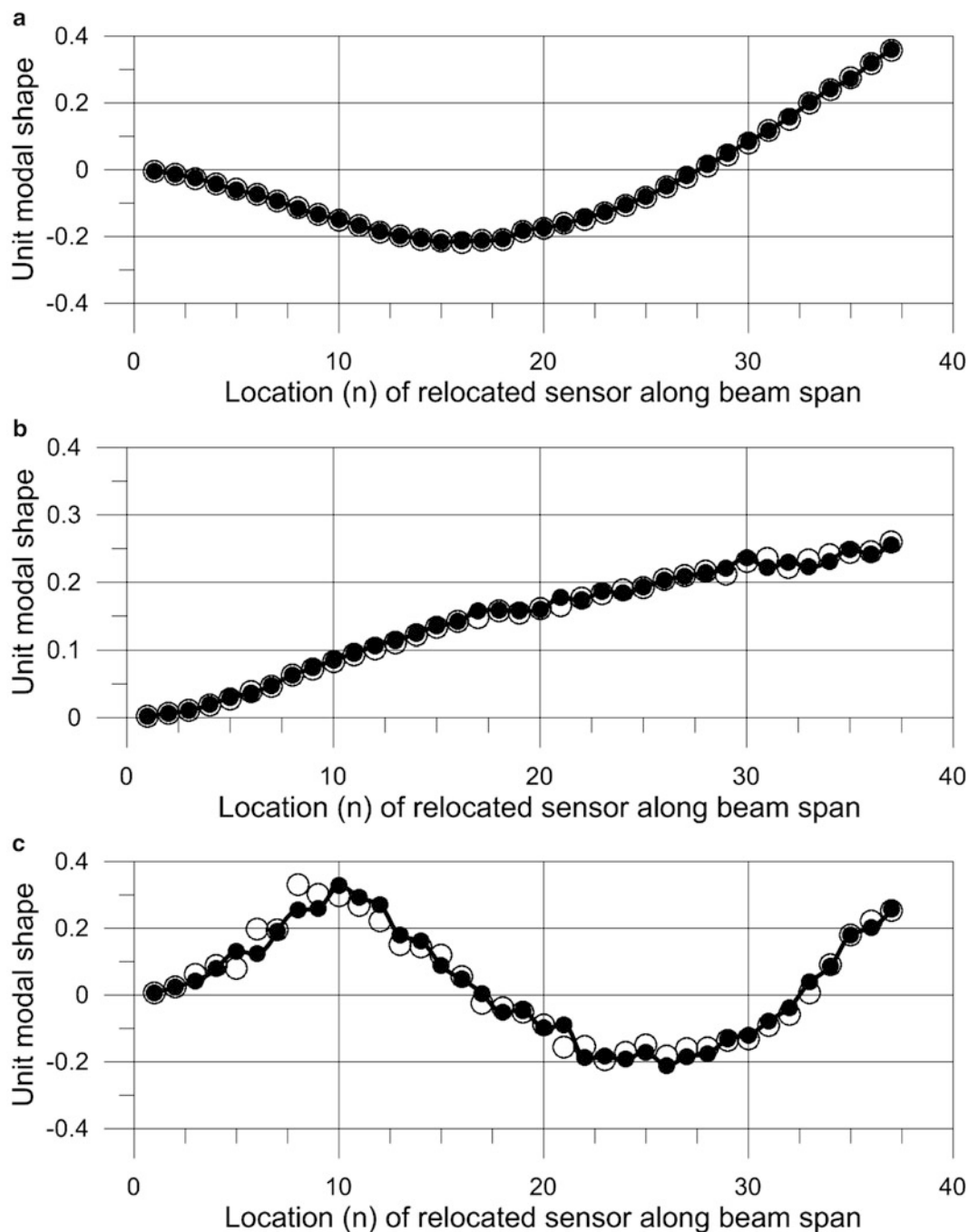


**Fig. 10.4** The unit time modulations of the dominant POD modes of the global database  $A_4$  and the local database  $A_3$

## 10.4 Experiment Repeatability

We have used a very low cost sensing-measuring technique to conduct a spatially distributed measurement of the transverse acceleration component not in space-fixed coordinate axes but in a geometry consistent space and time varying axis field. We use two sensors to perform  $N = 37$  spatial acceleration measurements. The measurement of acceleration is one part of the advanced modal analysis technique presented here. Thus, we naturally addressed the issue of how reliable is the technique. Is the experiment repeatable? To cope with issue, the typical experiment is repeated at least twice. From two samples one can construct many samples by simple combinations. Figure 10.5 presents the dominant POD modes for the two space-time samples, Test 1 and Test 2, of the same motion. These samples are generated by exciting the beam  $N/2$  times from nearly the same initial conditions. Despite the unavoidable small random errors in the initiation conditions, the databases are quite close since the shapes of the three first POD modes are very close. Figure 10.5 shows this result for the database  $A_3$  which is  $M = 97500$  time points long in the time dimension. We have small quantitative differences falling in the expected experimental error zone.

Another indication of the high level of repeatability of the experiment is the fact that the POD structure of the ensemble of signals mined by the fixed sensors is composed of a single dominant POD mode with uniform space modulation, see Fig. 10.6. The spatial uniformity strongly indicates that the motions are emanating from closely neighboring initial conditions. And the fact that the energy of the dominant mode is about 96 % of the database indicates that the signals collected by the fixed sensors are underlined at the level of 96 % by the same signal. The remaining 4 % is due to the uncertainties. The ideal case would be the 100 % level. But clearly we do need this level of accuracy. This is one of the novel points of this sensing technique. We can operate in a cloud of uncertainty in a useful way.

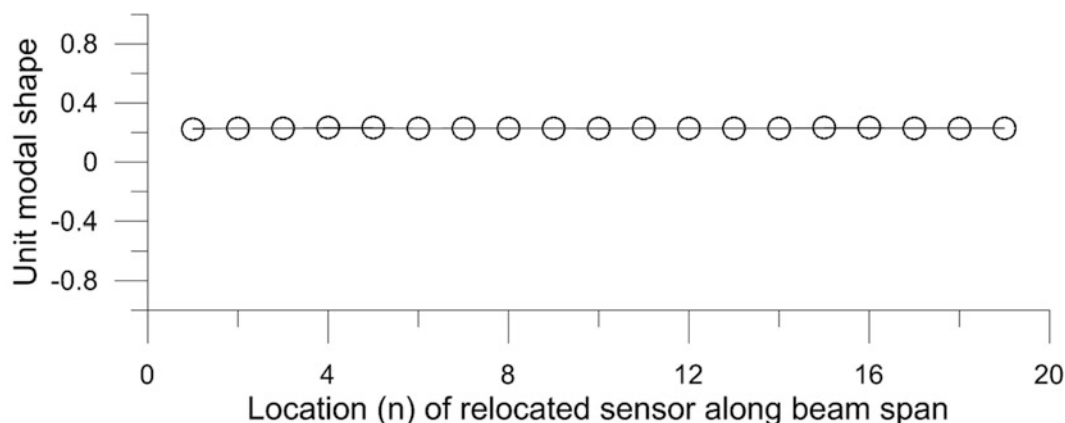


**Fig. 10.5** The unit shapes of the dominant POD modes of two space-time samples, Test 1 (*filled circle*) and Test 2 (*unfilled circle*) of the resolution of the acceleration vector field into the normal unit vector field defined by the normal to the beam surface. The database is mined by a relocated pair of sensors triggered simultaneously by a fixed sensor. (a) 1st mode, (b) 2nd mode, (c) 3rd mode

### 10.5 Normal Modes Relations

Regarding elastic structures, the main goal of the well-established and practiced notion of modal analysis is to determine either by means of theoretical-computational or experimental techniques the normal modes of vibration. For test and evaluation and structural health monitoring the challenge is whether it is possible to extract the normal modes of vibration from distributed time series of acceleration. The challenge is elevated more if one adds the fact that the time series are mined by a device whose sensing direction is not fixed, just as the accelerometers in our study here. Thus we address the issue of





**Fig. 10.6** The uniform unit shape of the dominant POD mode of the database mined by the fixed sensor

whether the shapes of the dominant POD modes represent the shapes of normal modes. This issue has been addressed by several researchers by using either ideal reduced beam models or experiment with very small planar motions [13, 14]. Here we do not restrict our motions. Thus we have data from full order dynamical systems allowed to perform spatial motions. The motions that we have measured are not planar. We have measured the projection of the acceleration vector field into a spatially distributed local transverse direction. We know that the elastic beam can vibrate into natural modes of bending. So here we compare the shapes of the three dominant POD modes to the shapes of the linear bending modes. Figure 10.7 reveals that the dominant POD modes are qualitatively quite similar to the bending linear normal modes (LNM) predicted by the classical Euler-Bernoulli beam model [15–17].

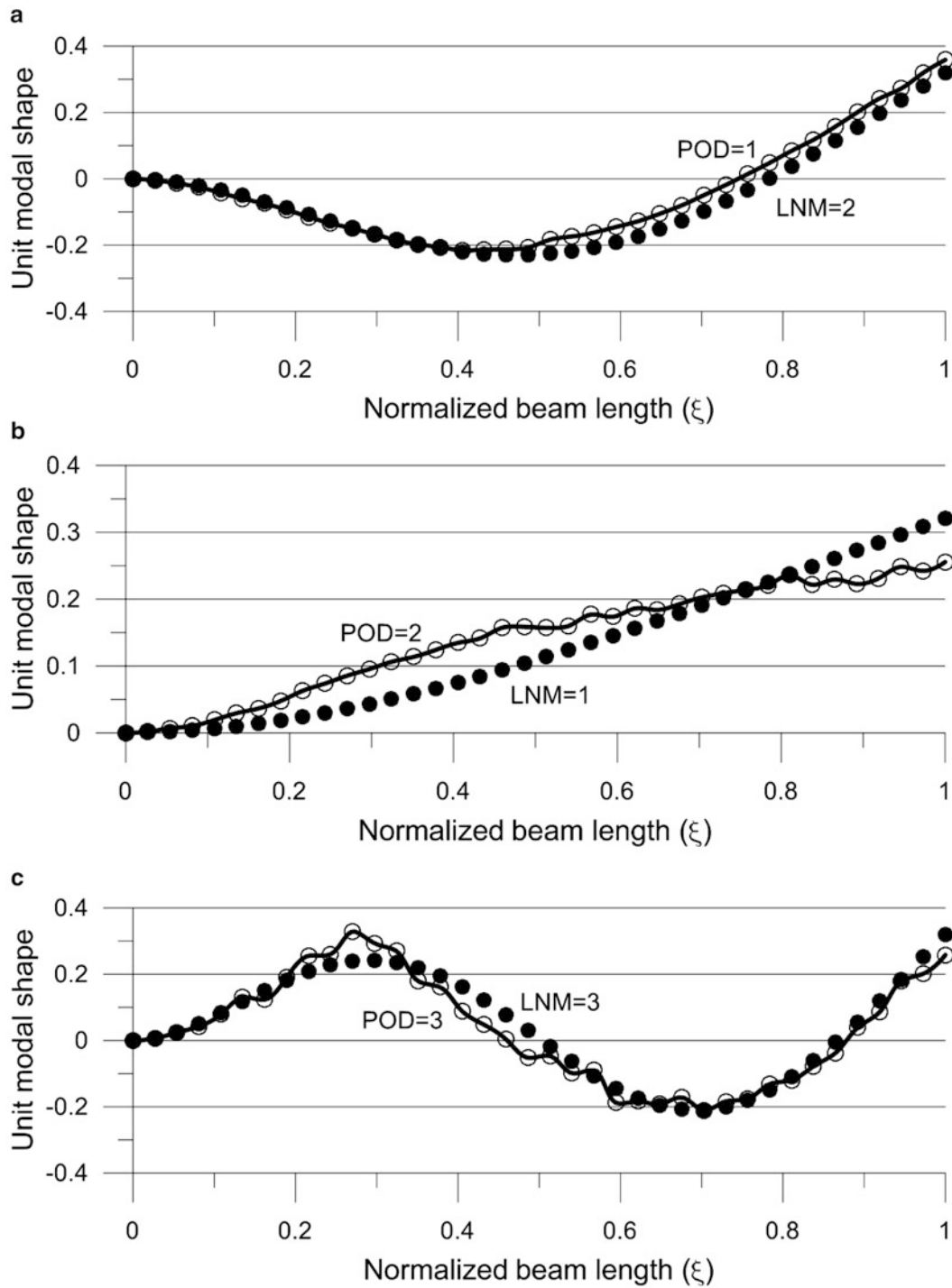
## 10.6 Natural Mitigation of Uncertainty

We have repeated the experiment  $N/2 + 1 = 19$  times. The nominal initial condition is pure initial deformation created quasi-statically with a mechanism. The beam is released nearly instantly. The created initial conditions are not quite the same. There are errors in the initial velocities. The errors contaminate the nominal initial conditions with fast oscillations of small amplitude. However, the motion is attracted by a slow invariant manifold. The fast oscillations decay very fast and the motion lands on the slow manifold and thus is very close to a motion initiated on the slow invariant manifold. The descent of the motion into an attracting slow invariant manifold reduces the magnitude of uncertainty in the initial conditions. The fact that POD mode 2 is qualitatively close to the fundamental bending mode predicted by the Euler-Bernoulli beam mode indicates strongly that this POD mode is very close to the fundamental bending mode of the physical beam under study. Thus this POD mode identifies the core slow vibrations of the long beam.

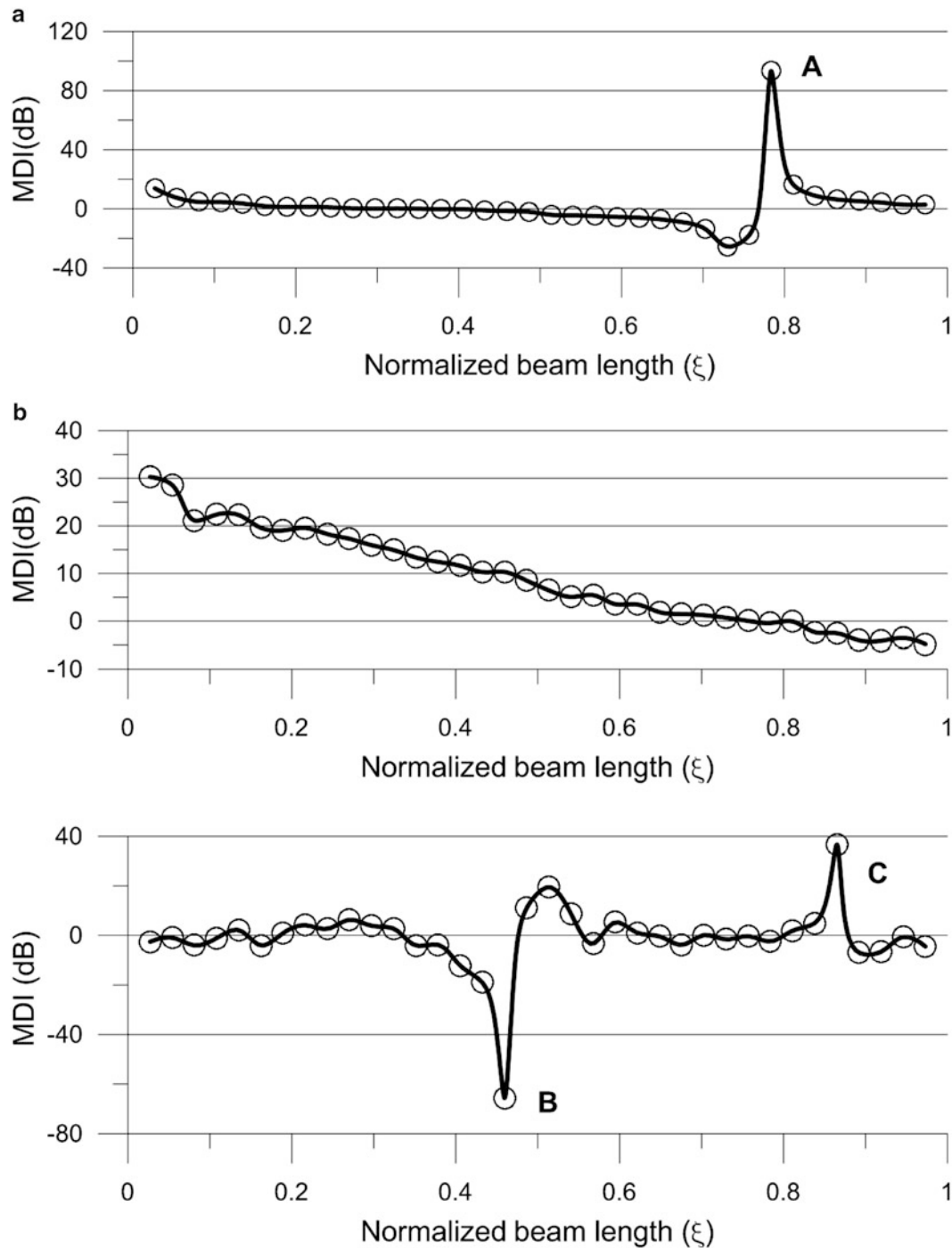
## 10.7 Detection of Anomalies

The aluminum beam structure is quite long and at the rest configuration is under considerable deformation by the action of its own weight. The beam region around the cantilevered end is under deformation whereas the rest undergoes a large displacement with small deformation. The POD modes characterize the motion from this deformed configuration. If the beam were quite short the POD modes would be very close to the linear normal modes. We consider the stretched beam by its own weight as “damaged” in the broad sense. We compare its POD modal shapes to those of the linear beam which can be considered a reference for the healthy beam in a non gravitational field.

Figure 10.8 reveals that the dominant POD modes of the space-time database of the transverse convected component of the acceleration differ from the normal modes of vibration in local regions and global regions. In particular, the POD modal shapes 1&3 differ in local regions from the normal modes. These local differences, region A in Fig. 10.8a and regions B and C in Fig. 10.8c, are stemming from the shift of the nodal points. The 2nd POD mode is qualitatively similar to the 1st bending linear mode. But Fig. 10.8b reveals a distributed difference which becomes large at the cantilevered beam end. This is due to the effect of the static deformation due to the beam weight.



**Fig. 10.7** Direct comparison of the dominant POD modal shapes of the geometry consistent space-time sample of the transverse acceleration vector field with the normal modes of the classical Euler-Bernoulli beam mode



**Fig. 10.8** Detection of modal deviation index (MDI) anomalies in the POD modal shapes of the beam pictured in Fig. 10.1. The modes of the linear beam are taken as a reference for the structural condition of the beam [6]

## 10.8 Conclusions and Discussion

The typical space-time matrix database-mined by a two relocated sensors monitored simultaneously by a fixed one-of the transverse acceleration field along a long flexible beam is highly coherent since its norm-based energy is practically concentrated at a small number of proper orthogonal decomposition (POD) modes. The POD analysis is done for a nested set of segments of the mined space-time database. The first two POD modes of the global database are not the same as those of the nested sub databases. This is an indication of nonlinear coupled vibrations. We find that the second POD mode is

qualitatively close to the fundamental bending mode which forms the core of the slow dynamics of the beam. But there are considerable quantitative differences which clearly indicate how the static deformation imposed by the gravitational field has influenced the shape of the fundamental nonlinear normal mode of vibration. The POD modes are used to detect anomalies in vibration behavior due to structural defects and deformation due to static forces. It is emphasized that this advanced modal analysis was performed on databases of a fully coupled acceleration vector field projected onto a fixed-flexible body axis field. The data were mined by a motion conforming triad of fixed and relocated, motion conforming accelerometers. The technique is model free and thus it can be used for test and evaluation of beam structures of arbitrary complex cross-sections. The proper orthogonal decomposition transform forms the basis for an advanced modal analysis tool since it can be used to evaluate the geometry consistent space-time databases of the acceleration vector field developed during the free motions of a beam structure.

**Acknowledgements** This research has been financed by the European Union (European Social Fund- ESF) and Greek national funds through the Operational Program “Education and Lifelong Learning” of the National Strategic Reference Framework (NSRF)-Research Funding Program: ARISTEIA II-project: IMS-PB DIAGNOSIS (code-4762).

## References

1. Doebling SW, Farrat CR, Prime MB (1998) A summary review of vibration-based damage identification methods. *Shock Vib Dig* 30(2): 91–105
2. Wang G, Pran K, Sagvolden G, Havsgard GB, Jensen AE, Johnson GA, Vohra ST (2001) Ship hull structure monitoring using fibre optic sensors. *Smart Mater Struct* 10:472–478
3. Georgiou IT, Schwartz IB, Emaci M, Vakakis A (1999) Interaction between slow and fast oscillations in an infinite degree-of-freedom linear system coupled to a nonlinear subsystem: theory and experiment. *J Appl Mech* 66:448–459
4. Georgiou IT (2005) Advanced proper orthogonal decomposition tools: using reduced models to identify normal modes of vibration and slow invariant manifolds in the dynamics of planar nonlinear rods. *Nonlinear Dyn* 41:69–110
5. Georgiou IT, Bajaj AK, Corless M (1998) Slow and fast invariant manifolds, and normal modes in a two- degree-of-freedom structural dynamical system with multiple equilibrium states. *Int J Non-Linear Mech* 33(2):275–300
6. Georgiou IT (2015) A single pair-of-sensors technique for geometry consistent sensing of acceleration vector fields in beam structures: detection and dissipation estimation by POD modes. *Meccanica*. DOI [10.1007/s11012-014-0091-y](https://doi.org/10.1007/s11012-014-0091-y)
7. Sirovich L (1987) Turbulence and the dynamics of coherent structures, Pt. 1. *Quart Appl Math* 45:561–571
8. Aubry N, Holmes P, Lumley LJ, Stone E (1988) The dynamics of coherent structures in the wall region of a turbulent boundary layer. *J Fluid Mech* 192:115–173
9. Cusumano JP, Sharkady MT, Kimble BW (1994) Experimental measurements of dimensionality and spatial coherence in the dynamics of a flexible-beam impact oscillator. *Philos Trans R Soc Lond* 34:421–438
10. Georgiou IT, Sansour J (1998) Analyzing the finite element dynamics of non-linear rods by the method of proper orthogonal decomposition. In: Idelsohn S, Onate E, Dvorkin E (eds) *Computational mechanics, new trends and applications*. CIMNE, Barcelona
11. Georgiou IT (2010) POD characterization of free coupled nonlinear vibrations in aluminum multi-beam structure. In: *Proceedings of the 16th US national congress of theoretical and applied mechanics*, State College, Pennsylvania, 27 Jun-2 Jul 2010
12. Georgiou I, Kintzios N (2012) Discovering irregular diagnostic proper orthogonal decomposition signatures in healthy marine ball bearings. In: *Proceedings of the ASME 2012 international mechanical engineering congress and exposition*, Huston, Texas, 9–15 Nov 2012
13. Fenny BF, Kappagantu R (1998) On the physical interpretation of proper orthogonal modes in vibrations. *J Sound Vib* 211(4):607–616
14. Fenny BF (2002) On proper orthogonal coordinates as indicators of modal activity. *J Sound Vib* 255(5):805–817
15. Soedel W (2003) *Vibrations of shells and plates*, 3rd edn. Marcel Dekker, Inc, New York
16. Newland DE (2005) *An introduction to random vibrations, spectral & wavelet analysis*, 3rd edn. Dover, New York
17. Ingard KU (1988) *Fundamentals of waves and oscillations*. Cambridge University Press, New York

# Chapter 11

## Comparison of Damage Classification Between Recursive Bayesian Model Selection and Support Vector Machine

Zhu Mao and Michael Todd

**Abstract** All damage identification activities inevitably involve uncertainties, and the resulting classification ambiguity in contaminated structural health monitoring (SHM) features can dramatically degrade the damage assessment capability. Probabilistic uncertainty quantification (UQ) models characterize the distribution of SHM features as random variables, and the UQ models facilitate making decisions on the occurrence, location, and type of the damages. A Bayesian framework will be adopted and the damage classification is transformed into a model selection process, in which the most plausible structural condition is determined by means of the recursively updated posterior confidence. In contrast to the probabilistic approach, machine learning is another candidate approach, which employs training data and extracts features from the recorded measurements. A support vector machine (SVM) is employed to classify the frequency response function data obtained from rotary machine under different damaged conditions. With different size of feature and different kernel functions, the classification of ball bearing damages are studied. Comparison between the Bayesian model selection approach and SVM is concluded in this paper.

**Keywords** Bayesian decision-making • Structural health monitoring • Damage localization • Support vector machine • Uncertainty quantification

### 11.1 Introduction

As the fundamental part of structural health monitoring (SHM), a comparison between two system statuses is deployed through the feature domain, and such features are extracted from physical understanding and/or field data acquisition. In reality, this type of decision-making, i.e., distinguishing one state from another, is always corrupted by uncertainties, such as lack of physical intuition, noisy measurements, and environmental/operational variability. To maintain an acceptable quality of SHM decision-making performance, numerous of realizations are often required, and two groups of evidence are compared in a statistical sense naively. To deal with the burden of extensive data acquisition, quantifying the uncertainty in the SHM feature evaluations is necessary. Thereby, the confidence of decision is described through the probabilistic uncertainty quantification (UQ) model, and the overall performance of SHM is enhanced [1–4].

Transfer function, also known as frequency response function (FRF), is one of the most widely-used features for SHM, for the clear physical interpretation and easy-accessibility. UQ models of different estimation algorithms regarding FRF features are established in our previous research, in which probability density functions of the estimates are derived analytically [5, 6]. By adopting the probabilistic UQ models, the confidence interval of decision boundaries are pre-defined, and all the testing samples falling outside of the boundaries are labeled as outliers. The percentage of outliers indicates if or not the testing statistics deviates from the undamaged baseline, thus detects damage occurrence.

Moreover, when the statistics of damaged conditions are also known beforehand, a damage classification can be deployed via selecting the most plausible probabilistic model. Specifically in this paper, a Bayesian framework is adopted, because the algorithm fuses the collected evidence to update prior confidence and thereby select the optimal model to characterize the data observation collected from unknown system condition.

As mentioned above, the uncertainty involved in SHM processes causes a lot of burden, especially when extracting sensitive and specific features from large volume of data set. Oftentimes, the great fuzziness and redundancy in the raw data encourage people to investigate powerful feature extraction methodologies. In the past decades, machine learning

---

Z. Mao • M. Todd (✉)

Department of Structural Engineering, University of California San Diego, La Jolla, CA 92093-0085, USA  
e-mail: [zmao@ucsd.edu](mailto:zmao@ucsd.edu); [mdtodd@ucsd.edu](mailto:mdtodd@ucsd.edu)

technologies have been widely applied to SHM, among which support vector machine (SVM) is particularly powerful for solving classification problems. Compared to the Bayesian model selection approach for damage classification, this paper adopts SVM to classify damage cases from the same test-bed.

A brief introduction of the SpectraQuest MFS vibration simulator system is given in Sect. 11.2, as well as a brief review of the FRF and the UQ model of its estimations. Bayesian model selection approach for classifying damage types will be given in Sect. 11.3, and SVM implementation, with a parametric study, is available in Sect. 11.4. In the end, a summary and comparison of the two approaches is given in Sect. 11.5.

## 11.2 Test-Bed and Uncertainty Quantification of FRF Estimations

The SpectraQuest MFS vibration system is adopted as the test-bed to compare the damage classification approaches, as Fig. 11.1 shows. In the simulator system, the bearing on right-hand side of the shaft is altered from undamaged bearing to damaged bearing with defected balls and defected outer race. Acceleration data in direction  $y$  and  $z$  are recorded, as denoted in Fig. 11.1, and the transfer function between the responses of those two directions are adopted as the damage index.

As the ratio between to power spectra, the definition of FRF is described in Eq. 11.1:

$$H(\omega) = \frac{V(\omega)}{U(\omega)}, \quad (11.1)$$

in which  $U$  and  $V$  are the Fourier transforms of theoretical input and output  $u(t)$  and  $v(t)$ . When the measurements are contaminated by noise (uncertainty), the realistic input and output are denoted as  $x(t)$  and  $y(t)$ , and the estimation of FRF is often calculated via certainty algorithms, called estimators. Equation 11.2 is the H-1 estimator of FRF, which is the ratio between cross- and auto-power density functions of (contaminated) input and output measurements:

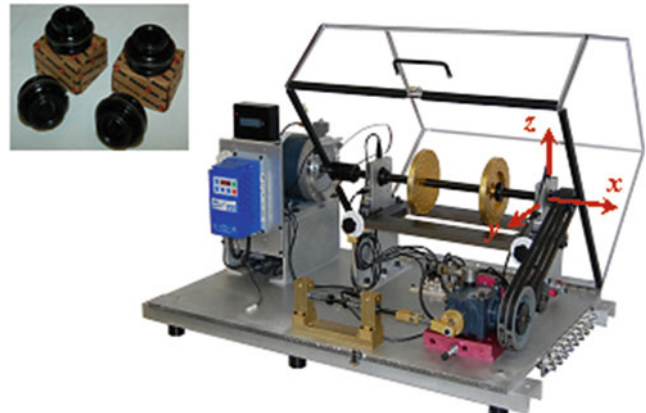
$$\hat{H}(\omega) = \frac{\hat{G}_{xy}(\omega)}{\hat{G}_{xx}(\omega)}, \quad (11.2)$$

where the  $\hat{\cdot}$  denotes the average of power spectra according to Welch's algorithm [7].

Figure 11.2 illustrates the FRF feature estimations for various damage conditions, both the magnitude and phase. There are undamaged baseline and other two types of damaged conditions included, as indicated by the three colors in Fig. 11.2. Obviously, the realizations of FRF are very noisy and overlapped at most of the frequency bins. Without investigating the randomness of estimations, it is hardly to make any valuable group classification judgments.

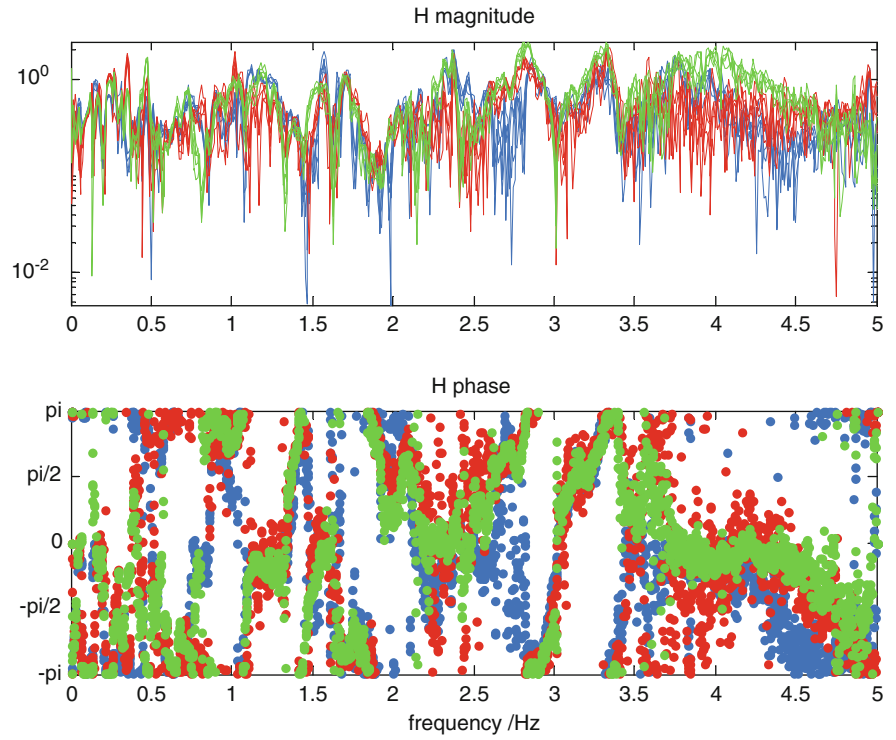
In the Welch's algorithm, the power spectra are estimated in an averaged fashion. If the number of averages is sufficient, the Gaussian distribution is hold asymptotically. The probability density functions of magnitude and phase estimations, as random variables, are derived in [8]:

$$p_m(z|M_j) = \frac{1}{\sigma\sqrt{2\pi}} e^{-\frac{(z-\mu_{m_j})^2}{2\sigma_{m_j}^2}}, \quad (11.3)$$



**Fig. 11.1** Rotary machine test-bed

**Fig. 11.2** FRF magnitude and phase estimations for baseline and two damaged conditions



where in the context of group classification,  $M_j$  is the  $j$ th condition of the structure, and  $\mu_m$  and  $\sigma_m$  are the mean and standard deviation of magnitude estimation respectively.

The probability density function of phase estimation  $p_\theta$  is:

$$p_\theta(z|M_j) = \frac{1}{2\pi} e^{-\frac{\mu_{R_j}^2 + \mu_{I_j}^2}{2\sigma_{\theta_j}^2}} + \frac{\eta_j}{2\sqrt{2\pi}\sigma_{\theta_j}} \cdot e^{-\frac{(\mu_{R_j} \sin(z) - \mu_{I_j} \cos(z))^2}{2\sigma_{\theta_j}^2}} \left(1 + \operatorname{erf}\left(\frac{\eta_j}{\sqrt{2}\sigma_{\theta_j}}\right)\right), \quad (11.4)$$

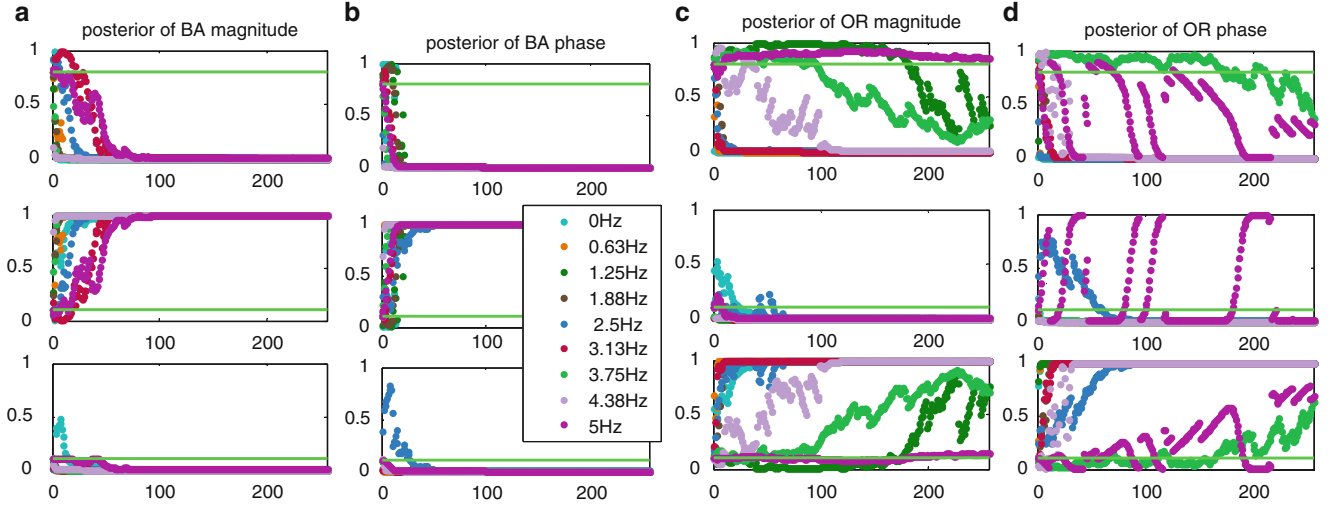
in which  $\eta_j = \mu_{R_j} \cos(z) + \mu_{I_j} \sin(z)$ , and  $\operatorname{erf}(\cdot)$  is error function. In Eq. 11.4,  $\mu_{R_j}$  and  $\mu_{I_j}$  represent the mean of real and imaginary parts of FRF estimation, while  $\sigma_{\theta_j}$  is the standard deviation of both parts.

### 11.3 Bayesian Model Selection for Damage Classification

Equation 11.5 demonstrates the Bayesian framework, which embeds prior knowledge into decision making, and updates the decision confidence when new data are available. The posterior probability  $p(M_j|D, \mathbf{M})$  of model (damage condition)  $M_j$  according to Bayes theorem:

$$p(M_j|D, \mathbf{M}) = \frac{p(D|M_j) p(M_j|\mathbf{M})}{p(D|\mathbf{M})}, \quad (11.5)$$

in which  $p(M_j|\mathbf{M})$  is the prior. Likelihood function  $p(D|M_j)$  is actually the PDF in Eqs. 11.3 and 11.4. Evaluating the total probability theorem, the total evidence for dataset  $D$  on the denominator can be calculated as Eq. 11.6:



**Fig. 11.3** Recursive posterior probability of model selection, at sample frequencies; *top*: baseline model; *middle*: damaged ball model; *bottom*: damaged outer race model. (a) Using FRF magnitude feature, damaged ball data, (b) Using FRF phase feature, damaged ball data, (c) Using FRF magnitude feature, damaged race data, (d) Using FRF phase feature, damaged race data

$$p(\mathbf{D}|\mathbf{M}) = \sum_{j=1}^n p(\mathbf{D}|M_j) \cdot p(M_j|\mathbf{M}), \quad (11.6)$$

where  $n$  is the dimension of model class  $\mathbf{M}$ . After running Eq. 11.6 in a recursive fashion for sufficient iterations, i.e., the posterior probability serves as the prior in the next iteration, and posterior updates are produced as the dataset is increased, the posterior  $p(M_j|\mathbf{D}, \mathbf{M})$  will tend towards 1 or 0, indicating acceptance or rejection of the  $j$ th model (damage condition).

In each class, the posterior probability of selecting among baseline (top), ball defect (middle), and race defect (bottom), as a function of number of iterations is plotted, and each color indicates a different frequency line. It is clear that in all cases, the posterior converges to the right number, i.e., converging to 1 if there is damage, and converging to 0 if not. The horizontal lines in green highlight the arbitrarily-picked prior probability before any testing information. In Fig. 11.3c, d, the convergence is not as decisive as Fig. 11.3a, b. That illustrates for damaged race, not all the sampled frequencies has the same detection capability

## 11.4 Support Vector Machine for Damage Classification

### 11.4.1 SVM and Kernelization

Different from the probabilistic approach using Bayesian framework, support vector machine (SVM) employs training data to form a hyperplane as the decision boundaries, in order to discriminate different sets of data. All the data points determining the hyperplane are called support vectors. Equation 11.5 describes the decision maker  $h^*$ , which maps feature vector  $\mathbf{x}$  into a binary space:

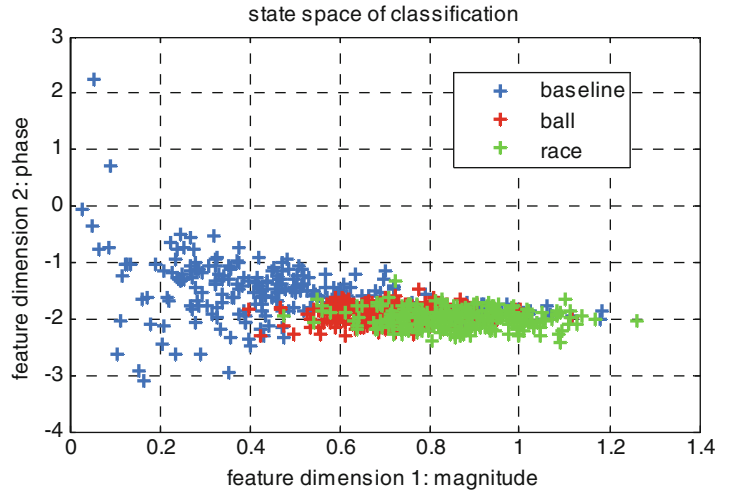
$$h(\mathbf{x}) = \begin{cases} 0 & \text{if } g(\mathbf{x}) > 0 \\ 1 & \text{if } g(\mathbf{x}) < 0 \end{cases}, \quad (11.7)$$

The function  $g^*$  forms a hyperplane in the feature domain, which is described as:

$$g(\mathbf{x}) = \mathbf{w}^T \mathbf{x} + \mathbf{b}. \quad (11.8)$$



**Fig. 11.4** Feature state space at a sample frequency line



For the realistic data presented in last section, the data from the classification model are mostly non-separable, thus the slack variables may be introduced to solve a soft margin problem. It is not always practical for highly overlapped/complicated feature spaces. Kernel functions are employed if necessary, to introduce extra feature dimensions, and all clusters are being better distinguished in a higher dimensional state, as Eq. 11.9 shows:

$$h(\mathbf{x}) = \text{sign} \left[ \sum_{i \in \text{SV}} y_i \alpha_i^* K(\mathbf{x}_i, \mathbf{x}) + \mathbf{b}^* \right]. \quad (11.9)$$

in which  $\mathbf{x}_i$  are all the support vectors,  $K(*,*)$  is the selected kernel function,  $\alpha_i$  is the Lagrange multiplier for constrained optimization, and  $y_i$  is the classification label of feature  $\mathbf{x}_i$ .

### 11.4.2 SVM Classification

Speaking of the cluster of features, a simplified condition is considered at the beginning for SVM analysis. Only a single frequency line is considered and the feature vector is defined as:

$$\mathbf{x} = [ |H(\omega)| \quad \angle H(\omega) ]^T \in \mathbb{R}^2. \quad (11.10)$$

In Eq. 11.10,  $\omega$  is a sample frequency, and apparently the feature  $\mathbf{x}$  is a 2-D vector. Figure 11.4 visualizes the feature vector, and the overlap of clusters is obvious.

In the context of SHM, SVM provides the boundary to separate damaged data from undamaged baseline. Figures 11.5 and 11.6 demonstrate such damage detection implementation on a binary case, with only ball damage involved. With about 250 testing cases in total, the classification result and the true condition for each test is plotted on the right. For each class, the percentage of correct labelling from SVM is calculated, for comparison with the random guess rate. In addition, the kernel trick in SVM increases the decision space dimensionality, so that the decision boundaries plotted are actually the projection of the real decision boundaries to the 2-D plane. Two different kernel realizations are adopted, namely linear kernel and Gaussian kernel, which is a more flexible radial bases function.

Comparing the rate of correct classification marked in the figures, the Gaussian kernel does better than the linear hyperplane separation. However, the performance of correct classification rate has to be compared considering all classes. For instance, if the classification is totally flipped (wrong), the binary classification rate will be 0%/0%, and 50%/50% will indicate an ideal random guess, and only 100%/100% means the perfect classification. The case of 0%/100% does not suggest a good classification, because in this scenario, the algorithm just classifies all the test cases into one class.

For the trinary classification problem, two damaged conditions need to be discriminated from the baseline, and this multi-class classification is implemented into three binary classifications. Each of the binary sub-problems is a “distinguishing one

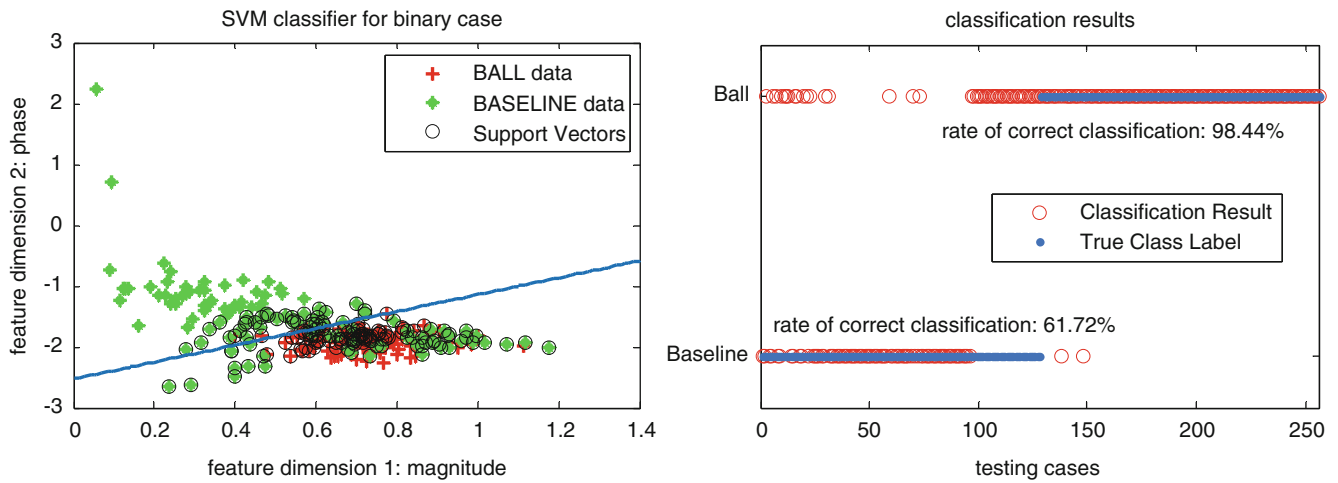


Fig. 11.5 SVM implementation for binary classification, linear kernel

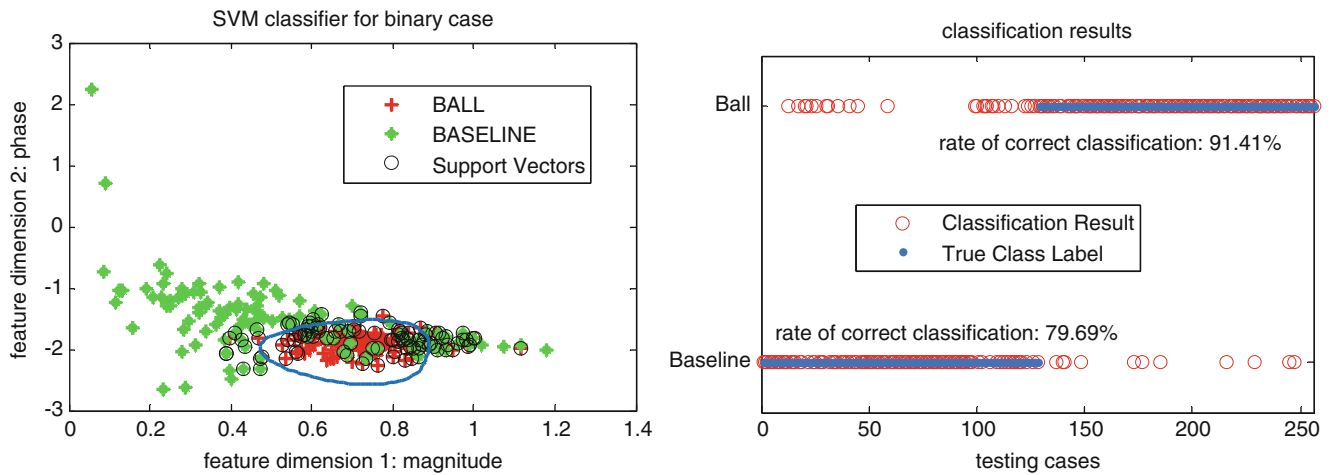


Fig. 11.6 SVM implementation for binary classification, Gaussian kernel

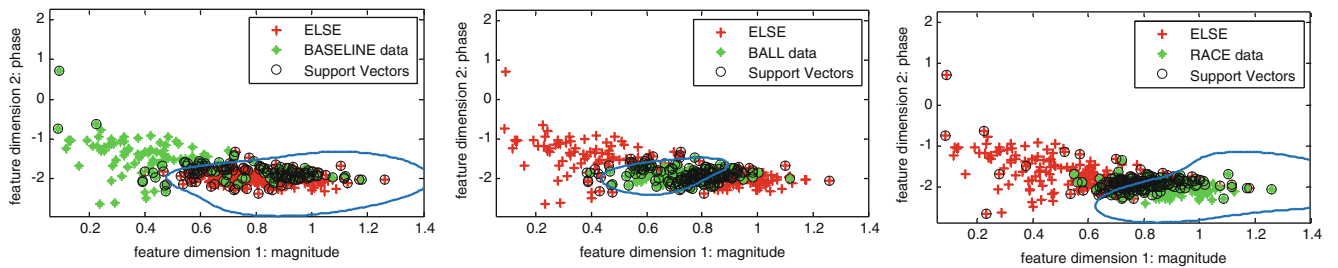
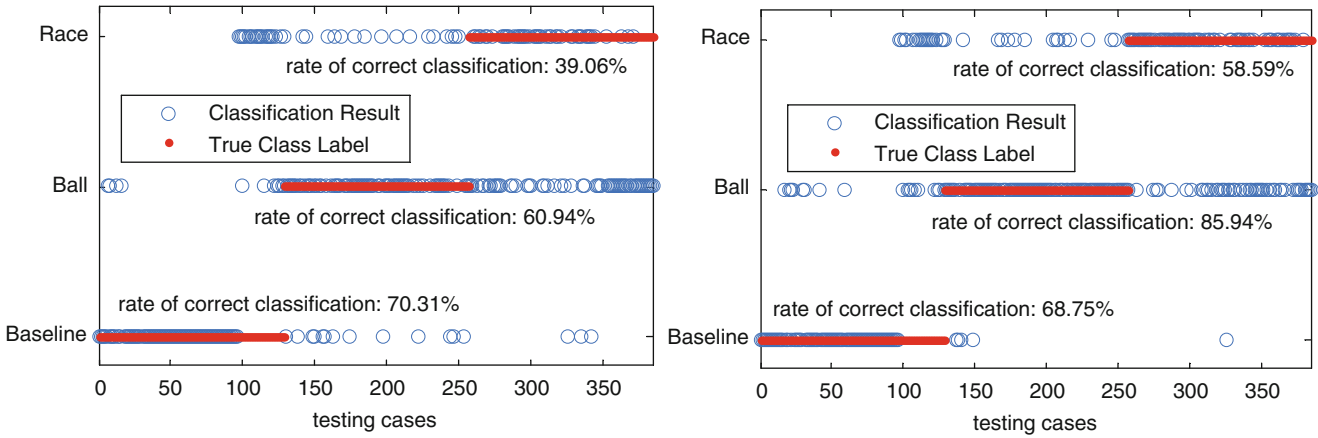


Fig. 11.7 SVM implementation for trinary classification, Gaussian kernel

from all the others” approach, which is essentially the same as damage detection. Specifically speaking, the one-versus-rest idea partitions the trinary classification into (1 vs. 2, 3), (2 vs. 3, 1) and (3 vs. 1, 2), all three sub-problems.

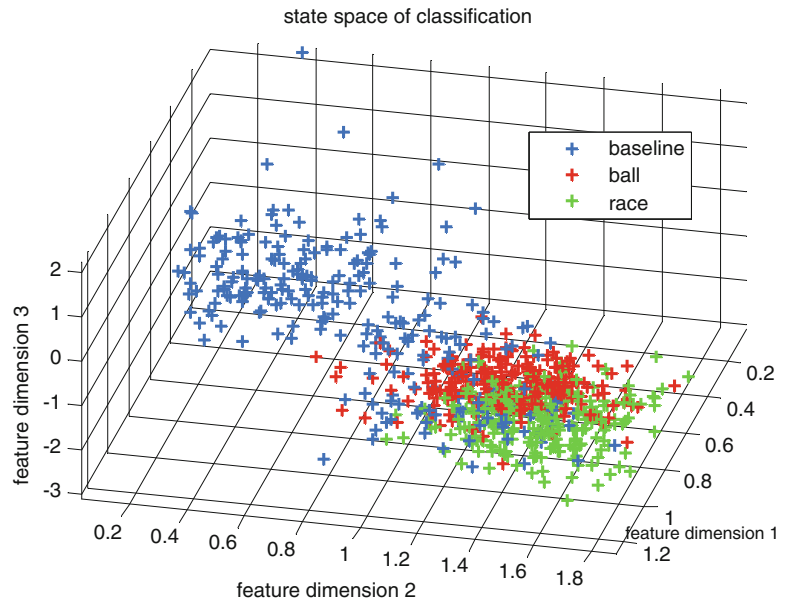
Because the Gaussian kernel outperforms slightly according to Figs. 11.5 and 11.6, the multi-class discriminations presented in Fig. 11.7 for each sub-problem employ Gaussian kernel. Just for a comparison, the result of “correct labeling” is also available in Fig. 11.8. In each sub-problem, the class to be distinguished is highlighted and the other two classes are grouped as “ELSE”.

The same as damage detection, the performance of SVM for trinary classification is evaluated via correct rate, plotted in Fig. 11.8. The same conclusion can be made, that the Gaussian function outperforms linear function due to the flexibility characteristics. Compared to the binary case, the SVM classifiers obtained from both kernel functions, in general, tag the



**Fig. 11.8** Correct classification rate for SVM implementation for trinary classification, *left*: linear kernel; *right*: Gaussian kernel

**Fig. 11.9** High-dimension feature state space projected to arbitrary three dimensions



data less accurate than the performance of binary case. This is mainly caused by the heavier complexity and ambiguity. The average rate of correct classification for each case is about 57 % and 71 %, which is lower than the binary classification, given the same feature dimension.

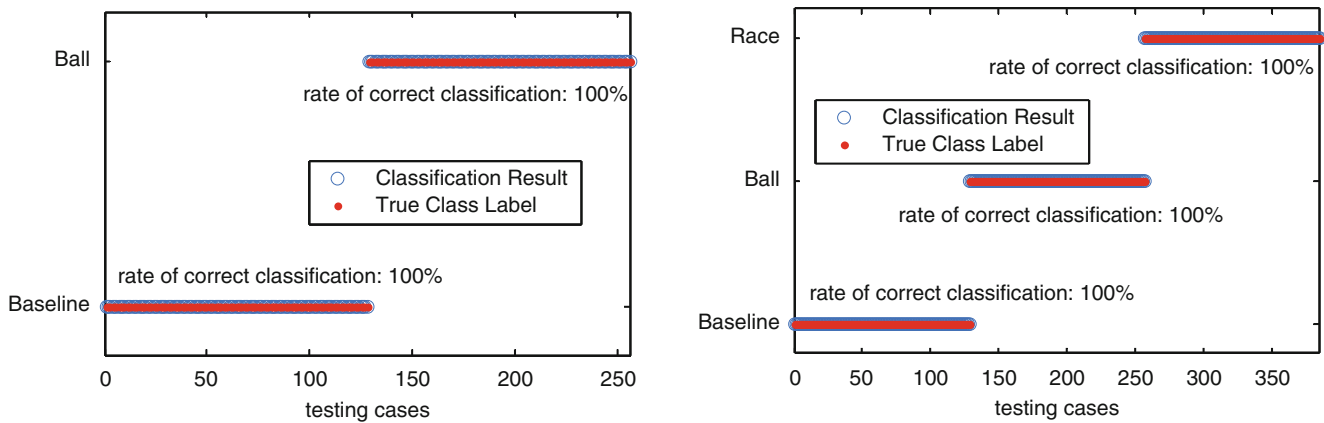
So far, all the damage detection/classification are implemented based upon the FRF feature at single frequency, and the correct labeling rate for binary and trinary is 85 % and 71 % respectively, using Gaussian kernel. In fact, a lot of information has not been utilized, because most of the spectral characteristics are thrown away when selecting the sample frequency. Instead of eliminating most of the FRF information, Eq. 11.11 defines the state space feature by using more frequency lines:

$$\mathbf{x} = [ |H(\omega_1)|, |H(\omega_2)| \cdots |H(\omega_n)|, \angle H(\omega_1), \angle H(\omega_2) \cdots \angle H(\omega_n) ]^T \in \mathbb{R}^{2n}. \quad (11.11)$$

in which  $n$  frequencies are considered to build up the new feature vector  $\mathbf{x}$ .

The new-established feature state has a lot more dimension. For example, if all the frequency lines are included in the vector  $\mathbf{x}$ , there will be around a thousand state space dimensions. Under this circumstance, the state space is not able to be visualized, and Fig. 11.9 only plots the projection to three arbitrary dimensions, which is the limit on a 2-D plane.

Given feature space with ultra-high dimension, Gaussian kernelization becomes burdensome and could not return a reliable classifier easily, especially due to the relative lack of training data. As a result, linear kernel function is adopted,



**Fig. 11.10** Rate of correct classification via SVM classifiers, linear kernel, *left*: binary classification; *right*: trinary classification

for both binary and trinary classification. By using the high-dimensional feature, the rates of correct classification for both binary and trinary cases are 100 %, as shown in Fig. 11.10, which means all the test cases are correctly labeled.

## 11.5 Summary and Conclusion

This paper compares two strategies of damage detection and classification, namely a Bayesian model selection approach and support vector machine classification. Bearing defects on rotary machine is selected as the test-bed to implement the strategies. In the Bayesian approach, it takes tens of samples for the posterior probability of selecting/denying a model to saturate to either 1 or 0, but for SVM, the training and testing will take longer time. In SVM approach, the performance for binary classification is better than for trinary cases, because of the lower complexity, and higher-dimensional features will lead to a more specific classification. On the other hand, higher-dimensional feature spaces will cause more computational burden in the SVM training procedure, which is a major drawback compared to Bayesian approach. Among the two types of kernel functions, SVM with linear kernel function separates data with a hyperplane and has the advantage of relatively faster training, while Gaussian kernel has better flexibility to handle more complicated data sets. This gets verified by high-dimensional features, where Gaussian kernel may not converge to a decision boundary with limited training sets. Although the SVM is computational expensive, compared to the Bayesian approach, it is better at handling high-dimensional features, because when the feature space expands, the joint probability density function will have an exponentially increasing complexity, and the evaluation of likelihood functions will become troublesome.

**Acknowledgement** This research was supported by the research grant (UD130058JD) of the Agency for Defense Development of the Korean government and by the Leading Foreign Research Institute Recruitment Program through the National Research Foundation of Korea funded by the Ministry of Science, ICT and Future Planning (2011-0030065).

## Reference

1. Bendat JS, Piersol AG (1986) Random data: analysis and measurement procedures, 2nd edn. Wiley, New York
2. Brillinger DR (1981) Time series: data analysis and theory. McGraw-Hill, New York
3. Mace BR, Worden K, Manson G (2005) Uncertainty in structural dynamics. *J Sound Vib* 288:423–429
4. Mao Z, Todd MD (2012) A model for quantifying uncertainty in the estimation of noise-contaminated measurements of transmissibility. *Mech Syst Signal Process* 28:470–481
5. Mao Z, Todd MD (2013) Statistical modeling of frequency response function estimation for uncertainty quantification. *Mech Syst Signal Process* 38:333–345
6. Mao Z, Todd MD (2013) Optimal structural health monitoring feature selection via minimized performance uncertainty. *Key Eng Mater* 558:235–243
7. Welch PD (1967) The use of fast fourier transform for the estimation of power spectra: a method based on time averaging over short, modified periodograms. *IEEE Trans Audio Electroacoust* 15:70–73
8. Mao Z, Todd MD (2013) Bayesian updating of detection capability with frequency response function related structural health monitoring features. The proceedings of the 9th international workshop on structural health monitoring (IWSHM 2013), Stanford University, Palo Alto, CA

## Chapter 12

# A Comparative Study of Mode Decomposition to Relate Next-ERA, PCA, and ICA Modes

Ayad Al-Rumaithi, Hae-Bum Yun, and Sami F. Masri

**Abstract** This paper discusses a comparative study to relate parametric and non-parametric mode decomposition algorithms for response-only data. Three popular mode decomposition algorithms are included in this study: the Eigensystem Realization Algorithm with the Natural Excitation Technique (NExT-ERA) for the parametric algorithm, as well as the Principal Component Analysis (PCA) and the Independent Component Analysis (ICA) for the non-parametric algorithms. A comprehensive parametric study is provided for (i) different response types, (ii) excitation types, (iii) system damping, and (iv) sensor spatial resolution to compare the mode shapes and modal coordinates of using a 10-DOF building model. The mode decomposition results are also compared using a unique dynamic response data collected in a ship-bridge collision accident for ambient excitation with traffic loading, ambient excitation without traffic loading, and impulse excitation.

**Keywords** Mode decomposition • Modal analysis • Eigensystem realization analysis (ERA) • Natural excitation technique (NExT) • Principal component analysis (PCA) • Independent component analysis (ICA) • Ship-bridge collision

## Nomenclatures

$\ddot{X}(t), \dot{X}(t), X(t)$	The system acceleration, velocity and displacement, respectively.
$\Psi^{\text{TRU}}$	The true mode shape determined by the modal superposition method.
$\hat{\Psi}_{\ddot{X}}^{\text{ERA}}, \hat{\Psi}_{\dot{X}}^{\text{ERA}}, \hat{\Psi}_X^{\text{ERA}}$	The mode shapes estimated with the Eigensystem Realization Algorithm with Natural Excitation Method (NExT-ERA) for $\ddot{X}(t)$ , $\dot{X}(t)$ , and $X(t)$ , respectively.
$\hat{\Psi}_{\ddot{X}}^{\text{PCA}}, \hat{\Psi}_{\dot{X}}^{\text{PCA}}, \hat{\Psi}_X^{\text{PCA}}$	The mode shapes estimated with the Principal Component Analysis (PCA) method for $\ddot{X}(t)$ , $\dot{X}(t)$ , and $X(t)$ , respectively.
$\hat{\Psi}_{\ddot{X}}^{\text{ICA}}, \hat{\Psi}_{\dot{X}}^{\text{ICA}}, \hat{\Psi}_X^{\text{ICA}}$	The mode shapes estimated with the Independent Component Analysis (ICA) method for $\ddot{X}(t)$ , $\dot{X}(t)$ , and $X(t)$ , respectively.
$p^{\text{TRU}}$	The true modal coordinate determined by the modal superposition method.
$\hat{p}_{\ddot{X}}^{\text{ERA}}, \hat{p}_{\dot{X}}^{\text{ERA}}, \hat{p}_X^{\text{ERA}}$	The modal coordinates estimated with the Eigensystem Realization Algorithm with Natural Excitation Method (NExT-ERA) for $\ddot{X}(t)$ , $\dot{X}(t)$ , and $X(t)$ , respectively.
$\hat{p}_{\ddot{X}}^{\text{PCA}}, \hat{p}_{\dot{X}}^{\text{PCA}}, \hat{p}_X^{\text{PCA}}$	The modal coordinates estimated with the Principal Component Analysis (PCA) method for $\ddot{X}(t)$ , $\dot{X}(t)$ , and $X(t)$ , respectively.
$\hat{p}_{\ddot{X}}^{\text{ICA}}, \hat{p}_{\dot{X}}^{\text{ICA}}, \hat{p}_X^{\text{ICA}}$	The modal coordinates estimated with the Independent Component Analysis (ICA) method for $\ddot{X}(t)$ , $\dot{X}(t)$ , and $X(t)$ , respectively.

---

A. Al-Rumaithi • H.-B. Yun (✉)

Civil, Environmental and Construction Engineering, University of Central Florida, Orlando, FL, USA  
e-mail: [ayad.ali89@gmail.com](mailto:ayad.ali89@gmail.com); [Hae-Bum.Yun@ucf.edu](mailto:Hae-Bum.Yun@ucf.edu)

S.F. Masri

Civil and Environmental Engineering, University of Southern California, Los Angeles, CA, USA  
e-mail: [Masri@usc.edu](mailto:Masri@usc.edu)

## 12.1 Introduction

Mode decomposition techniques are popularly used in many identification applications of multi-degree-of-freedom (MDOF) dynamic systems. These techniques are generally categorized into parametric and non-parametric approaches. The experimental modal analysis is categorized into the parametric approach. The modal analysis can be further classified into input-output modal identification and output-only modal identification methods, depending on the use of the excitation data in its mode decomposition process. Since measuring the forces of MDOF systems is technically difficult and often expensive, the output-only modal identification method is used in many monitoring applications when the force measurement is not available, usually based on an assumption that the excitation input is a zero-mean Gaussian white noise. There are two main groups of the output-only modal identification method: frequency-domain and time-domain methods (Maia et al. 2003). The Eigensystem Realization Algorithm (ERA) combined with the Natural Excitation Technique (NExT) is a time-domain modal analysis technique that has been studied in numerous structural dynamics applications [1–3].

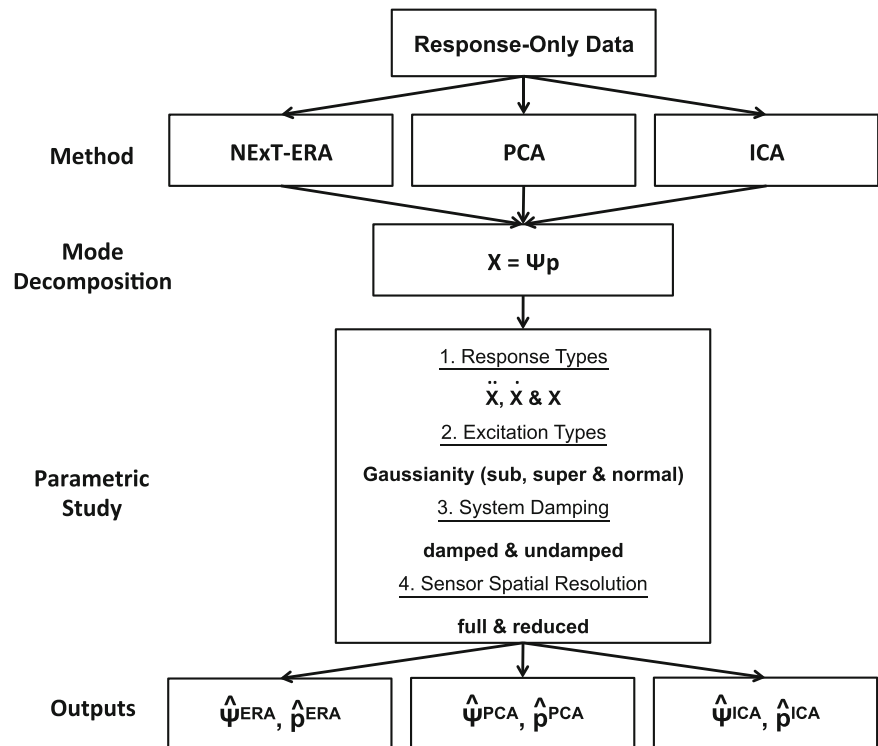
On the other hand, the Principal Component Analysis (PCA) and Independent Component Analysis (ICA) are categorized into the non-parametric mode decomposition approach, which are in a family of the Blind Source Separation (BSS) techniques. The mathematical models of these techniques are data-driven, rather than being based on physical assumptions such as the equation of motion. The identification is relatively simple and straightforward since the vibration modes can be identified from the columns of the transformation matrix that can be determined based on underlying statistics of the response data. The PCA, known also as the Proper Orthogonal Decomposition (POD), Second-Order Blind Identification (SOBI), or Karhunen-Loève (K-L) Decomposition, decomposes multivariate response data into statistically uncorrelated data using the second-order statistics, while the ICA decomposes the response data into statistically independent data using the fourth-order statistics.

The objective of this paper is to compare the parametric and non-parametric mode decomposition methods of NExT-ERA, PCA and ICA. Using response-only datasets collected in simulation and field tests, a parametric study was conducted to evaluate the sensitivity of the mode decomposition techniques to (i) response types, (ii) excitation types, (iii) system damping, and (iv) sensor spatial resolution. First, the simulation study is presented using 10-DOF building models subjected to impulse and random excitations. Then, the experimental study is presented using a full-scale suspension bridge under different excitation conditions in a ship-bridge collision accident, including ambient excitation with traffic loads, ambient excitation without traffic loads, and impulse excitation during the collision. In the simulation study, the mode shapes ( $\hat{\Psi}$ ) and modal coordinates ( $\hat{p}$ ) identified using NExT-ERA, PCA and ICA were compared with the true modes. In the experimental study,  $\hat{\Psi}$  and  $\hat{p}$  identified using PCA and ICA were compared with those using NExT-ERA. An overview of the proposed comparative study is shown in Fig. 12.1.

Prior to this study, analytical and experimental studies have made by researchers to relate the non-parametric modes to the parametric modes for vibrating structures. For PCA, Feeny and Kappagantu [4] related POD to free vibration and compared mode shapes and modal coordinates using low-dimensional numerical models. Feeny and Liang [5] related the proper orthogonal modes (POMs) to linear normal modes (LNMs) of lumped and continuous-mass systems. They found that POD agreed with LNMs under random excitation conditions. Kerschen et al. [6] presented an overview of the POD method for dynamic characterization and the order reduction of mechanical systems. They stated that POMs may be considered as an alternative to the linear mode shapes although they do not have the theoretical foundations. POMs and proper orthogonal values (POVs) provide a good characterization of the dynamics without requiring the knowledge of the structural matrices; thus POD can determine an appropriate embedding space for a low-dimensional structure. Zhou and Chelidze [7] compared the Algorithm for Multiple Unknown Signal Extraction (AMUSE), SOBI, and Ibrahim Time-Domain Modal Analysis (ITD) methods using noise-free response data for damped and undamped systems. Smith and Saitta [8] employed PCA for analysis and damage detection of complex structures, which was compared with multiple model-free data interpretation methods including the Correlation Analysis, Continuous Wavelet Transform (CWT), Short-Term Fourier Transform (STFT), and Instance-Based Method (IBM). Posenato et al. [9] applied PCA combined with the K-mean clustering for data mining to interpret multiple-model predictions. Antoni and Chauhan [10] compared SOBI with the Stochastic Subspace Identification (SSI) for an analytical 15-DOF system by comparing their mode shapes and natural frequencies. They found that the validity of is in principle limited to conservative systems, yet it is quite robust to this assumption.

For ICA, Roan et al. [11] applied ICA to detect and analyze gear tooth failure. Kerschen et al. (2006) related the vibration modes of mechanical systems to ICA modes for their mode shapes and modal coordinates. They found that the ICA modes agreed well with the vibrational modes for an undamped system subjected to impulse and uniform random excitation while a damped system gave higher discrepancy. Poncelet et al. [12, 13] compared the mode shapes and modal coordinates identified with ICA and SOBI to true ones. ICA gave a good agreement for weakly damped systems. SOBI gave smaller discrepancy for strongly damped systems than ICA. McNeil and Zimmerman [14] discussed the relationship between

**Fig. 12.1** Study overview for the performance evaluation of the mode decomposition using NExT-ERA, PCA and ICA



independent component and free-vibration modal responses using the free-vibrational modal responses of a diagonally-damped model through their simulation study. They deduced that undamped modal responses closely corresponded to independent components, while damped modal responses did not. Yang and Nagarajaiah [15] found that the time-domain ICA was limited to lightly damped structure, and SOBI lost robustness in nonstationary and unknown noisy environment. They proposed STFT-ICA for both lightly and highly damped structures.

More recently, the Sparse Component Analysis (SCA), as a novel BSS method, has been studied to estimate modal parameters for underdetermined problems: Yang and Nagarajaiah [15] applied SCA to the underdetermined problem where sensors were highly limited compared to the number of active modes. Yu et al. [16] applied SCA to estimate both time-invariant and time-varying modal parameters of a small-scale column in laboratory tests using a limited number of accelerometers.

In addition to the above studies that were conducted using numerical or laboratory models, the BSS methods were applied to some large-scale field structures. Oh et al. [17] applied Kernel PCA (KPCA) for the structural health monitoring of the Yeongjong suspension bridge in South Korea to perform data normalization and incorporate with a novelty index and generalized extreme value statistics for novelty detection. Kallinikidou and Yun [18] applied POD for long-term monitoring of the Vincent Thomas suspension bridge in California, U.S.A. The statistics of acceleration covariance matrices (ACMs) were evaluated, and the relation between POMs and vibrational mode shapes were studied. Yun et al. (2014) applied adaptive PCA to a tunnel structure to evaluate proximity excavation effects on the tunnel deformation using POMs and POVs using extensometers and tilt sensors.

Although the relationships between NExT-ERA, PCA, and ICA modes have been investigated in the above studies, they were conducted for a limited number of parameters that affect the performance of mode decomposition. This paper presents a comprehensive parametric study as shown in Fig. 12.1. Most of the previous studies were limited to using simulation models or small-scale models in the laboratory, and the relationship of the parametric and non-parametric mode decomposition has been rarely evaluated for full-scale field structures. The experimental evaluation in this study includes analysis for the impulse vibration, ambient vibration with traffic loads, and ambient vibration without traffic loads, which are unique datasets to investigate the performance of the mode decomposition for different excitation types.

This paper is organized as follows: the mathematical background of NExT-ERA, PCA and ICA methods are described in Sect. 12.2; the results of the simulation study using the 10-DOF building models are presented and discussed in Sect. 12.3; the results of the experimental study using the ship-bridge collision data are presented and discussed in Sect. 12.4; and finally the conclusions are given in Sect. 12.5.

## 12.2 Mode Decomposition Techniques

### 12.2.1 Eigen Realization Algorithm with Natural Excitation Technique (NExT-ERA)

In general, a MDOF linear system subjected to the forced vibration of ambient excitation, for  $m$  sensors that is larger than the degrees of freedom of the system and  $N$  data points over time, can be expressed as the following equation of motion:

$$\mathbf{M}\ddot{\mathbf{X}}(t) + \mathbf{C}\dot{\mathbf{X}}(t) + \mathbf{K}\mathbf{X}(t) = \mathbf{F}(t) \quad (12.1)$$

where;  $\mathbf{M}$ ,  $\mathbf{C}$  and  $\mathbf{K}$  are the  $(m \times m)$  mass, damping and stiffness matrices, respectively;  $\ddot{\mathbf{X}}(t)$ ,  $\dot{\mathbf{X}}(t)$ ,  $\mathbf{X}(t)$ , and  $\mathbf{F}(t)$  are the  $(m \times N)$  matrices of the system displacement, velocity, acceleration, and ambient excitation, respectively.

The Eigen Realization Algorithm (ERA) is an output-only modal analysis technique for a MDOF linear dynamic system with an assumption of impulse excitation [19]. Since ERA is designed for free vibration, the original ERA should be modified to deal with ambient excitation. The Natural Excitation Technique (NExT) [20] is commonly used with ERA for this modification as

$$\mathbf{M}\mathbf{R}_{X_{\text{ref}}\ddot{\mathbf{X}}}(\tau) + \mathbf{C}\mathbf{R}_{X_{\text{ref}}\dot{\mathbf{X}}}(\tau) + \mathbf{K}\mathbf{R}_{X_{\text{ref}}\mathbf{X}}(\tau) = \mathbf{R}_{X_{\text{ref}}\mathbf{F}}(\tau) \quad (12.2)$$

where  $\mathbf{R}(\ )$  is the cross-correlation function; and  $X_{\text{ref}}(\tau)$  is the reference displacement with a time lag,  $\tau$ . If the reference channel displacement and input force are statistically uncorrelated, the RHS of Eq. 12.2 vanishes. Using the following relationships

$$\mathbf{R}_{X_{\text{ref}}\dot{\mathbf{X}}}(\tau) = \dot{\mathbf{R}}_{X_{\text{ref}}\mathbf{X}}(\tau), \dots, \dots, \mathbf{R}_{X_{\text{ref}}\ddot{\mathbf{X}}}(\tau) = \ddot{\mathbf{R}}_{X_{\text{ref}}\mathbf{X}}(\tau) \quad (12.3)$$

Equation 12.3 becomes

$$\mathbf{M}\ddot{\mathbf{R}}_{X_{\text{ref}}\ddot{\mathbf{X}}}(\tau) + \mathbf{C}\dot{\mathbf{R}}_{X_{\text{ref}}\dot{\mathbf{X}}}(\tau) + \mathbf{K}\mathbf{R}_{X_{\text{ref}}\mathbf{X}}(\tau) = 0 \quad (12.4)$$

Then, the original ERA technique can be applied to Eq. 12.4 for the system modal parameters. In ERA, due to the noise in the data, the system order should be chosen to be higher than the real system order. Many studies, including Pappa et al. [2], discussed the system order role on the realization.

The mode condensation algorithm gives practical solution to distinguish between physical and noisy modes and perform the modal realization without the need to predefine the system order [2, 21]. Juang and Pappa [19] and Pappa et al. (1993) suggested different mode indicators to measure the accuracy of mode identification. These mode indicators are incorporated in the mode condensation algorithm in order to separate physical modes from the noisy modes. The consistent mode indicator (CMI) used in this study is expressed as (Pappas et al. 1993)

$$\text{CMI}_i = \text{EMAC}_i \cdot \text{MPC}_i \quad (12.5)$$

where  $\text{EMAC}_i$  is the extended mode amplitude coherence of mode  $i$ , which quantifies the temporal consistency of the identified mode, and  $\text{MPC}_i$ , the modal phase collinearity, quantifies the spatial consistency of the corresponding mode. Therefore  $\text{CMI}_i$  quantify both of the temporal and spatial consistency.  $\text{CMI}_i$ ,  $\text{EMAC}_i$ , and  $\text{MPC}_i$  have values from 0 to 100 %.

### 12.2.2 Principal Component Analysis (PCA)

The Principal Component Analysis (PCA) converts the response data that are correlated between sensor channels into *statistically uncorrelated* data as follows:

$$\ddot{\mathbf{X}}(t) = \Psi_{\ddot{\mathbf{X}}}^{\text{PCA}} p_{\ddot{\mathbf{X}}}^{\text{PCA}}(t), \quad \dot{\mathbf{X}}(t) = \Psi_{\dot{\mathbf{X}}}^{\text{PCA}} p_{\dot{\mathbf{X}}}^{\text{PCA}}(t), \quad \mathbf{X}(t) = \Psi_{\mathbf{X}}^{\text{PCA}} p_{\mathbf{X}}^{\text{PCA}}(t) \quad (12.6)$$



where  $p_{\ddot{X}}^{\text{PCA}}(t)$ ,  $p_{\dot{X}}^{\text{PCA}}(t)$ , and  $p_X^{\text{PCA}}(t)$  are the  $(m \times N)$  matrices of the modal coordinates for the system acceleration, velocity and displacement, respectively, which are statistically uncorrelated between the coordinate components;  $\Psi_{\ddot{X}}^{\text{PCA}}$  is the transformation matrix of the acceleration to be determined for the linear transformation from  $\ddot{X}(t)$  to  $p_{\ddot{X}}^{\text{PCA}}(t)$ ; and in the same manner for  $\dot{X}(t)$  and  $X(t)$ . The columns of  $\Psi_{\ddot{X}}^{\text{PCA}}$  represent the mode shapes of the response data.

The purpose of PCA is to find the orthonormal  $\Psi_{\ddot{X}}^{\text{PCA}}$ ,  $\Psi_{\dot{X}}^{\text{PCA}}$ , or  $\Psi_X^{\text{PCA}}$  matrices that make the components of  $p_{\ddot{X}}^{\text{PCA}}(t)$ ,  $p_{\dot{X}}^{\text{PCA}}(t)$ , or  $p_X^{\text{PCA}}(t)$  statistically uncorrelated by transforming the covariance matrix of the modal coordinates to a diagonal matrix. The uncorrelated modal coordinates can be determined by using the second-order statistics from

$$\sum_{\ddot{X}} = E \left[ p_{\ddot{X}}^{\text{PCA}} p_{\ddot{X}}^{\text{PCA T}} \right] = E \left[ \Psi_{\ddot{X}}^{\text{PCA}} p_{\ddot{X}}^{\text{PCA}} p_{\ddot{X}}^{\text{PCA T}} \Psi_{\ddot{X}}^{\text{PCA T}} \right] = \Psi_{\ddot{X}}^{\text{PCA}} \Gamma_{\ddot{X}} \Psi_{\ddot{X}}^{\text{PCA T}} \quad (12.7)$$

where  $\sum_{\ddot{X}}$  is the covariance matrix of  $\ddot{X}(t)$ ;  $\Gamma_{\ddot{X}}$  is the covariance matrix of  $p_{\ddot{X}}(t)$ . Equation 12.7 can be applied in the same manner for  $\dot{X}(t)$  and  $X(t)$ . PCA is the optimal linear algorithm since it obtains the minimum expected squared distance between the original signal and the dimension-reduced representation [6].

### 12.2.3 Independent Component Analysis (ICA)

The Independent Component Analysis (ICA) is another mode decomposition technique in the BSS family to convert the response data into *statistically independent* data by the following linear transformation:

$$\ddot{X}(t) = \Psi_{\ddot{X}}^{\text{ICA}} p_{\ddot{X}}^{\text{ICA}}(t), \quad \dot{X}(t) = \Psi_{\dot{X}}^{\text{ICA}} p_{\dot{X}}^{\text{ICA}}(t), \quad X(t) = \Psi_X^{\text{ICA}} p_X^{\text{ICA}}(t) \quad (12.8)$$

where  $p_{\ddot{X}}^{\text{ICA}}(t)$ ,  $p_{\dot{X}}^{\text{ICA}}(t)$ , and  $p_X^{\text{ICA}}(t)$  are the  $(m \times N)$  matrices of the modal coordinates for the system acceleration, velocity and displacement, which are statistically independent between the coordinate components;  $\Psi_{\ddot{X}}^{\text{ICA}}$  is the transformation matrix of the acceleration to be determined for the linear transformation from  $\ddot{X}(t)$  to  $p_{\ddot{X}}^{\text{ICA}}(t)$ ; and in the same manner for  $\dot{X}(t)$  and  $X(t)$ .

The objective of ICA is to find the mode shape matrices of  $\Psi_{\ddot{X}}^{\text{ICA}}$ ,  $\Psi_{\dot{X}}^{\text{ICA}}$ , or  $\Psi_X^{\text{ICA}}$ , which satisfy the components of  $p_{\ddot{X}}^{\text{ICA}}(t)$ ,  $p_{\dot{X}}^{\text{ICA}}(t)$ , or  $p_X^{\text{ICA}}(t)$  to be statistically independent. Several methods are available to find the mode shape matrices. One approach is to maximize the non-Gaussianity of  $p_{\ddot{X}}^{\text{ICA}}(t)$ ,  $p_{\dot{X}}^{\text{ICA}}(t)$ , or  $p_X^{\text{ICA}}(t)$  based on the kurtosis ( $k$ ) that is zero for Gaussian data [22]. The data with  $k > 0$  are called the super-Gaussian data, while the data with  $k < 0$  are called the sub-Gaussian data. The major differences between PCA and ICA include

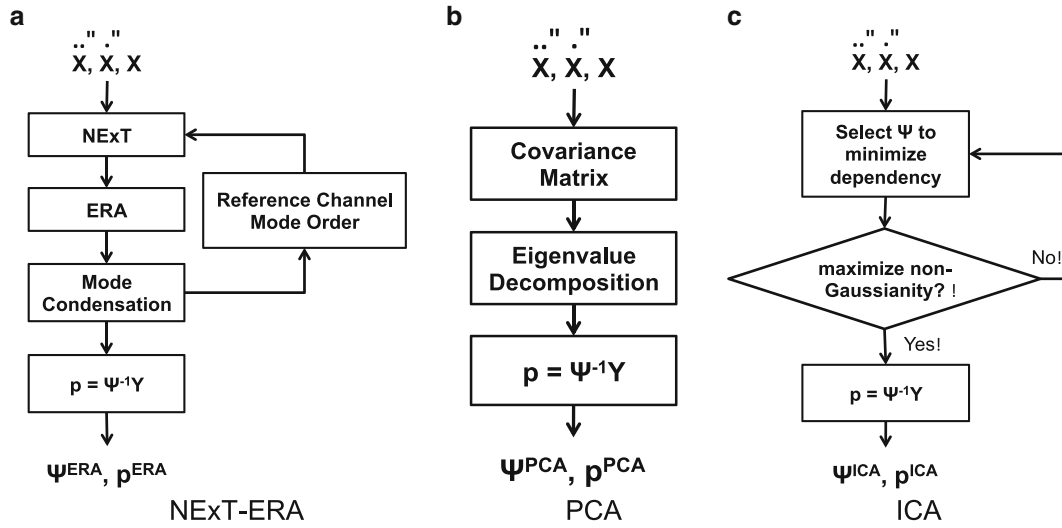
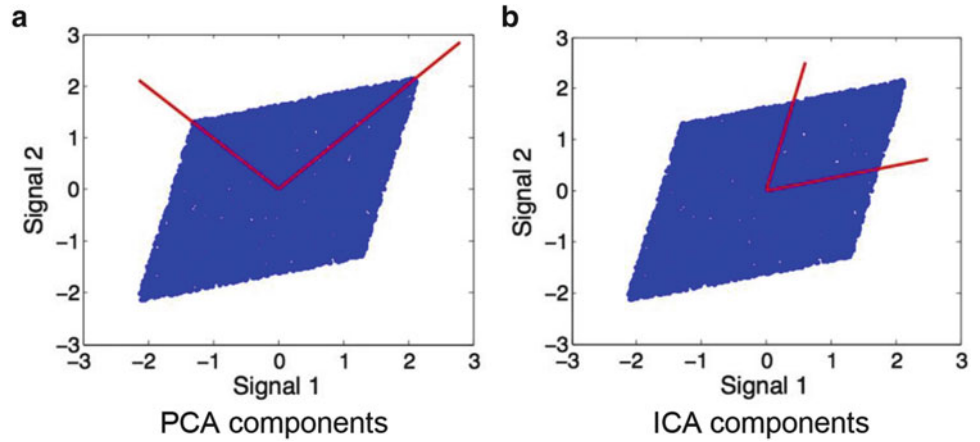
- PCA converts the system responses into statistically uncorrelated modal coordinates, while ICA converts the system responses into statistically independent modal coordinates.
- The PCA mode shape matrix (or transformation matrix) is orthonormal, while the ICA mode shape matrix is not necessarily orthonormal.
- The ICA modal coordinate (or transformed variable) has a unit variance, while the PCA modal coordinate does not necessarily have a unit variance.
- PCA works with both Gaussian and non-Gaussian response data, while ICA does not work with Gaussian response data.

Figure 12.2 shows that the identified PCA and ICA mode components can be different for the same bivariate uniform random variables since their mode decomposition criteria are different. In this paper, the PCA and ICA modes will be compared with the NExT-ERA or true modes for different conditions of response types, excitation types, system damping, and sensor spatial resolution using simulation models in Sect. 12.3 and a full-scale bridge in Sect. 12.4.

### 12.2.4 Mode Shapes and Modal Coordinates for Mode Decomposition Performance

In this study, the mode shapes and modal coordinates are used to evaluate the mode-decomposition performance of the NExT-ERA, PCA and ICA as

**Fig. 12.2** Comparison between PCA and ICA components for the bivariate uniform random variables



**Fig. 12.3** Procedures of NExT-ERA, PCA and ICA

$$p_Y(t) = \Psi_Y^{-1}Y(t) \tag{12.9}$$

where  $Y(t)$  is the system response of  $\ddot{X}(t)$ ,  $\dot{X}(t)$  or  $X(t)$ ;  $\Psi_Y$  is the matrix of the mode shapes or the transform matrix of NExT-ERA, PCA or ICA; and  $p_Y(t)$  is the modal coordinates of NExT-ERA, PCA or ICA. The procedures of NExT-ERA, PCA and ICA to obtain the mode shapes ( $\Psi$ ) and modal coordinates ( $p$ ) are illustrated in Fig. 12.3.

## 12.3 Simulation Study

### 12.3.1 Model Description

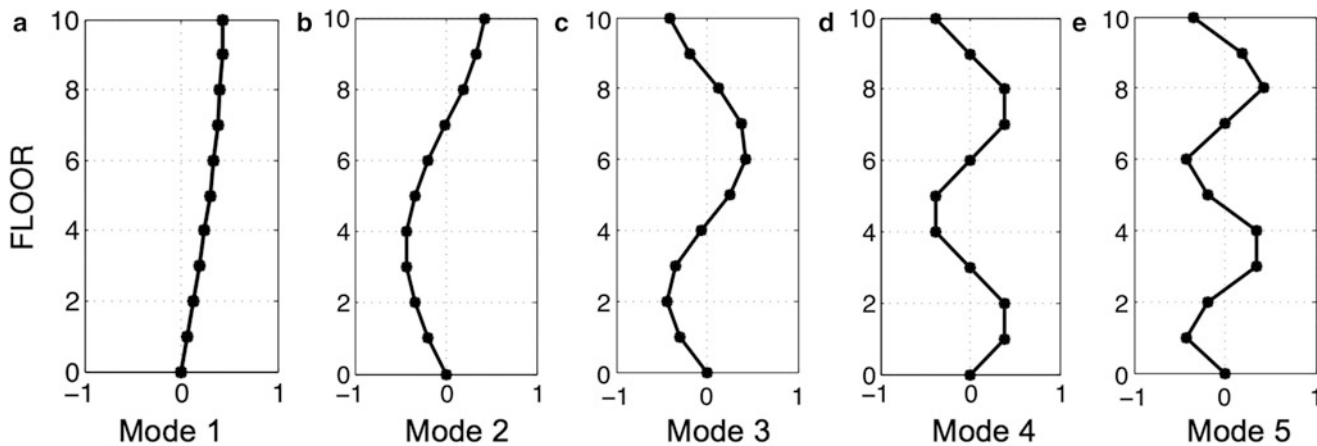
A 10-DOF multistory building model was developed, which was fixed at the bottom and free at the top. The simulation model can be expressed using the following linear equation of motion:

$$\mathbf{M}\ddot{X}(t) + \mathbf{C}\dot{X}(t) + \mathbf{K}X(t) = F(t) \tag{12.10}$$

where  $\mathbf{M}$ ,  $\mathbf{K}$ , and  $\mathbf{C}$  are the  $10 \times 10$  matrices of the mass, damping, and stiffness, respectively;  $F(t)$  is the  $(10 \times N)$  matrix of the external excitation;  $X(t)$  are the  $(10 \times N)$  matrix of the system displacement; and  $N$  is the number of data points. The mass was set to be 1 kg, and the stiffness was set to be 500 N/m for all floors. The simulation models were developed for two

**Table 12.1** The modal frequencies and damping ratios of the lightly damped and undamped simulation models

Mode no.	Natural frequency (Hz)	Damping ratio (%)		Mode no.	Natural frequency (Hz)	Damping ratio (%)	
1	0.53	0.26	0.00	6	5.22	2.32	0.00
2	1.58	0.71		7	5.88		
3	2.60	1.16		8	6.41		
4	3.56	1.58		9	6.8		
5	4.44	1.97		10	7.04		



**Fig. 12.4** Mode shapes of the 10-DOF simulation model

different damping cases to investigate the effects of the system damping. The first is a zero-damping case as  $\mathbf{C} = \mathbf{0}$ , and the other is the damping case of  $\mathbf{C} = 0.001\mathbf{K} + 0.001\mathbf{M}$ . Equation 12.10 can be solved using the modal superposition method by writing the response in term of the generalized response as

$$X(t) = \Psi p(t) \tag{12.11}$$

where  $\Psi$  is the mode shape matrix; and  $p(t)$  is the modal displacement.  $\Psi$  can be evaluated by the eigenvalue decomposition as follows

$$\Psi \Omega^2 \Psi^{-1} = \mathbf{M}^{-1} \mathbf{K} \tag{12.12}$$

where  $\Omega$  is the frequency matrix of the system.

Equation 12.10 can be converted into uncoupled differential equations as

$$\mathbf{M}_n p_{\ddot{x}}(t) + \mathbf{C}_n p_{\dot{x}}(t) + \mathbf{K}_n p_x(t) = \Psi^{-1} F(t) \tag{12.13}$$

in which are the diagonal matrices of  $\mathbf{M}_n = \Psi^{-1} \mathbf{M} \Psi$ ,  $\mathbf{C}_n = \Psi^{-1} \mathbf{C} \Psi$ , and  $\mathbf{K}_n = \Psi^{-1} \mathbf{K} \Psi$ . The uncoupled differential equations can be written as

$$p_{\ddot{x}}(t) + 2\omega\zeta p_{\dot{x}}(t) + \omega^2 p_x(t) = r_i(t) \tag{12.14}$$

where  $r(t)$  is the modal force of  $\mathbf{M}_n^{-1} \Psi^{-1} F(t)$ ;  $p_x(t)$  is the modal displacement.  $\omega$  and  $\zeta$  are the system modal frequency and the damping ratio vectors, respectively as

$$\omega = \Omega \dots \dots \dots \zeta = \frac{\mathbf{C}_n}{2\omega \mathbf{M}_n} \tag{12.15}$$

The modal frequencies and damping ratios of the lightly damped and undamped simulation models are summarized in Table 12.1, and the mode shapes are shown in Fig. 12.4.

**Table 12.2** Parameters evaluated in the simulation study

Parameters	Cases	Description
Excitation type	Gaussian	Ten Gaussian random excitations with the unit variance of $\sigma^2 = 1 \text{ N}^2$ applied on all floors, which are statistically independent between the sequences
	Uniform	Ten uniform random excitations with the amplitude between $-0.5$ and $0.5 \text{ N}$ applied on all floors, which are statistically independent between the sequences
	Impulse	Ten impulse excitations applied on all floors with the peak amplitude of $1.0 \text{ N}$
Response type	Acceleration (ACC)	Acceleration of the system response
	Velocity (VEL)	Velocity of the system response
	Displacement (DSP)	Displacement of the system response
System damping	Undamped	$\mathbf{C} = 0$
	Damped	$\mathbf{C} = 0.001\mathbf{K} + 0.001\mathbf{M}$
Sensor spatial resolution	Full (ten sensors)	All ten sensors measuring at all floors
	Reduced (five sensors)	Five sensors measuring at every other floors for the reduced spatial resolution

The modal displacement can be calculated as

$$p_X(t) = \int_0^t r(\tau) h_X(t - \tau) d\tau \quad (12.16)$$

in which

$$h_X(\tau) = \frac{1}{\omega_D} e^{-\zeta\omega\tau} \sin(\omega\tau) \quad (12.17)$$

where  $h_X(\tau)$  is the impulse response function for the system displacement.

The numerical simulation was conducted for three excitation cases: Gaussian random, uniform random and impulse excitations. For the Gaussian random excitation,  $F(t)$  was chosen to be the  $(10 \times N)$  matrix that consists of ten Gaussian-random sequences with the unit variance of  $\sigma^2 = 1 \text{ N}^2$ , which are mutually independent between the sequences. For the uniform random excitation,  $F(t)$  was chosen to be the  $(10 \times N)$  matrix that consists of ten uniform random sequences with the amplitude between  $-0.5$  and  $0.5 \text{ N}$ , which are mutually independent. For the impulse excitation,  $F(t)$  was chosen to be the  $(10 \times N)$  matrix of impulse excitation with the peak amplitude of  $1 \text{ N}$ .

The system responses were calculated for each excitation case. First, the modal displacement,  $p_X(t)$ , was calculated for the sampling frequency of  $100 \text{ Hz}$  and the total duration of  $900 \text{ s}$ . The modal velocity,  $p_{\dot{X}}(t)$ , and the modal acceleration,  $p_{\ddot{X}}(t)$ , were also computed in the same way using the first and second derivatives of the transfer function,  $h_i(\tau)$ . Then,  $X(t)$ ,  $\dot{X}(t)$  and  $\ddot{X}(t)$  of each floor mass was found by multiplying the modal coordinates,  $p_X(t)$ ,  $p_{\dot{X}}(t)$ , and  $p_{\ddot{X}}(t)$ , by the mode shape vector,  $\phi$ .

### 12.3.2 Analysis Results of the Simulation Data

Once the necessary system response data were obtained, a parametric study was conducted by comparing the NExT-ERA, PCA and ICA modes to the true modes. The comparison was conducted for different factors that could affect the mode-decomposition performance of each method including (i) excitation type, (ii) response type, (iii) system damping, and (iv) sensor spatial resolution. The parameters evaluated in the simulation study are summarized in Table 12.2.

In NExT-ERA, several user-defined parameters have to be specified, including the system order and reference channels. The mode condensation algorithm developed by Pappa and Zimmerman (1998) was used to evaluate the stabilization of the mode realization for the system orders from 10 to 30, which are equivalent to the maximum number of modes from 5 to 15. All channels were used as reference positions, but not simultaneously. Ten valid modes were selected based on the modes

with ten highest CMI values. All other modes having the CMI value less than 95 % were excluded. In PCA and ICA, no user-defined parameters are necessary since the analysis processes are solely data-driven, which does not require physical assumptions of the system.

### 12.3.3 Discussion of the Simulation Analysis Results

#### 12.3.3.1 Effects of the Response Types

In order to investigate the effects of the response types, the datasets of the acceleration (ACC), velocity (VEL), and displacement (DSP) were analyzed using NEX-T-ERA, PCA and ICA methods. The system was damped under the Gaussian random excitation. The full sensor spatial resolution (10 sensors) was used (see Table 12.2). After the analyses, the mode shapes ( $\hat{\Psi}$ ) and the modal coordinates ( $\hat{p}$ ) were obtained.

To measure the decomposition performance, the identified mode shapes and the modal coordinates were compared with the true mode shapes ( $\Psi^{\text{TRU}}$ ) and modal coordinates ( $p^{\text{TRU}}$ ) using two indicators: the mode assurance criterion (MAC) for the mode shapes, and the correlation coefficients for the modal coordinates (COR). MAC can be calculated as

$$\text{MAC} = \frac{|\hat{\Psi}^* \Psi^{\text{TRU}}|^2}{(\hat{\Psi}^* \hat{\Psi}) (\Psi^{\text{TRU}*} \Psi^{\text{TRU}})} \times 100 \% \quad (12.18)$$

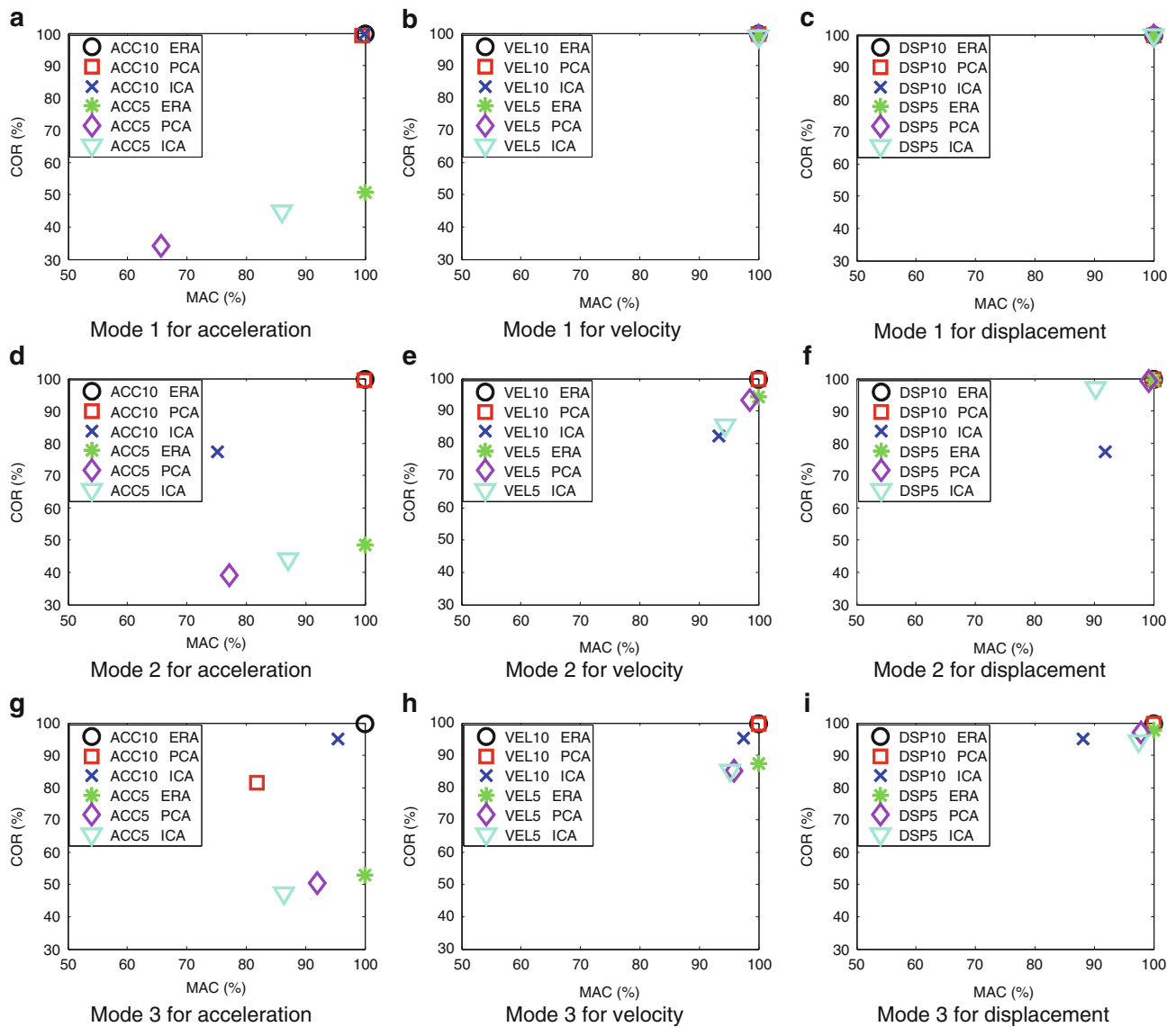
where \* represents transpose and conjugate;  $\hat{\Psi}$  is the identified mode shape vectors; and  $\Psi^{\text{TRU}}$  is the true mode shape vectors. Therefore, MAC can be a real number between 0 and 100 %, indicating 100 % when the estimated mode shape vectors are identical to the true mode shape vectors. COR can be computed as

$$\text{COR} = \frac{\left(\sum_{k=1}^n \hat{p}_k p_k^{\text{TRU}}\right)^2}{\left(\sum_{k=1}^n \hat{p}_k \hat{p}_k\right) \left(\sum_{k=1}^n p_k^{\text{TRU}} p_k^{\text{TRU}}\right)} \times 100 \% \quad (12.19)$$

where  $\hat{p}_k$  is the identified modal coordinate vectors;  $p_k^{\text{TRU}}$  is the true modal coordinate vectors;  $n = 10$  for the full sensor spatial resolution, and  $n = 5$  for the reduced sensor spatial resolution. COR can also be a real number between 0 % and 100 %, indicating 100 % when the estimated modal coordinate vectors are identical to the true modal coordinate vectors.

In Fig. 12.5, MAC and COR using NEX-T-ERA ( $\circ$ ), PCA ( $\square$ ), and ICA ( $\times$ ) are shown for the first three modes. In the plot, the x-axis shows MAC, and the y-axis shows COR. In addition, ACC, VEL and DSP indicate the response types, and the number ten indicates the *full* sensor-spatial resolution. The results of the reduced spatial resolution data (\*,  $\square$ ,  $\nabla$ ) shown with the number five in Fig. 12.5 will be discussed later in Sect. 3.3.4. For NEX-T-ERA ( $\circ$ ), both MAC and COR were equal to 100 % for all three modes and for all response types, which means that there is no error with NEX-T-ERA in  $\hat{\Psi}^{\text{ERA}}$  and  $\hat{p}^{\text{ERA}}$ . For PCA ( $\square$ ), the results were the same as NEX-T-ERA ( $\circ$ ), except MAC = 82 % in  $\hat{\Psi}_x^{\text{PCA}}$  and COR = 82 % in  $\hat{p}_x^{\text{PCA}}$  for mode 3 (Fig. 12.5g). For ICA ( $\times$ ), MAC and COR were equal to 100 % only in mode 1 for all response types (Figs. 12.5a–c). Therefore, the performance of the mode decomposition was observed the best with NEX-T-ERA, then with PCA, and the worst with ICA for these datasets.

The causes of the above errors in PCA and ICA were further investigated. Figure 12.6 shows the phase diagrams of the acceleration, velocity and displacement at Floors 1 and 2. To demonstrate the effect of the response type, a simple 2-DOF oscillator with the fixed-free boundaries was used to simulate the modal responses under the Gaussian random excitation. The same mass, stiffness, damping, which was used for the 10-DOF model in Sect. 12.3.1, were also used in this simulation. The correlation coefficients ( $\rho$ ) of the Floors 1 and 2 responses were measured at  $\rho = 0.1$  % for the acceleration,  $\rho = 50.2$  % for the velocity, and  $\rho = 90.2$  % for the displacement. The correlation coefficients show that the acceleration sequences are almost zero-correlated, and the displacement sequences are highly correlated. Two modes corresponded to the two responses were also identified using NEX-T-ERA, PCA and ICA. The directions of the two modes are shown as the two straight lines: the major mode direction is shown as 1 and the minor mode direction is shown as 2. The angles of the mode components were calculated, and the major component angle ( $\theta_1$ ) and the minor component angle ( $\theta_2$ ) are shown in the figure. The angle was measured in radian with respect to the horizontal line in the counter-clockwise direction.



**Fig. 12.5** Comparison of MAC and COR between the identified and true mode shapes and modal coordinates of the first three modes

The results show that the NExT-ERA mode components are identical to the true mode components. For PCA, the mode components for the velocity and displacement are identical to the true components in Figs. 12.6e, f, while the identified modes for the acceleration has an error in Fig. 12.6d. For ICA, errors are observed for all response types in Fig. 12.6g–i. The above results agree with the results in Fig. 12.5. It should be noted that the true, NExT-ERA, and PCA modes have  $|\theta_1 - \theta_2| = \pi/2$ , while the ICA modes do *not necessarily* have  $|\theta_1 - \theta_2| = \pi/2$ . It is because the singular value decomposition of the covariance matrix in PCA *mathematically* guarantees the orthogonality between the mode shapes, which is similar to the orthogonality between the *physical* mode shapes in NExT-ERA. The discrepancy between the true and ICA modes is because maximizing the non-Gaussianity of the resulting modal coordinates in ICA does not guarantee such orthogonality.

For the acceleration, the scattered data have a circular boundary due to the low statistical correlation although the data are measured at two adjacent floors. Therefore, PCA and ICA have errors in the mode decomposition since it is difficult to find the major directions of mode components in the circularly scattered data. For the velocity and displacement, the PCA modes become accurate because the data have high statistical correlation with the prominent directions of mode components. ICA still has the errors due to the non-orthogonal modes.

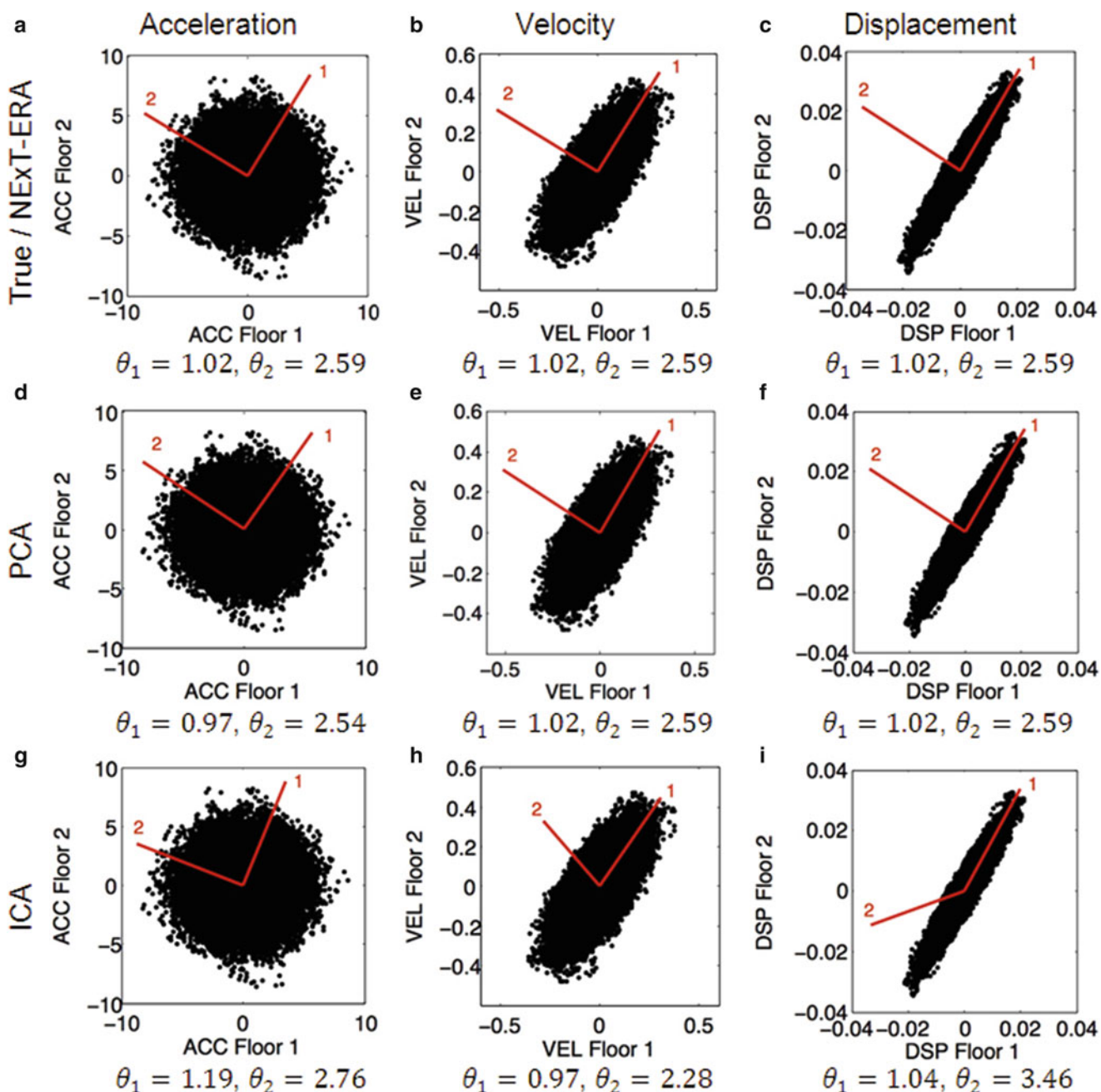
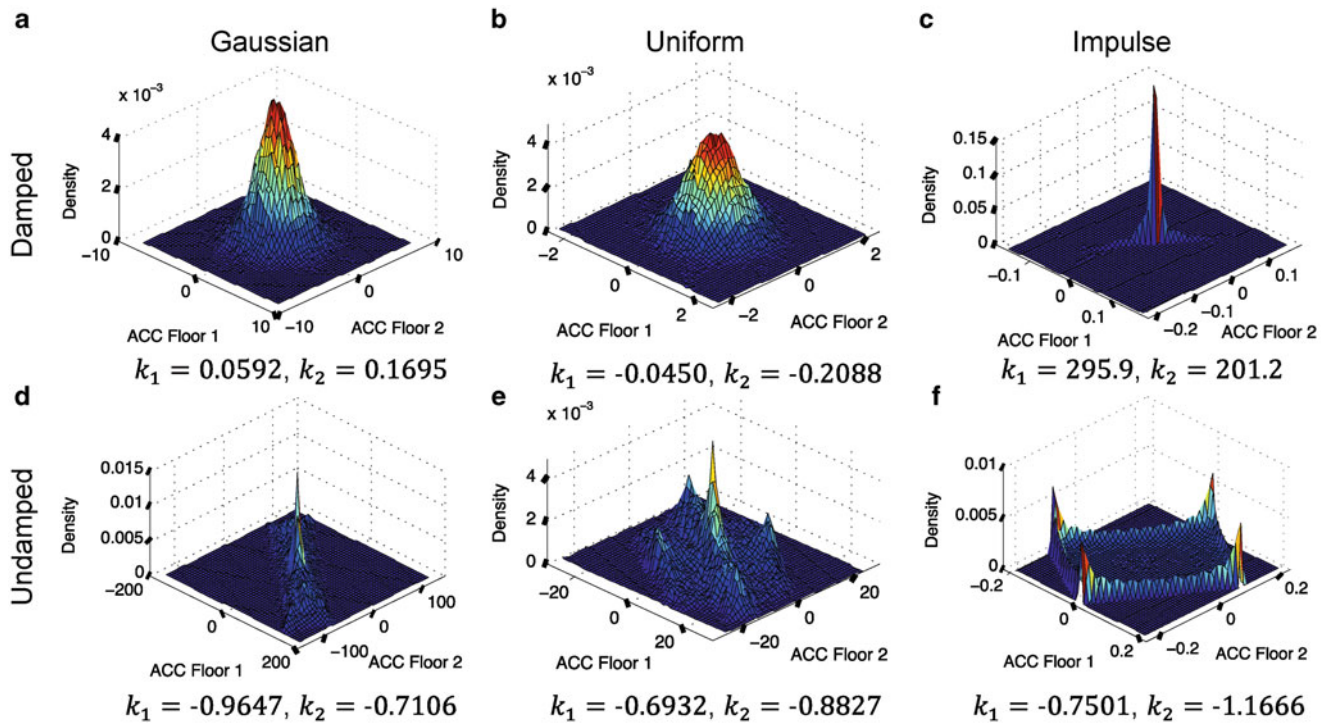


Fig. 12.6 The mode components of the true, NExT-ERA, PCA and ICA. The angles are shown in radian

### 12.3.3.2 Effects of the Excitation Types and System Damping

In Sect. 12.3.3.1, it was shown that ICA gave the highest error in the mode decomposition. The effects of the excitation types on the ICA modes are discussed in this section. Hyvärinen and Oja [22] stated that the fundamental restriction in ICA is that the independent components must be non-Gaussian since the distribution of any orthogonal transformation of the Gaussian variables  $(x_1, x_2)$  has exactly the same distribution as  $(x_1, x_2)$ , in which  $x_1$  and  $x_2$  are statistically independent. Consequently, the matrix  $\Psi^{ICA}$  is not accurately identifiable for Gaussian independent components. When one of the independent components is non-Gaussian, however, the ICA model can still be estimated. Kerschen et al. [23] evaluated ICA for undamped vibrating structures with impulse and uniform random excitations. According to them, the application of ICA is limited to a weakly damped system which typically has the damping ratios of less than 1%. Another limitation stated by them is that the number of sensors should always be chosen to greater than or equal to the number of active modes.



**Fig. 12.7** The joint probability density functions of the two acceleration sequences of the damped and undamped 2-DOF oscillator

**Table 12.3** Averaged MAC and COR of the two modes using the acceleration data

	Uniform		Gaussian		Impulse	
	Damped	Undamped	Damped	Undamped	Damped	Undamped
Avg. MAC (%)	90	35	57	67	92	100
Avg. COR (%)	90	42	59	83	88	100

Poncelet et al. [13] showed a similar result where the accuracy of ICA decreased as the system damping or mode number increased. McNeil and Zimmerman [14] also discussed the effect of the system damping. They deduced that undamped free-vibration modal responses closely corresponded to the independent components, while damped modal responses do not.

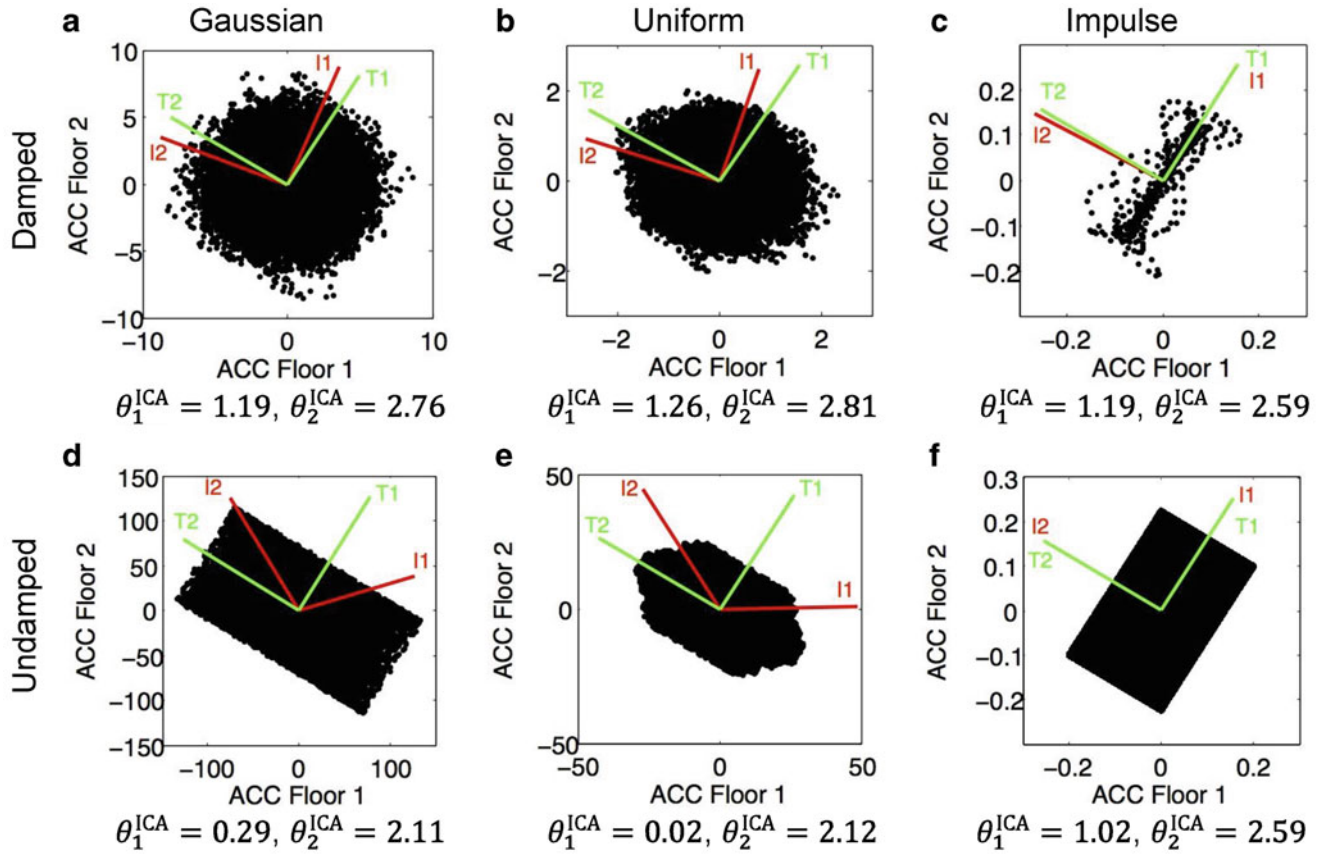
To demonstrate the effect of the excitation on ICA, the same 2-DOF oscillator in Sect. 12.3.3.1 was used with the Gaussian random, uniform random and impulse excitations. The excitation properties used in this simulation are described in Table 12.2. The joint probability density functions of the system responses are shown in Fig. 12.7. The kurtosis is used to measure the sharpness (or Gaussianity) of the probability distribution.

$$k(x) = \frac{E[x^4]}{(E[x^2])^2} - 3 \quad (12.20)$$

where  $E[x]$  is the expected value of the random variable,  $x$ ;  $k(x) = 3$  when  $x$  is the Laplace double exponential random variable;  $k(x) = 0$  when  $x$  is the Gaussian random variable; and  $k(x) = -1.2$  when  $x$  is the uniform random variable. Thus,  $k(x)$  is a positive value for the super-Gaussian random variable with a sharp peak, while  $k(x)$  is a negative value for the sub-Gaussian random variable with a flat peak. The kurtoses of the two accelerations are shown in the figure:  $k_1$  is for the acceleration with the fixed boundary, and  $k_2$  is for the acceleration with the free boundary.

Figure 12.7 shows that the joint distributions of the damped responses are closer to the Gaussian distribution than the undamped responses. Therefore, it can be seen that the system damping significantly increases the Gaussianity of the acceleration data. To understand the effects of the system damping and the Gaussianity of the system response on the ICA mode decomposition, the accuracy of the ICA modes is shown in Table 12.3 by averaging the MACs and CORs of the two modes using the acceleration data. The table shows that no error is observed only for the undamped system under the impulse excitation, which indicates that both system damping and non-impulse excitation reduces the accuracy of the ICA modes.





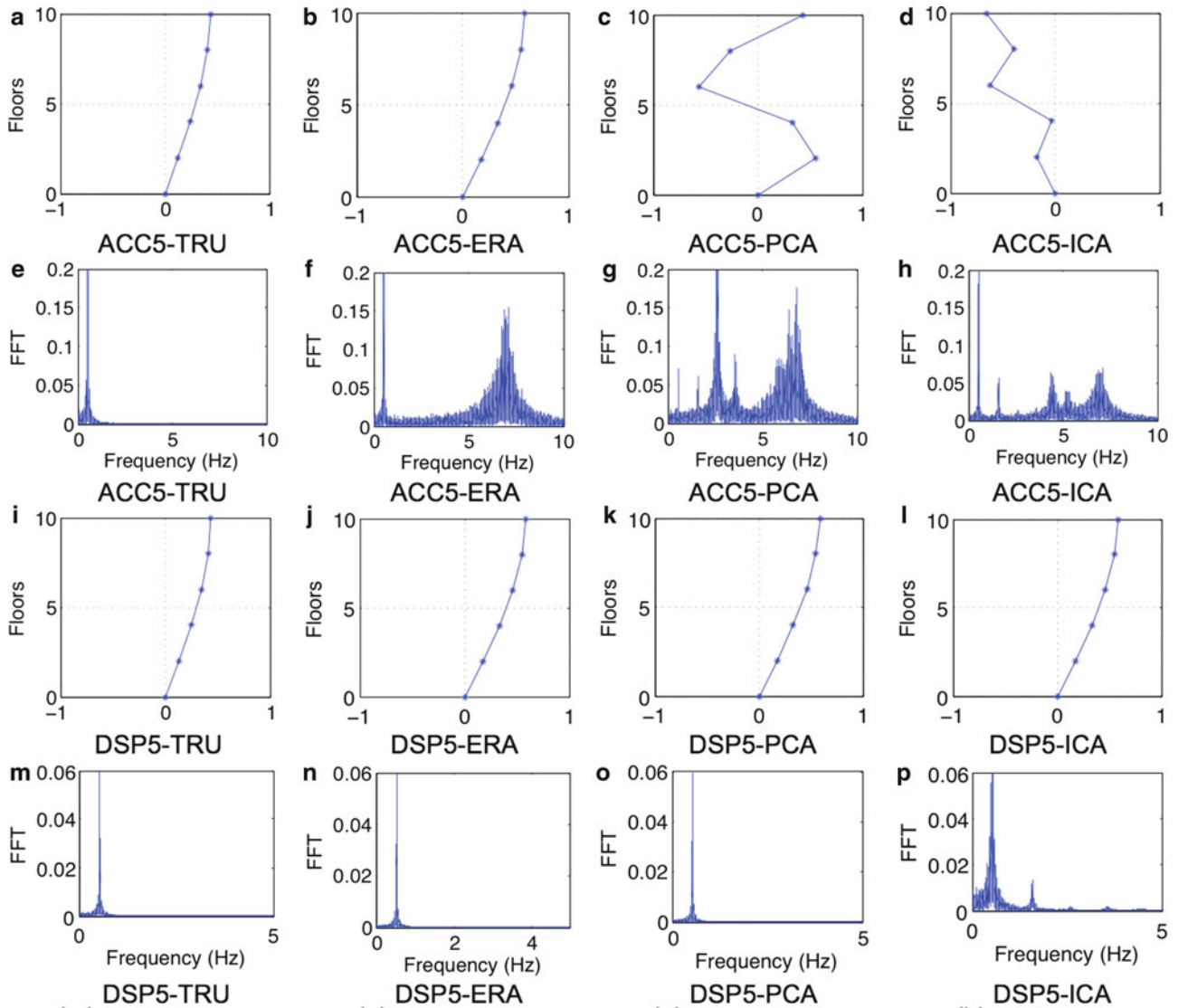
**Fig. 12.8** A comparison of true and ICA mode components for different excitation types using the acceleration data. The angles of the true modal components are  $\theta_1^{TRU} = 1.02$ , and  $\theta_2^{TRU} = 2.59$

Figure 12.8 compares the true modes (T1 and T2) and the ICA modes (I1 and I2) in the plots of the acceleration scattered data, indicating the major components (T1 and I1) and the minor components (T2 and I2). The results shown that the independent components had no errors only when the undamped system was subjected to the impulse excitation. The angle between I1 and I2 are also measured in radians and shown in the figure. Similar to the results in Fig. 12.6, the angles of the ICA modes are not necessarily perpendicular (i.e.,  $|\theta_1 - \theta_2| = \pi/2$ ), while the angles of the true modes are always perpendicular. For the damped systems, the ICA angles are close to  $\pi/2$  although the directions of the mode components are different from the true modes. This is a result of the response data being scattered in a circular boundary due to the strong Gaussianity with the Gaussian and uniform excitations (Fig. 12.8a, b). For the undamped system, ICA still gave significant errors although the data were correlated and the joint distributions were non-Gaussian (Fig. 12.8d, e). Only the case of the undamped system under the impulse excitation gave no error in the mode decomposition. The above results show that the accuracy of ICA is highly affected with the statistical distribution of the response data due to the system damping, and excitation types.

### 12.3.3.3 Effects of the Sensor Spatial Resolution

To understand the effects of the sensor spatial resolution, the same datasets of the 10-DOF damped system in Sect. 12.3.3.1 were used, but with the reduced sensor spatial resolution by using the five responses at every other floor (see Table 12.2). NExT-ERA, PCA, and ICA were applied using the reduced-resolution data, and the mode shapes ( $\hat{\Psi}$ ) and the modal coordinates ( $\hat{p}$ ) were identified. Then, the MAC and COR were calculated for  $\hat{\Psi}$  and  $\hat{p}$ , respectively.

The results of ERA (\*), PCA ( $\square$ ), and ICA ( $\nabla$ ) for the first three modes are shown in Fig. 12.5. Here, the number five indicates the *reduced* sensor-spatial resolution, and ACC, VEL and DSP indicate the response type. For the acceleration (Fig. 12.5a, d, and g) significant errors were observed in all identification methods, while the errors were observed least with



**Fig. 12.9** A comparison of the true and identified mode shapes and modal coordinates of mode 1. The natural frequency of mode 1 is 0.53 Hz. The modal coordinates are shown in frequency domain

the displacement (Fig. 12.5c, f, and i) for all identification methods. Among all cases, only the mode shapes identified with ERA gave no errors for all response types. This means that  $\hat{\Psi}_{\dot{X}}^{\text{ERA}}$ ,  $\hat{\Psi}_{\dot{X}}^{\text{ERA}}$ , and  $\hat{\Psi}_{\dot{X}}^{\text{ERA}}$  are robust to the 50 % reduction of the spatial resolution. In addition, both  $\hat{\Psi}$  and  $\hat{p}$  were less affected with the reduced spatial resolution in a lower mode.

The  $\hat{\Psi}$  and  $\hat{p}$  identified with NExT-ERA, PCA and ICA of mode 1 using the acceleration and displacement are compared with  $\Psi^{\text{TRU}}$  and  $p^{\text{TRU}}$  in Fig. 12.9. Using the acceleration data, the  $\hat{\Psi}_{\dot{X}}^{\text{PCA}}$  and  $\hat{\Psi}_{\dot{X}}^{\text{ICA}}$  were erroneously identified due to low statistical correlation between the acceleration sequences shown in Fig. 12.9c, d, which is the similar results discussed earlier in Fig. 12.6d, g. The  $\hat{p}_{\dot{X}}^{\text{ERA}}$ ,  $\hat{p}_{\dot{X}}^{\text{PCA}}$ , and  $\hat{p}_{\dot{X}}^{\text{ICA}}$  also gave erroneous frequency peaks as shown in Fig. 12.9f–h. With the displacement data, the  $\hat{\Psi}$  and  $\hat{p}$  become more accurate for all methods. Using the displacement data, the  $\hat{\Psi}$  and  $\hat{p}$  were accurately identified with NExT-ERA and PCA, while ICA gave errors in the identification due to the combined effects of the system damping and the Gaussianity of the displacement data that were discussed in Sect. 12.3.3.2.

In summary, the above simulation results show that the PCA modes can be used as alternative structural modes of a low degree-of-freedom system. The accuracy of the PCA modes is best with the displacement, and worst with the acceleration. The PCA modes can be used when the number of sensors is reasonably smaller than the system order. On the other hand, the ICA modes are significantly different from the structural modes because the ICA mode shapes are not necessarily orthogonal. The accuracy of the ICA modes is largely affected by the excitation types and system damping, which are not practical to

be used as alternative structural modes. The identification of the modal coordinates is more sensitive to the sensor spatial resolution for all methods than the identification of the mode shapes.

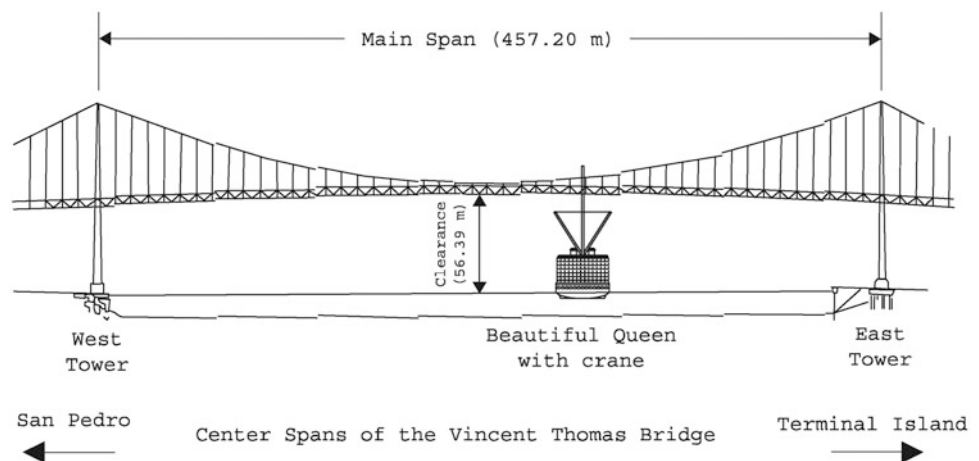
## 12.4 Field Study Using a Full-Scale Suspension Bridge

### 12.4.1 Measurements of Bridge Responses in Ship-Bridge Collision Accident

The Vincent Thomas Bridge (VTB) located in San Pedro, California in the U.S.A. was used in this experimental study (Fig. 12.10). The bridge is an 1,850-m long cable-suspension bridge with a main span length of 457 m, two-suspended side spans of 154 m each, and two 10-span cast-in-place concrete approaches of 545-m length on the both ends. In 2006, there was a collision between the bridge and a cargo ship that was passing underneath it. The freight-loading crane on the cargo ship struck the bridge main span from the side. About 30 min after the collision, the vehicular traffic on the bridge was stopped by the bridge authority to investigate potential damage. As the result, moderate damage was found on the bridge maintenance scaffold installed at the bridge main span. The investigation continued for about 2 h having no traffic on the bridge, and then the vehicular traffic was reopened. A detailed description of the ship-bridge collision accident can be found in Yun et al. [3].

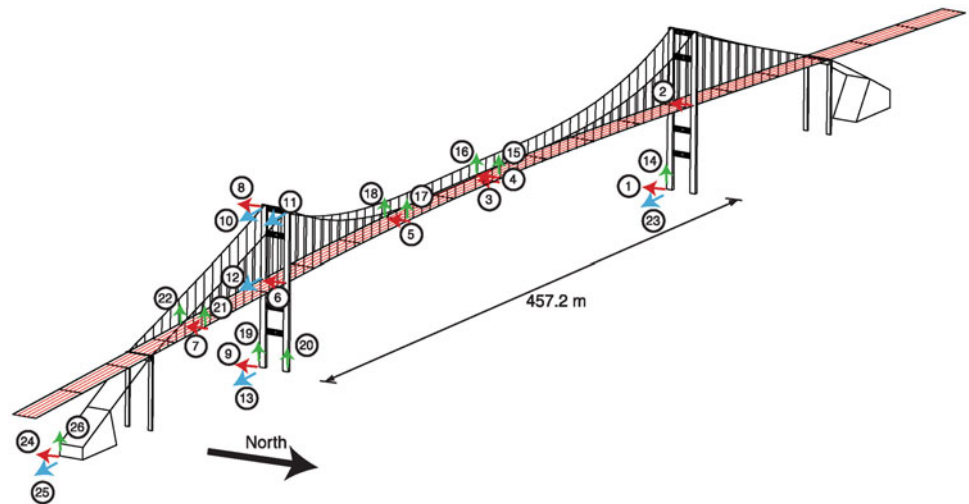
With a web-based continuous bridge monitoring system installed on the bridge in 2005, the dynamic responses of the bridge were measured in the ship-bridge collision accident. The bridge responses were measured at the sampling rate of 100 Hz using the 26 force-balance accelerometers installed on the bridge deck, piers and anchorage as shown in Fig. 12.11. The accelerometers were connected to a data acquisition system with the 24-bit analog-digital converter via sensor wires. A detailed description of the data acquisition system and the web-based bridge monitoring system can be also found in Yun et al. [3].

The acceleration data of the normal traffic, ship collision, and no-traffic conditions were pre-processed to obtain the filtered acceleration, velocity and displacement data that are necessary for the proposed comparative study. For each excitation type, the acceleration data was first divided into 15-min time histories. Then, the DC and linear trend were removed from the time histories. A 5% cosine-tapered window was applied before the high pass filter of 0.1 Hz with filter order of two and the low pass filter of 30 Hz with order of 4 were applied. Numerical integration was used to obtain the velocity. The same pre-process method was applied before and after the numerical integration for the displacement. Channel 4 was excluded in the analysis due to sensor malfunction. The above preprocessing procedures are shown in Fig. 12.12. Sample bridge responses during the ship-bridge collision after the pre-processing are shown in Fig. 12.13.

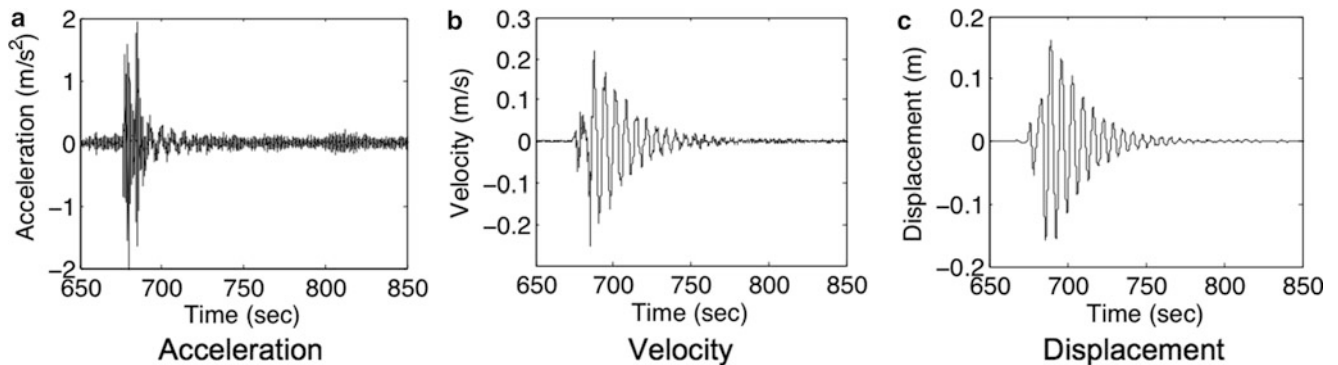
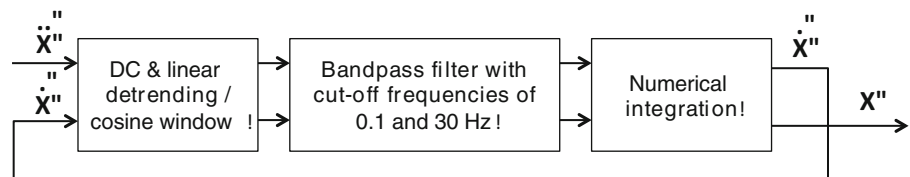


**Fig. 12.10** The ship-bridge collision by the onboard crane of the cargo ship [3]

**Fig. 12.11** The sensor locations and directions on the bridge [3]



**Fig. 12.12** The preprocessing procedures to obtain the acceleration, velocity and displacement data of the bridge responses



**Fig. 12.13** Bridge response at channel 3 during the ship-bridge collision after the preprocessing

### 12.4.2 Analysis Results of the Experimental Data

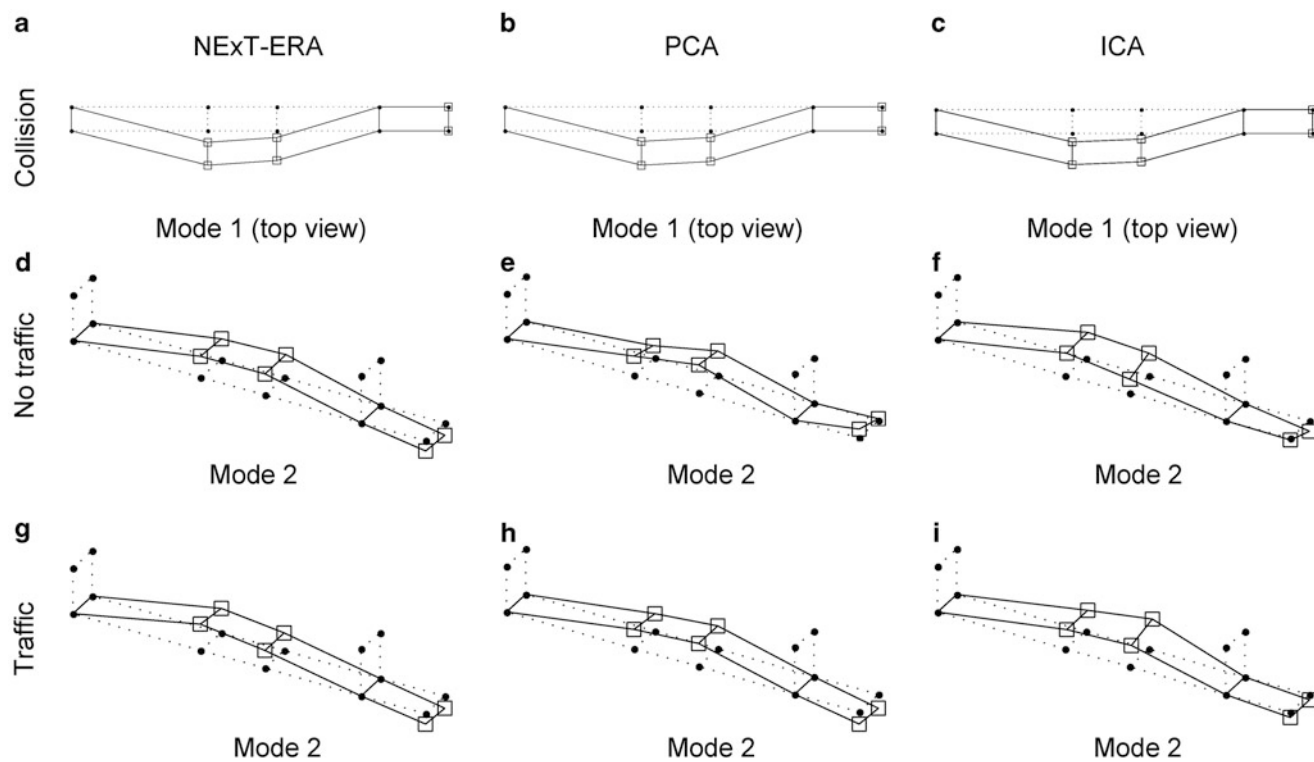
The bridge response data for the traffic, no-traffic and collision excitation cases were analyzed using NExT-ERA, PCA and ICA. Only 12 sensor channels on the bridge deck were used. For NExT-ERA, all channels were used as reference channels but not simultaneously. The system order was set to be 100. The modes were then condensed by choosing the ones with the CMI value higher than 70 %. A total of 15 modes were identified in each case. Among the 15 modes, the first 5 modes were considered in the study. The modal frequencies and damping ratios identified with NExT-ERA are summarized in Tables 12.4 and 12.5. The mode shapes and modal coordinates were calculated using NExT-ERA, PCA and ICA methods for the different response types, and for the different excitation types. The sample mode shapes are shown in Fig. 12.14, and the FFT of the modal coordinates are shown in Fig. 12.15. Mode 1 was not realized in NExT-ERA since the acceleration data contained weak vibration components in the lateral direction of the bridge under the ambient excitation without traffic loads. The modal parameters identified in this study agreed with those in previous studies [3, 24, 25].

**Table 12.4** Identified modal frequencies (Hz) using NExT-ERA

Mode	Traffic			No traffic			Collision		
	ACC	VEL	DSP	ACC	VEL	DSP	ACC	VEL	DSP
1	0.175	0.170	0.166	–	0.174	0.181	0.149	0.151	0.143
2	0.233	0.233	0.232	0.245	0.226	0.246	0.231	0.233	0.228
3	0.55	0.539	0.537	0.529	0.552	0.540	0.534	0.534	0.535
4	1.393	1.401	1.393	1.400	1.397	1.397	1.382	1.391	1.404
5	1.867	1.876	1.860	1.901	1.887	1.896	1.859	1.864	1.870

**Table 12.5** Identified damping ratio (%) using NExT-ERA

Mode	Traffic			No traffic			Collision		
	ACC	VEL	DSP	ACC	VEL	DSP	ACC	VEL	DSP
1	47.761	3.846	2.250	–	0.240	2.445	8.587	3.526	1.828
2	2.321	2.461	2.599	0.149	5.509	2.398	2.640	6.897	3.692
3	5.656	1.417	0.651	2.141	0.916	0.564	1.414	1.095	1.403
4	1.480	0.591	1.328	0.437	1.156	1.324	1.589	1.050	1.448
5	1.817	1.667	1.503	1.401	1.296	1.175	2.419	1.763	1.842

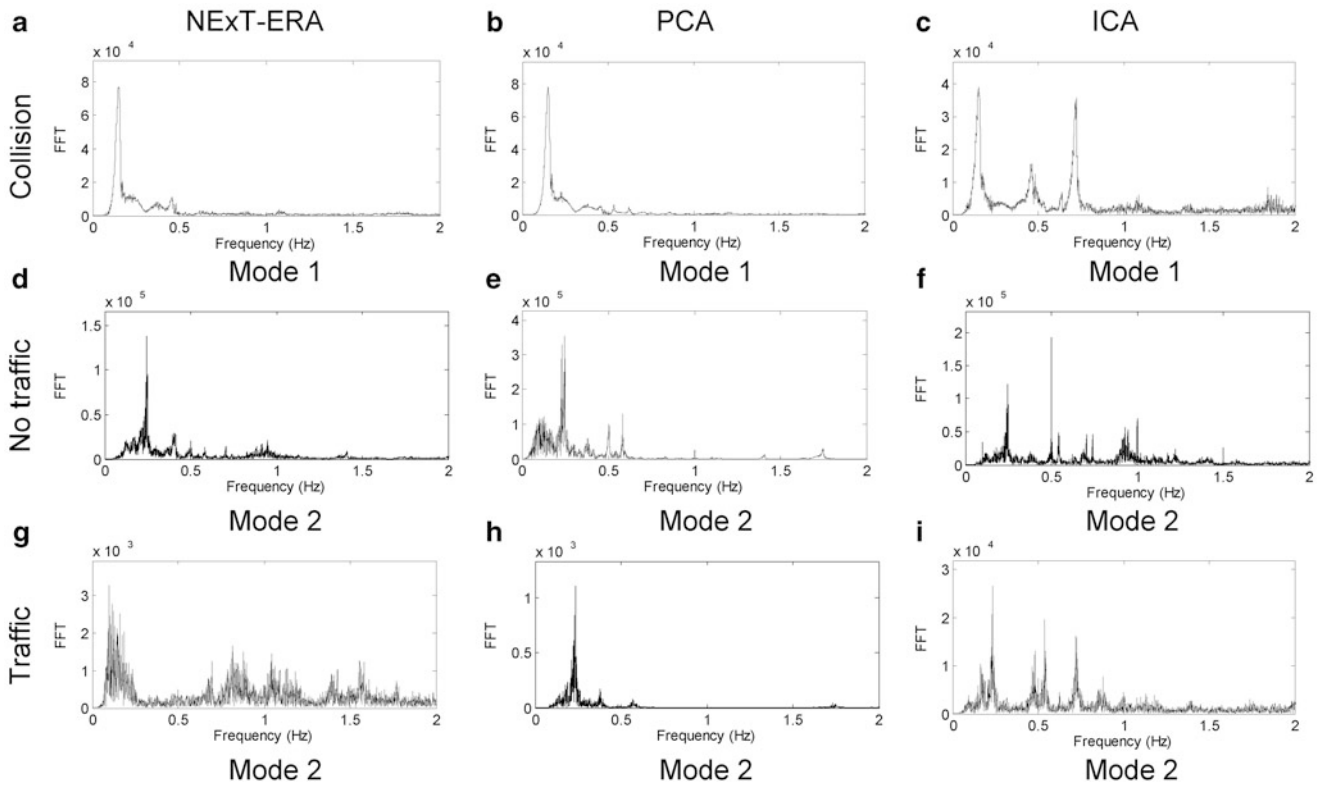


**Fig. 12.14** Mode shapes identified using NExT-ERA, PCA and ICA methods for the velocity data

### 12.4.3 Discussion on the Experiment Results

MAC was calculated to compare  $\hat{\Psi}^{PCA}$  and  $\hat{\Psi}^{ICA}$  with  $\hat{\Psi}^{ERA}$ , and COR was calculated to compare  $\hat{\rho}^{PCA}$  and  $\hat{\rho}^{ICA}$  with  $\hat{\rho}^{ERA}$ . The results for the first five modes are shown for different excitation types in Fig. 12.16. For each ‘response type’–‘identification method’ case shown in the legend, the average distance from the upper-right corner is calculated and ranked in Table 12.6. Overall, the DSP-PCA modes ( $\square$ ) were closest to the DSP-ERA modes for the excitation and response types. There were more discrepancies in  $\hat{\rho}$  than  $\hat{\Psi}$  for both PCA and ICA, which would be due to the relatively sparse sensor network on the bridge. The above result is similar to the simulation results in Sect. 12.3.

In PCA,  $\hat{\Psi}^{PCA}$  agreed most with  $\hat{\Psi}^{ERA}$  for the collision excitation, and least for the no-traffic excitation. This is because the PCA modes could be decomposed more accurately with the collision excitation than ambient excitations as illustrated earlier in Figs. 12.6 and 12.7. Figure 12.17 shows the statistical distributions of the bridge responses under different excitations.



**Fig. 12.15** Modal coordinates identified using NEXt-ERA, PCA and ICA methods for the velocity data. The natural frequencies identified by NEXt-ERA are 0.170 Hz for mode 1, and 0.233 Hz for mode 2

**Table 12.6** The averaged errors of the PCA and ICA methods and their ranking in Fig. 12.14 for the first five modes

All			Traffic			No traffic			Collision		
Rank	Method	Error	Rank	Method	Error	Rank	Method	Error	Rank	Method	Error
Errors in the identified mode shapes											
1	DSP-PCA	21.3	1	VEL-PCA	16.1	1	DSP-PCA	28.6	1	DSP-PCA	12.9
2	VEL-PCA	21.4	2	DSP-PCA	22.7	2	VEL-PCA	33.5	2	VEL-PCA	14.4
3	ACC-PCA	40.9	3	ACC-PCA	54.2	3	VEL-ICA	37.1	3	ACC-PCA	24.9
4	VEL-ICA	45.5	4	ACC-ICA	54.2	4	ACC-PCA	44.4	4	VEL-ICA	38.6
5	ACC-ICA	50.3	5	DSP-ICA	59.7	5	DSP-ICA	53.5	5	ACC-ICA	34.4
6	DSP-ICA	53.5	6	VEL-ICA	60.8	6	ACC-ICA	65.3	6	DSP-ICA	47.3
Errors in the identified modal coordinates											
1	DSP-PCA	58.3	1	DSP-PCA	55.3	1	DSP-PCA	63.2	1	DSP-PCA	56.5
2	VEL-PCA	75.8	2	VEL-PCA	83.8	2	VEL-PCA	69.5	2	VEL-PCA	74.1
3	VEL-ICA	81.8	3	DSP-ICA	86.7	3	VEL-ICA	73.7	3	VEL-ICA	82.7
4	DSP-ICA	86.7	4	VEL-ICA	88.9	4	DSP-ICA	87.8	4	DSP-ICA	85.7
5	ACC-PCA	90.9	5	ACC-PCA	91.9	5	ACC-PCA	94.1	5	ACC-PCA	87.5
6	ACC-ICA	94.9	6	ACC-ICA	92.5	6	ACC-ICA	97.6	6	ACC-ICA	95.3

It shows that the distributions of the responses are closer to a Gaussian distribution under the ambient excitations with traffic and no-traffic loads than the impulse excitation, which also explains why the PCA modes are closer to the NEXt-ERA modes under the collision excitation. The response type also affected the accuracy in  $\hat{\Psi}^{PCA}$ : the highest accuracy with the displacement and the lowest accuracy with the acceleration.

In ICA, there were large discrepancies between the ICA and NEXt-ERA modes for all excitation and response types. It indicates that the ICA modes are generally incompatible to the NEXt-ERA modes of the suspension bridge. The discrepancies would be due to the non-orthogonal ICA modes as shown in the simulation results in Sect. 12.3.3.2.

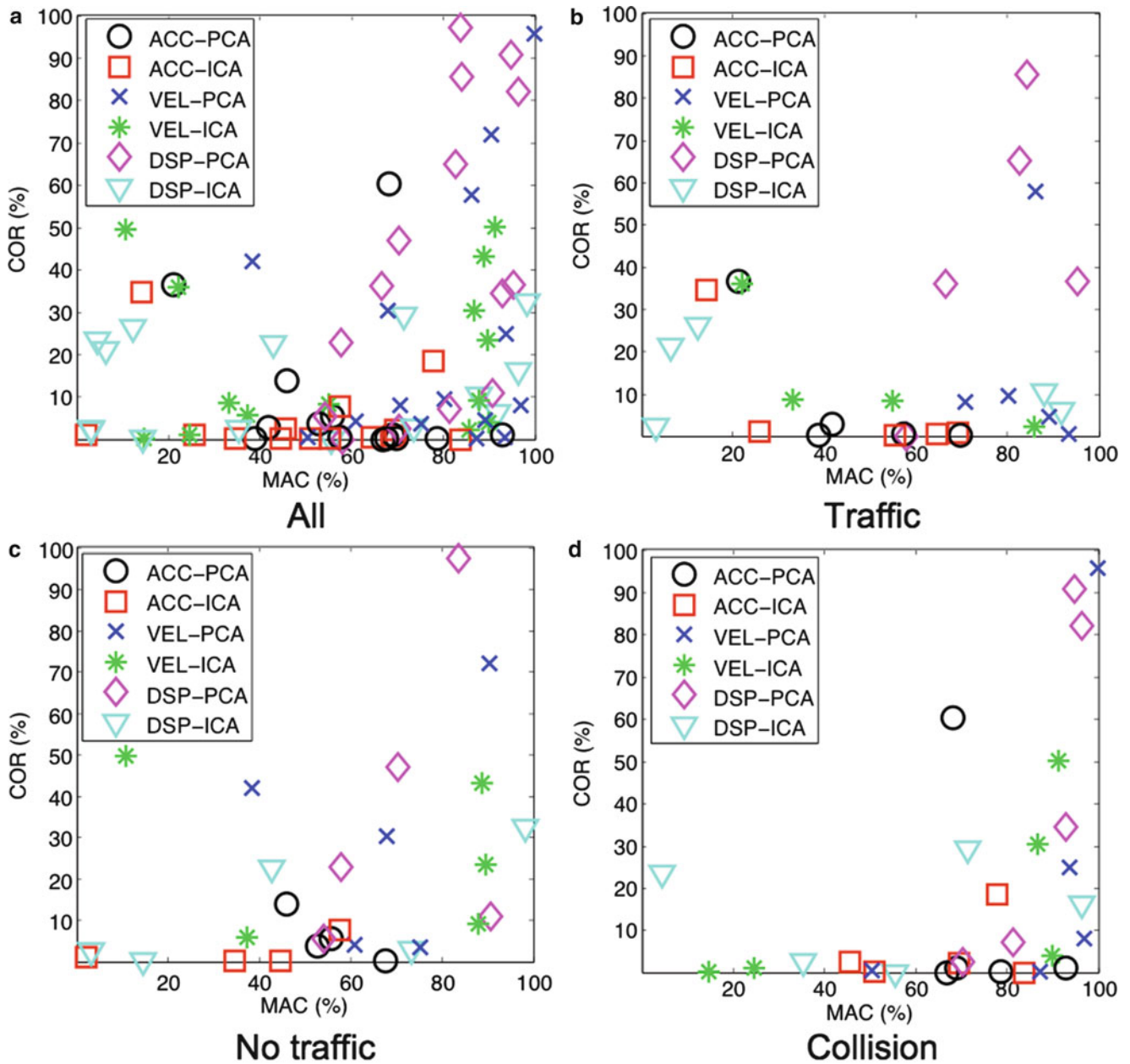


Fig. 12.16 Comparison of MAC and COR between PCA and NExT-ERA, and between ICA and NExT-ERA for different response types

## 12.5 Conclusions

In this study, the PCA and ICA modes were related to the NExT-ERA modes to investigate whether the non-parametric modes could be used as alternative structural modes. A parametric study was conducted to understand the effects of the response types, excitation types, system damping, and sensor spatial resolution through the simulation and experimental tests. Major findings in the parametric study include:

- The PCA modes could be used as alternative structural modes when the system has a low degree-of-freedom system and the displacement (or velocity) data are available. The ICA modes have significant errors when the system has damping or is subjected to ambient excitations, which cannot be used as alternative structural modes for general purposes.
- In the simulation tests, a higher accuracy was found in the order of NExT-ERA > PCA > ICA, compared to the true mode shapes and modal coordinates. In the experimental tests, the PCA modes were closer to the NExT-ERA modes than the

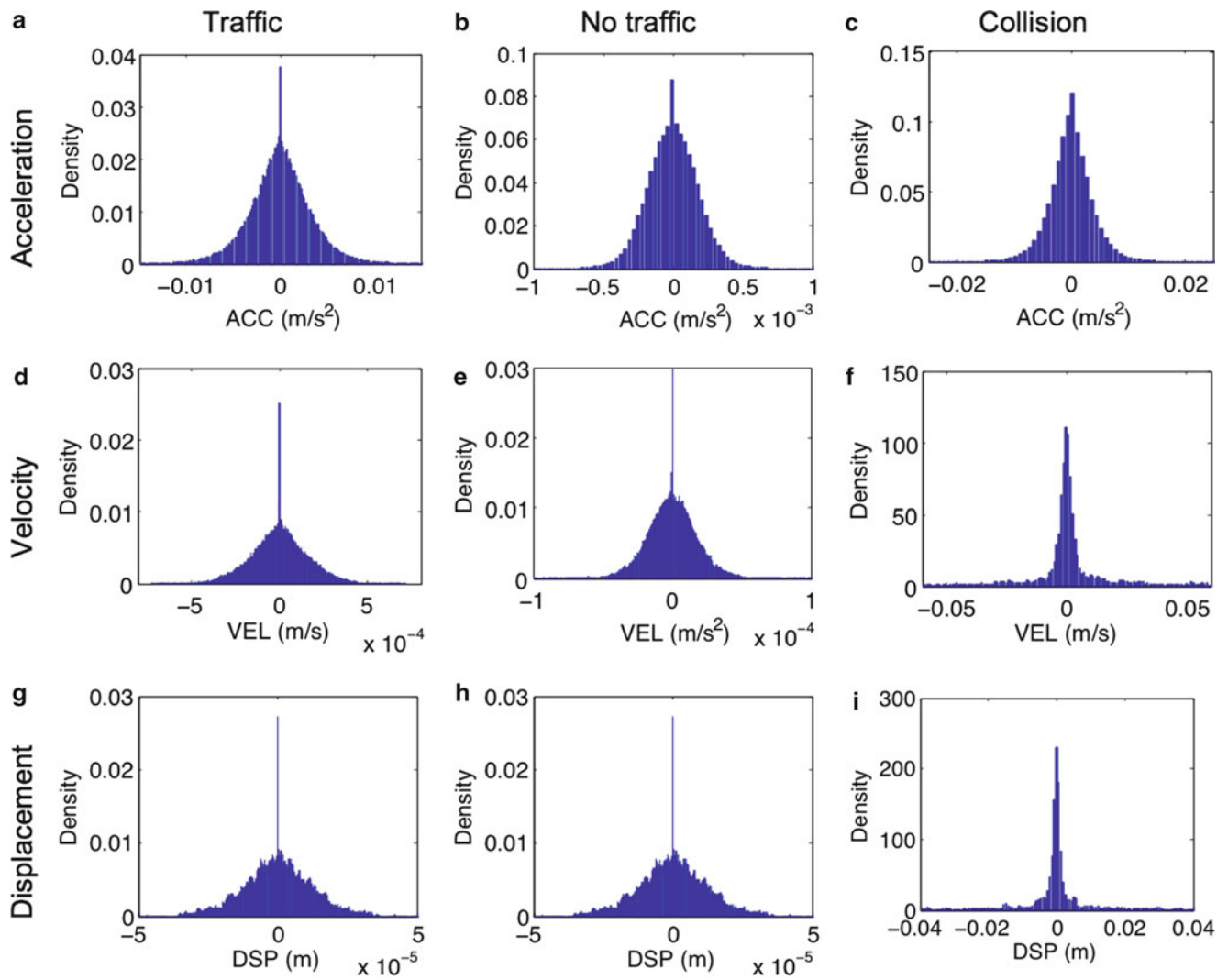


Fig. 12.17 Statistical distributions of the bridge responses at channel 3 under different excitations

ICA modes. The PCA mode shapes are orthogonal due to the singular value decomposition of the covariance matrix of the response data, while the ICA mode shapes are not necessarily orthogonal since maximizing the non-Gaussianity does not mathematically guarantee the orthogonal modes.

- In both PCA and ICA, the accuracy of the mode decomposition is affected by the response types in the order of displacement > velocity > acceleration. It is because the acceleration data are scattered without prominent directions due to low correlation between the sensor measurements. The accuracy of the PCA (and ICA) modes increases with the displacement and velocity since the statistical correlation is larger in these responses which contain dominant low-frequency contents. Therefore, the PCA identification would be limited to low structural modes.
- The ICA modes are significantly affected by the system damping. It is because the system damping increases the Gaussianity of the response data. ICA requires non-Gaussian multivariate responses [22], which are often violated under ambient excitation. The simulation results showed that the ICA identification had no error when the system has no damping and is subjected to impulse excitation.
- The PCA modes are more accurate with impulse excitation than ambient excitation. In the experimental study, the PCA mode shapes agreed most with the LNMs under the collision excitation and worst under the ambient excitation without traffic loads.

**Acknowledgements** This study was supported in parts by grants from the U.S. National Science Foundation (NSF), the Air Force Office of Scientific Research (AFOSR), and the National Aeronautics and Space Administration (NASA). The assistance of A. Shakal of the California Geology Service and L.-H. Sheng of the California Department of Transportation (Caltrans) is appreciated.



## References

1. Pappa RS, Elliott KB, Schenk A (1992) A consistent-mode indicator for the eigensystem realization algorithm. *J Guid Control Dyn* 16(5):852–858. Retrieved from <http://hdl.handle.net/2060/19920015464>
2. Pappa RS, James GH, Zimmerman DC (1998) Autonomous modal identification of the space shuttle tail rudder. *J Spacecr Rockets* 35(2):163–169. doi:10.2514/2.3324
3. Yun H, Nayeri R, Tasbihgoo F, Wahbeh M, Caffrey J, Wolfe R, Sheng L-H (2008) Monitoring the collision of a cargo ship with the Vincent Thomas Bridge. *Struct Control Health Monit* 15(2):183–206. doi:10.1002/stc.213
4. Feeny B, Kappagantu R (1998) On the physical interpretation of proper orthogonal modes in vibrations. *J Sound Vib*. Retrieved from <http://www.sciencedirect.com/science/article/pii/S0022460X97913869>
5. Feeny BF, Liang Y (2003) Interpreting proper orthogonal modes of randomly excited vibration systems. *J Sound Vib* 265(5):953–966. doi:10.1016/S0022-460X(02)01265-8
6. Kerschen G, Golinval J, Vakakis AF, Bergman LA (2005) The method of proper orthogonal decomposition for dynamical characterization and order reduction of mechanical systems: an overview. *Nonlinear Dyn* 41(1–3):147–169. doi:10.1007/s11071-005-2803-2
7. Zhou W, Chelidze D (2007) Blind source separation based vibration mode identification. *Mech Syst Signal Process* 21(8):3072–3087. doi:10.1016/j.ymssp.2007.05.007
8. Smith IF, Saitta S (2008) Improving knowledge of structural system behavior through multiple models. *J Struct Eng* 134(4):553–561. doi:10.1061/(ASCE)0733-9445(2008)134:4(553)
9. Posenato D, Lanata F, Inaudi D, Smith IFC (2008) Model-free data interpretation for continuous monitoring of complex structures. *Adv Eng Inform* 22(1):135–144. doi:10.1016/j.aei.2007.02.002
10. Antoni J, Chauhan S (2013) A study and extension of second-order blind source separation to operational modal analysis. *J Sound Vib* 332(4):1079–1106. doi:10.1016/j.jsv.2012.09.016
11. Roan MJ, Erling JG, Sibul LH (2002) A new, non-linear, adaptive, blind source separation approach to gear tooth failure detection and analysis. *Mech Syst Signal Process* 16(5):719–740. doi:10.1006/mssp.2002.1504
12. Poncelet F, Kerschen G, Golinval J (2006) Experimental modal analysis using blind source separation techniques. *International Conference on . . .* Retrieved from <http://orbi.ulg.ac.be/handle/2268/18770>
13. Poncelet F, Kerschen G, Golinval J-C, Verhelst D (2007) Output-only modal analysis using blind source separation techniques. *Mech Syst Signal Process* 21(6):2335–2358. doi:10.1016/j.ymssp.2006.12.005
14. McNeill S, Zimmerman D (2010) Relating independent components to free-vibration modal responses. *Shock Vib* 17:161–170. doi:10.3233/SAV-2010-0504
15. Yang Y, Nagarajaiah S (2013) Output-only modal identification with limited sensors using sparse component analysis. *J Sound Vib* 332(19):4741–4765. doi:10.1016/j.jsv.2013.04.004
16. Yu K, Yang K, Bai Y (2014) Estimation of modal parameters using the sparse component analysis based underdetermined blind source separation. *Mech Syst Signal Process* 45(2):302–316. doi:10.1016/j.ymssp.2013.11.018
17. Oh CK, Sohn H, Bae I-H (2009) Statistical novelty detection within the Yeongjong suspension bridge under environmental and operational variations. *Smart Mater Struct* 18(12):125022. doi:10.1088/0964-1726/18/12/125022
18. Kallinikidou E, Yun H (2013) Application of orthogonal decomposition approaches to long-term monitoring of infrastructure systems. *J Eng Mech* 139:678–690. doi:10.1061/(ASCE)EM.1943-7889.0000331
19. Juang JN, Pappa RS (1985) An eigensystem realization algorithm for modal parameter identification and model reduction. *J Guid Control Dyn* 8(5):620–627. Retrieved from <http://doi.aiaa.org/10.2514/3.20031>
20. James GH, Carne TG, Lauffer JP (1993) The Natural Excitation Technique (NExT) for modal parameter extraction from operating wind turbines. System 1–46. Sandia National Laboratories. Retrieved from <http://vibration.shef.ac.uk/doc/1212.pdf>
21. Nayeri RD, Tasbihgoo F, Wahbeh M, Caffrey JP, Masri SF, Conte JP, Elgamal A (2009) Study of time-domain techniques for modal parameter identification of a long suspension bridge with dense sensor arrays. *J Eng Mech* 135(7):669. doi:10.1061/(ASCE)0733-9399(2009)135:7(669)
22. Hyvärinen A, Oja E (2000) Independent component analysis: algorithms and applications. *Neural Netw: the official journal of the International Neural Network Society* 13(4–5):411–430. Retrieved from <http://www.ncbi.nlm.nih.gov/pubmed/10946390>
23. Kerschen G, Poncelet F, Golinval J-C (2007) Physical interpretation of independent component analysis in structural dynamics. *Mech Syst Signal Process* 21(4):1561–1575. doi:10.1016/j.ymssp.2006.07.009
24. Luş H, Betti R, Longman R (1999) Identification of linear structural systems using earthquake-induced vibration data. *Earthq Eng Struct Dyn* 28:1449–1467
25. Smyth AW, Pei J-S, Masri S (2003) System identification of the Vincent Thomas Suspension Bridge using earthquake records. *Earthq Eng Struct Dyn* 32:339–367
26. Maia NMM, Silba JMM (1997) *Theoretical and experimental modal analysis*. Research Studies Press LTD, England
27. Mariani R, Dessi D (2012) Analysis of the global bending modes of a floating structure using the proper orthogonal decomposition. *J Fluids Struct* 28:115–134. doi:10.1016/j.jfluidstructs.2011.11.009
28. Yang Y, Nagarajaiah S (2012) Time-frequency blind source separation using independent component analysis for output-only modal identification of highly damped structures. *J Struct Eng* 1780–1793. doi:10.1061/(ASCE)ST.1943-541X.0000621
29. Yun H-B, Park S-H, Mehdawi N, Mokhtari S, Chopra M, Reddi LN, Park K-T (in press) Monitoring for close proximity tunneling effects on an existing tunnel using principal component analysis technique with limited sensor data. *Tunn Undergr Space Technol*

# Chapter 13

## Comparison of Different Approaches for the Model-Based Design of Experiments

Ina Reichert, Peter Olney, Tom Lahmer, and Volkmar Zabel

**Abstract** Before starting an experiment it is wise to make close investigations on the structure to be examined and the possible designs of the experiment. The optimal design of the measurement setups is acquired by using mathematical optimization methods which are supported by numerical simulations of the structure and its behavior. The numerical model can then be used to verify the resulting design of the experiment and both of them can be validated by monitoring an existing structure. The aim of this paper is to undertake this first step to confirm the optimal design of experiments which is gained by three different approaches and testing them on a numerical model. These methods are: the reduction of parameter uncertainties by using the Fisher Information Matrix, the second approach is made by the minimization of the mean-squared errors between the assumed true solution and the solution of the inverse problem and as third approach the so-called sigma-point method is used where for the mean-squared error biased estimators for the parameter identification problem are used.

**Keywords** Design of experiments • Fisher Information Matrix • Mean-squared errors • Sigma-point method • Sensor placement

### 13.1 Introduction

It is truly helpful to conduct experiments in order to gain more information about a process or a structure, which is more probable in the field civil engineering. In fact, there are different types of experiments; they can be divided into long-term and short-term monitoring as well as those that take place in the field or in laboratories. Nevertheless, each type comes with its own restrictions and difficulties. Therefore, it is useful and promising to do an optimal design of experiments, DoE, which leads to effective, time and cost saving measurements.

Since most improvements in strategies for the design of experiments (DoE) were done in approximately the last 100 years [8], a number of methods were developed dealing with optimal design. This paper is to be seen as the extension a former conference paper [9] by adding a third method for comparison and discussion. Firstly, the classic approach with the Fisher Information Matrix (FIM) [1, 11] is chosen. The main known disadvantage of the FIM is that systematic errors can not be taken into account. Secondly, the optimal design is gained by the calculation of the mean-squared error (MSE) [2, 5, 7] between the exact and estimated parameters of interest. Lastly, a relatively new approach, the sigma-point method (SP) [6, 10], is considered. Finally these three methods are tested on a cantilever beam, which serves as the application example. The three mentioned approaches are then compared based on the results of this example and conclusions are drawn in order to also make further investigations.

---

I. Reichert (✉) • P. Olney  
Bauhaus-Universität Weimar, Faculty of Civil Engineering, Research Training Group 1462, Berkaer Str. 9, 99425 Weimar, Germany  
e-mail: [ina.reichert@uni-weimar.de](mailto:ina.reichert@uni-weimar.de); [peter.olney@uni-weimar.de](mailto:peter.olney@uni-weimar.de)

T. Lahmer • V. Zabel  
Bauhaus-Universität Weimar, Faculty of Civil Engineering, Institute of Structural Mechanics, Marienstr. 15, 99423 Weimar, Germany  
e-mail: [tom.lahmer@uni-weimar.de](mailto:tom.lahmer@uni-weimar.de); [volkmar.zabel@uni-weimar.de](mailto:volkmar.zabel@uni-weimar.de)

## 13.2 Methods for Model-Based Design of Experiments

For the optimal design of any experiment, a model of the process or structure is needed. This model is then used to find the optimal design which leads to the least uncertainty in the measurement results corresponding to one specific method. It can also be used to make a comparison between different DoE approaches. In this paper, the optimal design refers to the sensor positions that should be optimized in order to estimate certain model parameters.

In the following the “exact” measurement data,  $y$ , which does not contain any noise, is corrupted by two different types of noise. On the one hand, this is random noise,  $\varepsilon_i$ , with zero mean and given variance,  $\sigma^2$ . On the other hand, it is a systematic error,  $\beta_i$ , which is considered as relative to the data value since its true structure is unknown.  $\beta_i$  is added to the “exact” measurement data  $y$ . The inclusion of both types of noise produces artificial measurement data  $u$  as follows:

$$u(\theta, x^j, t_i) = y(\theta, x^j, t_i) + \delta_i, \quad (13.1)$$

where  $\theta$  is the vector of parameters,  $x^j$  and  $t_i$  correspond to the discrete spatial and temporal domain as well as  $\delta_i$  represents the noise term and can as described in [3] either be a random noise  $\varepsilon_i$  or a systematic one  $\beta_i$ .

### 13.2.1 Fisher Information Matrix

As described in Uciński [11], the Fisher Information Matrix (FIM) can be derived using the Cramér-Rao inequality as a lower bound estimate of the covariance matrix of parameters. This leads to a probabilistic definition of optimal sensor placement. Most simulations of civil engineering structures use deterministic models and methods, therefore this original form of the FIM cannot be used directly for the design of experiments, but has to be modified under certain assumptions. A basic one is that the numerical model sufficiently represents the considered structure. The most common approach is to consider the numerical model response as a measured response by the addition of noise. When this noise is taken as a random variable with a probability distribution, then a relation between the probabilities and model responses can be made. Considering this along with spatially uncorrelated errors [11], the FIM becomes

$$M = \frac{1}{\sigma^2} \sum_{j=1}^{n^{\text{sens}}} \int_0^{t_f} \left( \frac{\partial y(\theta, x^j, t_i)}{\partial \theta} \right)^T \left( \frac{\partial y(\theta, x^j, t_i)}{\partial \theta} \right) dt, \quad (13.2)$$

where  $y$  solves the forward problem,  $\theta$  are the parameters of interest,  $x$  is the spatial variable and  $t$  is the temporal one. The measurements are taken over a finite time interval,  $t_f$ . The standard deviation of the measurement error is  $\sigma$ , constant for all measurement locations.

From this brief overview, it becomes immediately clear that only random errors can be considered directly with the FIM, a potential disadvantage when systematic errors are large. Different criteria exist for evaluating and comparing FIMs, which also may return different results as to which sensor configuration is optimal. As described in [11], optimal sensor positioning should minimize some real-valued function,  $J$ . One example is the D-optimality criterion:

$$J(M) = \det(M^{-1}). \quad (13.3)$$

While many other criteria exist and there is still some debate about which one is the best to use, an advantage of the D-optimality condition is that it is independent of the scaling of the parameters (units) [4]. This criterion will be used in this discussion for these and other reasons. This choice is immaterial as long as it is consistent when the comparison is made between measurement setups.

### 13.2.2 Mean-Squared Errors

The second method uses the minimization of the difference between the “exact” solution for the parameters  $\theta$  and its estimate  $\hat{\theta}$ . Therefore, first the form of the data has to be defined, assuming a linear relation between model input and output. In this case the data  $u$  consists of the “exact” solution  $y$  and an error term  $\delta_i$  which is described by Eq. (13.1), where  $\delta$  can describe a systematic error,  $\beta$ , a random one,  $\varepsilon$ , or both together as explained in Sect. 13.2. The experiment has to be set up in such a way that it leads to the best approximation of the unknown vector of parameters  $\theta$ . Firstly, a sufficient number

of experiments has to be chosen. If the problem is well-posed, which is the case in this article, the number of experiments or in this instance sensors  $n^{\text{sens}}$  has to satisfy the inequality  $n^{\text{sens}} \geq n$ , where  $n$  represents the number of parameters  $\theta$  [5].

A cost function has to be set up. This leads to the usage of the mean-squared error (MSE) which is expressed by

$$\mathbf{MSE}(\hat{\theta}) = \mathbf{E}\|\hat{\theta} - \theta\|^2 \quad (13.4)$$

and which should be minimized by

$$\min \mathbf{E}\|\hat{\theta} - \theta\|^2 \quad (13.5)$$

as written in [2] to find the optimal experimental design.

Once the number of sensors is defined, the optimal positions have to be found. The description of the noisy measurements as given in Eq. (13.1) is used for the minimization of the difference between the “exact” measurement data and the ones corrupted by any noise  $\delta_i$ . The measurement data depends on the parameters  $\theta$ , the sensor positions  $x^j$  and the time  $t_i$ . The corresponding cost function that depends on the parameters  $\theta$  and which should be minimized is expressed by

$$\min_{\theta} J(\theta, x^j, t_i) = \min_{\theta} \sum_{j=1}^{n^{\text{sens}}} (y(\theta, x^j, t_i) - u(\theta, x^j, t_i))^2. \quad (13.6)$$

After a certain number of iteration steps of the optimization, the gained parameters serve as the estimated ones  $\hat{\theta}$  and lead to the mean-squared error given by

$$\mathbf{MSE}(\hat{\theta}, x^j) = \|\hat{\theta}(x^j) - \theta(x^j)\|^2. \quad (13.7)$$

The value of the MSE is then used as the selection criteria for finding the best sensor positions  $x^j$  where the corresponding  $\mathbf{MSE}(\hat{\theta}, x^j)$  is minimal.

### 13.2.3 Sigma-Point Method

Taking the ideas of [6] a new approach for optimal experimental design was formed in [10], the so-called Sigma-point method, SP. First of all, noisy measurements,  $u$ , have to be produced. This is again done by adding  $2mK$  noise terms  $\delta_i$  to the “exact” measurement data,  $y$ , as in Eq. (13.1) which lead to  $(2mK)$  noisy measurement data sets with  $m$  being the number of parameters to be estimated and  $K$  being the number of temporal measurement points. From these samples  $(2mK)$  parameter vectors,  $\hat{\theta}_i$ , can be identified and the mean,  $\bar{\theta}$ , and covariance matrix,  $C_{\theta, \text{SP}}$ , as written in [10] can be derived by

$$\bar{\theta} = \sum_{i=1}^{2mK} w_i^m \hat{\theta}_i \quad \text{and} \quad (13.8)$$

$$C_{\theta, \text{SP}} = \sum_{i=1}^{2mK} w_i^c (\hat{\theta}_i - \bar{\theta}) (\hat{\theta}_i - \bar{\theta})^T, \quad (13.9)$$

where  $w_i^m$  and  $w_i^c$  represent weights, which are considered here as constant, such that the calculation of the mean,  $\bar{\theta}$ , and the covariance matrix,  $C_{\theta, \text{SP}}$ , are defined by

$$\bar{\theta} = \frac{1}{2mK} \cdot \sum_{i=0}^{2mK} \hat{\theta}_i \quad \text{and} \quad (13.10)$$

$$C_{\theta, \text{SP}} = \frac{1}{2mK - 1} \cdot \sum_{i=0}^{2mK} (\hat{\theta}_i - \bar{\theta}) (\hat{\theta}_i - \bar{\theta})^T. \quad (13.11)$$

where the mean values,  $\bar{\theta}$ , of the parameters could be replaced by the “exact” ones,  $\theta$ , as we are dealing with artificially created data and the true solution is known.

With this approach it is not only possible to consider random noise, but it can also handle constant systematic errors. The estimation of the bias is then made by

$$\widehat{\text{Bias}} = \bar{\theta} - \hat{\theta}_0, \quad (13.12)$$

but only if  $\bar{\theta} \neq \hat{\theta}_0$ .

There are now two ways that lead to the optimal sensor positions. One way is the calculation of the mean-squared error between the “exact” solution,  $\theta$ , and the estimated mean one,  $\bar{\theta}$ , similar to Eq. (13.7) by

$$\text{MSE}(\bar{\theta}, x^j) = \|\bar{\theta}(x^j) - \theta(x^j)\|^2. \quad (13.13)$$

and evaluating its minimum to take the corresponding sensor positions as optimal. The second way is to use an optimality criterion like in Eq. (13.3) on the covariance matrix,  $C_{\theta,SP}$ , but in this case for the sake of stability the T-optimality criterion

$$J(C_{\theta,SP}) = \text{tr}(C_{\theta,SP}) \quad (13.14)$$

is used and again the optimal sensor setup is found where  $J$  is minimal.

### 13.3 Application on a Cantilever Beam

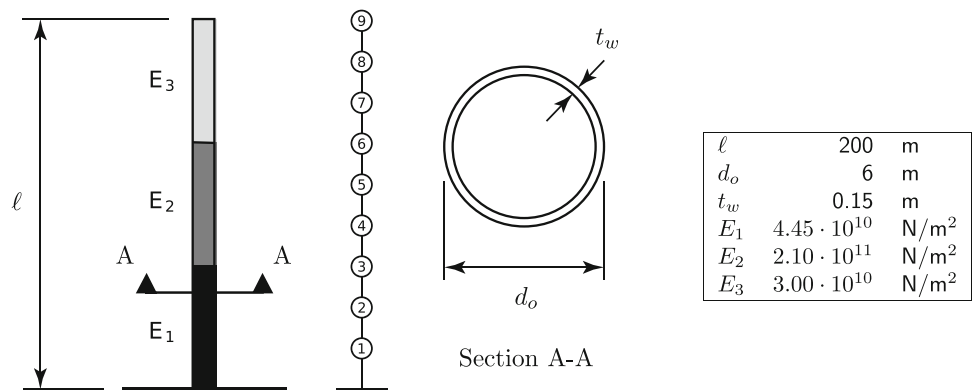
#### 13.3.1 Numerical Model

In order to compare the results from applying the three different design of experiment strategies introduced, a tower-like structure is considered as depicted in Fig. 13.1. The tower is separated into three equal length sections each corresponding to a different material with Young’s modulus,  $E_i$ . Although three materials are modeled, the density is kept constant at  $2,550 \text{ kg/m}^3$ . A finite element model using nine Bernoulli beam elements of equal length (3 per material) is used to model the structure. There is no modal damping included in the discretized system. A dynamic simulation is computed using an harmonic excitation with the seventh eigenfrequency applied on all nodes of the system, only considering the steady state response. Design of the input loading for optimal experiments is outside the scope of this paper.

Acceleration time histories taken at specific locations  $x^j$  and corrupted by the afore mentioned two types of noise are considered as the measurement data. The random error is hereby represented by a normal distribution  $\varepsilon_i = \mathcal{N}(0, \sigma^2)$  with zero mean and the standard deviation  $\sigma = 0.005$ . For the systematic error a relative description is used, so the systematic error is 5 % of the exact value of the acceleration time history. The initial guesses for the values of the Young’s modulus is set to 90 % of the “exact” values and for the sigma-point method  $m = 3$  as we are dealing with three parameters and in order to reduce computing time  $K = 50$ , which leads to 300 samples per setup.

Since the model response is taken at discrete positions  $x^j$ , the optimal sensor positions are found by evaluating all combinations of three sensors  $n^{\text{sens}}$  at nine possible positions  $n^{\text{pos}}$ . This leads to 84 combinations which have to be calculated.

**Fig. 13.1** Sketch of the cantilever beam with discrete sensor positions, cross section A-A and values of the material properties [9]



Their values of the D-optimality criterion for the FIM approach, the mean-squared error as well as the MSE and the T-optimality criterion for the SP method are serving for sorting the sensor setups for each method in order to gain the best one, respectively.

### 13.3.2 Results: Comparison Between FIM, MSE and SP

The comparisons of the results of the three methods for the two different types of noise are shown in the Tables 13.1 and 13.2. The tables contain the best, second best and worst value for the D-optimality criterion of the Fisher Information Matrix (FIM) on one side and the values of the mean-squared error for MSE and SP as well as the value of the T-optimality criterion for the SP-method corresponding to this particular design of sensors on the other side. The rows below belong to the cases respectively. In Table 13.1 the comparison for the random error and in Table 13.2 the one for the systematic one is given.

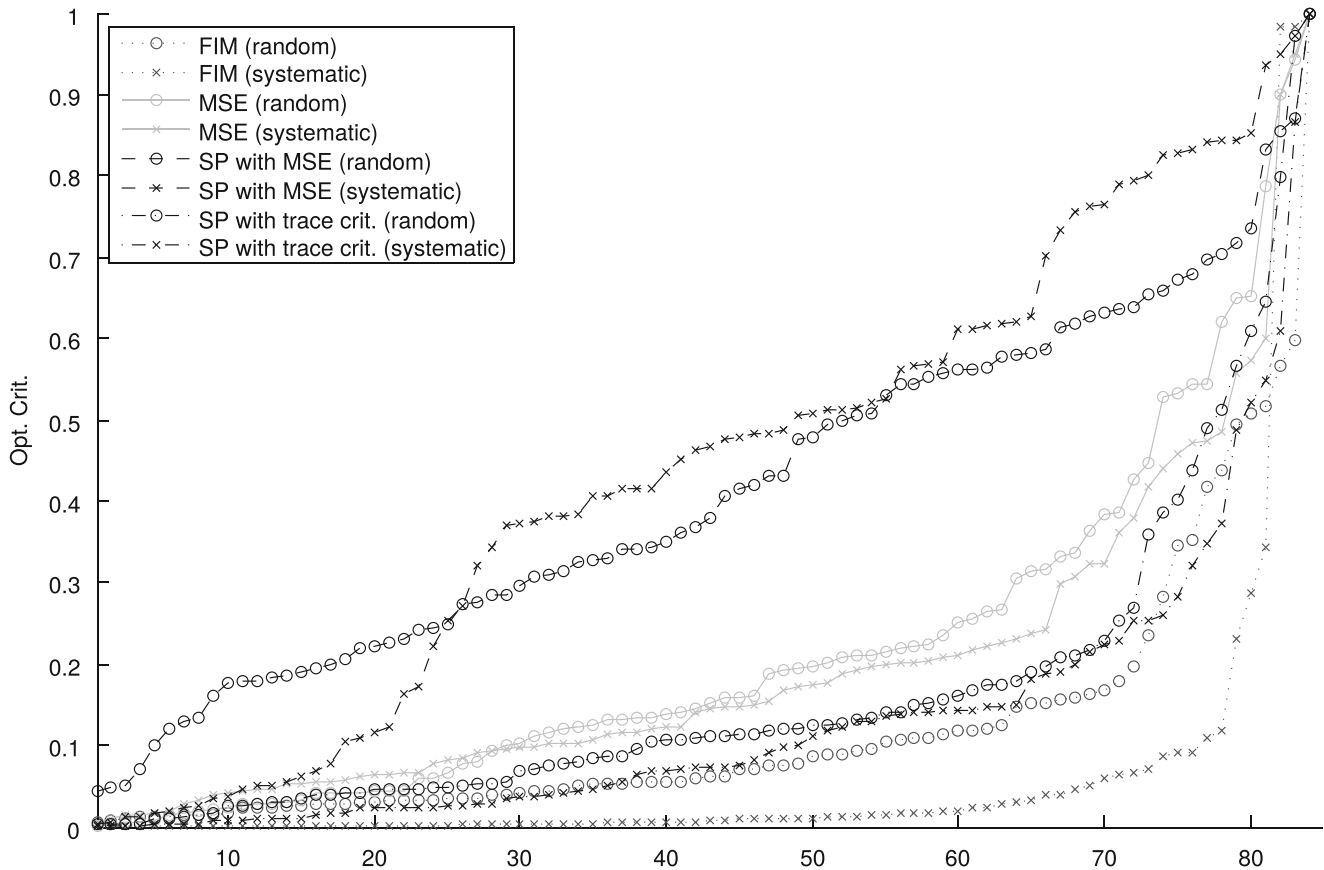
Additionally Fig. 13.2 shows the behavior of the different DoE approaches for the respective optimality criterion depending on the rank of the setups. Where the slope is steep, neighboring (in rank) setups can lead to much better or worse results in finding the “exact” parameters. This can be especially seen for the sigma-point method while using the MSE as the evaluation criterion for the whole range, but also all other methods show an even steeper growth for the last 10–20 ranks. On the opposite side the slopes for the FIM, MSE and SP while using the T-optimality criterion for the first 60–70 ranks are rather flat. It can be concluded that in rank neighboring setups give equally good estimates of the unknown parameters.

**Table 13.1** Random error: Overview of normalized values of D-optimality criterion of FIM, MSE as well as mean-squared error and T-optimality criterion of SP (Opt. Crit.) for the two best and the worst design corresponding to each method and their values for the other methods, respectively

Design	FIM		MSE		SP with MSE		SP with trace crit.	
	Opt. Crit.	Rank	Opt. Crit.	Rank	Opt. Crit.	Rank	Opt. Crit.	Rank
[5 6 9]	0.005	1	0.042	17	0.134	8	0.108	41
[2 5 9]	0.009	2	0.027	11	0.248	25	0.132	53
[1 3 4]	1.000	84	0.943	83	0.477	49	0.176	63
[3 6 7]	0.096	54	0.001	1	0.284	28	0.012	7
[3 4 5]	0.151	65	0.004	2	0.120	6	0.128	52
[4 8 9]	0.046	33	1.000	84	0.871	83	0.151	57
[1 5 6]	0.059	42	0.267	63	0.044	1	0.218	69
[4 5 6]	0.016	9	0.111	31	0.048	2	0.047	22
[4 7 8]	0.076	47	0.222	57	1.000	84	0.229	70
[2 6 7]	0.025	14	0.031	14	0.329	36	0.002	1
[2 3 6]	0.024	11	0.787	81	0.581	65	0.002	2
[1 6 8]	0.155	67	0.006	4	0.327	35	1.000	84

**Table 13.2** Systematic error: Overview of normalized values of D-optimality criterion of FIM, MSE as well as mean-squared error and T-optimality criterion of SP (Opt. Crit.) for the two best and the worst design corresponding to each method and their values for the other methods, respectively

Design	FIM		MSE		SP with MSE		SP with trace crit.	
	Opt. Crit.	Rank	Opt. Crit.	Rank	Opt. Crit.	Rank	Opt. Crit.	Rank
[5 6 9]	0.000	1	0.017	5	0.373	78	0.108	41
[2 5 9]	0.000	2	0.092	27	0.011	15	0.132	53
[2 4 8]	1.000	84	0.115	37	0.321	76	0.086	36
[2 3 7]	0.019	59	0.007	1	0.002	5	0.004	4
[3 5 9]	0.011	49	0.010	2	0.001	4	0.104	39
[1 2 7]	0.005	41	1.000	84	0.038	32	0.140	55
[4 5 9]	0.023	62	0.055	16	0.003	1	0.026	26
[3 5 9]	0.011	49	0.010	2	0.005	2	0.001	4
[4 6 7]	0.038	66	0.363	71	1.000	84	0.028	28
[3 5 7]	0.005	37	0.379	72	0.018	6	0.000	1
[3 4 5]	0.010	47	0.440	74	0.051	12	0.001	2
[5 7 8]	0.001	13	0.167	48	0.025	8	1.000	84



**Fig. 13.2** Behavior of the optimality criterion (Opt. Crit.) of the three introduced methods (FIM, MSE and SP) for random and systematic noise depending on the rank of the sensor setups

### 13.4 Discussion and Conclusion

Tables 13.1 and 13.2 show no sensor setup (design) is mentioned at least twice in each table. This leads to the conclusion that the optimal designs differ between the different considered methods for one type of noise. Since no common measure for all methods exists, the questions of how to compare the results and to decide which setup is the best one are open. In future work, this drawback should be overcome by finding a compatible measure. Another remedy could be made by taking real experiments in order to validate the aforementioned methods.

One could also go back to the theory behind the methods and see that the Fisher Information Matrix can only be used for random noise. So, it is not recommended to use this method also for systematic errors. This effect can also be seen in the results, since the best two designs for FIM do not depend on the noise type, only the worst one is different. The same case holds for using the T-optimality criterion on the sigma-point method where all three (best, second best and worst) depicted designs are the same for random and systematic noise. These findings lead to the necessity of a more careful consideration of the noise occurring in any experiment. First of all, the type of noise is important to know. Further research will deal with the influence of different noise levels and the corruption of measurements by both random and systematic noise at the same time.

For practical use, it is also important to think about computational costs. The FIM is very fast, but as a big disadvantage it can only deal with random noise. The MSE is computationally more intensive, but gives results for both error types in a reasonable time. Whereas considering that  $2mK$  samples per sensor design have to be calculated for the SP method it takes a lot of computational time in order to get results.

Concerning the application example, it was determined, that the loading has a large influence on the quality of the estimated parameters. It is highly recommended to also take into account the type of loading for design of experiments as it can improve the identification of the model parameters. Future work should also include more parameters of the experiment, such as sampling rate, types of sensors and resolution. In addition, an extension to the continuous case for the spatial domain,  $x$ , has to be done.

## References

1. Bandemer H, Bellmann A (1994) Statistische Versuchsplanung. BG Teubner, Leipzig
2. Bardow A (2006) Optimal experimental design for ill-posed problems. In: 16th European symposium on computer aided process engineering and 9th international symposium on process systems engineering. Elsevier, Amsterdam, pp 173–178
3. Coleman HW, Steele WG Jr (1989) Experimentation and uncertainty analysis for engineers. Wiley, New York
4. Goodwin GC, Payne RL (1977) Dynamic system identification: experiment design and data analysis. Academic, New York
5. Haber E, Horesh L, Tenorio L (2010) Numerical methods for the design of large-scale nonlinear discrete ill-posed inverse problems. *Inverse Prob* 26(2):025002
6. Julier SJ, Uhlmann JK (1996) A general method for approximating nonlinear transformations of probability distributions. Technical report, technical report, robotics research group. Department of Engineering Science, University of Oxford, Oxford
7. Lahmer T (2011) Optimal experimental design for nonlinear ill-posed problems applied to gravity dams. *Inverse Prob* 27(12):125005
8. Lye LM (2002) Design of experiments in civil engineering: are we still in the 1920s. In: Proceedings of the 30th annual conference of the Canadian Society for Civil Engineering, Montreal, QC, June
9. Reichert I, Olney P, Lahmer T (2014) Comparison of different model-based design of experiment approaches under moderate errors. In: Proceedings of the 12th International Probabilistic Workshop, Weimar, Germany
10. Schenkendorf R, Kremling A, Mangold M (2009) Optimal experimental design with the sigma point method. *IET Syst Biol* 3(1):10–23
11. Uciński D (2005) Optimal measurement methods for distributed parameter system identification. CRC Press, Boca Raton



# Chapter 14

## Sensitivity Analysis for Test Resource Allocation

Chenzhao Li and Sankaran Mahadevan

**Abstract** To predict the response of a system with unknown parameters, a common route is to quantify the parameters using test data and propagate the results through a computational model of the system. Activities in this process may include model calibration and/or model validation. Data uncertainty has a significant effect on model calibration and model validation, and therefore affects the response prediction. Data uncertainty includes the uncertainty regarding the amount of data and numerical values of data. Although its effect can be qualitatively observed by trying different data sets and visually comparing the response predictions, a quantitative methodology assessing the contributions of these two types of data uncertainty to the uncertainty in the response prediction is necessary in order to solve test resource allocation problems. In this paper, a novel computational technique based on pseudo-random numbers is proposed to efficiently quantify the uncertainty in the data value of each type of test. Then the method of auxiliary variable based on the probability integral transform theorem is applied to build a deterministic function so that variance-based global sensitivity analysis can be conducted. The resultant global sensitivity indices quantify the contribution of data value uncertainty of each type of test to the uncertainty in the response prediction. Thus a methodology for robust test resource allocation is proposed, i.e., quantifying the number of each type of tests so that the response predictions using different data set are consistent.

**Keywords** Resource allocation • Model calibration • Model validation • Global sensitivity analysis

### 14.1 Introduction

System response prediction is one of the main objectives in engineering research. Basically, prediction is the activity to estimate the system response at an untested configuration using available model and test information. Prediction under uncertainty for a complicated system generally includes two steps: (1) build a computational model  $Y = F(X; \theta_m)$  to represent the system, where  $Y$  is the system response, and  $X$  is a vector of model input, and  $\theta_m$  is a set of unknown model parameters; (2) quantify and propagate the uncertainty in  $X$  and  $\theta_m$  through the model  $Y = F(X; \theta_m)$  in order to quantify the uncertainty in system response. In step one,  $Y = F(X; \theta_m)$  can be: (1) physics-based model, e.g., finite element model; or (2) data-driven model, e.g., regression model with input–output data [1–3]. In step 2, model inputs  $X$  are generally measurable in each test, and their uncertainty is aleatory (i.e., nature variability across tests). In contrast, model parameters  $\theta_m$  are fixed but unknown values, and their uncertainty is epistemic (due to lack of information). While the variability in  $X$  can be quantified by direct measurement and distribution fit, the uncertainty quantification of  $\theta_m$  relies on statistical inferences using input–output measurements. Activities to quantify the uncertainty in  $\theta_m$  may include: (1) model calibration to compute the uncertainty in  $\theta_m$ ; (2) model validation to assess the quality of model calibration; and (3) uncertainty integration to combine the information in model calibration and validation. Both model calibration and validation require test data.

The problem of resource allocation arises from the fact that test data are uncertain. Data uncertainty includes the uncertainty regarding the number of data and numerical values of data. Data uncertainty has a significant effect on model calibration and model validation, and therefore affects the response prediction. In other words, another set of calibration/validation test data may give a distinct system response prediction. Generally, test resource allocation is an activity of optimization before conducting the actual tests. Calibration tests and validation tests are two different categories of tests. Data obtained in calibration test reduce the uncertainty in model parameters thus reduce the uncertainty in prediction. In case of considering model calibration only, generally the resource allocation optimization is to select test type and number to minimize the uncertainty in the prediction [4, 5]. In contrast, data obtained in validation test may indicate that the model

---

C. Li • S. Mahadevan (✉)

Department of Civil & Environmental Engineering, Vanderbilt University, VU Station B #351831, Nashville, TN 37235-1831, USA  
e-mail: [sankaran.mahadevan@vanderbilt.edu](mailto:sankaran.mahadevan@vanderbilt.edu)

calibration is not exactly valid thus the uncertainty reduction obtained in model calibration should be discounted, which indicates more uncertainty in the prediction. In the resource allocation considering both calibration test and validation test [6], resource allocation optimization needs to select test type and number of tests of each type to obtain robust prediction, i.e., how many tests of various types are necessary such that the prediction is consistent using different sets of test data. The second optimization is discussed in this paper, using a comprehensive approach that includes both model calibration and model validation.

The rest of this paper is organized as follows. Section 14.2 proposes a novel seed-based method to capture the uncertainty in data value. Section 14.3 builds a framework of optimization for robust resource allocation. In Sect. 14.4, two numerical examples of different configurations are given to illustrate the propose framework.

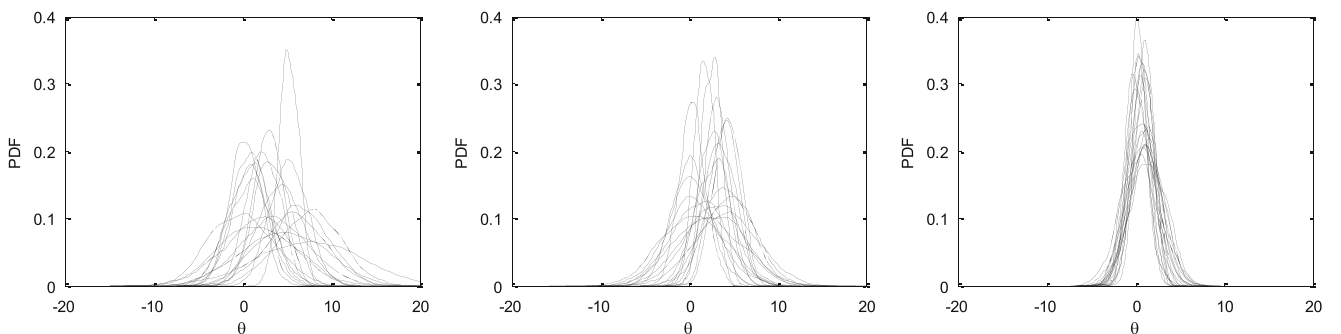
## 14.2 Seed-Based Method for Data Value Uncertainty

Since resource allocation is an optimization handling data uncertainty before actual tests are conducted, synthetic test data are necessary in resource allocation. The generation of synthetic test data includes two cases:

1. Limited tests of each type have been conducted. Based on these test data, synthetic test data can be generated using algorithms such as bootstrapping [7];
2. No test has been conducted. In this case, synthetic data can be generated based on the nominal values or the prior mean values of model parameters; due to the discrepancy between the synthetic data and the real data caused by the difference between the nominal values and the true values, repeated resource allocation optimizations trying different nominal values may be required.

In any case above, at data size  $N_i$ , the data value uncertainty is represented by the difference between multiple sets of data. In robust test planning, it is desired that the contribution of data uncertainty to the uncertainty of the prediction be small such that consistent response predictions can be obtained for every other data sets. Generally, the contribution of data value uncertainty reduces as data number increases. One example is Bayesian inference, which is used as the model calibration methodology in this paper. In Fig. 14.1, each sub-figure contains a family of posterior distributions obtained by same data number but different data values. From left to right, the sub-figures use more and more data points. Figure 14.1 illustrates the decreased variation of posterior distributions with increased data number. Across the family members, the decreased variation of the posterior includes two aspects: (1) the decreased variation of the mean values, roughly meaning that the centers of the family members are closer; (2) the decreased variation of the variance in each PDF, roughly meaning that the lengths of intervals covered by the family members are closer. If the posterior distribution of  $\theta$  is propagated for prediction, the response prediction is expected to more consistent as data number increases.

As robust resource allocation requires consistent prediction across different data sets, it is necessary to develop a methodology quantifying the contribution of data uncertainty to the prediction variation. Contribution assessment of uncertainty generally uses global sensitivity analysis (GSA). Consider a model  $Y = F(X)$  where  $X = \{X^1, \dots, X^N\}$  is a vector of model inputs. GSA measures the contribution of each component of  $X$  to the uncertainty of  $Y$  [8]. Two global sensitivity indices have been developed in the literature based on the law of total variance and Sobol's variance decomposition theorem [9]: first-order index and total effects index. For a particular model input  $X^i$ , the first-order index is



**Fig. 14.1** Posterior distribution of a model parameter as increased test data number

defined as  $S_1^i = V\left(E\left(Y|X^i\right)\right)/V(Y)$ ; and the total effects index is defined as  $S_T^i = 1 - V\left(E\left(Y|X^{-i}\right)\right)/V(Y)$  where  $X^{-i}$  means all the inputs other than  $X^i$ . The first-order index measures the contribution of the variable  $X^i$  by itself; in contrast, the total effects index contains not only the contribution of  $X^i$ , but also the interaction effect of  $X^i$  with other inputs. One assumption in the GSA is that each model input  $X$  is represented by a continuous probabilistic distribution (normal, uniform, etc.). However, as explained earlier, the data value uncertainty is only represented by the difference of multiple data sets of the same size, and no probabilistic distribution is directly available to represent it. Therefore, an explicit variable with a probability distribution to represent the data value uncertainty is pursued.

Recall the generation of synthetic data. It is basically a process of generating random numbers, usually accomplished by programming languages. The random number generation in programming languages is pseudo-random, which means that the resultant random numbers are not unpredictable at all, but are generated by deterministic algorithms such as Mersenne Twister generator [10], combined multiplicative recursive generator [11] or Wichmann-Hill generator [12]. These generators use a positive integer known as seed to generate a random number of various distribution types, and a new seed is deterministically computed before generating the next random number, and different seed values leads to different random numbers.

Therefore, if a code is used to generate synthetic data, the result is determined once the initial seed value is given. This initial seed, denoted by  $K$ , is considered as the random variable controlling the generation of synthetic data. At give data size, the initial seed  $K$  captures the data value uncertainty due to the one-to-one mapping between the value of  $K$  and the generation of synthetic data. It is equally possible for any positive integer to be used as a seed, so theoretically  $K$  has a discrete uniform distribution  $U_d(1, n_c)$  where the upper bound  $n_c$  is a very large positive integer decided by the specific programming language and computer. But in practice we can define the bounds of this discrete uniform distribution, depending on how many different possible data sets are adequate to represent the data value uncertainty.

One more step is needed to apply this seed method to global sensitivity analysis. Although the initial seed  $K$  captures data value uncertainty for a given data size, its distribution is discrete while the global sensitivity analysis requires continuous random variables. Therefore another auxiliary variable  $U_K$  [13], which is the CDF value of  $K$ , is introduced to represent  $K$ . The mapping between the value of  $U_K$  and the value of  $K$  is:

$$K = a + \lfloor U_K (b - a + 1) \rfloor \quad (14.1)$$

where  $a$  and  $b$  are the lower and upper bound respectively, and  $\lfloor \cdot \rfloor$  is the floor function. Now assuming that the uncertainty in a model parameter  $\theta_m$  is quantified by test data from different types of tests, a deterministic relationship from  $U_K$  to the quantified distribution of  $\theta_m$  is established as:

$$H\left(U_{K_1}, \dots, U_{K_q} \mid N_1 = n_1, \dots, N_q = n_q\right) \rightarrow f_{\theta_m} \quad (14.2)$$

where  $N_i$  is the data number of the  $i^{\text{th}}$  type of test ( $i = 1, \dots, q$ ), and  $U_{K_i}$  is the corresponding auxiliary variable capturing the data uncertainty in the  $i^{\text{th}}$  type of test, and  $f_{\theta}$  is the quantified distribution of  $\theta_m$ . Basically, Eq. (14.2) indicates that the quantified distribution of  $\theta_m$  is fixed as data number and data values of each type of test are fixed.

### 14.3 Framework of Optimization for Robust Resource Allocation

As shown in Eq. (14.2), at  $U_{K_i} = u_{K_i}$  and  $N_i = n_i$  ( $i = 1, \dots, q$ ), the data of each type of test are deterministic so that the calibrated joint distribution for all the model parameter  $\theta_m$  is fixed. As this joint distribution is propagated into the computational model  $Y = F(X; \theta_m)$  along with the known distribution of  $X$ , the predicted distribution  $f_Y(y)$  for the system response  $Y$  is also fixed, as shown in Eq. (14.3):

$$H\left(U_{K_1}, \dots, U_{K_q} \mid N_1 = n_1, \dots, N_q = n_q\right) \rightarrow f_Y(y) \quad (14.3)$$

As discussed in Sect. 14.2, the objective in resource allocation is to obtain consistent prediction of the system response under different set of test data. As shown in Fig. 14.1, this consistency can be verified in two aspects: (1) small variation of the mean value of prediction; and (2) small variation of the variance of the prediction. Equations for these two aspects derived from Eq. (14.3) are:

$$\mu_Y = H_1 \left( U_{K_1}, \dots, U_{K_q} \mid N_1 = n_1, \dots, N_q = n_q \right) \quad (14.4)$$

$$V_Y = H_2 \left( U_{K_1}, \dots, U_{K_q} \mid N_1 = n_1, \dots, N_q = n_q \right) \quad (14.5)$$

Thus two deterministic functions for GSA are established, where  $\mu_Y$  and  $V_Y$  are the mean value and variance of the prediction.

Application of Eqs. (14.4) and (14.5) in GSA assesses the contribution of data value uncertainty in each type of test to the uncertainty in the mean value and variance of the prediction. Generally it is expected that  $U_{K_i}$  will cause smaller uncertainty to  $\mu_Y$  and  $V_Y$  as  $N_i$  increases. However, this tendency cannot be revealed if we directly use the first-order or total effects index. They are normalized indices revealing the comparative contribution. However, this means that the index of  $U_{K_i}$  will increase purely due to the decreased contribution of  $U_{K_j}$  ( $i \neq j$ ), even if its absolute contribution stays the same. Thus a measurement of absolute contribution is pursued. This paper resolves this problem using the non-normalized first-order index:

$$S_{K_i}^M = V \left( E \left( Y \mid U_{K_i} \right) \right) \quad (14.6)$$

where  $M$  can be  $\mu_Y$  or  $V_Y$ .

In the optimization of resource allocation, a cost function is expected to be minimized while the contribution of each  $U_{K_i}$  is smaller than a threshold. If the expense of a type  $i$  test is  $C_i$  and threshold is assumed for  $\mu_Y$  and  $V_Y$  separately, the optimization can be expressed as:

$$\begin{aligned} \text{Min } & \sum_{i=1}^q C_i N_i \\ \text{s.t. } & S_{K_i}^{\mu_Y} \leq \lambda_{\mu_Y}^{K_i}, S_{K_i}^{V_Y} \leq \lambda_{V_Y}^{K_i} \end{aligned} \quad (14.7)$$

where  $\lambda_{\mu_Y}^{K_i}$  and  $\lambda_{V_Y}^{K_i}$  is the threshold for the  $i^{\text{th}}$  type of test with respect to  $\mu_Y$  and  $V_Y$ , correspondingly.

Eq. (14.7) is a complicated integer optimization problem, where model calibration and validation need to be repeated for each generation of the test data to evaluate the constraint function. Integer optimization is sometimes solved using a relaxation approach [14], where the integer constraint is first relaxed, and the integers nearest to the resulting optimal solution are used in a further solution of the original (unrelaxed) problem. Unfortunately, this approach is not applicable to the solution of Eq. (14.7), because the constraint functions are defined and computed only for integer-valued decision variables, i.e., number of tests. It is not possible to generate test data for a non-integer number of tests.

In this paper, a greedy approach is used to solve the optimization in Eq. (14.7):

1. Set the initial values of  $N_i$  ( $i = 1, \dots, q$ ) at 1 and conduct the GSA using Eq. (14.4), (14.5), and (14.6).
2. Set the threshold of  $\lambda_{\mu_Y}^{K_i}$  and  $\lambda_{V_Y}^{K_i}$ . In the optimization, the types of tests with more contribution at  $N_i = 1$  deserve larger number of tests. Thus in this paper, the threshold for  $\mu_Y$  is set as a percentage of the maximum  $S_{K_i}^{\mu_Y}$  at  $N_i = 1$ ; and the threshold for  $V_Y$  is set as a percentage of the maximum  $S_{K_i}^{V_Y}$  at  $N_i = 1$ . For  $\mu_Y$  or  $V_Y$ , each type of test uses the same threshold, so  $\lambda_{\mu_Y}^{K_i}$  and  $\lambda_{V_Y}^{K_i}$  reduce to  $\lambda_{\mu_Y}$  and  $\lambda_{V_Y}$ . For example, the numerical examples in Sect. 14.4 chooses this percentage as 15 %, so the thresholds are:  $\lambda_{\mu_Y} = 0.15 \max(S_{K_i}^{\mu_Y} \mid N_i = 1)$ ,  $\lambda_{V_Y} = 0.15 \max(S_{K_i}^{V_Y} \mid N_i = 1)$ .
3. Increase  $N_i$  by 1 if  $S_{K_i}^{V_Y} > \lambda_{\mu_Y}$  or  $S_{K_i}^{\mu_Y} > \lambda_{V_Y}$ , i.e., the data value uncertainty in the  $i^{\text{th}}$  type of test caused more uncertainty than the threshold either to  $\mu_Y$  or  $V_Y$ ;
4. Repeat Step 3 until  $S_{K_i}^{V_Y} > \lambda_{\mu_Y}$  and  $S_{K_i}^{\mu_Y} > \lambda_{V_Y}$  for ( $i = 1, \dots, q$ ), i.e., the contribution of data value uncertainty in any type of test is less than the thresholds.

Thus a framework of robust resource allocation using the seed-method, the auxiliary variable method, and the GSA is established. In Sect. 14.4, two numerical examples are used to illustrate the proposed framework.

## 14.4 Numerical Examples

### 14.4.1 Mathematical Example

This subsection presents a simple illustrative example to demonstrate the proposed framework of robust resource allocation. It is assumed that a system output is the sum of two sub-system outputs, and each sub-system has separate model inputs and model parameters:

$$Y = Y_1 + Y_2, Y_1 = X_1\theta_1, Y_2 = X_2\theta_2 \quad (14.8)$$

The model inputs  $X_1$  and  $X_2$  are independent Gaussian variables. Model parameters  $\theta_1$  and  $\theta_2$  have unknown deterministic values. Bayesian inference is used to calibrate model parameters using synthetic data and assigned prior distributions. It is assumed that posterior distributions of  $\theta_j$  are directly used to predict  $Y$ , thus in this example only model calibration is required to quantify  $\theta_j$ . Two types of tests are available: test to measure  $Y_1$  at input  $X_1$  and test to measure  $Y_2$  at input  $X_2$ . It is assumed that in each test the value of model input  $X_j$  is measured accurately, but  $Y_j$  is measured with a measurement error  $\epsilon_j$  ( $j = 1, 2$ ). Synthetic data are generated using Eq. (14.8), the nominal value of  $\theta_j$ , and the measurement error. Numerical details of this example are listed in Table 14.1.

The robust test planning is conducted following the four steps in Sect. 14.3:

1. The GSA is firstly conducted at  $N_1 = N_2 = 1$ . The absolute contributions of data value uncertainty in two types of test are:  $S_{K_1}^{\mu_Y} = 458$ ,  $S_{K_2}^{\mu_Y} = 1044$ ,  $S_{K_1}^{V_Y} = 1.64 \times 10^4$ ,  $S_{K_2}^{V_Y} = 1.39 \times 10^5$ ;
2. The threshold for  $\mu_Y$  and  $V_Y$  are chosen as:  $\lambda_{\mu_Y} = 0.15 \max \left( S_{K_i}^{\mu_Y} \mid N_1 = 1, N_2 = 1 \right) = 156$ ,  $\lambda_{V_Y} = 0.15 \max \left( S_{K_i}^{V_Y} \mid N_1 = 1, N_2 = 1 \right) = 2.08 \times 10^4$ ;
3. Increase  $N_i$  by 1 until  $S_{K_i}^{V_Y} > \lambda_{\mu_Y}$  and  $S_{K_i}^{\mu_Y} > \lambda_{V_Y}$ ; the details for this iteration are shown in Table 14.2.

The optimization for the illustrative example terminates at  $N_1 = 6$ ,  $N_2 = 9$ , meaning that more tests to measure  $Y_2$  are needed to achieve a robust prediction of  $Y$ . Figure 14.2 also visually verifies this result. In Fig. 14.2, the family of PDFs at each sub-figure shows the effect data value uncertainty at given data number. As more data number are applied, the family members become more concentrated, meaning reduced contribution of data value uncertainty to the prediction.

### 14.4.2 Multi-Level Problem

A multi-level structural dynamics challenge problem provided by Sandia National Laboratories [15] is shown in Fig. 14.3. Level 1 contains three mass-spring-damper dynamic components in series, and a sinusoidal force input is applied to  $m_1$ .

**Table 14.1** Numerical details of the illustrative example

Prior distributions of model parameters	$\theta_1 \sim N(5, 0.5)$ , $\theta_2 \sim N(10, 1)$
Distributions of model inputs	$X_1 \sim N(100, 5)$ , $X_2 \sim N(50, 5)$
Measurement errors	$\epsilon_1 \sim N(0, 50)$ , $\epsilon_2 \sim N(0, 40)$
Nominal values of model parameters	$\theta_1^N = 5$ , $\theta_2^N = 10$

**Table 14.2** Optimization details of the illustrative example

$(N_1, N_2)$	$S_{K_1}^{\mu_Y}$	$S_{K_2}^{\mu_Y}$	$S_{K_1}^{V_Y}$	$S_{K_2}^{V_Y}$
(1,1)	459	1,044	16,392	138,541
(2,2)	388	764	17,959	103,315
(3,3)	323	601	15,054	77,532
(4,4)	255	410	11,873	57,018
(5,5)	199	337	11,854	40,986
(6,6)	150	217	7,692	30,033
(6,7)	150	179	7,716	23,192
(6,8)	150	182	7,772	22,565
(6,9)	150	140	7,707	18,977

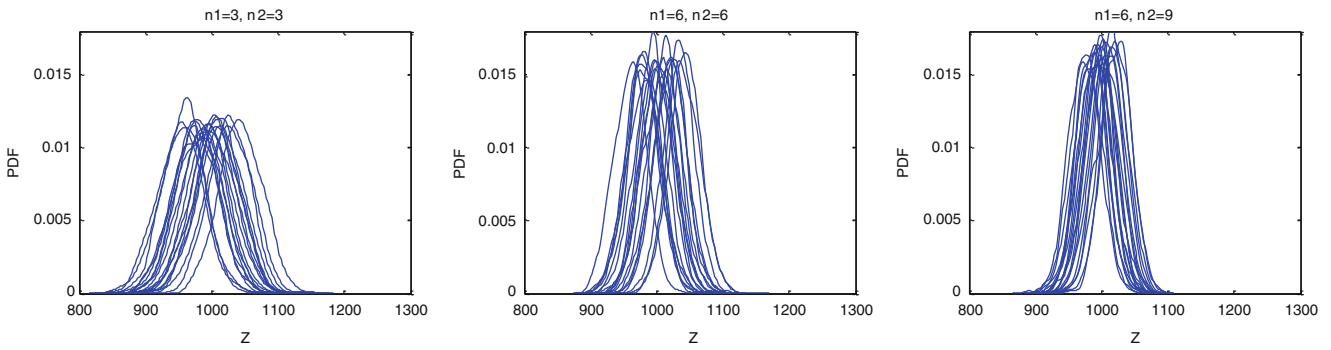


Fig. 14.2 Prediction as increased test data number

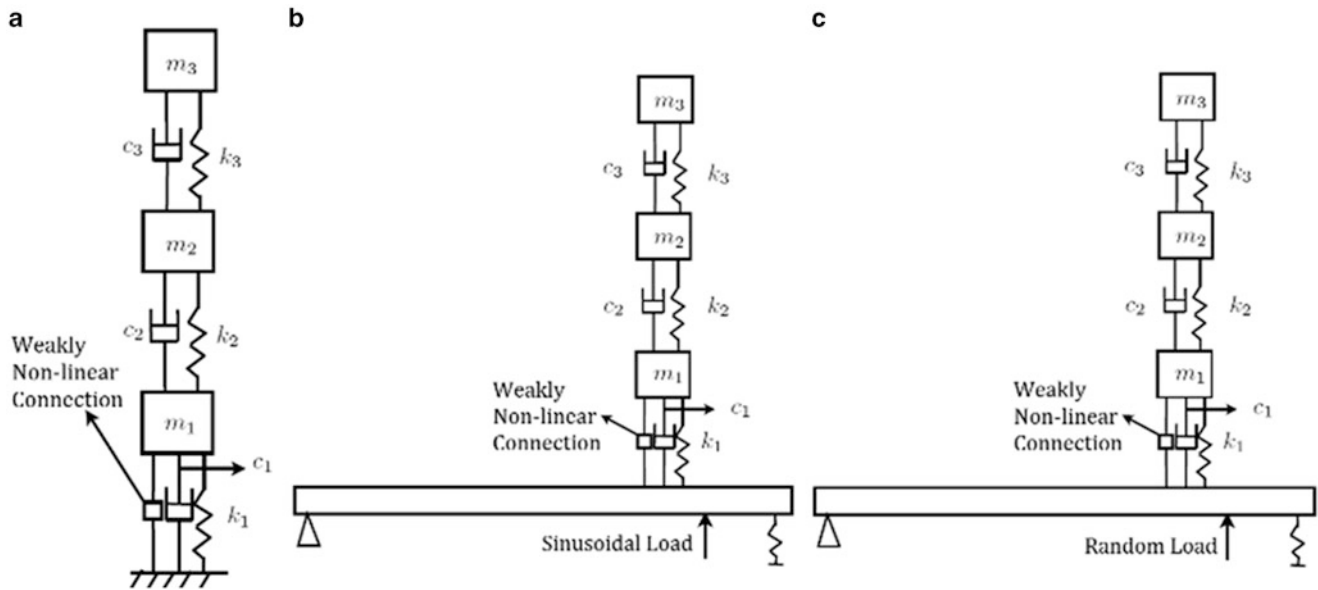


Fig. 14.3 Structural dynamics challenge problem. (a) Level 1, (b) Level 2, (c) Level 3

At Level 2, the dynamic system is mounted on a beam supported by a hinge at one end and a spring at the other end; another sinusoidal force input is applied on the beam. The configuration of the system level is the same as Level 2, but the input is a random process loading. Here Level 1 and Level 2 are defined as lower levels, and experimental data are only available at lower levels. All levels share three model parameters of spring stiffnesses  $k_i$  ( $i = 1, 2, 3$ ). The objective in this numerical example is to predict the maximum acceleration at  $m_3$  for the system level configuration.

In a multi-level problem, the lower levels and the system level constitute a hierarchy, sharing a set of model parameters ( $\theta$ ) to be calibrated. In order to predict the system level output when data are only available at lower levels, a reasonable route is to quantify the model parameters using lower level data, and propagate the results through the computational model at the system level. The procedure to predict the system level output can be found in Ref. [16], and a brief introduction is given here:

1. Model calibration by Bayesian inference. Three calibrations are possible: (1) calibration using the data from Level 1 alone; (2) calibration using the data from Level 2 alone; (3) calibration using the data from both Level 1 and Level 2. For a model parameter  $\theta$ , the posterior distributions from the calibrations above are denoted as  $f(\theta|D_1^C)$ ,  $f(\theta|D_2^C)$ , and  $f(\theta|D_1^C, D_2^C)$ , respectively.
2. Model validation using the model reliability metric at lower levels. The resultant model validity at Level 1 and Level 2 are denoted as  $P(G_1)$  and  $P(G_2)$ , respectively.
3. Uncertainty integration by the roll-up method. The integrated distribution for a model parameter  $\theta$  is in Eq. (14.9), where  $P(G_1') = 1 - P(G_1)$  and  $P(G_2') = 1 - P(G_2)$ .

**Table 14.3** Numerical details of the multi-level problem

Prior distributions of model parameters	$K_1 \sim N(5000, 500), K_2 \sim N(10000, 1000), K_3 \sim N(9000, 900)$
Measurement errors	$\epsilon_1 \sim N(0, 100), \epsilon_2 \sim N(0, 400)$
Nominal values of model parameters	$K_1^N = 5500, K_2^N = 9500, K_3^N = 8800$

**Table 14.4** Optimization details of the multi-level problem

$(N_1, N_2, N_3, N_4)$	$S_{K_1}^{\mu_Y}$	$S_{K_2}^{\mu_Y}$	$S_{U_{K_3}}^{\mu_Y}$	$S_{K_4}^{\mu_Y}$	$S_{K_1}^{V_Y}$	$S_{K_2}^{V_Y}$	$S_{U_{K_3}}^{V_Y}$	$S_{K_4}^{V_Y}$
(1,1,1,1)	401	23	147	13	831,223	324,801	56,590	88,297
(2,2,2,2)	231	114	108	446	417,587	359,898	26,889	687,488
(3,3,3,3)	166	23	162	29	455,399	426,526	25,324	47,175
(4,4,4,3)	102	21	147	11	324,321	365,224	22,686	55,704
(5,5,5,3)	61	20	144	13	283,422	322,376	21,332	61,831
(6,6,6,3)	38	19	126	14	181,811	290,937	17,728	68,511
(7,7,7,3)	22	17	111	16	144,947	255,802	20,771	75,866
(8,8,8,3)	16	15	100	17	126,595	226,772	21,952	79,556
(9,9,9,3)	8	14	91	18	108,430	206,501	24,446	84,001
(9,10,10,3)	7	12	78	19	112,662	182,936	29,802	86,057
(9,11,11,3)	7	11	67	19	119,376	162,681	35,286	86,797
(9,12,12,3)	7	10	57	20	116,832	148,899	42,855	86,486
(9,13,12,3)	7	8	57	20	119,997	124,831	40,493	85,393
(9,14,12,3)	8	8	57	20	119,913	122,778	40,345	84,689

4. System response prediction. The integrated distributions of  $\theta$  are propagated into the computational model at the system level to predict the system response.

$$\begin{aligned}
f\left(\theta \mid D_1^{C,V}, D_2^{C,V}\right) &= P(G_1) P(G_2) f\left(\theta \mid D_1^C, D_2^C\right) + P(G_1^*) P(G_2) f\left(\theta \mid D_2^C\right) \\
&+ P(G_1) P(G_2^*) f\left(\theta \mid D_1^C\right) + P(G_1^*) P(G_2^*) f(\theta)
\end{aligned} \quad (14.9)$$

Four types of tests are available in this multi-level problem: (1) test to provide calibration data at Level 1; (2) test to provide validation data at Level 1; (3) test to provide calibration data at Level 2; and (4) test to provide validation data at Level 2. The number of tests for each type is denoted as  $N_1, N_2, N_3$ , and  $N_4$ , respectively. The measurement error at Level 1 and Level 2 are denoted as  $\epsilon_1$  and  $\epsilon_2$ . Similar with the illustrative example, synthetic data are generated based on model input, nominal values of the model parameters, and measurement error. In this problem, the model inputs at each level are fixed. Numerical details of this problem are shown in Table 14.3.

The robust test planning is conducted following the four steps in Sect. 14.3:

1. The GSA is firstly conducted at  $N_1 = N_2 = N_3 = N_4 = 1$ . For the mean value of the prediction, the absolute contributions of data value uncertainty in four types of test are:  $S_{K_1}^{\mu_Y} = 401$ ,  $S_{K_2}^{\mu_Y} = 23$ ,  $S_{U_{K_3}}^{\mu_Y} = 147$ ,  $S_{K_4}^{\mu_Y} = 13$ ; for the variance of the prediction, the absolute contributions of data value uncertainty in four types of test are  $S_{K_1}^{V_Y} = 8.31 \times 10^5$ ,  $S_{K_2}^{V_Y} = 3.25 \times 10^5$ ,  $S_{U_{K_3}}^{V_Y} = 5.66 \times 10^4$ ,  $S_{K_4}^{V_Y} = 8.83 \times 10^4$ ;
2. The threshold for  $\mu_Y$  and  $V_Y$  are chosen as:  $\lambda_{\mu_Y} = 0.15 \max\left(S_{K_i}^{\mu_Y} \mid N_1 = N_2 = N_3 = N_4 = 1\right) = 60$ ,  $\lambda_{V_Y} = 0.15 \max\left(S_{K_i}^{V_Y} \mid N_1 = N_2 = N_3 = N_4 = 1\right) = 1.25 \times 10^5$ ;
3. Increase  $N_i$  by 1 until  $S_{K_i}^{V_Y} > \lambda_{\mu_Y}$  and  $S_{K_i}^{V_Y} > \lambda_{V_Y}$ ; the details for this iteration are shown in Table 14.4.

Some observations for this multi-level problem can be obtained from Table 14.4:

1. As  $N_i$  increases but is still small, the contribution of data value uncertainty may increase. For example, as  $(N_1, N_2, N_3, N_4)$  increases from (1,1,1,1) to (2,2,2,2),  $S_{K_2}^{\mu_Y}$  increases from 23 to 114 and  $S_{K_4}^{V_Y}$  increases from 88,297 to 687,488 dramatically. The reason is that at small sizes data sets can be very different from each other.
2. As  $N_i$  keeps increasing, the contribution of data value uncertainty globally shows a decreasing tendency; however local increases are observed, caused by numerical errors in the GSA when the contribution itself is comparatively small.

The optimization for the illustrative example terminates at (9, 14, 12, 3), meaning that only a small number of validation tests at Level 2 are needed, compared to the other three steps of tests, in order to achieve a robust prediction of the maximum acceleration of mass 3 at the system level.

## 14.5 Summary

A framework of robust test planning is established in this paper. Robust prediction is obtained for a given number of tests at which the contribution of data value uncertainty is reduced below a threshold. First a novel seed-based computational technique based on pseudo-random numbers is proposed to efficiently represent the uncertainty in the data values for a given data size (i.e., number of tests). Then the contribution of data value uncertainty is quantified by the proposed seed-based method and global sensitivity analysis. Then an optimization for robust test planning is proposed to reduce the contribution of data value uncertainty to the overall prediction uncertainty. This optimization is solved by a greedy methodology.

**Acknowledgements** The research in this paper is partially supported by funds from Sandia National Laboratories through contract no. BG-7732 (Technical Monitor: Dr. Angel Urbina). This support is gratefully acknowledged. The authors also appreciate valuable discussions with Shankar Sankararaman (NASA Ames) and Joshua Mullins (Sandia National Laboratories).

## References

1. Rajashekhar MR, Ellingwood BR (1993) A new look at the response surface approach. *Struct Saf* 12:205–220
2. Rasmussen CE, Williams CKI (2006) *Gaussian Processes for Machine Learning*. MIT Press
3. Ghanem R, Spanos PD (1990) Polynomial chaos in stochastic finite elements. *J Appl Mech* 57(1):197–202, no 89
4. Liepe J, Filippi S, Komorowski M, Stumpf MPH (2013) Maximizing the information content of experiments in systems biology. *PLoS Comput Biol* 9(1). e1002888
5. Sankararaman S, McLemore K, Mahadevan S, Bradford SC, Peterson LD (2013) Test resource allocation in hierarchical systems using Bayesian networks. *AIAA J* 51(3):537–550
6. Mullins J, Li C, Mahadevan S (2014) Optimal selection of calibration and validation test samples under uncertainty. In *IMAC XXXII*. Orlando, FL
7. O'Hagan A, Stevens JW (2003) Assessing and comparing costs: how robust are the bootstrap and methods based on asymptotic normality? *Health Econ* 12(1):33–49
8. Saltelli A, Ratto M, Andres T, Campolongo F, Cariboni J, Gatelli D, Saisana M, Tarantola S (2008) *Global sensitivity analysis: the primer*. John Wiley & Sons
9. Sobol IM (2001) Global sensitivity indices for nonlinear mathematical models and their Monte Carlo estimates. *Math Comput Simul* 55(1–3):271–280
10. Matsumoto M, Nishimura T (1998) Mersenne twister: a 623-dimensionally equidistributed uniform pseudo-random number generator. *ACM Trans Model Comput Simul* 8(1):3–30
11. L'ecuyer P (1999) Good parameters and implementations for combined multiple recursive random number generators. *Oper Res* 47(1): 159–164
12. Matteis A, Pagnutti S (1993) Long-range correlation analysis of the Wichmann-Hill random number generator. *Stat Comput* 3(2):67–70
13. Sankararaman S, Mahadevan S (2013) Separating the contributions of variability and parameter uncertainty in probability distributions. *Reliab Eng Syst Saf* 112:187–199
14. Schrijver A (1998) *Theory of linear and integer programming*. John Wiley & Sons
15. Red-Horse JR, Paez TL (2008) Sandia National Laboratories validation workshop: structural dynamics application. *Comput Meth Appl Mech Eng* 197(29–32):2578–2584
16. Li C, Mahadevan S (2014) Uncertainty quantification and output prediction in multi-level problems. In: 16th AIAA Non-Deterministic Approaches Conference, American Institute of Aeronautics and Astronautics



# Chapter 15

## Predictive Validation of Dispersion Models Using a Data Partitioning Methodology

Gabriel Terejanu

**Abstract** Validation of models used in safety-critical applications requires an extensive validation protocol to build confidence in their predictive capability. A recent predictive validation methodology, introduced by the author and collaborators, is applied in this study to validate the predictions of a Gaussian puff dispersion model. The methodology is based on cross-validation principles in the context of predicting unobserved or difficult to observe quantities of interest. The challenge in this context is that predictions of quantities of interest have no associated observations that they can be compared to. Thus, assessing how close predictions are from observations using validation metrics such as root-mean-square error is not feasible. The study addresses the issue of partitioning the data into a calibration and a validation set, and defining relevant validation metrics based on sensitivity analysis that can support the ultimate goal of predictive modeling. While the framework is general and can be applied to a wide range of problems, in this paper it is used to find an optimal partition of chemical concentration sensors to assess the validity of Gaussian puff predictions in a region of interest.

**Keywords** Data partitioning • Predictive validation • Bayesian inference • Cross-validation • Gaussian plume models

### Nomenclature

$p(\cdot)$	Probability density function (pdf)
$p(\cdot \cdot)$	Conditional pdf
$F(t), G(t)$	Cumulative distribution function (cdf)
$d(F(t), G(t))$	Distance between two cdfs
$\theta$	Model parameters
$D_c, D_v$	Calibration and validation data
$M_D, M_Q$	Data and quantity of interest (QoI) metric
$M_D^*, M_Q^*$	Data and QoI thresholds
$s_k, s^*$	$k$ th partitioning of the data and optimal partition
$\mathcal{N}(\mu, \sigma^2)$	Gaussian density function with mean $\mu$ and variance $\sigma^2$
$\log \mathcal{N}(\mu, \sigma^2)$	Log-normal density function with mean $\mu$ and variance $\sigma^2$

### 15.1 Introduction

Model validation is defined as the process of determining whether a mathematical model is a sufficient representation of reality from the perspective of the intended uses of the model [1, 4, 5]. Generally, the validity of a computational model is often determined by simply comparing the output of the model with experimental data [6, 8, 13–17]. However, many of these procedures neglect the most common use case, where data is not available to directly assess predictions of the quantities of interest (QoI). This paper examines this type of situations in which models are used to make predictions at scenarios where experimental data is not available, referred here as *prediction scenarios*. Here, scenario is defined as the set of conditions (inputs) of the physical system or experiment to be simulated by the model. Several issues make the problem of prediction

---

G. Terejanu (✉)

Department of Computer Science and Engineering, University of South Carolina, 315 Main St., Columbia, SC 29208, USA  
e-mail: [terejanu@cec.sc.edu](mailto:terejanu@cec.sc.edu)

a challenging one: experiments may be impractical or impossible due to various factors such as financial and regulatory constraints or physical limitations. Furthermore, the only experimental data available may come from legacy experiments and may be incomplete. Despite these difficulties, the assessment of QoI prediction quality is required to decide whether the model can be reliably used from the perspective of its intended use.

In general, the standard validation procedure requires the data to be partitioned in two datasets: the *calibration* (or training) set and the *validation* set. The calibration dataset is used to calibrate the model, and then the prediction outputs of the calibrated model are compared with the data in the validation set. A reasonable discrepancy between predictions and data increases the credibility of the model while a large discrepancy may invalidate the model. The initial step raises the question of how to partition the data, but the answer is far from trivial. Cross-validation attempts to address this issue by using multiple splits of the data and averaging the results of the model discrepancy from each split. However, existing cross-validation techniques do not address validating the model with respect to the QoI, but only with respect to the data. On the other hand, the more recently developed QoI-driven validation addresses the issue of prediction, but has not yet explored the issue of partitioning the data in depth.

Babuška et al. [7] presented a systematic approach to assess predictions using Bayesian inference and what they call a validation pyramid. Experimental scenarios of varying complexity are available that suggest an obvious hierarchy on which to validate the model. In their calibration phase, Bayesian updating is used to condition the model on the observations available at lower levels of the pyramid. The model's predictive ability is then assessed by further conditioning using the validation data at the higher levels. One advantage of their approach is that the prediction metric is directly related to the QoI. This approach relies on a subjective partition of the data, which is argued that is made clear by the experimental set-up and validation pyramid. However, in practice this is often not the case. The distinction between calibration and validation scenarios depends on the sensitivity of uncertain parameters with respect to the observables, which is not so clear without a more comprehensive analysis.

To avoid a subjective choice of the calibration set, the author and collaborators [12] have recently introduced a more rigorous and quantitative process inspired by cross-validation to partition the data into calibration and validation sets. In contrast to previous works, this approach does not require a single partitioning, nor does it use averages of estimators over multiple splits [2, 3, 20]. Instead, it considers all possible ways to split the data into disjoint calibration and validation sets which satisfy a chosen set size. Then by analyzing several splits, the optimal partitioning is chosen by requiring that it satisfies the following desiderata: (1) the model is sufficiently informed by the calibration set, and is thus able to reproduce the data, and (2) the validation set challenges the model as much as possible with respect to the QoI. Once the optimal split is found, the validity of the model is determined using the same procedure introduced by Babuška et al. [7].

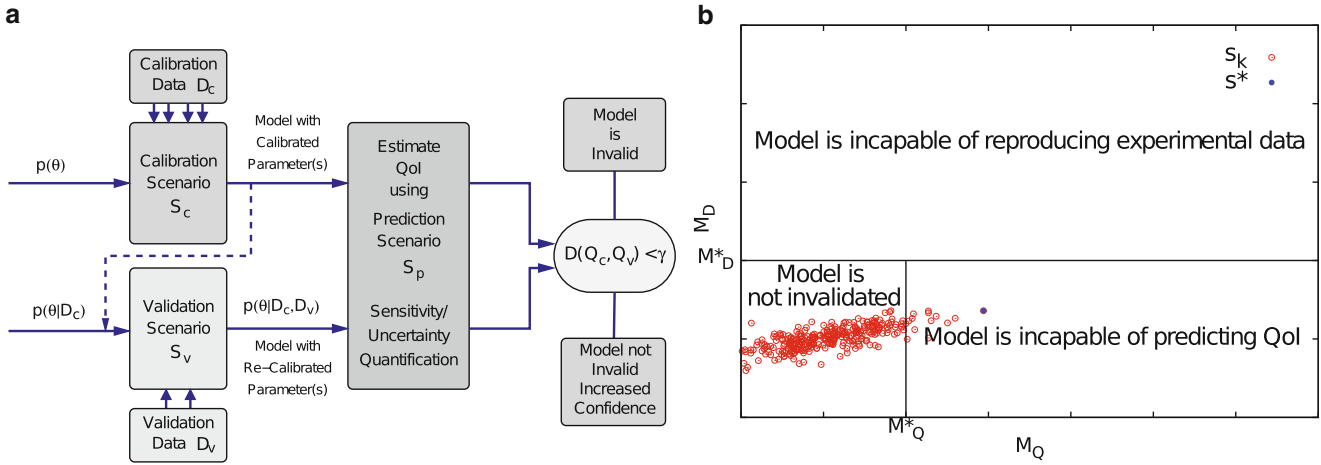
In this paper, this cross-validation inspired data partitioning is used to find an optimal partition of chemical concentration sensors to assess the validity of Gaussian plume predictions in a region of interest that lacks measurements. While intuition prompts one to construct the validation set from data provided by sensors that are closest to the prediction scenario, the analysis here reveals the contrary. Namely, it is shown that the best split in calibration and validation sets for this particular application involves selecting the most distant sensors from the region of interest in the validation set and the closest in the calibration set. This data partitioning methodology is introduced in the next section, followed by the numerical results on a Gaussian puff model.

## 15.2 Data Partition Methodology for Validation of Predictive Models

The QoI-driven model validation framework introduced by Babuška et al. [7] is depicted in Fig. 15.1a. Compared with other validation methods, the QoI-driven model validation tests the model with respect to the QoI which is not directly observable. Given that no data is available to be compared with the QoI prediction, this methodology consists of judging the validity of the model with respect to the discrepancy between two predictions of the same model. One prediction is given by a model updated with calibration data and the other by a model updated with all the data (calibration and validation). Since this QoI-driven validation is done in the presence of measurement and parametric uncertainty, Bayesian inference [10, 11] is used to determine the posterior and predictive distributions. In this context, Bayesian updating is performed on a calibration set, and then a prediction of the QoI is made using the updated model. A subsequent update is performed using a validation set followed by an additional prediction with the newly updated model. Finally, the two predictions are compared to assess the model's predictive capabilities.

Given  $D_c$  the calibration data, and  $\theta$  the uncertain model parameters, with prior probability density function (pdf)  $p(\theta)$ , Bayes' rule states that the posterior pdf  $p(\theta|D_c)$  is given by

$$p(\theta|D_c) \propto p(D_c|\theta)p(\theta), \quad (15.1)$$



**Fig. 15.1** Validation of predictive models. (a) QoI-driven validation cycle. (b) Cross-validation inspired data partitioning

where  $p(D_c|\theta)$  is the likelihood of observing data  $D_c$  given parameter values. Similarly, a second posterior pdf  $p(\theta|D_c, D_v)$  can be obtained using all the available data. The degree of knowledge, or rather the uncertainty, about the parameter values is completely accounted for by these posterior pdfs, which are then propagated through the model to obtain the predictive pdfs of the QoI, which can then be compared to determine the validity of the model.

The QoI driven model assessment developed in [7] requires a metric to compare predictions of the QoI obtained from the calibration and validation sets. Since predictions are probabilistic in nature, the metric used has to be compatible with probabilistic inputs. Ideally this metric would measure in the units of the QoI, allowing for easy interpretation by decision-makers on how consistent the predictions are. Ferson et al. [9] argue that Kantorovich metric can both accommodate probabilistic inputs and be expressed in terms of QoI units. Kantorovich metric calculates the area between two cdfs  $F(t)$  and  $G(t)$  and it is used to measure the disagreement between the two probabilistic predictions.

$$d(F(t), G(t)) = \int_{-\infty}^{\infty} |F(t) - G(t)| dt \quad (15.2)$$

The data partitioning methodology proposed by the author and collaborators [12], leverages this QoI-driven framework but in addition instead of relying on a subjective data split, uses a quantitative process to determine an optimal split. Here, optimality is given by the partitioning of the data that satisfies the following desiderata: (1) the model is sufficiently informed by the calibration set, and is thus able to reproduce the observed data, and (2) the validation set challenges the model as much as possible with respect to the quantity of interest. First, a model incapable of reproducing observations should not be used to predict unobservable quantities of interest. Specifically in the case of Bayesian updating, the prior information and observed data must be sufficient to produce a satisfactory posterior distribution for the model parameters. Second, the validation set should be the most challenging possible to assess QoI predictions. In other words, the model is required to perform well on even the most challenging of validation sets; otherwise, one cannot be confident in its predictive capability with respect to the QoI.

Two metrics need to be defined to judge how well the model meets these two criteria. One metric to measure how well the model is reproducing the data and the other to measure the predictive performance of the model. Let  $M_D$  and  $M_D^*$  denote the data reproduction metric and threshold respectively. Similarly,  $M_Q$  and  $M_Q^*$  are used to measure the discrepancy in the QoI prediction. While the data partitioning procedure can accommodate any suitable metrics, in this work both the data and QoI metric are given by the Kantorovich metric defined in Eq.(15.2). In the case of the data reproducibility, the area metric is defined between the empirical distribution of the data and the predictive distribution of the observable. For QoI assessment, the area metric is defined between the predictive distribution of the QoI given the calibration data and the predictive distribution of the QoI conditioned on all the data (calibration and validation).

Given  $N$  observations, we denote the size of the calibration set by  $N_C$  and the size of the validation set by  $N_V$ ,

$$N_C + N_V = N. \quad (15.3)$$

Note that it could be the case that each of the  $N$  observations in fact represents a set of observations, if, for instance, repeated experimental measurements are taken at the same conditions. As with many validation schemes, the selection of the calibration, or training, set size is important. This set size can vary greatly [2, 3], and the particular choice could impact the final conclusion and must be made with care. Of particular concern is providing enough data so that all parameters of the model are sufficiently informed by the inverse problem. If the model were to fail with respect to the data metric, the issue may not be the model itself but too small a calibration set size. In this case one should perform further analysis to determine the source of this discrepancy and increase the calibration set size if necessary. Regardless, the partitioning framework is generally applicable to whatever this size might be.

To determine the optimal split, all possible partitions of the data respecting (15.3) are considered. By considering all admissible partitions, one can determine which observations are most influential with respect to the QoI. However, the drawback of this approach is evident: consider the model performance for all partitions of the data. This yields a combinatorially large number of partitions, whose exact number is given by the binomial formula:

$$P = \binom{N}{N_C} = \frac{N!}{N_C!N_V!}. \quad (15.4)$$

Here these partitions, or splits, are denoted by  $\{s_k\}$ , where  $k = 1, 2, \dots, P$ . The computational impact of this becomes even more significant while solving  $P$  Bayesian inverse problems using Eq.(15.1). This is an area for improvement and it is set as subject of future work.

With the solutions obtained from the inverse problems one can evaluate the performance of the model by computing the data and QoI metrics. These can be visualized on a Cartesian grid where the  $x$  and  $y$  axes correspond to the metrics  $M_Q$  and  $M_D$ , respectively, and each point corresponds to a single partition of the data into a calibration and validation set, see Fig. 15.1b. The optimal partition  $s^*$  is given by the following optimization problem which requires the calibration data to sufficiently inform the model to reproduce the data and the validation data to maximize the prediction metric.

$$s^* = \arg \max_{s_k, M_D(s_k) < M_D^*} M_Q(s_k). \quad (15.5)$$

The optimal partition for the results shown above is highlighted in Fig. 15.1b. After identifying the optimal partition one can compare model's predictive performance against the threshold  $M_Q^*$ . If  $s^*$  fails to satisfy the threshold then it can be concluded that the model is invalid given the observations available. In the case where  $s^*$  does not violate the tolerance set by the decision-maker, it can be concluded that the model is not invalidated given the observations. This does not guarantee that the model is valid, only that one cannot demonstrate otherwise. This may prompt the acquisition of additional observations to challenge the model. The process to obtain these additional experimental measurements may be supplemented by performing optimal experimental design [19]. If, however, we cannot obtain more data, then the process is complete, and we conclude that the model has not been invalidated. The general algorithm can be summarized in Algorithm 1.

---

#### Algorithm 1 Data partitioning algorithm

---

- 1: Define data metric and threshold,  $M_D$  and  $M_D^*$
- 2: Define prediction metric and threshold,  $M_Q$  and  $M_Q^*$
- 3: Given  $N$ , choose the calibration set size,  $N_C$ , such that

$$N_C + N_V = N.$$

- 4: Generate all possible partitions of the data  $\{s_k\}_{k=1}^P$ , where  $P = \binom{N}{N_C} = \frac{N!}{N_C!N_V!}$
  - 5: Solve  $P$  inverse problems for partitions  $\{s_k\}_{k=1}^P$ .
  - 6: For each partition  $s_k$ , compute  $M_D(s_k)$ .
  - 7: Solve an additional inverse problem using all available data (calibration and validation)
  - 8: For each partition  $s_k$ , compute  $M_Q(s_k)$ .
  - 9: Find optimal partition  $s^* = \arg \max_{s_k, M_D(s_k) < M_D^*} M_Q(s_k)$
  - 10: Compare  $M_Q(s^*)$  with  $M_Q^*$ .
-

### 15.3 Data Partitioning for a Gaussian Puff Model

This section describes an application of determining the optimal partition for a Gaussian puff model. The model in Eq. (15.6) is given by the steady-state Gaussian plume solution to the advection-diffusion equation under assumptions of isotropic diffusion and constant wind velocity,  $u = 1$ , which is sufficiently large such that the longitudinal diffusion term can be neglected [18]. Here  $c(x, y)$  is the ground concentration at an  $(x, y)$  location,  $Q$  is the release mass,  $H = 1$  is the height of the release and  $K = 1$  is the eddy diffusivity.

$$c(x, y) = \frac{Q}{2\pi Kx} \exp\left(-\frac{u(y^2 + H^2)}{4Kx}\right) \epsilon_{\text{meas}} \tag{15.6}$$

In this study, it is considered that a set of six noisy concentration readings are available corresponding to the six sensors depicted in Fig. 15.2a. Both the release mass and the wind velocity are considered uncertain. Given these six measurements, the goal is to divide them in a calibration and validation set, both containing three data points, in order to assess the capability of the model to predict the concentration in the region of interest shown also in Fig. 15.2a. The distribution of the measurement noise and the prior distribution for the release mass and the wind velocity are given as follows.

$$p(\epsilon_{\text{meas}}) = \log \mathcal{N}(0, 1), \quad p(Q) = \log \mathcal{N}(2, 10), \quad p(u) = \mathcal{N}(2, 0.5) \tag{15.7}$$

The synthetic measurement data is generated from the true model where  $Q = 1$  and  $u = 1$ . For a specific run, the measurements obtained for various sensors as well as the distance of these sensors to the region of interest are given in Table 15.1. Given the distances from the region of interest, see Table 15.1 and Fig. 15.2a, intuitively, one would expect that the optimal split would be to have the validation set comprising readings of sensors (4, 5, 6) and calibration set comprising readings of sensors (1, 2, 3). For this split the data metric is found to be  $M_D = 1.03$  and the QoI metric  $M_Q = 0.27$ . The data metric is well within the tolerance of the measurement noise  $M_D^* = 1.75$ , however the question is whether this split challenges the model enough with respect to the QoI.

However, the data partitioning methodology introduced in the previous section, after computing the metrics for all possible partitions of size three, gives the optimal split as the calibration set comprising of sensors (3, 5, 6) and the validation set comprising of sensors (1, 2, 4). In this case the  $M_D = 1.09$  and the QoI metric  $M_Q = 0.61$ . Again, the data metric indicates

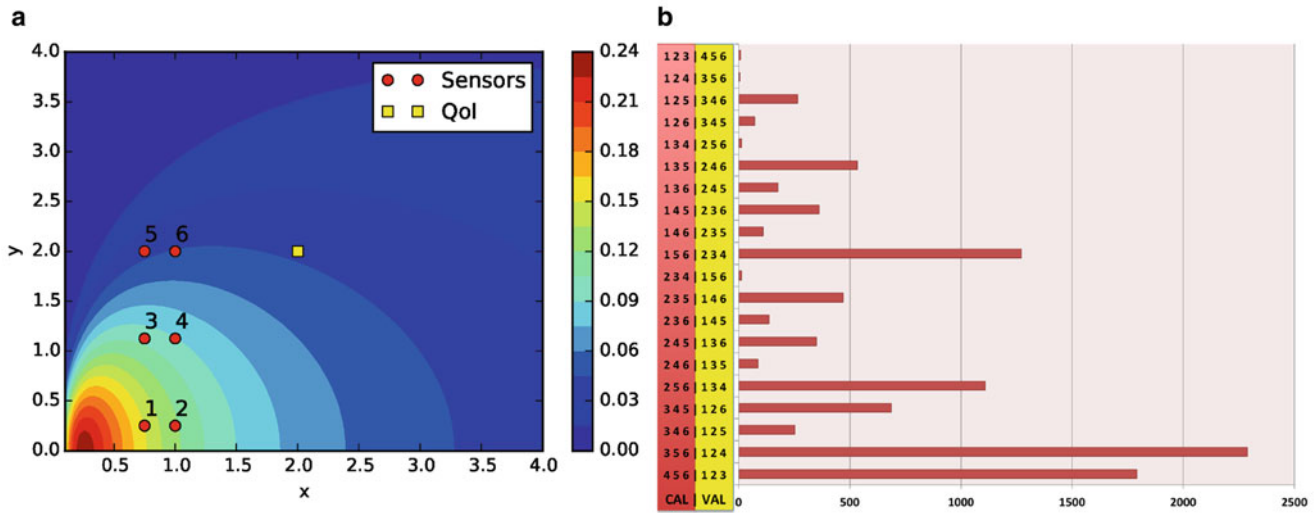


Fig. 15.2 Numerical results. (a) True concentration field, location sensors and region of interest. (b) Optimal split distribution given 10,000 trial

Table 15.1 Measurements for a specific run and distance of various sensors to the region of interest

Sensor	1	2	3	4	5	6
Measurement	0.16	0.11	0.19	0.06	0.10	0.04
Distance	2.15	2.01	1.52	1.39	1.25	1.00

that the model is well calibrated, and as compared with the previously intuitive split, the QoI metric for the optimal split is almost three times as challenging. Also note that validation set contains sensors, which are farther away from the region of interest instead of closer to it.

Obviously, the results are conditioned on the measurements available, and one may question the finding as being particular to the instance of measurement noise. To address this issue, a number of 10,000 trials have been performed, each corresponding to different measurement noise instances. For each trial the optimal split has been identified, and the overall distribution of the optimal split has been plotted in Fig. 15.2b. Note that most of the time the validation sets chosen contain sensors that are farther away from the region of interest instead of closer to it, which further motivates the uses this quantitative process to identify the partitioning of the data. In addition, note that the intuitive split at the top of Fig. 15.2b has produced very few optimal splits in the 10,000 trials, which prompts one to carefully consider the problem of partitioning the data in calibration and validation sets.

## 15.4 Conclusion

A data partitioning methodology has been introduced to determine the optimal split in calibration and validation sets to assess the predictive capability of a model. This cross-validation inspired methodology is applied in the context of unobserved QoIs, where the quality of the QoI prediction is determined via a sensitivity analysis approach. This procedure is used to determine the optimal partition of chemical concentrations to assess the predictive capability of a Gaussian plume models. For the example considered in this study, it is shown that the validation set should contain sensors farther away from the region of interest rather than closer as it might be dictated by intuition.

## References

1. AIAA Computational Fluid Dynamics Committee on Standards (1998) AIAA guide for verification and validation of computational fluid dynamics simulations. AIAA, G-077-1998
2. Alqallaf F, Gustafson P (2001) On cross-validation of bayesian models. *Can J Stat* 29(2):333–340
3. Arlot S, Celisse A (2010) A survey of cross-validation procedures for model selection. *Stat Surv* 4:40–79
4. ASME Committee V&V 10 (2006) Standard for verification and validation in computational solid mechanics. ASME
5. ASME Committee V&V 20 (2009) Standard for verification and validation in computational fluid dynamics and heat transfer. ASME
6. Babuška I, Nobile F, Tempone R (2008) A systematic approach to model validation based on Bayesian updates and prediction related rejection criteria. *Comput Methods Appl Mech Eng* 197:2517–2539
7. Babuška I, Nobile F, Tempone R (2008) A systematic approach to model validation based on bayesian updates and prediction related rejection criteria. *Comput Methods Appl Mech Eng* 197(29–32):2517–2539 [validation challenge workshop]
8. Balci O (1997) Verification validation and accreditation of simulation models. In: Proceedings of the 29th winter simulation conference, WSC '97. IEEE Computer Society, Washington, pp 135–141
9. Ferson S, Oberkampf WL, Ginzburg L (2008) Model validation and predictive capability for the thermal challenge problem. *Comput Methods Appl Mech Eng* 197(29–32):2408–2430
10. Howson C, Urbach P (1989) Scientific reasoning: the bayesian approach. Open Court Publishing Company, Chicago
11. Jaynes ET (2003) Probability theory: the logic of science. Cambridge University Press, Cambridge
12. Morrison RE, Bryant CM, Terejanu G, Prudhomme S, Miki K (2013) Data partition methodology for validation of predictive models. *Comput Math Appl* 66(10):2114–2125
13. Oberkampf W, Roy C (2010) Verification and validation in scientific computing. Cambridge University Press, Cambridge
14. Oberkampf WL, Trucano TG (2007) Verification and validation benchmarks. Technical Report SAND2007-0853, Sandia National Laboratories, Unlimited Release
15. Roache PJ (2008) Perspective: validation-what does it mean? *ASME J Fluids Eng* 131(3):1–3
16. Roache PJ (2009) Fundamentals of verification and validation. Hermosa Publishers, Albuquerque
17. Sargent RG (1998) Verification and validation of simulation models. In: Proceedings of the 30th winter simulation conference, WSC '98. IEEE Computer Society Press, Los Alamitos, pp 121–130
18. Stockie J (2011) The mathematics of atmospheric dispersion modeling. *SIAM Rev* 53(2):349–372
19. Terejanu G, Upadhyay RR, Miki K (2012) Bayesian experimental design for the active nitridation of graphite by atomic nitrogen. *Exp Therm Fluid Sci* 36:178–193
20. Vehtari A, Lampien J (2002) Bayesian model assessment and comparison using cross-validation predictive densities. *Neural Comput* 14: 2439–2468

# Chapter 16

## SICODYN Research Project: Variability and Uncertainty in Structural Dynamics

Sylvie Audebert

**Abstract** The idea underlying the SICODYN (Simulations credibility via test-analysis CORrelation and uncertainty quantification in structural DYNamics) funded research project is to give easy tools, based on tested methodologies, to a priori estimate the confidence associated to a dynamical simulation-based prediction. The project is based on a complex built-up pump in industrial environment. Gathering 13 French academic and industrial partners, it is organized in 6 parts. In Part 1, an inventory of the benchmarks in structure dynamics and a review of methods leading to credible models are performed. Experimental benchmarks based on in-situ measurements permit the quantification of experimental variability, related to nominally-identical structures or due to operator and modal identification methodology (Part 2). Numerical benchmarks (Part 3) lead to observe the corresponding total numerical variability. Part 4 is devoted to test-analysis correlation methods. In Part 5, both parametric and non parametric methods are confronted in order to quantify the parametrical and model-form uncertainties, either in a deterministic (method of intervals . . . ) or probabilistic context. The objective of Part 6 is to estimate the capacity of uncertainty quantification methods to represent the observed numerical variability, and to select, or adapt, some of them, to propose simple tools usable in industrial context.

**Keywords** Vibrating mechanics • Numerical and experimental benchmarks • Modal characteristics • Uncertainty quantification

### 16.1 Context and Objectives

A main objective of industrial companies is to quantify the confidence they have in numerical models used either in design purpose or in expertise purpose. The systems of interest include proposed or existing systems that operate at design conditions, at off-design conditions and at failure-mode conditions that apply in accident scenarios. In particular, the dynamical behaviour of engineered systems that equip power plants must be confidently predicted. The numerical models built to do so in a design purpose must be able to represent the characteristics of the structure itself, its coupling with its environment, the usually unknown excitations and the corresponding error sources and uncertainties; in an expertise purpose, when measurements can be carried out on the existing structure and used to improve the numerical-experimental correlation, the numerical models are generally generic and must be able to reproduce the behaviour of the whole family of nominally-identical structures.

### 16.2 Scientific Structuration of SICODYN Project

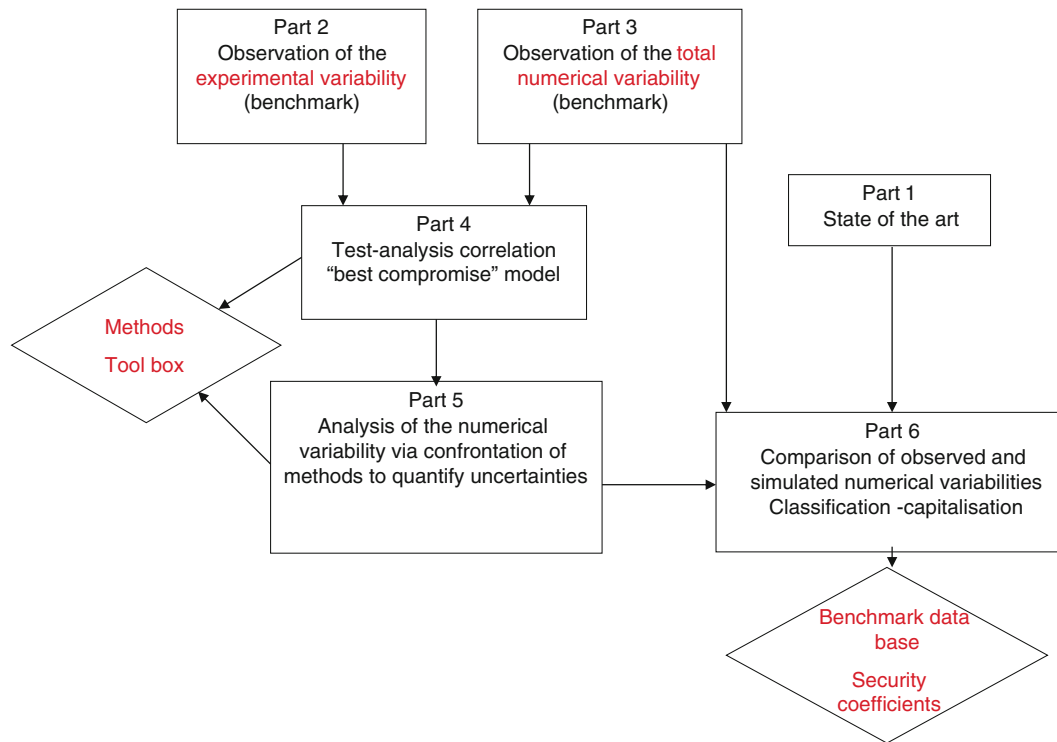
The funded FUI (Fonds Unique Interministériel) 2012–2016 project, untitled SICODYN, follows the international 2008–2010 SICODYN benchmark [1, 2]. It is based on a complex built-up demonstrator in industrial environment. The project gathers 13 French academic and industrial partners [3].

The idea underlying the project is to give easy tools, based on tested methodologies, to a priori estimate the confidence associated to a dynamical simulation-based prediction [4–7]. The general organization of the six interconnecting parts of the project is described in Fig. 16.1. The quantities of interest are the modal characteristics of the mechanical system (eigenfrequency, modeshape and modal damping). In Part 1, an inventory of the benchmarks in structure dynamics and a

---

S. Audebert (✉)

Acoustics and Mechanical Analyses Department, Electricité De France Research & Development, EDF Lab Clamart, 1 av. du Général de Gaulle, Clamart Cedex 92141, France  
e-mail: [sylvie.audebert@edf.fr](mailto:sylvie.audebert@edf.fr)



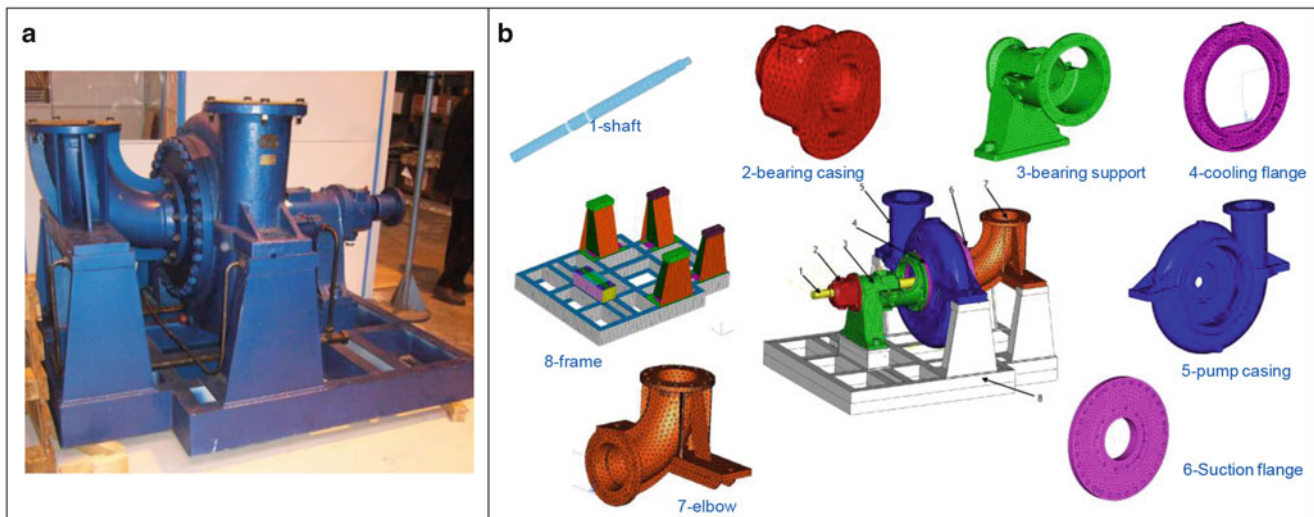
**Fig. 16.1** Organization of the six parts of the SICODYN project

review of methods leading to credible models are performed: test-analyses methods and ways to estimate the total uncertainty. In Part 2, experimental benchmarks based on laboratory and in-situ measurement campaigns permits the quantification of experimental variability, related to nominally-identical structures or due to operator and modal identification methodology. In addition, two laboratory devices are designed and used in order to improve and validate the numerical representation of a bolted assembly at macro-level. A numerical benchmark (Part 3) on the pump assembly considered in its work environment (complex boundary conditions that are frame fixed in concrete and connections with suction and delivery pipes) leads to observe the total numerical variability, which takes into account the parametric and model form uncertainty. Part 4 is devoted to test-analysis correlation and model updating, using notably a collection of numerical results and a collection of experimental measurements [8]. Methods to elaborate the best-estimate model, which both insures fidelity to measured data and robustness relatively to uncertainties, are comparatively tested. In Part 5, both parametric and non parametric methods are confronted in order to quantify the uncertainties, either in a deterministic (method of intervals . . .) or probabilistic context [9–11]. In Part 6, the observed (via the benchmark) and simulated (in Part 5) numerical variabilities will be compared. The most appropriate uncertainty quantification methods a priori represent the observed numerical variability, from an industrial point of view, will be selected and possibly derived in simple security coefficients and margins applied in classes of dynamical problems to determine, or simple tools usable in industrial context.

### 16.3 Description of the Demonstrator

The chosen equipment is a pump used in EDF thermal units (Fig. 16.2). It is a one-stage booster pump, composed of a diffuser and a volute, with axial suction and vertical delivery (body with volute called “snail”), mounted on a metallic frame. It was designed 40 years ago by Sulzer Pumps. The bolted built-up structure contains eight main components.





**Fig. 16.2** The pump assembly and its main components. (a) The pump assembly. (b) CAD models of the pump components

## 16.4 Innovative Characteristics and Technological Challenges

The main innovative characteristics of SICODYN project are following:

- Organization of an experimental benchmark in situ, with independent teams, in view of observing the variability of modal properties of a built-up structure (related to specimen, measurement means, identification methodology)
- Organization of a numerical benchmark in condition of a study performed by a design office, in view of observing the total numerical variability of a dynamic simulation
- Application of methods tested on academic structures to complex industrial large number of degree of freedom structures
- Improvement of the modeling at macro-level of bolted structure assemblies
- Taking into account the environment, represented by complex boundary conditions
- Model improvement by adaptation and comparison of numerical-experimental correlation methods
- Numerical estimation of the model form uncertainty, and not only the parametrical uncertainty
- Improvement of the model robustness relative to uncertainties
- Confrontation of observed and numerical variabilities, and elaboration of recommendations for the use of numerical methods to a priori estimate the confidence of simulation-based predictions
- Establishment of empirical laws to a priori estimate the credibility related to a dynamic simulation result

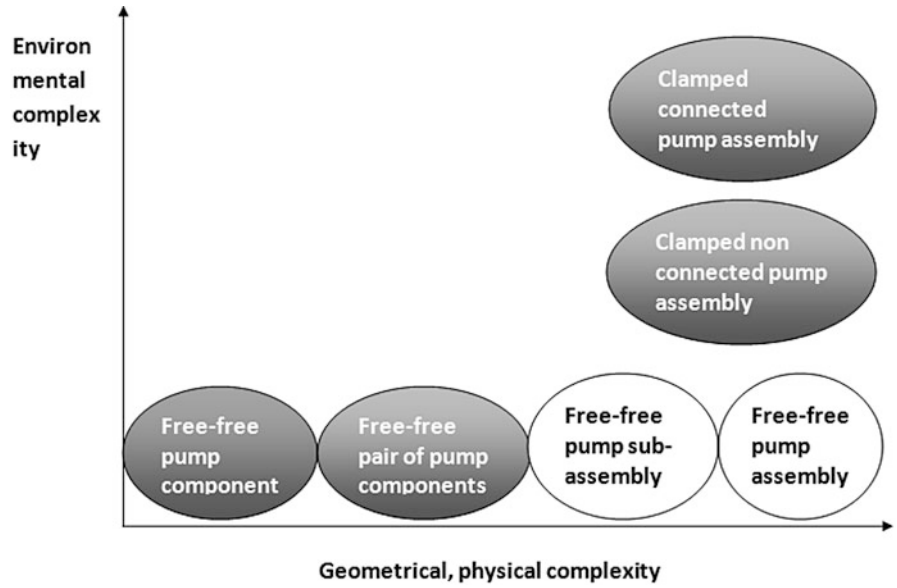
## 16.5 Benchmarks Purpose (Parts 2 and 3)

The benchmark purpose is clearly to observe, from an *industrial* point of view, that is in the real conditions of an engineering study, the variability of computational blind and experimental modal results. The general Verification and Validation (V&V) comprehensive methodology based on benchmarks described in [4] can be kept in mind and successfully applied within the purpose of the observation of the numerical or experimental variability: a step-by-step procedure from the free-free separate components to the built-up system with complex boundary conditions is so here applied.

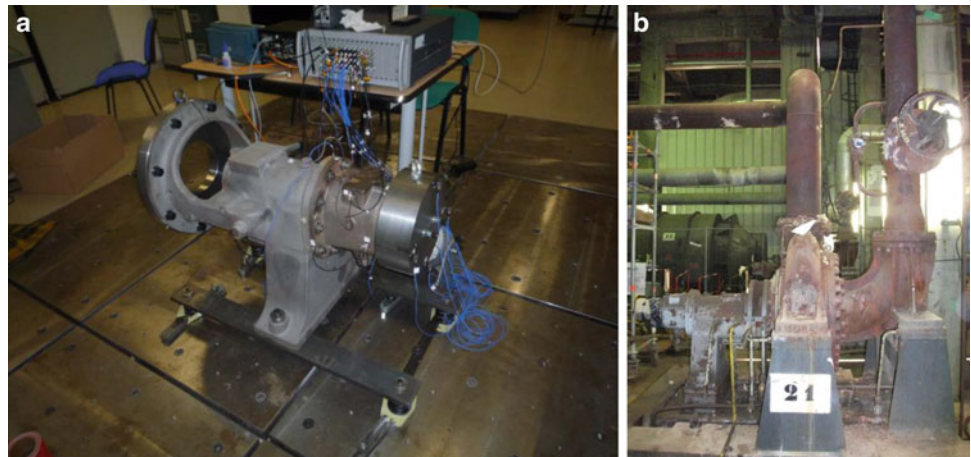
The dynamical systems of interest used for the benchmarking operations have been determined more and more the complexity of both the system and the boundary conditions, following the hierarchical process presented in Fig. 16.3:

- The eight free-free pump components;
- A two-component sub-assembly (Fig. 16.4a);
- The clamped pump assembly, not connected to pipes;
- The clamped pump assembly, connected to pipes (Fig. 16.4b).

**Fig. 16.3** The hierarchical procedure



**Fig. 16.4** The two-component assembly tested in laboratory and the pump in its industrial environment. (a) The two-component sub-assembly. (b) The pump, frame in concrete, connected to pipes, in thermal power plant



For each dynamical system, the modal basis on the bandwidth [0 Hz; 300 Hz] must be determined.

The number of independent blind simulated predictions and measurements are given in Table 16.1. Complementary simulations and corresponding experimental analyses have been performed by one partner only on a free-free pump sub-assembly and on the free-free pump assembly.

**Table 16.1** Number of independent benchmark simulated predictions and measurements

	Number of simulations	Number of measurements
Free-free pump components	8–10	0–1
Free-free pair of components	3	3
Free-free sub-assembly	1	1
Free-free pump assembly	1	1
Non connected clamped pump assembly	10	2
Connected pump assembly	7	5

### 16.5.1 Numerical Benchmarks

The numerical benchmarks have been organized in the framework of 2008–2010 international SICODYN benchmark [1, 2] and Part 3 of 2012–2016 SICODYN project. The industrial point of view is taken into account by the fact that (1) here input benchmark data are not equally determined for all the partners, in order to consider their inherent uncertainty (data provided by EDF are but paper plans of the assembled pump and its parts, and CAD models of the eight main pump components) (2) the chosen demonstrator is an industrial structure in use in EDF thermal units: it is well-representative of modeling and boundary conditions complexity; (3) reference experimental data have been partially obtained in situ. Concerning benchmark data, material characteristic values are chosen by partners. Representation of pump components, boundary conditions and connections between components is left free choice.

This original benchmark approach, described in [1, 2, 12], is well adapted to the questions an industrial company must answer and critical decisions it must take: what is the confidence level of the simulation-based predictions provided by design offices? Are they sufficiently robust to uncertainties to authorize the cancellation or the decrease of experimental tests which characterize the dynamical behavior?

### 16.5.2 Experimental Benchmarks

The experimental modal analysis campaigns have been performed in the framework of 2008–2010 international SICODYN benchmark [1, 2] and Part 2 of 2012–2016 SICODYN project. The configurations of interest are the following:

- shaft and impeller system, bearing support and pump casing in free-free conditions;
- bearing support and bearing casing system in free-free conditions (three experimental modal bases);
- shaft, bearing support, cooling flange and bearing casing sub-assembly in free-free conditions (one experimental modal basis);
- pump assembly in free-free conditions (one experimental modal basis);
- non rotating in situ non connected pump assembly, frame fixed in concrete (two experimental modal bases relative to two specimens);
- non rotating in situ pump assembly, connected to delivery and suction pipes, frame fixed in concrete (two experimental modal bases on one specimen, three experimental modal bases on another specimen).

As for numerical benchmarks, no precise instructions on the number of sensors, the excitation type or the identification methods to be used are given to the partners. The observed experimental variability so attached to measurement “reference” data is to be considered during test-analysis correlation.

## 16.6 Quantification of the Numerical Uncertainties (Part 5)

Besides the observation of variabilities thanks to benchmarking operations, a priori quantification of numerical uncertainties is performed using methods able to represent the observed level of uncertainties. Methods to do so must be able to address both parametrical and model-form uncertainties. Model-form uncertainty originates from assumptions or simplifications of known, or unknown, phenomena that must be represented in the numerical simulation. Some of the modeling assumptions that influence simulation results in structural dynamics include the use of 1D, 2D, or 3D representation to model a component of the structure, the method through which contact and boundary conditions are represented. Thus, attempt to quantify the effect of model-form uncertainty and, as a consequence, the total numerical uncertainty have been far less encountered [13]. The methods to quantify the total numerical uncertainty, applied on the pump assembly, are (1) the generalized probabilistic approach, including both the model-parameter uncertainties and the model form uncertainties in a separate way [14], (2) the lack of knowledge theory [15], which is based on intervals whose bounds are probabilistic, and (3) the combined use of the component mode synthesis and the probabilistic uncertainty analysis [10]. The comprehensive approach, that is application of these methods to a complex industrial dynamical system with large uncertainties, and confrontation of so estimated uncertainties with the observed variability, is a main challenge of the SICODYN project.

**Acknowledgements** The support of the FUI (Fonds Unique Interministériel) is gratefully acknowledged. The 13 partners currently involved in 2012–2015 SICODYN project are: AIRBUS Defence & Space, CETIM, EDF R&D, LMT ENS Cachan, Institut FEMTO-ST UMR CNRS 6174, LAMCOS UMR CNRS 5259 INSA Lyon, MSME UMR-CNRS 8208, NECS Numerical Engineering and Consulting Service, PHIMECA Engineering, SAMTECH, SOPEMEA, SULZER Pompes France, VIBRATEC.

## References

1. Audebert S (2010) SICODYN international benchmark on dynamic analysis of structure assemblies: variability and numerical-experimental correlation on an industrial pump. *Méc Ind* 11(6):439–451
2. Audebert S (2014) SICODYN international benchmark on dynamic analysis of structure assemblies: variability and numerical-experimental correlation on an industrial pump (Part 2). *Mec Ind* 15(1):1–17
3. Audebert S (2014) FUI 2012–2015 SICODYN project (pour des Simulations crédibles via la Corrélacion calculs-essais et l'estimation des incertitudes en DYNamique des structures). In: Proceedings IXxe symposium vibrations, shocks and noise, Aix en Provence, France, 17–19 June 2014
4. Roy CJ, Oberkampf WL (2011) A comprehensive framework for verification, validation, and uncertainty quantification in scientific computing. *Comput Methods Appl Mech Eng* 200:2131–2144
5. Unal C, Williams B, Hemez F, Atamturktur SH, Mc Clure P (2011) Improved best estimate plus uncertainty methodology, including advanced validation concepts, to licence evolving nuclear reactors. *Nucl Eng Des* 241:1813–1833
6. Atamturktur S, Hemez F, Williams B, Tome C, Unal C (2011) A forecasting metric for predictive modelling. *Comput Struct* 89:2377–2387
7. Pilch M, Trucano TG, Helton JC (2011) Ideas underlying the quantification of margins and uncertainties. *Reliab Eng Syst Saf* 96:965–975
8. Oberkampf WL, Barone MF (2006) Measures of agreement between computation and experiment: validation metrics. *J Comput Phys* 217: 5–36
9. Audebert S, Zentner I, Mikhevitch A (2011) Variability and propagation of uncertainties on modal simulations of a built-up structure (SICODYN benchmark). In: de Roeck G, Gegrande G, Lombaert G, Müller G et al (eds) Proceedings of the 8th international conference on structural dynamics, ISBN 978-90-760-1931-4, EUROODYN 2011, Leuven, 4–6 July 2011, pp 3000–3007
10. Audebert S, Fall-Lo F (2013) Uncertainty analysis on a pump assembly using component mode synthesis. In: Papadrakakis M, Papadopoulos V, et al (eds) Proceedings of COMPDYN 2013 4th ECCOMAS thematic conference on computational methods in structural dynamics and earthquake engineering, Kos Island, 12–14 June 2013
11. Hinke L (2008) Modelling approaches for the low-frequency analysis of built-up structures with non-deterministic properties. Phd thesis, University of Southampton, Faculty of Engineering, Science and Mathematics, Institute of Sound and Vibration Research, <http://eprints.soton.ac.uk>, April 2008
12. Audebert S, Ghavarian S, Kaici C (2014) Benchmark on modal characterization of built-up structures: numerical variability and test-analysis correlation on an industrial pump. In: Sas P, Moens D, Denayer H (eds) Proceedings XXVIe international ISMA noise and vibration engineering conference – ISMA2014, Leuven, 15–17 Sept 2014
13. Van Buren KL, Hall TM, Gonzales LM, Hemez FM, Anton SR (2015) A case study to quantify prediction bounds caused by model-form uncertainty of a portal frame. *Mech Syst Signal Process* 50–51:11–26
14. Batou A, Soize C, Audebert S (2015) Model identification in computational stochastic dynamics using experimental modal data. *Mech Syst Signal Process* 50–51:307–322
15. Daouk S, Louf F, Dorival O, Audebert S (2015) Stochastic modeling of uncertainties: a review of basic methods and application to simple and complex structures, in press

# Chapter 17

## Experimental Variability on Modal Characteristics of an In-Situ Pump

Sylvie Audebert, Anne Coulon, Marie-Ange Andrianoely, Stéphane Muller, and Emmanuel Foltête

**Abstract** Considering that experimental data, usually considered as the reference in test-analysis correlation and model updating purpose, must also be concerned with uncertainty quantification, the experimental variability on modal characteristics of two nominally-identical pumps in industrial environment is observed, via a benchmark between 5 independent teams. Free choice is let to determine the number and the type of sensors, the excitation means, the number of excitation points and the modal identification method. Variabilities relative to the operator and pump specimen are addressed; moreover specific variability relative to the modal identification phase can be quantified using the same experimental test runs.

Due to differences on experimental meshes, from 27 to 138 measurement points, a SEREP expansion on a finite element mesh is first performed, allowing the comparison of experimental modal bases. Global variability observed, based on half paired among identified eigenmodes (within 10 % frequency gap and 50 % MAC criteria), shows a 2 % mean frequency gap and 32 % mean damping ratio gap. Unit-to-unit variability, essentially attributed to different actual bolted torque levels at component connections and pipe-to-pump connections, and realization of the frame fixation on concrete, shows 10 % mean frequency gap and 28 % mean damping gap. Specific variability due to modal identification operator, as a component of the global variability, is still significant with a number of identified modes that varies by a factor of 2; the so paired modes show 1 % mean frequency gap and 24 % mean damping ratio gap.

**Keywords** Vibrating mechanics • Experimental benchmark • Modal characteristics • In situ measurement • Experimental variability

### 17.1 Context and Objectives

Experimental modal data resulting from in situ measurements are used in industrial context to characterize the dynamical behavior of a new-designed structure or to expertise a system with potentially vibrating problems; they are generally collected simultaneously to the elaboration of a numerical model of the structure considered, which can then be tuned using measurement data. Like numerical models, which intend to represent the dynamical behavior of nominally-identical systems, complete information on experimental modal data must include the overall range of measurements, attached to a given experimental data. Concerning the eigenfrequency variability, the overall range of measurements is  $[f_k^{\min}, f_k^{\max}]$ , where  $f_k^{\min}$  and  $f_k^{\max}$  respectively denote lower and upper bounds within which the measured eigenfrequency  $f_k$  is expected to be observed for a similar structure. The control parameters that can explain the experimental variability are the sensor type and location, the excitation type and location, the identification method used and its parameters, the system specimen considered.

---

S. Audebert (✉)

Acoustics and Mechanical Analyses Department, Electricité de France Research & Development,  
EDF Lab Clamart, 1 avenue du Général de Gaulle, Clamart Cedex 92141, France  
e-mail: [sylvie.audebert@edf.fr](mailto:sylvie.audebert@edf.fr)

A. Coulon  
VIBRATEC, 28 chemin du petit bois, BP 36, Ecully Cedex 69131, France

M.-A. Andrianoely  
LAMCOS, INSA Lyon, Bâtiment Jean d'Alembert, 18-20 rue des Sciences, Villeurbanne Cedex 69621, France

S. Muller  
AIRBUS Defence & Space, 51-61 route de Verneuil, BP 3002, Les Mureaux Cedex 78133, France

E. Foltête  
Institut FEMTO-ST, 24 chemin de l'épitaphe, Besançon 25000, France

The first objective of the study is to characterize the overall range of measurements, as a result of benchmarking operation applied on the Booster pump of the SICODYN funded French research project [1, 2]; the second objective is to quantify the effect of some particular control parameters on the observed variability.

## 17.2 Description of the Dynamical System

The chosen equipment is a pump used in EDF thermal units (Fig. 17.1). It is a one-stage booster pump, composed of a diffuser and a volute, with axial suction and vertical delivery (body with volute called “snail”), mounted on a metallic frame.

This main bolted assembly was designed forty years ago by Sulzer Pumps.

The principal characteristics of the pump are:

- the power of the pump is 135 kW;
- the dimensions of the pump without support are approximately  $1\text{ m} \times 1\text{ m}$ ;
- the mass of pump and support is approximately 2,800 kg;
- the material of the pump is cast iron and steel;
- the nominal rotational speed is 1,500 rpm and the flow rate in nominal conditions is  $620\text{ m}^3/\text{h}$ ;
- the shaft is supported in radial direction by two plain bearings (unknown stiffness and damping linearised characteristics) and in axial direction by a roller;
- the impeller and shaft are connected by keys.

In this study, the pump is not rotating and not coupled to the engine that permits to put it to operation. The boundary conditions are: frame fixed in concrete, pump assembly connected to delivery and suction pipes.



**Fig. 17.1** The pump, frame in concrete, connected to pipes, in thermal power plant

### 17.3 Test Specifications and Settings

Five independent teams are invited to perform an experimental modal analysis of two specimen of the similar pump assembly (Table 17.1) in the frequency bandwidth [0 Hz; 300 Hz]. Free choice is let to determine the number and the type of sensors, the excitation means, the number of excitation points and the modal identification method.

As a consequence of the proposed method, actual settings of the experimental modal analyses performed can be different from one partner to another. All partners excited the pump using a shock hammer. The frequency resolution varied from 0.078 to 0.25 Hz. Measurements were collected using an average of five replicates, excepted for one partner, who used an average of 25 replicates. Linearity and reciprocity tests were carried out by four partners among five. The identification methods applied were generally similar (Table 17.2).

Details on impact and measurement points are given in Table 17.3. The number of impact points varies from 3 to 9 ; the number of measurement points, where tri-axial accelerometers are located, varies from 27 to 138. It can be noticed that the pump itself can be lightly or heavily instrumented; instrumentation of the pipes, useful for the characterization of the boundary condition to be included within modeling purpose, can be different too. The experimental mesh geometries are directly measured by each team in situ, and no numerical model was supplied for the measurement.

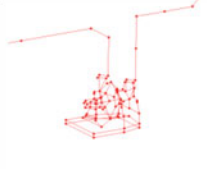
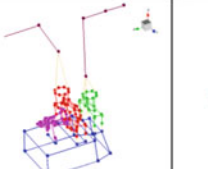

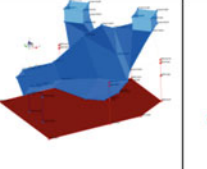
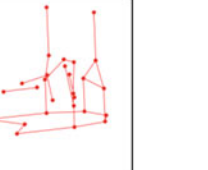
**Table 17.1** Number of experimental modal analyses per pump specimen

	Number of experimental modal analyses
Pump 1	3
Pump 2	3

**Table 17.2** Actual settings of experimental analyses

Partner	Pump	Excitation type	Impact points	Frequency bandwidth (Hz)	Frequency sampling rate (Hz)	Number of means	Identification method	Linearity, reciprocity tests
1	1 2	Shock hammer	3	[0–400]	0.25	5	LSCF LMS Polymax	OK
2	2		4	[0–320]	0.078	5		
3	1		3	[0–300]	0.16	3		OK
4	1		9	[0–500]	0.122	5	OK	
5	2		6	[0–512]	0.122	25	LSCF, LCF, SAPP, LMS	OK

**Table 17.3** Impact and measurement points (X: horizontal, Y: vertical, Z: horizontal along rotor axis)

Partner	1	2	3	4	5
	Impact points				
Number	3	4	3	9	6
Position Direction	X: flange suction elbow Y: flange delivery casing Y: top casing	X, Y: flange suction elbow X, Y: flange delivery casing	X, Y, Z : casing fixation	X, Y: elbow fixation X, Y: casing-frame fixation X, Y : suction elbow flange X, Y: delivery casing flange X : top casing	X, Y, Z : suction elbow flange X, Y, Z: flange delivery casing
	Measurement points				
					
Pump	60	109	43	17	
Frame	16	20	20	8	6
Pipes	14	9	8	2	7
Total	90	138	91	27	

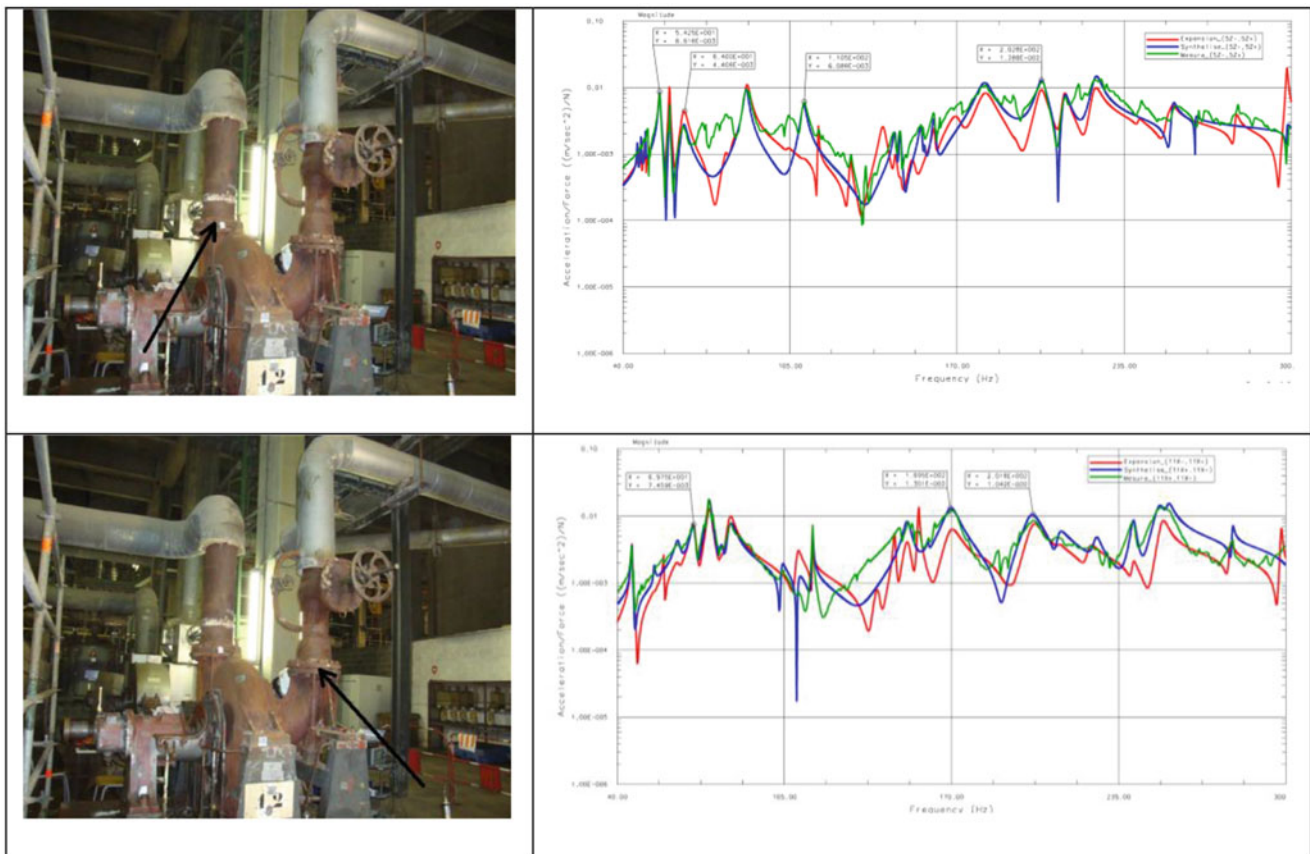


Fig. 17.2 Comparison of measured, synthesized and expanded FRF at two different point locations

## 17.4 SEREP Expansion and Its Validation

To allow comparison of experimental data relatively to measurement meshes presented in Table 17.3, too different to be directly compared, a SEREP expansion [3] is preliminary performed from the heaviest experimental mesh (considered as the reference) on a finite element mesh of the pump assembly. The system of interest being the pump itself, this operation does not take into account vibrating information measured on the pipes; consequently the pipes are considered in the finite element FE model using equivalent mass and stiffness representations. As a first element of expansion validation, Fig. 17.2 shows the frequency response functions FRF at two locations, that respectively are connections of the pump with suction and delivery pipes, directly measured, synthesized from identified eigenmodes, and expanded on the FE element mesh via SEREP method: satisfactory correlation can be obtained on main eigenmodes, depending on the point location considered.

Second element of expansion validation can be performed via the comparison of expanded/experimental MAC and autoMAC matrices (Fig. 17.3). The overall modes are very well correlated with diagonal MAC numbers generally greater than 0.9. The dispersion along diagonal line, that can be shown around modes 10–17, is already present in autoMAC, proving that it is not caused by expansion operation.

## 17.5 Observed Global Experimental Variability

A first topic of significance is the observation of the global experimental variability, considering all sources of discrepancy. Attempt is made to pair the identified modes by four partners, relatively to two pump specimens. Around four overall eigenmodes can be paired among eight, based on a 50 % MAC number and 10 % maximum frequency gap criteria. Considering these paired eigenmodes, the mean frequency gap shows a low 2 % value, whereas the damping ratio gap, with a mean value of 32 %, can reach more than 60 % (Table 17.4).



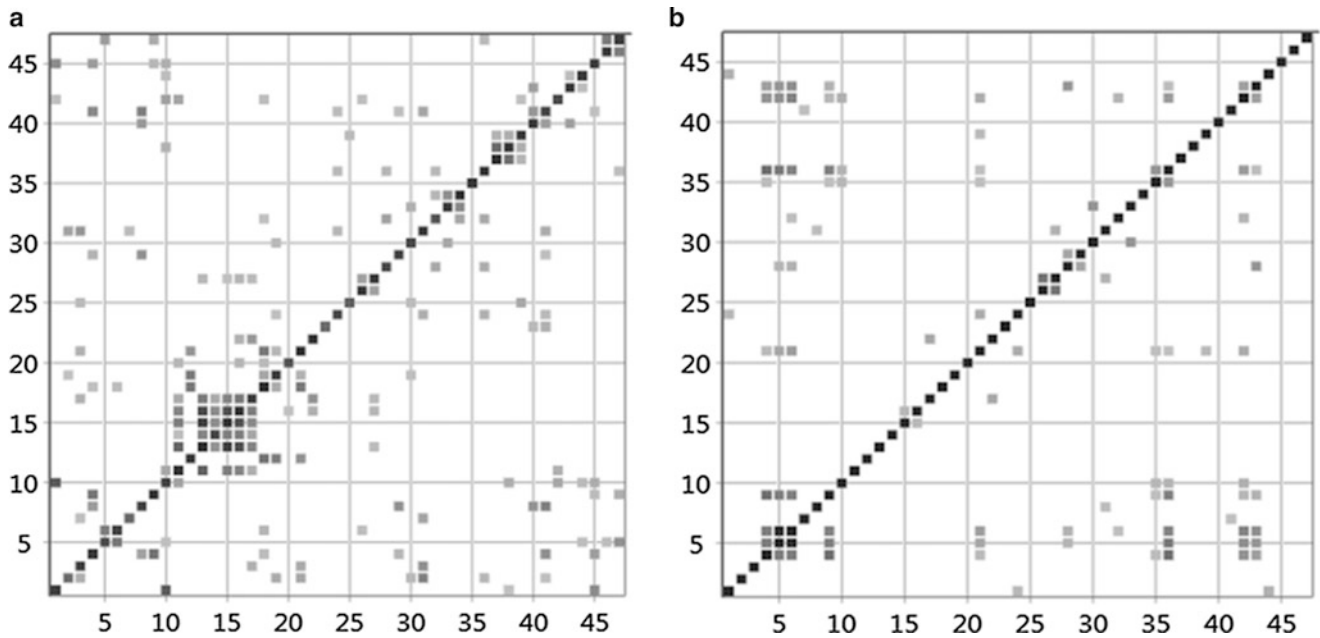


Fig. 17.3 Comparison of expanded/experimental MAC matrix and autoMAC matrix

Table 17.4 Global variability: compared modal bases

	Partner 1				Partner 2, ref: partner 1, pump 2			Partner 3, ref: partner 1, pump 1			Partner 4, ref: partner 1, pump 1		
	Pump 2		Pump 1		Pump 2			Pump 1			Pump 1		
	Mode	Freq. (Hz)	Mode	Freq. (Hz)	Mode	Freq. (Hz)	MAC	Mode	Freq. (Hz)	MAC	Mode	Freq. (Hz)	MAC
1	15	54.3	6	60.2	7	54.8	82.8	1	60.5	92.0	3	60.2	83.7
2	17	63.6	8	71.1							4	72.3	64.8
3	18	69.7	9	74.5				2	74.4	72.5			
4	21	83.8	10	82.5	8	69.5	80.2	3	83.4	91.5			
5	22	88.2	7	67.9	10	82.4	74.8						
6	32	161.1			16	161.6	52.3						
7	34	180.8	15	169.9	17	175.9	82.2	7	188.6	76.9			
8	38	211.6			18	196.2	52.2						
9	44	278.3	25	284.5				10	284.4	83.2			

### 17.6 Observed Unit-to-Unit Variability

Unit-to-unit variability can be quantified by comparing identified modal bases relative to two nominally-identical pump assemblies, obtained by the same operator and using the same identification method. Pairing criteria applied, minimum 50 % MAC number and maximum 20 % frequency gap, allow to pair the main overall eigenmodes, as indicated in Table 17.5. The ten so paired modes show a 0.77 mean MAC coefficient, 10 % mean frequency gap and 28 % mean damping gap, for reduced damping values comprised between 0.2 % and 4.5 %. Unit-to-unit variability can essentially be attributed to different actual bolted torque levels at component connections and pipe-to-pump connections, and realization of the frame fixation on concrete. The latter boundary condition can effectively vary a lot from one specimen to another, in direct relation to the aging process of the concrete.

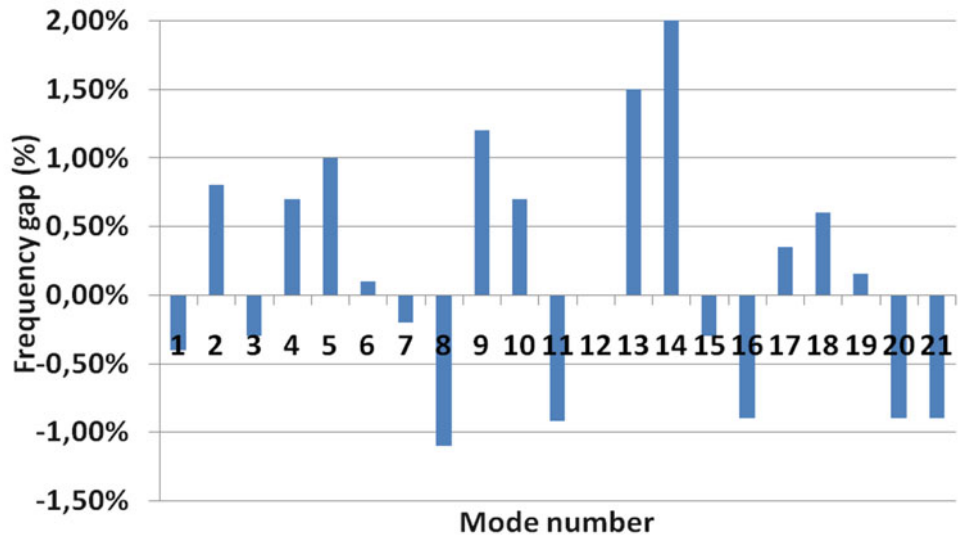
### 17.7 Observed Identification Variability Due to Operator

In order to quantify variability due to operator during the modal identification procedure, two independent operators were asked to perform it from the same test runs, using the same modal identification method and the same software, on the

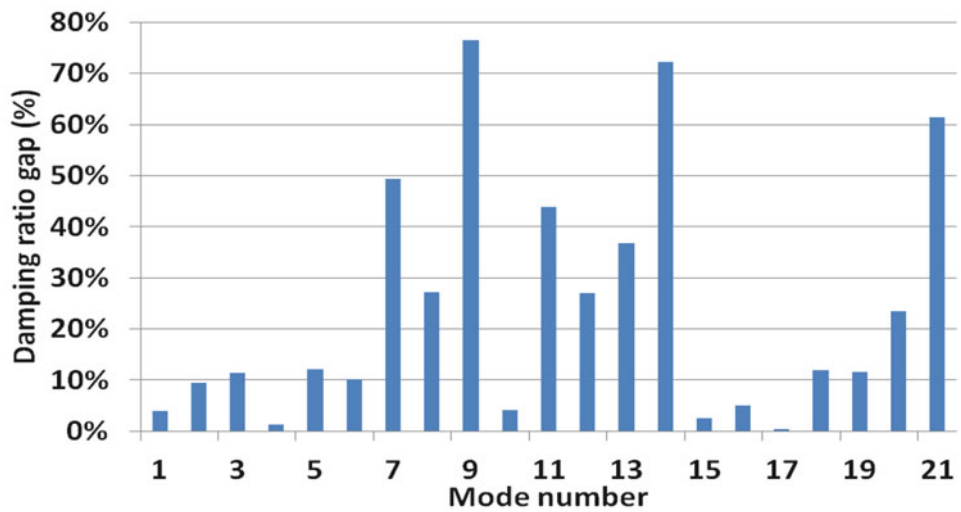
**Table 17.5** Compared modal bases of two nominally-identical pump assemblies

	Pump 1		Pump 2		Frequency gap (%)	MAC (%)	Damping ratio gap (%)
	Mode number	Frequency (Hz)	Mode number	Frequency (Hz)			
1	6	60.2	15	54.3	11.0	93.4	27
2	7	67.9	20	80.3	-15.4	64.8	43
3	8	71.1	17	63.6	11.7	86.6	11
4	9	74.5	21	83.8	-11.1	87.5	34
5	10	82.5	18	69.7	18.3	88.1	41
6	11	98.6	24	110.1	-10.4	51	20
7	15	169.9	34	180.8	-6.1	87.7	36
8	16	186.7	38	211.6	-11.8	84.2	24
9	17	191.3	37	202.6	-5.6	71.8	29
10	25	284.5	44	278.3	2.2	53.1	11

**Fig. 17.4** Identification variability due to operator: frequency gap



**Fig. 17.5** Identification variability due to operator: damping ratio gap



frequency bandwidth [30 Hz; 400 Hz]. It must be first noted that the number of modes so identified varies from 22 to 51, among which 21 could be paired. If frequencies of these 21 paired eigenmodes are identified with satisfactory accuracy, with a mean and a maximal frequency gaps of 1 % and 2 % respectively (Fig. 17.4), larger discrepancy can be observed on damping ratios with a mean and a maximal gaps of 24 % and 76 % respectively (Fig. 17.5), with values varying from 0.4 % to 4 %.

## 17.8 Conclusion

As a part of the SICODYN funded French research project, an experimental modal benchmark is performed on two nominally-identical Booster pumps in industrial environment, between five independent teams, whose free choice is let to determine the number and the type of sensors, the excitation means, the number of excitation points and the modal identification method. The first objective is to characterize the overall range of measurements. The second objective is to quantify the effect of some particular control parameters on the observed variability: unit-to-unit and operator variabilities are so proposed to be addressed. Moreover specific variability relative to the modal identification phase can be quantified using the same experimental test runs by two independent operators.

Due to differences on experimental meshes, from 27 to 138 measurement points, a SEREP expansion on a finite element mesh is first performed, allowing the comparison of experimental modal bases. Global variability observed, based on half paired among identified overall eigenmodes (within 10 % frequency gap and 50 % MAC criteria), shows a 2 % mean frequency gap and 32 % mean damping ratio gap. Unit-to-unit variability, essentially attributed to different actual bolted torque levels at component connections and pipe-to-pump connections, and realization of the frame fixation on concrete, shows 10 % mean frequency gap and 28 % mean damping ratio gap. Specific variability due to modal identification operator, as a component of the global variability, is still significant with a number of identified modes that varies by a factor of 2; the so paired modes show 1 % mean frequency gap and 24 % mean damping ratio gap. These quantitative results could be considered comparatively to those obtained on a portal frame in laboratory conditions [4].

It should be remained that the observed ranges of damping ratio, quite high, are relative to low values; nevertheless this result is an element that confirms the difficulty to precisely identify this modal characteristic.

Lesson to draw is that the mode pairing operation is quite difficult and generally allows only about half modes to be paired, if experimentation and identification are performed by different operators. On the contrary, unit-to-unit variability study, without the operator effect, allows a better pairing of overall eigenmodes. This must be kept in mind when quantification of variability, in terms of frequency and damping ratio gaps and MAC values, evidently carried out but on the paired modes, is used in test-analysis or uncertainty purpose.

All the experimental results and the corresponding range are used in Parts 4 and 5 of SICODYN project, respectively concerned with test-analysis correlation and uncertainty quantification. An example is the model identification in computational stochastic dynamics using experimental modal data [5].

**Acknowledgements** The support of the FUI (Fonds Unique Interministériel) is gratefully acknowledged. The 13 partners currently involved in 2012–2015 SICODYN project are: AIRBUS Defence & Space, CETIM, EDF R&D, LMT ENS Cachan, Institut FEMTO-ST UMR CNRS 6174, LAMCOS UMR CNRS 5259 INSA Lyon, MSME UMR-CNRS 8208, NECS Numerical Engineering and Consulting Service, PHIMECA Engineering, SAMTECH, SOPEMEA, SULZER Pompes France, VIBRATEC.

## References

1. Audebert S (2010) SICODYN International Benchmark on dynamic analysis of structure assemblies: variability and numerical-experimental correlation on an industrial pump. *Méc Ind* 11(6):439–451
2. Audebert S (2014) SICODYN International benchmark on dynamic analysis of structure assemblies: variability and numerical-experimental correlation on an industrial pump (part 2). *Mec Ind* 15(1):1–17
3. OCallahan J, Avitabile P (1989) System equivalent reduction expansion process (SEREP). In: Proceedings of the 7th international modal analysis conference, Las Vegas, pp 29–37
4. Van Buren KL, Hall TM, Gonzales LM, Hemez FM, Anton SR (2015) A case study to quantify prediction bounds caused by model-form uncertainty of a portal frame. *Mech Syst Signal Process* 50–51:11–26
5. Batou A, Soize C, Audebert S (2015) Model identification in computational stochastic dynamics using experimental modal data. *Mech Syst Signal Process* 50–51:307–322

# Chapter 18

## Variability of a Bolted Assembly Through an Experimental Modal Analysis

Sami Daouk, François Louf, Christophe Cluzel, Olivier Dorival, and Laurent Champaney

**Abstract** Industrial structures are mainly assemblies with complex geometries and non-linear characteristics. Friction and joint preload added to fabrication imperfections lead to a substantial gap between numerical models and real structures. In order to develop accurate generic models, it is then necessary to quantify the behavior variability, especially the one related to the joint conditions. The first part of this paper describes the iterative sizing procedure of an academic assembly which characteristics may vary depending on several input variables (e.g. value of the bolt torque, number and position of preloaded bolts, etc.). The properties of the bolted joint were optimized in order to satisfy a set of conditions in terms of tangential slipping, normal displacement and maximum stress level. The second part concerns the experimental modal analysis of the assembly. The main purpose is to characterize the relationship that exists between the input variables and the measured eigenfrequencies and modal damping of the assembly.

**Keywords** Experimental variability • Bolted joints • Uncertainty quantification • Modal analysis • Modal damping

### 18.1 Introduction

Mechanical systems are commonly analyzed assuming that the mathematical models are deterministic and the input data is precisely defined. Nevertheless, in most cases, parameters of the mathematical-mechanical model linked to geometry, boundary conditions and material properties can neither be identified nor modeled accurately. The need to address data uncertainties is now clearly recognized, and over the past decades there has been a growing interest in stochastic modeling and application of probabilistic numerical methods [1, 2].

It is our will to have a better understanding of experimental variability, especially in case of bolted assemblies. In fact, even though the sources of uncertainties can be well identified, the characterization of their influence on the dynamic behavior is still not well known. The main objective of this study is then to quantify the influence of joint parameters on the dynamic response of a bolted joint. Some relevant parameters to be considered are the value of the bolt preload, the number and position of preloaded bolts and lubrication conditions. To achieve that, it is necessary to have a bolted joint with binding conditions that can be easily varied. It is clear that a low level of effort in the joint, the variation of the parameters mentioned earlier will not cause any significant change in the dynamic response of the connection. However, in case of heavy loads, sliding in the joint may appear in different areas of contact, i.e. the contact between the parts and the contact between bolts and parts. This sliding will be source of energy dissipation and thus contribute to a variation of eigenfrequencies and modal damping. However the application of high stress levels in dynamic is not possible with an experimental material of reasonable size. One interesting solution is to take advantage of the dynamic load amplification at resonance and build parts to store elastic and kinetic energy and raise the stress levels in the joint. Eccentric masses (kinetic energy) were added and linked to the bolted joint of interest by long beams (elastic energy). The conversion of kinetic energy into elastic energy from the masses to the beams enables the transfer of the desired efforts to the central bolted joint.

---

S. Daouk (✉) • F. Louf • L. Champaney  
LMT (ENS-Cachan, CNRS, Université Paris Saclay), 61 avenue du Président Wilson, 94235 Cachan, France  
e-mail: [sami.daouk@lmt.ens-cachan.fr](mailto:sami.daouk@lmt.ens-cachan.fr)

C. Cluzel  
LMT (ENS-Cachan, CNRS, Université Paris Saclay), 61 avenue du Président Wilson, 94235 Cachan, France  
IUT-SGM, rue du Père Jarlan, 91025 Evry, France

O. Dorival  
Université de Toulouse, Institut Clément Ader (ICA); INSA, UPS, Mines Albi, ISAE, 135 av. de Rangueil, 31077 Toulouse Cedex, France

The first part of this paper describes the iterative sizing procedure of a bolted assembly which properties were optimized in order to satisfy a set of conditions in terms of sliding and maximum stress level. The second part presents the experimental procedure and the first results of an experimental modal analysis of the assembly. The purpose is to find the relationship that exists between the input variables and the eigenfrequencies and modal damping of the assembly.

## 18.2 Sizing Procedure

### 18.2.1 Estimation of Eigenfrequencies and Frequency Responses

The first step in the sizing procedure of the bolted joint is to estimate the first eigenfrequencies of the assembly in free-free vibrations, in particular the ones associated with bending modes. Considering a structure with cylindrical symmetry, there will only be symmetric or anti-symmetric modes. The exact values of the eigenfrequencies can be found, but in order to avoid time-consuming calculations, approximations were made. For this, the Rayleigh quotient method is used assuming a simple polynomial form of the eigenmode that will lead to an overestimation of the exact desired eigenfrequency.

For instance, Fig. 18.1 shows the simplified model associated to the first eigenmode, i.e. a symmetric bending mode. The experimental modal analysis will be carried out with free-free boundary conditions, so two rigid body modes are possible in case of a planar study: a transverse translating movement and a rotation about the out-of-plane axis. If we study a symmetric mode, there can not be any rotation, which explains the choice of the boundary conditions at  $x = 0$ . The remaining degree of freedom is important: if eliminated, the center of gravity of the deformed configuration will not be the same as that of the non-deformed configuration, which contradicts an important property of structures vibrating in free-free conditions.

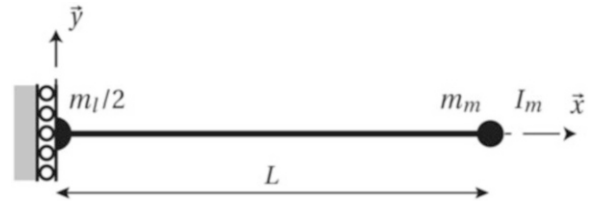
Let  $V_{s,1}(x)$  be a kinematically admissible displacement field describing the first symmetric bending mode of the structure. Several forms of the field  $V_{s,1}(x)$  were considered, such as the sum of a rigid translating mode and a mode deforming the structure such as  $V_{s,1}(x) = a + x^2$  or  $V_{s,1}(x) = a + \frac{Lx^2}{2} - \frac{x^3}{6}$ . For each form, we write the Rayleigh quotient as:

$$R(V_{s,1}) = \frac{\int_0^L EI(V_{s,1}''(x))^2 dx}{\int_0^L \rho S(V_{s,1}(x))^2 dx + \frac{1}{2}m_l(V_{s,1}(0))^2 + m_m(V_{s,1}(L))^2 + I_m(V_{s,1}'(L))^2} \quad (18.1)$$

where  $E$ ,  $\rho$ ,  $L$ ,  $S$  and  $I$  are respectively the Young's modulus, the density, the length, the section and the second moment of area of the beam;  $m_l$  is the mass of the central bolted joint of interest;  $m_m$  is the mass of an eccentric mass and  $I_m$  its moment of inertia about an axis passing through its center and orthogonal to the  $x$ -axis.

Then we search for the coefficient  $a$  that minimises the Rayleigh quotient and then the corresponding eigenfrequency. The latter is compared to the eigenfrequency of a numerical beam model that has the same geometry, masses, inertia and material properties. That's how we can find the best approximate displacement field  $V_{s,1}(x)$  describing the first eigenmode. The same procedure is followed for the other eigenmodes of interest.

Once the different eigenmodes of interest are known, it is possible to estimate the frequency response of the structure at a given forced excitation which maximum is set at 1,000 N in our study case (maximum force level of the shaker used).



**Fig. 18.1** Model used to estimate the first eigenmode (symmetric bending mode)

In particular, we seek to estimate the oscillation amplitude at resonance, assuming a low modal damping, but obviously not zero. When considering the forced vibrations problem in case of a viscoelastic material with low damping, the magnitude of the amplitude  $q_i(\omega_i)$  associated to the mode  $i$  writes:

$$|q_i(\omega_i)| = \frac{F U_i(x_0)}{\omega_i C_i} \quad (18.2)$$

where  $\omega_i$  is the angular eigenfrequency of mode  $i$ ,  $F$  is the magnitude of a punctual harmonic load applied at the point  $x = x_0$  at  $\omega_i$ ,  $U_i(x)$  is the shape of the eigenmode  $i$  (that was approximated previously using the Rayleigh quotient method) and  $C_i$  is the viscous damping coefficient. This relationship is obviously independent of the type of problem (bending, tension, torsion) so it will be possible to find the amplitude at resonance in all cases of interest.

For instance, in case of the first symmetric bending mode of the structure, we find the magnitude of  $q(\omega_{s,1})$  as:

$$|q(\omega_{s,1})| = \frac{4Fm_l + 5F\rho SL}{8Im_l E\zeta + 16Im_m E\zeta + 16ILSE\zeta\rho} \quad (18.3)$$

where the modal damping ratio  $\zeta$  has been introduced.

Then the bending moment in the beam around the  $z$ -axis at resonance is:

$$M_{z,s,1}(x) = |q(\omega_{s,1})| V_{s,1}''(x) = -\frac{I(L-x)E(8Fm_m + 3F\rho SL)}{8Im_l E\zeta + 16Im_m E\zeta + 16ILSE\zeta\rho} \quad (18.4)$$

which leads to the shear force

$$Q_{s,1}(x) = |q(\omega_{s,1})| V_{s,1}'''(x) = -\frac{IE(8Fm_m + 3F\rho SL)}{8Im_l E\zeta + 16Im_m E\zeta + 16ILSE\zeta\rho} \quad (18.5)$$

and the bending normal stress in the beam can be found as:

$$\sigma_{s,1}(x) = \frac{M_{z,s,1}(x)}{I} \frac{D}{2} = -\frac{D(L-x)E(8Fm_m + 3F\rho SL)}{2(8Im_l E\zeta + 16Im_m E\zeta + 16ILSE\zeta\rho)} \quad (18.6)$$

In our calculations, a modal damping ratio  $\zeta = 0.2\%$  was considered for all studied modes. This value is relatively low and leads to a higher estimation of the amplitudes and stress levels, but then the sizing procedure remains conservative.

## 18.2.2 Optimization of the Design of the Bolted Joint

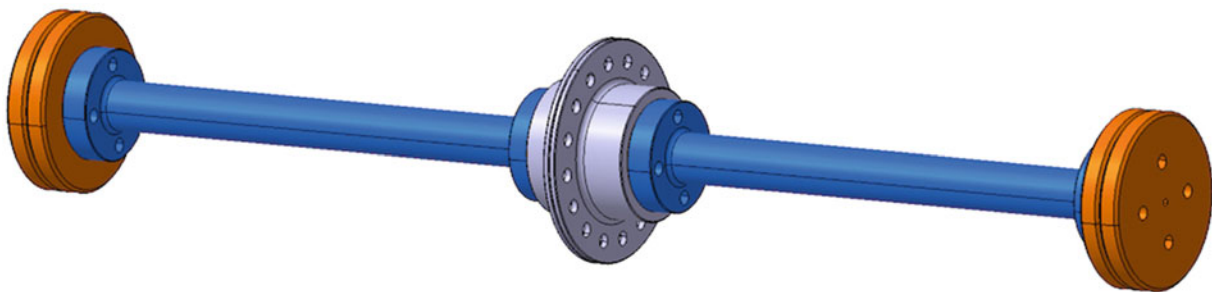
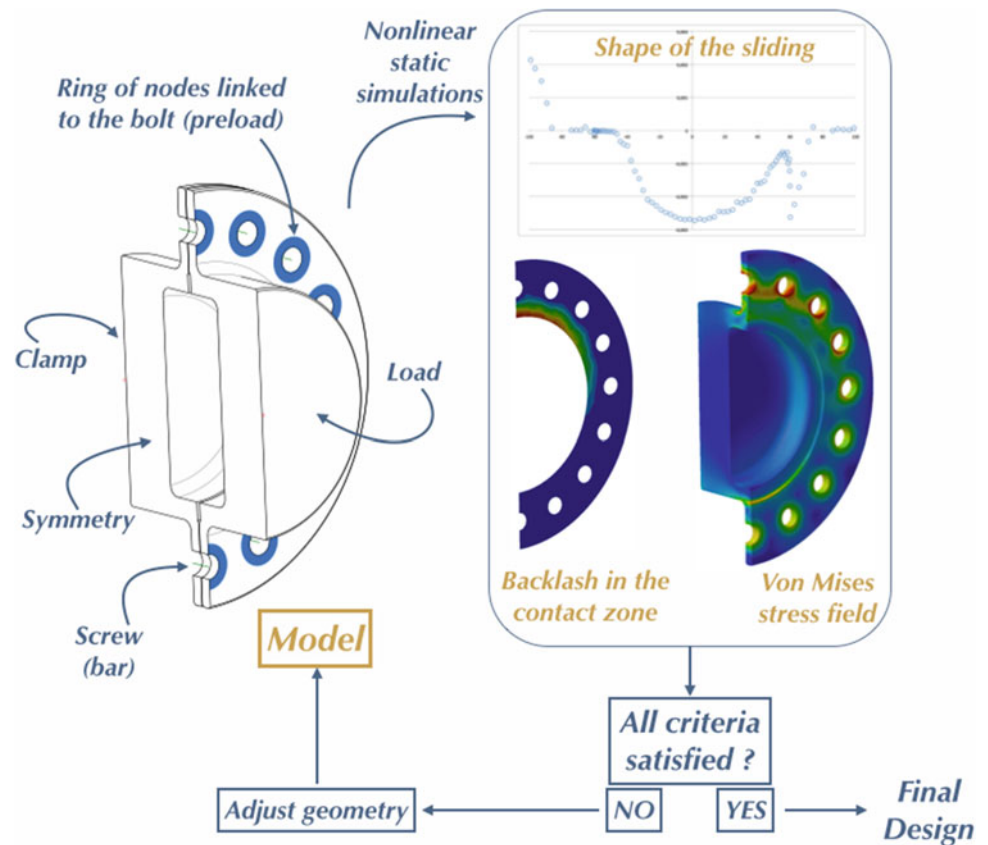
After estimating the eigenfrequencies and calculating the stress levels in the model, we proceeded to the optimization of the design of the bolted joint regarding the moments and stresses generated in the beams at resonance. The preload range that was considered goes from 20% to 80% of the yield strength of the screws.

In particular, it is necessary that the joint resists but also works in a significant way at resonance:

- in the preload range considered, we wish to have local backlash in the contact zone between the parts, in the order of 0.05 mm for an average preload ;
- in the preload range considered, we wish to have local sliding between the parts, in the order of 0.005 mm for an average preload.

The second step of the sizing procedure is then to perform nonlinear static simulations to visualize these effects, and increase them, if necessary, by changing the geometry. These calculations are performed for a given geometry of the parts of the bolted joint and for a precise eigenmode. The value of the load is given by the previous step of the sizing procedure. For instance, in case of the first symmetric bending eigenmode, the load to apply is the bending moment and shear force given by relations (18.4) and (18.5). A Coulomb friction model without kinetic effects was considered with a coefficient of friction of 0.2 (steel-steel). In addition to the values of slipping and backlash in the contact zone, it is essential to check the stress levels in both parts, which may not exceed 400 MPa in order to remain in the elastic range and avoid damaging the parts.

**Fig. 18.2** Optimization procedure of the design of the bolted joint



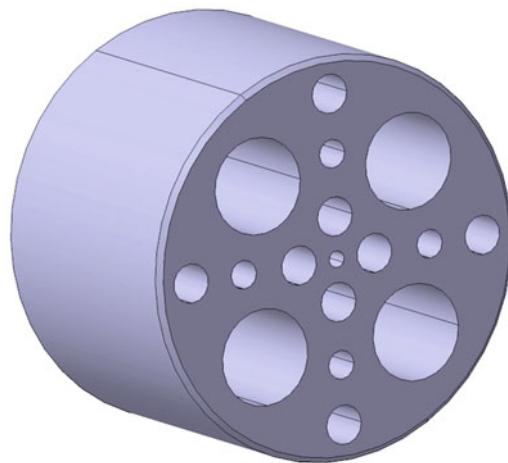
**Fig. 18.3** Final design of the assembly

As shown in Fig. 18.2, the last step is the adjustment of the characteristics of the parts in order to reach the desired sliding, backlash and stress levels, mainly for the first symmetric and anti-symmetric bending eigenmodes. In fact, these modes will have the most significant effect on the bolted joint. For that, the stiffness, mass and inertia of the parts of the joint are modified while minimizing the dissipation in the other joints of the assembly, namely between beams and masses, and between parts of the joint and beams. Figure 18.3 presents the final design of the assembly resulting from the sizing procedure, where 16 bolts can be loaded in the central joint of interest. The assembly has been designed so that the eigenfrequencies are separated and the first ones associated to bending modes are less than 1 kHz.

The evaluation of the energy dissipated only in the bolted joint can be done by carrying out differential identifications. That's why a reference part shown in Fig. 18.4 was designed as a rigid part with a simple geometry of the same length as the bolted joint under study. It is also mounted to the beams in a similar way and has equal bending and torsion moments of inertia. Its mass may vary by filling the holes or not in order to be consider the case of eight, twelve or sixteen loaded bolts.

In order to evaluate the dissipation in the bolted joint of interest, the same experiments are carried out on the assembly with the joint and the assembly with the reference part. When applying the same energy through the shaker, for a given mode, the difference in the elastic energy of the beams between both assemblies leads to the energy dissipated in the central bolted joint.

**Fig. 18.4** Reference part built to evaluate the energy dissipated only in the bolted joint



### 18.3 Evaluation of Modal Damping

When the structure is lightly damped, its distribution is almost always not well known, and it is usually necessary to make an assumption about the distribution. A first method considers that damping is constant depending on the level of vibrations, which makes it precise in case of a low loading level only. That is mainly due to the fact that experimental control is automatic and vibrating at the natural frequency is too risky to inject a high load. This approach considers the frequencies  $f_{i,1}$  and  $f_{i,2}$  of the bandwidth at  $-3$  dB of the maximum of the transfer function around the resonant frequency  $f_i$ . The corresponding damping ratio  $\zeta_i$  is given by the relation:

$$\zeta_i = \frac{f_{i,2} - f_{i,1}}{2 f_i} \quad (18.7)$$

Another method is the *Specific Damping Capacity*  $\psi$  that intends to measure damping for a given deformed shape such as a modal shape. It is expressed as a ratio of the energy dissipated per cycle and the elastic energy (or energy stored) per cycle:

$$\psi = \frac{W_d}{W_e} \quad (18.8)$$

where the dissipated energy  $W_d$  can be calculated by summing the power injected in the assembly per cycle as:

$$W_d = \int_0^T \mathbf{F} \cdot \mathbf{v} \, dt = \int_0^T \mathbf{F} \cdot d\mathbf{u} \quad (18.9)$$

$\mathbf{F}$  being the effort applied through the shaker and  $\mathbf{v}$  the velocity of vibrations, and the elastic energy  $W_e$  can be calculated on both beams as:

$$W_e = 2 \int_0^L \frac{M_f^2}{2 EI} \, dx \quad \text{in case of bending modes} \quad (18.10)$$

When using this energy ratio to evaluate damping, no assumption is made about the relationship between damping and the level of vibrations. This measure leads then to a better characterization of modal damping for any loading level in the joint. The *Specific Damping Capacity* can be related to the modal damping ratio via the relation:

$$\psi_i = 4\pi \frac{\zeta_i}{\sqrt{1 - \zeta_i^2}} \quad (18.11)$$



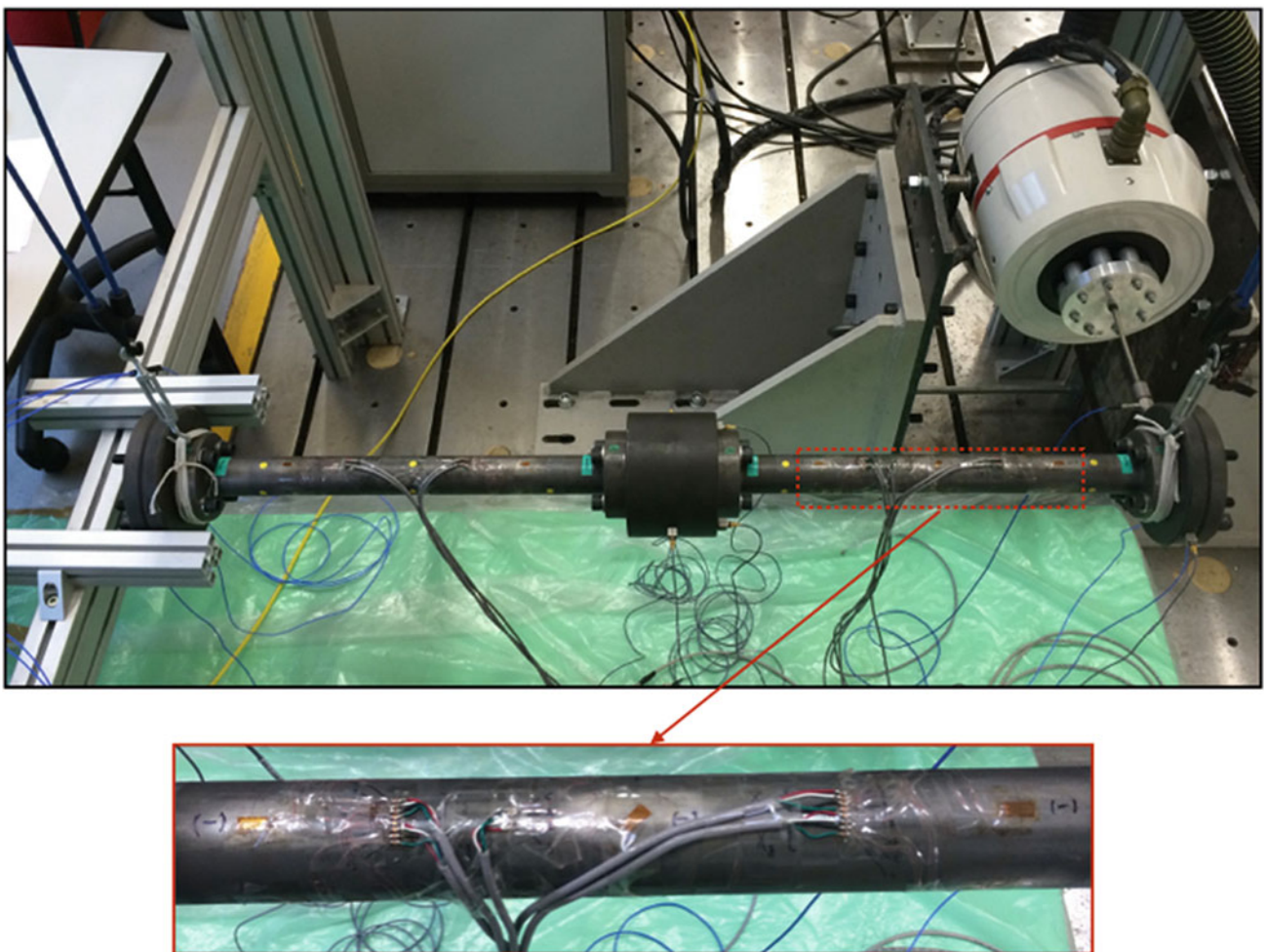
## 18.4 Experimental Procedure

Several experimental tools are needed in order to measure finely the quantities of interest. Single and triaxial accelerometers were used to measure the natural frequencies of the assembly. The use of accelerometers is also necessary in order to measure the energy applied through the shaker. Strain gages are another important tool that was used. To evaluate the magnitude of the efforts in the bolted joint, twenty strain gages were glued on the beams as shown in Fig. 18.5. They were arranged in eight half bridges (four in the horizontal plane and four in the vertical plane) to measure bending, and one full bridge to measure torsion. The evaluation of the strain magnitude in the beams leads to the elastic energy of the assembly (mainly stored in the beams).

The experimental procedure is structured into two parts. First, it is necessary to carry out a modal analysis of the reference assembly. This will validate that all manipulations and tests that will be carried out are without risk on the joint. In fact, as the vibration at a natural frequency will result in a dynamic amplification whose magnitude is unknown, an upper bound of the amplitude of the loads in the joint is needed in order to keep the strain in the elastic range. A second objective of studying the reference assembly is to have the reference information necessary for the differential identifications of the energy dissipated in the bolted joint.

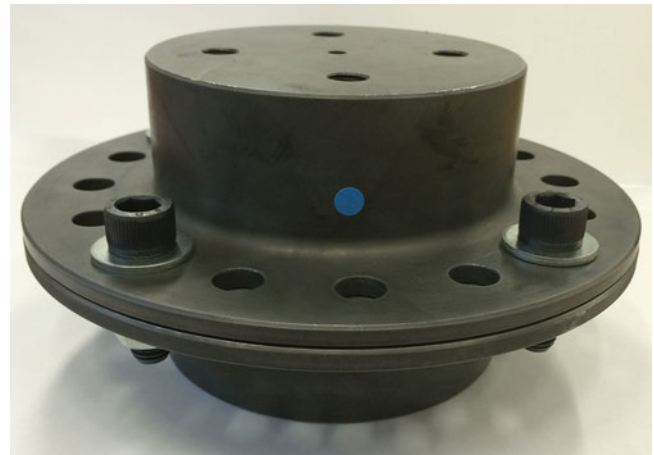
The analysis of the reference assembly includes three steps:

- the first step is to determine the eigenfrequencies and eigenmodes under 1 kHz. These quantities are measured for a low loading level firstly by using a hammer and then through a white noise applied by the shaker,



**Fig. 18.5** The reference assembly analyzed in free-free vibrations

**Fig. 18.6** The bolted joint under study



- the second step is to evaluate modal damping, by using the methods presented in Sect. 18.3. The results of all methods should be the same in case of light loads,
- the last step is the measurement of the variation of eigenfrequencies and modal damping depending on the applied load.

The second part of the experimental procedure is the study of the dynamic behavior of the bolted joint. At first, we carry out the same tests performed on the reference assembly. This step is essential to the success of the differential analysis which includes two aspects:

- the eigenfrequency variation: it could be either linked to the damping variation or to the stiffness variation resulting from the deformation of the thin support plates of the joint (thickness of 6 mm), as shown in Fig. 18.6.
- the damping variation: it is evaluated by considering the energy variation between both assemblies (the one with the bolted joint and the reference assembly).

Finally, the modification of joint conditions (e.g. value of the joint preload, number and position of preloaded bolts, ...) leads to the characterization of their influence on the dynamic behavior of the joint.

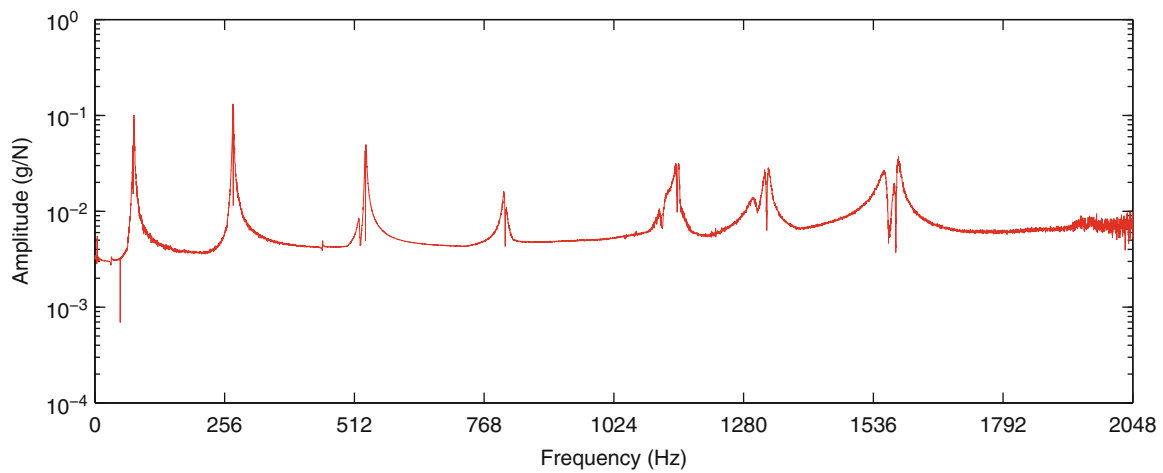
## 18.5 First Results

The first experimental results presented in Fig. 18.7 show the eigenfrequencies of the reference assembly under 2 kHz. The values are smaller than the ones of the numerical model, but without a major gap.

The first work was focused on the first eigenfrequency, which is associated to a symmetric bending mode. We noticed that the value of the eigenfrequency decreases when the load increases. It is hoped that, as the bolt torque and the number of preloaded bolts increase, the contact becomes more rigid, which leads to an increase of the measured natural frequencies.

## 18.6 Conclusions and Future Work

The first part of the paper described the iterative sizing procedure of a bolted assembly where the joint conditions may vary. The properties of the bolted joint were optimized in order to satisfy a set of conditions in terms of tangential slipping, backlash and maximum stress level. The second part described the methods used to evaluate modal damping experimentally and presented the experimental procedure. The frequency response function of the reference assembly shows that the eigenfrequencies are coherent with the numerical model. The future work is firstly to analyze the variation of eigenfrequencies and modal damping. Then, the modal analysis of assembly with the bolted joint will be performed. The purpose is to characterize the relationship that exists between the different joint conditions and the measured eigenfrequencies and modal damping of the assembly.



**Fig. 18.7** The frequency response function of the reference assembly showing the eigenfrequencies under 2 kHz

In the framework of the SICODYN Project [3, 4], initiated in 2012 and carried out till 2016, the experimental modal analysis will be extended to the case of a booster pump studied within its industrial environment. That would lead to a better understanding of experimental variability and then to an assessment of the ability of parametric and non-parametric probabilistic numerical methods to consider and propagate uncertainties in bolted assemblies.

**Acknowledgements** This work has been carried out in the context of the FUI 2012–2016 SICODYN Project (SIMulations credibility via test-analysis COrrelation and uncertainty quantification in structural DYNAMics). The authors would like to gratefully acknowledge the support of the FUI (Fonds Unique Interministériel).

## References

1. Matthies HG, Brenner CE, Bucher CG, Guedes Soares C (1997) Uncertainties in probabilistic numerical analysis of structures and solids-stochastic finite elements. *Struct Saf* 19:283–336
2. Schuëller G (2001) Computational stochastic mechanics – recent advances. *Comput Struct* 79:2225–2234
3. Audebert S (2010) SICODYN international benchmark on dynamic analysis of structure assemblies: variability and numerical-experimental correlation on an industrial pump. *Mech Ind* 11(6):439–451
4. Audebert S, Mikchevitch A, Zentner I (2014) SICODYN international benchmark on dynamic analysis of structure assemblies: variability and numerical-experimental correlation on an industrial pump (part 2). *Mech Ind* 15:1–17

# Chapter 19

## Bottom-Up Calibration of an Industrial Pump Model: Toward a Robust Calibration Paradigm

A. Kuczkowiak, S. Huang, S. Cogan, and M. Ouisse

**Abstract** The calibration of complex industrial structures using vibration test data is an important step toward improving the credibility of model-based decisions for a specified application. Meanwhile, the state-of-practice in industry is to use computer-aided design software that produce very refined finite element meshes thus creating an impractical bottleneck in the iterative calibration process. This paper illustrates a two level bottom-up approach that requires testing at both the component and assembled levels. Initially, a global sensitivity analysis is performed on the complete model to rank the model components in terms of their influence on the quantities of interest. Selected components are then calibrated using dedicated tests before being integrated as a Craig-Bampton superelement into the global assembly. At the top level, model calibration is restricted mainly to the component interface properties. Since test data is available only for a single pump, a deterministic calibration paradigm is applied here. This two level procedure is illustrated on a detailed model of a pump that is studied in the framework of the French nationally funded project SICODYN. A robust calibration methodology will also be outlined for future work in order to account for lack of knowledge in the final operational boundary conditions of the pump.

**Keywords** Test-analysis correlation • Sensitivity analysis • Craig-Bampton substructuring • Model calibration • SICODYN project

### 19.1 Introduction

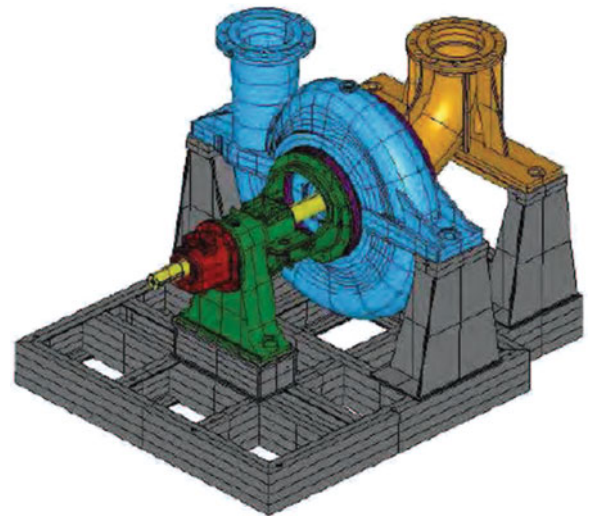
The calibration of complex industrial structures using vibration test data is an important step toward improving the credibility of model-based decisions for a specified application. This paper is a contribution within the SICODYN project [1], which is briefly described. The research project SICODYN (SIMulations credibility via test-analysis CORrelation and uncertainty quantification in structural DYNAMics) is based on an a complex built-up demonstrator (cf. Figs. 19.1 and 19.2) in industrial environment : it gathers 13 French partners, both academic and industrial. The idea underlying this project is to provide tools, based on tested methodologies, to estimate a priori the confidence associated with a dynamical simulation-based prediction.

More precisely, one objective of this project is to obtain credible finite element (FE) model able to predict identified modal data with a given accuracy. This step is commonly referred to as model calibration [2, 3]. Various calibration strategies exist:

- **Reference basis methods** [4, 5]. A class of nonparametric identification methods that solve a constrained optimization problem to obtain perturbations of the stiffness and mass matrices for the nominal finite element model based on a set of measured eigensolutions. This kind of method is useful for some limited applications but not within the framework of Validation and Verification (V&V).
- **Deterministic local methods** [2, 6]. A class of parametric identification methods that solve a nonlinear constrained optimization problem to obtain deterministic estimates of local stiffness and mass properties based on a set of measured eigensolutions. Due to its simplicity, this kind of method is the most conventional approach in model calibration where fidelity-to-data is optimized.
- **Statistical local methods** [7, 8]. A class of parametric identification methods that solve a nonlinear constrained optimization problem to obtain statistical estimates of local stiffness and mass properties based on a set of measured eigensolutions.

---

A. Kuczkowiak • S. Huang • S. Cogan (✉) • M. Ouisse  
Department of Applied Mechanics, FEMTO-ST Institute - 24, rue de l'Épitaphe, 25000 Besançon, France  
e-mail: [antoine.kuczkowiak@femto-st.fr](mailto:antoine.kuczkowiak@femto-st.fr); [scott.cogan@univ-fcomte.fr](mailto:scott.cogan@univ-fcomte.fr)

**Fig. 19.1** Built-up demonstrator**Fig. 19.2** CAD demonstrator

- **Robust local methods** [9]. A class of parametric identification methods that solve a nonlinear constrained optimization problem to obtain either deterministic or statistical estimates of local stiffness and mass properties based on a set of measured eigensolutions. A robust satisficing<sup>1</sup> approach is adopted to find an adequate compromise between fidelity-to-data and robustness to lack of knowledge in the system and its environment.

As indicated previously reference basis methods are not suitable for model calibration within the framework of V&V, which is the preferred framework for demonstrating the credibility of models. Since only a single measurement is available, statistical local methods can also not be performed. Hence, a deterministic local method is preferred here.<sup>2</sup> Meanwhile, the state-of-practice in industry—and especially here—is to use computer-aided design software that produce very refined finite element meshes thus creating an impractical bottleneck in the iterative calibration process.

First of all, the present work aims to provide a two level bottom-up calibration approach suitable for dealing with industrial FE models. At the end, a calibrated FE model capable of predicting the identified modal data—when the pump is not connected—is found. However, when connected, the structural dynamic behavior will inevitably change. In such cases, can we to quantify the predictability of calibrated model under untested conditions? Since the answer is not trivial, dedicated approaches have to be performed. The second objective is to describe a robust calibration strategy in order to emphasize the tradeoff between fidelity-to-data and robustness-to-uncertainty for further work.

<sup>1</sup>Contraction between *satisfy* and *suffice*. More details can be found pp. 38–39 in [10].

<sup>2</sup>Robust local methods and their possible applications within the framework of the SICODYN project are however discussed at the end of the paper.

## 19.2 FE Model Calibration of an Industrial Pump

### 19.2.1 Introduction

The model calibration of an industrial pump is detailed in this section. The objective is to obtain a predictive FE model which is one objective stated within the framework of the SICODYN project. As indicated previously, the SICODYN project is composed of several partners, each of which have the freedom to propose and apply their preferred strategy. The description below is the approach proposed by the Department of Applied Mechanics, FEMTO-ST Institute in Besançon, France.

The initial discrepancy between simulation predictions and test data is expressed in Table 19.1 and emphasizes that the model does not provide an accurate representation of the reality. The model is actually capable of predicting only two modes. Blank entries in Table 19.1 indicate that the MAC (Modal Assurance Criterion) between numerical and experimental eigensolutions is below 60 %, rendering a comparison between eigenfrequencies impossible.

### 19.2.2 Reduced-Order Model (ROM) Construction

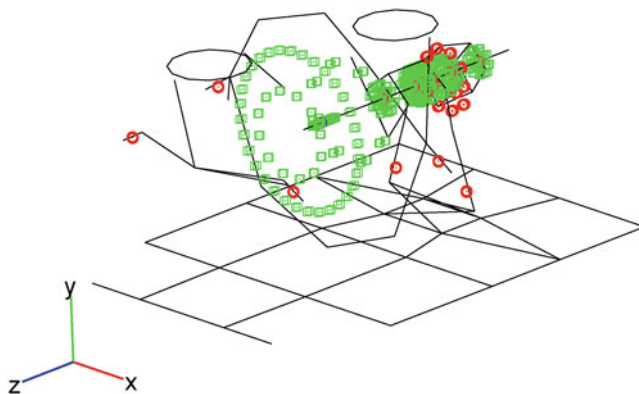
The full FE model available contains around 10 million nodes which is unmanageable within a standard calibration framework. Although one possible solution is to design an efficient fast running model (e.g. a metamodel, see for instance [11]), the preferred way here is to reduce the FE model: the fixed interface Craig-Bampton substructuring technique [12] is used. The full FE model includes seven substructures (or superelements), namely: the bearing casing, the bearing support, the cooling flange, the pump casing, the suction flange, the elbow, and the frame. For each substructure  $s$  with  $N_s$  dofs, the basis  $\mathbf{T}^{(s)} \in \mathbb{R}^{N_s \times c_s}$  is computed:

$$\mathbf{T}^{(s)} = \left[ \mathbf{T}_G^{(s)} ; \boldsymbol{\psi}^{(s)} \right], \quad (19.1)$$

where  $\mathbf{T}_G^{(s)}$  are the static responses to unit displacement at each degrees of freedom (dofs) of interface and  $\boldsymbol{\psi}^{(s)}$  the natural modes when the dofs of each interface are assumed to be fixed. The ROM is depicted in Fig. 19.3.

**Table 19.1** Discrepancy between model prediction and test data before calibration

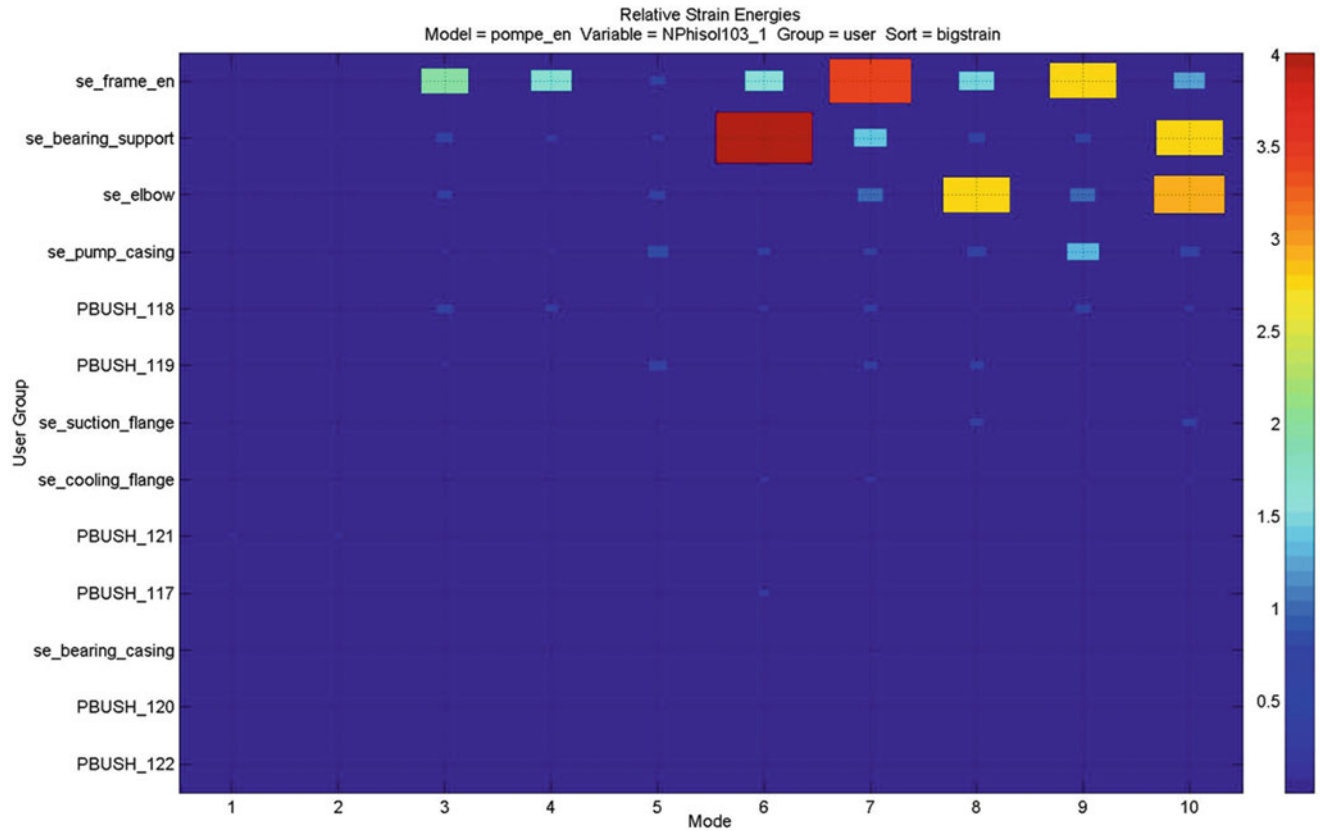
Mode	Test (Hz)	Mode	Model (Hz)	Error (%)	MAC (%)
1	76.8	3	98.4	16.4	93.3
2	134.4				
3	162				
4	211.9	7	189.7	-10.5	60.4
5	233.4				
6	251.2				



**Fig. 19.3** Reduced-order model

**Table 19.2** Accuracy of the ROM

Name	Mass (kg)	Full 3D model (number of nodes)	Reduced order model (number of nodes)	Eigenfrequency (Hz)	Error (%)
Bearing casing	19	337,410	111	1,016–1,581	0.5–11.7
Bearing support	123	1,702,818	228	244–883	0.5–4.5
Cooling flange	13	384,324	20	239–1,234	1.5–5.6
Pump casing	951	875,736	114	432–1,310	1.4–7.1
Suction flange	212	480,414	80	566–2,167	2.2–9.2
Elbow	208	1,792,350	47	294–857	0.5–4.1
Frame	788	4,113,240	27	43–210	0.2–1.5
Total	2,314	9,686,292	627		

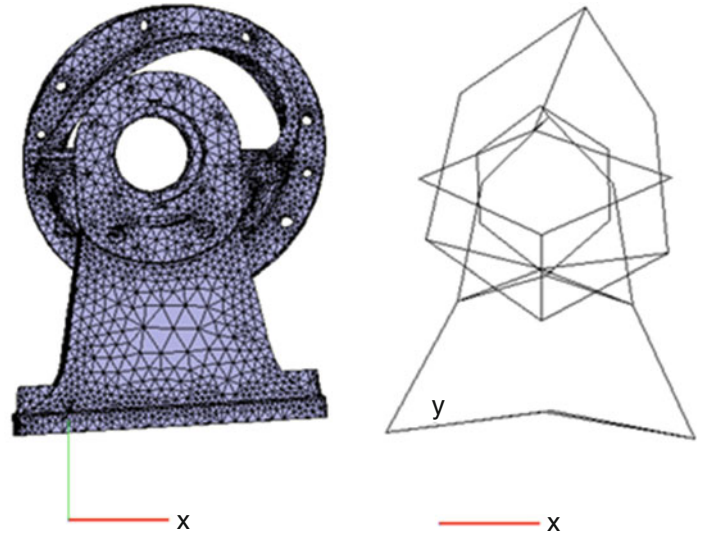
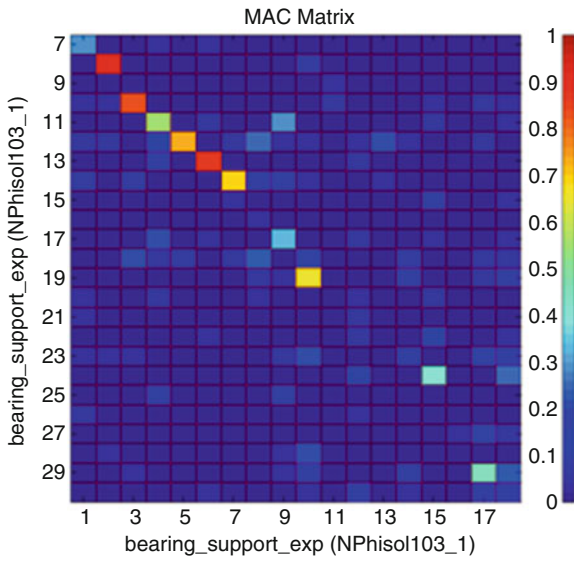
**Fig. 19.4** Relative strain energies for each superelement

The accuracy of the ROM is expressed by Table 19.2 where a modal analysis has been performed for each superelement as well as the full FE model and the reduced one with free-free boundary conditions. Except for the bearing casing, prediction errors with the ROM are below 10% while the size of the FE model is drastically reduced, thus improving the feasibility of the iterative calibration process.

### 19.2.3 Sensitivity Analysis and Calibration at the Component Level

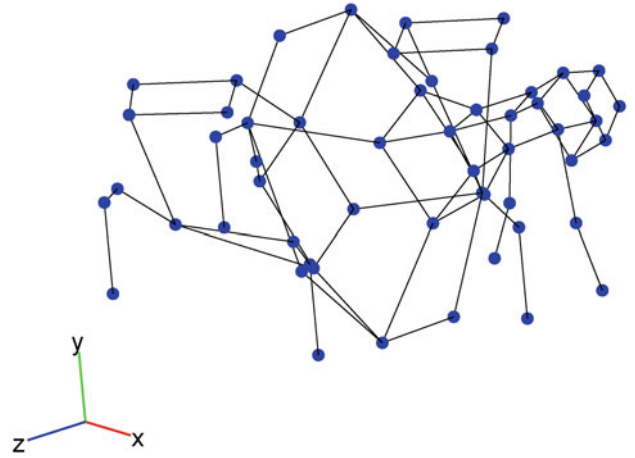
A sensitivity analysis [13] is then performed in order to rank input variables with respect to their deterministic influence on features of interest. The relative strain energy is an efficient indicator to assess the impact of modifications on structural dynamics: the higher this energy for a given superelement, the more sensitive this superelement will be.

Figure 19.4 plots the relative strain energy for each superelement: only few of them seems to be influent. Dedicated tests at the component level are used in order to calibrate only the most influential substructures. For instance, Fig. 19.5 illustrates the level of correlation between test and model at the component level, namely the bearing support.



**Fig. 19.5** Calibration at the component level

**Fig. 19.6** Experimental mesh



#### 19.2.4 Calibration of the ROM at the Assembled Level

Experimental modal data are available at the assembled level and the experimental mesh contains 55 nodes (three dofs/node) and is depicted in Fig. 19.6. Since the ROM is already constructed, the calibration parameters are either the interface between superelements or a weighting (non-physical) coefficient for each superelement. Though other cost functions are available for model calibration (see for instance, the Extended Constitutive Relation Error—ECRE [14]), here a simple and inexpensive output-based cost function is used. Calibration parameters  $\mathbf{p}^*$  minimize the function

$$g = \sum_{\nu} |\omega_{\nu} - \omega_{\nu}^{\text{test}}|_2 + \sum_{\nu} |\phi_{\nu} - \pi \phi_{\nu}^{\text{test}}|_2, \quad (19.2)$$

where  $(\omega_{\nu}, \phi_{\nu})$  and  $(\omega_{\nu}^{\text{test}}, \phi_{\nu}^{\text{test}})$  are respectively the calculated and the experimental eigensolutions (taken as the reference) and  $\pi$  is the transformation matrix between the numerical mesh and the experimental one.

Before optimizing  $g$ , the active calibration parameters have to be defined. Toward this end, a Morris sensitivity analysis [15] is performed in order to select the most sensitive variables. Such an approach is a global sensitivity analysis and has the objective to compute the sensitivity of parameters by calculating several times the elementary effect of each parameter. The sensitivity indicators are the mean and the standard deviation of the elementary effect. The mean gives information about the overall influence and the standard deviation indicates if the parameters have a coupling effect with other(s) parameter(s) or



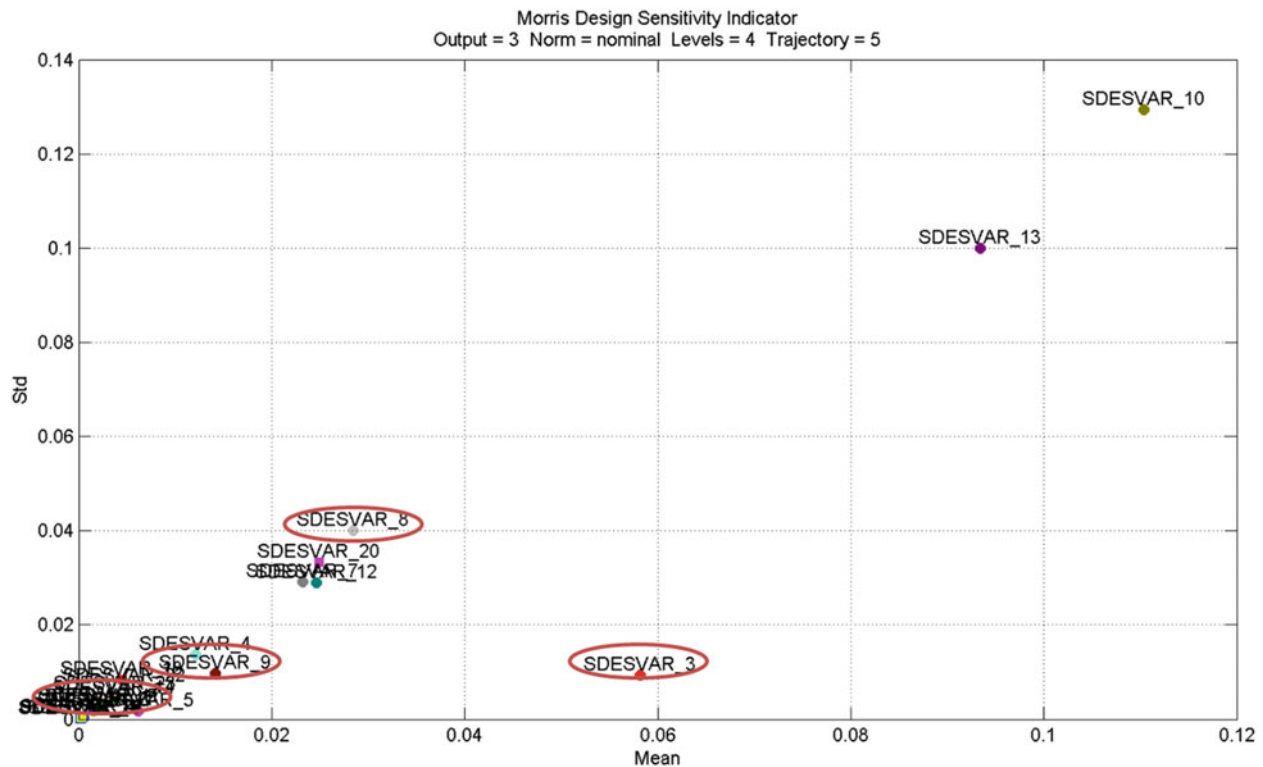


Fig. 19.7 Morris sensitivity analysis

Table 19.3 Discrepancy between model prediction and test data after calibration

Mode	Test (Hz)	Mode	Model (Hz)	Error (%)	MAC
1	76.8	3	77.3	0.7	91.1
2	134.4	5	133.7	-0.5	75.5
3	162	6	154	-4.9	93.7
4	211.9	7	199.2	-6	92.2
5	233.4	9	214.4	-8	88.8
6	251.2	10	224.8	-10.6	86.0

a non-linear effect. Figure 19.7 plots the mean and the standard deviation of each elementary effect. The selected calibration parameters are encircled (see Fig. 19.7). One can see that some selected calibration parameters are not very sensitive and vice versa. For instance, the variable SDESVAR 10 is the frame and its properties are well-known. Hence, a high sensitivity is not a sufficient criterion to select variable as a calibration parameter. Based on engineering judgment, a variable must be poorly known in order to be candidate as a calibration parameter. The selected calibration parameters are thus both sensitive and uncertain.

At the end, this bottom-up calibration yields a predictive FE model. For example, Table 19.3 provides the eigenfrequencies predicted by the calibrated model as well as their relative errors (in %) when compared to experimental eigenfrequencies and the corresponding MAC values. This table emphasizes also the good agreement between simulation prediction and test data after the calibration process.

### 19.3 Toward a Robust Calibration Paradigm

The proposed calibration strategy was applied on the pump considered without a connection with the piping. More precisely, the pump is connected to piping: it is the real operational boundary conditions. This real boundary condition are thus not taken into account in the construction of the FE model and it is well known that this kind of boundary condition strongly modifies the structural dynamic behavior. Furthermore, such types of connection are extremely difficult to model. One of the

main reason is that piping can be considered to be flexible and thus contains vibration modes. Furthermore, these types of connection are variables: pipes are unique in each power plant and thus boundary conditions are not the same in one location or in another. That is why, these types of connection can reasonably be assumed to be uncertain.

In presence of lack of knowledge, deterministic calibration makes no sense since the calibrated design with the highest fidelity-to-data (or fidelity-optimal design) strongly depends on (potential) wrong assumption. For instance, if the boundary conditions of the pump are modeled in two different ways, it is clear that two different fidelity-optimal designs—i.e. both designs can predict the data with the same fidelity-to-data—could be found. This is directly related by the fact that, during the calibration process and in presence of uncertainty, calibration parameters are compensating each others [16]. Hence, the conventional approach that selects the model with the highest fidelity-to-data is not sufficient to demonstrate the credibility of models. It turns out that exploring robustness in addition to fidelity lends credibility to the model, ensuring model predictions can be trusted even when lack-of-knowledge in the modeling assumption and/or input parameters result in unforeseen errors and uncertainties.

Rooted in info-gap theory [10], robust calibration approaches [9] is the preferred way for exploring the robustness-to-uncertainty. Nevertheless, it has been also demonstrated in [9] that improving both robustness-to-uncertainty and fidelity-to-data are antagonistic. The inherent antagonistic nature of these components leads to fundamental trade-offs that forms the basis of the new model calibration paradigm. Typical robust calibration approach is briefly described.

Model predictions can be denoted by

$$\mathcal{M}(\mathbf{p}, \mathbf{u}) = \mathbf{y}, \quad (19.3)$$

where  $\mathbf{p}$  are the calibration parameters (or model input parameters),  $\mathbf{u}$  the uncertain parameters and  $\mathbf{y}$  the response feature of interest. For instance, here, calibration parameters could be the stiffness at the interface between two superelements and uncertain parameters could be the boundary conditions. The FE model is used to predict eigensolutions, which are the response features of interest.

The objective is to study the robustness of the model fidelity to experimental data in presence of lack of knowledge in the boundary conditions. The discrepancy between the simulated eigensolutions and the experimental ones (seen here as the reference) can be assessed with a metric  $\mathcal{D}(\mathbf{p}, \mathbf{u})$  defined as the norm of the difference between test data  $\mathbf{y}^{\text{test}}$  with the results obtained from the model  $\mathcal{M}(\mathbf{p}, \mathbf{u})$ :

$$\mathcal{D}(\mathbf{p}, \mathbf{u}) = \|\mathbf{y} - \mathbf{y}^{\text{test}}\|_{\mathcal{N}}, \quad (19.4)$$

where  $\mathcal{N}$  is the norm dependent on the type of data that the model predicts. For instance, in the case of the pump,  $\mathbf{y}$  is a vector of eigenfrequencies, then the norm  $\mathcal{N}$  would simply be the  $\ell^2$ -norm. Finally, the smaller  $\mathcal{D}(\mathbf{p}, \mathbf{u})$  is, the better the model is. Nevertheless, the model is assumed to be predictable when

$$\mathcal{D}(\mathbf{p}, \mathbf{u}) \leq d_c, \quad (19.5)$$

where  $d_c \geq 0$  is the greatest level of discrepancy that can be tolerated.

Info-gap model of uncertainty  $\mathcal{U}(\alpha, \mathbf{u}^0)$  is used to represent the uncertainty in the system. Hence,

$$\mathbf{u} \in \mathcal{U}(\alpha, \mathbf{u}^0), \quad (19.6)$$

with  $\alpha \in \mathbb{R}_+$  the unknown horizon of uncertainty which measures the distance—or the gap—between the estimate  $\mathbf{u}^0$  and the whole possibilities in the set  $\mathcal{U}(\alpha, \mathbf{u}^0)$ . Many different info-gap models of uncertainty are available (see pp. 20–30 in [10]): for instance, the info-gap relative error model is

$$\mathcal{U}(\alpha, \mathbf{u}^0) = \left\{ \mathbf{u} : \left| \frac{\mathbf{u} - \mathbf{u}^0}{\mathbf{u}^0} \right| \leq \alpha \right\}. \quad (19.7)$$

The model of uncertainty  $\mathcal{U}(\alpha, \mathbf{u}^0)$  is actually an unbounded family of nested convex sets of realizable designs.

The info-gap theory is a decision theory and one of the main feature in this approach is the robustness function  $\hat{\alpha}$ . Broadly speaking, the robustness of decision to choose  $\mathbf{p}$  is the greatest horizon of uncertainty that can be tolerated without exceeding the critical performance  $d_c$ . Hence, the robustness function is expressed as a function of the design  $\mathbf{p}$  and the critical performance requirement  $d_c$ . It is written by

$$\hat{\alpha} = \hat{\alpha}(\mathbf{p}, d_c) = \max\{\alpha : \max_{\mathbf{u} \in \mathcal{U}(\alpha, \mathbf{u}^0)} \mathcal{M}(\mathbf{p}, \mathbf{u}) \leq d_c\}. \quad (19.8)$$

The conventional approach in model calibration methods seeks to maximize solely the fidelity-to-data. Thus, the fidelity-optimal parameters are obtain by

$$\mathbf{p}^* = \arg \min_{\mathbf{p}} \{\mathcal{M}(\mathbf{p}, \mathbf{u}^0)\}. \quad (19.9)$$

Nevertheless, this conventional approach does not take into account the uncertainty in  $\mathbf{u}$ . On the contrary, robust calibration approach aims to choose  $\mathbf{p}$ —the robust parameters—in such a way to minimize the impact of  $\mathbf{u}$  on the system performance. For a given tolerable threshold  $d_c$ , the robust parameters  $\mathbf{p}^R$  are the ones which maximize the robustness function. The robust-optimal parameters are

$$\mathbf{p}^R = \arg \max_{\mathbf{p}} \{\hat{\alpha}(\mathbf{p}, d_c)\}. \quad (19.10)$$

Initially formulated in [9], the tradeoff between fidelity-to-data and robustness-to-uncertainties expresses that *Robustness improves as fidelity deteriorates*. Because the info-gap models of uncertainty have the properties to be nested, the robustness function is monotonically increasing. Hence, let  $d_c$  and  $d'_c$ , two different level of fidelity, then:

$$d_c < d'_c \Rightarrow \hat{\alpha}(\mathbf{p}, d_c) \leq (\mathbf{p}, d'_c). \quad (19.11)$$

Equation (19.11) asserts that, for any given model, specified by  $\mathbf{p}$ , the robustness-to-uncertainties increases as the required fidelity is relaxed. Typical tradeoffs between fidelity-to-data and robustness-to-uncertainties are emphasized by exploring the robustness curve. The reader can refer to [17, 18] for various illustrations of robust calibration strategy.

To sum-up, the important steps toward a robust calibration are:

- Construct a metamodel with the objective to replace the functional  $\mathcal{M}$ ;
- Propose an adequate info-gap model of uncertainty capable of modeling the lack of knowledge in boundary conditions;
- Compute the robustness curves with the objective to study the tradeoffs.

These steps will be performed in order to tackle the robust calibration strategy on the pump, the structure of interest within the SICODYN project framework.

## 19.4 Conclusions

The first objective was to provide a two-level bottom-up calibration approach suitable for dealing with industrial FE models. This approach was illustrated on a pump, the structure of interest within the SICODYN project framework. At the end, a calibrated FE model capable of predicting the identified modal data was found. Nevertheless, in presence of lack of knowledge, maximizing solely the fidelity-to-data is not the best way to improve the credibility of the model [9]. The second objective was to formulate a robust calibration methodology for future work in order to account for lack of knowledge in the final operational boundary conditions of the pump.

## References

1. Audebert S (2010) Sicodyn international benchmark on dynamic analysis of structure assemblies: variability and numerical-experimental correlation on an industrial pump. *Mec Ind* 11(06):439–451
2. Mottershead JE, Friswell MI (1993) Model updating in structural dynamics: a survey. *J Sound Vib* 167(2):347–375
3. Hemez FM, Farrar CR (2014) A brief history of 30 years of model updating in structural dynamics. In: Foss G, Niezrecki C (eds) *Special topics in structural dynamics*, vol 6. Springer, Berlin, pp 53–71
4. Baruch M (1982) Optimal correction of mass and stiffness matrices using measured modes. *AIAA J* 20(11):1623–1626
5. Berman EJ, Nagy A (1983) Improvement of a large analytical model using test data. *AIAA J* 21(8):1168–1173
6. Mottershead JE, Link M, Friswell MI (2011) The sensitivity method in finite element model updating: a tutorial. *Mech Syst Signal Process* 25(7):2275–2296
7. Govers Y, Link M (2010) Stochastic model updating-covariance matrix adjustment from uncertain experimental modal data. *Mech Syst Signal Process* 24(3):696–706

8. Goller B, Broggi M, Calvi A, Schueller GI (2011) A stochastic model updating technique for complex aerospace structures. *Finite Elem Anal Des* 47(7):739–752
9. Ben-Haim Y, Hemez FM (2011) Robustness, fidelity and prediction-looseness of models. *Proc R Soc A* 468:227–244
10. Ben-Haim Y (2006) *Information-gap theory: decisions under severe uncertainty*, 2nd edn. Academic, London
11. Doebling SW, Hemez FM, Schultze JF, Cundy AL (2002) A metamodel-based approach to model validation for nonlinear finite element simulations. In: *International modal analysis conference XX*, Los Angeles, 4–7 Feb 2002
12. Craig RR, Bampton MCC (1968) Coupling of substructures for dynamic analyses. *AIAA J* 6(7):1313–1319
13. Saltelli A, Chan K, Scott EM (2000) *Sensitivity analysis*, vol 134. Wiley, New York
14. Deraemaeker A, Ladevèze P, Leconte P (2002) Reduced bases for model updating in structural dynamics based on constitutive relation error. *Comput Methods Appl Mech Eng* 191:2427–2444
15. Morris MD (1991) Factorial sampling plans for preliminary computational experiments. *Technometrics* 33(2):161–174
16. Atamturktur S, Liu Z, Cogan S, Juang H (2014) Calibration of imprecise and inaccurate numerical models considering fidelity and robustness: a multi-objective optimization-based approach. *Struct Multidiscip Optim*. doi:[10.1007/s00158-014-1159-y](https://doi.org/10.1007/s00158-014-1159-y)
17. Pereira D, Cogan S, Sadoulet-Reboul E, Martinez F (2013) Robust model calibration with load uncertainties. In: *Topics in model validation and uncertainty quantification*, vol 5. Conference proceedings of the society for experimental mechanics series 41. Springer, New York, pp 89–97
18. Van Buren KL, Atamturktur S, Hemez FM (2014) Model selection through robustness and fidelity criteria: modeling the dynamics of the cx-100 wind turbine blade. *Mech Syst Signal Process* 43(1):246–259

# Chapter 20

## Model Validation in Scientific Computing: Considering Robustness to Non-probabilistic Uncertainty in the Input Parameters

Greg Roche, Saurabh Prabhu, Parker Shields, and Sez Atamturktur

**Abstract** The origin of the term validation traces to the Latin *valere*, meaning *worth*. In the context of scientific computing, validation aims to determine the worthiness of a model in regard to its support of critical decision making. This determination of worthiness must occur in the face of unavoidable idealizations in the mathematical representation of the phenomena the model is intended to represent. These models are often parameterized further complicating the validation problem due to the need to determine *appropriate* parameter values for the *imperfect* mathematical representations. The determination of worthiness then becomes assessing whether an unavoidably imperfect mathematical model, subjected to poorly known input parameters, can predict sufficiently well to serve its intended purpose. To achieve this, we herein evaluate the agreement between a model's predictions and associated experiments as well as the robustness of this agreement given imperfections in both the model's mathematical representation of reality as well as its input parameter values.

**Keywords** Robustness to uncertainty • Experiment-based validation • Uncertainty quantification • Bounded uncertainty • Parameter variability

### 20.1 Introduction

Despite their sophistication, computer models can only provide approximations of the reality they are built to represent. As the famous declaration of statisticians George Box and Norman Draper reminds us, “all models are wrong, but some are useful.” Thus, the *raison d'être* of a model is not to be a *correct* representation of reality, but to include sufficient realism to be *useful* in decision making. In this paper, we are concerned with assessing the usefulness of mechanistic models which aid in our understanding of the underlying phenomena. We should therefore consider the three distinct components of the development process for such models:

- (a) the domain in which the problem will be evaluated, typically defined by the control parameters that dictate the environmental or operational conditions of the system,
- (b) the mathematical representation of the underlying processes, also referred to as model form, defined in accordance with the identified domain,
- (c) the input parameters that characterize the properties of the system of interest in accordance with the mathematical representations.

Proper determination of the domain is one of the key aspects of predictive modeling. The domain of applicability must be strictly determined based upon what is necessary for decision making as the model's internal structure will be determined

---

G. Roche • S. Prabhu  
Clemson University, Clemson, SC 29634, USA

P. Shields  
Applied Building Sciences, Inc., Chapin, SC 29036, USA

S. Atamturktur (✉)  
Glenn Department of Civil Engineering, Clemson University, Clemson, SC 29634, USA  
e-mail: [sez@clemson.edu](mailto:sez@clemson.edu)

according to this domain. Herein, we will conveniently<sup>1</sup> assume that the model developer has identified the suitable domain (item a) and focus our attention on the selection of a model form and its associated parameter values (items b and c).

Item b declares that no model form is a perfect representation of reality. Item b is closely associated with item c and their close association raises the following question: Should we use parameter values that suitably compensate for the model form's imperfectness or rather those that most accurately depict the real parameters? The former is typically what is achieved by calibrating model parameters against experiments and of course, the latter is only possible if the parameter has a physical, measurable meaning (i.e. density of a material, geometric dimension, etc.). How should we approach this problem then if a model's parameters have no physical meaning, or worse, if those with physical meaning are wrongly excluded during model idealization?

As seen, a great many complications arise in the selection of input parameters for imperfect model forms while no universally accepted approach exists to help in their determination. *Hence, the only logical way of approaching this problem is to ensure that the selected mathematical representation (i.e. model form) must not only provide sufficiently accurate predictions of observable reality,<sup>2</sup> but that it must do so given uncertainty in its own parameter values.* The capability of a model form in accommodating parametric uncertainties is termed robustness. A model is said to be robust if a small change in parameter values results in model predictions that are within acceptable fidelity bounds [1–4]. Models that afford higher uncertainties while staying robust with respect to the predictions of interest would therefore be preferable.

Section 20.2 of this paper overlays the proposed approach to evaluating fidelity and robustness of model predictions. The development of a case study application involving the proposed approach is presented in Sect. 20.3. Section 20.4 presents a discussion of the implications of this approach using the case-study application along with generalizations to a wide range of practical problems. Finally, Sect. 20.5 concludes the paper and discusses limitations of the proposed approach as well as the future direction for improvement.

## 20.2 Methodology

Consider a model with parameters whose variability is represented by bounded uncertainty, defining the model's parameter space. If that model is a locally proper, continuous function, then within the bounds of its uncertain parameter space, a *small* change in the input parameters around their nominal values will yield a *small* change in the model's output. The implication is that for a compact space of input parameters, the model's output will be compact (i.e. closed and bounded) (see Fig. 20.1). The compact input space can be defined for instance by a predefined window of uncertainty around the nominal values. Within the compact output, we can identify the realizations, which satisfy a certain error tolerance when compared with experimental observation. Here, we introduce the concept of a *satisfying boundary*<sup>3</sup> that encompasses all the model input parameter sets which satisfy this prescribed error tolerance. From another perspective, this boundary marks the periphery beyond which lie combinations of parameter values which yield unacceptable model predictions. This satisfying boundary is expected to monotonically increase in size as the error tolerance becomes less and less stringent, as shown in Fig. 20.2.

Obviously, the satisfying boundary is strongly dependent upon the model form itself. Hence, among alternative model forms with the same set of uncertain parameters, the model with a larger satisfying boundary should be preferred as it can accommodate increased uncertainty in its parameters while meeting the error tolerance requirement. In our study, we build upon this concept and closely integrate two independent pieces of information: a satisfying boundary that is intrinsic to the model form and the bounded space that is intrinsic to the uncertain model parameters.

Here, we determine a model's *probability of satisfying* a given error tolerance for a given level of uncertainty in its parameters. Hence, for a given error tolerance and uncertain parameter space, a model's performance can be quantified by comparing the parameter values contained within the satisfying boundary to those contained within the uncertain parameter space. The ratio of points within the satisfying boundary to the total number of values in the uncertain parameter space yields the model's probability of satisfying the error tolerance. Figure 20.3 demonstrates such a case for a two-parameter model.

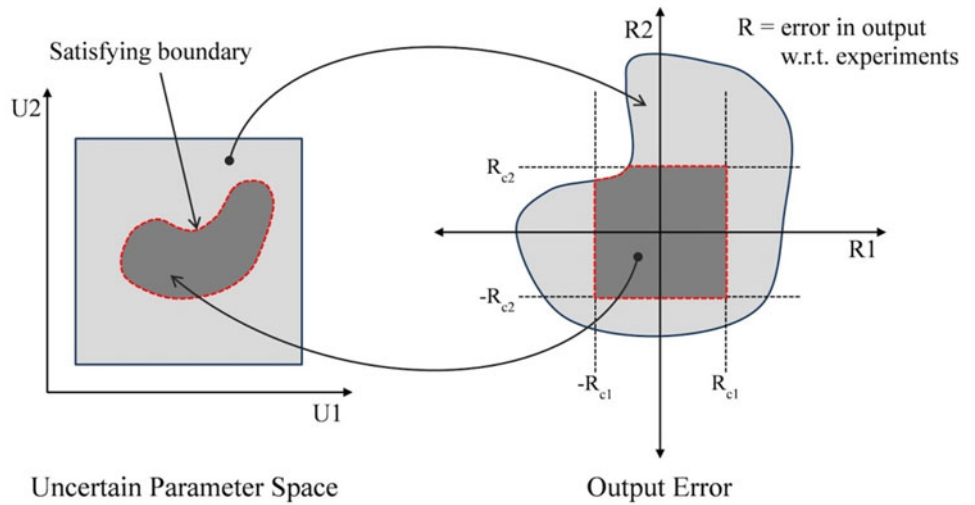
Knowing the satisfying boundary can help determine the impact of parameter uncertainty on the output of a model. For instance, if 100 % of the parameter value sets within the parameter space are effectively contained within the satisfying

<sup>1</sup>Note that we have also conveniently assumed that model yields converged solutions within the time and spatial domains and that numerical uncertainties are of little importance.

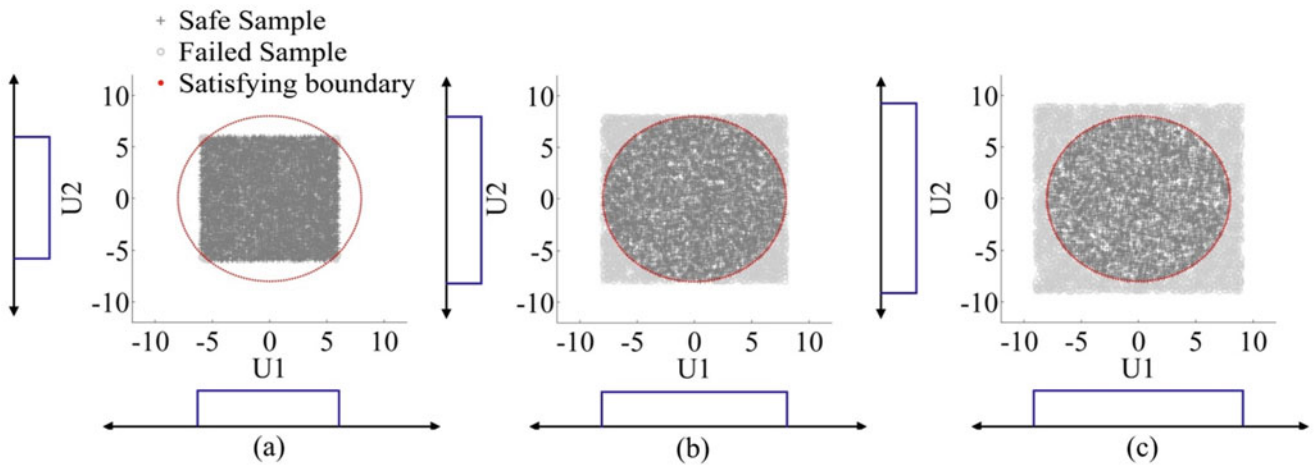
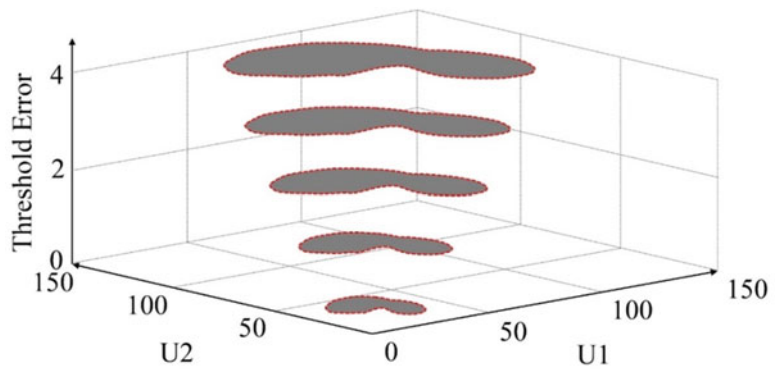
<sup>2</sup>Of course, the observables must be in sufficient quality and quantity to identify the model's flaws.

<sup>3</sup>For a model with two parameters, the size of a satisfying boundary would be defined by its area, while for a model with multiple parameters, the size would be defined by a hypervolume.

**Fig. 20.1** Conceptual figure showing the mapping from uncertain parameter space to output space and the compact satisfying boundary



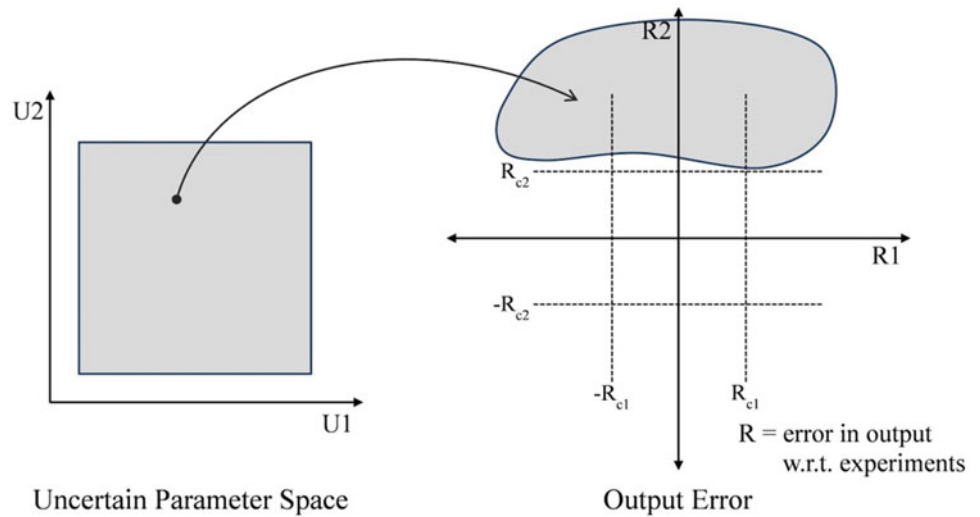
**Fig. 20.2** A schematic representation of the satisfying boundary monotonically increasing with increasing error tolerance in the predictions (i.e., decreasing fidelity)



**Fig. 20.3** Probability of satisfying the error tolerance for a two-parameter model given three distinct parameter spaces are (a) 99 %; (b) 79 %; and (c) 62 %

boundary, parameter uncertainty can be deemed inconsequential as the model predictions satisfy the error tolerance requirement regardless of parameter uncertainty. Thus, the model form can be said to be robust and able to make reliable predictions. However, if this is not the case, then we can resort to quantifying the probability that the model output will satisfy the error tolerance given the uncertainty of its parameters. If the probability of satisfying is inordinately low, it may indicate a problem with either (1) the model form or (2) the nominal parameter values suggesting that we must invest in developing a better model form or in better defining our parameters. Figure 20.4 demonstrates such a case where the probability of satisfying the error tolerance is 0 %. As the uncertain parameter space expands, some model instances may begin to satisfy

**Fig. 20.4** Conceptual figure showing the absence of a satisfying boundary as output errors fall outside the error tolerance



**Table 20.1** Input values for the portal frame

Property description	Beams and columns
All member lengths (in.)	120
Cross-sectional area (in. <sup>2</sup> )	4.44
Moment of inertia (in. <sup>4</sup> )	48.0
Young's modulus (ksi)	29,000

the error threshold leading to a counterintuitive increase in probability of satisfying with increasing parameter uncertainty. Such behavior can point to the imperfections in either the model form or the nominal parameter values.

While parametric uncertainties can be reduced by additional data collection and further analysis, we should first inquire as to whether a reduction in parameter uncertainty will improve the usefulness of the model. It is logical that if the parameter uncertainty has only a modest impact on a model's probability of satisfying a prescribed error tolerance, the dedication of resources towards reducing such uncertainty would seem frivolous and inefficient. Hence, in our evaluation, we do not require that a single value be specified for the uncertainty in a model's input parameters. Instead, an array of differing levels of uncertainty can be studied to observe how a model's probability of satisfying the fidelity tolerance changes with varying levels of parametric uncertainty. Of course, a higher probability of satisfying relates to an increase in the worthiness of a model for its intended use. Such trade-off analysis allows us to measure the impact of efforts aimed at reducing uncertainty.

### 20.3 Proof-of-Concept Demonstration: Steel Moment Resisting Frame

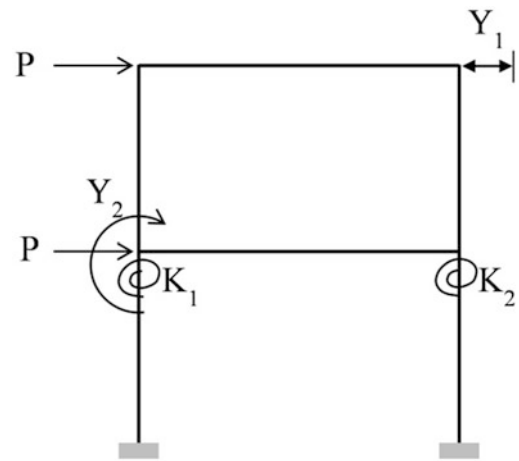
In steel frame structures, the connection stiffness values are typically highly uncertain due to the natural variability of material properties and geometries as well as the construction practices used to erect them [5, 6]. Hence, these parameters are treated as uncertain parameters to be calibrated within this study.

#### 20.3.1 Description of Frame Structure

The 2-D frame shown in Fig. 20.4 is constructed with vertical columns that rest on fixed supports, while the beams are rigidly connected to the columns at both levels. The connections at the top of the first story columns are assumed to be imprecisely known and thus, modeled with uncertain stiffness. Here, the connections are represented with linear rotational springs. All members of the portal frame have uniform dimensions with the geometric data and material properties provided in Table 20.1. Static, horizontal loads are applied to the portal frame as shown and the members are oriented to bend about their strong axes.



**Fig. 20.5** Single-bay, two-story portal frame with rotational springs at the top of the first story columns



**Table 20.2** Exact values and simulation ranges for input parameters  $K_1$  and  $K_2$

	$K_1$	$K_2$
Exact value	10	10
Lower bound	5	5
Upper bound	15	15

### 20.3.2 Synthetic Experiments and Competing Model Forms

In the development of the mathematical representation, a number of simplifying assumptions may be established or idealizations may take place leading to multiple competing model forms. In this section, we demonstrate how the probability of satisfying the error tolerance can be used to compare three distinct model forms with varying levels of model imperfectness (i.e. prediction bias).

Experimental data describing the frame's translation and rotation response at each connection (while subjected to the loading conditions shown in Fig. 20.5) is synthesized using the so-called *exact* model built using the Timoshenko beam theory [7]. This exact model not only accurately accounts for the effects of axial, shear, and flexural deformations but also uses the nominal values of  $K_1$  and  $K_2$  (Table 20.1).

Alongside the exact model, two inexact (biased) model forms are built: one that underestimates and one that overestimates the shear area within the Timoshenko beam matrices. Hence, the two inexact models will inaccurately account for the shear deformations, while all three models will contain uncertainty as to which values of  $K_1$  and  $K_2$  are *appropriate* for the analysis. These inaccurate and imprecise models will thus result in unavoidable disagreements between predictions and experiments offering a decision maker three alternative options.

## 20.4 Assessment of Uncertainties Steel Moment Resisting Frame

### 20.4.1 Exact Model with Uncertain Input Parameters

The exact values for  $K_1$  and  $K_2$  as well as the bounds of the parameter space are provided in Table 20.2. For the various combinations of  $K_1$  and  $K_2$ , the model predictions are compared to the synthetic experimental data to calculate the prediction error. Here, two outputs of the frame are selected namely the rotation at the first story and the translation at the top story (marked as  $Y_1$  and  $Y_2$  respectively in Fig. 20.5). The corresponding prediction error  $R_1$  and  $R_2$  are the percentage difference with respect to the exact model. Figure 20.6 illustrates the relationship between the error in the model output (i.e. lack of fidelity) and the two parameter values.

Subsequently, satisfying boundaries are generated for varying error tolerances,  $R_c$ , shown in Fig. 20.7.  $R_c$  is varied from 0 % to 5 % prediction error in steps of 0.5 %. In Fig. 20.7, each contour corresponds to an error tolerance level  $R_c$  such that all instances of  $K_1$  and  $K_2$  that lie within the contour satisfy the error tolerance. As expected of a continuous system, the satisfying boundaries are nested with their size increasing as error tolerance increases. The model form used in the development of this figure was "exact," which is why the nominal parameter values are encompassed within the satisfying boundaries.

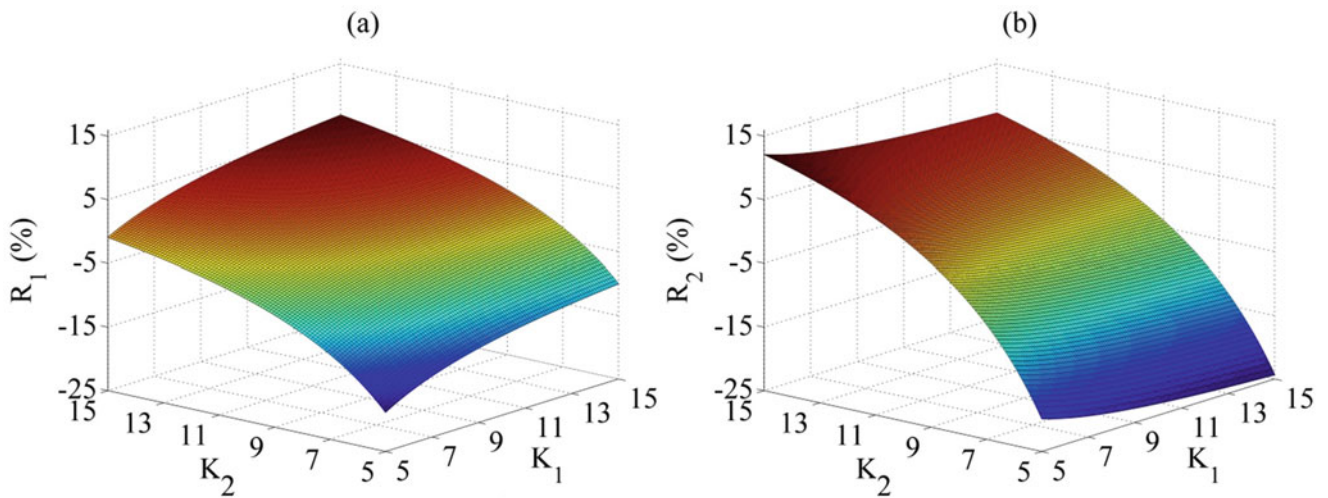


Fig. 20.6 Three-dimensional representation of prediction errors  $R_1$  and  $R_2$  in the exact model

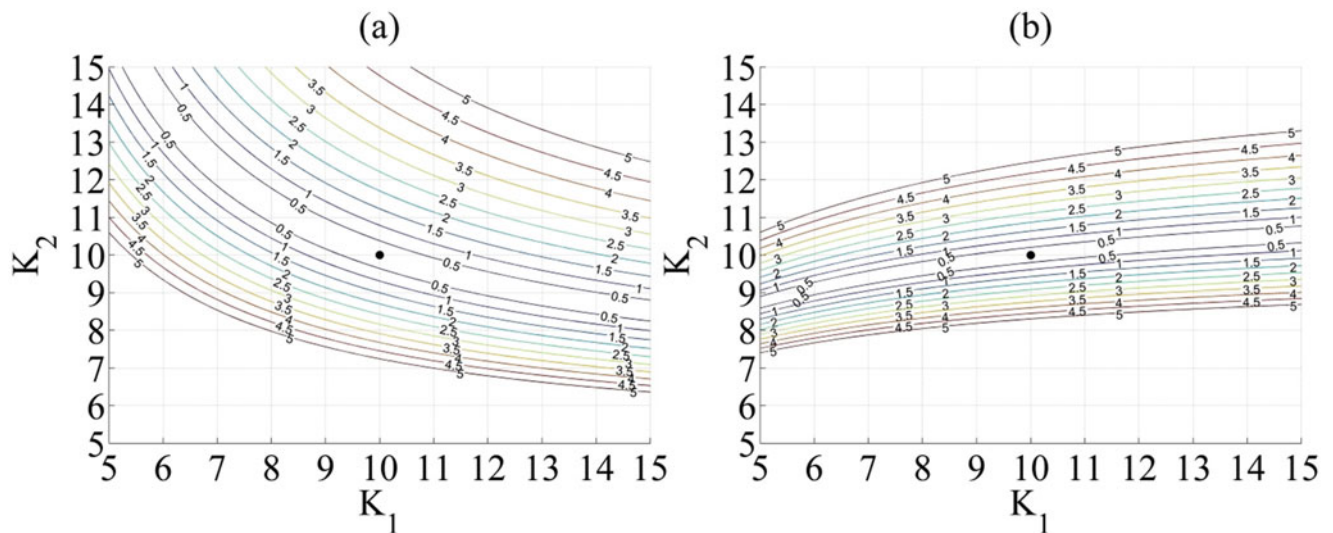
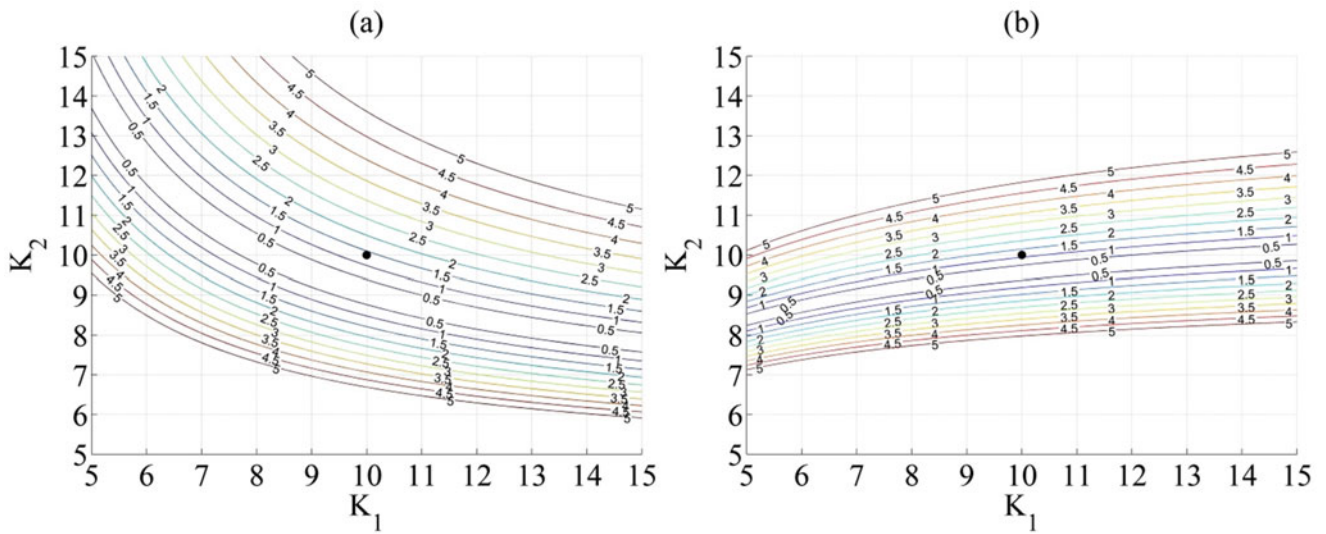


Fig. 20.7 Nested sets of satisfying boundaries for increasing levels of error tolerance for the exact frame model for (a) output  $Y_1$  and (b)  $Y_2$ . The black dot represents the location of the nominal parameter values

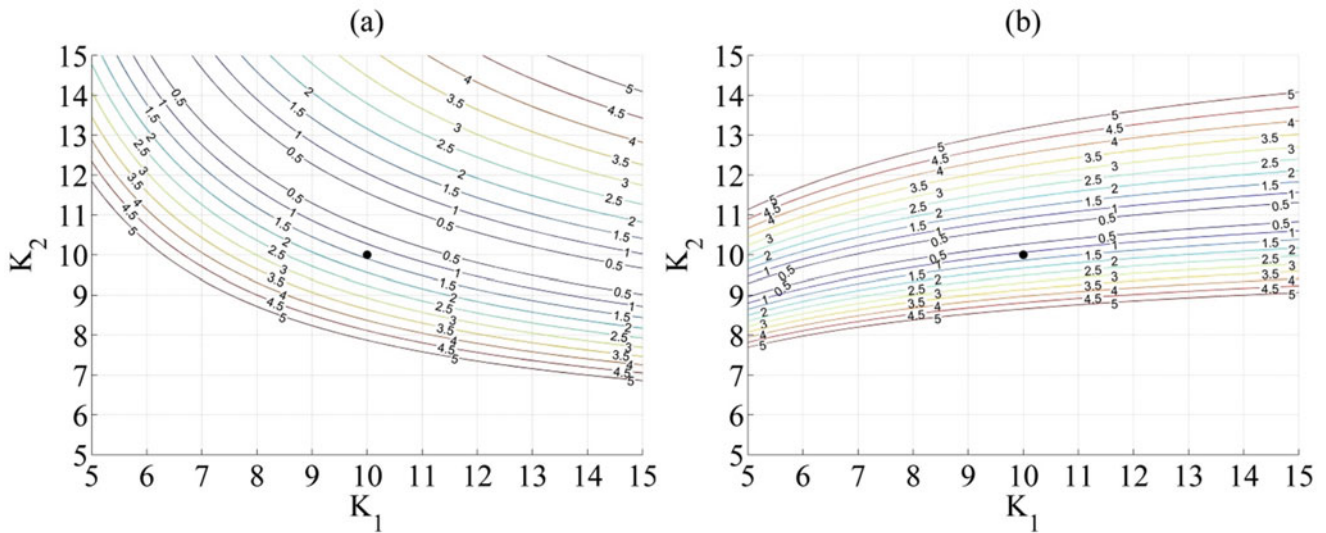
### 20.4.2 Inexact Models with Uncertain Input Parameters

The two inaccurate finite element models studied herein underestimate and overestimate the shear area of the beam and column elements by 25 % (i.e., 75 and 125 % shear area, respectively). This intentional error is meant to mimic a possible modeling mistake as it results in biased model predictions. The satisfying boundaries for the two inexact models are shown in Figs. 20.8 and 20.9.

As seen in Fig. 20.8, the underestimation of shear deformation causes the satisfying boundaries to shift downwards, which is evident when compared to the corresponding satisfying boundaries obtained from the unbiased model shown in Fig. 20.7. An important observation we can garner from Fig. 20.7 is that the nominal parameter values represented by the black dot ( $K_1 = K_2 = 10$ ) in Fig. 20.8 are no longer encompassed by the initial (smallest) satisfying boundaries. This is the result of the inherent bias in the predictions of these two inexact models. Figure 20.9 shows the satisfying boundaries for the frame model with the shear area overestimated by 25 % and a bias in the opposite direction.



**Fig. 20.8** Nested sets of satisfying boundaries for increasing levels of error tolerance for the biased frame model (25 % lower shear area) for (a) output  $Y_1$  and (b)  $Y_2$ . The *black dot* represents the location of the nominal parameter values



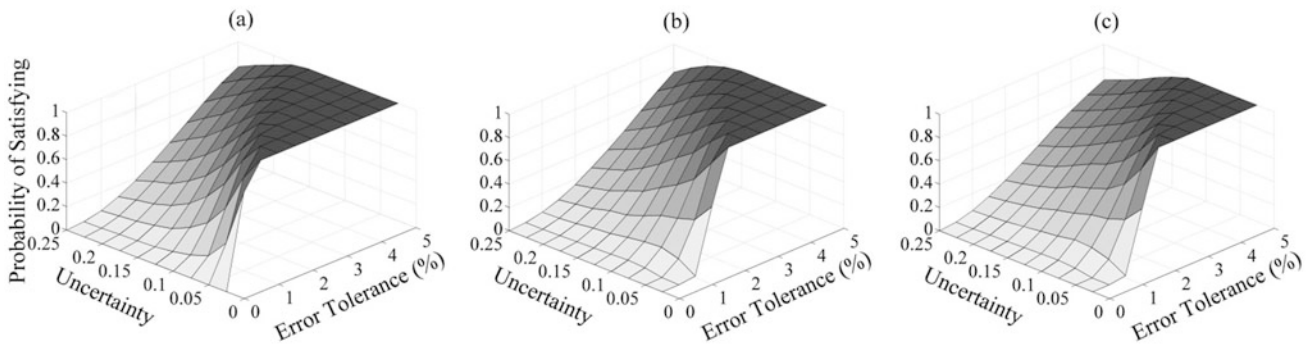
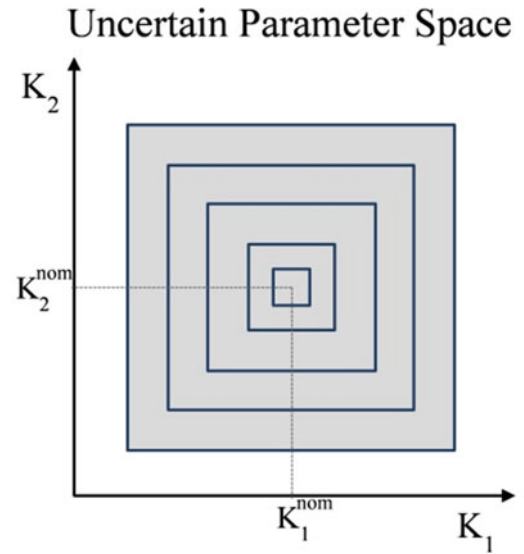
**Fig. 20.9** Nested sets of satisfying boundaries for increasing levels of error tolerance for the biased frame model (25 % higher shear area) for (a) output  $Y_1$  and (b)  $Y_2$ . The *black dot* represents the location of the nominal parameter values

### 20.4.3 Utilizing the Satisfying Boundaries

The satisfying boundaries for the three competing models (one exact and two inexact) shown in the previous section are used herein to evaluate the probability of satisfying predefined error tolerances considering the bounds of uncertain parameter spaces. In this evaluation, multiple parameter spaces that are nested around the nominal values ( $K_1 = K_2 = 10$ ) are considered. These nesting parameter spaces increase in size from 5 to 50 % of their nominal values in steps of 5 % as show in Fig. 20.10.

This evaluation is repeated for increasing levels of error tolerance throughout a range of 0–5 %, in steps of 0.5 %. Figure 20.11 displays the relationship between the varying levels of error tolerance in model predictions, the parameter uncertainty and the subsequent probability that the model satisfies this predefined error tolerance. Since two outputs, namely the rotation at the first story and the translation at the top story of the steel frame, are considered, the joint probability of satisfying the error tolerance in both outputs is calculated (see Fig. 20.11).

**Fig. 20.10** Nested parameter spaces with increasing uncertainty bounds



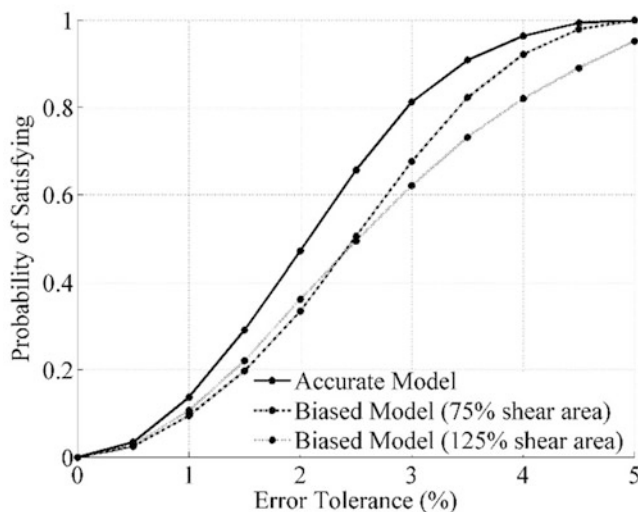
**Fig. 20.11** Three-dimensional plot showing trade-off between probability of satisfying, error tolerance and parametric uncertainty for the (a) accurate model, (b) inaccurate model with 25 % underestimated shear area and (c) inaccurate model with 25 % overestimated shear area

It can be observed from Fig. 20.11 that as error tolerance increases so too does the probability of satisfying the error tolerance. The rate of increase depends on the level of bounded uncertainty. When the uncertainty in the parameters is low, the probability is observed to increase at a more rapid rate than when the uncertainty in the parameters is high. The light region in Fig. 20.11 represents the situation where the model is not suitable for its intended use (as defined by the error tolerance) given the available knowledge (as defined by the parametric uncertainty). On the other hand, the dark region in Fig. 20.11 represents the situation where the model is a good fit for its intended use. This region is obtained when the experimental uncertainty approaches lower values and when the error tolerance approaches higher values. The model with the exact form (Fig. 20.11a) displays larger dark region compared to the two inexact models (Fig. 20.11b, c). Hence, Fig. 20.11 can be used as a diagnostic tool to identify the usefulness of a computer model.

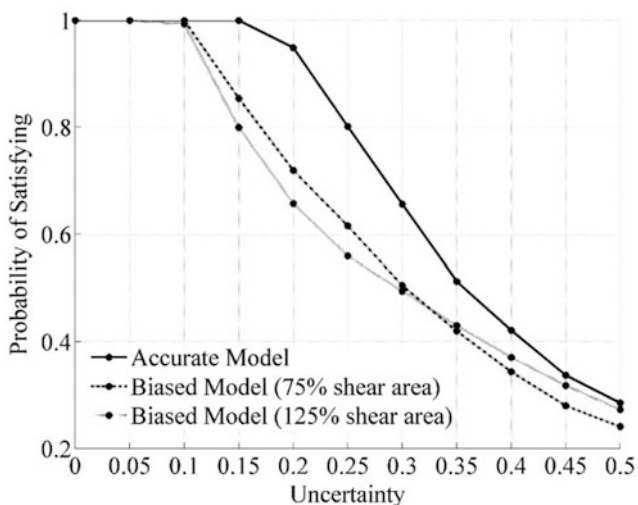
Figure 20.12 depicts the relationship between the probability of satisfying the error tolerance and the error tolerance itself for 30 % uncertainty in  $K_1$  and  $K_2$ . As can be seen in Fig. 20.12, for an error tolerance of 0 %, the corresponding probability of satisfying this tolerance is 0 %, meaning that no model form can accommodate the given level of uncertainty and satisfy the required error tolerance. Only by increasing the error tolerance does the probability of satisfying this tolerance increases. It can be observed in Fig. 20.12 that the exact model consistently yields a higher probability of satisfying the error tolerance compared to the two inexact models. Furthermore, exact model's probability of satisfying the error tolerance increases more rapidly with error tolerance (higher slope) than the two imperfect models. Although Fig. 20.12 demonstrates this observation for a constant level of uncertainty, this finding is noted to be valid throughout the entire parameter space evaluated herein.

Figure 20.13 plots probability of satisfying the error threshold of 3 % as a function of uncertainty in the input parameters. This plot allows the model developer to observe a potential improvement that can be gained in the probability of satisfying the desired error tolerance by reducing the uncertainty in the input parameters. For instance, if the developer of the exact model wants to ensure at least 90 % probability of satisfying the 3 % error tolerance, then it is clear that resources must be

**Fig. 20.12** Probability of satisfying as a function of prediction error for a 30 % uncertainty in  $K_1$  and  $K_2$



**Fig. 20.13** Probability of satisfying as a function of parameter uncertainty for a constant error tolerance ( $R = 3\%$ )

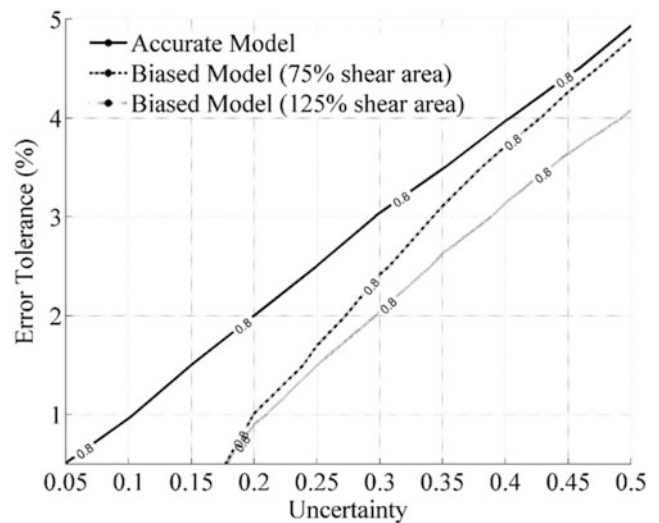


allocated to ensure that the uncertainty in the input parameters is lower than 20 %. On the other hand, Fig. 20.13 also shows that for uncertainty levels of 15 %, the exact model yields predictions that are 100 % within the error tolerance. Hence, from this figure, a modeler can deduce that allocating resources for reducing uncertainty below 10 % is not justifiable.

Also note in this figure that, for small levels of parameter uncertainty, all three competing model forms yield the same probability of satisfying the error threshold (i.e. 100 %). Hence, in this particular example, if uncertainty in the parameters is less than 10 %, attempts to improve model fidelity to reduce model bias are not justifiable. Increased levels of parameter uncertainty however lead to a reduction in this probability of satisfying the error tolerance and hence the role of bias once again becomes important. For very high levels of parameter uncertainty, all three models converge to unacceptably low probabilities of satisfying the error tolerance. Figure 20.13, like Fig. 20.12, can be used as a comparative tool and aid in model selection. For instance, a decision maker may establish a minimum probability of satisfying requirement and subsequently evaluate which model performs best given varying degrees of parameter uncertainty.

Alternatively, one can evaluate the relationship between the fidelity of model predictions and parameter uncertainty for a given probability of satisfying (shown for 80 % in Fig. 20.14). The two inexact models are inadmissible when the parameter uncertainty is less than 18 %. This can be explained by the fact that, for the biased models, the nominal parameters lie outside of the satisfying boundary (recall Figs. 20.8 and 20.9) resulting in the parameter spaces corresponding to low uncertainty falling entirely outside the satisfying boundary. This concept, demonstrated earlier in Fig. 20.4, supplies a means for diagnosing fundamental flaws in either our model forms or the values associated with the parameters of these model forms.

**Fig. 20.14** Prediction error as a function of parameter uncertainty for a constant probability of satisfying ( $P_s = 80\%$ )



## 20.5 Conclusion

In numerical modeling, uncertainties arise due to imprecisely-known input parameter values just as biases arise from our imperfect understanding of the underlying physics. This manuscript has presented a method to evaluate the usefulness of models for their intended use given the availability of information. This evaluation is completed considering three criteria. The first criterion, which relates to a model's intended use, involves the desired fidelity of model predictions to experimental observation. The second criterion, which relates to the availability of information, concerns how well a model can maintain these desired fidelity levels given uncertainty in its input parameters. The last criterion combines the first two criteria by assessing a model's probability of satisfying a predefined error tolerance requirement.

In this paper, we introduced the concept of a satisfying boundary, which maintains a compact form for proper continuous functions. Deriving the satisfying boundary of a 2-dimensional model allows us to visually observe the trade-off between the allowable error in the model predictions and the probability of achieving predictions that indeed satisfy this tolerance for a given uncertainty in model parameters. This evaluation can be repeated for various levels of parameter uncertainty to investigate the aforementioned qualities. This process allows us to observe how the model reacts to uncertainty in its input parameters.

Here, the individual tasked with validating the model must establish certain adequacy criteria regarding the tolerable error in model predictions or the desired probability of ensuring that the model satisfies this tolerable error. For a given level of uncertainty, only one of these two criteria need be known or defined, from which the third can then be determined. In these instances, knowledge of the trade-offs between these two criteria can afford a decision maker useful insight in selecting the most useful or appropriate values based upon the model's intended application.

The discussion in this paper is limited to proper continuous functions to ensure compactness of the satisfying boundary. For our application, satisfying this requirement locally around the nominal values of uncertain parameters is sufficient. However, relaxing this assumption may result in discontinuous or non-compact satisfying boundaries. Therefore, future work is necessary to explore this occurrence in hopes of determining its implications and how model validation should occur in these instances.

## References

- Weinmann A (1991) Uncertain models and robust control. Springer-Verlag, Vienna
- Elishakoff I (1995) Essay on uncertainties in elastic and viscoelastic structures: from A. M. Freudenthal's criticisms to modern convex modeling. *Comput Struct* 56(6):871–895
- Ben-Haim Y (2001) Information-gap decision theory: decisions under severe uncertainty. Academic Press, San Diego, California, USA
- Atamturktur S, Liu Z, Cogan S, Juang CH (2014) Calibration of imprecise and inaccurate numerical models considering fidelity and robustness: a multi-objective optimization based approach. *Struct Multidiscip Optim*. doi:10.1007/s00158-014-1159-y
- Sakurai S, Ellingwood B, Koshiyama S (2001) Probabilistic study of the behavior of steel frames with partially restrained connections. *Eng Struct* 23(11):1410–1417
- Díaz C, Victoria M, Querin OM, Martí P (2012) Optimum design of semi-rigid connections using metamodels. *J Constr Steel Res* 78:97–106
- Hartmann F, Katz C (2004) Structural analysis with finite elements. Springer-Verlag, Berlin

# Chapter 21

## Robust-Optimal Design Using Multifidelity Models

Kendra Van Buren and François Hemez

**Abstract** Applications in engineering analysis and design have benefited from the use of numerical models to supplement or replace the costly design-build-test paradigm. Previous work has acknowledged that design optimization should not only consider the performance of the model, but also be as insensitive as possible, or robust, to sources of uncertainty that are used to define the simulation. Clearly, evaluating robustness to sources of uncertainty can be computationally expensive, due to the number of iterations required at every step of the optimization. Multifidelity techniques have been introduced to mitigate this computational expense by taking advantage of fast-running lower-fidelity models or emulators. Herein, to achieve robust design, we argue that it is more effective to reduce the total range of variation in model performance rather than to reduce the standard deviation of model performances due to uncertainty in calibration variables of the model. We utilize a multifidelity approach to apply this paradigm to a sub-problem of the NASA Uncertainty Quantification Challenge problem, which is a high-dimensional and nonlinear MATLAB-based code used to simulate dynamics of remotely operated aircraft developed at NASA Langley. This method demonstrates an alternative and computationally efficient approach to robust design.

**Keywords** Robust design • Multi-fidelity optimization • Metamodels • Uncertainty • Info-gap

### 21.1 Introduction

Numerical models have become accepted to study the behavior of complex phenomena that are difficult or costly to measure experimentally. As such, numerical models can be used to replace the costly design, build, test cycle by being able to study the behavior of candidate designs. For example, in wind energy applications, numerical models have been proposed to study the placement of wind turbines within a wind farm, such that power output can be maximized and fatigue failure due to wind-to-turbine and turbine-to-turbine interactions can be minimized [1]. Optimization techniques can be exploited to efficiently search for the best-performing design, however, the added computational cost of performing an optimization often necessitates the use of a fast-running emulator to expedite the analysis.

Herein, we assume that models are defined using calibration variables,  $\theta$ , and design parameters,  $p$ . Calibration variables are parameters of the model that are introduced due to modeling assumptions, for example parameters that describe material strength, such as a linear young's modulus. Calibration variables will carry some uncertainty because of inherent variability in manufactured products, and because of our inability to perfectly represent physics in a numerical model. Design parameters are those that are known, for example the dimensions of a building. It is emphasized that the "best" design is unknown, however, once a design is chosen the design parameters are known exactly. Thus, the goal of robust design is to find the design, as defined by the design parameters,  $p$ , whose predicted performance is as insensitive as possible to uncertainty introduced by the calibration variables,  $\theta$ .

In robust design, it is common for these uncertainties to be described using probability distributions; however, the formulation of probability distributions can affect the conclusions of the robustness analysis [2]. A typical approach to probabilistic-based robust design is to assume the form of probability definitions and then minimize the uncertainty, as described by hyper-parameters of the probability distributions. Which probability distribution (uniform law, normal law, beta law?) to assume might be a challenging proposition. In some applications it may be more appropriate to apply a

---

K. Van Buren (✉)  
Los Alamos National Laboratory, NSEC, 87545 Los Alamos, New Mexico, USA  
e-mail: [klvan@lanl.gov](mailto:klvan@lanl.gov)

F. Hemez  
Los Alamos National Laboratory, XTD-IDA, 87545 Los Alamos, New Mexico, USA  
e-mail: [hemez@lanl.gov](mailto:hemez@lanl.gov)

non-probabilistic methodology if little is known about the actual behavior of the calibration variables, such that unwarranted assumptions about probability functions are minimized. One such alternative to describe uncertainties is info-gap decision theory, which does not require the formulation of probability laws if such information is not available [3]. Rather, uncertainties are treated as a Knightian uncertainty, or info-gap, in which no assumption is made about the shape of the uncertainty distribution.

There can also be a high computational cost to robust design. The computational expense often arises due to the fact that the numerical model must be executed several times to explore the variability defined by the uncertain calibration variables. Exploring the performance of competing designs by optimizing the design parameters, adds another “layer” of numerical simulations. Often, the high-fidelity, physics-based numerical simulation can be replaced with a mathematical-based surrogate model, also known as a metamodel (or emulator), that is computationally insignificant to evaluate. It is emphasized that metamodels offer an additional source of uncertainty when pursuing robust design [4]. In some applications, there can also exist physics models of varying levels of complexity that can be used to simulate the same phenomena of interest. It is commonly desired to utilize the physics-based numerical model of highest fidelity, however, this option might be infeasible due to the computational demands required by the simulation. For these reasons, multi-fidelity approaches have been proposed, whereby the high-fidelity numerical model is supplemented by simulations from either a lower-fidelity physics-based model or a mathematical-based surrogate model [5].

Herein, we describe our approach to robust design in which we incorporate our non-probabilistic definition of robustness, as defined by info-gap decision theory, into a multi-fidelity optimization framework. The remainder of the paper is organized as follows. In Sect. 21.2 we present our approach to robust design in the context of info-gap decision theory. This approach is then implemented into the multi-fidelity paradigm, as described in Sect. 21.3. As a proof-of-concept, we demonstrate the approach on a sub-model of the NASA Challenge Problem, as discussed in Sect. 21.4. The drawbacks of our approach, avenues for future work, and overall conclusions are summarized in Sect. 21.5.

## 21.2 Info-Gap Approach to Robust Design

This section provides an overview of info-gap decision theory (IGDT) such that the reader has an understanding for how robustness is defined in our analysis. Herein, robustness describes the worst-case performance predicted by the model whereas opportuneness describes the best-case performance. Further details of IGDT and its implementation can be found in [3] and [6, 7]. We emphasize that a model that is robust to uncertainties is one that can tolerate a high level of uncertainty with the guarantee of delivering an expected performance. Hence we do not attempt to describe the probability law of performance, for a given design, using statistical sampling. Instead we search for the worst-case and best-case performances that meet user-defined performance requirements.

Implementation of IGDT necessitates the combination of three attributes: (i) the model, (ii) the performance criterion, and (iii) the info-gap model used to represent what is unknown about the decision. As described previously, we assume that a model is defined by its calibration variables,  $\theta$ , and design parameters,  $p$ . The model represents the relationship between these inputs and model outputs,  $y$ , as described in Eq. 21.1:

$$y = f(\theta; p). \quad (21.1)$$

Performance, denoted herein as  $R$ , is a scalar quantity used to determine the ability of the model to satisfy a critical performance value,  $R_C$ . The performance quantifies the ability of the design to meet an expected performance criterion, for example maximum deflection due to external loads, as suggested in Eq. 21.2:

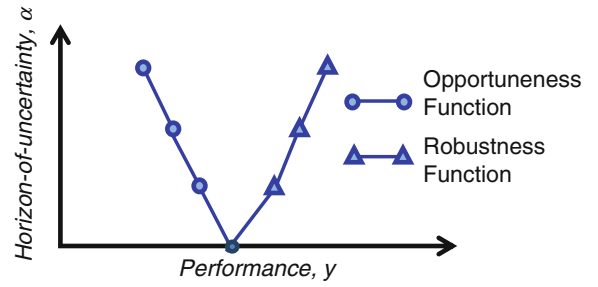
$$R(p) = y \leq R_C. \quad (21.2)$$

The uncertainty that we wish to be robust to originates from the uncertain calibration variables. The info-gap model,  $U(\alpha; \theta_0)$ , describes how the uncertain calibration variables,  $\theta$ , vary with respect to their nominal values or settings. The nominal values,  $\theta_0$ , denote the best-available knowledge that is used as the starting point of the analysis. The “distance” between the current knowledge,  $\theta_0$ , and hypothetical settings,  $\theta$ , which could be selected for decision-making, is parameterized using a single scalar quantity,  $\alpha$ , denoted as the horizon-of-uncertainty:

$$U(\alpha; \theta_0) = \{\theta : \|\theta - \theta_0\| \leq \alpha\}, \alpha \geq 0. \quad (21.3)$$



**Fig. 21.1** Nominal info-gap plot with opportuneness and robustness functions



When  $\alpha = 0$ , the uncertain variables remain fixed at their nominal settings,  $\theta = \theta_0$ . As the horizon-of-uncertainty increases, the calibration variables,  $\theta$ , are allowed to vary and more settings are taken into consideration. Each setting leads to a different model that can be evaluated against the performance criterion, as defined in Eq. 21.2. Equation 21.3 shows that, at a fixed horizon-of-uncertainty,  $\alpha$ , the set  $U(\alpha; \theta_0)$  defines a family of models that can be explored to search for variability in performance, given the amount “ $\alpha$ ” of calibration variable uncertainty.

With these three attributes defined, robust design in the context of an info-gap analysis searches for the design that is defined using calibration variables,  $\theta$ , that can potentially deviate from the best-available knowledge  $\theta_0$  by the greatest amount  $\alpha$ , and simultaneously satisfy the performance criterion of Eq. 21.2. When searching for the worst-case performance, robustness is achieved if the model can tolerate deviations from its nominal settings, as quantified in Eq. 21.3, while delivering the expected level of performance,  $R_C$ , as quantified in Eq. 21.2. Conversely, opportuneness is achieved if the best-case performance of the model, as it deviates from its nominal settings Eq. 21.3, improves the critical performance level,  $R_C$ , of Eq. 21.2.

Conceptually, the robustness,  $\hat{\alpha}$ , of an info-gap analysis quantifies the degradation of performance as the horizon-of-uncertainty  $\alpha$  increases, while the opportuneness,  $\hat{\beta}$ , quantifies the potential improvement in performance. Mathematically, these functions depend on the target critical performance,  $R_C$ , and are defined as:

$$\hat{\alpha} = \arg \max_{\alpha \geq 0} \left\{ \alpha : \max_{p \in U(p_0; \alpha)} R(p) \leq R_C \right\} \text{ and } \hat{\beta} = \arg \min_{\alpha \geq 0} \left\{ \alpha : \min_{p \in U(p_0; \alpha)} R(p) \leq R_C \right\}. \quad (21.4)$$

Solving the robustness and opportuneness conditions defined in Eq. 21.4 involves two nested optimization problems. This can be computationally expensive, especially if large numbers (for example, more than five or six each) of design parameters,  $p$ , and calibration variables,  $\theta$ , are considered. To bypass this difficulty, we focus on a multi-fidelity approach of the inner optimization, as discussed further in Sect. 21.3 at a fixed horizon-of-uncertainty  $\alpha$ . The worst-case and best-case performances are searched for, given that the uncertain calibration variables are allowed to vary within their lower and upper bounds. Strictly speaking, a critical level of performance,  $R_C$ , need not be defined when the robustness and opportuneness functions are explored, as described previously.

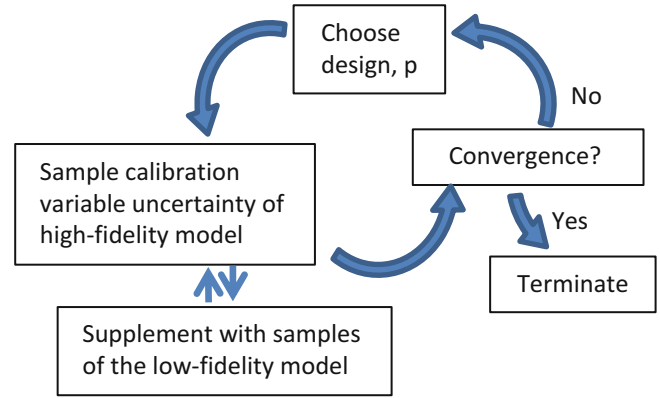
A representative info-gap plot is provided in Fig. 21.1, where smaller performance values are more desirable than larger performance values. As the horizon-of-uncertainty  $\alpha$  increases, the best-case and worst-case performances start to deviate from the nominal performance, as demonstrated by the notional shapes of the opportuneness and robustness functions. The info-gap plot of Fig. 21.1 quantifies, first, by how much model predictions vary and, second, the range of predictions that are obtained at any given horizon-of-uncertainty.

### 21.3 Optimization Using Multifidelity Approach

In this section, we discuss how the info-gap concept of Sect. 21.2 is incorporated into the multi-fidelity framework. The goal is essentially to incorporate into the design optimization a criterion for reducing the range of predicted performance values at a particular horizon-of-uncertainty,  $\alpha$ . Herein, we place a particular emphasis on reducing the range of predictions, however, it is easily amenable to incorporate other performance criteria into the optimization. One could elect, for example, to optimize the mean (average) or worst-case performance given the uncertainty of calibration variables,  $\theta$ .

The basic paradigm for how the multi-fidelity approach can be applied to a robust design optimization is illustrated in Fig. 21.2. At any iteration within the robust design optimization, a candidate design,  $p$ , is chosen, as indicated by the box at the top of the figure. To determine the range of performances, which is used to quantify the robustness of the design, an

**Fig. 21.2** Flowchart of the multi-fidelity optimization process



optimization routine is required that searches for the minimum and maximum performances of the candidate design. Clearly, it is computationally expensive to repeat this optimization for all candidate designs that are evaluated in the optimization routine. For computational efficiency, a relatively small number of samples of the high-fidelity model is supplemented with a large number of samples taken using the low-fidelity model, as shown by the boxes in the lower left of Fig. 21.2. This multi-fidelity step provides a real potential to significantly reduce computational demands, because fewer evaluations of the high-fidelity model are required. It is emphasized, however, that the multi-fidelity framework can only provide an approximation of the statistics that would have been obtained if only the high-fidelity model were utilized. The multi-fidelity sampling provides the information necessary to evaluate the robustness. We then return to the outer optimization loop, where we decide whether we have converged to the robust-optimal design and therefore terminate, or if a new candidate design is chosen and the process repeated.

Herein, the multi-fidelity approach implemented in [5] is utilized to approximate the statistic,  $\hat{s}_A$ , used to define the performance of a given design. This approximation combines predictions from the high-fidelity model (with a small number of evaluations) and low-fidelity model (with a large number of evaluations), as shown in Eq. 21.5:

$$\hat{s}_A = a_n + \kappa (b_m - b_n), \quad m > n. \quad (21.5)$$

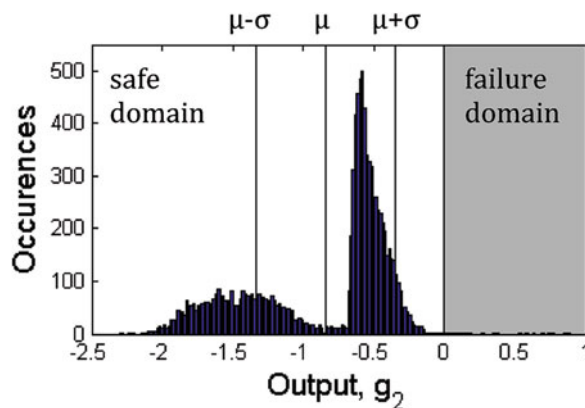
where  $a_n$  indicates estimation of the statistic using  $n$  simulation runs from the high-fidelity model,  $b_n$  and  $b_m$  indicate estimation of the statistic using  $n$  and  $m$  simulation runs from the low-fidelity model, and  $\kappa$  is used to control how much correction we are willing to accept from the low-fidelity model. Herein the statistic,  $\hat{s}_A$  that we are evaluating is the range of performance predictions. The high-fidelity model is sampled  $n$  times, indicated by the  $a_n$  evaluations, and the low-fidelity model is sampled at the same  $n$  settings as the high-fidelity model, indicated by the  $b_n$  evaluations. Due to the computational efficiency of the low-fidelity model, it is sampled an additional  $m$  times, indicated by the  $b_m$  evaluations. Ideally, the number of times that the low-fidelity model is sampled will be much larger than then the number of times the high-fidelity model is sampled. It is emphasized however, that there is no guarantee for the global optima of the low-fidelity model to be at the same location as the high-fidelity model.

## 21.4 Application to the NASA Uncertainty Quantification Challenge Problem

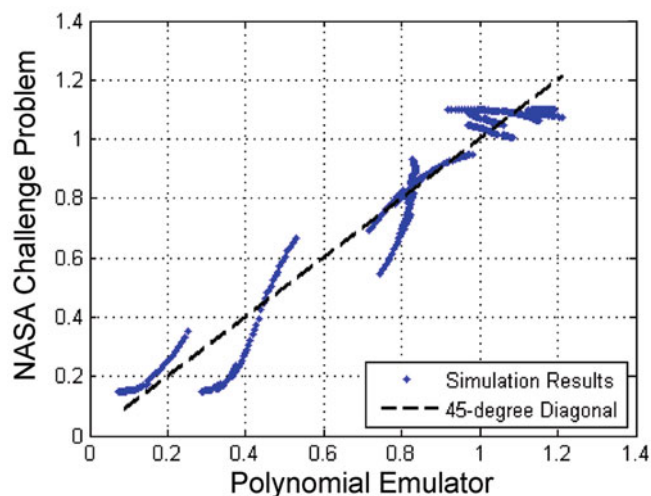
In this section, we utilize the NASA Uncertainty Quantification Challenge problem to demonstrate our approach to robust design, as discussed in Sects. 21.2 and 21.3, in a multi-fidelity optimization framework. The NASA challenge problem is used to describe dynamics of the Generic Transport Model, remotely operated aircraft developed by the NASA Langley Research Center. The numerical model is provided to us as an executable Matlab™ code that we treat as a black-box problem [8, 9]. Five submodels are used to define the problem. Herein, we demonstrate the multi-fidelity optimization on one submodel of the problem. The submodel is defined by a total of five variables, three of which we define as calibration variables and two as design parameters, as indicated in Eq. 21.6:

$$y = f(\theta_1, \theta_2, \theta_3, p_1, p_2). \quad (21.6)$$

**Fig. 21.3** Monte carlo sampling results of the submodel output



**Fig. 21.4** Goodness of fit of the polynomial emulator to the NASA subproblem

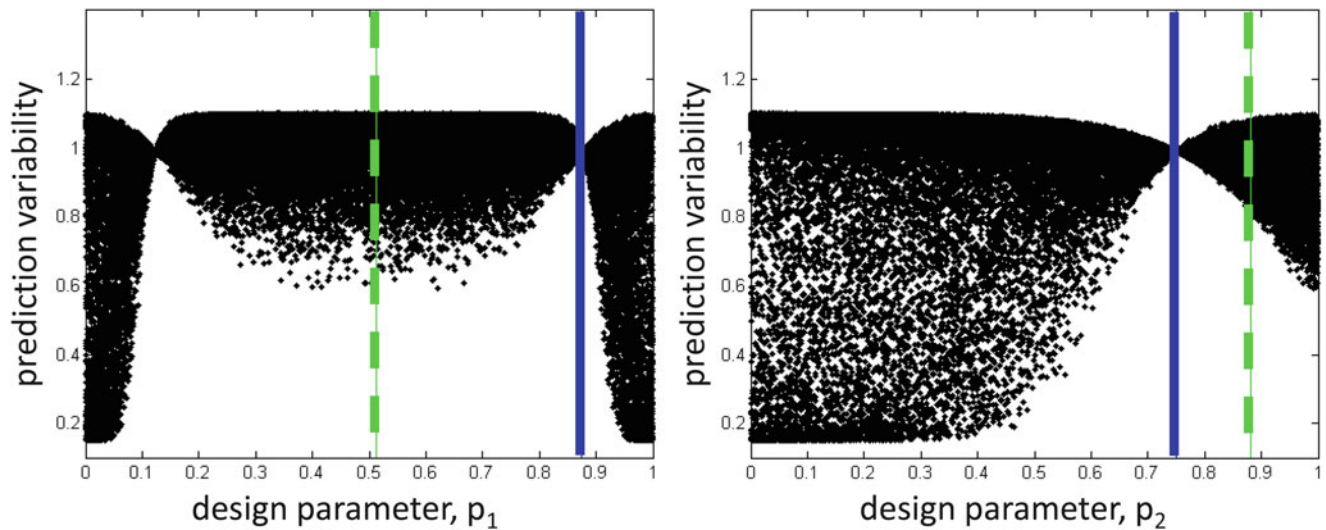
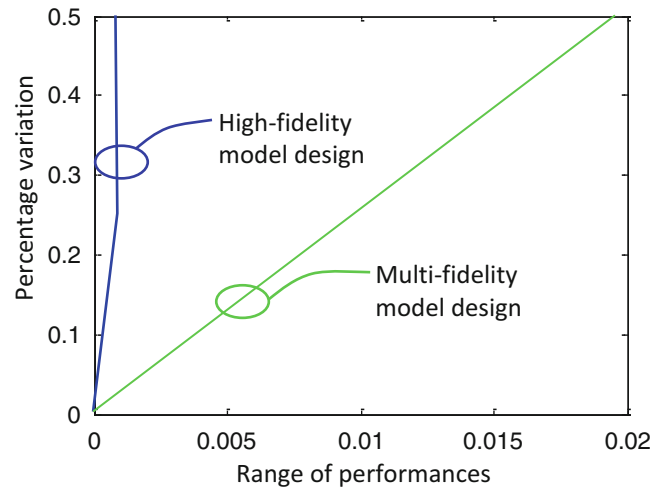


In accordance with the discussion in Sects. 21.2 and 21.3, we wish to optimize the pair of design parameters  $(p_1; p_2)$  to search for the design that meets the user-defined performance requirement,  $R_C$ , while being as robust as possible to the uncertainty defined for the triplet of calibration variables  $(\theta_1; \theta_2; \theta_3)$ . Monte Carlo sampling of the model demonstrates that the model output is highly nonlinear, as shown in Fig. 21.3. The vertical black lines indicate the mean and  $\pm$  one standard deviation range of the output. The grey region indicates the model output that has entered the failure domain, as defined by the NASA challenge problem moderators. The main takeaway message of Fig. 21.3 is that there is no guarantee that the model output can be accurately described by its mean and standard deviation, or any other type of commonly used probability distribution function. This observed nonlinearity further motivates the need to optimize the robustness of the model through use of the overall range of predictions obtained in the model output.

A polynomial emulator of the model is developed to be utilized as the low-fidelity counterpart in the multi-fidelity optimization. We use a third order polynomial model of the five variables  $(p_1; p_2; \theta_1; \theta_2; \theta_3)$ , trained using 243 runs of the high-fidelity model from a five-level full factorial design. The goodness-of-fit of the emulator is shown in Fig. 21.4, whereby the predictions of the polynomial emulator are plotted with respect to the x-axis, and the predictions of the submodel of the NASA problem are plotted on the y-axis. The black, dashed line plotted on the 45-degree diagonal represents what the comparison would look like if there were perfect agreement between the emulator and the NASA submodel. In this case however, the emulator is only able to capture some of the global trends of the NASA submodel. While this may not be the best-possible goodness-of-fit, it is representative of the fact that a low-fidelity model is not guaranteed to accurately capture the behavior of a high-fidelity model. The goal here is not to find the best-fit emulator for the challenge problem, but rather to see how well the multi-fidelity optimization works when an emulator that captures the overall trend of the model is used to supplement the numerical model calculations.

We perform an unconstrained optimization, meaning that we attempt to find the design with the least amount of variability regardless of the response. Constraints can be easily added to the procedure such that other design requirements, for example minimum deflection or stresses, are also met. Because the NASA submodel is relatively cheap to execute, a global optimization search using only the high-fidelity model is also performed to search for the robust-optimal design. A comparison of the two designs, obtained either by direct optimization of the high-fidelity model or through the multifidelity

**Fig. 21.5** Info-gap robustness of the robust-optimal models



**Fig. 21.6** Monte carlo sampling of the uncertain calibration variables plotted against  $p_1$  (left) and  $p_2$  (right)

optimization procedure, is given in Fig. 21.5. The figure shows the robustness functions of the two design optimization strategies. Each robustness function maps the variability of design performance (horizontal axis) as the three calibration variables deviate more-and-more from their nominal values (vertical axis). As expected, there is less variability in the model output of the design obtained through direct optimization of the high-fidelity model than there is with the design provided by the multi-fidelity framework. This is to be expected due to the fact that optimization utilizing only the high-fidelity model is more likely to converge to the global optimum.

Monte Carlo sampling of the uncertain calibration variables is performed next to investigate the behavior of the model and understand why the robust-optimal designs obtained using the multi-fidelity and high-fidelity optimizations behave differently. The variation of predictions with respect to the two design parameters are plotted in Fig. 21.6, with the first design parameter,  $p_1$ , shown on the left and the second design parameter,  $p_2$ , shown on the right. Each black dot represents a performance predicted by the model of Eq. 21.6 for a given set of design parameters ( $p_1; p_2$ ), and when the triplet of calibration variables ( $\theta_1; \theta_2; \theta_3$ ) is “sampled.” The vertical green dashed lines indicate the design parameter values obtained through the multi-fidelity optimization, and the vertical blue solid lines indicate the design parameter values obtained through the optimization that utilizes only the high-fidelity model. It is shown that the optimization using only the high-fidelity model is able to converge to the global optimum, as evidenced by the reduced range of variability in the scatter. The multi-fidelity approach, however, comes close but is unable to accurately identify the global optimum. This finding clearly shows the difficulty of the multi-fidelity optimization to converge to the global optima. We believe that the explanation for this difficulty, in addition to relying on the approximated statistic given in Eq. 21.5, is the fact that the low-fidelity surrogate model is not an accurate representation of the high-fidelity model, as evidenced in Fig. 21.4.

## 21.5 Conclusions

This manuscript discusses a multifidelity approach to robust design whereby we utilize a non-probabilistic robustness criterion as defined by info-gap decision theory. In doing so, the uncertainty in design parameters is treated differently from the uncertainty in the calibration variables. Whereas design parameters are uncertain because the “best” design is unknown, calibration variables are uncertain because of inherent variability. Thus, the goal is to identify the robust-optimal design whose predicted performance is as insensitive as possible to uncertainties in the calibration variables. We do not seek a design that delivers the absolute “best” performance, rather, one that delivers a performance which meets the user-defined requirement while being as insensitive, or robust, as possible to the calibration variable uncertainty. Herein, we define our robustness criterion in the context of info-gap decision theory. In doing so, we remove the need for any unwarranted assumption about the formulation of probability distribution functions used to describe uncertainty in the problem. The robustness criterion is incorporated into a multifidelity approach to optimization, which has the potential to significantly reduce the cost of a robust design optimization.

Our approach is demonstrated on a submodel of the NASA Uncertainty Quantification Challenge problem. It is shown through Monte Carlo sampling that the model output is highly nonlinear, and that it would be potentially misleading to describe its uncertainty by its mean and standard deviation. Utilized in the analysis is the original physics-based code to represent our high-fidelity model, and a polynomial-based emulator used to represent the low-fidelity model. We demonstrate that using an optimization procedure of the high-fidelity model only is able to converge to the global maximum of the optimization, however, the multi-fidelity approach is unable to do so with a similar level of accuracy. This is likely due to the fact that there is no guarantee that the global minimum of our low-fidelity model will match the global minimum of the high-fidelity model. For applications where the low-fidelity model is a fast running mathematical surrogate, not necessarily grounded in physics, it is obvious that the high-fidelity model is more trustworthy. However, in applications where the low-fidelity model is based on physics principles, it may be unclear which model should be trusted more. How to efficiently combine the predictions of low-fidelity and high-fidelity models based on their respective levels of trustworthiness, is a direction of research that warrants more work in the future.

Future work includes extending the analysis to an application whereby the low-fidelity model is a physics-based model rather than a mathematical surrogate. Further, we would like to extend the current analysis to cases where the calibration space of the high-fidelity model is of a different nature than the calibration space of the low-fidelity model. Addressing these topics should help demonstrate further the potential that a multifidelity simulation approach offers for uncertainty quantification and robust design.

**Acknowledgements** The first author acknowledges support from the Advanced Scientific Computing program at the Los Alamos National Laboratory (LANL). The second author is grateful for support provided by the Advanced Certification Campaign at LANL. LANL is operated by the Los Alamos National Security, L.L.C., for the National Nuclear Security Administration of the U.S. Department of Energy under contract DE-AC52-06NA25396.

## References

1. Linn R, Koo E (2011) Wind blade: coupled turbine/atmosphere modeling. Los Alamos national laboratory turbine-turbine interaction workshop, Los Alamos
2. Park GJ, Lee TH, Lee KH, Hwang KH (2006) Robust design: an overview. *AIAA J* 44(1):181–191
3. Ben-Haim Y (2006) Info-gap decision theory: decisions under severe uncertainty, 2nd edn. Academic, Oxford
4. Apley DW, Liu J, Chen W (2005) Understanding the effects of model uncertainty in robust design with computer experiments. *ASME J Mech Des* 128(4):945–958
5. Ng LWT, Willcox KE (2014) Multifidelity approaches for optimization under uncertainty. *Inter J Numer Methods Eng* 100(10):746–772
6. Van Buren KL, Atamturktur S, Hemez FM (2014) Model selection through robustness and fidelity criteria: modeling the dynamics of the CX-100 wind turbine blade. *Mech Syst Signal Process* 43(1–2):246–259
7. Hemez FM, Ben-Haim Y (2004) Info-gap robustness for the correlation of tests and simulations of a non-linear transient. *Mech Syst Signal Process* 18:1443–1467
8. Jordan TL, Bailey RM (2008) NASA langley’s AirSTAR testbed – a subscale flight test capability for flight dynamics and control system experiments, AIAA guidance, navigation, and control conference and exhibit, Honolulu, 18–21 Aug 2008
9. Foster JV, Cunningham K, Fremaux CM, Shah GH, Stewart EC, Rivers RA, Wilborn JE, Gato W (2005) Dynamics modeling and simulation of large transport airplanes in upset conditions. AIAA guidance, navigation, and control conference and exhibit, San Francisco, 15–18 Aug 2005

# Chapter 22

## Robust Modal Test Design Under Epistemic Model Uncertainties

Fabien Maugan, Scott Cogan, Emmanuel Foltête, and Aurélien Hot

**Abstract** A wide variety of model-based modal test design methodologies have been developed over the past two decades using a non-validated baseline model of the structure of interest. Due to the presence of lack of knowledge, this process can lead to less than optimal distributions of sensors and exciters due to the discrepancy between the model and the prototype behaviors. More recent strategies take into account statistical variability in model parameters but the results depend strongly on the hypothesized distributions.

This paper provides a decision making tool using a robust satisficing approach that provides a better understanding of the trade-off between the performance of the test design and its robustness to model form errors and associated imprecisions. The latter will be represented as an info-gap model and the proposed methodology seeks a sensor distribution that will satisfy a given design performance while tolerating a specified degree of modeling error. The evolution of this performance for increasing horizons of uncertainty is an important information for the test planner in choosing the total number of sensors.

**Keywords** Sensor placement • Robustness • Info-gap • Uncertainty • Lack of knowledge

### 22.1 Introduction

The increasing size and complexity of spacecraft structures make it necessary to plan base excitation tests in view of performing a modal identification. This can be particularly important when the identified behaviors are to be used in test-analysis correlation or model calibration procedures. The performance of a test design is generally measured in terms of its ability to excite and observe the target modes of interest.

Therefore in the past three decades, a wide variety of deterministic model-based strategies have been developed to define an optimal configuration of sensors and actuators. In most cases, an optimal design is one which provides the best observability and distinguishability of the identified eigenmodes. For example, methodologies based on the Guyan reduction [10, 11], the effective independence criteria [8], the constraint energy of the structure [7], the QR decomposition of the modal matrix [13] or the Orthogonal Maximum Sequence (OMS) [3].

Improvements in computing resources and an increased awareness of the importance of uncertainties in engineering decision-making has given rise to stochastic approaches such as presented in [1] based on residuals, in [12] using the entropy, or in [5] where classical sensor location methodologies are employed to examine the influence of parametric uncertainties. However, these methodologies are not necessarily well adapted to lack of knowledge in the finite element model resulting, for example, from poorly understood behavior laws, neglected physics, or other commonly encountered sources of ignorance. Indeed, model-based test design is generally based on non-validated finite element models. In the space industry, the structural FEM is generally composed of different subsystems models provided by the subcontractors. All of these models have different degrees of accuracy in modeling the true hardware behavior and this situation often leads to significant errors in the predicted modal forms due to poorly estimated stiffness, mass and damping properties. The impact of these errors on the modal properties of the structure are discussed in [9], and various solutions have been proposed to propagate uncertainties through the finite element model in order to determine the corresponding uncertainties in the modal

---

F. Maugan (✉) • S. Cogan • E. Foltête  
FEMTO-ST Institute Applied Mechanics Department, 24 chemin de l'Épitaphe, 25000 Besançon, France  
e-mail: [fabien.maugan@femto-st.fr](mailto:fabien.maugan@femto-st.fr)

A. Hot  
Spatial Center of Toulouse, 18 avenue Edouard Belin, 31401 Toulouse cedex 9, France

properties [2, 4]. A robust sensor placement methodology accounted for imprecise parameter estimations was proposed [15]. This paper takes a second look at this robust satisficing methodology and proposes a more efficient approach for selecting sensor degrees of freedom.

## 22.2 Robust Test Design Methodology

It is widely recognized that random uncertainties in a system and its environment must be taken into account in most engineering design processes [14] and an overview of robust design strategies in structural dynamics can be found in [16]. However, uncertainty can arise in many forms and modeling errors are not necessarily random in nature. For example, errors in model form or imprecise parameter values often require non-probabilistic approaches to be accounted for correctly. Moreover, the concept of robust design is not restricted exclusively to structural design, it is also a useful concept in the development of algorithms. In the following, we seek to define a new strategy in order to maximize the robustness of a model-based sensor placement design for vibration tests to errors in the finite element model.

A sensor distribution should be able to observe and distinguish the set of target structural eigenmodes. In a standard deterministic approach, a single modal basis of the baseline model is used. In what follows, an approach based on a set of model bases will be used all of which are realizations consistent with the assumed modeling errors. The first step is to obtain these modal bases consists in establishing a model linking the unknown model inputs with the target eigenmodes of the structure :

$$M(\mathbf{m}_i) = \Phi_i \quad (22.1)$$

In order to account for model uncertainties, the approach adopted here consists in sampling the uncertain model design space to generate a set of modal bases  $\Phi$  such as  $\Phi = [\Phi_1, \dots, \Phi_N]$  by running  $N$  times the finite element model. Within the framework of the info-gap theory, this sampling must be done following an uncertain model  $\mathcal{U}(\alpha, \mathbf{m}^{(0)})$  where  $\mathbf{m}$  is the vector of uncertain parameters,  $\mathbf{m}^{(0)}$  is the nominal parameter values, and  $\alpha$  the horizon of uncertainty. This model must represent the physics of the parameter uncertainty and define an interval in the uncertain design space where the unknown parameters are allowed to vary. In the context of this paper, a simple envelope-bound model is used:

$$\mathcal{U}(\alpha, \mathbf{m}^{(0)}) = \left\{ \mathbf{m} : \left| \mathbf{m}_i - \mathbf{m}_i^{(0)} \right| < \alpha w_i \mathbf{m}_i^{(0)}, i = 1, \dots, p \right\} \quad (22.2)$$

Once the sample is computed, the target behaviors of the uncertain system responses must be extracted. For this purpose, a Singular Value Decomposition (SVD) [6] of the  $\Phi$  matrix is performed such as  $U \Sigma V^T = \Phi$ . The results are three matrices which can be describe in a mechanical way by:

- $U$  : orthogonal matrix containing the left singular vectors that are the singular directions, also called proper orthogonal modes (POM)
- $\Sigma$  : pseudo-diagonal matrix containing the singular values, also called proper orthogonal values (POV) and linked to the POM energy
- $V$  : orthogonal matrix containing the right singular vectors, temporal modulation of POMs

The singular values given by this decomposition allows to build a reduced but representative subspace to model the system by only choosing the higher singular values and there corresponding singular vectors. If the modeling errors have only a weak impact on the structural behavior, then this subspace will not doubt be reduced to the baseline eigenmodes. However, as uncertainty increases the realizable modal space can become richer. If the discrepancy between the baseline modes and the modified ones is large enough, the subspace will gain new vectors in order to take into account this new behaviors. The dimension of this subspace conditions the number of points to instrument with sensors in order to observe all the linear independent phenomena.

The reduced problem can be written as:

$$(U_r^T * K * U_r - \omega_v^2 U_r^T * M * U_r) * c_v = 0 \quad (22.3)$$

Where  $U_r$  is composed of the selected singular vectors of  $U$ . Solving the above system yields an approximation to the eigensolutions of the system  $(K - \omega_v M) \varphi_v = 0$ .

This new system produces a reduced modal basis  $\tilde{\Phi}$  which contains the main behaviors the structure can adopt for a given horizon of uncertainty. The robust sensor distribution methodology must then find the locations that maximize the identification and the distinguishability within this modal space. That is why  $\tilde{\Phi}$  will be decomposed by QR algorithm such as  $QR = \tilde{\Phi}^T E$  in order to find the optimal sensor distribution. This kind of decomposition has already been used to determine test design [13] but is here directly applied on the selected subspace given by the SVD. The QR decomposition is performed on  $\tilde{\Phi}^T$  and yields:

- $Q$  : orthogonal matrix
- $R$  : rectangular up matrix
- $E$  : permutation matrix

The question is now how to assess the robustness to lack of knowledge in the finite element model of the sensor distribution. A useful figure of merit is based on the distinguishability of the eigenmodes corresponding to a given eigenbasis realization. Qualitatively, a set of eigenmodes is considered to be distinguishable when no single eigenvector can be written as a linear combination of the remaining eigenvectors in the basis. In [15] the distinguishability of an eigenbasis is quantified thanks to the condition number of the sensor matrix  $\Phi_s$ , which is the modal matrix reduced to the degrees of freedom attached to a sensor. Indeed, distinguishability improves with decreasing condition number. The performance requirement can be then define as the maximal condition number of the sensor matrix tested on all the sampled modal basis for a given horizon of uncertainty must be below a limit  $\kappa_c$ .

$$\max (\text{cond}(\Phi_s)) \leq \kappa_c \quad (22.4)$$

The robustness function determination can easily be deduced from the performance requirement by looping on the horizon of uncertainty. These curves are a very useful decision making tool which allows to compare the evolution of the robustness of different designs.

$$\tilde{\alpha} = \max \left\{ \alpha, \max_{\mathbf{m} \in U(\alpha, \mathbf{m}^0)} (\text{cond}(\Phi_s)) \leq \kappa_c \right\} \quad (22.5)$$

### 22.3 Numerical Applications

The previously described methodology will now be illustrated on a fixed-free beam of steel with a 50 mm per 50 mm section and a total length of 1 m. At the middle of this simple beam is added a 1 kg lumped mass which will modify the baseline modes of the structure. Two test cases will be investigation: the first introduces uncertainty in the value of the lumped mass while the second introduces uncertainty in its location.

In the first test case, the uncertainty will only concern the value of the mass ( $\mathbf{m} = m$ ) which is allowed to vary between 0.1 and 10 times its initial value in order to obtain at one extreme a classical fixed-free beam behavior without added mass and at the other extreme, an approximately clamped condition at the mass point. The corresponding uncertainty model is indicated in Eq. (22.6) with  $\alpha$  between 0 and 9 and is based on a modified form of the envelope-bound model:

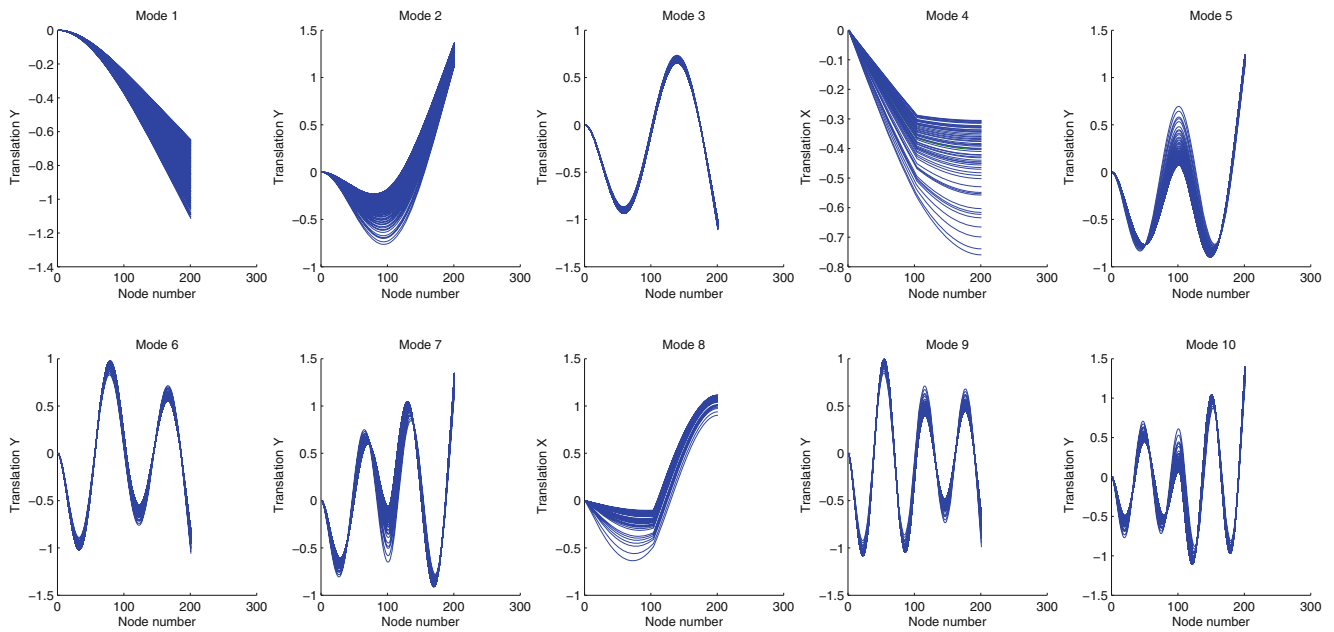
$$m \in U(\alpha, m^0) = \left\{ m : m^0 \left( 1 - \frac{\alpha}{10} \right) \leq m \leq m^0 (1 + \alpha) \right\} \quad (22.6)$$

The advantages of this structure are the absence of local modes, the presence of both bending and longitudinal modes, and the smoothness of the evolution in its behavior even for severe horizons of uncertainty.

In the second test case, the uncertainty will be applied to the location of the mass on the beam ( $\mathbf{m} = m_x$ ) which is closer to future industrial applications. In a practical way, the mass is here connected to the beam center thanks to a rigid link. The maximal authorized uncertainty is 10 cm from the initial position, that can represent the uncertainty in an equipment position in the very early phases of a structure design. The model of uncertainty is based on the envelope bound model available in Eq. (22.7). This new configuration will create strongly altered modes for bending modes at high horizons of uncertainty, and show the interest of a robust approach of a test design.

$$m_x \in U(\alpha, m_x^0) = \left\{ m_x : m_x^0 (1 - \alpha) \leq m_x \leq m_x^0 (1 + \alpha) \right\} \quad (22.7)$$





**Fig. 22.1** Variation in deformed shapes

### 22.3.1 First Test Case

#### 22.3.1.1 Modal Basis Sampling

In order to efficiently explore the uncertain design space in order to generate a set of realizations for the modal bases, the sampling will be performed through a Monte-Carlo approach with a logarithmic repartition. In Fig. 22.1 the dispersion in the deformed shapes due to the variation of the mass value is shown for the first ten modes of the structure and with the maximal allowed horizon of uncertainty ( $\alpha = 9$ ). The first two longitudinal modes are retained in this study and correspond to modes 4 and 8. We confirm that the variations in mass have a more significant impact on the displacement fields when located near a crest of the baseline modes.

#### 22.3.1.2 Singular Value Decomposition

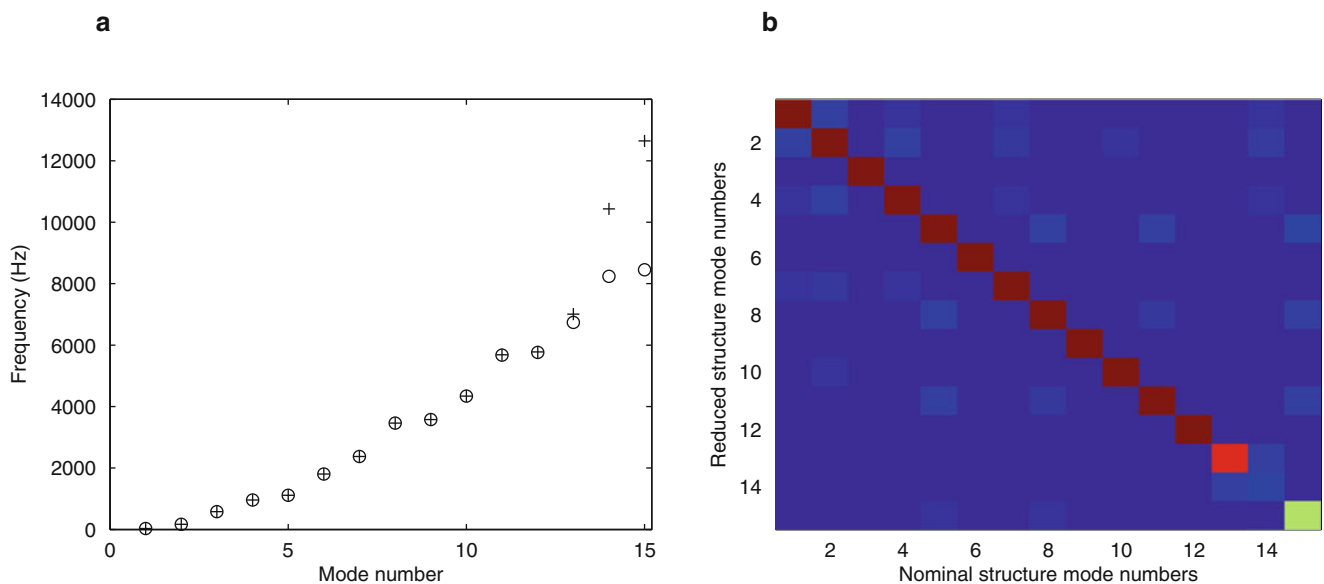
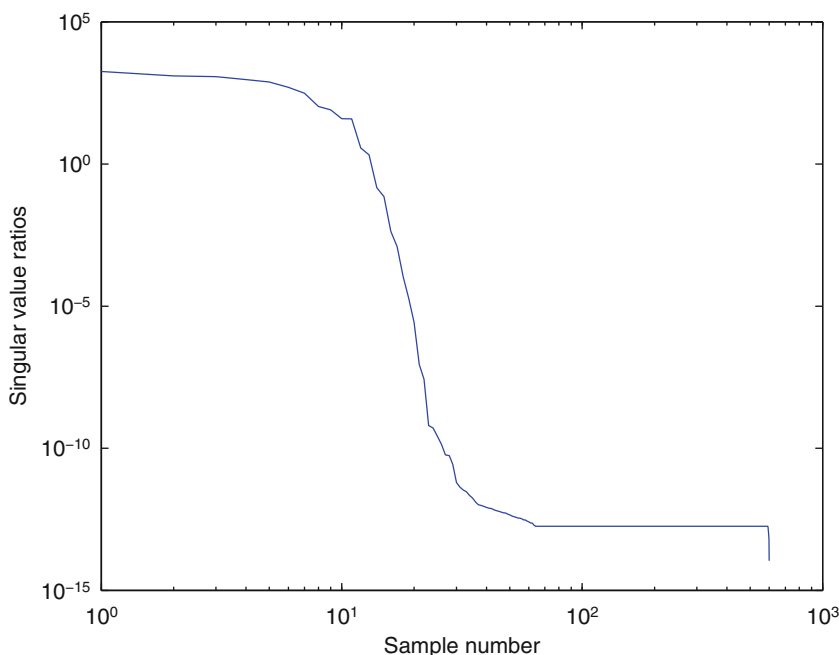
The SVD of this sample yields the distribution of singular values presented in Fig. 22.2. The reduction of the system must be made by selecting the largest singular values. The chosen criteria is that the ratio between a given value and the largest singular value must be above  $10^{-5}$ , which is a common threshold in methodologies using SVD. In the present case, 15 singular values are retained while the sampling is performed on modal basis containing only ten modes. The corresponding singular vectors will be used to define the reduced problem (see Eq. (22.3)).

This new system produces a reduced modal basis  $\tilde{\Phi}$  synthesizing the response of the unknown system. In Fig. 22.3, the 15 eigenmodes of the reduced system are compared to the first 15 natural modes of the structure and we note that the reduced model reproduces the first 13 structural modes. The remaining reduced modes are due to the discrepancies in the first 13 baseline modes.

#### 22.3.1.3 QR Decomposition

The results from the SVD provide a subspace of realizable system behaviors for a given horizon of uncertainty. The QR decomposition is then used to select the optimal sensor locations which corresponds to the subset of model degrees of freedom yielding the most linearly independent modal submatrix. Figure 22.4 shows the result of this placement procedure for the test structure, once again for the maximum horizon of uncertainty. In this case, the observation of the ten first modes

**Fig. 22.2** Singular values profile



**Fig. 22.3** Comparison between reduced modes (*plus sign*) and natural modes (*open circle*) eigenfrequencies (a) MAC between reduced modes and natural modes (b)

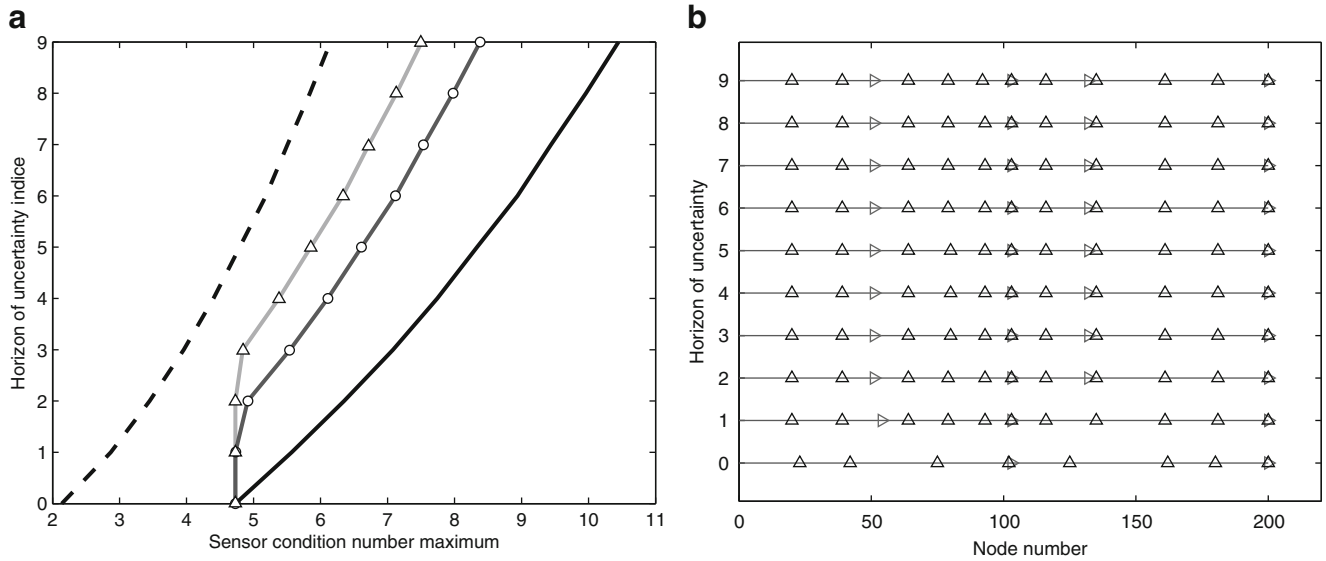
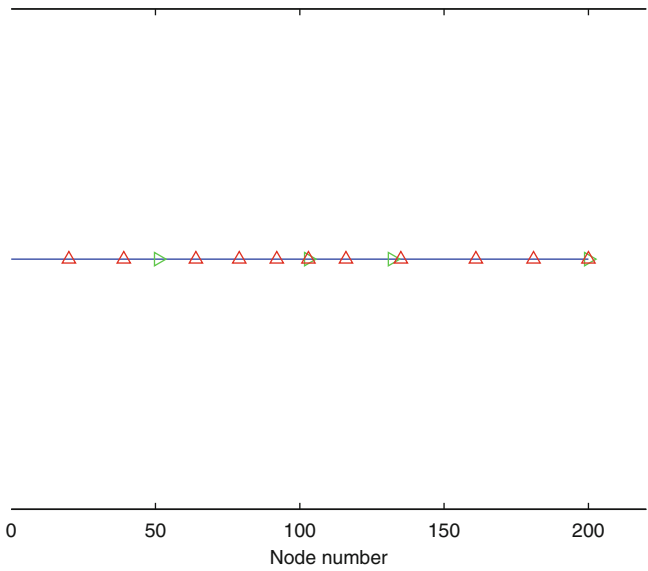
over the uncertain design space requires fifteen sensors. Eleven of them are along the Y direction in order to observe the bending modes while the remaining sensors are along the X direction.

**22.3.1.4 Robustness Curves**

Once the methodology to obtain the sensor distribution for a given horizon of uncertainty is established, the robustness curves can be computed by looping over the horizon of uncertainty and determining the modal basis among the available samples that maximizes the condition number of the sensor matrix.

The results are presented in Fig. 22.5. In (a), the robustness curves are obtained under various conditions. The two curves without markers delimit the domain of robustness. The dashed one represents the robustness computed with a sensor placed

**Fig. 22.4** Sensor placement



**Fig. 22.5** Robustness curves (a) sensor locations (b)

at each translational degree of freedom of the structure and is used here as a reference. The solid black curve is computed only with ten sensors obtained using the deterministic algorithm with a horizon of uncertainty of 0. Intermediate behaviors are shown with the curves with open circle and cross markers obtained for singular value thresholds of  $10^{-5}$  and a  $10^{-7}$  respectively. As expected, the design yielding the greatest number of sensors (cross markers) is the more robust. The last thing to highlight in the graph is the fact that the three solid curves begin at the same point. This is due to the fact that at zero horizon of uncertainty, the methodology yields exactly the same design as the deterministic design solution. In (b) the sensor distributions given by the methodology for several horizon of uncertainty are shown, with the same color code than Fig. 22.4. As previously explained, without lack of knowledge, ten sensors are enough to observe the beam oscillations. New sensors are then added with increasing uncertainty up to a horizon of uncertainty equal to 3. Beyond this value, no improvement in the design is obtained by adding additional sensors while maintaining the same threshold criteria.

### 22.3.2 Second Test Case

The second test case studies the impact of uncertainty in the location of the lumped mass. As seen in Fig. 22.6 mode shapes can change significantly for more severe horizons of uncertainty. For example, the modes six and seven (graph 10) and eight and nine (graph 11) for severe uncertainty are drawn separately for the sake of readability. The methodology is applied here only to the first nine bending modes of the structure.

The resulting robustness curves are shown in Fig. 22.7. The solid black curve corresponds to a deterministic sensor design and the sudden change in slope at approximately 7% uncertainty is due to the appearance of strongly modified mode shapes. The dashed black curve corresponds to the robust sensor design for each horizon of uncertainty and it is seen that the sensor distribution evolves efficiently with respect to the deterministic design to account for new behaviors.

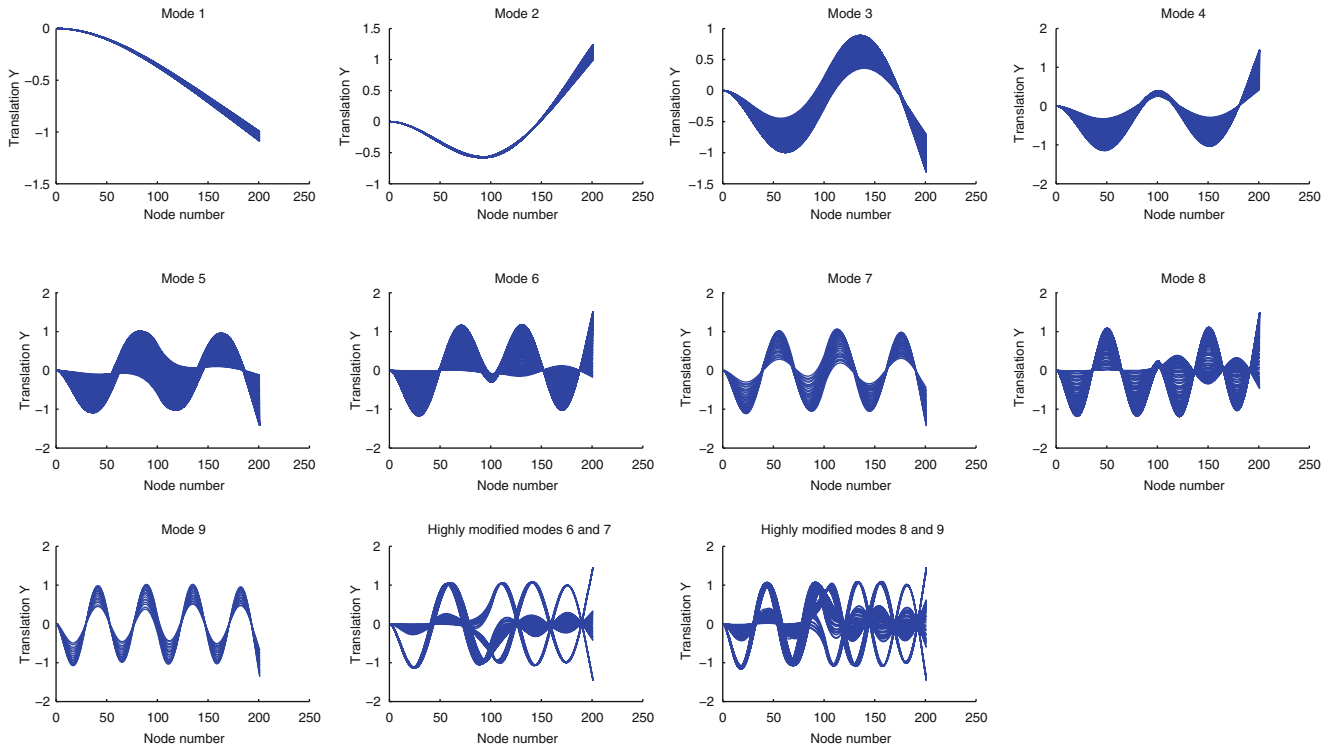


Fig. 22.6 Dispersion due to mass location

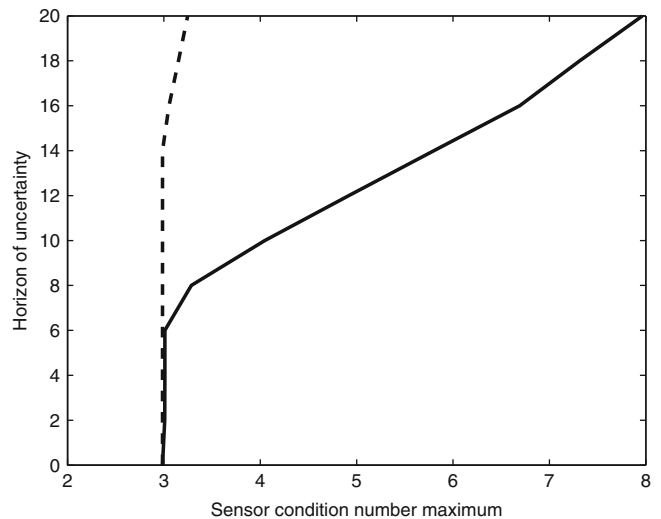


Fig. 22.7 Robustness curves

## 22.4 Conclusion

A global methodology for preparing a robust vibration test design with respect to epistemic model uncertainties has been proposed where lack of knowledge has been represented in the framework of the info-gap decision theory. The proposed robust satisficing approach can include a wide range of modeling errors since it is based on a set of modal bases representing different horizons of uncertainty. This methodology combines the singular value and QR decompositions to yield an efficient sensor placement technique applicable in an industrial context. Further work will aim at extending the approach to implicitly include triaxial sensors.

**Acknowledgements** The authors would like to thank the CNES-Toulouse and the Région Franche-Comté for their generous financial support.

## References

1. Abdelghani M, Friswell MI (2007) Sensor validation for structural systems with multiplicative sensor faults. *Mech Syst Signal Process* 21:270–279
2. Balmes E (2004) Uncertainty propagation in experimental modal analysis. In: *International modal analysis conference*
3. Balmes E (2005) Orthogonal maximum sequence sensor placements algorithms for modal tests, expansion and visibility. In: *International modal analysis conference, Orlando*
4. Ben-Haim Y (2006) *Info-gap, decision theory, decisions under severe uncertainty*, 2nd edn. Academic, London
5. Castro-Triguero R, Murugan S, Gallego R, Friswell MI (2013) Robustness of optimal sensor placement under parametric uncertainty. *Mech Syst Signal Process* 41:268–287
6. Golub G, Kahan W (1965) Calculating the singular values and pseudo-inverse of a matrix. *J Soc Ind Appl Math B Numer Anal* 2(2):205–224
7. Hemez F, Farhat C (1994) An energy based optimum sensor placement criterion and its application to structural damage detection. In: *International modal analysis conference*, pp 1568–1575
8. Kammer DC (1991) Sensor placement for non-orbitmodal identification and correlation of large space structures. *J Guid Control Dyn* 14(2):251–259
9. Kammer DC (1992) Effect of model error on sensor placement for on-orbit modal identification of large space structures. *J Guid Control Dyn* 15(2):334–341
10. Kammer DC, Falnigan CC, Dreyer W (1986) A super-element approach to test-analysis model development. In: *Proceedings of the fourth international modal analysis conference*, pp 663–673
11. Lallement G, Ramanitranjan A, Cogan S (1998) Optimal sensor deployment: application to model updating. *J Vib Control* 4:29–46
12. Papadimitriou C, Beck JL, Au SK (2000) Entropy-based optimal sensor location for structural model updating. *J Vib Control* 6:781–800
13. Schedlinski C, Link M (1996) An approach to optimal pick-up and exciter placement. In: *Proceedings of the 14th international modal analysis conference*, pp 1–7
14. Schueller GI (2007) On the treatment of uncertainties in structural mechanics and analysis. *Comput Struct* 85:235–243
15. Vinot P, Cogan S, Cipolla V (2005) A robust model-based test planning procedure. *J Guid Control Dyn* 28:571–585
16. Zang C, Friswell MI, Mottershead JE (2005) A review of robust design and its application in dynamics. *Comput Struct* 83:315–326

# Chapter 23

## Clustered Parameters of Calibrated Models When Considering Both Fidelity and Robustness

Sez Atamturktur, Garrison Stevens, and Yuting Cheng

**Abstract** In computer modeling, errors and uncertainties inevitably arise due to the mathematical idealization of physical processes stemming from insufficient knowledge regarding accurate model forms as well as the precise values of input parameters. While these errors and uncertainties are quantifiable, compensations between them can lead to multiple model forms and input parameter sets exhibiting a similar level of agreement with available experimental observations. Such non-uniqueness makes the selection of a single, best computer model (i.e. model form and values for its associate parameters) unjustifiable. Therefore, it becomes necessary to evaluate model performance based not only on the fidelity of the predictions to available experiments but also on a model's ability to sustain such fidelity given the incompleteness of knowledge regarding the model itself, such an ability will herein be referred to as robustness. In this paper, the authors present a multi-objective approach to model calibration that accounts for not only the model's fidelity to experiments but also its robustness to incomplete knowledge. With two conflicting objectives, the multi-objective model calibration results in a family of non-dominated solutions exhibiting varying levels of fidelity and robustness effectively forming a Pareto front. The Pareto front solutions can be grouped depending on their *nature of compromise* between the two objectives, which can in turn help determine clusters in the parameter domain. The knowledge of these clusters can shed light on the nature of compensations as well as aid in the inference of uncertain input parameters. To demonstrate the feasibility and application of this new approach, we consider the computer model of a structural steel frame with uncertain connection stiffness parameters under static loading conditions.

**Keywords** Model calibration • Info-gap decision theory • Non-dominated sorting genetic algorithm (NSGA-II) • K-means clustering • Multi-objective optimization

### 23.1 Introduction

Regardless of sophistication and extent of detail included, computer models at best approximate the segment of reality they are built to represent. Thus, the use of computer models for decision making mandates that the validity (i.e. worthiness) of model predictions be assessed. Traditionally, this process has solely focused on the fidelity of model predictions to experiments. However, when evaluated according to a fidelity metric alone, compensations between uncertainties and errors that originate from various sources during the model development process can inflate the apparent capabilities of inferior models. Such compensations can lead to multiple models yielding predictions of similar fidelity to the available experiments, widely referred to as non-uniqueness [1].

Non-uniqueness occurs when an incorrectly assigned parameter value compensates for another incorrect parameter value or acts to offset model bias. Compensations between parameters may occur when correlated parameters are calibrated simultaneously (which can be prevented by calibrating each parameter using an independent observable) or when available experimental observations are insufficient (which can be alleviated by further data collection). Compensations may also result from the definitions of the test-analysis correlation metrics, for instance when errors in predictions of multiple outputs are lumped together in one metric. In such situations, considering errors in each of the outputs separately might be useful in determining what role compensations play during model calibration. Compensations might also be due to the inherent imperfectness of model form in that the model parameters might be calibrated to values that counter the model bias. In such situations, explicitly considering the model bias through the training of an independent error model can alleviate the problem. Oftentimes, all of these factors take place in varying degrees making it difficult to come up with one overarching solution.

---

S. Atamturktur (✉) • G. Stevens • Y. Cheng  
Glenn Department of Civil Engineering, Clemson University, Clemson, SC, USA  
e-mail: [sez@clemson.edu](mailto:sez@clemson.edu)

These compensations during parameter calibration make it difficult (and in fact, unjustifiable) to select one set of calibrated parameter values. This difficulty can be alleviated by ensuring the robustness of a model's fidelity against uncertainty in the calibrated input parameters. Robustness in model predictions, as defined by the info-gap decision theory, means that the model predictions reproduce observables within a predefined fidelity threshold even when the inherent uncertainties are considered. Hence, what might be a viable approach to address the difficulties model calibration faces due to compensations is to seek parameter value sets that not only yield a satisfying level of agreement with observations but also do so while being able to accommodate variability in their own imperfectness.

The above statement effectively converts model calibration into a multi-objective problem with two conflicting objectives (see Ben-Haim and Hemez [2] for a discussion on the conflicting nature of fidelity and robustness), in which one objective cannot be improved without compromising the other. Accordingly, in this study, model calibration is treated as a multi-objective problem by considering both the model's fidelity to measurements and robustness of this fidelity to parameter uncertainty. Multi-objective optimization supplies a family of plausible solutions each with a different compromise between the conflicting objectives, known as Pareto front, which visually displays the trade-off between these two conflicting objectives.

The shape of the Pareto front depends on the nature of the optimization problem. Herein, the desired outcome for the robustness objective (horizon of uncertainty) is the larger-the-better and the outcome for the fidelity objective (error threshold) is the smaller-the-better, which leads to a monotonically increasing Pareto front. Such Pareto front shapes tend to have distinct regions depending on the nature of the compromise between objectives: regions where gains and losses between objectives are not balanced (gaining in one objective implies a significant loss in the other) and a region where gains and losses between objectives are balanced. These distinct regions on the Pareto front tend to be associated with distinct clusters in the input parameter space. Knowing the distribution of input parameters in the input space can allow (i) the modeler to evaluate the extent of the compensation between model input parameters and (ii) aid in the decisions regarding the inferred parameter values.

This paper is organized as follows. Section 23.2 provides a background review of earlier reported studies in which clustering of Pareto optimal solutions is evaluated. Section 23.3 presents a discussion on the multi-objective model calibration integrated with clustering algorithms as well as an overview of the algorithms implemented for both multi-objective optimization and clustering. Section 23.4 illustrates its application by means of a case study of a two bay, two story steel moment resisting frame with imprecisely known connection parameters. Section 23.5 concludes the study by overviewing both the contributions and limitations of the proposed methodology.

## 23.2 Background Review

Cluster analysis divides a dataset into distinct groups, referred to as "clusters," where data points within a cluster are similar to one another and different from the data points of other clusters. Clustering is used to discover hidden "structures" within a given set of data. Cluster analysis identifies patterns among data points to group similar data together, revealing relationships in the data that were previously unknown. Analyzing the data in clusters helps to outline hidden correlations within the system at hand. Furthermore, revealing relationships in the system informs decision makers who need extensive knowledge of the system to implement it for its intended use. Cluster analysis is widely used in many fields, such as data mining [3], exploratory data analysis [4] and vector quantization [5].

Cluster analysis has previously been used to cluster Pareto optimum solutions to aid in the selection of a single optimum solution (especially when the Pareto front contains a larger number of solutions). For instance, Zio and Bazzo [6] proposed a two-steps procedure to reduce the number of optimal solutions in the Pareto front. In their study, a subtractive clustering algorithm is used to cluster the solutions into "families." For each family, a "head of the family" is selected to effectively reduce the number of possible solutions on the Pareto front aiding the decision making process. Finally, they represented and analyzed the reduced Pareto front by Level diagrams. Veerappa and Letier [10] implemented a hierarchical clustering method and clustered the Pareto optimal solutions based on the cost-weighted Jaccard distance function for cost-value based requirements selection problem. Jaccard distance measures the similarity (or lack thereof) between clusters as the ratio of their intersection over their union. The cost-weighted Jaccard distance function is a version of Jaccard distance that applies weights based on the importance of each objective.

## 23.3 Methodology

### 23.3.1 Fidelity in Model Calibration

Combined effects of incompleteness of model form and the imprecision in the input parameters yield deviations between model predictions and observable reality. Such deviations can be quantified as shown in Eq. 23.1:

$$R(k) = |M(k) - E| \quad (23.1)$$

where,  $k$  represents the imprecise parameters to be calibrated selected based on their sensitivity and uncertainty,  $R(k)$  represents the fidelity metric (error) between model prediction,  $M(k)$ , and experimental observation,  $E$ .

Given the inevitable uncertainties in experimental observations and numerical calculations, aiming to reach a perfect agreement between model predictions and experimental observations would have little meaning. A more rational approach instead is to aim to reach *sufficient* agreement between the two. Herein, sufficiency can be defined by a preset fidelity threshold as shown in Eq. 23.2:

$$|M(k) - E| < Rc \quad (23.2)$$

where  $Rc$  indicates the error tolerance (which is related to desired level of fidelity) between model prediction and experiment.

### 23.3.2 Overview of Info-Gap Decision Theory

Info-gap decision theory supplies a non-probabilistic approach to decision making under uncertainty. The Info-gap approach uses convex, nested sets of uncertainty models to quantify the allowable range of uncertainty the system can tolerate before it fails to meet the preset performance criteria [7].

$$U(\alpha, \tilde{k}) = \left\{ k : \left| \frac{k - \tilde{k}}{\tilde{k}} \right| \leq \alpha \right\}, \alpha \geq 0 \quad (23.3)$$

Equation 23.3 shows the info-gap model with uncertain calibrated parameters. In this equation,  $k$  once again represents imprecise parameters and  $\tilde{k}$  represents the nominal values for these parameters, which herein will be obtained through calibration. The nominal values are the vector of best estimate model parameters that result in the smallest error between experiments and simulations [8]. The uncertainty in parameters, commonly referred to as horizon of uncertainty, is represented by notation  $\alpha$ .

$$\widehat{R}(\alpha) = \max_{k \in U(\alpha, \tilde{k})} R(k) \quad (23.4)$$

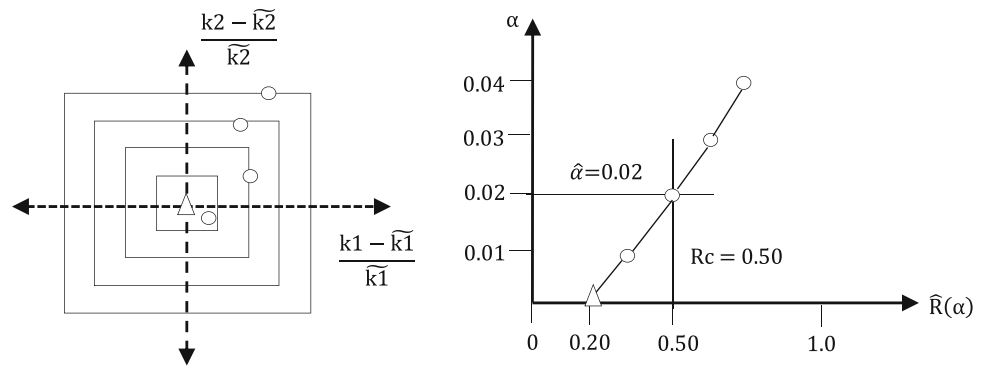
The function  $R(k)$  represents the fidelity of the model considering uncertain calibrated parameters. By increasing the model's horizon of uncertainty,  $\alpha$ , the uncertain parameters are allowed to vary within a defined range. For each given value of  $\alpha$ , the uncertain parameters will result in a new worst-case fidelity as shown in the Fig. 23.1 (left). Therefore,  $\widehat{R}(\alpha)$  is a non-decreasing function of  $\alpha$  as shown in Fig. 23.1 (right).

As shown in Fig. 23.1, as the horizon of uncertainty increases,  $\widehat{R}(\alpha)$  eventually exceeds the predefined value of fidelity threshold,  $Rc$ . The maximum horizon of uncertainty in which uncertain parameters are allowed to vary without failing to satisfy the fidelity requirement is defined as  $\widehat{\alpha}$ , as shown in Eq. 23.5. Thus, a larger  $\widehat{\alpha}$  is desired and representative of greater robustness of the model.

$$\widehat{\alpha} = \max \left\{ \alpha : \widehat{R}(\alpha) \leq Rc \right\} \quad (23.5)$$



**Fig. 23.1** Illustration of info-gap robustness with (left) worst case predictions given varying horizons of uncertainty and (right) monotonically increasing robustness curve



### 23.3.3 Overview of Multi-objective Optimization

Multi-objective problems arise when multiple objectives influence the problem in a conflicting manner. Multi-objective optimization supplies a means to obtain solutions for such problems in that conflicting objectives are optimized simultaneously under given constraints. Multi-objective optimization can be expressed as shown in the following equation:

$$\begin{aligned} \text{Minimize : } & Y(x) = [f_1(x), f_2(x), \dots, f_k(x)] \\ \text{Subject to : } & h(x) \leq 0 \end{aligned} \tag{23.6}$$

where  $f$  represents the each objective function and  $h$  represents the constrain function.

Multi-objective optimization results in a set of compromising solutions, which represent the trade-off between conflicting objectives. Referred to as Pareto front, these compromising solutions provide the optimal solutions in the solution space, within which improving one objective is not possible without degrading the other(s). It must therefore be obvious to the reader that when multiple objectives are not conflicting, obtaining a single optimal solution becomes possible and multi-objective optimization would not be needed.

Once the Pareto front is determined, decision makers can select solution within this optimal solutions set taking the trade-off between multiple objectives into account. The shape of Pareto front has important significance for this study as it indicates the nature of the trade-off between the different objective functions. The shape of the Pareto front can be used to infer the nature of the relationship between objectives. For instance, in Fig. 23.2, regions where the slope of the Pareto front is steep (or shallow) indicate solutions where slight improvement in one objective requires a significant sacrifice in the other. In Fig. 23.2, three distinct regions can be identified with distinctly different trade-off characteristics (indicated with gray highlights).

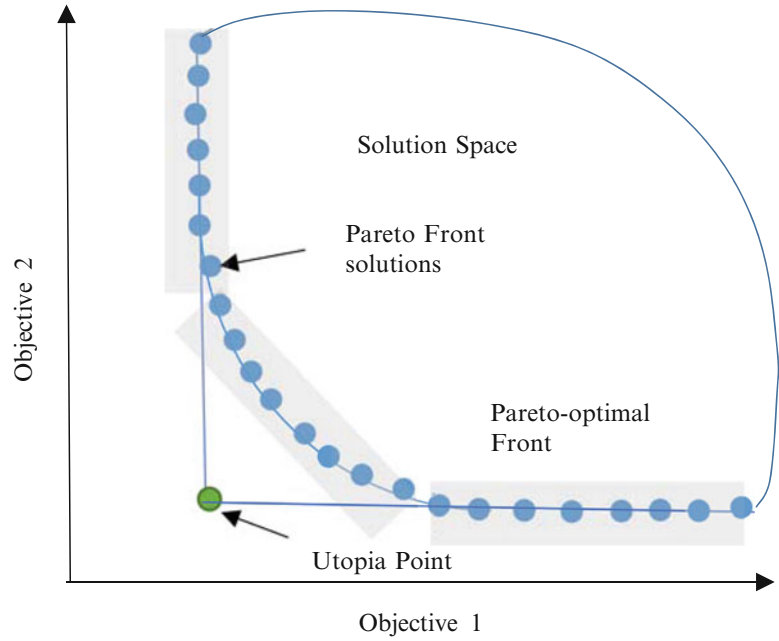
### 23.3.4 Application of K-Means Clustering to Pareto Front

K-means clustering belongs to partitioning methods, one of the most commonly used clustering algorithms due to its implementation simplicity and computational efficiency. K-means clustering algorithm is a centroid based clustering method [9] that partitions data into a user-defined number of clusters, each of which is associated with a centroid.

The main procedure of K-means clustering algorithm can be broken down into four components (i) selecting a user defined number of data points as the initial set of cluster centroids, (ii) assigning each point to the cluster with the nearest centroid, (iii) recalculating the centroid of each cluster, and (iv) repeating assignment of each point to the cluster with the nearest centroid.

The algorithm starts with randomly choosing the number the predefined number of solutions in the Pareto front as an initial set of cluster centroids. Then, each solution in the Pareto front is assigned to the cluster with nearest centroid. The “nearest centroid” is measured by the Euclidean distance between each solution in the Pareto front and the corresponding closest centroid. To express the formulation of Euclidean distance, let us consider a N-dimensional Pareto front set which contains  $n$  solutions,  $N_n = (x_1, x_2, \dots, x_n)$ , where these  $n$  solutions are partitioned into  $m$  sets,  $H = (h_1, h_2, \dots, h_m)$ , where  $m \leq n$ .

**Fig. 23.2** Representative shape of Pareto Front



$$d_n^m = \sum_{x \in H_i} \|x - C_i\|^2 \quad (23.7)$$

where  $m$  represents the number of centroids (i.e. number of clusters) and  $C_i$  represents the centroid of each cluster.

According to the distances calculated in Eq. 23.7, each of the  $n$  data-points are assigned to the nearest one of the  $m$  centroids and next, the centroid of each cluster is recalculated. This iterative procedure is repeated, until the convergence condition is satisfied or when the iterative procedure reaches the predefined number of iterations. The convergence condition is satisfied when the distribution of clusters do not change more than a predefined amount by recalculating the centroid of each cluster.

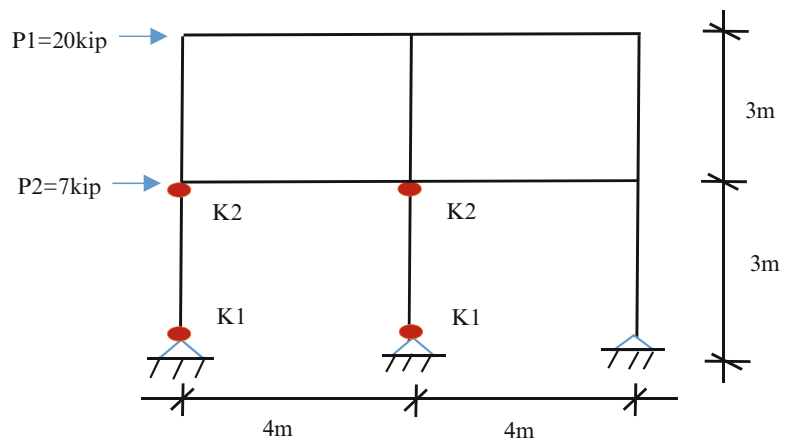
K-means clustering algorithm assigns solutions in the Pareto front into non-overlapping clusters, where solutions within a cluster have similar characters. For instance, within one cluster, we may observe that the value of objective 2 exhibits small changes for varying values of objective 1. What is interesting to note that if the problem in hand is constituted of proper continuous functions, then each of clusters in Pareto front would be associated with parameters that also have *similar* values. Observing the clusters formed in the parameter space corresponding to the clusters in the solution space can help decision makers evaluate the effect of compensations in model calibration and aid in the model parameter selection (note that we are indicating an inverse analysis from the solution space to the parameter space).

## 23.4 Case Study

The proposed methodology is demonstrated on a case study of a two bay, two story steel moment resisting frame, shown in Fig. 23.3. The frame is built with beams and columns that have uniform cross-sections. Two external horizontal, static loads are applied to the top and the first story of this steel moment resisting frame (Fig. 23.3). It is assumed that the loads applied do not cause deformations beyond the elastic range. Material properties and physical dimensions of the portal frame members are provided in Table 23.1.

Connection stiffness between the substructures in steel moment resisting frames is typically highly uncertain. In the frame system shown in Fig. 23.3, four linear rotational springs are assigned to represent beam to column connections located at the top and bottom of the first story left and center columns. The stiffness of these rotational springs are represented by parameters  $K1$  and  $K2$ . All other beam to column connections are assumed rigid and columns are pin connected to the foundation. The connection stiffness values,  $K1$  and  $K2$ , are treated as the calibration parameters. The exact stiffness values of those linear rotational springs are provided in Table 23.2 along with their plausible ranges (i.e. parameter space).

**Fig. 23.3** Steel moment resisting frame with linear rotational springs



**Table 23.1** Material properties and physical dimensions for the portal frame

	Beam	Column
Length (m)	4	3
Cross section area (m <sup>2</sup> )	0.05	0.05
Moment of inertia (m <sup>4</sup> )	0.1	0.05
Young's modulus (Pa)	2,000	2,000
Shear area coefficient	0.95; 1; 1.05	0.95; 1; 1.05
Poisson's ratio	0.3	0.3

**Table 23.2** Calibrated parameters and NSGA-II simulation ranges

	K1 (N-m)	K2 (N-m)
Exact value	33,000	40,000
Upper bound	132,000	160,000
Lower bound	3,300	4,000

### 23.4.1 Multi-objective Optimization: Robustness Versus Nominal Fidelity

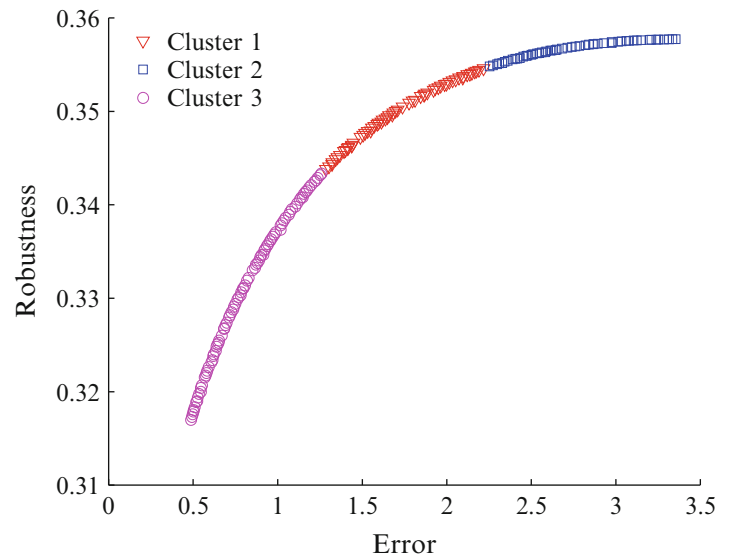
In this case study, the error between model predictions and measured observables as well as the robustness of the model predictions given uncertain parameters are implemented as objectives. A finite element model is developed and used to predict the maximum lateral displacement at the first story of the portal frame under static lateral loading. Synthetic experimental data are obtained by using sets of input parameters with exact values while model predictions are obtained in a separate process using sets of parameters with imprecise values. Inaccurately calibrated parameters result in disagreements between predictions and experiments for maximum lateral displacement at the first story, quantified by the fidelity metric (refer back to Eq. 23.1). According to the proposed procedure explained in Sects. 23.3.1 and 23.3.2, the fidelity threshold,  $R_c$ , is predefined to equal 0.5 and the horizon of uncertainty,  $\alpha$ , is varied from 0.01 to 0.5 by a step size of 0.1. NSGA-II is implemented to solve the multi-objective optimization problem with 100 generations with 200 individuals in each to obtain the Pareto front.

The conflicting relationship between objectives develops as robustness to parameter uncertainty should decrease when the fidelity threshold is increase [2]. Thus, the shape of the Pareto front reflects this monotonic trade-off relationship between the two objectives. K-means clustering algorithm is implemented to cluster the solutions in the Pareto front using three clusters. The number of clusters to evaluate is determined by considering the change in slope of the Pareto front (recall Fig. 23.2).

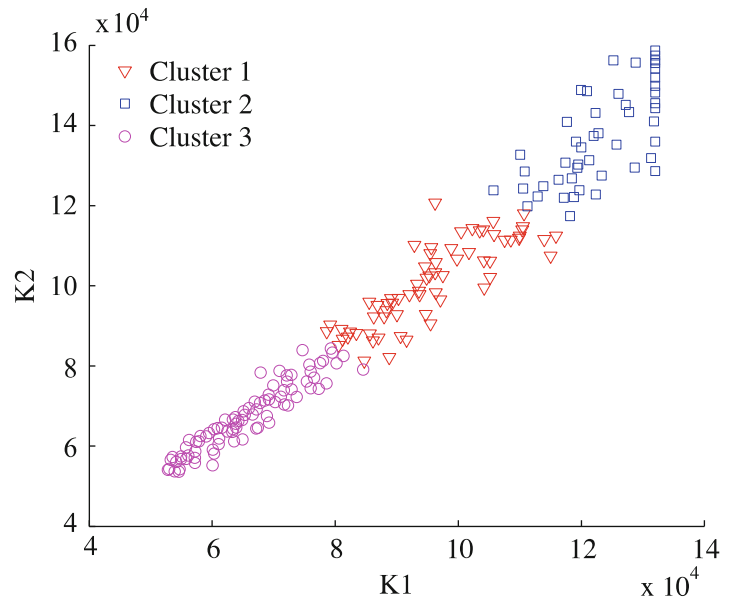
The result of a clustered multi-objective optimization is shown in Fig. 23.4, which provides a clear visualization of the spread of solution groups along the Pareto Front. The distribution of calibrated parameters corresponding to each cluster is shown in Fig. 23.5. It should be noted that this case study resulted in a partial Pareto front, which is possible with the NSGA-II algorithm. Decision makers may use information gained from the clusters to select a parameter set with which model outcomes balance both of the objectives. Decision makers may first select the cluster containing the most solutions satisfying their requirements. Next, the parameter sets corresponding to this cluster may be determined.

In Fig. 23.5, the correlation between the two calibration parameters is evident, illustrated by the linear distribution of parameter sets. There clearly exists a relationship where K1 increases K2 also increases.

**Fig. 23.4** Distribution of robustness and error for the 100th generation



**Fig. 23.5** Distribution of calibrated input parameters for the 100th generation

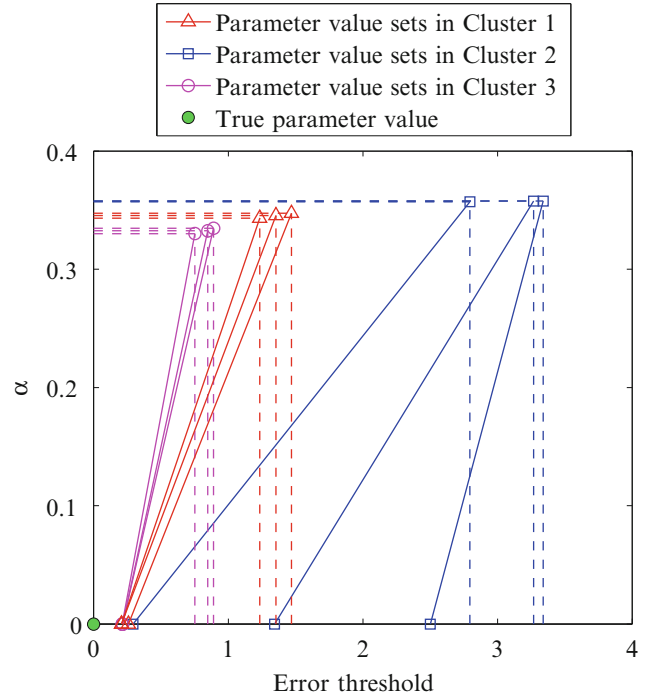


### 23.4.2 Multi-objective Optimization: Robustness Versus Fidelity Threshold

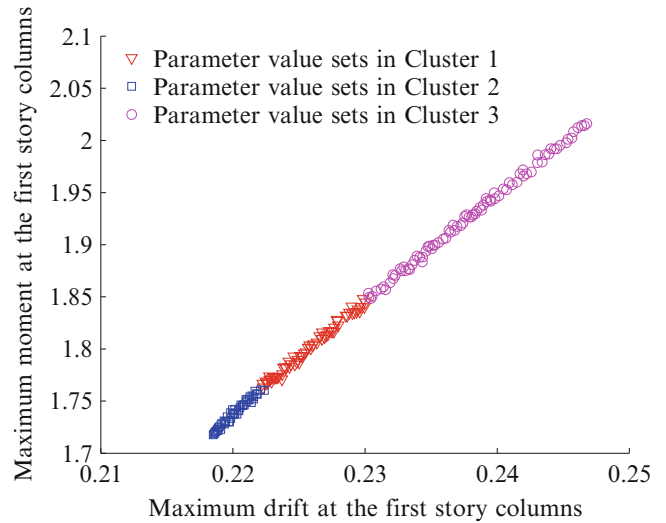
According to the methodology presented in Section 23.3.2, a larger robustness is desired meaning the model is capable of higher uncertainty in parameters. The fidelity threshold quantifies the error between predictions and measurements. Hence, minimizing the fidelity threshold corresponds to a low level of error allowed between predictions and experiments. Maximizing the robustness causes the corresponding fidelity threshold to increase. This trade-off relationship between the two objectives is revealed by the shape of the Pareto front. NSGA-II is implemented to solve the multi-objective optimization problem with 100 generations and 200 individuals in each generation. K-means clustering algorithm is applied to the solutions. Figure 23.6 presents a robustness function (recall Fig. 23.1 right) for a select number of Pareto optimal solutions. Plotting robustness functions for the Pareto optimal solutions then effectively results in the Pareto front itself (notice the similarity between Figs. 23.4 and 23.6).

### 23.4.3 New Predictions for Portal Frame by Using Parameter Sets in Each of Clusters

In this section, a series of new predictions for the steel moment resisting frame is presented. Based on the parameter sets shown in Fig. 23.5. Each of these parameter sets is used in the finite element model to predict the maximum lateral displacement (drift), maximum moment and maximum shear force at the first story as well as the maximum lateral displacement at the roof of the portal frame. The following results show that using parameter value sets in each cluster results in a different prediction as well as solutions that are clustered (Figs. 23.7, 23.8, and 23.9).

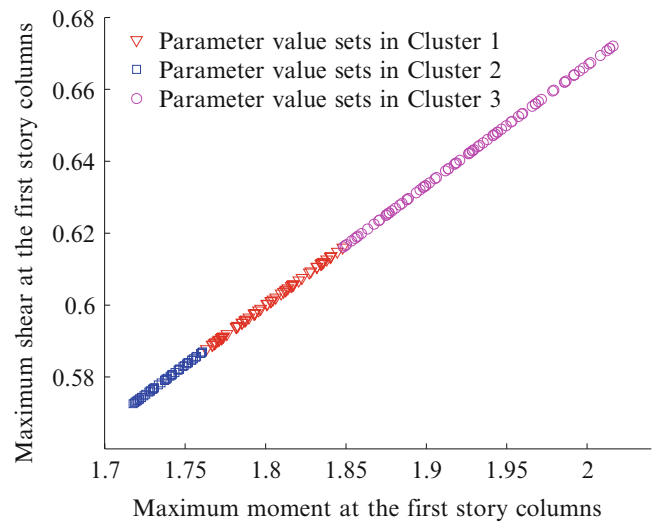


**Fig. 23.6** Distribution of robustness and error threshold for each cluster

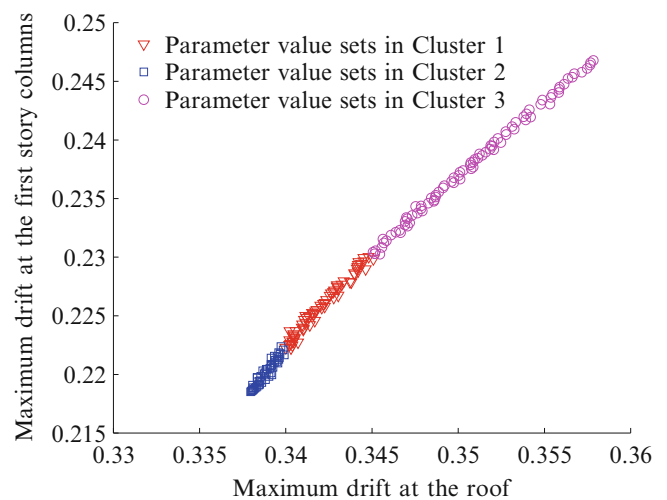


**Fig. 23.7** First story maximum drift versus maximum moment

**Fig. 23.8** First story maximum moment versus maximum shear



**Fig. 23.9** Roof maximum drift versus first story maximum drift



## 23.5 Conclusion

Model calibration considering both the model's fidelity to measurements and robustness to parameter uncertainty results in a multi-objective problem. Multi-objective optimization provides insight to the trade-off between objectives through a Pareto front. However, understanding the compromise between parameters alone is not sufficient information for decision makers, who are often required to select a best-performing data, which maintains each of their requirements. The selection task becomes more burdensome when the set of non-dominated solutions is large. For this reason, the authors proposed a methodology that implements the k-means clustering algorithm to cluster the solutions in the Pareto front making the selection task more feasible. The main idea of this methodology is to categorize possible solutions into different groups based on their spread on the Pareto front. Calibrated parameter values may then be selected from among these groups of solutions.

Furthermore, this study can also help decision makers to select among the clusters obtained. This can be achieved by evaluating the distribution of calibration parameters within each cluster. A key benefit of clustering Pareto front solutions is the ability to evaluate the extent of the compensation between model input parameters. Clusters with large distributions indicate severe compensations between parameters. Therefore, model developer may select a parameter set with the least amount of compensations, or determine steps to reduce compensations if the compensations are too large.

The proposed methodology has been applied to case study with a steel moment resisting frame. The results show that this methodology makes it more feasible to select the optimal group of solutions, which will narrow down the range to select calibration parameters. A separate robustness analysis presents the trade-off between robustness to uncertainty parameters and fidelity threshold. Hence, within a certain fidelity threshold, the model can tolerate the maximum allowable level of uncertainty.

## References

1. Berman A, Flannelly WG (1971) Theory of incomplete models of dynamic structures. *AIAA J* 9(8):1481–1487
2. Ben-Haim Y, Hemez FM (2004) Robustness-to-uncertainty, fidelity-to-data and prediction looseness of models. In: *Proceedings of the 22nd international modal analysis conference (IMAC-XXII)*, pp 26–29
3. Fayyad UM, Piatetsky-Shapiro G, Smyth P, Uthurusamy R (1996) *Advances in knowledge discovery and data mining*. AAAI Press/MIT Press, Menlo Park
4. Xu R, Wunsch D (2005) Survey of clustering algorithms. *Neural Networks, IEEE Transactions* 16(3):645–678
5. Yair E, Zeger K, Gersho A (1992) Competitive learning and soft competition for vector quantizer design. *Signal Processing, IEEE Transactions* 40(2):294–309
6. Zio E, Bazzo R (2011) A clustering procedure for reducing the number of representative solutions in the Pareto Front of multiobjective optimization problems. *Eur J Oper Res* 210(3):624–634
7. Ben-Haim Y (2006) *Info-gap decision theory: decisions under severe uncertainty*. Academic Press, Oxford
8. Atamturktur S, Liu Z, Cogan S, Juang H (2014) Calibration of imprecise and inaccurate numerical models considering fidelity and robustness: a multi-objective optimization-based approach. *Struct Multidiscip Optim* 50(6):1–13
9. Awasthi P, Balcan MF (2013) Center based clustering: a foundational perspective. Survey chapter in *handbook of cluster analysis* (manuscript)
10. Veerappa V, Letier E (2011) Understanding clusters of optimal solutions in multi-objective decision problems. In: *19th IEEE international conference on requirements engineering (RE)*, IEEE, pp 89–98

# Chapter 24

## Uncertainty Propagation Combining Robust Condensation and Generalized Polynomial Chaos Expansion

K. Chikhaoui, N. Kacem, N. Bouhaddi, and M. Guedri

**Abstract** Among probabilistic uncertainty propagation methods, the generalized Polynomial Chaos Expansion (gPCE) has recently shown a growing emphasis. The numerical cost of the non-intrusive regression method used to compute the gPCE coefficient depends on the successive Latin Hypercube Sampling (LHS) evaluations, especially for large size FE models, large number of uncertain parameters, presence of nonlinearities and when using iterative techniques to compute the dynamic responses. To overcome this issue, the regression technique is coupled with a robust condensation method adapted to the Craig-Bampton component mode synthesis approach leading to computational cost reduction without significant loss of accuracy. The performance of the proposed method and its comparison to the LHS simulation are illustrated by computing the time response of a structure composed of several coupled-beams containing localized nonlinearities and stochastic design parameters.

**Keywords** Robustness • Uncertainty • Generalized polynomial chaos expansion • Component mode synthesis • Meta-model

### 24.1 Introduction

In structural mechanics and in practically all branches of industry, when parametric uncertainty is incorporated in the mathematical model, its propagation is needed to evaluate how the randomness of input parameters affects the computed outputs and to handle, consequently, more and more realistic behaviors. In a probabilistic framework, statistical approaches such as the well-known Latin Hypercube Sampling (LHS) [1] use a great number of samples of random variables for reasonable accuracy and therefore require a prohibitive computation time. On the other side, among other non statistical approaches, the generalized polynomial chaos expansion (gPCE) [2] has shown a growing emphasis in recent years due to its simple implementation and high performance. It combines polynomial basis vectors and deterministic coefficients, which can be computed by means of intrusive or non-intrusive approaches [3]. In the context of the latter, more advantageous than the former since it considers the original FE model as a black box, among other existing methods [4], regression technique permits to estimate the gPCE coefficients by minimizing the difference between the referential LHS response and the approximation, corresponding to a set of random variables chosen among combinations of Hermite polynomial roots.

Nevertheless, the most expensive part of its implementation lies in the successive LHS evaluations. To overcome this issue, we focus, in this paper, on coupling the non-intrusive regression technique with a robust condensation method adapted to the Craig-Bampton component mode synthesis (CBCMS). In fact, the prohibitive cost of prediction is due to: the computational time of the full model using direct analysis, the computation of reduction basis for each random sample while propagating uncertainties and the number of iterations necessary to obtain accurate approximations using iterative techniques in presence of nonlinearities. Consequently, model condensation must be applied. Furthermore, the use of the CBCMS [5, 6] allows considering some substructures, which are uncertain and/or containing localized nonlinearities, being condensed independently of the others. Nevertheless, the main issue lies on forming a robust enriched condensed Craig-Bampton Transformation (CBT) [6, 7] which takes into account uncertainties and localized nonlinearities.

---

K. Chikhaoui • N. Kacem (✉) • N. Bouhaddi  
FEMTO-ST Institute, UMR 6174, Applied Mechanics Laboratory, University of Franche-Comté, 24 Chemin de l'Épitaphe, 25000 Besançon, France  
e-mail: najib.kacem@femto-st.fr

K. Chikhaoui • M. Guedri  
National High School of Engineers of Tunis (ENSIT), University of Tunis, 5 Avenue Taha Hussein, BP 56, Bâb Manara, Tunis, Tunisia



In the literature, some works focus on coupling uncertainty propagation methods and condensation techniques in order to attain a robust design. In [8], the authors implemented the CMS taking into account stochastic aspect to compute frequency linear structures responses using stochastic spectral FE method (SSFEM). In [9], a reduced-order model (ROM) is integrated into SSFEM, using a basis spanned by displacements and derivatives of displacements, and implemented to optimize the shape of a linear shell structure. Afonso et al. [10] implemented Monte Carlo (MC) method and Probabilistic Collocation Method (PCM) based on reduced-order modeling (ROM) approach incorporated via proper orthogonal decomposition method (POD).

The main originality of this paper lies on combining gPCE and robust CBCMS in order to obtain a metamodel, which allows computing stationary temporal solution of large size stochastic periodic structures containing local nonlinearities, with high accuracy and low computational cost.

## 24.2 Theoretical Backgrounds

### 24.2.1 Generalized Polynomial Chaos Expansion (gPCE)

Thanks to the generalization of the PC approach [2], several types of random variables and orthogonal polynomials are taken into account to develop its expansion. In this section, a compact form of the gPCE formulation is presented [2–4]. The gPCE of second order random variable is a decomposition, truncated by retaining only terms of the polynomials with degree up to  $p$ , of the form

$$Y = \sum_{\alpha=0}^P y_{\alpha} \Phi_{\alpha}(\xi) = y^T \Phi(\xi), \quad (24.1)$$

where  $y_{\alpha}$  are the unknown deterministic coefficients,  $\Phi_{\alpha}$  the multivariate polynomials of  $d$  independent random variables  $\xi = \{\xi_i(\theta)\}_{i=1}^d$  and  $\alpha$  the multidimensional index such as  $|\alpha| = \sum_{i=1}^d \alpha_i$ .

The number of terms retained in Eq. 24.1 is defined as

$$P + 1 = (d + p)! / d! p!. \quad (24.2)$$

Solving the gPCE consists on computing the coefficients  $y_{\alpha}$ . Hence, the non-intrusive regression method is implemented, in its standard form, minimizing the difference between the gPCE approximate solution and the exact one as follow

$$\tilde{y} = \underset{y}{\text{Arg min}} \frac{1}{N} \sum_{n=1}^N [\{Y^{(n)}\} - y^T \Phi(\xi^{(n)})]^2. \quad (24.3)$$

The solution considered as exact is a set of LHS responses  $\{Y^{(n)} = y(\xi^{(n)}), n = 1, \dots, N\}$  computed corresponding to a set of random variables  $\Xi = \{\xi^{(n)}\}_{n=1}^N$  called experimental design (ED).

The final obtained approximate solution of Eq. 24.3 is of the form

$$\tilde{y} = (\Phi^T \Phi)^{-1} \Phi^T \{y\} = \Phi^+ \{y\} \quad (24.4)$$

where  $\Phi_{nj} \equiv (\Phi_j(\xi^{(n)}))_{n=1, \dots, N}$  is called the data matrix.  
 $j = 0, \dots, P$

A necessary condition for the numerical stability of the regression approximation is choosing an ED of size  $N \geq P + 1$  which ensures the well-conditioning of the matrix  $(\Phi^T \Phi)$  which will be inverted. The selection of the ED is carried out using two different methods; according to the first one, the ED is chosen randomly with respect to the probability distribution of the random variables, the second method consists on selecting the ED, in a deterministic way, among Hermite polynomial roots [3]. In fact, the roots of the Hermite polynomial of degree  $p + 1$  are at first computed, then all their possible combinations  $(p + 1)^d$  are calculated and finally these roots combinations are classified such that the following variable

$$\zeta_N(\xi^{(n)}) = 2\pi^{-d/2} \exp\left(-\frac{1}{2}\xi^{(n)2}\right) \quad (24.5)$$

is maximized or  $\xi^{(n)2}$  minimized. The roots combinations retained to create the ED are subject to another selection [4]. Indeed, to ensure that the invertible matrix  $(\Phi^T \Phi)$  is well-conditioned, a condition number  $\kappa$  defined as

$$\kappa = (\Phi^T \Phi)^{-1} \cdot \Phi^T \Phi \quad (24.6)$$

must be minimized, where  $\cdot$  is the 1-norm of the matrix. To the smallest value of  $\kappa$  corresponds a number  $N$  of roots combinations which verify Eq. 24.5 and thus create the ED needed for gPCE coefficients.

Once obtained, the estimated coefficients give the final gPCE as a metamodel of the form

$$\tilde{Y} = \tilde{\mathcal{M}}(X(\xi)) = \sum_{\alpha=0}^P \tilde{y}_{\alpha} \Phi_{\alpha}(\xi), \quad (24.7)$$

In uncertainty analysis, some statistical quantities have to be calculated. The mean and the variance are respectively given

$$\text{by } \tilde{\mu}_Y = \tilde{y}_0 \text{ and } \tilde{\sigma}_Y^2 = \sum_{\alpha=0}^P \tilde{y}_{\alpha}^2.$$

Note that the  $N$  successive deterministic FE evaluations needed for LHS method is the most expensive part of the gPCE implementation especially for large size FE models, large number of uncertain parameters, presence of nonlinearities and when using iterative techniques to compute dynamic structure responses. To overcome this issue, the regression technique is coupled with a robust condensation method adapted to the CBCMS.

### 24.2.2 Model Condensation

In nonlinear dynamics, a mechanical system can generally be represented in the time domain by the following differential equation

$$\begin{cases} [M] \{\ddot{y}\} + [B] \{\dot{y}\} + \{f_{int}\} = \{f_{ext}\} \\ \{y\}(t_0) = \{y\}_0, \{\dot{y}\}(t_0) = \{\dot{y}\}_0 : \text{ initial conditions} \end{cases} \quad (24.8)$$

where  $[M]$  and  $[B]$  stand for the mass and damping matrices of the system,  $\{f_{ext}\}$  the exciting force and  $\{f_{int}\} = ([K] + \{f_{NL}\}(\{y\}, \{\dot{y}\})) \{y\}$  the internal force vector,  $[K]$  is the stiffness matrix.

Modeling complex structures requires large size FE models for satisfying accuracy. To overcome the high computational cost of the analysis, a reduced order model has to be designed using only few normal modes with respect to the frequency range of interest. Therefore, the projection of the time response on an adequate condensation basis, considering the variable transformation  $\{y(t)\} = [T] \{q(t)\}$  to generalized coordinates, is needed. Hence, the equation of motion Eq. 24.8 becomes

$$[T]^T [M] [T] \{\ddot{q}(t)\} + [T]^T [B] [T] \{\dot{q}(t)\} + [T]^T \{f_{int}\}_r = [T]^T \{f_{ext}\}, \quad (24.9)$$

where the index  $r$  denotes the term reduced,  $[T]^T [M] [T] = [M]_r$ ,  $[T]^T [B] [T] = [B]_r$ , in this case, the internal force vector is expressed as

$$\{f_{int}\}_r = [T]^T ([K] + \{f_{NL}\}([T] \{q\}, [T] \{\dot{q}\})) [T] \{q\}. \quad (24.10)$$

The time solution of the Eq. 24.9 can be approximated by using the Newmark nonlinear time integration scheme, which allows expressing the displacement and the velocity at the instant  $t_{n+1}$  as a function of their expression at  $t_n$ .

The implementation of the Newmark method permits to write the equation of motion Eq. 24.9 in an incremental form

$$([K_{eff}]_r)_n \Delta \{q\}_n = \Delta (\{f_{eff}\}_r)_n \quad (24.11)$$

where  $([K_{eff}]_r)_n$  is the instantaneous (effective) stiffness matrix function of the tangent stiffness matrix  $([K_T]_r)_n = \partial(\{f_{ini}\}_r)/\partial [T] \{q\}_n$  obtained by applying the Newton iterative scheme.

### 24.2.3 Robust Craig-Bampton Component Mode Synthesis Method (CBCMS)

Dividing the complete structure into several components (substructures) is interesting in the case of presence of uncertainties and localized nonlinearities in large size complex structures. It permits to apply the adequate condensation technique to each component independently of the others.

In deterministic linear case, the reduced model is obtained using standard CBCMS [5, 6] of the linear system in its blocked interface configuration. In this case, the CBT is defined, for a substructure  $k$ , as

$$\{y\}^k = \begin{Bmatrix} y_j \\ y_i \end{Bmatrix}^k = \begin{bmatrix} I_{jj} & 0 \\ \psi_{ij} & \varphi_i \end{bmatrix}^k \begin{Bmatrix} q_j \\ q_c \end{Bmatrix}^k = [T_{CB}]^k \{q\}^k \quad (24.12)$$

where  $\{y_i\}^k$  are the interior coordinates transformed to the blocked junctions modal coordinates  $\{q_c\}^k$ ,  $\{y_j\}^k$  are the junction coordinates denoted as constraint coordinates  $\{q_j\}^k$ ,  $[\psi_{ij}] = -K_{ii}^{-1} K_{ij}$  is the static subbasis which contains the constraint modes,  $I_{jj}$  is the identity matrix, and  $[\varphi_i]$  is the dynamic one containing the truncated normal modes basis at blocked interfaces ( $\{y_j\} = 0$ ) of the corresponding component. Nevertheless, using standard CBT requires computing more and even all normal modes for accurate results, which leads to a prohibitive computation cost.

In stochastic case with localized nonlinearities, the standard CBT  $[T_{CB}]$  cannot satisfy the required accuracy and robustness of the model. Therefore, adding a complementary basis  $[\Delta T]$  is necessary in order to form an enriched CBT (ECBT)  $[T_{ECB}]$ . The obtained basis, for each sub-structure, is thus of the form

$$[T_{ECB}]^k = \begin{bmatrix} T_{CB} \\ \Delta T \end{bmatrix}^k. \quad (24.13)$$

The complementary basis is a set of static residuals calculated according to the type of enrichment.

For each component  $k$ , to enrich the basis by taking into account stochastic aspect, the residual vectors are static responses with correspondence to a set of residual forces  $[F_S]$  presenting the stochastic effects. These forces are generated depending on the stochastic zones of the mass and stiffness matrices [8]. The first complementary subbasis  $[\Delta T_S]^k$  is thereafter obtained and added to the standard Craig-Bampton one.

To take into account localized nonlinearity effects, another type of complementary subbasis  $[\Delta T_{NL}]^k$  has to be created [7] as a set of static responses corresponding to unit residual force vectors  $\{F_i\}^k$  with respect to each nonlinear degree of freedom (dof)  $i$  for each component  $k$ .

The CBT can also be enriched if the external loading effect is considered [6]. Thus, an additional subbasis  $[\Delta T_E]^k$  must be computed using a set of unit static loadings  $\{F_E\}^k$  imposed on internal excited substructure dofs.

Consequently, the final enriched basis has the following form

$$[T_{ECB}]^k = \begin{bmatrix} T_{CB} \\ \Delta T_S \\ \Delta T_{NL} \\ \Delta T_E \end{bmatrix}^k = \begin{bmatrix} I_{jj} & 0 & 0 & 0 \\ \psi_{ij} & \varphi_i & \Delta T_S & \Delta T_{NL} \\ & & \Delta T_S & \Delta T_{NL} \\ & & & \Delta T_E \end{bmatrix}^k \quad (24.14)$$

Note that a singular value decomposition (SVD) is needed to ensure linear independence of the vectors forming each complementary subbasis and also carried out on  $[T_{ECB}]^k$  to ensure the linear independence of the subbases and thus the well-conditioning of the ECBT. The synthesis of the complete structure requires finally the assembly of the different CBT matrices according to the hypothesis of continuity of displacements at junction dofs.

### 24.2.4 Robust Metamodel Combining CBCMS and gPCE

The CBCMS and the gPCE methods were previously independently presented. The main aim of this paper is to couple them in order to replace large size dynamical structures with considerably condensed and sufficiently accurate metamodel. Indeed, we propose to compute the succession of  $N$  deterministic responses of LHS simulations  $\{Y^{(n)} = y(\xi^{(n)}), n = 1, \dots, N\}$ ,

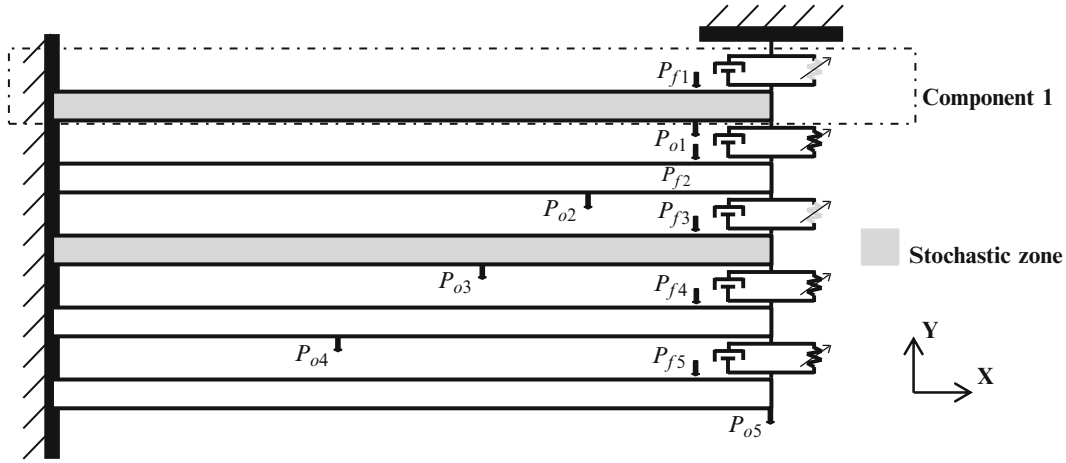


Fig. 24.1 Coupled beams structure

needed for the gPCE regression method implementation (Eq. 24.4), using the ECBT Eq. 24.14. The notion of robustness consists, in our study, on satisfying two different criterions; the accuracy of the responses and the gain in terms of computational time. To verify the first criterion, a set of temporal statistic moments  $\mathcal{M}_i$ , also called times indicators or energy criterions, has to be calculated in order to quantify the response accuracy in terms of amplitude and periodicity errors. These moments are expressed as [11]

$$\mathcal{M}_i = \int_{-\infty}^{+\infty} (t - t_s)^i y(t)^2 dt \quad (24.15)$$

where  $y(t)$  is the temporal response,  $i$  the order of the moment and  $t_s$  the temporal shift chosen in our case as  $t_s = 0$ .

The total energy of the response  $E = \mathcal{M}_0$  permits the verification of the accuracy in term of amplitude.  $\mathcal{M}_1/\mathcal{M}_0 = T$  and  $\mathcal{M}_2/\mathcal{M}_0 - (\mathcal{M}_1/\mathcal{M}_0)^2 = D^2$  are respectively the central time and the root mean square duration computed to verify the accuracy of the response in term of periodicity.

A numerical application is presented in Sect. 24.3 in order to illustrate the main features of the proposed robust metamodel designed to analyze the dynamic behavior in presence of uncertainties and localized nonlinearities.

## 24.3 Numerical Application

### 24.3.1 Proposed Structure and Validation Process

The proposed academic structure, Fig. (24.1), is composed of five identical beams loaded in pure flexion. The discretization of each beam into 20 elements (two dofs per node:  $v_y, \theta_z$ ) leads to a 200 dofs FE model. The beams are of rectangular section with  $b = 3 \times 10^{-2}m$  and  $h = 1 \times 10^{-2}m$ , length  $L_b = 5 \times 10^{-1}m$ , Young modulus  $E_0 = 2.1 \times 10^{11}Pa$ , density  $\rho_0 = 7800 kg.m^{-3}$  and Poisson's ratio  $\nu = 0.3$  and are submitted each one to a localized excitation force (N)  $P_f = 10 \times \cos(2\pi f_1 t)$ , where  $f_1 = 82.96 rad.s^{-1}$  is the first eigenfrequency, according to the  $v_y$  dof ( $Y$  direction). The five beams are coupled using five local dampers such as  $c = 10^2 N.s.m^{-1}$ , five linear springs  $k_0 = 10^6 N.m^{-1}$  and nonlinear ones  $k_{NL} = 10^{11} N.m^{-1}$ . Several observation points  $P_{oj}$  ( $j = 1, 2, \dots$ ) are considered to evaluate the efficiency of the proposed metamodel.

The stationary temporal response evaluation is done in the time interval  $[0-0.5 s]$ , divided into steps of  $10^{-4}s$ , in which the stationary regime is already attained.

To apply the CBCMS method, the complete structure is divided into substructures. In fact, being in the case of periodic structure, we propose to consider each set of coupling elements (localized damper, linear and nonlinear springs) and a beam as a substructure (Fig. 24.1). The first and the third components are considered as two stochastic zones in which the Young modulus of the beam and the linear coupling stiffness are supposed to be uncertain parameters such as

**Table 24.1** Model size and associated temporal moments

Methods		Model (dofs)	E		T		D <sup>2</sup>	
			E × 10 <sup>4</sup> (m <sup>2</sup> .s)	Error (%)	T × 10 <sup>2</sup> (s)	Error (%)	D <sup>2</sup> × 10 <sup>3</sup> (s)	Error (%)
LHS (A)	LHS-REF	200	15.93	0.00	49.93	0.00	82.03	0.00
	LHS-ECBT	24	15.78	0.94	49.92	0.02	82.01	0.02
REG (B)	REG-2-REF	200	15.75	1.13	49.84	0.18	82.26	0.28
	REG-4-REF	200	15.88	0.31	49.86	0.14	82.19	0.19
	REG-2-ECBT	24	15.45	3.01	49.82	0.22	82.31	0.34
	REG-4-ECBT	24	15.57	2.26	49.85	0.16	82.23	0.24

$$E = E_0 (1 + \sigma_E \xi_E) \quad \text{and} \quad k = k_0 (1 + \sigma_k \xi_k) \quad (24.16)$$

where  $\xi_E$  and  $\xi_k$  are two random variables of respectively uniform and lognormal probability distributions and  $\sigma_E = \sigma_k = 10\%$  are the considered dispersions. The effect of the stochastic aspect of the uncertain parameters is shown using the MAC (Modal Assurance Criterion) [6] matrix, which compares the normal modes of the deterministic model to the means of the modes of the stochastic model computed with correspondence to each random variable.

The proposed metamodel results are discussed with respect to the responses considered as reference, computed using LHS method using 1,000 samples of random variables. In fact, the process of evaluation of the metamodel efficiency is as follow

- (A) Implementing the 1,000 samples LHS method on: 1- the complete model (projection on complete eigenvectors basis) denoted LHS-REF, 2- the reduced model (projection on the ECBT matrix) denoted LHS-ECBT;
- (B) Implementing the regression gPCE: 1- on the complete model for two gPCE orders (2 and 4) denoted respectively REG-2-REF and REG-4-REF, 2- combined with the ECBT (proposed metamodel) also for two gPCE orders, denoted respectively REG-2-ECBT and REG-4-ECBT.

## 24.4 Results and Discussion

The ECBT matrix contains  $n_j = 8$  junctions dofs,  $n_i = 8$  retained normal modes and  $n_e = n_{eS} + n_{eNL} + n_{eE} = 2 + 5 + 1 = 8$  enriching static residual vectors, where  $n_{eS}$  corresponds to the stochastic enrichment,  $n_{eNL}$  to the nonlinear one and  $n_{eE}$  to the external force enrichment. Hence, the size of the ECBT transformation matrix is  $200 \times 24$ , which signify that the reduction ratio of the full problem is of 88 % (200 dofs).

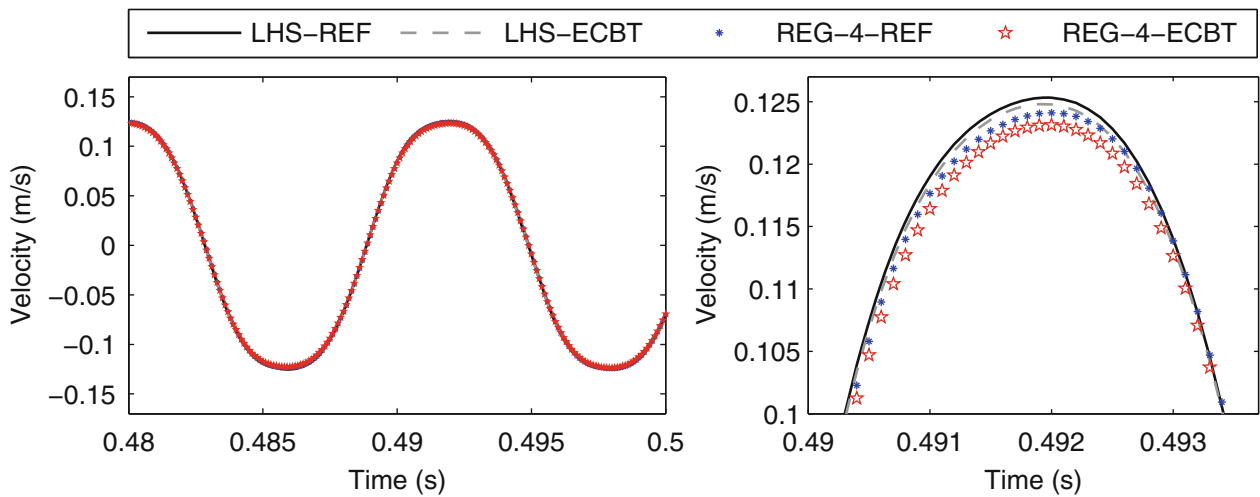
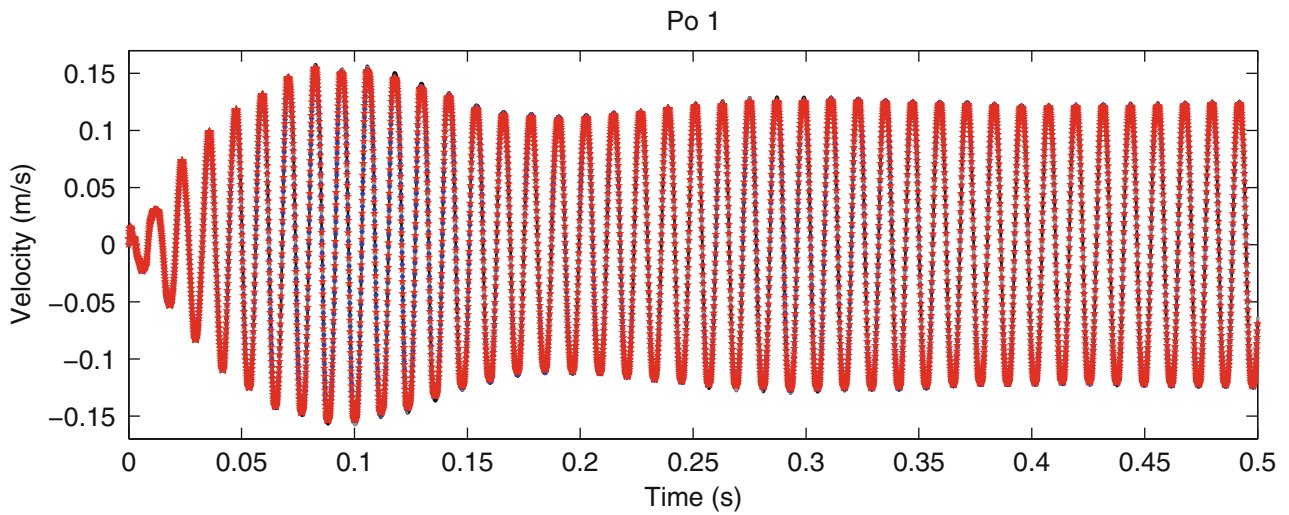
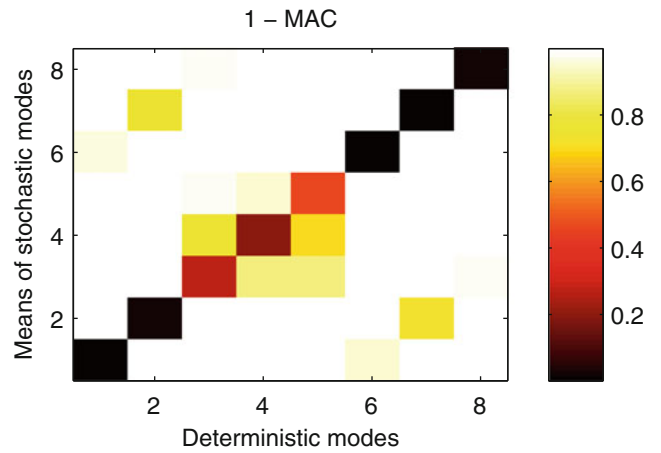
For a second order gPCE, the ED is of size 31 random variables combinations chosen with correspondence to the conditions defined in Eqs. 24.5 and 24.6 among 81 Hermite polynomial roots combinations ( $(p+1)^d = 3^4 = 81$ ) and then transformed with respect to the probability distributions (Table 24.1). For the fourth order, 84 random variables are needed among 625 possible combinations.

Figure 24.2 shows the stochastic effect on the model normal modes through the MAC matrix. Figures 24.3 and 24.4 illustrates the comparison between the means of stochastic velocities obtained by implementing the different methods with correspondence to the above proposed process (A and B) at two chosen observation points  $P_{o1}$  and  $P_{o4}$ .

The MAC matrix, presented in Fig. 24.2, illustrates the stochastic effect on the eight first modes retained for ECBT. Indeed, the level of uncertainty is not high but sufficient to show the interest of the stochastic enrichment. Consequently, the level of nonlinearities is chosen to be low in order to ensure the contribution of each type of enrichment in the ECBT. In fact, high level of nonlinearities leads to a negligible stochastic enrichment contribution in the ECBT and thus enriching using only nonlinear effect is sufficient.

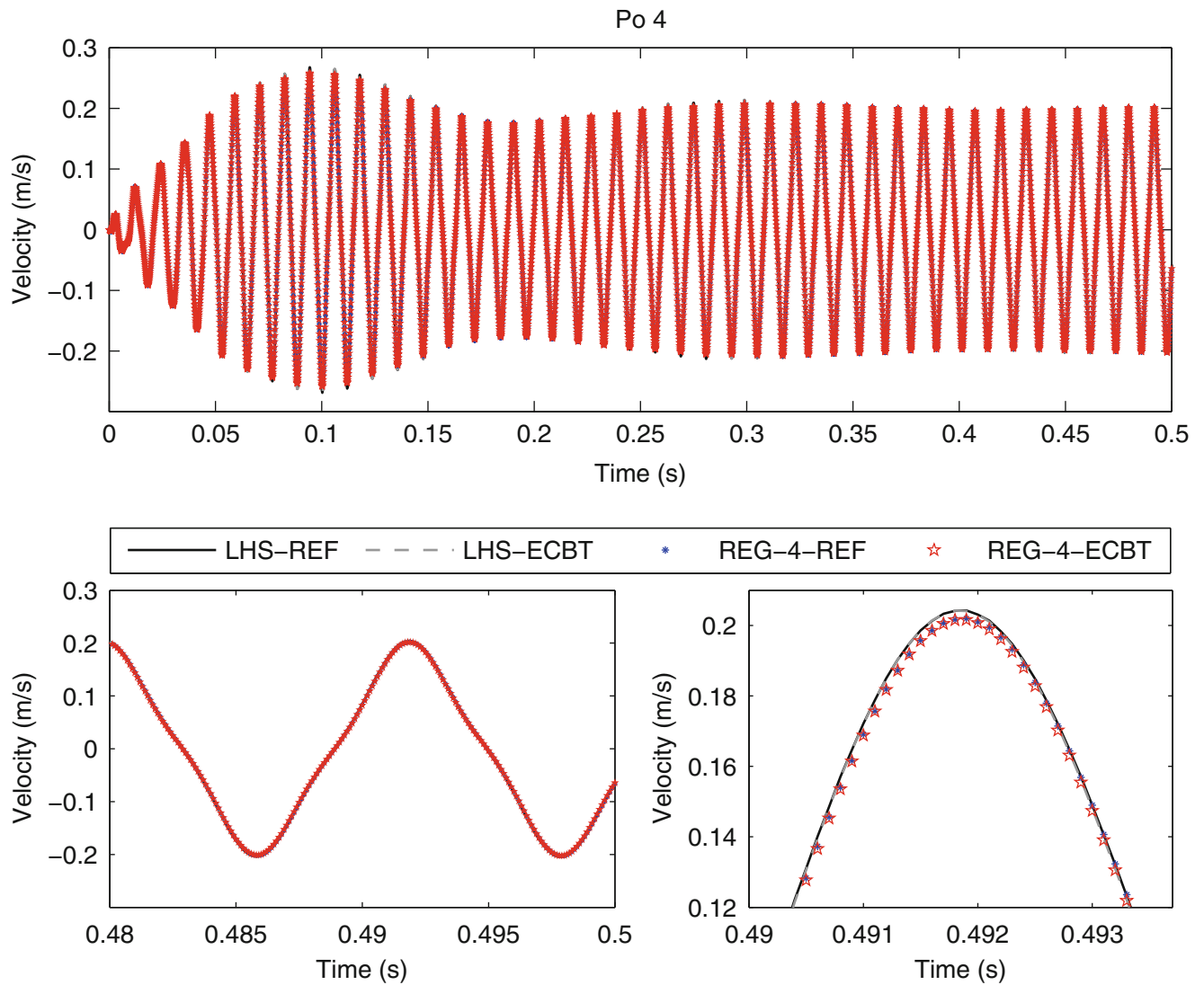
The obtained results of different implemented models are compared in terms of accuracy and time consuming by means of the CPU computation time and the temporal moments  $E$ ,  $T$  and  $D^2$  (Tables 24.1 and 24.2). In fact, Table 24.1 recalls the size of the problems to be solved and gives the values of the associated temporal moments and Table 24.2 contains different computational time values.

**Fig. 24.2** MAC matrix comparing the deterministic normal modes and the means of the stochastic ones



**Fig. 24.3** Mean of the stochastic velocity at the observation point  $P_{o1}$  computed on the reference (complete) model (REF) and the condensed one (ECBT) using LHS and fourth order gPCE methods

The results displayed in Figs. 24.3 and 24.4 show that the proposed metamodel can replace the original one without a significant loss of accuracy with respect to the reference results computed by LHS method on the full structure. Note that the higher the order of the gPCE is, the more accurate the results are, the longer the required computational time is, as shown in



**Fig. 24.4** Mean of the stochastic velocity at the observation point  $P_{o4}$  computed on the reference (complete) model (REF) and the condensed one (ECBT) using LHS and fourth order gPCE methods

**Table 24.2** Computational CPU time

Methods		CPU (min)	CPU (%)
LHS (A)	LHS-REF	6049.10	100
	LHS-ECBT	4405.13	72.82
REG (B)	REG-2-REF	201.19	3.33
	REG-4-REF	463.99	7.67
	REG-2-ECBT	155.40	2.57
	REG-4-ECBT	399.61	6.61

Table 24.2. Only the fourth order gPCE approximations are presented, the second order gPCE results are discussed through their temporal moments presented in Table 24.1. The ECBT efficiency can be at first evaluated comparing the two first curves (Figs. 24.3 and 24.4) and the two first lines of Table 24.1, which show that the amplitude and periodicity errors between the results of the LHS method on full and condensed model are very small.

Table 24.2 shows that the computation time can be reduced by 93.4 % when implementing the proposed metamodel, and it increases when the gPCE order is higher. Note that despite the fact that the example is not sufficiently representative in size and uncertain parameter number to show the efficiency of the CBCMS, the gain of nearly 30 % attained when implementing

ECBT with LHS or gPCE reflects more than 30 h of time reduction (1 % of gain is 61 min). For larger size examples, and also when using properly optimized algorithms, the robust CBCMS contribution should be more illustrated.

## 24.5 Concluding Remarks

In this paper, a robust metamodel is proposed in order to approximate structure behaviors in presence of uncertainties and localized nonlinearities. This metamodel is obtained by the combination between the parametric uncertainty propagation method and a robust CMS approach. The efficiency of the metamodel was successfully evaluated on the temporal response approximations of the coupled beams structure with respect to the reference LHS method results, thanks to different verified robustness criterions. The reduction in terms of time consuming and model size using the comparison of the computation times and temporal moments prove the efficiency and the usefulness of the proposed metamodel for the robustness analysis of large size nonlinear stochastic model.

## References

1. Helton JC, Davis FJ (2003) Latin hypercube sampling and the propagation of uncertainty in analyses of complex systems. *Reliab Eng Syst Saf* 81:23–69
2. Xiu D, Karniadakis GE (2002) The Wiener-Askey polynomial chaos for stochastic differential equations. *SIAM J Sci Comput* 24(2):619–644
3. Berveiller M (2005) *Eléments finis stochastiques : Approches intrusive et non intrusive pour des analyses de fiabilité*, Ph.D. thesis. Université BLAISE PASCAL - Clermont II, Aubière
4. Blatman G, Sudret B (2010) An adaptive algorithm to build up sparse polynomial chaos expansions for stochastic finite element analysis. *Probab Eng Mech* 25:183–197
5. Craig RR Jr, Bampton MCC (1968) Coupling of substructures for dynamic analyses. *AIAA J* 6(7):1303–1319
6. Lombard JP (1999) *Contribution à la réduction des modèles éléments finis par synthèse modale*, Ph.D. thesis. Université de Franche-Comté, France
7. Bouazizi ML, Guedri M, Bouhaddi N (2006) Robust component modal synthesis method adapted to the survey of the dynamic behavior of structures with localized nonlinearities. *Mech Syst Signal Process* 20:131–157
8. Guedri M, Bouhaddi N, Majed R (2006) Reduction of the stochastic finite element models using a robust dynamic condensation method. *J Sound Vib* 297:123–45
9. Maute K, Weickum G, Eldred M (2009) A reduced-order stochastic finite element approach for design optimization under uncertainty. *Struct Saf* 31:450–459
10. Afonso SMB, Motta RS (2013) Structural optimization under uncertainties considering reduced-order modeling, 10th world congress on structural and multidisciplinary optimization, Orlando, 19–24 May 2013
11. Hemez FM, Doebling SW (2003) From shock response spectrum to temporal moments and vice-versa, international modal analysis conference (IMAC-XXI), Kissimmee, 3–6 Feb 2003



# Chapter 25

## Robust Updating of Operational Boundary Conditions for a Grinding Machine

Elvio Bonisoli and Marco Brino

**Abstract** Operational boundary conditions of actual structures are often a crucial and difficult aspect in model updating of CAD/CAE models based on dynamic tests and experimental modal identification.

In this work two grinding machines are experimentally tested through roving hammer impact tests. Due to the importance of comparing two different solutions of grinding structures involving traditional cast-iron or a new polymeric concrete, actual operational boundary conditions, consisting in industrial supports acting on a not-well-known pavement, are taken into account.

Their effects affect the dynamic behaviour, in particular at low frequencies and they are the main updating parameters of the CAD/CAE models.

Gradient-based optimization and genetic algorithms are implemented to reduce modal parameters errors in the identification and updating phase of parametric models to demonstrate feasibility and improvements of robust numerical models, in order to evaluate effective improvements of the material choice for the grinding machine.

**Keywords** Updating • Optimization • Elastic supports • Experimental modal analysis • Finite element model

### 25.1 Introduction

In this paper the study of the effect of the operational boundary conditions, compared with the result of an experimental campaign, is presented, performing EMA (Experimental Modal Analysis) [1].

Even though in real world no kind of constraint (such as clamp, or simple support in particular) is *ideal* (which means that the displacement in correspondence of the constraint is identically zero), in most cases the choice of considering this ideal condition does not imply a significant error in the results.

But if this case does not apply, the error might be large and the results need to be carefully processed and criticised.

Model Updating techniques [2] might help in case of discrepancies between numerical and experimental data are due to uncertainties that comes from the material properties.

To allow the boundary conditions to model non-ideal behaviour, springs connecting the structure to the pavement may be used, but it is not trivial the choice of the values of the stiffness in the relative directions.

Here a step-by-step optimisation strategy is proposed to find reliable and stable parameters (the stiffness values) and then to obtain a good correlation between experimental and numeric.

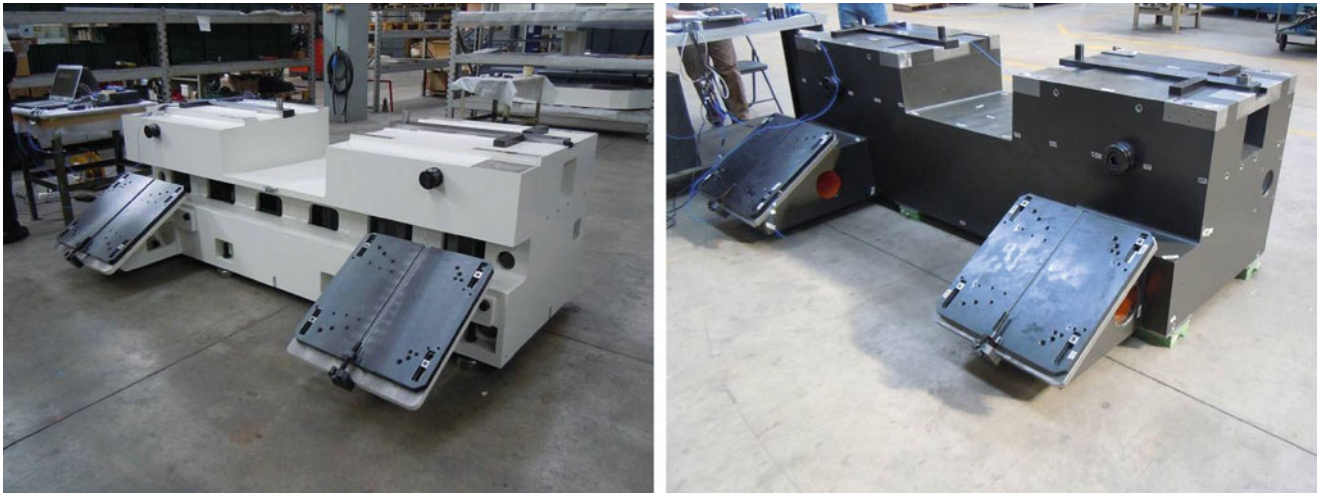
### 25.2 Test Structures and Experimental Modal Analysis

The structures, subject of the experimental campaign, are two bases for grinding machines. These structures differ one another on the material they are made of: one is made of cast-iron, historically used since the conception of the bases, while the other is made of stone-cast, recently adopted because of its lower cost and the simpler manufacturing process.

Figure 25.1 shows the two test structures.

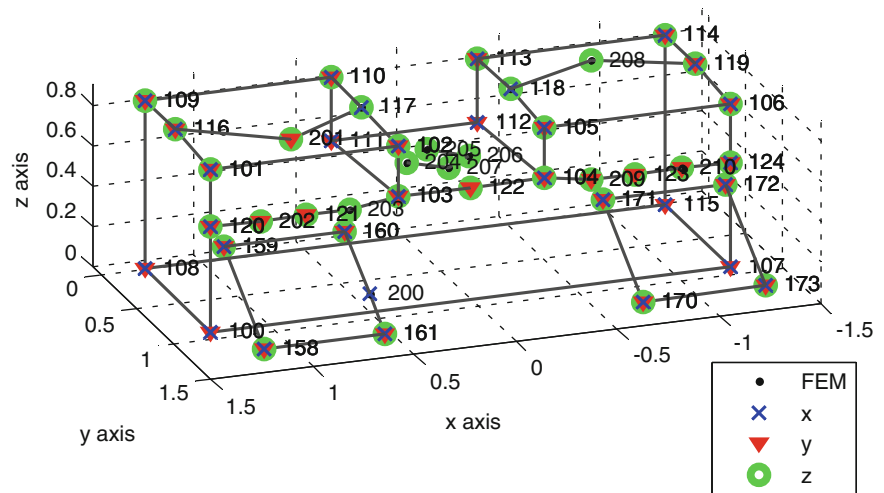
---

E. Bonisoli (✉) • M. Brino  
Department of Management and Production Engineering, Politecnico di Torino, Corso Duca degli Abruzzi 24,  
Torino 10129, Italy  
e-mail: [elvio.bonisoli@polito.it](mailto:elvio.bonisoli@polito.it)



**Fig. 25.1** Cast-iron (*left*) and stone-cast (*right*) structures pictures

**Fig. 25.2** Accelerometers locations



The total masses of the two structures are basically the same, but while the metallic one has cavities inside in order to lower the mass involved without affecting the structural characteristics, the polymeric concrete, due to its lower density and mechanical properties, needs more material to fit the structural requirements and then no cavities are necessary.

The experimental modal analysis was performed using *roving hammer* technique with accelerometer acquisitions to identify possible natural frequencies that might be excited during the regular operation of the grinding process. Another parameter that is important to compare the structures is the modal damping.

In a roving hammer acquisition the choice of the location of the accelerometers used as reference is crucial and may affect a lot the quality and reliability of the consequent results. So, the sensor placement positions were chosen running the MoGeSeC algorithm [3, 4], which basically evaluates, through all the translational degrees of freedom of the nodes in the Finite Element Model and the related eigenvectors of the selected modes, the progressive optimal selection of experimental areas where is maximal the larger modal displacements and the independency of the modal description. Thus, a related property is that all the entire geometry is involved and, in particular, suitable candidates are zones on external surfaces, available for EMA.

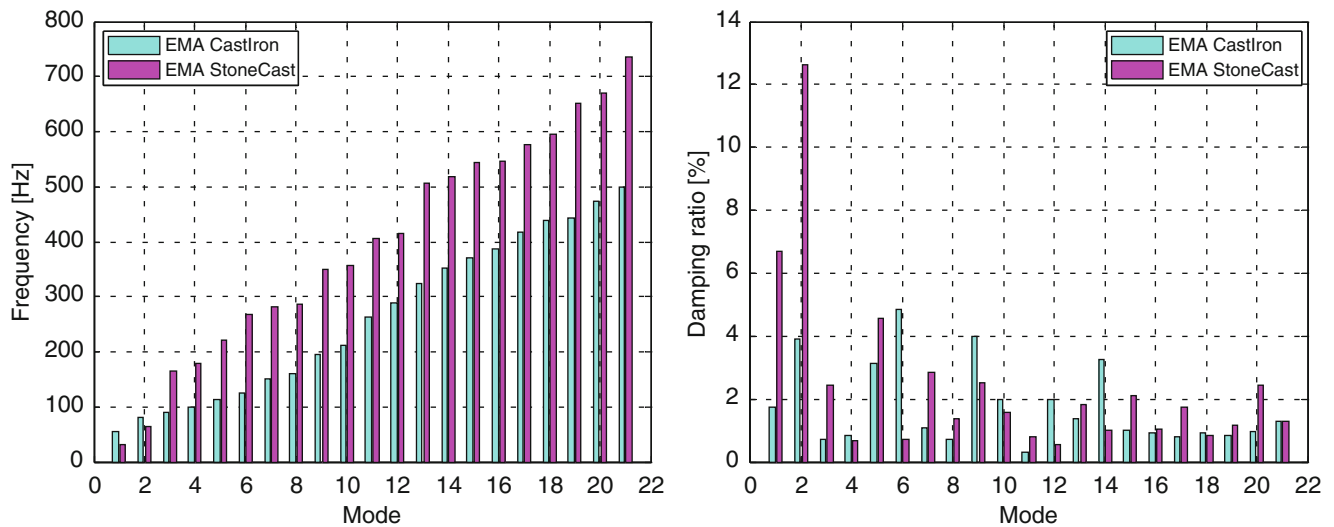
After this suggested pattern as locations for accelerometers, geometrically interesting regions are analysed and chosen to set the final choice of locations. The locations suggested are shown in Fig. 25.2.

For both test cases natural frequencies, modal damping ratios and mode-shapes were identified, and their values are summarised in Table 25.1 and graphically compared one another in Fig. 25.3.

Even though there is not a one-to-one relationship between the modes of the two structures, the charts in Fig. 25.3 show that in general the cast-iron structure has lower frequencies with respect to the stone-cast one, and lower damping ratios.

**Table 25.1** Comparison of identified EMA parameters between cast-iron and stone-cast structures

Cast-iron structure				Stone-cast structure			
Mode	Freq. [Hz]	Damp [%]	Mode-shape description	Mode	Freq. [Hz]	Damp [%]	Mode-shape description
1st	54,1	1,74	Rigid-body rotational z (global)	1st	32,4	6,69	Rigid-body rotational z (global)
2nd	80,1	3,91	1st bending yz of motors m.(global)	2nd	64,4	12,6	Rigid-body rotational x (global)
3rd	89,7	0,71	Symmetric bending xy of motor m	–			
4th	98,8	0,83	Bending xy of motor mounting $x < 0$	–			
5th	113	3,12	Opposite bending yz of motor ms	3rd	165	2,43	Opposite bending yz of motor ms
6th	126,3	4,85	Bending yz of motor mounting $x < 0$	4th	180	0,69	Symmetric bending xy of motor ms
7th	150	1,1	Symmetric torsional y of motor ms	–			
8th	161	0,7	Parallel torsional y of motor mount	–			
9th	194	4,01	1st bending xz (global)	5th	221	4,55	1st bending xz (global)
–				6th	268	0,72	Symmetric bending xy of motor m
–				7th	283	2,83	1st bending yz (global)
–				8th	286	1,38	Symmetric bending yz of motor ms
10th	212	1,99	1st torsional x (global)	9th	349	2,53	1st torsional x (global)
–				10th	357	1,57	Opposite bending yz of motor ms
11th	263	0,32	1st bending xy (global)	11th	407	0,80	1st bending xy (global)
12th	289	1,97	torsional x of motor mount $x > 0$	12th	415	0,54	Symmetric torsional x of motor ms
13th	324	1,36	Torsional x of motor mount $x < 0$	13th	507	1,82	
14th	353	3,26		14th	518	1,02	
15th	370	1,01		15th	543	2,09	
–				16th	546	1,05	
16th	387	0,91	2nd bending xz (global)	17th	576	1,74	2nd bending xz (global)
17th	417	0,79	not well identified (global)	18th	595	0,84	



**Fig. 25.3** Comparison of natural frequencies and damping ratios of Cast-iron EMA vs. Stone-cast EMA

In the cast-iron structure the two plates are clamped to the main body using two beams each, arranged in “I” position, which are then the most compliant element of the structure: the lower frequencies then involve these components while the *global* mode-shapes occur at higher values. In the stone-cast structure, instead, the plates are fixed on supports that are a single part with the main body, the *global* modes occur already at lower frequencies.

### 25.3 Finite Element Models

In an era where every designed structure is validated using virtual prototypes, the presence of experimental data raises the need to use them as reference to a finite element model. The numerical simulations were performed using the geometry supplied from the CAD models of the two structures, and using tetrahedral elements to mesh the relative bodies. A general idea on the density of nodes is shown in Fig. 25.4, considering that the aim of the simulation were to compute about the first 20/25 modes, thus a coarse mesh is enough to reach a reasonably accuracy of the results for lower modes.

Both structures, which are certainly heavy (about 4 tons of weight) are lean on the floor with 8 tuneable mountings. The tuning possibility allows the height of the mounting to be adapted in order of distributing the weight with uniform load among them.

Three different boundary constraint types were chosen to model the connection with the floor (Fig. 25.5):

- all 8 mountings fixed (clamped) – Study 1;
- 2 mountings fixed, 6 mounting simply supported (sliders) – Study 2;
- all 8 mountings simply supported – Study 3.

For Study 3 the trivial consideration is that the first three modes will be the rigid body motions allowed by the simply supported condition of the sliders, while for Study 1 is reasonable the doubt that even though the structures are very heavy, a fixed condition is too stiff, also considering that the tuning of the mountings is not perfect and some of them are less loaded and then more subject of sliding.

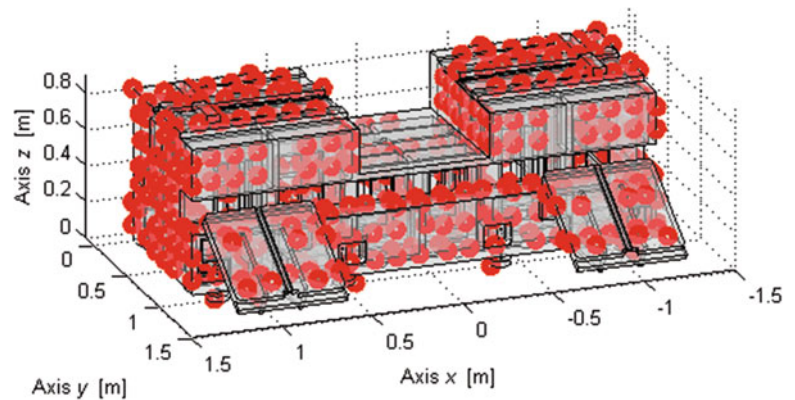


Fig. 25.4 CAD-CAE simplified model

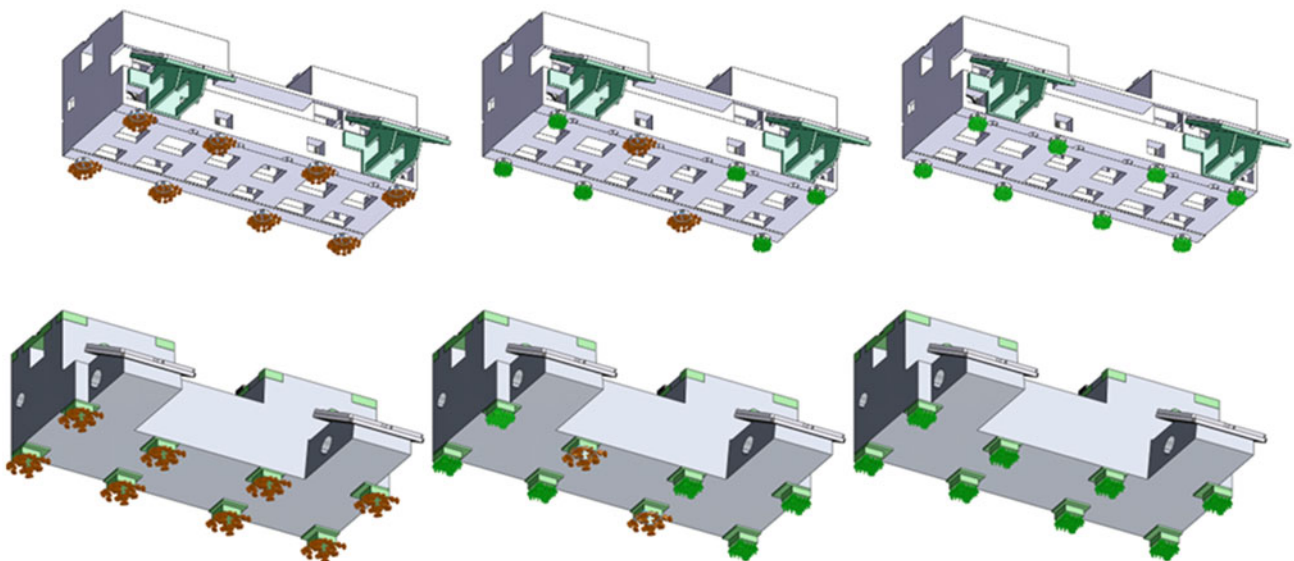
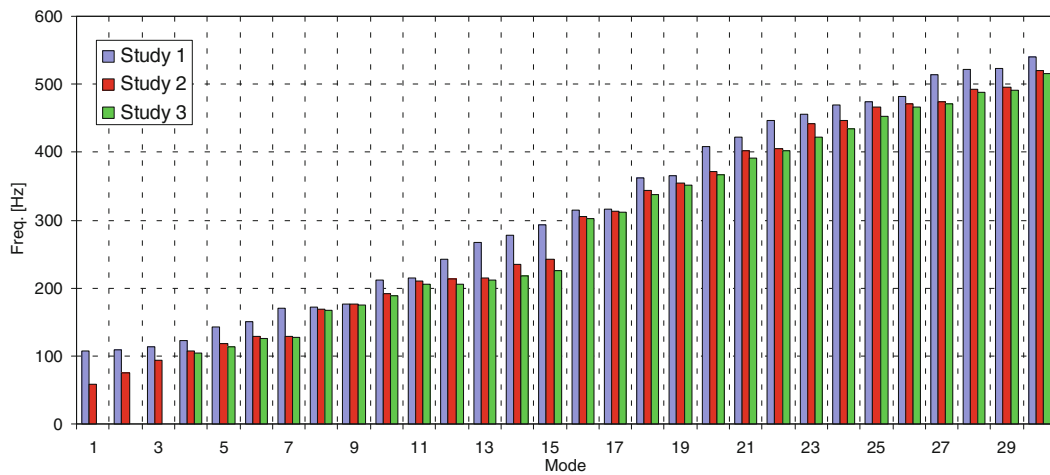
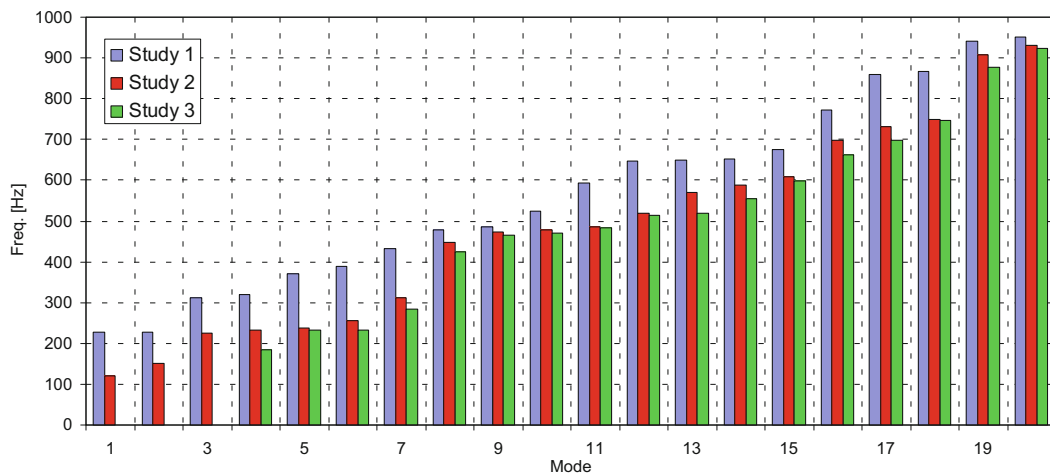


Fig. 25.5 Boundary conditions for mountings for cast-iron (*upper*) and stone-cast cases: Study 1 (*left*), Study 2 (*middle*) and Study 3 (*right*)



**Fig. 25.6** Comparison of the natural frequency of the three FEA studies for cast-iron model



**Fig. 25.7** Comparison of the natural frequencies of the three FEA studies for stone-cast model

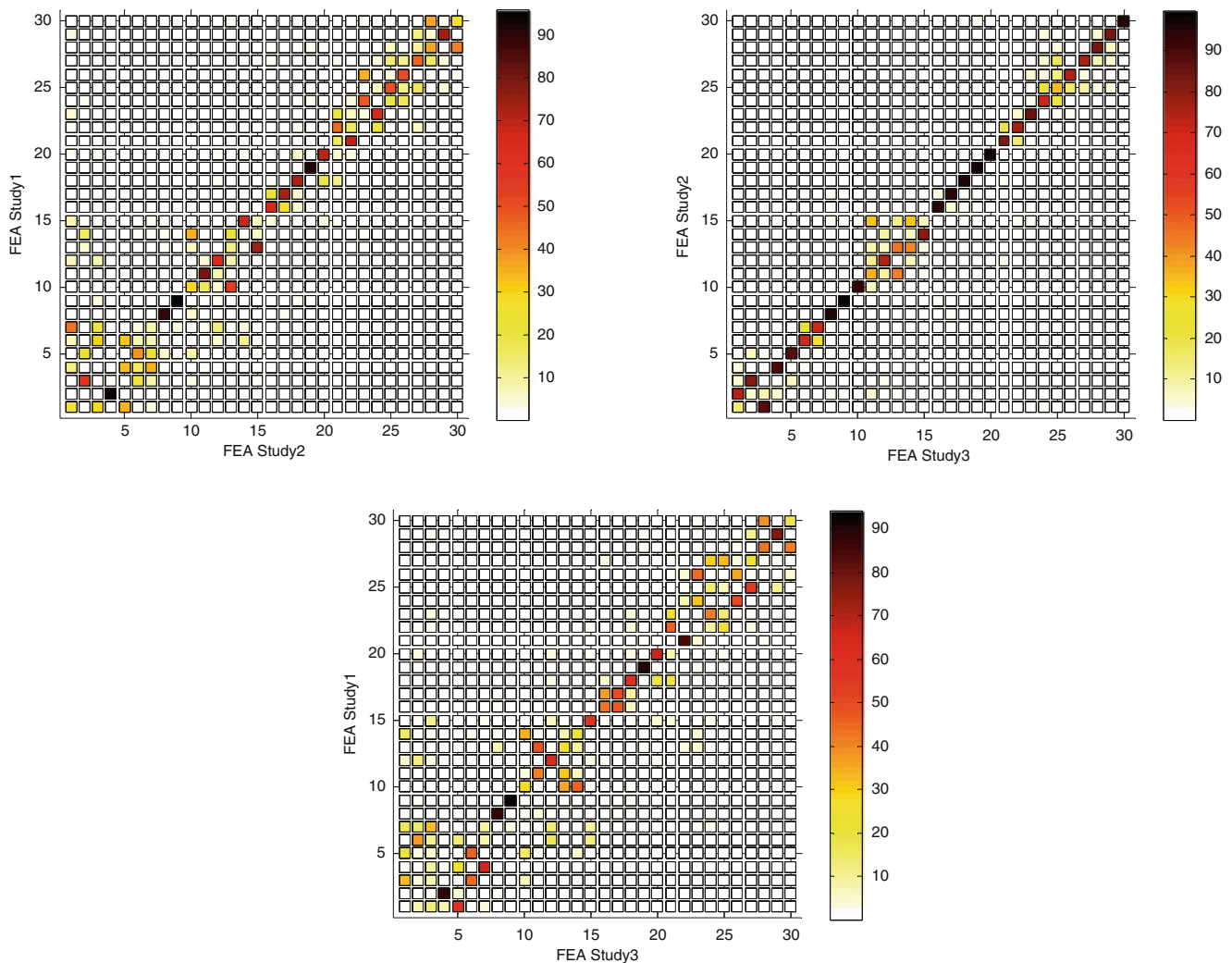
Study 2 seems to be a good compromise between the two extreme cases but anyway the choice of which of the mountings is to be fixed is not straightforward.

Figures 25.6 and 25.7 confirm these hypotheses showing, in particular, that the frequencies of Study 1 are larger, the frequencies of Study 3 are lower and, then, the frequencies of Study 2 are in between.

A comparison among the mode-shapes can be performed using the MAC index [5], introduced in Eq. 25.1, to evaluate the relationship that each mode has with respect to the modes of the other two studies, with different boundary conditions. These plots are shown in Figs. 25.8 and 25.9, and the most interesting is the comparison between Study 2 and Study 3, where there are switches among the rigid body motions and all the other modes are fairly correspondent, for the structure in cast-iron, while for the second structure this consideration is not of the same strength even though is the best among the three combinations.

## 25.4 Elastic Supports and Optimization Process

A first consideration on the correlation between the experimentally identified parameters and the correspondent values obtained from the relative numerical simulation shows that none of the studies actually fits. Even Study 2 is quite far from the expectations.



**Fig. 25.8** MAC comparison of the mode-shapes of the three FEA studies for cast-iron model

The resulting consideration is then that the grounding supports are compliant and must be considered as elastic supports, with two parameters each: one is the normal stiffness and the other is the transversal stiffness (in-plane).

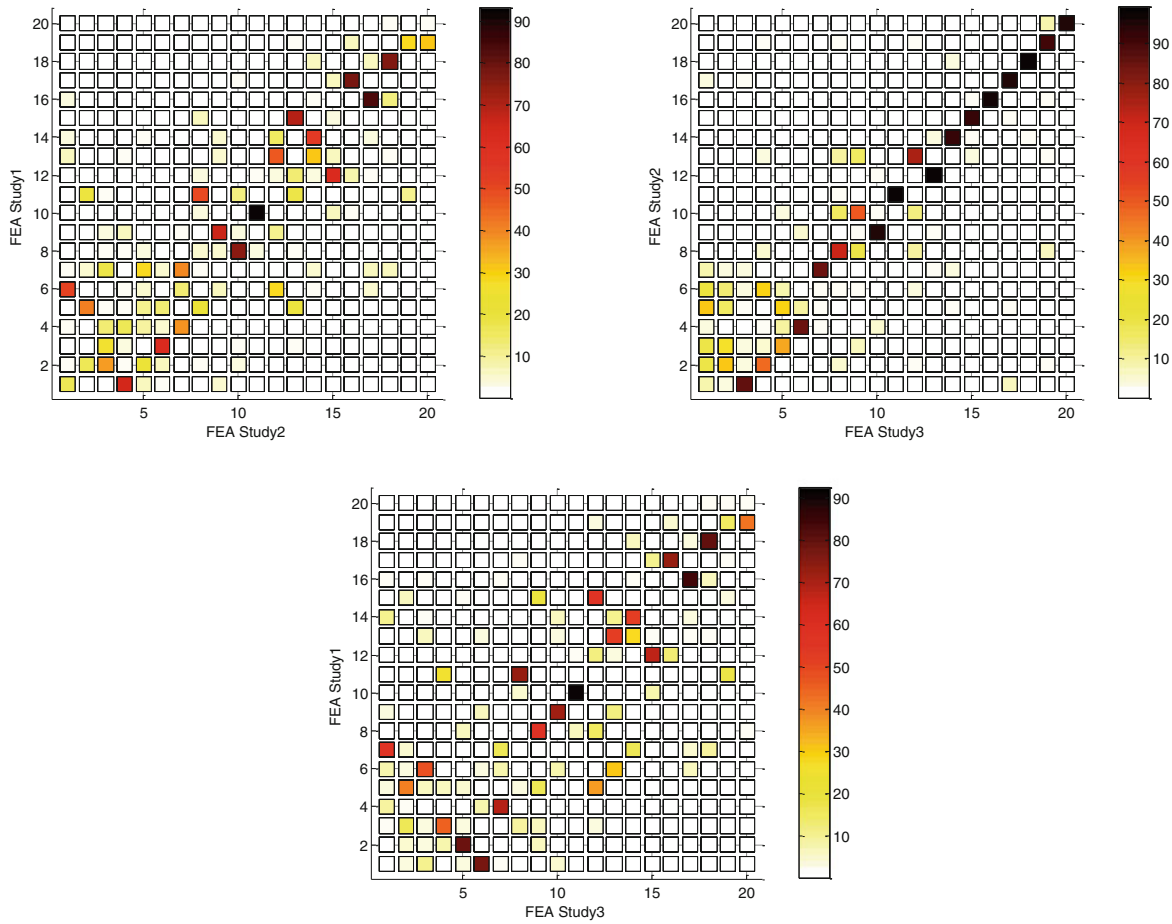
The values of these stiffness are not known a priori, and this implies the use of an optimisation strategy to find the values that best fit the experiments.

To perform a reliable and effective optimisation, the following strategy is described in steps:

- analysis of the model with reasonable values of stiffness (same values of each of the 8 supports) that are chosen as a starting point (picture or frame of the system);
- first optimisation run (same values for each support) using the values of the previous step as first guess, and then comparing the results of the optimal values with two different algorithms;
- second optimisation run with different values for first guess;
- third optimisation with increase of the number of design parameters; now each support has its own values of normal stiffness and transversal stiffness.

For each of these steps the reliability and stability of the solution found is checked running a second attempt using the optimal values of the previous run as first guess.

The two algorithm used in the optimisation are gradient-based and MATLAB tools *fmincon* [6, 7] and *Pattern Search* [8]. An alternative approach used by authors for small FE model is the *Genetic Algorithm* technique. In these cases it is not considered because it would not be effective with long and slow computation of the single analysis, and the total computational cost spent only for getting the first iteration would be too large.



**Fig. 25.9** MAC comparison of the mode-shapes of the three FEA studies for stone-cast model

Fmincon compares the gradients for each direction of the objective function is evaluated and the maximum slope is considered to compute the next iteration. This technique has the drawback of computing the partial derivatives for each iteration, but the advantage of following the quickest path.

Pattern Search, instead, computes the partial derivatives on the first iteration only, and then that direction is followed for all the subsequent iterations, unless the slope sign is changed: only in this case the partial derivatives are evaluated again. The advantage is that the time between two iterations is drastically reduced, but the path followed to reach the optimum might be longer, because it is not guaranteed to be the quickest.

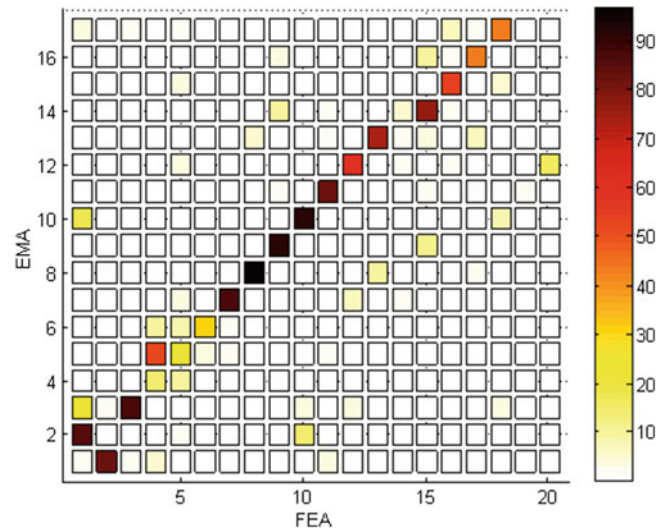
The objective function chosen is a composition of the error in term of frequencies and the discrepancy in term of mode-shapes, evaluated using MAC index, and is shown in Eq. 25.1:

$$\begin{aligned}
 ObjFnc &= (1 - Err) \cdot MAC \\
 Err &= \frac{1}{n} \sum_{r=1}^n \left[ \min_{j,k} \left| \frac{f_{j,EMA} - f_{k,FEA}}{f_{j,EMA}} \right| \right] \\
 MAC &= \frac{1}{n} \sum_{r=1}^n \left[ \max_{j,k} \frac{(\Phi_{j,EMA}^T \Phi_{k,FEA})^2}{(\Phi_{j,EMA}^T \Phi_{j,EMA}) (\Phi_{k,FEA}^T \Phi_{k,FEA})} \right]
 \end{aligned} \tag{25.1}$$

The function is to be *maximised* and weighted in the same way between eigenvalues and eigenvector errors, in order to reach the optimal values.

Details and results are now shown for all the steps.

**Fig. 25.10** MAC comparison of the mode-shapes between the three FEA studies for the first manual choice of stiffness



**Table 25.2** Design parameters for the optimisation with bounds, first guess and optimal values

Symbol	Lower bound [N/m]	First guess [N/m]	Upper bound [N/m]
$k_z$	1	$10^9$	$10^{12}$
$k_{xy}$	1	$10^3$	$10^{10}$

### 25.4.1 Starting Point

From a qualitative comparison of the three cases of operative boundary conditions, in particular regarding the similarities with the rigid body motions and the experimental mode-shapes of the very first modes, it is chosen to set a normal stiffness much larger than the transversal one. This would also fit the role of a simple support with transversal displacement reduced by friction effects. The normal stiffness is set with a value comparable with the stiffness of steel material.

As first approximations, all the supports are considered to be equal to each other, and then a single value of normal stiffness and a single value of transversal stiffness is applied, and the values are:

- Normal stiffness  $k_z = 10^9$  N/m;
- Transversal stiffness  $k_{xy} = 10^3$  N/m;

In Fig. 25.10 the MAC index of this starting point between EMA and FEA is proposed.

### 25.4.2 First Optimisation

The values set in the previous paragraph is chosen as first guess for the optimization and summarized in Table 25.2, with their relative bounds.

In the following figures (Figs. 25.11 and 25.12) the results of the optimisation processes for both the algorithms are shown.

### 25.4.3 Optimisation with Different Starting Point

The reliability of the values obtained with the previous optimisation are checked running a second process with different values of first guess, taking into account the order of magnitude of the values obtained before. The aim is to verify that the maximisation of the objective function reached a *global* instead of a *local* point.

For this attempt, the first guess values are summarised in Table 25.3.

In the following figures (Figs. 25.13 and 25.14) the results of the optimisation processes for both the algorithms are shown.



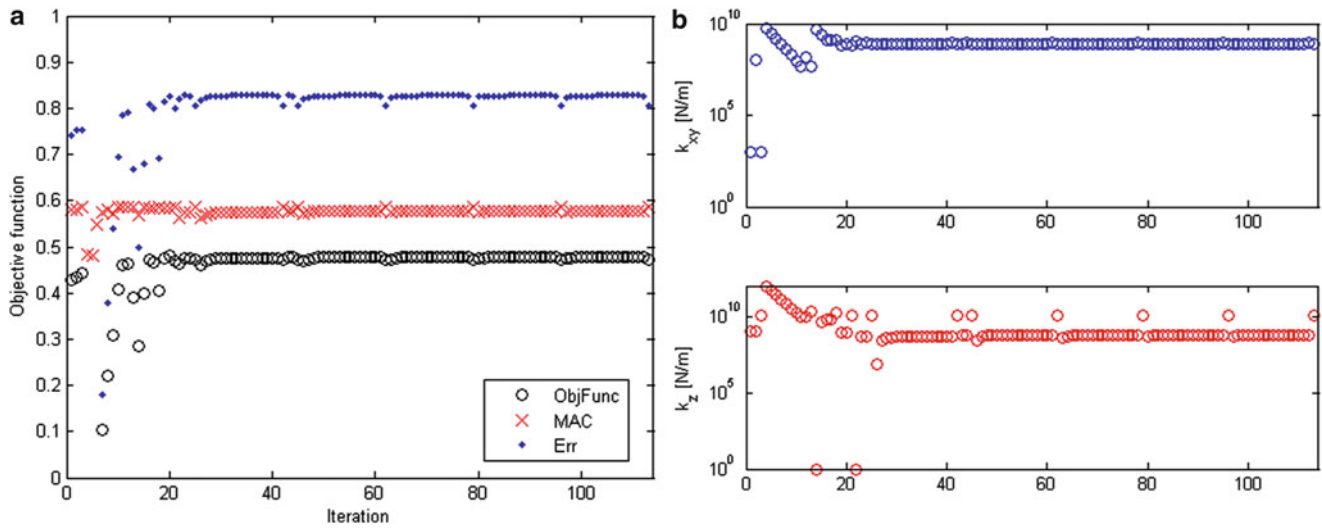


Fig. 25.11 Objective function (left) and parameters (right) trends with respect to the iterations for *fmincon* algorithm

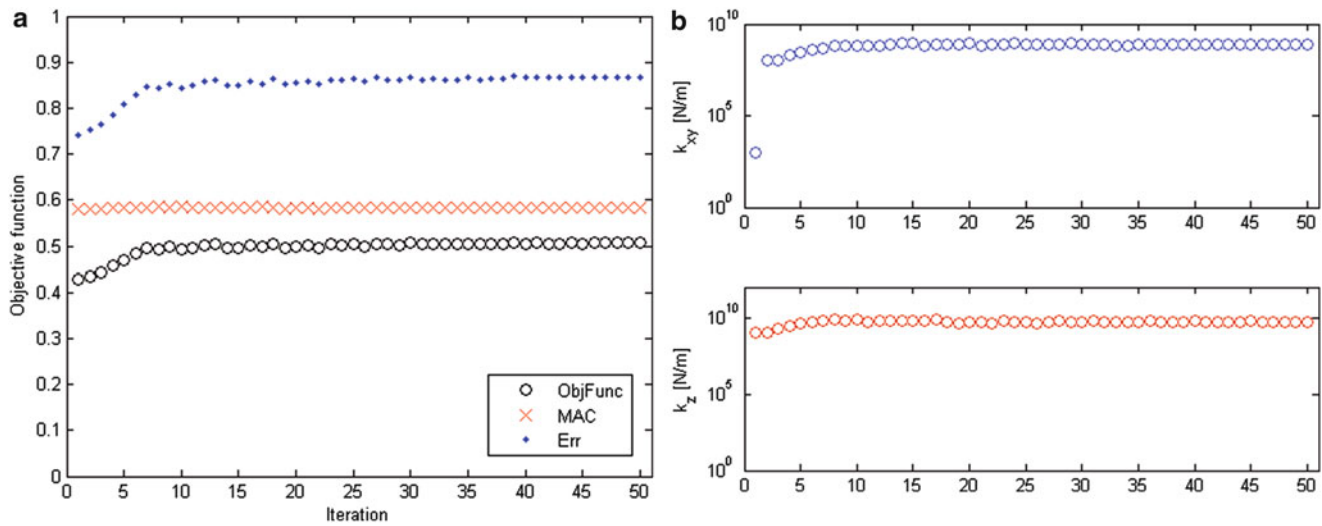


Fig. 25.12 Objective function (left) and parameters (right) trends with respect to the iterations for *patternsearch* algorithm

Table 25.3 Design parameters for the optimisation with bounds, first guess and optimal values

Symbol	Lower bound [N/m]	First guess [N/m]	Upper bound [N/m]
$k_z$	1	$4 \cdot 10^9$	$10^{12}$
$k_{xy}$	1	$8 \cdot 10^8$	$10^{10}$

### 25.4.4 Full Optimisation with Separate Values for Supports

The last step, after the reliability of the model is proved, the optimization is extended allowing the supports to be independent and then assigning different values for the normal stiffness and different values for transversal stiffness.

The relative 16 design parameters with lower bounds, upper bounds, first guess and optimal values are summarised in Table 25.4.

Then, in Figs. 25.15 and 25.16 the trends of objective function and parameters choice are shown

Then the final resulting MAC with the optimum values is shown in Fig. 25.17.

After the results of the optimal values, a visual comparison and a MAC plot of the mode-shapes between EMA and FEA eigenvectors. In Figs. 25.18 and 25.19 the qualitative comparison of the 3D views of the deformed configuration of some representative global modes are shown.

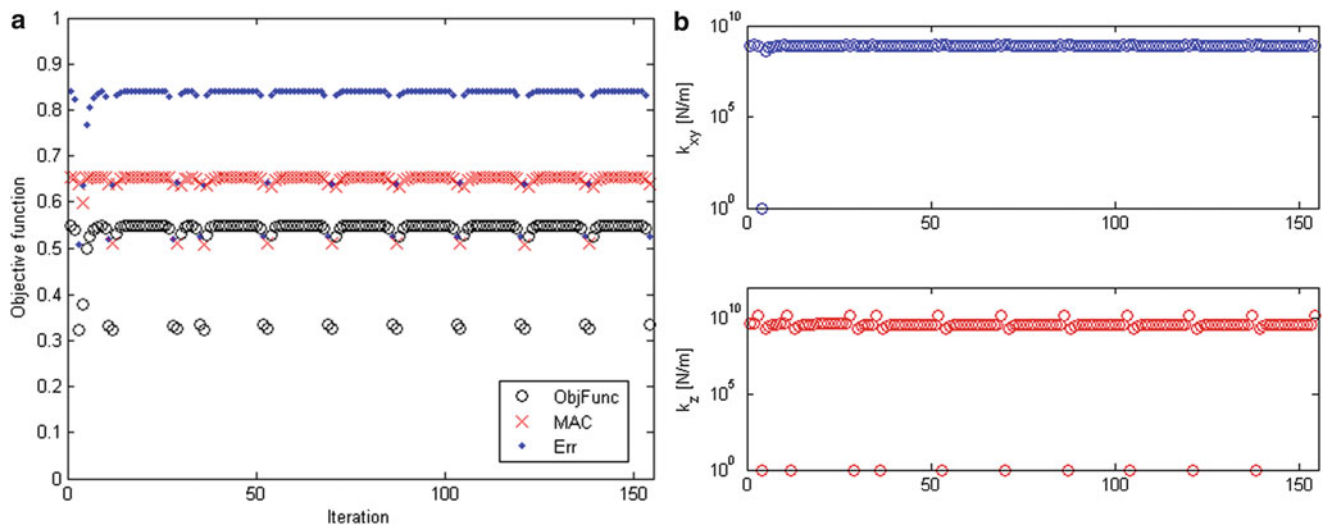


Fig. 25.13 Objective function (left) and parameters (right) trends with respect to the iterations for *fmincon* algorithm

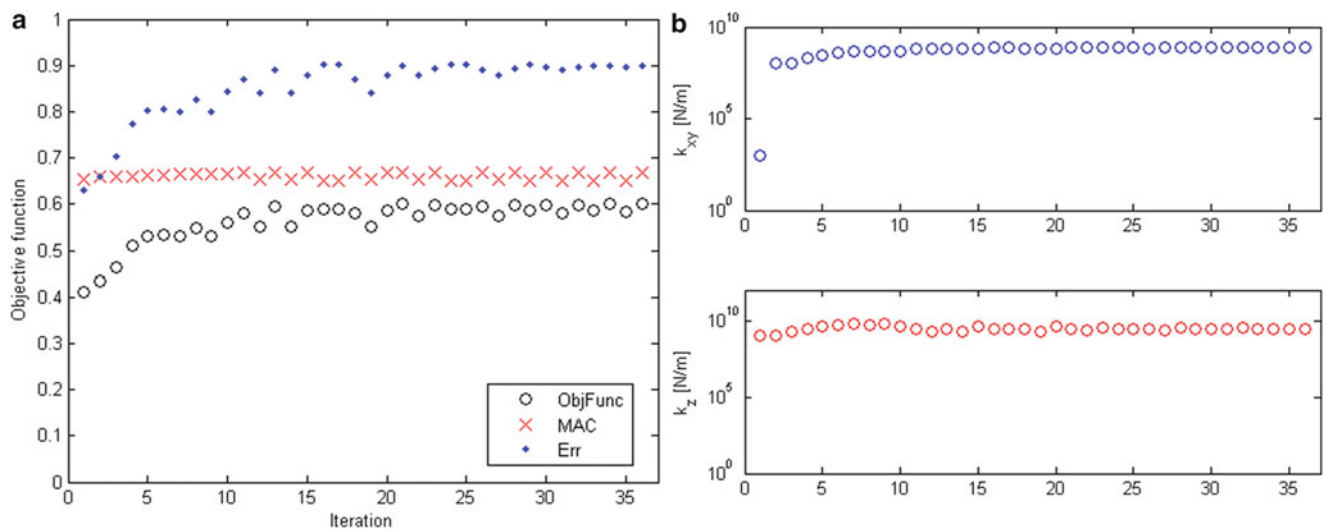


Fig. 25.14 Objective function (left) and parameters (right) trends with respect to the iterations for *patternsearch* algorithm

Table 25.4 Design parameters for the optimisation with bounds, first guess and optimal values

Support ID	Symbol	Lower bound [N/m]	First guess [N/m]	Upper bound [N/m]
1	$k_{1,z}$	1	$4 \cdot 10^9$	$10^{12}$
2	$k_{1,xy}$	1	$8 \cdot 10^8$	$10^{10}$
	$k_{2,z}$	1	$4 \cdot 10^9$	$10^{12}$
3	$k_{2,xy}$	1	$8 \cdot 10^8$	$10^{10}$
	$k_{3,z}$	1	$4 \cdot 10^9$	$10^{12}$
4	$k_{3,xy}$	1	$8 \cdot 10^8$	$10^{10}$
	$k_{4,z}$	1	$4 \cdot 10^9$	$10^{12}$
5	$k_{4,xy}$	1	$8 \cdot 10^8$	$10^{10}$
	$k_{5,z}$	1	$4 \cdot 10^9$	$10^{12}$
6	$k_{5,xy}$	1	$8 \cdot 10^8$	$10^{10}$
	$k_{6,z}$	1	$4 \cdot 10^9$	$10^{12}$
7	$k_{6,xy}$	1	$8 \cdot 10^8$	$10^{10}$
	$k_{7,z}$	1	$4 \cdot 10^9$	$10^{12}$
8	$k_{7,xy}$	1	$8 \cdot 10^8$	$10^{10}$
	$k_{8,z}$	1	$4 \cdot 10^9$	$10^{12}$
	$k_{8,xy}$	1	$8 \cdot 10^8$	$10^{10}$

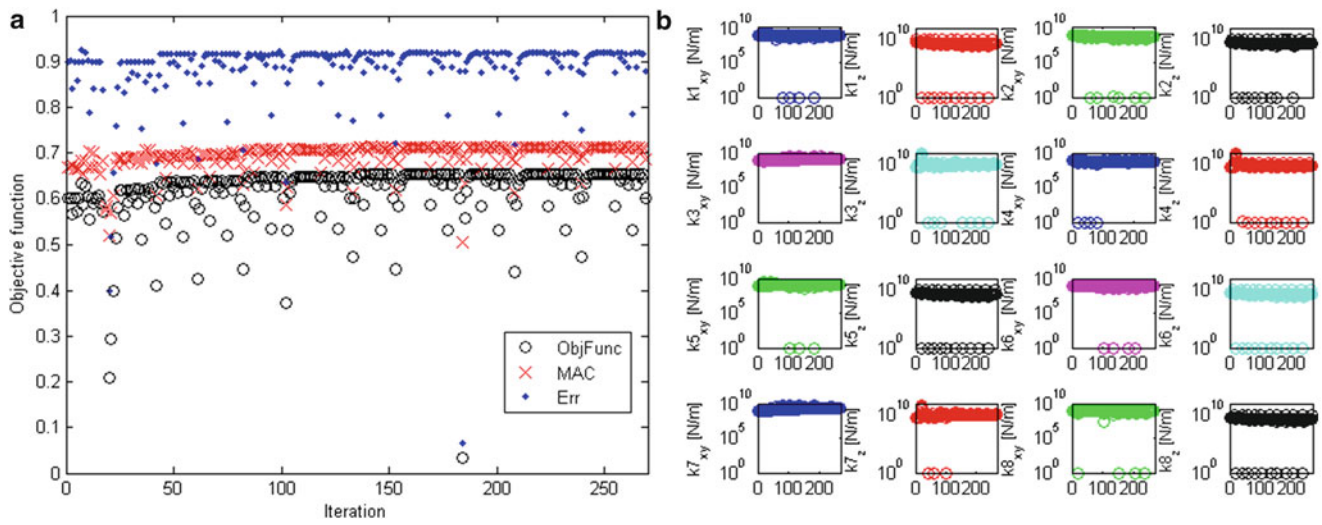


Fig. 25.15 Objective function (left) and parameters (right) trends with respect to the iterations for *fmincon* algorithm

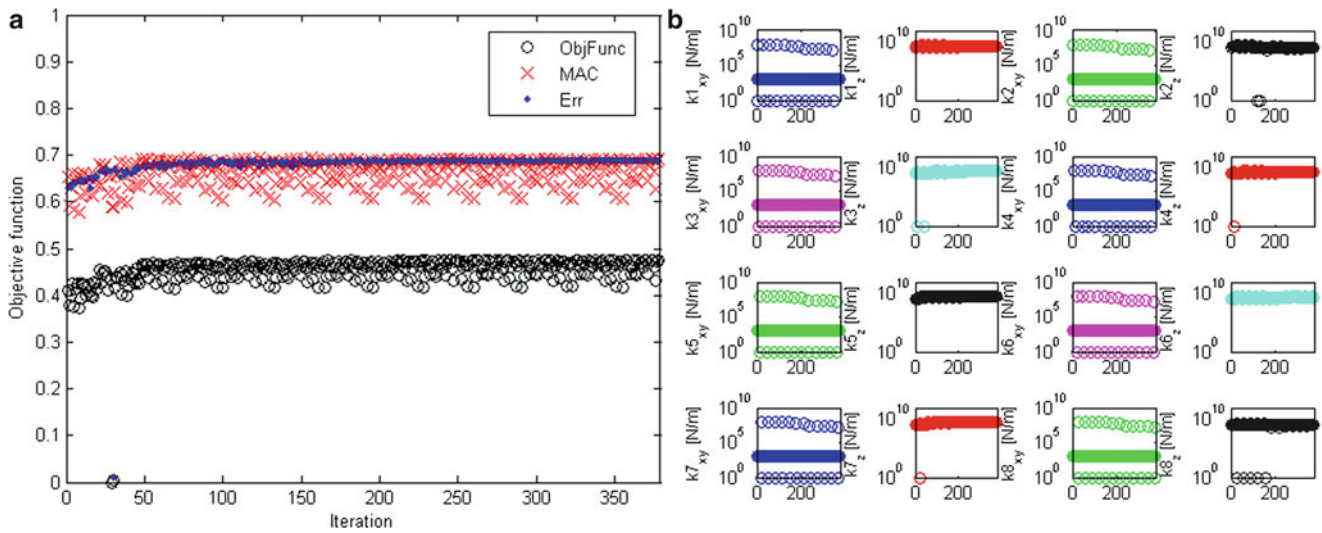
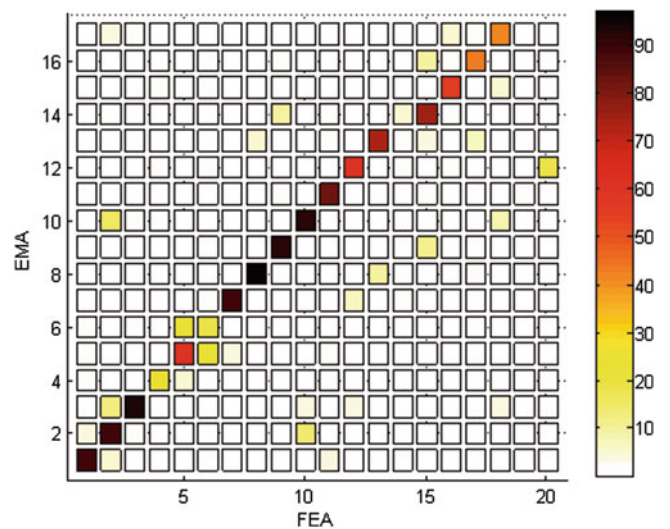


Fig. 25.16 Objective function (left) and parameters (right) trends with respect to the iterations for *patternsearch* algorithm

Fig. 25.17 Resulting MAC with the optimum values



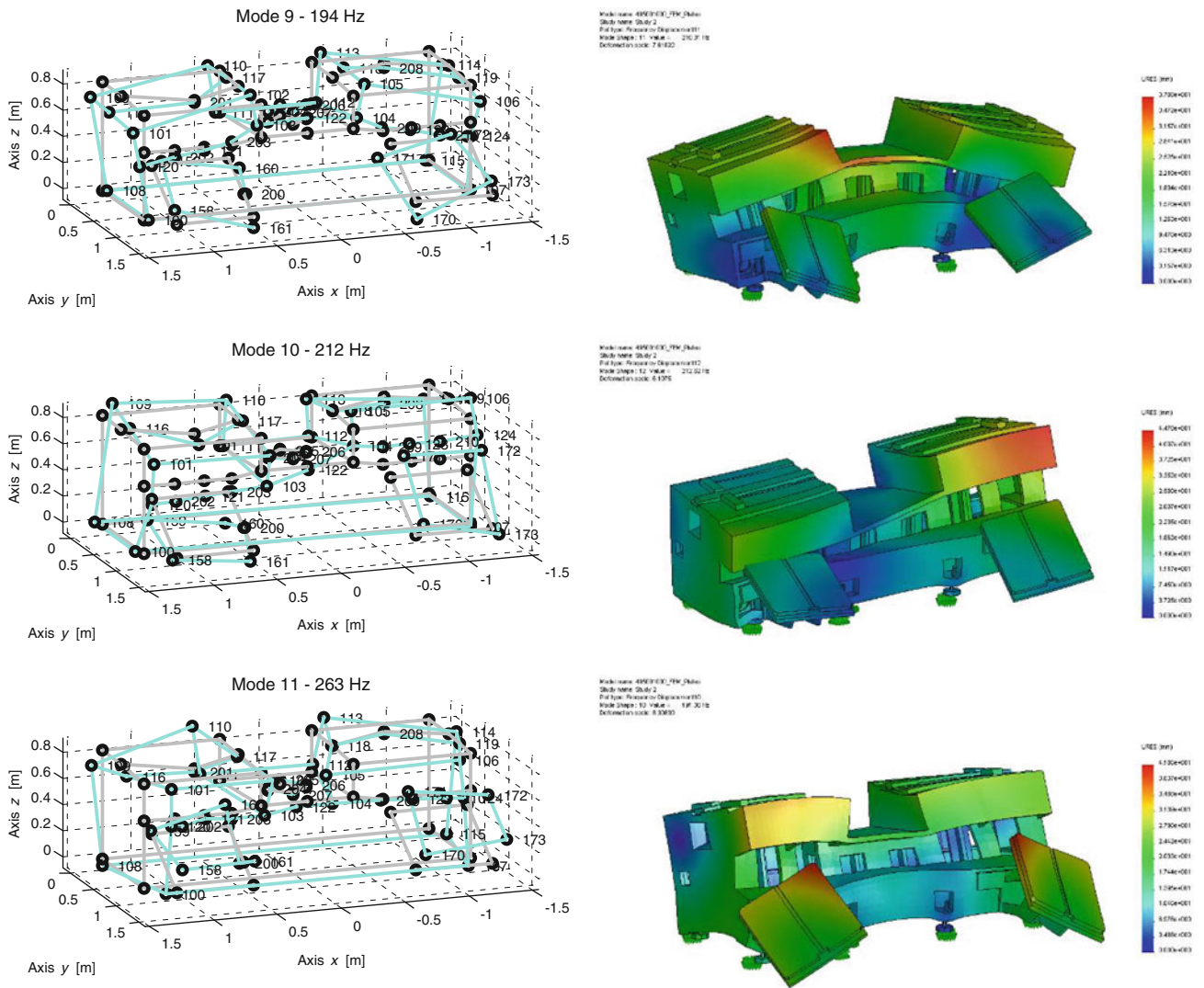


Fig. 25.18 Visual mode-shape comparison EMA-FEA of the cast-iron model

## 25.5 Conclusions

The two test structures subject of this work presented a case where the boundary constraint are not trivial to model and choose.

If the two extreme studies (all mountings clamped or all mountings supported) might be intuitively not suggested, the intermediate condition is difficult to set because of the non-trivial choice of which of the mountings are to be clamped.

The values of stiffness of elastic supports are obtained using an optimisation process and the comparison in terms of frequencies and mode-shapes are presented.

Optimal values of stiffness are reported reaching an fair correlation with experimental results. The stone-cast structure was proved to have better dynamic behaviour with respect to the cast-iron one, thus lower cost meets performances that are more suitable for a grinding machine.

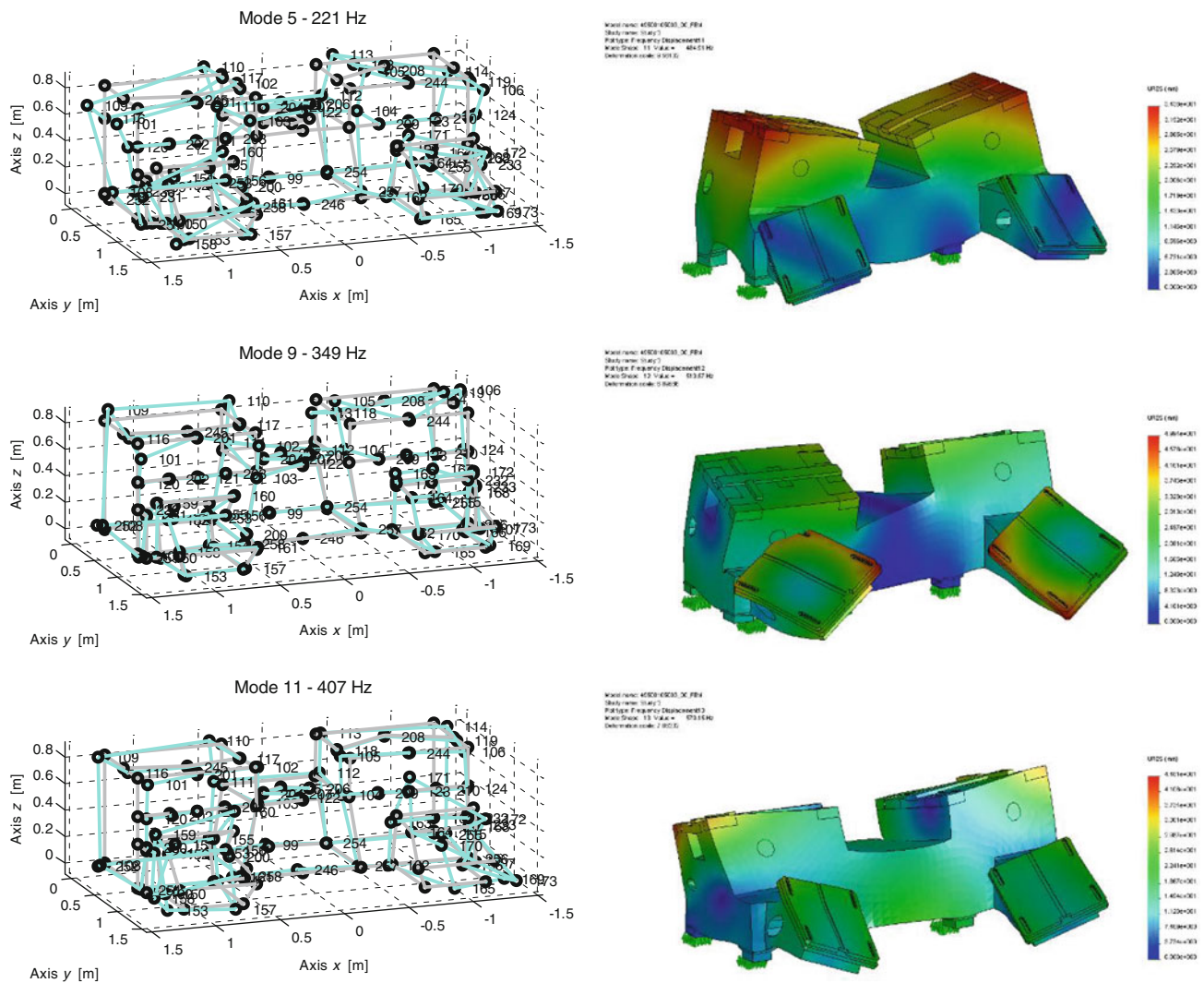


Fig. 25.19 Visual mode-shape comparison EMA-FEA of the stone-cast model

**Acknowledgment** This work was performed under a research project with Fives Giustina. The authors would like to thank Dr. Aldo Antonino, Dr. Sergio Giusto and Dr. Enrico Bruno from Giustina for their enthusiasm and driving force in the project.

## References

1. Maia MMN, Silva JMM (1997) Theoretical and experimental modal analysis. Wiley, New York/USA
2. Friswell MI, Mottershead JE (1995) Finite element model updating in structural dynamics. Dordrecht, Kluwer
3. Bonisoli E, Delprete C, Rosso C (2009) Proposal of a modal-geometrical-based master nodes selection criterion in modal analysis. Mech Syst Signal Process 23:606–620
4. Bonisoli E, Delprete C, Rosso C (2011) A modal-geometrical selection criterion for master nodes: numerical and experimental testing. Proceedings of the XXIX IMAC, pp 281–295
5. Allemang RJ, Brown DL (1982) A correlation coefficient for modal vector analysis. Proceeding of the I IMAC, pp 110–116
6. Han SP (1977) A globally convergent method for nonlinear programming. J Optim Theory Appl 22(3):297–309
7. Powell MJD (1978) A fast algorithm for nonlinearly constrained optimization calculations. Lect Notes Math 640. Springer Verlag, pp. 144–157
8. Conn AR, Gould NIM, Toint PL (1997) A globally convergent augmented lagrangian barrier algorithm for optimization with general inequality constraints and simple bounds. Math Comput 66(217):261–288

# Chapter 26

## Impact of Numerical Model Verification and Validation Within FAA Certification

David M. Moorcroft and Joseph Pellettiere

**Abstract** The mission of the Federal Aviation Administration (FAA) is to provide the safest, most efficient aerospace system in the world. The FAA Aircraft Certification Service is responsible for the design and production approval and airworthiness certification of all U.S. civil aviation products. Historically, design approval has required physical tests, however the FAA allows for the use of modeling and simulation (M&S) to demonstrate compliance with federal regulations. This allows an applicant to reduce the number of tests required to certify a design by relying on the results of M&S. As with all M&S use, verification and validation are fundamental in establishing the credibility of the computational models of aircraft components. Through several government-industry workshops, there is an apparent need for better guidance and training for both parties to understand how to communicate M&S and Verification and Validation (V&V) activities to support certification decisions. Current efforts focus on the level of detail required to document the M&S and V&V activities by an applicant such that the FAA can make an informed certification decision resulting in safe aircraft.

**Keywords** Verification • Validation • Regulatory • Decision making • Aircraft certification

### 26.1 Background

The Federal Aviation Administration (FAA) is one of the federal agencies that require a safety demonstration of commercial equipment before it can be used. The FAA's standards and regulations are designed to protect occupants in the event of an aircraft crash. As part of these regulations, dynamic testing and occupant injury assessment have been required for seats in newly certified aircraft since the adoption of Title 14 Code of Federal Regulations part 25.562 and similar regulations in parts 23, 27, and 29 [1].

Part 25.562(b) states that "Each seat type design approved for crew or passenger occupancy during takeoff and landing must successfully complete dynamics tests or be demonstrated by rational analysis based on dynamic tests of a similar type seat..." The inclusion of this statement in the regulatory language, "... demonstration by rational analysis ...", provided the necessary basis to develop Advisory Circular (AC) 20-146 to incorporate the use of modeling and simulation (M&S) in certification programs for the various categories of aircraft and rotorcraft [2]. The AC provides high-level guidance on the validation of numerical seat models. AC 20-146 identifies three main groups to which the use of M&S may be applicable: applicants including the seat as part of the aircraft type design, seat manufacturers, and seat installers. Two possible uses for M&S in certification programs include establishing the critical seat installation or configuration that will be tested, potentially reducing the number of required certification tests and demonstrating compliance of changes made to an existing certified seat system.

In addition to AC 20-146, SAE International has published Aerospace Recommended Practice (ARP) 5765, Analytical Methods for Aircraft Seat Design and Evaluation [3]. The document is the result of work done by the SAE SEAT committee, which is an industry group that produces industry standards and recommended practices. ARP 5765 was created to define specifications for virtual Anthropomorphic Test Devices (v-ATDs) suitable for aviation impact test simulations, to provide procedures for validation of both lumped mass and detailed finite element seat models, and to convey the current best

---

D.M. Moorcroft (✉)

Biodynamics Research Team, Federal Aviation Administration Civil Aerospace Medical Institute,  
PO Box 25082, Oklahoma City, OK 73125, USA  
e-mail: [david.moorcroft@faa.gov](mailto:david.moorcroft@faa.gov)

J. Pellettiere

Crash Dynamics, Federal Aviation Administration Aviation Safety, Washington, DC, USA

practices to assist engineering analysts in developing accurate models. Part of the purpose of this ARP is to provide additional detail that was not contained in AC 20-146 and provide details on practices to develop a model that can be used in the certification process.

### **26.1.1 Physical Testing**

Data available from tests conducted to support certification of seat systems may not be sufficient to develop or validate models. Seat certification has historically been accomplished through physical testing and has been treated as deterministic. The results of a particular test are either a pass or fail of all of the requirements levied upon it. If a test is considered a failure, then those results would not be forwarded to the regulating authority as part of the certification package. This approach limits certification test data to only being usable as a point validation since it only represents a single possibility of what might happen to a seating system and only under acceptable conditions. Another issue is the lack of repeated tests from which confidence intervals can be derived. Industry typically considers every developmental test a potential certification test and is not required to repeat a successful test. If a successful test was repeated and it subsequently resulted in a failure, then the previous test results can be called into question, jeopardizing the certification of that configuration. This is a significant disincentive to conducting repeats. Simply put, once a seat passes the test condition, from an industry standpoint, it is best to let it be and move on to the next configuration. Yet another issue is the cost of conducting tests that generate sufficient data to develop or validate models. Repeating tests solely to generate additional data for model validation adds significant cost to a program. Other cost burdens include any additional instrumentation or data processing required to support model validation. A certification test is normally conducted with only the instrumentation necessary to gather the data to make a pass or fail determination in accordance with the regulations. Model validation, however, may levy additional data requirements that will increase testing costs for the industry. Without clear benefits established and consistency across the industry, any manufacturer would view this as an increased cost burden.

### **26.1.2 Regulatory Acceptance**

AC 20-146 was developed as a response to the public Law HR 1000 under section 757, Streamlining Seat and Restraint System Certification Process and Dynamic Testing Requirements [4]. The AC was part of the plan that promoted alternative methods of compliance, which in this case includes using M&S in the certification process. The application of the AC and use of M&S also has the potential to improve certification efficiency by providing a better understanding of the system behavior which can reduce the number of test failures.

The use of M&S in certification has been either investigated or accepted by the FAA for cabin interiors, bird strike, fuselage crashworthiness, and engine blade failure [5]. Other federal agencies have also explored the use of M&S in certification, including the Federal Highway Administration for roadside safety structures [6] and the Food and Drug Administration for medical devices [7].

## **26.2 Verification and Validation**

Modeling and simulation used to support certification, so called certification by analysis (CBA), will require substantiation in the form of verification and validation (V&V). AC 20-146 provides high-level guidance on the validation of seat models. Note that the original version, published in 2003, does not contain the term verification. Several commercial codes were identified as being acceptable and a brief description of time steps is included, but otherwise the topic of code and solution verification is absent. The forthcoming revision will likely include more discussion on the topic and will include definitions from the American Society of Mechanical Engineers Guide for Verification and Validation in Computational Solid Mechanics (ASME V&V 10-2006) [8].

The AC does a better job of addressing validation, although the focus is on full system tests/models. General validation criteria are listed, which require the validation conditions to be similar to the model use conditions. This agrees with the ASME V&V 10-2006 specification that validation is done for an intended use. Application specific validation criteria are thoroughly discussed while providing only rudimentary suggestions for the methods of comparison, i.e. validation metrics,

and acceptance values. These criteria are focused almost exclusively on system level certification system response quantities (SRQs), i.e. the data channels used to make a pass/fail decision. Support channels are mostly excluded.

One of the original purposes of the SAE ARP was to provide additional recommendations on the methods of V&V. The first edition of the ARP, published in 2012, did not include a V&V section, but a forthcoming revision will. The recommendations are not yet at the level of a step-by-step guide, but additional information is provided on expectations for verification, component model validation, and system response quantities of interest, including support channels. This document also provides more detailed recommendations for validation metrics and acceptance limits.

The forthcoming revisions for both AC 20-146 and ARP 5765 references ASME V&V 10-2006, specifically the definitions and process map. The methods suggested for aviation seats are rudimentary by the standards of V&V 10-2006, specifically as it relates to uncertainty quantification (UQ). As mentioned previously, aircraft seat testing is treated as deterministic and limited information is available to attempt even basic UQ. The revised AC 20-146 will likely include a recommendation to apply a factor of safety to some critical SRQs in an attempt to account for testing and modeling uncertainties.

### **26.2.1 Code Developer Support**

Multiple commercial code developers, along with the developers of the virtual ATDs, have supported the efforts of the FAA and industry, through the SAE SEAT committee. Additionally Livermore Software Technology Corporation (LSTC) has hosted the LS-DYNA<sup>®</sup> Aerospace Working Group for several years [<http://awg.lstc.com/>]. The Aerospace Working Group (AWG) develops and publishes aerospace test cases and modeling guidelines for the non-linear analysis program LS-DYNA<sup>®</sup>. The working group originally focused on engine blades, but has recently created a group to address cabin interiors. The hope is that this group, and perhaps others like it, will provide the aviation industry with more information on code verification and quality assurance.

## **26.3 Communicating Results**

With the end goal of being able to incorporate certification by analysis (CBA), objective methods of determining model acceptance must be explored. A certification engineer may not be an experienced analyst, but will still be required to evaluate the analysis. To aid in CBA decisions, an applicant must communicate to the decision maker, i.e. the certification engineer, the methods used to model the physical system, the validity of that model, and how the results relate to a regulatory submission.

### **26.3.1 Coordination and Planning**

AC 20-146 emphasizes early and thorough communication between an applicant and the certifying authority. The FAA coordination process presented in the AC is extracted from FAA Order 8110.4C [9]. FAA coordination is essential to ensure the proper and timely execution of any certification program. When M&S is to be included in the certification plan, the following applicant actions are recommended:

- Acquaint the FAA personnel with the project.
- Discuss and familiarize the FAA with details of the design.
- Identify, with the FAA, applicable certification compliance paragraphs.
- Negotiate with the FAA where the applicant will utilize computer modeling and specify the intent and purpose of the analysis.
- Establish means of compliance either by test, by rationale analysis (i.e., computer modeling), or both, with respect to the certification requirements.
- Establish the validation criteria for the computer model relative to its application for certification.
- Prepare & obtain FAA Aircraft Certification Office (ACO) approval of the certification plan.



The certification plan document should contain:

- A description of the seat system to be modeled.
- A description of the software to be used in the analysis, including the operating assumptions and limitations of the software.
- A description of how compliance will be shown.
- A description of material data sources.
- A list of validation methods, including a description and justification of the failure modes/theories.
- An interpretation of results.
- Substantiation documentation and data submittal package.

### 26.3.2 *M&S Documentation*

The applicant must create a document that provides the numerical results and comparisons to test data when computer modeling is submitted as engineering data. This document is known as the Validation and Analysis Report (VAR). As recommended in AC 20-146, this report should contain:

- Purpose of Computer Model
- Overview of Seating System
- Software and Hardware Overview
- Description of the Computer Model
  - Engineering Assumptions
  - Modeling of the Physical Structure
  - Material Models
  - Constraints
  - Load Application
  - Occupant Simulation
  - General Analysis Control Parameters
- Results Interpretation
- Ultimate Margin of Safety

SAE ARP 5765 provides additional detail on the contents of this report. The structure is based on US Department of Health and Human Services, Food and Drug Administration documentation guidance [7]. The ARP specifies the following sections:

- Executive Summary
- Introduction
- Numerical Implementation (code details)
  - v-ATD
- Seat System Geometry
- Material Models and Material Properties
- Mesh
- Boundary and Initial Conditions
- Post-Processing & Results
- Validation
- Model Use
- Limitations
- Conclusion

This document is essentially the combination of three documents. The first component is a detailed description of the numerical model including how the model was constructed and the sources of material properties. This includes information related to the physical system, such as dimensions, tolerances, and materials. The next component is a verification and

validation report, which includes the comparator test data and the results of quantitative comparisons. The third component could be considered a test report for the model use simulations, i.e. details that are included in a test report when generating certification data. This includes conformity of the test article, use of acceptable loading conditions, use of acceptable ATDs, and data outputs that meet regulatory pass/fail criteria.

The final two sections of the report are of particular interest to the decision maker. The limitations section must address the extrapolation limits of the model, the uncertainties related to modeling practice and material properties, and should include sensitivity analyses. The culmination of the document is then a recommendation for a positive certification decision. As such, this report must convince the decision maker, through the accumulation of evidence, that the model is capable of accurately predicting the system response for the intended use.

## 26.4 Decision Making

Modeling and simulation has been used in the certification process for several different programs including seat systems, certification of a novel design aircraft fuselage, and design of derivative engine fan blades. Currently these approvals have been made on a case-by-case basis. As discussed above, there are numerous documents that recommend procedures for an applicant to follow. As these documents mature, recommended practices can become standards and the FAA will be able to define an equivalent level of safety for M&S data. Hence the use of M&S can follow general guidance in much the same way that physical test data are used.

Verification and validation is fundamental in establishing the credibility of the computational models of aircraft components. When M&S results are to be submitted as engineering data, it is only through V&V that the decision maker can have confidence in the accuracy and applicability of the M&S. Due to the nature of certification approvals, documentation is the key. This is the means for an applicant to communicate the assumptions and descriptions of the physical processes, modeling techniques, verification methods, validation results, and limitations. For validation documentation, ASME 10-2006 suggests two questions be answered:

- Are the approximations and uncertainties inherent in the modeling approach appropriate for the intended application?
- Are the model and experiments adequate to predict the intended system responses for the reality of interest?

Perhaps most important for certification, the V&V documentation should address limits on the use of the model. The intended use of the model is to generate certification data at an untested location in the design space. Knowledge of the engineering assumptions, the region of applicability for material properties, and the similarity between model use and validation conditions provides confidence in the extrapolation. Sensitivity analysis is recommended throughout the model validation process to determine the sensitivity to model inputs that are difficult to measure, e.g. friction, or inputs that are not known with high certainty. Sensitivity analyses can be used to document the sensitivity of the model under different conditions. This includes checking the sensitivity of the model for future use and extrapolation and for the justification of specific model inputs where the data were not explicitly known. If the conclusions of the analysis are significantly dependent on the assumptions and/or simplifications in the model, the analyst should conduct a sensitivity analysis of the parameters associated with those assumptions and/or simplifications.

### 26.4.1 Decision Makers

Certification decisions are made by Aircraft Certification Office (ACO) engineers. They are experts on the regulatory aspects of aircraft components, federal regulations, FAA policies and orders, airworthiness directives, exemptions, and industry standards. ACO cabin interior engineers typically have a structural qualification such as a mechanical engineering background. They are not expected to be experts in every software code that could be used to generate certification data. Because of this, it is important that an applicant use the certification plan document and the validation and analysis report to provide sufficient information for the ACO to make an informed decision.

The ACO also has the ability to bring in FAA subject matter experts to assist in the decision making process. The subject matter experts can provide knowledge of the specific software codes, general V&V best practices, and testing uncertainties. Recognizing testing uncertainties, within the backdrop of deterministic certification testing, and definition of appropriate accuracy requirements, also plays a key role in the success of certification by analysis.

### **26.4.2 *Level of Detail***

Through several government-industry workshops, it has become apparent that there is a need for better guidance and training for both parties to understand how to communicate M&S and V&V activities to support certification decisions. Current efforts focus on the level of detail required to document these activities by an applicant so the FAA can make an informed certification decision that ensures aviation safety. Potential applicants have suggested a streamlined approach to documentation, expressing that much of the information is contained in other documents or is an analyst's decision. We hypothesize two underlying issues that explain this situation.

The first is a possible misunderstanding of the role of M&S/V&V documentation in the certification process. In a typical physical certification test, a FAA witness can inspect the physical test article and observe the test. In certification by analysis, the ACO must rely solely on the validation and analysis report to make a decision. In this regard, the documentation of the modeling techniques, the verification and validation activities, and the extrapolation simulations must stand-in for the ability to view a physical seat.

The second issue is that companies may not have allocated sufficient time for an analyst to thoroughly document the M&S activities. Analysts have suggested that once a simulation shows positive results, company management believes that that portion of the project is complete and the analyst should move on to the next project. At this point, it seems that it is important for the regulatory authorities, to make it clear how important proper documentation is to the acceptance of modeling and simulation for certification data.

### **26.4.3 *Discrepancies***

AC 20-146 states that failure to satisfy all validation criteria does not automatically preclude the model from being validated. The applicant and the ACO engineer should evaluate whether the deviations impact the ability of the model to predict credible results and determine if deviations from the validation criteria are acceptable. In addition, the applicant may present evidence to show that the deviation is within the inherent reliability and statistical accuracy of the test measurements. The applicant should quantify any discrepancies between the results obtained from analysis and the dynamic test data for those parameters that are critical to the application of the analysis. Additional data from previous testing, data available from component tests, and support from classical engineering methods can all be used to support a positive certification decision when discrepancies occur.

### **26.4.4 *Documentation of Validation***

AC 20-146 states that the applicant is entitled to validation documentation, supplied by the FAA, indicating that the computer model is capable of generating certification data. This will allow the applicant to avoid revalidating the same model each time it produces certification data. It also avoids having to revalidate if business must be conducted at an ACO different from the ACO that approved the original validation. Possible items to include in the validation documentation are:

- The FAA's acceptance of the computer model to produce certification data.
- Identification of the software version and hardware platform used to build and run the computer model.
- A description of any limitations on the application of the computer model.
- The FAA's expectations for how the applicant will maintain configuration control of the model.
- Other items as agreed to between the ACO and the applicant.

## **26.5 Conclusion**

An important point to consider is that the application of verification and validation still relies heavily on testing. The V&V activities are focused on the comparison of the M&S with the physical test data. Part of this is that current regulations which may change as M&S and V&V mature. As they mature, the reliance on full scale testing may be reduced, but this may be supplanted by the need to conduct smaller scale component tests following a building block approach. This way, the M&S

can be validated in smaller portions with a smaller extrapolation to the full system response. The amount of testing and at what level then becomes one of the future uncertainties.

The FAA has several guidance documents allowing the incorporation of M&S data into the certification process. In the future, these documents will be expanded to provide additional details and clarity. New guidance material may be developed to discuss the use of M&S to demonstrate the crashworthiness of full aircraft with performance based requirements. These updates will incorporate the evolving material on verification, validation, and uncertainty quantification and how they might affect any decisions. However, the use of M&S does not remove the need for high quality physical test data.

Currently V&V is an integral step in the decision making process for certification decisions when M&S is used. Without V&V, the numerical data will not be accepted as certification data. Even with rigorous V&V, care must be taken to ensure that a quality V&V process is followed that is relevant to the purpose of the certification project.

**Disclaimer** The findings and conclusions in this paper are the opinions of the author(s) and should not be construed to represent any agency determination or policy. Certification approvals are based on federal regulations, official FAA policy, and certification engineers.

## References

1. Code of Federal Regulations Title 14, Part 25 (2014) Airworthiness standards: transport category airplanes, subpart C – structure. U.S. Government Printing Office, Washington, DC
2. Federal Aviation Administration Advisory Circular (AC) 20-146 (2003) Methodology for dynamic seat certification by analysis for use in parts 23, 25, 27, and 29 airplanes and rotorcraft. Federal Aviation Administration, Washington, DC
3. SAE Aerospace Recommended Practice 5765 (2012) Analytical methods for aircraft seat design and evaluation. SAE International, Warrendale
4. Wendell H. Ford Aviation Investment and Reform Act for the 21st century. Public Law 106-181, House Resolution 1000, 2000
5. Federal Aviation Administration Policy ANE-2006-33.94-2 (2009) Use of structural dynamics analysis methods for blade containment and rotor unbalance tests. Federal Aviation Administration, Washington, DC
6. Ray M, Mongiardini M, Plaxico C, Anghileri M (2010) Procedures for verification and validation of computer simulations used for roadside safety applications. National Cooperative Highway Research Program project 22-24, report no 179. Transportation Research Board of the National Academies, Washington, DC
7. Reporting of Computational Modeling Studies in Medical Device Submissions (2014) Draft guidance for industry and food and drug administration staff. U.S. Department of Health and Human Services, Food and Drug Administration, Document no 1807, Washington, DC
8. ASME V&V 10-2006 (2006) Guide for verification and validation in computational solid mechanics. The American Society of Mechanical Engineers, New York
9. Federal Aviation Administration Order 8110.4C (2005) Type certification. Administration

# Chapter 27

## The Role of Model V&V in the Defining of Specifications

Todd Simmermacher, Greg Tipton, Jerry Cap, and Randy Mayes

**Abstract** Model validation plays an important role in estimating the confidence in a simulation. Many times, the simulation is the only source of response that is available. When an expensive simulation is developed, the predictions from that simulation will usually be used in an absolute sense, with more conservatism added if the model validation analysis indicates low confidence. The results of the simulation could be scaled based upon the confidence of the model. This paper will describe how the outcome of a model validation exercise determines the conservatism applied to the environmental specifications and the estimation of margins derived from those simulations.

**Keywords** Validation • Specifications • Qualification • Uncertainty • Model

### 27.1 Introduction

Model validation and uncertainty quantification has, from necessity, become increasingly embedded into the design and qualification process. Model results are not being used in a vacuum for high consequence decisions, but are compared and formally evaluated against relevant experimental data. The degree and rigor to which the evaluation is performed varies widely based upon programmatic constraints such as budget, schedule, and risk tolerance of the end user of the results.

Model validation and uncertainty quantification has a large body of literature that has advanced the field. The iconic reference is [1]:

*Verification:* The process of determining that a model implementation accurately represents the developer's conceptual description of the model and the solution to the model.

*Validation:* The process of determining the degree to which a model is an accurate representation of the real world from the perspective of the intended uses of the model.

The objective of verification is to confirm that the computational representation of the mathematics of the model is, in fact, representing the intended mathematics to some quantified degree. There will be errors due to discretization and convergence of solvers, but these errors should be quantified and included in the uncertainty estimates. The verification of a simulation involves both the analysis code used to develop the simulation, as well as the specific model that is implemented in the code. Verification involves comparison to known analytical solutions and other known solutions to the mathematics that is implemented in the analysis code. The specific model that is developed in the analysis code also requires verification to insure that the assumptions made by the analyst are being correctly represented such that the analysis code provides a valid simulation.

The objective of validation, in contrast, is to evaluate the appropriateness of the assumed computational model of the system of interest. Whereas verification is purely an evaluation of the mathematics of the model, validation is the tie to the physical system and experimental data. Validation involves identifying quantities of interest such as peak velocity, maximum temperature, gRMS (standard deviation of a time signal in the units of acceleration of gravity), or other scalar measures that represent the end use of the model. The results of a model validation effort should also include an uncertainty analysis of the experimental and analysis processes as well as the confidence in the comparison. This information is important to assess the adequacy of the model and to inform the risk affiliated with using the simulation results.

This paper will demonstrate a few examples where the adequacy of the model influences how the model results are utilized. Typically, regardless of the results of the validation, the model is still useful. A very poor model may only be good

---

T. Simmermacher (✉) • G. Tipton • J. Cap • R. Mayes  
Sandia National Laboratories, PO Box 5800, Albuquerque, NM 87123, USA  
e-mail: [twsimme@sandia.gov](mailto:twsimme@sandia.gov)

for relative comparisons between modeled configurations; however, it can still provide valuable insight. Many times, the model is assessed to be fair to good, and can still be used for its intended application. How the model results are used can be affected by the results of a validation. Results from a fair model may be modified by a safety or uncertainty factor whereas results from a good model may be used with no modification.

The first two examples where the adequacy of the model influences how the model results are utilized is for component test specifications. Specifically, this paper will focus on component mechanical shock test specification and component random vibration test specification. These two examples show how simulation results and the adequacy of the results are used for development of component test specifications. The final example in this paper demonstrates where the quality of the model necessary for decision making is determined by the outcome of the analysis. The example is the calculation of failure margins. It is shown that if the predicted margin is large, then a large effort into improving the model and doing model validation may not be worth the expense.

## 27.2 Component Specification

An application that requires a high fidelity, validated model is the derivation of test environments to be used to qualify components for use in a full system. A full system model is developed and simulations of the various environments that have been defined as requirements for the system are used to define component level laboratory tests. These laboratory level tests are designed to represent the in service excitation such that a component can be adequately tested without requiring the hardware to represent the full system.

The environments at the component level can be derived from either a full system physical test or from a computational simulation. Both the test and the computational simulations have limitations in the level of fidelity in replicating the operational environment, however, typically the test results are assumed to be sufficiently representative to develop component test specifications. Computational simulations, however, require model validation for the results to be considered valid for further use. The reality is for many applications, the model will be used unless it is excessively wrong.

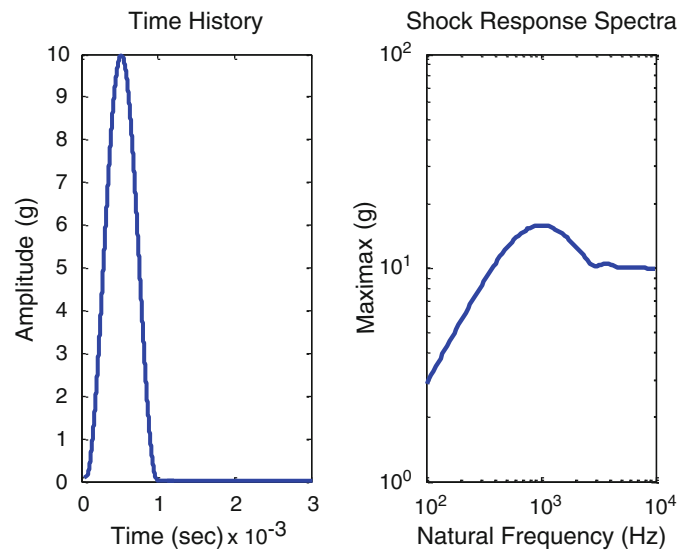
How the results from a simulation are used can be affected by the outcome of the model validation [2]. A model that is shown to be highly predictive with little uncertainty will be used with confidence and with little modification. If the model is shown to be a poor representation of reality or with a large degree of uncertainty, a large safety factor or scaling may be applied to ensure conservatism in the final test specification. Declaring a priori how the results of a simulation are going to be used, processed, and modified based upon the fidelity demonstrated by the validation is as important as declaring the model validation metric and acceptance criteria. In this case, identifying the modifications to the data that will be performed on the data for various levels of success is important so that the processing can be agreed upon prior to adjudicating the model. This assures that the process can be developed in an objective manner.

## 27.3 Component Mechanical Shock Test Specification

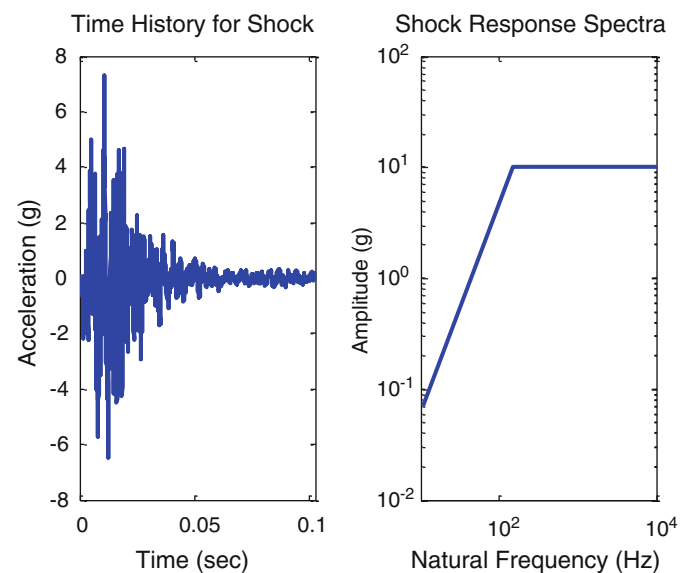
High level mechanical shock test specifications are simulated on either a drop table or a resonant plate or beam test setup. The shock specifications for either test are shown in Figs. 27.1 and 27.2. For a drop table, the test specification is in the form of a haversine. The duration and amplitude of the haversine are the parameters to be specified. The duration is determined by the bandwidth of the shock. Normally the specification is developed by enveloping the test or model data in the shock response spectra (SRS) domain. The amplitude and duration of the haversine is adjusted until the SRS of the haversine is higher in amplitude than the data being enveloped. An important feature of the SRS is that the high frequency asymptote has amplitude equal to the peak acceleration of the corresponding time history. It is this characteristic that will be used in the development that follows.

A shock can also be simulated on a resonant beam or plate fixture (Fig. 27.2). This shock is appropriate for a pyro shock type application where there is ringing affiliated with the operational environment. The resonant test is performed by fixing the test article to a flat plate or beam, then exciting the plate or beam by firing a projectile at the fixture. As with the haversine, there are two parameters that are needed to define the resonant plate test, the amplitude and the “knee” frequency. The amplitude is determined by the magnitude of the impact. The knee frequency is defined as the break point where the slope changes in the SRS which is 200 Hz in Fig. 27.2. The knee frequency is controlled by the first natural frequency of the beam or plate used as a fixture for the test. By adjusting the size or thickness of the beam or plate, the knee frequency can be tuned.

**Fig. 27.1** Representative haversine



**Fig. 27.2** Representative resonant plate specification

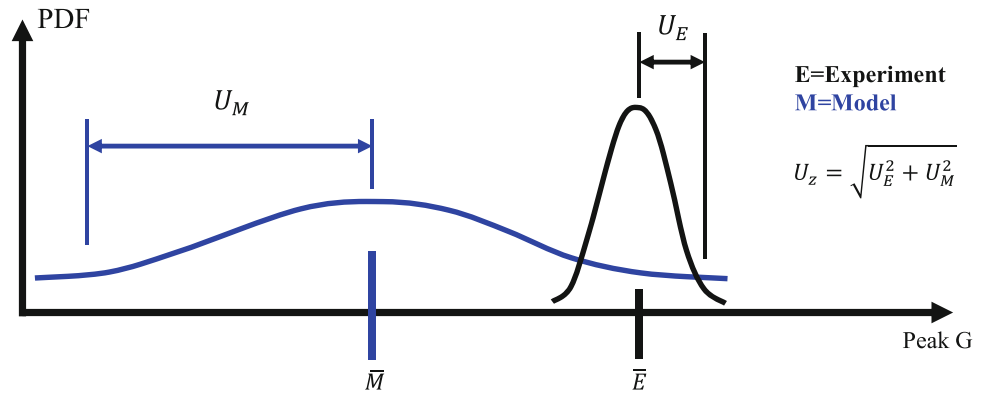


For the application described in [2], the duration of the haversine is assumed to have been determined through a combination of test data and model results. By reviewing data from both validation tests and simulation results, the frequency content of the SRS was estimated and was assumed known. The model results were to be used to determine the amplitude of the haversine for use in a component level test specification. The validation of the model was performed at the response level. Each measurement location was judged individually against test data to determine the degree of conservatism present in the model. The model was then used to simulate similar, untested environments and the results were used to derive a composite shock specification for the various components in the system.

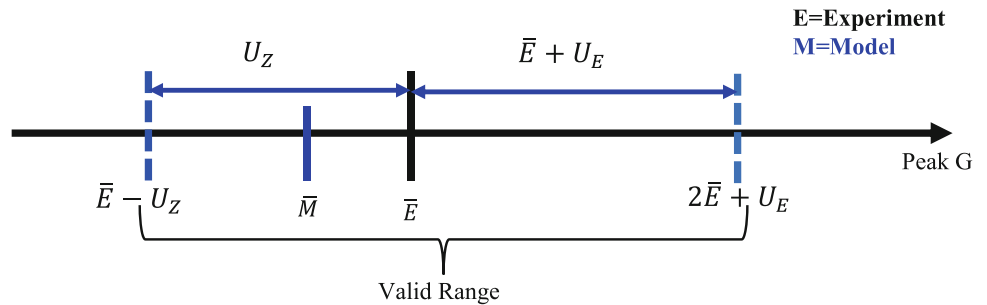
The model validation conditions and the resulting acceptance of the data are characterized by the quantities identified in Fig. 27.3. The mean of the quantity of interest (QOI) from the model ( $\bar{M}$ ) and the mean of the QOI from the experiment ( $\bar{E}$ ) are defined relative to the probability distribution of the model and experimental QOI. The uncertainty is given as a standard deviation of the respective distributions. The appropriate standard deviation for which to define  $U_M$  and  $U_E$  based upon the PDF of the model and experimental uncertainty is negotiated with a team consisting of the customer, test engineers, analysts, and environment engineers.

The criteria developed in [2] are shown in Figs. 27.4 and 27.5. The underlying model to be validated is linear, however localized non-linearities exist in the physical system. At the locations where the response is predominately linear, the criterion uses a combination of model and experimental uncertainty. At locations where the response is influenced by a local nonlinearity, the linear model should be conservative. This definition favors a conservative model which is preferable for component qualification. A component that passes an over-test is guaranteed to function in the operational environment

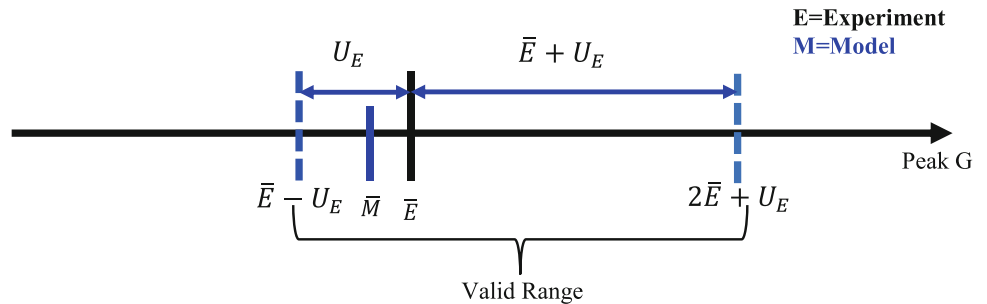
**Fig. 27.3** Model and experimental probability density functions definitions



**Fig. 27.4** Graphical representation of validation metric for a linear model in a linear regime



**Fig. 27.5** Graphical representation of validation metric for a linear model in a nonlinear regime



while a significantly under-tested component may have an undetected failure prior to reaching the full environment. An overly conservative specification, however, can add unnecessary cost to the design in an effort to overly ruggedize the component. A factor of two in conservatism was negotiated to be acceptable for the application and is based on the rule of thumb for enveloping SRS responses that the peak acceleration of the resulting specification should not be over a factor of two from the underlying data.

For a location where the response is predominately linear, the model is considered valid if the model is within the root mean square of the model and experimental uncertainty below the mean of the experiment or within sum of the mean of the experiment plus the experimental uncertainty above the mean of the experiment (Fig. 27.4). The example in Fig. 27.4 shows a valid model that is slightly non-conservative in predicting peak acceleration. This allowed for the possibility that the model results could under-predict the test, but still be considered valid.

For a location where the response is primarily non-linear (Fig. 27.5), the expectation is that a linear model should predict that location conservatively, and therefore the valid region for the model only spans between the experimental data and the same upper bound as Fig. 27.4. This restriction only allows for the experimental uncertainty at the lower bound.

Once the simulation results have been determined to be valid, the amplitude of the haversine can be set. If the valid prediction was higher than the experimental measurement, the peak acceleration was used directly from the model. However, if the valid prediction was lower than the experimental measurement, the amplitude of the haversine was set to twice the predicted level. This insured that the component specification was conservative.

A similar metric could be used to define a resonant plate test. The knee frequency, which is similar to the duration of the haversine, would be determined a priori from legacy data or through analysis of relevant test and model data. The amplitude of the resonant plate specification would be set exactly as described above for a haversine.



## 27.4 Component Random Vibration Test Specification

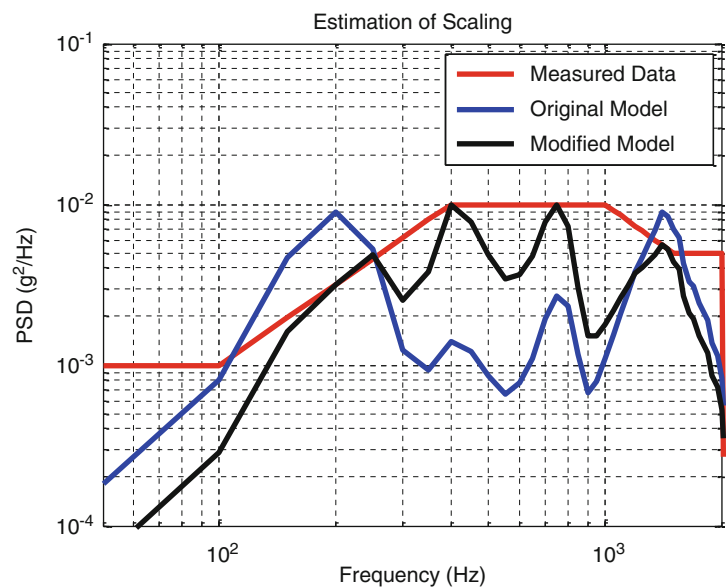
For random vibration, the test specification is defined in terms of the power spectral density (PSD). The duration of the test specification is determined by either the duration of the operational environment or a scaling based on maintaining the fatiguing nature of the insult that is determined by a variation of Miners fatigue life model. This scaling will compress the time necessary to perform the test by increasing the amplitude of the test specification. The test specification is derived from either operational, laboratory, or simulation data. The specification is defined by simplifying the underlying data by generating a straight line envelope of the data, with some conservatism added to account for variability and uncertainty.

Model validation for random vibration can be performed in a few different ways. A simple metric is a specification on the natural frequencies of the system to be within a certain percentage of the experimental frequencies as determined by a modal test. Typically 5 % is assumed to be a reasonable error. A more rigorous metric is based on the least favorable response (LFR) and is developed by [3]. The LFR is attractive because it compares a weighted integral over multiple frequency ranges to determine validity. The integration minimizes the sensitivity of the metric to small errors in natural frequency that can be due to model errors or unit to unit variability.

Once the validity of the model has been established, the data is available to define specifications. Typically, due to uncertainty in the loadings, errors and uncertainty in the model, and variability in the hardware, the simulation results will differ from test data or legacy test specifications derived for a similar system. Since the model results may be the only data available to specify component specifications, processing of the simulation results is needed to normalize the results to a known basis. A method to normalize the data has been developed by [4]. This technique was developed to utilize the model results at locations that were unmeasured during a laboratory or field test. This assumes that the model is compared at measurement locations and the degree of similarity is defined at these equivalent locations. A frequency dependent scaling factor is then defined that corrects the simulation results to the measured results. This frequency dependent scaling is then applied to model results for unmeasured nearby locations. The assumption is that the bias error for nearby locations is similar to the bias error observed at the measured locations.

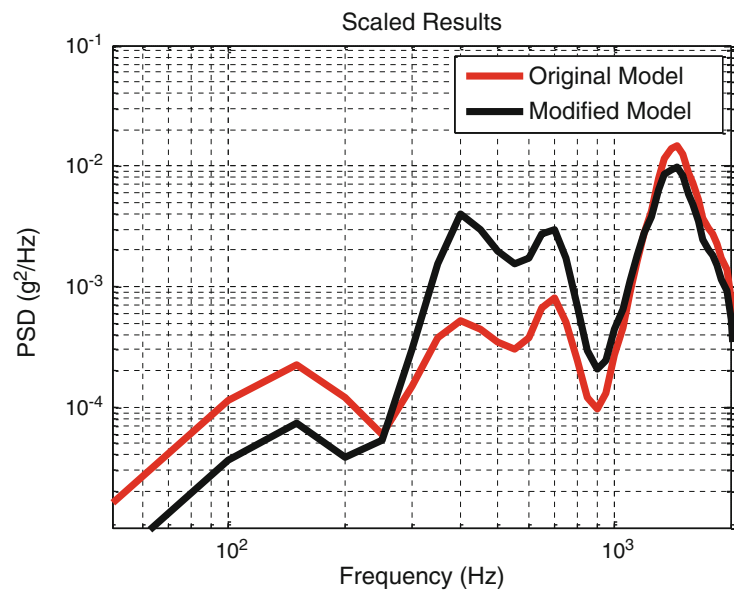
The correction procedure is demonstrated in Fig. 27.6. The processing begins by either enveloping measured data or using legacy test specifications that currently exists. This is depicted as the red line in Fig. 27.6. The raw model results are shown in blue in Fig. 27.6. A frequency dependent function is defined as the ratio of the red curve and the blue curve evaluated at the peaks. For the example in Fig. 27.6 this gives a value of the function at four frequencies. The ratios are then interpolated to the remaining frequencies in the bandwidth of interest. Finally the model data is scaled using this frequency dependent function with the result given as the black curve in Fig. 27.6. Note that the peaks in the modified simulation data match the envelope of the measured data exactly as defined. The valleys are also corrected. This is critical for a properly defined test specification to insure that the test does not attempt to overdrive these regions of low response.

Once the frequency dependent scaling has been defined for a location, this function is assumed to be valid at nearby locations. The definition of nearby is based on engineering judgment and should be determined by a team including the



**Fig. 27.6** Localized bias correction using peak scaling

**Fig. 27.7** Localized bias correction



environments engineer, analyst, and customer. The scaling is then used to modify predictions at locations of interest where no test data were collected. Figure 27.7 shows an example of nearby results scaled using the frequency dependent function determined in Fig. 27.6. Note that the mid frequencies are amplified as a result of the scaling. The model under-predicted this frequency range at the measurement location and this amplification is carried through to the other locations as desired.

## 27.5 Quantifying Margins and Uncertainties

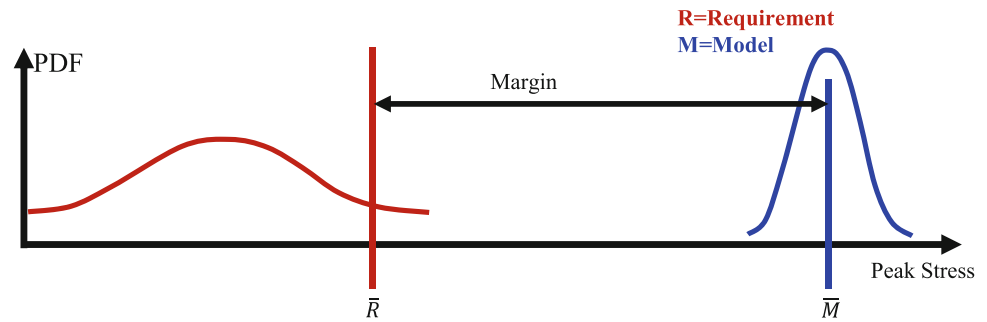
The final example is an application where the model results are used to determine the margin in a system. Quantification of margins and uncertainties has become increasingly important in high consequence applications [5, 6]. An example application is depicted in Fig. 27.8. The requirement is a hard limit based off of some measured operational data. The operational environment is random and has some distribution. The requirement is derived by defining some level of conservatism with some confidence factor. This then identifies the deterministic value of the requirement, in this case peak stress at some location. The model will be used to evaluate the capability of the component by simulating environments much higher than the requirement until a failure is predicted by the model. The probability of failure is then estimated by propagating uncertainty in the parameters through the model and estimating the potential distributions of the peak stress.

The acceptance criteria of the model being deemed valid are determined in a large part by the amount of margin demonstrated in the simulation. In Fig. 27.8, a system with a large degree of margin is shown. The model can have a large amount of uncertainty and the margin would still be large. In this case, a very refined model with minimal uncertainty may be as effective as a cruder model with large uncertainty. If the model is being used solely for margin assessment, an extensive, time consuming model development and model validation effort might not be worth the expense.

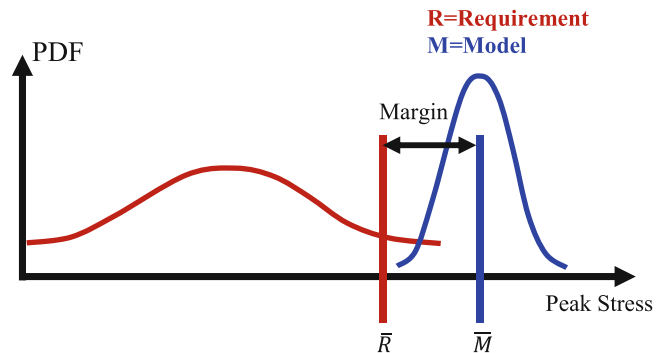
Figure 27.9 demonstrates a system with a small degree of margin with respect to the requirement. In this case, the margin is small and the required confidence in the model results is much higher than the situation in Fig. 27.8. Here, large uncertainty in the model could indicate the possibility of negative margin which could imply that the system does not meet its requirements. A large model validation and characterization effort would be demanded for this situation prior to any assessment of the margin.

In the quantification of margin using modeling results, the required confidence in the model is dependent on the demonstrated margin. The results of the simulation determine the acceptance criteria for the model validation. This dependence on the simulation requires an initial estimate of the margin. A rough or initial model might be used to estimate the degree of margin present in the design. Then the path for model development can be planned and executed to the appropriate level.

**Fig. 27.8** Quantification of margin and uncertainty



**Fig. 27.9** Quantification of margin and uncertainty



## 27.6 Conclusions

Three examples of where the outcome of a model validation exercise determines how the data from the simulation is used have been presented. In two of these examples the end result of the model is not a yes/no decision, but the simulation results are used to provide test specifications for designers to assess their components against. The third example shows where the quality of the model necessary for decision making is driven by the outcome of the analysis. These examples again show that the application that the model was developed for drives how the model validation is performed.

**Acknowledgement** Sandia National Laboratories is a multi-program laboratory managed and operated by Sandia Corporation, a wholly owned subsidiary of Lockheed Martin Corporation, for the U.S. Department of Energy's National Nuclear Security Administration under contract DE-AC04-94AL85000.

## References

1. AIAA (1998) Guide for the verification and validation of computational fluid dynamics simulations. American Institute of Aeronautics and Astronautics, AIAA-G-077-1998
2. Mayes RL (2008) Developing adequacy criterion for model validation based on requirements. In: Proceedings of the international modal analysis conference, Orlando
3. Urbina A, Ross M, Paez TL (2012) Assessment of the accuracy of a model for use in prediction of component environment. In: Proceedings of the 53rd AIAA/ASME/ASCE/AHS/ASC structures, structural dynamics, and materials conference, Honolulu
4. Cap JS (2014) A method for reducing the effect of biased data on the derivation of test specifications. Sandia National Laboratories internal white paper, 5 May 2014
5. Pilch M, Trucano TG, Helton JC (2006) Ideas underlying quantification of margins and uncertainties (QMU): a white paper. Sandia National Laboratories internal report, SAND2006-5001
6. Diegert K, Klenke S, Novotny G, Paulsen R, Pilch M, Trucano T (2007) Toward a more rigorous application of margins and uncertainties within the nuclear weapons life cycle – a Sandia perspective. Sandia National Laboratories internal report, SAND2007-6219

# Chapter 28

## A Perspective on the Integration of Verification and Validation into the Decision Making Process

Kenneth T. Hu, Angel Urbina, and Joshua Mullins

**Abstract** As more and more high-consequence applications such as aerospace systems leverage computational models to support decisions, the importance of assessing the credibility of these models becomes a high priority. Two elements in the credibility assessment are verification and validation. The former focuses on convergence of the solution (i.e. solution verification) and the “pedigree” of the codes used to evaluate the model. The latter assess the agreement of the model prediction to real data.

The outcome of these elements should map to a statement of credibility on the predictions. As such this credibility should be integrated into the decision making process. In this paper, we present a perspective as to how to integrate these element into a decision making process. The key challenge is to span the gap between physics-based codes, quantitative capability assessments (V&V/UQ), and qualitative risk-mitigation concepts.

**Keywords** Verification • Validation • Credibility • Decision making • Risk

### Nomenclature

V&V Verification and validation  
UQ Uncertainty quantification  
M&S Modeling and simulation

### 28.1 Introduction

Verification and validation (V&V) of physics based models has progressed quickly in the past few decades. Modeling and simulation (M&S) is now an everyday activity, and is routinely used to influence decisions. Engineering decisions are made based on both testing and M&S information. In our engineering context, the decision often relates to whether a system or components meet a requirement. In addition to the best action (accept vs. reject), sometimes the decision itself must be changed when there is not enough information (redesign/add margin, or gather additional information – i.e. renegotiate the intended uses). Decision theory tells us that the best action must be selected based on the available information.

Engineering decisions are based on requirements, but there are many levels of requirements. “This system must provide function A” is derived to “Component W must provide output X when input Y is above Z”, and this is finally translated to “a *validated* simulation of Component W must show that output X is provided when input Y is above Z, with 99 % confidence.” An M&S requirement like this needs a specification of validated, often based on adequacy criterion.

What is the appropriate level of abstraction to request M&S information or provide requirements? At some point these derived and translated requirements and adequacy criteria are no longer representative or useful for answering the actual question of interest. In addition, the M&S capabilities to meet those requirements are unlikely to exist, at least with any degree of credibility. This is also a problem for experimental work.

The phrase ‘intended use’ of M&S is similarly vague. A common definition is the way M&S results will impact the decision. We will define an intended use of a simulation to be the presentation of simulation results to satisfy – partially or wholly – a specific requirement. It is not useful to set intended uses that exceed the predictive capability (the ability to

---

K.T. Hu • A. Urbina (✉) • J. Mullins  
Sandia National Laboratories, PO Box 5800, MS 0828, Albuquerque, NM 87185, USA  
e-mail: [aurbina@sandia.gov](mailto:aurbina@sandia.gov)

make predictions with any confidence or credibility). It is equally unhelpful to request simulation results that are irrelevant or lack traceability to the original requirements. Instead the intended uses must be negotiated so that they are both useful to decision makers, and achievable by the M&S/V&V analysts. *The main questions that arise here are: at what level should requirements be provided to the M&S analysts, and how should intended uses be justified?* We will focus on the second question.

In the waterfall development concept [1], the decision maker derives and translates requirements down to specific M&S predictions and adequacy criteria – answering the question “How good is good enough?”. This is an extremely difficult process, since it is entirely subjective and is done without knowledge of the M&S capabilities. If the M&S analyst somehow meets this requirement, then the model is *valid* or *accredited*, and its results can be used to cover higher level requirements. If the requirement is not met, significant rework is required. For the reasons described above, this has never been a practical approach. We argue that the “translation” of M&S requirements should actually be a negotiation of capability vs. intended use. Building an argument for covering requirements must be done based on knowledge of M&S capabilities, and as those capabilities evolve, or more information about capabilities is uncovered, the intended uses must change.

If we accept that M&S requirements will evolve as a negotiation between intended uses versus capabilities, we still need a framework for comparing the two. We propose that decision theory is a suitable approach – the predictive capability must be good enough for the customer to feel they can make a high quality AND risk-informed (see definition below) decision about intended use. A high quality decision is one where you are confident that the action taken was the best available, based on the available information. Too often, decisions are poor quality because we lack the proper information and a consistent process to analyze the information. We maintain that high quality, risk-informed decisions are possible, but they require a combination of predictions, uncertainty analysis, and credibility assessments. The ability to make such a decision is related to the available information (predictions, tests, uncertainty analysis) and the quality of that information (credibility).

This paper will dig deeper into this argument with the goal of exposing a gap between the stated purpose of V&V and the practical aspects of decision support. The authors’ aim for this paper is not to state a position as to how V&V should be done but to start the conversation about our role in making engineering decisions.

We start with some crucial terminology, but we stress that these are working definitions that we apply to the contents of this paper and are not assumed to be universally accepted.

- Verification – the process of confirming that a governing equation has been properly implemented into a mathematical model and solved correctly
- Validation – the process of confirming that a governing equation and the associated model are indicative of reality for a target application
- Uncertainty quantification – the process of mathematically characterizing unknown/random features and variables in a target application and predicting their influence on a quantity of interest
- Value – the benefit achieved as a result of a particular event
- Risk – the expected loss associated with a particular event or set of events
- Risk management – the identification, assessment, and prioritization of risks followed by coordinated and economical application of resources to minimize, monitor, and control the probability and/or impact of unfortunate events [2]
- Credibility – the believability of a message or conclusion, as determined by objective and subjective components including the expertise of the source and the quality and completeness of the available information

As a starting point for this paper, we conducted a limited review of published work on this topic [3–7]. This is not an exhaustive literature search but provides a means to identify established processes in other organizations, and understand the concepts and principles and cultural issues to explain why they work. One formal framework to establish confidence in an extrapolated system level model response within the context of nuclear weapons was proposed at Sandia National Laboratories (referred to as Sandia hereafter) and it is referred to as Risk Informed Decision Analysis (RIDA). A central statement of RIDA which provides the main motivation for this research states [8]:

“Whatever mathematical form an application of Risk Informed Decision Analysis (RIDA) to a stockpile lifecycle decision might take, it requires that all uncertainties be identified and characterized. This includes the separate quantification of both variability (i.e., aleatoric uncertainty) and lack-of-knowledge uncertainty (i.e., epistemic uncertainty), as well as definitions of “other factors” and quantified characterizations of their individual contributions to uncertainty. RIDA also requires attention to uncertainties in requirements and decision criteria, such as definitions of performance thresholds that are fundamental to the decision making. In addition, RIDA requires complete transparency of all the information to make the decision process understandable, traceable, and reproducible (documented).”

A key feature in the statement above is the last sentence which implies a formal process leading to the decision making effort, in order to achieve the required level of transparency. Addressing this fact in a systematic way is what motivates this

paper and thus, we organize this paper by posing questions and providing commentary – not answers. The “best” way to support and influence engineering decisions, based on M&S, V&V, and UQ evidence, is very much open to debate. The questions are posed at three levels.

First level:

1. What is the relationship between V&V, credibility, and uncertainty?
2. How does V&V/UQ evidence and communication impact risk perception?
3. What is and how to characterize risk?
4. What is the “decision rule” that takes into account all the available information to make an engineering decision? What principles underlie this rule? Risk management? Value maximization?

Second level

1. In the presence of risk, how to allocate resources towards testing, M&S, V&V, UQ, etc.?
2. What is the best process to determine whether a model is valid?
3. What is the role of the Subject Matter Expert and peer review?

Third level:

1. What validation metric should I use?
2. How many Monte Carlo samples do I need?
3. How good is good enough? Is my model valid?

The questions at the third level are representative of much of the published work in the V&V and UQ fields. Indeed the focus of V&V and UQ research at Sandia has been on developing methods, metrics, heuristics, etc. The second level is more general, asking questions about the processes of an engineering organization. The first level is the most abstract – dealing with the concepts and principles that govern how decisions are made. In this paper, we focus on first level – the most abstract. The hope is that providing clarity on the principles will highlight the cultural and procedural changes that are required to connect M&S, V&V, and UQ work to decision making. Then the detailed, practical questions of methods and metrics will become more meaningful.

## 28.2 How Are M&S, V&V/UQ and Credibility Connected to Decision Making and Risk?

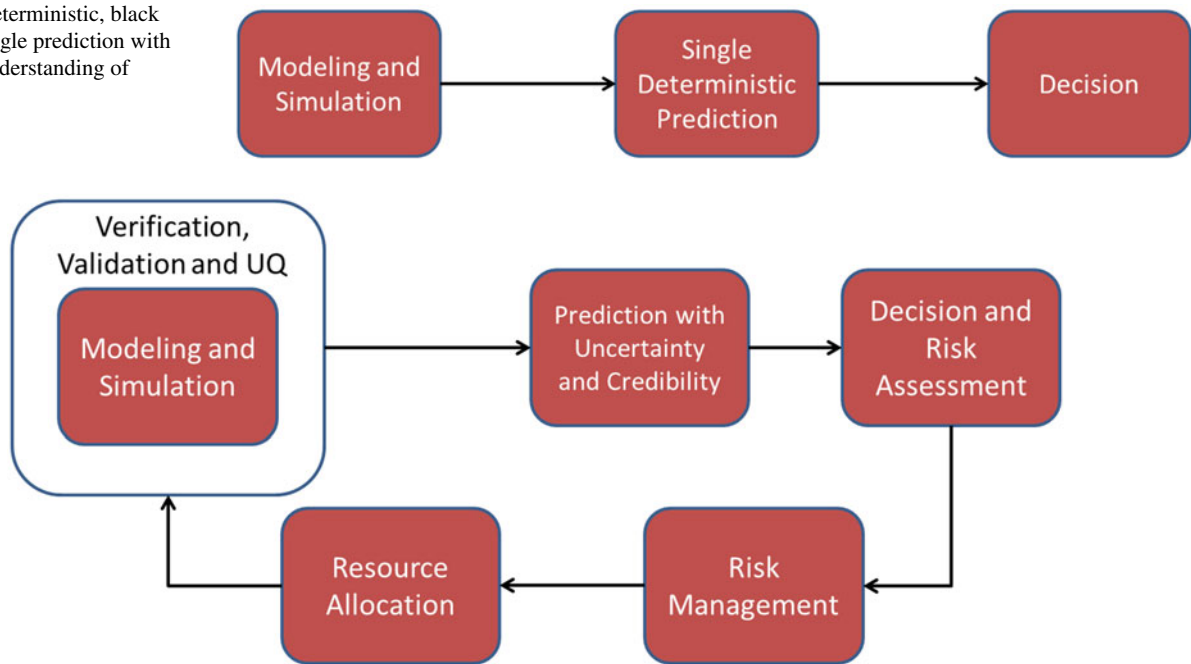
The answer to this question has everything to do with the engineering culture. *A fundamental question is: what is the effect of a certain activity – testing, M&S, V&V, UQ, etc. – in the total uncertainty vs. credibility space.* For example, doing UQ improves the understanding of uncertainty in predictions but the particular method used to quantify the uncertainty can introduce epistemic uncertainty; in addition, the boundary conditions might not be well characterized, reducing the credibility of the result (garbage in, garbage out). So in this case, perhaps the fidelity of our uncertainty calculations are increased, but the credibility of our results could potentially go down. Credibility is a subjective thing, and institutional knowledge and experience are key inputs. *The second question is how uncertainty and credibility maps to decision making and risk.*

To begin addressing the topic of this section, we have arbitrarily divided the problem into two broad categories: (1) where V&V/UQ is not part of the process and (2) where V&V/UQ is integrated into the workflow. These categories are illustrated below and some commentary on each one is made. To reiterate, the purpose of this paper is not to critique any particular approach or to suggest one is superior to another but merely to contrast between them and highlight the positive aspects and shortcomings of each one.

### 28.2.1 Case 1: A Deterministic Workflow

The first case, shown in Fig. 28.1, represents a workflow that is pervasive in many industries. It involves a deterministic M&S single prediction with no formal understanding and treatment of uncertainty or credibility. This leads to a decision which can be characterized as uninformed (i.e. sources of uncertainty not identified and/or incorporated into the analysis) and thus yielding little understanding of value and risk. In this case, the decision maker relies on expert opinion and “tribal knowledge” to prescribe a level of risk associated with the M&S predictions that are presented. In such a scenario, the concept of “I trust this predictions because analyst XYZ made them and has years of experience in this field” are commonplace and

**Fig. 28.1** Deterministic, black box M&S single prediction with little to no understanding of uncertainty



**Fig. 28.2** M&S with elements of V&V and UQ incorporated into the process

serve as the basis for assigning credibility to an M&S body of work. One issue with the previous statements is that it is a subjective and biased way of assigning credibility of M&S prediction. We are not discounting the value of experience in the process of decision making but it is possible that a less experienced analyst could provide similar or even technically superior predictions yet his/her results will be highly questioned and at worse, dismissed mainly based on perception. We feel this is one of the biggest risks in not having a systematic approach to determining credibility in an M&S prediction. On the positive side, this approach has been in place for many years and it is used by industry to inform and guide decisions on a regular basis. Both analysts and decision makers are comfortable with this mainly due to familiarity with this.

### 28.2.2 Case 2: An M&S and V&V/UQ Integrated Workflow

In contrast to Case 1, the second case, shown schematically in Fig. 28.2, represents an attempt to integrate the elements of V&V/UQ into the decision making process. It is noted from the figure that the process is not linear or serial but a recursive process where feedback loops help to enhance various aspect of the process. M&S, when elements of V&V and UQ are integrated into the process, will yield predictions plus an estimate of uncertainty and an assessment of credibility. This provides the basis for formal risk analysis, given the activities that were and were not performed, which we believe will lead to better informed decisions. This knowledge leads naturally to risk management/mitigation opportunities. Figure 28.2 includes the pieces that we believe are necessary, but not sufficient, for supporting decisions.

This figure leads to many different discussion topics, described over the next few paragraphs.

- Decisions must be made with some purpose or context beyond model predictions, which we define as the intended uses of M&S. To reiterate, the intended use is an argument that the presented M&S evidence proves that a requirement is satisfied. We will adopt the concept of “use risk” [5] to mean the risk that an intended use argument is flawed. This could occur for many reasons, which we leave for future discussion. This concept of use risk should drive the development, verification, validation, and eventual use of models.
- The depiction as a loop is an attempt to contrast this approach from a waterfall method. Each iteration should improve the convergence of predictive capability and intended uses. The loop is completed when modeling results are communicated to decision makers.

- We believe that distinct concepts of uncertainty and credibility are useful in this setting. We also envision that this identification of uncertainties and risks will naturally lead to a formulation in which the optimal allocation of resources, to reduce risk and improve decisions, can be achieved. This is further explored later in this paper.

We note that a decision can be made in both cases presented above. However, the first case must rely entirely on “intangibles” like assumptions, experience, credibility of the person(s) informing the process, etc., while the second provides the necessary evidence to make a defensible, high-quality, informed decision. Since risk assessment is an intrinsic element in this workflow, it is possible to introduce risk management and mitigation processes into the workflow. This is a fundamentally different way of thinking; one that emphasizes a system’s engineering approach to the problem. In other words by looking at the “big picture”, it can enable to make informed decisions at the analysis level.

To enable the upper left box in Fig. 28.2 (i.e. the integration of M&S and V&V/UQ), we have developed an integrated M&S/V&V/UQ workflow and it is shown in Fig. 28.3. The value proposition of this integrated workflow is the identification of an end-to-end path which includes elements of V&V/UQ leading to a customer driven deliverable.

In the context of Fig. 28.2 which includes elements of credibility and risk assessment, the integrated workflow is envisioned to aid in the following ways. It clearly outlines the steps that are needed to comprehensively perform an end-to-end M&S activity with the proper context in mind. It provides an opportunity to adjust the scope of the effort by “pruning” those elements (i.e. the boxes in the workflow) that are unattainable due to funding, schedule and/or technical impediments. It is this “pruning” of elements that introduce risk in to the process. For example, if the Code Verification element, which addresses how good is the software that is used to run an analysis, is “pruned”, the net effect is felt downstream of this element. Thus there is a significant risk involved (and a corresponding reduction in credibility) due to this step being eliminated from the workflow. At this point, there is no formal quantification of the amount of risk that is introduced into the process by “pruning” any particular box or boxes in the workflow. This is a qualitative assessment. Future research will be needed to determine if there is any practical way to quantify this. Also the amount of risk is highly dependent on the context (or intended use) of the M&S activity. For example, if the analysis is mainly to understand a relative behavior of a quantity of interest, then the risk is fairly low. Conversely, if the analysis is supporting a major decision say, certification of an airplane, then the risk associated with the “pruning” of the Code Verification element is fairly high. It is thus imperative that both the context *and* the workflow that leads from requirements to deliverables are well defined.

### 28.2.3 *Communication of Credibility as a Function of M&S, V&V and UQ*

The credibility of a computational simulation analysis has historically been based largely on the experience of the analyst using a tool and judgment by that analyst on the suitability of the results produced for a particular application. At Sandia, we developed the Predictive Capability Maturity Matrix (PCMM) [9] to provide more structure and formality in assessing the credibility of an M&S analysis for a target application. This framework aims at reducing the ambiguity in such assessments, and to provide specificity as to what should be assessed and communicated to the analyst’s customer. PCMM evaluations have the potential to provide information for effective planning as well as for communication. The PCMM is based on six evaluation dimensions, or elements, that are deemed fundamentally important to the quality of an M&S analysis. These elements address (1) the fidelity in representing physics, including the material models; (2) the geometric fidelity in representing the system or subsystem element being modeled; (3) the completeness in addressing whether the computational simulation code has been verified from a software assurance point of view and (4) verified from a solution convergence point of view; (5) assessments against experimental data; and (6) the evaluation of uncertainty in the results due to uncertainties such as the input information used to characterize the specific geometry, environment, and material properties for the application. The current tool used at Sandia to perform the PCMM assessment is shown in Fig. 28.4.

## 28.3 Resource Allocation

When the result of the risk assessment is unacceptable, a mitigation strategy must be undertaken. Here we refer to this process as risk management. When the M&S analysis is done deterministically as in Case 1, risk management decisions must be made based largely on expert judgment. While domain experts frequently understand which aspects of their models are inadequate (w.r.t. physics fidelity or numerical resolution), they are not likely to be able to gauge the relative contributions of these aspects in the overall system prediction. By including UQ and credibility assessment in the analysis and decision process,



# V&V/UQ CompSim Workflow

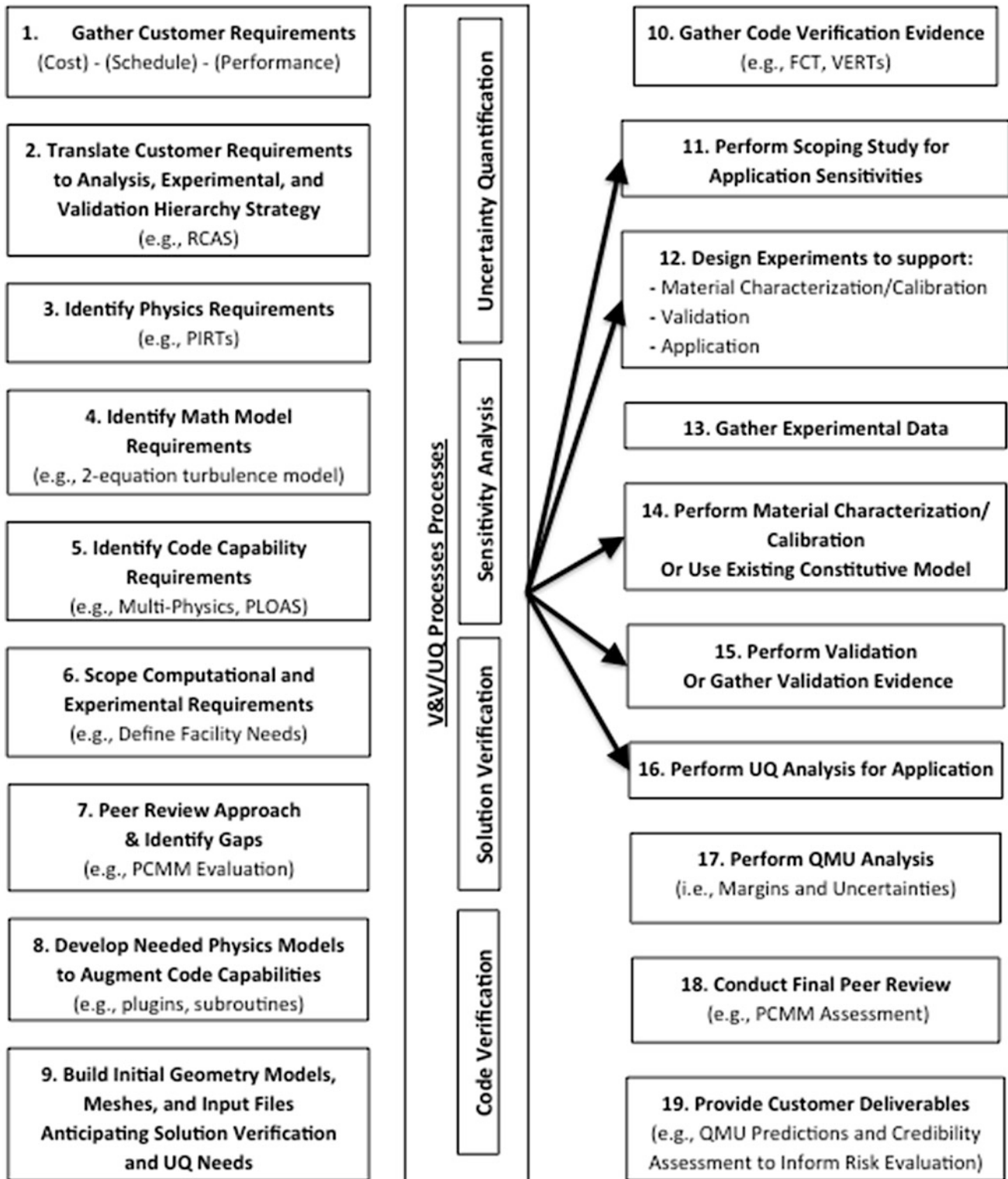


Fig. 28.3 Integrated M&S/V&V/UQ workflow

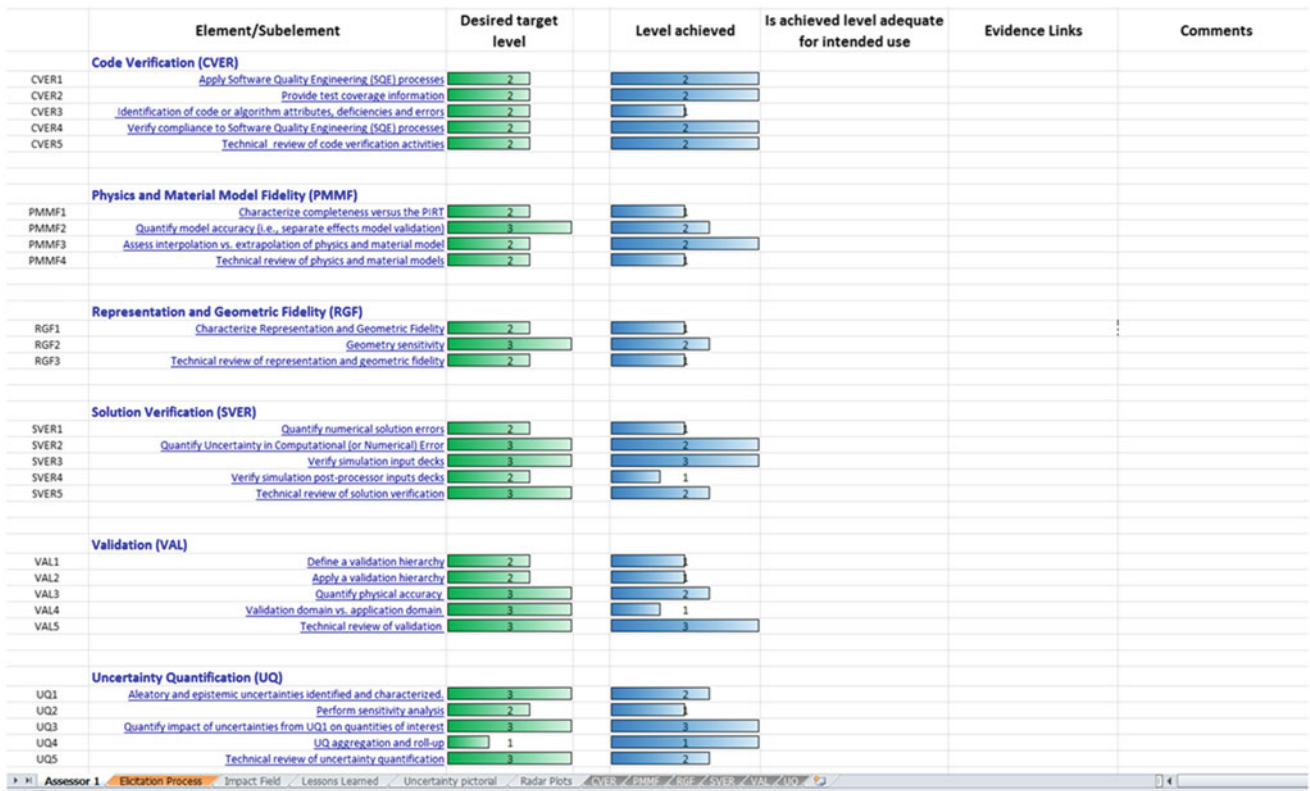


Fig. 28.4 PCMM tool’s main assessment sheet

the plans for future work can instead be made in a quantitative way that takes a comprehensive view of the system and the contributions of error and uncertainty sources to the various aspects of the system prediction. Since this risk management process is subject to budget constraints, an important issue is the proper allocation of resources to achieve the maximum benefit.

We explore a quantitative risk reduction-based strategy for resource allocation [10, 11]. Classically, the risk of an event (e.g. system failure) has two key components: (1) the probability of the event and (2) the consequences of the event. These two components have a simple, logical relationship, in which the risk  $S$  is a product of the consequence of an event  $L$  and the probability of the event  $P(L)$ .

$$S = L * P (L)$$

Within this context, risk can be viewed as the expected value of the cost of a particular failure scenario. For some systems, a relatively large failure probability does not pose a great risk because the failure event will not result in any particularly severe consequences. Therefore, the events of greatest concern are those that have both high probability and extreme consequence (e.g. human life loss and/or major property destruction). In many applications, there are many different potential risk events, and the overall system risk  $S_T$  is the summation of all of  $m$  discrete risk scenarios.

$$S_T = \sum_{i=1}^m L_i P (L_i)$$

Designers and decision-makers have little control over the consequences of an event, so risk minimization is achieved by reducing the probability of the negative events. This reduction is significantly enabled by minimizing prediction uncertainty while maintaining prediction accuracy (i.e. low bias).

From an economic perspective, it is not logical to spend large resources on UQ without also considering the total benefit of the analysis. Since risk can be directly interpreted as a cost, it provides a convenient space to analyze design and management decisions. The total cost of the UQ activities can then be viewed as a “risk” event with 100 % probability since the cost is

always incurred once the spending decision is made. Then, a reasonable overall goal for the decision maker is to minimize the total risk coming from these two components (the failure risk  $S_f$  and the UQ/model development cost  $S_d$ ). This view leads to the following formulation for determining how much UQ spending is enough:

$$\begin{aligned} S_d &= 1 * L_d \\ S_f &= p_f * L_f \\ S_T &= S_d + S_f \end{aligned}$$

Here,  $L_d$  is the total cost of UQ/development activities,  $p_f$  is the system failure probability, and  $L_f$  is the consequence of system failure. It is assumed that  $L_f$  is a constant that the decision maker cannot control, and  $L_d$  is the primary decision variable during the resource allocation phase of the process. With the overall goal of minimizing  $S_T$  the spending budget  $L_d$  must now be selected based on its impact on  $p_f$ , which is a dependent variable in the analysis that is affected by UQ and credibility assessment. The primary challenge is that the functional relationship between spending activities and failure probability reduction is never explicitly known. However, this framework emphasizes the importance of looking at these decisions at the level of the system prediction rather than making refinement decisions locally without specific regard for their overall impact.

Potential spending decisions that could be made include model selection, model improvement, and test selection. Since these are topics unto themselves in the literature and the intent of this paper is to provide a high-level framework for decision-making, we only mention them briefly here. Uncertainty propagation can be prohibitively expensive due to the large number of model evaluations that are needed. As a result, models of lower fidelity/complexity including reduced-order, reduced-physics, and mathematical surrogate models are often used for UQ activities. There is a tradeoff decision of accuracy vs. efficiency when selecting among these candidate models. Any of them may potentially be improved/refined, or they may be selected adaptively for different predictions. Additionally, these candidate models must be calibrated and validated, which couples the modeling decisions with test selection decisions. The number and type of calibration and validation tests that are performed impacts the quality of the models and therefore the quality of the prediction and associated UQ. For each of these decisions, the important consideration is the impact on the overall prediction uncertainty since it is directly tied to the system failure probability component of the total risk. This context for the decisions is critical to efficient resource allocation.

## 28.4 Summary

In this paper, we present a perspective of how elements of V&V/UQ and Credibility could be incorporated into the decision process. We acknowledge that this spans many topics, including: modeling, V&V/UQ methods, credibility assessments, risk management, and requirements management/systems engineering. We have developed an integrated workflow that is useful in understanding sources of use risk in the end-to-end analysis. To properly establish the importance of these sources of risk, it is imperative that both the context *and* the workflow that leads from requirements to M&S deliverables are well defined. We argue that the commonly discussed waterfall approach is impractical, and instead propose negotiation of intended uses. At present, risks arising from “pruning” elements in the workflow are mainly qualitatively defined. A quantitative solution is a future research direction which once established, will enable a more formal and mathematical treatment of the larger issue of resource allocation.

**Acknowledgments** The authors thank Simone Youngblood at JHU Applied Physics Laboratory, and Jason Jarosz at Sandia for many helpful discussions. Sandia is a multi-program laboratory operated by Sandia Corporation, a Lockheed Martin Company, for the United States Department of Energy’s National Nuclear Security Administration under Contract DE-AC04-94AL85000.

## References

1. Mayes RL (2009) Developing adequacy criterion for model validation based on requirements. In: IMAC-XXVII, Society for Experimental Mechanics, Orlando
2. Hubbard DW (2009) The failure of risk management: why it’s broken and how to fix it, 1st edn. Wiley, New York
3. Elele JN (2009) Assessing risk levels of verification, validation, and accreditation of models and simulations. In: Proceedings of modeling and simulation for military operations IV, SPIE, Orlando

4. Elele JN, Smith J (2010) Risk-based verification, validation, and accreditation process. In: Proceedings of modeling and simulation for defense systems and applications V, SPIE, Orlando
5. Youngblood SM et al (2011) Risk based methodology for verification, validation, and accreditation (VV&A) M&S use risk methodology (MURM). Johns Hopkins University Applied Physics Laboratory, Laurel. Report NSAD-R-2011-011
6. Nitta CK, Logan RW (2004) Qualitative and quantitative linkages from V&V to adequacy, certification, risk, and benefit/cost ratio. Lawrence Livermore National Laboratory, Livermore. Report UCRL-TR-205809
7. Blattnig SR et al (2009) Towards a credibility assessment of models and simulations. American Institute of Aeronautics and Astronautics, 2009002E
8. Pilch M et al (2006) Ideas underlying quantitative margins and uncertainty (QMU): a white paper. Sandia National Laboratories, SAND2006-5001, Unlimited Distribution
9. Oberkampf WL et al (2007) Predictive capability maturity model for computational modeling and simulation. Sandia National Laboratories, SAND2007-5948
10. Mullins J, Mahadevan S (2014) Variable-fidelity model selection for stochastic simulation. Reliab Eng Syst Saf 131:40–52. doi:[10.1016/j.ress.2014.06.011](https://doi.org/10.1016/j.ress.2014.06.011)
11. Mullins J, Li C, Mahadevan S, Urbina A (2014) Optimal selection of calibration and validation test samples under uncertainty. In: Conference proceedings of the society for experimental mechanics. Model validation and uncertainty quantification, vol 3. Orlando, pp 391–401

# Chapter 29

## A MCMC Method for Bayesian System Identification from Large Data Sets

P.L. Green

**Abstract** This paper addresses the situation where, with the aim of performing Bayesian system identification, one is presented with a very large set of training data (such that, because of computational restraints, only a subset of this data can be used). Presented here is a novel Markov chain Monte Carlo (MCMC) method which, by using concepts from the well-known Simulated Annealing algorithm, can ‘absorb’ subsets of training data in a smooth and continuous manner. This allows the user to track quantities of interest (such as the mean posterior parameter estimates) as a large set of training data is absorbed, terminating the algorithm when these quantities are judged to have converged. Furthermore, the algorithm is able to quickly absorb relatively uninformative data and concentrate instead on data sets which have a greater influence on the posterior parameter distribution (thus reducing computational cost).

**Keywords** Bayesian inference • Markov chain Monte Carlo • Shannon entropy • Big data

### 29.1 Introduction

Defining  $\mathcal{M}$  as one of a set of candidate models and  $\boldsymbol{\theta} \in \mathbb{R}^{N_\theta}$  as the vector of parameters within that model then it is well known that, to access the probability of  $\mathcal{M}$  and  $\boldsymbol{\theta}$  conditional on some training data  $\mathcal{D}$ , one can simply apply Bayes’ theorem in a sequential manner:

$$P(\boldsymbol{\theta}|\mathcal{D}, \mathcal{M}) = \frac{P(\mathcal{D}|\boldsymbol{\theta}, \mathcal{M})P(\boldsymbol{\theta}|\mathcal{M})}{P(\mathcal{D}|\mathcal{M})}, \quad P(\mathcal{M}|\mathcal{D}) = \frac{P(\mathcal{D}|\mathcal{M})P(\mathcal{M})}{P(\mathcal{D})}. \quad (29.1)$$

$P(\boldsymbol{\theta}|\mathcal{M})$  and  $P(\mathcal{M})$  are priors—probability distributions which represent one’s knowledge of the system before the data was known—while  $P(\boldsymbol{\theta}|\mathcal{D}, \mathcal{M})$  and  $P(\mathcal{M}|\mathcal{D})$  are known as the posterior parameter and posterior model distributions respectively.  $P(\mathcal{D}|\boldsymbol{\theta}, \mathcal{M})$ —the probability of witnessing the data  $\mathcal{D}$  given a model  $\mathcal{M}$  with parameters  $\boldsymbol{\theta}$ —is known as the likelihood and requires the definition of a ‘prediction-error model’ whose parameters, conveniently, can be included in  $\boldsymbol{\theta}$ .  $P(\mathcal{D}|\mathcal{M})$  not only acts as a normalising constant for the posterior parameter distribution but also provides evidence for the model  $\mathcal{M}$  in the second application of Bayes’ theorem and, as such, is commonly referred to as the ‘model evidence’. Bearing in mind its role as a normalising constant, the model evidence is defined as

$$P(\mathcal{D}|\mathcal{M}) = \int P(\mathcal{D}|\boldsymbol{\theta}, \mathcal{M})P(\boldsymbol{\theta}|\mathcal{M})d\boldsymbol{\theta}. \quad (29.2)$$

A particularly useful aspect of adopting this approach is that, with regard to the posterior model distribution, models tend to be ‘rewarded’ with high probabilities if they are able to replicate a set of training data without being overly complex. In other words, the successful evaluation of  $P(\mathcal{M}|\mathcal{D})$  can be used to help one select a model which is not over-fitted (see [1] for more details).

In situations where the response of  $\mathcal{M}$  with parameters  $\boldsymbol{\theta}$  is intractable, then a numerical simulation is required to evaluate the posterior parameter distribution at a particular point  $\boldsymbol{\theta}$ . In such a scenario one can choose to generate samples from  $P(\boldsymbol{\theta}|\mathcal{D}, \mathcal{M})$  using Markov chain Monte Carlo (MCMC) methods (which involve the generation of an ergodic Markov chain whose stationary distribution is equal to some target which, in this case, is the posterior parameter distribution).

---

P.L. Green (✉)

Department of Mechanical Engineering, University of Sheffield, Sir Frederick Mappin Building, Mappin Street, S1 3JD, South Yorkshire, UK

Institute for Risk and Uncertainty, The Quadrangle, University of Liverpool, Brownlow Hill, Liverpool L69 3GH, UK

e-mail: [P.L.Green@liverpool.ac.uk](mailto:P.L.Green@liverpool.ac.uk)

MCMC is particularly useful as it provides a relatively cheap way of generating samples from a potentially high-dimensional probability distribution. Early MCMC methods such as the Metropolis algorithm [2] can be used to sample from a distribution proportional to  $P(\boldsymbol{\theta}|\mathcal{D}, \mathcal{M})$ , which avoids the need to evaluate the high-dimensional integral given by Eq. (29.2) (but, as a result, prevents one from analysing the posterior model distribution). Since then an array of advanced algorithms [3–6] have been developed which allow one to evaluate both the posterior parameter and posterior model distributions.

This brings one to the motivation behind the current paper: while MCMC methods are undoubtedly powerful they can prove to be rather expensive if one is using a large set of training data. This is simply because, to evaluate the posterior parameter distribution at a single point one has to, using numerical simulation techniques, analyse the ability of the model to replicate the whole data set  $\mathcal{D}$ . This issue is becoming increasingly common place as wireless sensors become cheaper and more reliable—simply put, it is easy to install a large network of sensors but it is difficult to analyse the resulting large data sets. This paper presents a MCMC algorithm which is designed to deal with this ‘big data’ phenomenon.

## 29.2 Background

The algorithm proposed here builds on two other pieces of work, which are briefly introduced in this section. The first is the Data Annealing (DA) [7] algorithm—an MCMC method which was designed to deal with large data sets. Briefly stated, DA involves using MCMC to target the distribution:

$$\pi(\boldsymbol{\theta}) \propto P(\mathcal{D}_1^N|\boldsymbol{\theta})P(\boldsymbol{\theta}) \quad (29.3)$$

where  $\mathcal{D}_1^N = \{\mathcal{D}_1, \mathcal{D}_2, \dots, \mathcal{D}_N\}$  is a small subset of the training data. One begins with a small value of  $N$  before allowing it to increase as the Markov chain evolves. This has the effect of gradually increasing the effect of the data on the posterior parameter distribution (in a similar manner to the well-known Simulated Annealing algorithm [8]). One then simply stops the algorithm when it is judged that a sufficient amount of information has been inferred from the data. While DA provides a faster way of dealing with large data sets it has a disadvantage: one doesn’t know before-hand how the addition of some new data points will alter the target distribution. Not only can this slow the convergence of the MCMC method being employed but can also lead to wasted time, where the algorithm is ‘absorbing’ data points which have very little influence over one’s parameter estimates.

In the current paper the aim is to improve the performance of DA using the concept of ‘highly informative training data’ [9], where one separates out smaller ‘information rich’ sets from a larger set of training data. Specifically, the aim is to develop a variant of DA which will quickly ‘skip over’ uninformative data and, as a result, focus on the data which contains a large amount of information about one’s parameter estimates.

## 29.3 Proposed Method

### 29.3.1 Basic Methodology

Consider beginning with a small subset  $\mathcal{D}_1^N$  of a large set of training data. To introduce this data in a smooth and continuous manner one can use MCMC to target

$$\pi_{\beta_j}(\boldsymbol{\theta}|\mathcal{D}_1^N) \propto P(\mathcal{D}_1^N|\boldsymbol{\theta})^{\beta_j} P(\boldsymbol{\theta}) \quad (29.4)$$

while  $\beta_j$  is steadily increased from 0 to 1—at this point the proposed algorithm uses the same procedure as Simulated Annealing (where the increasing sequence of  $\beta$  values is the annealing schedule). Once  $\beta = 1$  and  $\mathcal{D}_1^N$  has been fully ‘annealed in’ then one can introduce a further  $k$  data points by targeting:

$$\pi_{\beta_j}(\boldsymbol{\theta}|\mathcal{D}_1^{N+k}) \propto P(\mathcal{D}_1^N|\boldsymbol{\theta})P(\mathcal{D}_{N+1}^{N+k}|\boldsymbol{\theta})^{\beta_j} P(\boldsymbol{\theta}) \quad (29.5)$$

(assuming mutual independence between  $P(\mathcal{D}_1^N|\boldsymbol{\theta})$  and  $P(\mathcal{D}_{N+1}^{N+k}|\boldsymbol{\theta})$ ) and, once again, use  $\beta$  to gradually increase the influence of this new data. The aim here is to ensure that relatively uninformative data is annealed in quickly thus allowing the algorithm to focus on absorbing more informative data. To achieve this, one can aim to use an annealing schedule which will ensure that the information in the data—measured using the Shannon entropy in this case—is introduced at a constant rate. Expressions detailing how such an annealing schedule can be created are derived in the next section.

### 29.3.2 Constant Entropy Variation

At this point it is convenient to write the target PDF as

$$\pi = \frac{\exp(-\beta \hat{J}_L - J_L - J_P)}{Z} \quad (29.6)$$

where

$$\hat{J}_L = -\ln P(\mathcal{D}_{N+1}^{N+k} | \theta), \quad J_L = -\ln P(\mathcal{D}_1^N | \theta), \quad J_P = -\ln P(\theta). \quad (29.7)$$

Furthermore, the notation  $\pi = \pi^*/Z$  will be used (where  $Z$  is the normalising constant of  $\pi^*$ ). One begins by first proving the following relations:

$$\frac{d\pi^*}{d\beta} = -\hat{J}_L \pi^*, \quad \frac{dZ}{d\beta} = -Z E[\hat{J}_L], \quad \frac{d\pi}{d\beta} = \pi(E[\hat{J}_L] - \hat{J}_L). \quad (29.8)$$

The Shannon entropy of the target distribution is

$$S = \beta E[\hat{J}_L] + E[J_L] + E[J_P] + \ln(Z) \quad (29.9)$$

as so the aim here is to evaluate the derivative:

$$\frac{dS}{d\beta} = \frac{d}{d\beta} (\beta E[\hat{J}_L]) + \frac{d}{d\beta} (E[J_L]) + \frac{d}{d\beta} (\ln(Z)). \quad (29.10)$$

Using the relations in Eq. (29.8), the first term of Eq. (29.10) is:

$$\frac{d}{d\beta} (\beta E[\hat{J}_L]) = E[\hat{J}_L] + \beta \frac{d}{d\beta} \int \hat{J}_L \pi d\theta \quad (29.11)$$

$$= E[\hat{J}_L] + \beta (E[\hat{J}_L]^2 - E[\hat{J}_L^2]) = E[\hat{J}_L] - \beta \text{Var}(\hat{J}_L), \quad (29.12)$$

while the second term is:

$$\frac{d}{d\beta} (E[J_L]) = \frac{d}{d\beta} \int J_L \pi d\theta \quad (29.13)$$

$$= \int J_L \pi (E[\hat{J}_L] - \hat{J}_L) d\theta \quad (29.14)$$

$$= E[J_L] E[\hat{J}_L] - E[J_L \hat{J}_L] = -\text{Cor}(J_L, \hat{J}_L) \quad (29.15)$$

(where ‘Cor’ represents the unnormalised correlation coefficient) and, finally, the third term is:

$$\frac{d}{d\beta} (\ln Z) = \frac{1}{Z} (-Z E[\hat{J}_L]) = -E[\hat{J}_L]. \quad (29.16)$$

From this it follows that:

$$\frac{dS}{d\beta} = -\beta \text{Var}(\hat{J}_L) - \text{Cor}(J_L, \hat{J}_L) \quad (29.17)$$

and so, to ensure that one's annealing schedule guarantees that the change in Shannon entropy of the posterior parameter distribution is equal to some predefined limit  $\Delta S$ , one should select  $\beta$  according to:

$$\beta_{j+1} = \beta_j - \frac{\Delta S}{\beta_j \text{Var}(\hat{J}_L) + \text{Cor}(J_L, \hat{J}_L)}. \quad (29.18)$$

### 29.3.3 Does Data Reduce Uncertainty?

A flaw in the algorithm presented thus far is that it is based on the assumption that new data will reduce one's uncertainty in the parameter estimates (and therefore reduce the Shannon entropy of the posterior parameter distribution). This is not always the case—it is easy to envisage a scenario where some new data contradicts the old data. However, one can make use of the classic result:

$$E[\text{Var}(\boldsymbol{\theta}|\mathcal{D})] = \text{Var}(\boldsymbol{\theta}) - \text{Var}(E[\boldsymbol{\theta}|\mathcal{D}]) \quad (29.19)$$

which states that, on *average*, new data must reduce the variance of the posterior parameter distribution. The upshot of this is that the algorithm needs to be altered slightly to allow for the fact that new data will not always reduce the Shannon entropy of the target distribution. To do so one simply needs to anneal according to:

$$\beta_{j+1} = \beta_j - \frac{\Delta S}{\beta_j \text{Var}(\hat{J}_L) + \text{Cor}(J_L, \hat{J}_L)} \quad (29.20)$$

subject to the constraints that

$$\beta_j < \beta_{j+1} \leq 1, \quad -\Delta S_{\text{lim}} < \Delta S < \Delta S_{\text{lim}}. \quad (29.21)$$

This ensures that the annealing schedule is still strictly increasing and that the absolute change in Shannon entropy is always less than some predefined limit  $\Delta S_{\text{lim}}$ .

## 29.4 Example

Here the algorithm is used to identify the linear stiffness  $k$ , nonlinear stiffness  $k_3$  and damping  $c$  present in a forced Duffing oscillator:

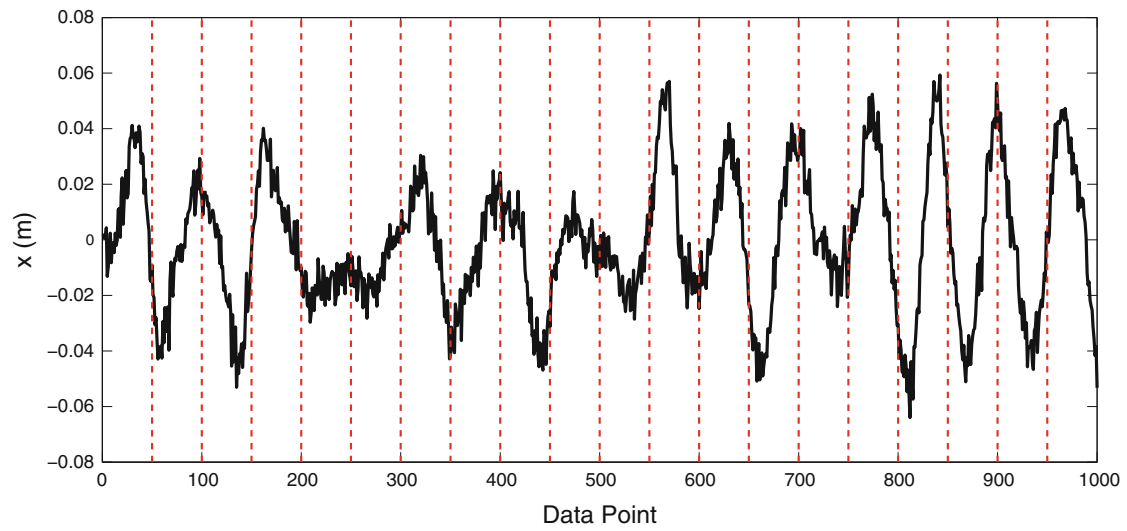
$$m\ddot{x} + c\dot{x} + kx + k_3x^3 = F \quad (29.22)$$

where  $F$  is zero-mean Gaussian white noise. These parameters were to be inferred using a set of time history data which had been artificially corrupted with Gaussian 'measurement noise'. This full set of data was delivered to the algorithm in 50 point segments, as shown in Fig. 29.1. A Gaussian prediction-error model with standard deviation  $\sigma$  was used to form the likelihood (where  $\sigma$  was included in  $\boldsymbol{\theta}$  as a parameter to be estimated). Furthermore, Gaussian prior distributions were employed—the true parameter values as well as the moments of  $P(\boldsymbol{\theta}|\mathcal{M})$  are given in Table 29.1.

Setting  $\Delta S_{\text{lim}} = 1$  the algorithm was run, and the sequence of annealing schedules shown in Fig. 29.2 were realised. It is interesting to note that not all of the data led to a decrease in Shannon entropy (although most of it did) and that, after annealing in the first 40 segments, the algorithm was able to quickly absorb the remaining data.

It was noted earlier that one can simply track properties of interest until, once they are judged to have converged, the algorithm can be terminated. Figure 29.3 shows how the posterior parameter distribution converged to and narrowed around the true parameter values as data was added. It is interesting to note that other properties can also be monitored—using MCMC to estimate the covariance matrix of the posterior parameter distribution, Fig. 29.4 shows how the negative correlation between the linear and nonlinear stiffness terms become increasingly obvious as more training data was used.

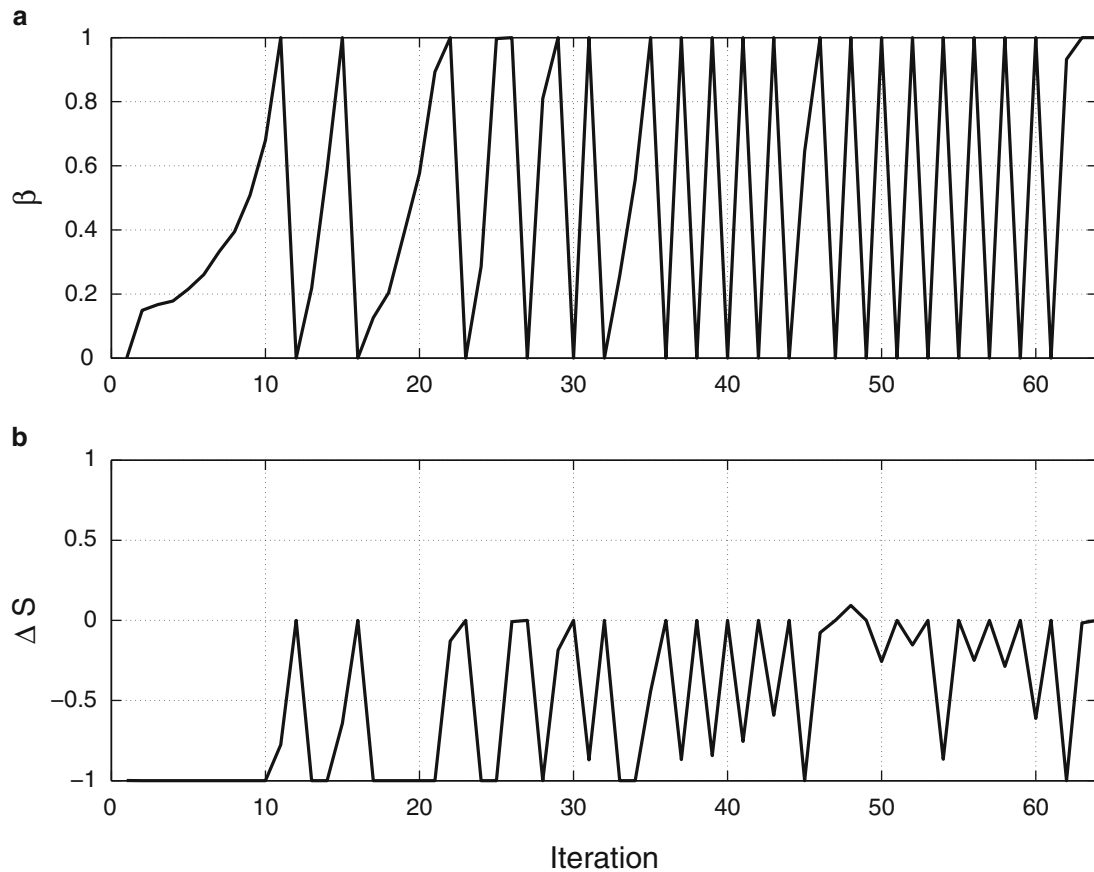




**Fig. 29.1** Training data

**Table 29.1** True parameter values and moments of prior distributions

Parameter	True value	Prior mean	Prior standard deviation	Units
$k$	100	150	30	N/m
$c$	0.05	0.02	0.02	Ns/m
$k_3$	100,000	40,000	20,000	N/m <sup>3</sup>
$\sigma$	0.005	0.0045	0.002	—



**Fig. 29.2** Resulting annealing schedules

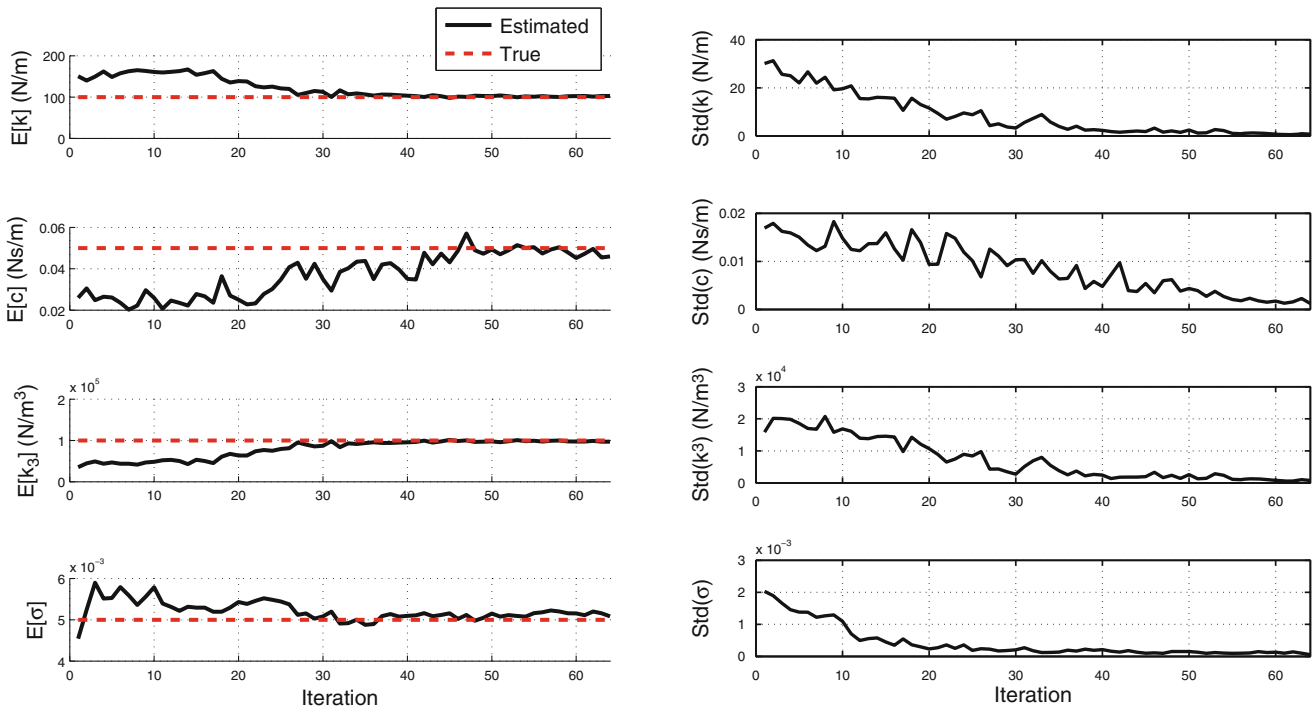
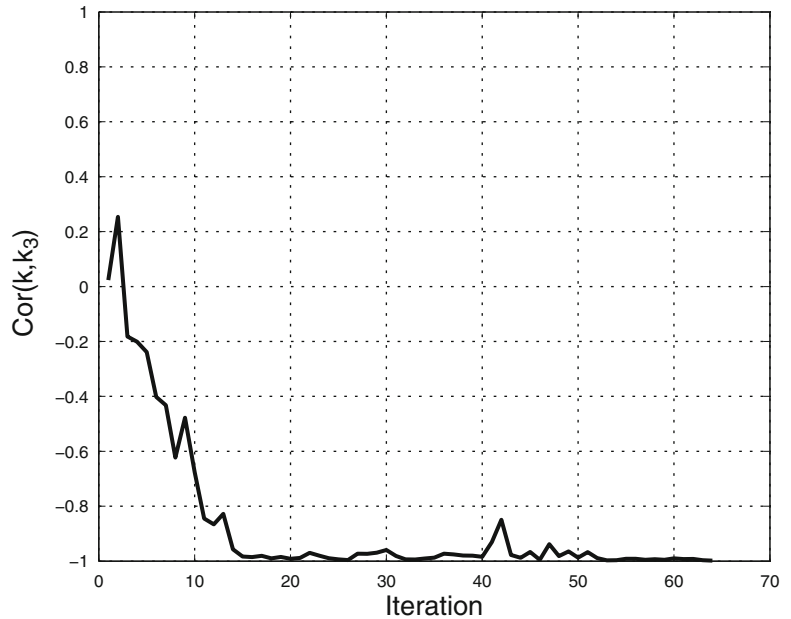


Fig. 29.3 Tracking the mean and standard deviation of the posterior parameter distribution as training data is added

Fig. 29.4 Tracking the (normalised) correlation between  $k$  and  $k_3$  as training data is added



### 29.5 Conclusions

In this paper a MCMC algorithm is presented which, via a Bayesian framework, can be used to infer probabilistic parameter estimates from large data sets. Simply stated, the algorithm is able to divide a large data set into smaller subsets which can then be ‘absorbed’ in a gradual and continuous manner. The algorithm is designed such that relatively uninformative data is absorbed quickly, thus allowing it to focus on data which will have a greater influence over the uncertainty in one’s parameter estimates. Furthermore it allows for the fact that, in some cases, new data can provide contradictory information which leads to an increase in uncertainty. The performance of the algorithm is demonstrated using a simulated example.

**Acknowledgements** The author would also like to acknowledge funding from the EPSRC programme grant ‘Engineering Nonlinearity’ EP/K003836/1.

## References

1. Muto M, Beck JL (2008) Bayesian updating and model class selection for hysteretic structural models using stochastic simulation. *J Vib Control* 14(1–2):7–34
2. Metropolis N, Rosenbluth AW, Rosenbluth MN, Teller AH, Teller E (1953) Equation of state calculations by fast computing machines. *J Chem Phys* 21(6):1087–1092
3. Green PJ (1995) Reversible jump Markov chain Monte Carlo computation and Bayesian model determination. *Biometrika* 82(4):711–732
4. Skilling J (2006) Nested sampling for general Bayesian computation. *Bayesian Anal* 1(4):833–859
5. Ching J, Chen YC (2007) Transitional Markov chain Monte Carlo method for Bayesian model updating, model class selection, and model averaging. *J Eng Mech* 133(7):816–832
6. Beck JL, Zuev KM (2013) Asymptotically independent Markov sampling: a new Markov chain Monte Carlo scheme for Bayesian inference. *Int J Uncertain Quantif* 3(5):445–474
7. Green PL (2014) Bayesian system identification of a nonlinear dynamical system using a novel variant of simulated annealing. *Mech Syst Signal Process*. doi:10.1016/j.ymsp.2014.07.010
8. Kirkpatrick S, Gelatt CD, Vecchi MP (1983) Optimization by simulated annealing. *Science* 220(4598):671–680
9. Green PL, Cross EJ, Worden K (2014) Bayesian system identification of dynamical systems using highly informative training data. *Mech Syst Signal Process*. doi:10.1016/j.ymsp.2014.10.003

# Chapter 30

## Bayesian Inference for Damage Detection in Unsupervised Structural Health Monitoring

Reza Mohammadi-Ghazi and Oral Buyukozturk

**Abstract** This paper presents a preliminary study on developing a new algorithm for making inference on the unsupervised structural health monitoring problems in a Bayesian framework. The main constraint in such problems, besides their unsupervised nature, is the small size of data set. Secondly, most often, there is no numerical model or enough empirical data for computing an appropriate prior density for Bayesian data analysis. Gaussian Mixture Model (GMM) and Kernel Density Estimate (KDE) are the main tools which are used in this paper for density estimation under the constraint on the size of data sets. To solve the second issue, an empirical Bayesian approach is employed for computing a prior density without any model; therefore, this algorithm provides an approximation to the standard Bayesian inference technique. An important aspect of the proposed algorithm is that it provides posterior probabilities for the intact or damaged states of the structure. Such results can be directly used for cost analysis and decision making in such unsupervised problems. The efficacy of the algorithm is experimentally verified by testing a three-story two-bay steel laboratory structure. The results show that the algorithm can effectively detect and localize the damages.

**Keywords** Uncertainty quantification • Structural health monitoring • Bayesian inference • Empirical Bayes • Gaussian mixture model • Kernel density estimate

### 30.1 Introduction

The goal of structural health monitoring (SHM) is to ensure safe operation and maintenance cost reduction of various mechanical systems from civil to aerospace structures. Vibration-based SHM is one of the main and most applicable methodologies for monitoring large scale complex structures. Basically, vibration-based SHM can be defined as detection/localization of damage by employing appropriate techniques for solving an inverse problem given only the vibrational response of structure. Non-unique solutions for such ill-posed inverse problem, variability of system's physical properties, and measurement noise are the main sources of uncertainties in vibration-based SHM. From the practical point of view, quantification of such uncertainties is essential for applicability of a damage detection algorithm; otherwise, its results cannot be used for decision making process which is the last link in any monitoring system in real world.

The vibration-based damage detection algorithms can be categorized into two main subgroups: model-based and data-based. Uncertainty quantification (UQ) for model-based methods is usually referred to statistical modeling techniques for computing the distribution of some characteristics of interest [1–6]. Tuning a model with experimental data in a Bayesian framework [7] and model updating for the case of incomplete data [8] are examples statistical modeling for the sake of damage detection. The propagation of uncertainties through the estimation of the models' characteristics is the modern aspect of UQ for statistical modeling. In data-based approach, which is the topic of the current paper, the concept of UQ is mostly referred to computing the confidence one may have on the final results of an algorithm. Finding the probability density function (PDF) associated with the different states, intact/damaged, of the system can be regarded as the ultimate goal of UQ in data-based approach. Note that such quantification takes care of the measurement uncertainties and their propagation into the data analysis process. This task is too difficult to do if some information is available from all states of the structure; nevertheless, this condition is not satisfied in most SHM problems. Empirical data from all damaged states of the system is not available when it is being monitored and the problem of simulating all possible damage scenarios in the structure is computationally intractable. Thus, such a problem is unsupervised, meaning that there is no information from some states of the structure. A two-phase approach has been proposed for this problem in [9] which estimates the PDF of some modal

---

R. Mohammadi-Ghazi • O. Buyukozturk (✉)

Department of Civil and Environmental Engineering, Massachusetts Institute of Technology, 77 Massachusetts Ave, Cambridge, MA, USA  
e-mail: [obuyuk@mit.edu](mailto:obuyuk@mit.edu)

properties of the structure as the initialization phase. Then, for the monitoring phase, the structure is tested periodically and the same properties are estimated for each test. The structure is classified as damaged if the difference between the new data and the baseline is greater than a pre-defined threshold. The main issue regarding this approach is defining an appropriate threshold which can significantly affect the robustness of SHM algorithms and false positive/negative rates. This issue is more critical for the algorithms that consider modal properties since they are also highly sensitive to environmental effects.

Another approach for UQ of such unsupervised problems is hypothesis testing. This method has been applied to some damage detection problems and the results have been verified both numerically and experimentally in [6, 10]. In another study, this technique has been employed and experimentally verified for the case of using multiple damage sensitive indices while the size of data set is small [11]. Basically, one of the main strengths of hypothesis testing is its stability and low error compared to other inference algorithms when the size of available data set is small even though the problem is unsupervised [11–14]. Note that this method represents the uncertainties in terms of  $p$ -values which are the probability of accepting a null hypothesis. The concept is completely different from the actual probability associated with a certain state of structure. Therefore, the results of this statistical data analysis cannot be directly used for standard decision making which needs the actual probabilities of events.

The objective of the current study is to propose an appropriate methodology for computing the true probability associated with the intact/damaged state of structures without any information about their damaged states. The statistical data analysis is performed in a Bayesian framework. The main challenge of Bayesian data analysis for data-based SHM, in addition to other issues regarding the unsupervised problems, is to come up with appropriate prior distributions while there is no model available for the structure. Bayesian inference with empirical prior [15–17] and generative statistical models for density estimation are the two main techniques which are implemented in the proposed algorithm of this paper. The efficacy of the methodology has been experimentally verified by testing a three-story two-bay steel laboratory structure with several damage scenarios.

## 30.2 Available Data

The first determining factor for any inference problems is the type and characteristics of the available data. In vibration-based SHM, infinite number of states can be assumed for the damaged structure depending on the location, type, and severity of the defect. As it was mentioned before, providing empirical or simulated data for all of these states is impossible. Simulating only few of damaged states also does not help since there is no way of verifying the simulation results before the occurrence of damage. Therefore, there are only two sets of available data at each sensor location: (1) the data from the intact state of the structure that could be empirical or simulated and denoted by  $\mathbf{X}_I$ ; (2) the data from the structure while being monitored in an unknown state. The second set of available data is denoted by  $\mathbf{X}_t$  and basically used for making inference about the state of the system. Note that, simulation can help for generating data for the intact state of structure since the results are verifiable. It is also noteworthy that in some special cases there may be some data available from the damaged states of the structure which might have been occurred in the past. However, such data sets may not be significantly useful since they are associated with very special states. Thus, we try to use the least amount of data one may have to ensure the generalization of the algorithm.

The raw data in vibration-based SHM is the time series measured by sensors. Most often, such raw data is not an appropriate input for the algorithms. Therefore, a pre-processing is usually conducted on the time series for extracting some damage sensitive features to be used as the input to the damage detection algorithms. In this work, data is mostly referred to the features extracted from the time series unless otherwise stated and the data analysis is conducted in the feature space. The features are also extracted via an energy-based approach for capturing nonlinear effects of damage which is presented in [11]. The size and dimensionality of the data in feature space are two significant factors for solving the problem. Curse of dimensionality [14] is out of the scope of this paper; whereas, the techniques for dealing with small data size is briefly addressed in the next sections.

## 30.3 Bayesian Inference Model Calibration

This section provides a brief review of Bayes theorem as it applies to vibration-based SHM problems for the sake of inference. Then it point out the challenges due to unsupervised nature of the problem to be addressed in the next sections.

By UQ in this paper we try to answer this question: Given  $\mathbf{X}_I$  and  $\mathbf{X}_t$  at each sensor location, what is the probability of damage being proximal to each sensor? More formally, we are interested in computing  $P(S_D | \mathbf{X}_t)$ , where  $P$  stands for probability and  $S_D$  is the set containing all possible damaged state of the system. Denoting  $S_I$  as the intact state of the system, the probability of interest according to the Bayes rule is

$$P(S_D | \mathbf{X}_t) = 1 - P(S_I | \mathbf{X}_t) = 1 - \frac{P(\mathbf{X}_t | S_I) P(S_I)}{P(\mathbf{X}_t)} \quad (30.1)$$

where  $P(\mathbf{X}_t | S_I)$  is the likelihood which is a function of  $\mathbf{X}_t$  with  $S_I$  fixed;  $P(S_I)$  is prior that indicates one's previous estimate of probability that the state is intact;  $P(\mathbf{X}_t)$  is marginal likelihood. By considering  $S_D$  as the set of all possible damaged states it is clear that the type of damage is ignored. In other words, normal functionality of the structure is what matters in this formulation. Since computing probability requires integration of the density functions over some interval, the problem can be equivalently defined as to computing the posterior probability distribution of the intact state of the system given the abovementioned data,  $p(S_I | \mathbf{X}_t)$ . According to the Bayes' theorem

$$p(S_I | \mathbf{X}_t) = \frac{p(\mathbf{X}_t | S_I) p(S_I)}{p(\mathbf{X}_t)} \quad (30.2)$$

where  $p(\cdot)$  is the probability distribution;  $p(S_I | \mathbf{X}_t)$  is the posterior density of intact state given the new data from testing the structure;  $p(\mathbf{X}_t | S_I)$  is the likelihood;  $p(S_I)$  is the prior density of the intact state; and  $p(\mathbf{X}_t)$  is the marginal likelihood distribution of the test data.

The most difficult term of Eq. (30.2),  $p(\mathbf{X}_t)$ , is usually unnecessary to compute. Once the likelihood and prior distributions are known it is sufficient to note that the posterior density is proportional to  $p(\mathbf{X}_t | S_I) p(S_I)$ , the product of likelihood and prior density. To get around with computing the marginal likelihood, a Markov chain Monte Carlo (MCMC) algorithm can be used to sample from the posterior density considering only the mentioned proportionality.

So far, we have not used the data from the intact state of the system,  $\mathbf{X}_I$ . Basically, this data, which may be empirical or simulated, is hidden in the expression of likelihood. If a density is fitted to  $\mathbf{X}_t$ , it can be regarded as the probability distribution associated with the likelihood since the state is fixed and known to be intact. The first question that may arise is how to estimate the density given  $\mathbf{X}_I$ ? To answer this question some generative density estimation techniques such as Gaussian Mixture Model (GMM) and Kernel Density Estimation (KDE) are used. Choosing between these two techniques depends on the size of data set. GMM can be employed in the case of large data set; otherwise, one may use KDE instead if the data set is too small. The second question is what if there is no empirical baseline data,  $\mathbf{X}_I$ , available? In this case, one may use numerical models for simulating the intact state of the system. In fact, it is impossible to make inference in vibration-based SHM without any baseline. All of that so called baseline-free methods implicitly consider a baseline, either empirical or numerical. For instance, when comparing the empirical modal properties of a beam with the closed form solution of Euler-Bernoulli beam, the closed form solution is the baseline indeed. The last question is how to deal with the variation of the characteristics of the intact state due to environmental effect? The detailed answer to this question is out of the scope of this paper but, to briefly address this issue we propose the regression methods. If the data from the intact state in different environmental conditions are available or can be simulated, the expected  $S_I$  can be predicted via regression models to be used for estimating the density of likelihood.

The last term to be determined in Eq. (30.2) is the prior density,  $p(S_I)$ . By definition, in the standard Bayesian inference the prior is the uncertainty about the intact state before considering any evidence. For instance, a model that shows the evolution of the system over time would be helpful for determining the prior. It is possible to obtain such models in special cases like for some mechanical systems which are under mass production; nevertheless, these models are very difficult to obtain for a system which has only a unique instance in real world. Two possible solutions for obtaining a valid prior in such problems are: (1) using non-informative priors; (2) using empirical prior which leads to an approximation to the standard Bayesian inference. Approaching the problem using non-informative priors distribution usually requires computationally expensive iterative methods to obtain an appropriate such a density for high dimensional feature space [18]. Herein, the empirical Bayes (EB) approach is taken mostly for the sake of computational efficiency. Note that EB provides an approximation to the standard Bayesian inference since it uses the observed data for tuning the parameters of prior. In this paper we utilize the two data sets  $\mathbf{X}_I$  and  $\mathbf{X}_t$  in an estimator called James-Stein estimator [15] for approximating the parameters of prior density. The James-Stein estimator has been used mainly for analyzing categorical data like the study by Morris [17]. What follows is the adaptation of this method for the unsupervised problem of our interest.

Assume that the unknown prior density has  $k$  parameters  $\theta_1 \cdots \theta_k$ . To start estimating the parameters, also assume that there is independent unbiased estimates  $\eta_1 \cdots \eta_k$  of the prior parameters such that  $E[\eta_i] = \theta_i$ . This set can be regarded as an appropriate approximation for the unknown parameters if the variance of this set is very small. Otherwise, if the variance is large or unknown, which is true for most of the times, but there exists another set of such estimate for the parameters denoted by  $\tilde{\theta}_1 \cdots \tilde{\theta}_k$ , how can one obtain a set of the prior parameters,  $\hat{\theta}_1 \cdots \hat{\theta}_k$ , which are preferred over the other sets? An interesting approach, which is proposed in [15] and used in some studies such as in [17], is using shrinkage coefficients to obtain the new estimator as

$$\hat{\theta}_i = (1 - b_i) \eta_i + b_i \tilde{\theta}_i \quad (30.3)$$

where  $b_i$  is the shrinkage coefficient belongs to  $[0,1]$  interval. If  $b_i = 0$ , there is no shrinkage and the parameters are determined by  $\eta_i$  and the converse is true if  $b_i = 1$ . Intuitively, the choice of  $b_i$  can be linked to a loss function that measures how good is each of the estimates  $\eta_i$  and  $\tilde{\theta}_i$ . One such measures is sum of squared error the variance of which is denoted by  $\sigma_e^2$ . Thus, the shrinkage coefficients are defined as [15, 17]

$$b_i = \frac{\sigma_\eta^2}{\sigma_\eta^2 + S_e} \quad (30.4)$$

Once the shrinkage coefficients are known, the parameters for the prior distribution can be immediately computed from Eq. (30.3).

To apply this approach to the SHM problem being discussed in this study, one should figure out the two sets of  $\eta_1 \cdots \eta_i$  and  $\tilde{\theta}_1 \cdots \tilde{\theta}_k$ . Before choosing these two sets, let's first discuss two extreme cases of our specific problem regarding the James-Stein estimator. The first extreme case is when the measurement is taken in a short time after the measurement for  $\mathbf{X}_I$  such that the evolution of the structure during the time is negligible. In addition, the system has not experienced any significant extreme loading. For this case, the prior density would be very close to, or even the same as, the density of the data obtained from the intact structure,  $\mathbf{X}_I$ . For the second extreme case, assume that a perfect model is available for the system is available such that the model accounts for all possible events from extreme loading to variability of the structural properties during the time. Such model would provide exactly the same information as the new measurement does at each sensor location. Thus, the prior in this case would be the density of the new measurements  $\mathbf{X}_t$ . However, a proper prior in reality is something between these two extreme cases. It is immediate from Eq. (30.3) that the James-Stein model can takes into account both the extreme cases as well as other cases in between by setting  $\eta_1 \cdots \eta_i$  and  $\tilde{\theta}_1 \cdots \tilde{\theta}_k$  equal to the parameters of the distributions of  $\mathbf{X}_I$  and  $\mathbf{X}_t$ , respectively. This is where the EB enters when the new measurements are used for approximating the prior. The shrinkage coefficients are the last parameters to be defined for completing the model for empirical prior. Equation (30.4) cannot be directly used in our problem because this equation was proposed for categorical data for which the variance of the parameters can be estimated; whereas, in our problem each of the data sets  $\mathbf{X}_I$  and  $\mathbf{X}_t$  provides only one set of parameters. However, the same concept can be used when the variance of the parameters are not available. Basically,  $b$  is a measure of confidence one may have about the second set of parameters  $\tilde{\theta}_1 \cdots \tilde{\theta}_k$ . Similarly, a distance between the densities associated with  $\mathbf{X}_I$  and  $\mathbf{X}_t$  can be used instead of the variance of error in Eq. (30.4). For the moment assume that these densities are Gaussian, an alternative definition for  $b_i$  may be proposed as

$$\hat{b}_i = \frac{\beta_{II}^2}{\beta_{II}^2 + \beta_{tI}^2} \quad (30.5)$$

where  $\beta_{II}^2$  is the maximum squared Mahalanobis distance of the points in the cluster formed by  $\mathbf{X}_I$  to the mean value of the same cluster;  $\beta_{tI}^2$  is the squared Mahalanobis distance between the mean value of  $\mathbf{X}_t$  from the distribution of  $\mathbf{X}_I$ . The choice of Mahalanobis distance is due to some of its special properties such as it is scale invariant. For more information about the superiority of this distance over Euclidian distance for comparing distributions the readers are referred to [11–13]. Note that there is no lack of generality by making the assumption of normality for the two densities. The reason is that both densities can be approximated by a weighted average of some Gaussian distributions via GMM or KDE depending on the size of the data set. Once the densities for both data sets are determined the procedure described in Eqs. (30.3), (30.4) and (30.5) can be applied for any pairs of the Gaussian components from the two clusters. Therefore, the number of Gaussian components of the prior density is equal to the multiplication of the number of components in the densities of  $\mathbf{X}_I$  and  $\mathbf{X}_t$ . In the case of small data size, it is usually reasonable to assume that the density of  $\mathbf{X}_t$  consists of only one Gaussian due to repeatability of the test. This assumption, if verified by the tests of normality, can help for reducing the computational cost of the algorithm.

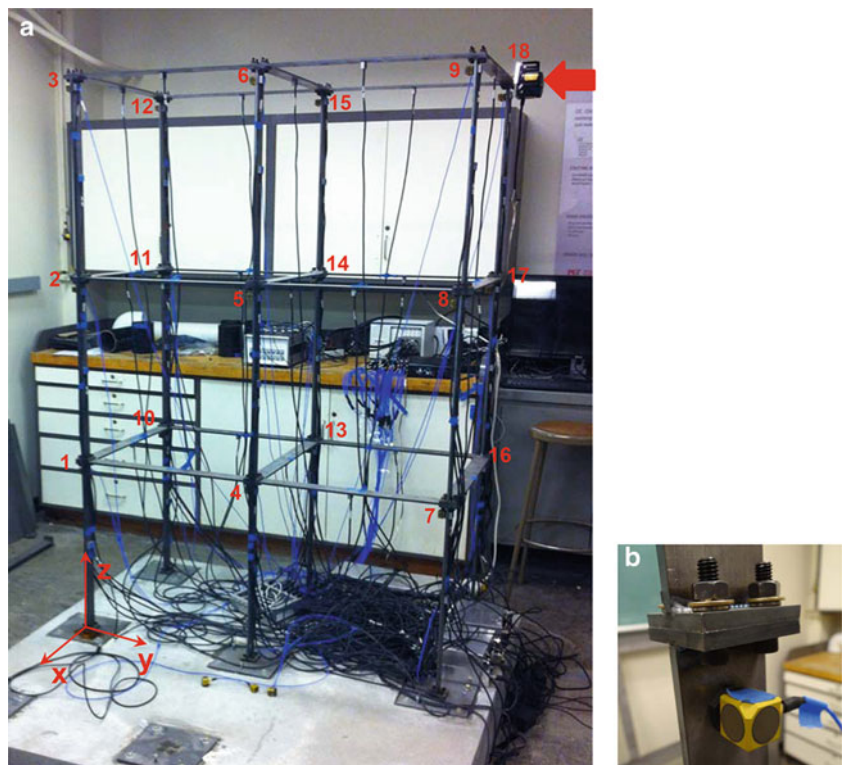
### 30.4 Probability Estimation

For computing the posterior probability of intact/damaged state of the system, Eq. (30.1), both densities for the likelihood and prior should be integrated over an interval or a specific zone. The determination of this zone depends on one's definition of the intact state of the system. For instance, the mentioned zone may be defined via a decision boundary around the data from the intact state. The problem of obtaining the best decision boundary has been well studied for years; however, integration inside of an irregular zone can be computationally expensive. To get around this issue we propose an alternative approach using the concept of confidence intervals. In fact, the integration zone is proposed to be considered as the  $(1-\alpha)\%$  confidence interval of each component of the Gaussian mixtures. The parameter  $\alpha$  is basically the significance level of the statistical analysis. There are efficient algorithms for computing the integrals over these zones which are defined by simple intervals in one-dimensional feature space and ellipsoids in higher dimensions. The weighted average of the probabilities from all of the intervals using  $\alpha_i$  yields the ultimate result.

### 30.5 Experimental Setup and Verification Results

The proposed algorithm has been verified by testing a three-story two-bay steel laboratory structure shown in Fig. 30.1. The structure has been instrumented by 18 triaxial piezoelectric accelerometers attached close to the connections as shown in Fig. 30.1b. The damage scenario in this study is bolt loosening at node #1. The excitation is white Gaussian noise which is produced by a shaker located at the top corner close to the node #18 (Fig. 30.1). Only 10 tests has been done on the structure in each state, intact or damaged, and only the  $z$ -direction of the acceleration data is used for feature extraction.

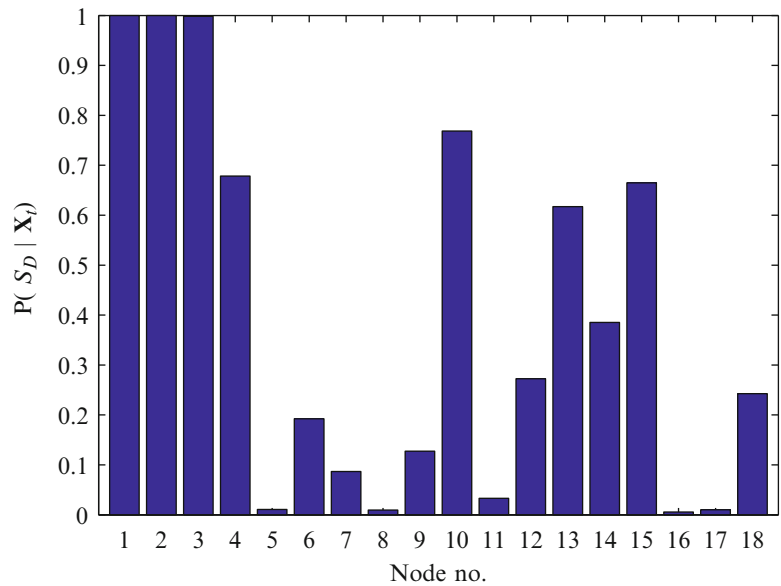
The parameter  $\alpha$  for computing the posterior probability of damage, Eq. (30.1), was set to 0.05, meaning that the 95 % confidence intervals of mixture components of the intact density were considered as the safe regions. The probabilities at different sensor locations for the mentioned damage scenario are shown in Fig. 30.2. Clearly, the posterior probability of damage is higher at the location of damage or its proximity. Note that this algorithm, contrary to many other damage detection algorithms, does not use any threshold; instead, it provides true probabilities which can be directly used for decision making. The probabilities at and around the damage location is significantly higher than other locations although many other nodes are affected by the damage. The reason for high probability at the other nodes is the small size of the prototype and its small damping. This suggests the importance of consideration of size and damping of the system for sensor placements.



**Fig. 30.1** The experimental setup; (a) The three-story two-bay laboratory steel structure; the shaker is at the top corner shown by an *arrow* close to sensor #18; (b) one of the connections with a sensors glued next to that



**Fig. 30.2** Posterior probability of damage given the new measurements



## 30.6 Conclusion

The preliminary study on an empirical Bayesian inference algorithm for uncertainty quantification in unsupervised structural health monitoring problems with constraints on the size of the data set was presented. An important issue in such problems is that there is usually no model available for the prior density of the intact or damaged states of the system. To solve this problem, first, a model similar to the idea of James-Stein estimator is developed. This model uses the likelihood density, which is obtained from the test data on the intact structure, and the density of the new measurements to approximate an appropriate prior density for the structure. Therefore, the proposed algorithm provides an approximation to standard Bayesian inference as it constructs the prior density using the data itself.

The constraint on the size of data set was considered on the density estimation techniques. GMM is used for density estimation of reasonably large data set while KDE can be used in the case that the size of available data is small. Note that the method is applicable even if just one test is available. Each pair of mixture components of the likelihood and new measurement densities gives one component for the prior density. For computing the probability, a specific region should be considered. Herein, the  $(1-\alpha)\%$  confidence interval of each component of the Gaussian mixtures is considered as the safe region.

Experimentally verified results show that the algorithm can effectively detect and localize the damage by assigning true posterior probability of damage to each sensor location. Such results can be directly used in cost analysis and decision making.

**Acknowledgment** The authors acknowledge the support provided by Royal Dutch Shell through the MIT Energy Initiative, and thank chief scientist Dr. Sergio Kapusta, project managers Dr. Keng Yap and Dr. Yile Li, and Shell-MIT liaison Dr. Jonathan Kane for their oversight of this work. Also, thanks are due to Dr. Michael Feng and his team from Draper Laboratory for their collaboration in the development of the laboratory structural model and sensor systems.

## References

1. Plessis G, Lallemand B, Tison T, Level P (2000) Fuzzy modal parameters. *J Sound Vib* 233(5):797–812
2. Bae HR, Grandhi RV, Canfield RA (2004) An approximation approach for uncertainty quantification using evidence theory. *Reliab Eng Syst Saf* 86:215–225
3. Kess HR, Adams DE (2007) Investigation of operational and environmental variability effects on damage detection algorithms in a woven composite plate. *Mech Syst Signal Process* 21:2394–2405
4. Wei DL, Cui ZS, Chen J (2008) Uncertainty quantification using polynomial chaos expansion with points of monomial cubature rules. *Comput Struct* 86:2102–2108

5. Fricker TE, Oakley JE, Sims ND, Worden K (2011) Probabilistic uncertainty analysis of an FRF of a structure using Gaussian process emulator. *Mech Syst Signal Process* 25:2962–2975
6. Mao Z (2012) Uncertainty quantification in vibration-based structural health monitoring for enhanced decision-making capability. Ph.D. dissertation in structural engineering, University of California, San Diego
7. Yuen KV, Au SK, Beck JL (2004) Two-stage structural health monitoring approach for phase I benchmark studies. *J Eng Mech ASCE* 130(1):16–33
8. Ching J, Muto M, Beck JL (2006) Structural model updating and health monitoring with incomplete modal data using Gibbs sampler. *Comput Aid Civ Infrastruct Eng* 21:242–257
9. Beck JL, Au SK (2001) Monitoring structural health using a probabilistic measure. *Comput Aid Civ Infrastruct Eng* 16:242–257
10. Sankararaman S, Mahadevan S (2013) Bayesian methodology for diagnosis uncertainty quantification and health monitoring. *Struct Control Health Monit* 19:88–106
11. Mohammadi Ghazi R, Buyukozturk O (2014) Assessment and localization of active discontinuities using energy distribution between intrinsic modes, *Proceedings of IMAC XXXII*
12. Fukunaga K (1990) *Introduction to statistical pattern recognition*, 2nd edn. Academic Press, Boston
13. Rice J (2007) *Mathematical statistics and data analysis*, 3rd edn. Duxbury Press, Belmont, California
14. Hastie T, Tibshirani R, Friedman J (2009) *The elements of statistical learning: data mining, inference, and prediction*, 2nd edn, Springer series in statistics. Springer, New York
15. James W, Stein C (1961) Estimation with quadratic loss. In: *Proceedings of the fourth Berkeley symposium on mathematical statistics and probability*, vol 1, University of California Press, pp 361–379
16. Krutchkoff RG (1972) Empirical Bayes estimation. *Am Stat* 26(5):14–16
17. Morris CN (1983) Parametric empirical Bayes inference: theory and applications. *J Am Stat Assoc* 78(381):47–55
18. Berger JO, Bernardo JM (1992) On the development of the reference prior (with discussion). *Bayesian statistics*, vol 4. Oxford University Press, Oxford, U.K, pp. 35–60

# Chapter 31

## Reducing MCMC Computational Cost with a Two Layered Bayesian Approach

Ramin Madarshahian and Juan M. Caicedo

**Abstract** One of the major challenges in the implementation sampling techniques in the Bayesian approaches is the computational cost involved with the estimation of the likelihood and/or posterior, especially in problems where the models being updated are computationally expensive. This paper proposes the use of surrogate models in a two-layer Bayesian approach to reduce the computational cost of estimating these PDF. In the first layer, the posterior is written in a traditional manner. The second layer attempts to estimate the PDF of the first layer with a surrogate model. Only a few runs of the structural model are needed to create the required samples. Preliminary results are shown with a numerical example to identify the stiffness of a structural system. Only ten simulations of the structural model are used to estimate the posterior PDF.

**Keywords** Bayesian inference • MCMC • Metamodel • Model updating • Computational cost

### 31.1 Introduction

Modeling is an abstraction of reality that lets a designer or engineer perform simulations with a “real” object or structure without testing it physically. However, the result of our simulations are as good as our models. More complex models could translate into more accurate predictions, but also require more computational power. The time taken to run computational models of structures can range from a few seconds to weeks or more, depending on the type of model, and the technology used to run it. The computational time to run a model becomes one of the main challenges in model updating. These techniques require the estimation of the model response with different values of parameters [1–3] in a fashion similar to optimization problems [4]. The computational demands are even higher when model updating is done in a probabilistic fashion [5] and algorithms such as Gibbs sampling [6] are used. Running a model many times is not feasible given the current computational resources available for most researchers and engineers.

Model approximation techniques are very helpful in these computationally-expensive scenarios [7, 8]. These techniques develop simplified models of the more complex and computationally expensive model. The first step in most approximation methods is experimental design. Experimental design uses different methods, such as factorial, Latin hypercube, orthogonal arrays, importance sampling, and sequential or adaptive methods to determine the places where the expensive computational model is sampled [9–12]. One of the most popular sampling methods is Markov Chain Monte Carlo (MCMC). It is very common in Bayesian problems, and the goal is getting samples from the posterior. Importance sampling is a kind of improved MCMC, in which by selecting a better probability distribution function, the efficiency of the algorithm is improved without sacrificing the accuracy [13]. The design space can be modified based on feedback information from sampling. Sampling methods can help to identify a more attractive region in the design space and also detect more significant variables, including their interaction [14]. The second step is selecting a new model to represent the computationally expensive model.

These approximated models are known as metamodels or surrogate models. The ideal metamodel should be accurate enough to replace the original model within only a fraction of the computational time. Furthermore, the metamodel should be easy to implement [7, 14, 15]. So far, many metamodels have been suggested in the literature. Among the most common are Polynomial, Gaussian process, Support Vector Machine (SVM), Kriging, and Artificial Neural Network models [16–19]. The fitting process is the next step in the process after the selection of an appropriate metamodel. The fitting method may be changed depending on the metamodel. The last step is model validation, which is an important task that should be done

---

R. Madarshahian (✉) • J.M. Caicedo  
University of South Carolina, 300 Main St., Columbia, SC 29208, USA  
e-mail: [mdrshhn@email.sc.edu](mailto:mdrshhn@email.sc.edu); [caicedo@cec.sc.edu](mailto:caicedo@cec.sc.edu)

before using a metamodel as the surrogate model. Different metrics are suggested in the literature for validation. The study of residuals, the difference of predicted values and actual values at sampled points, mean and root mean square error, or cross-validation are some of the popular metrics for validation [8, 20].

Bayesian model updating is a powerful method to infer the probability of the parameters given some experimental data. MCMC algorithms like Gibbs sampling and the Metropolis-Hasting algorithm are used intensively in these kinds of problems [6]. However, when the model is computationally expensive, using MCMC methods is not feasible. Computationally expensive models can be approximated by metamodels, reducing the computational time. This paper proposes the implementation of a metamodel to the posterior PDF obtained, rather than on the model itself. A simple example of a one degree of freedom (DOF) structure is used to illustrate the application of the technique. Even though the model is not computationally expensive, conclusions about potential time savings can be drawn based on the number of times that the SDOF model is run.

## 31.2 Methodology

### 31.2.1 Bayesian Modeling

The Bayes theorem can be described by considering two events,  $A$ , and  $B$ .

$$p(B|a) = \frac{P(B)p(a|B)}{p(a)} \quad (31.1)$$

where  $p(a)$  can be obtained by the law of total probability [21]. In the modeling field, Bayesian inference is one of the most common, and arguably one of the most powerful probabilistic methods. Using Bayes it is possible to consider the parameters of a model in a random fashion and infer unobserved probability distributions of parameters of interest based on the observed data. Denoting the observed data by  $D$ , and the vector of model parameter(s) by  $\theta$ , Bayes theorem can be written as:

$$p(\theta|D) = \frac{p(\theta)p(D|\theta)}{p(D)} \quad (31.2)$$

where  $p(\theta|D)$  is called the posterior PDF and it describes the probability of the parameters given the data ( $D$ ).  $p(D|\theta)$  is the likelihood PDF, and describes the probability of the sampled data given a specific value of  $\theta$ . Since the dominator of Eq. (31.2) is not a function of  $\theta$  it is usually considered a normalization constant. Therefore, Eq. (31.2) can be written as follows:

$$p(\theta|D) \propto p(\theta)p(D|\theta) \quad (31.3)$$

Solving Eq. (31.3) in a close form is not a trivial task. One numerical approximation consists of getting samples of  $\theta$  that follow the posterior PDF by using MCMC algorithms. However, the number of samples needed to implement these algorithms is usually large. If the model is computationally expensive, the time required to perform the updating might not be feasible.

### 31.2.2 Two Layer Bayesian Method

Metamodeling can be used to reduce the computational time required to perform model updating. Traditionally, the computationally expensive model is replaced with a suitable metamodel before updating. This paper proposes to implement the updating process in two layers or steps. The computationally expensive model is used in the first layer of the analysis. Only a few points of the posterior PDF are calculated in this layer. Then, a second analysis is done to approximate the PDF using a metamodel. The parameters of the metamodel can be estimated with a new Bayesian inference process. This second analysis is considered the second layer.

In this paper we assume that the summation of several normal distributions is a suitable model. The validity of this assumption is not treated here given that the main focus of this paper is the proof of concept. The two layers of calculation are defined as follows: For the first ‘‘layer’’ the posterior is defined by the equation:

$$p(\theta|D) = \alpha_1 p(\theta) p(D|\theta) \quad (31.4)$$

where  $\alpha_1$  is the scaling factor,  $D$  is the experimental data, and  $\theta$  is the vector of parameter(s). Then, the posterior is approximated by:

$$Mm(\theta_{Mm}) = \sum_i c_i N(\mu_i, \sigma_i) \quad (31.5)$$

where  $Mm$  is the metamodel, and  $c_i$ ,  $\mu_i$ , and  $\sigma_i$  are the  $i$ th scale factor, mean and standard deviation respectively. Now, the task at hand is to estimate the values of  $c_i$ ,  $\mu_i$ , and  $\sigma_i$ , having the limited information from the original posterior PDF ( $D_{Mm}$ ). If  $\theta_{Mm} = [c_i, \mu_i, \sigma_i]$ , then

$$p(\theta_{Mm}|D_{Mm}) = \alpha_2 p(\theta_{Mm}) p(D_{Mm}|\theta_{Mm}) \quad (31.6)$$

where  $\alpha_2$  is the scale factor for the second layer. The likelihood for the second layer is assumed Gaussian and it is defined as:

$$p(D_{Mm}|\theta_{Mm}) = \frac{1}{\sigma \sqrt{2\pi}} e^{-\frac{(D_{Mm} - Mm(\theta_{Mm}))^2}{2\sigma^2}} \quad (31.7)$$

### 31.3 Example

A single degree of freedom (SDOF) system is used here to illustrate the application of the technique. This is not a computationally expensive model but allows us to test if the proposed technique produces valid results with a simple problem. The stiffness ( $K$ ) in this model is the parameter to be updated, while the mass ( $M$ ) is assumed known. The value of  $M$  is set to 100 kg. The “true” distribution for the stiffness is assumed to be normal with a mean of 1,000 N/m and a standard deviation of 10 N/m. Ten realizations of the frequencies are theoretically obtained and considered as experimental data. These frequencies are shown in Table 31.1

First, the posterior PDF of  $K$  is estimated using a traditional Bayesian inference without the use of the metamodel. Then, the proposed two layer technique is implemented. Since the metamodel introduces some errors, the differences between the two methods are discussed. The python package PyMC is used [22] to sample the posterior PDFs.

#### 31.3.1 Inference Without Using the Metamodel

The natural frequency of a SDOF with small damping ratios can be estimated using the equation

$$\omega_t = \sqrt{\frac{K}{M}} \quad (31.8)$$

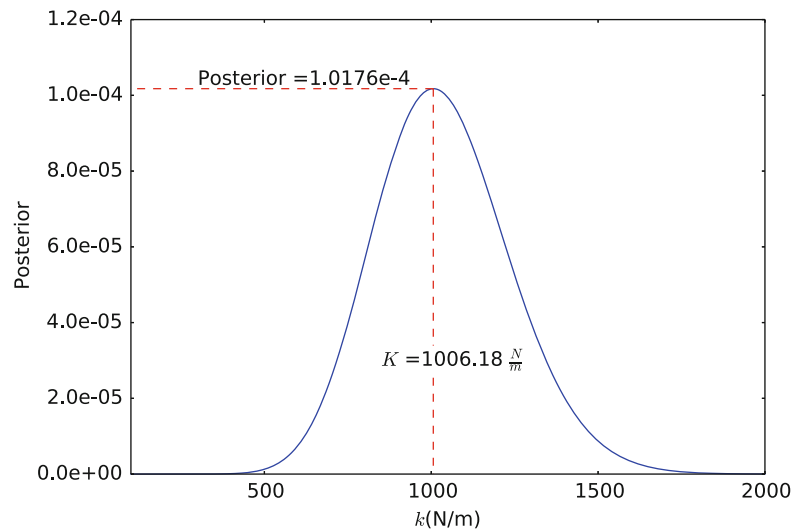
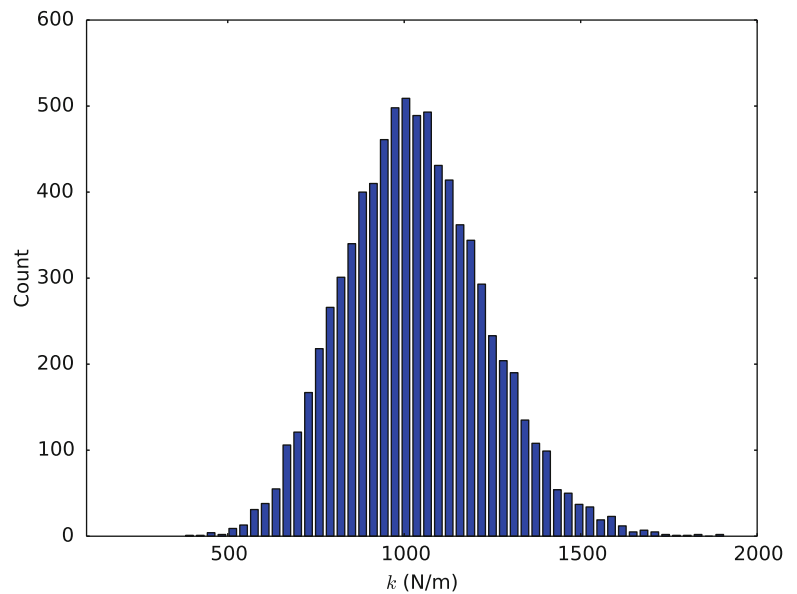
The likelihood is assumed to be Gaussian and it is calculated as follows

$$p(\omega_e|K) = \prod_{i=1}^n \frac{1}{\sigma \sqrt{2\pi}} e^{-\frac{(\omega_t - \omega_{e_i})^2}{2\sigma^2}} \quad (31.9)$$

where  $n$  is the number of experimental frequencies ( $\omega_e$ ), and  $\sigma$  is the standard deviation of the likelihood function. The value of  $\sigma$  is considered deterministic for simplicity, but it can be set as a free parameter in the updated process. Figure 31.1 shows the likelihood function for the case when  $\sigma = 1$ . The value of maximum probability density given the experimental data shown in Table 31.1 is  $K = 1,006$  N/m.

**Table 31.1** Simulated experimental natural frequencies  $\omega_e$

Test no.	$\omega_e$	Test no.	$\omega_e$
#1	3.2058	#6	3.1673
#2	3.2184	#7	3.1759
#3	3.1677	#8	3.1264
#4	3.1554	#9	3.1911
#5	3.1415	#10	3.1708

**Fig. 31.1** Posterior of the SDOF**Fig. 31.2** Posterior of the SDOF

A MCMC sampling method is implemented to generate a chain to represent the distribution of  $K$ . As expected, the histogram obtained from the samples has the same shape as the posterior function in the Fig. 31.1.

This analysis assumes a uniform distribution for  $K$ . Also since  $K$  cannot take negative values, a condition was added to make the probability zero for any negative values. A total of 10,000 samples are generated and the first 2,000 are discarded. Figure 31.2 shows the histogram of the obtained samples. A mean value of  $\mu_K = 1,034.84$  N/m was obtained. Also the interval with the 95 % Highest Posterior Density (HPD) was obtained as [642, 1,428] N/m. The theoretical mean value of  $K$  is 1,000 N/m and the value of highest likelihood is  $K = 1,006$  N/m. Both are located in the HPD interval. Finally the standard deviation of the samples was calculated as 203 N/m.

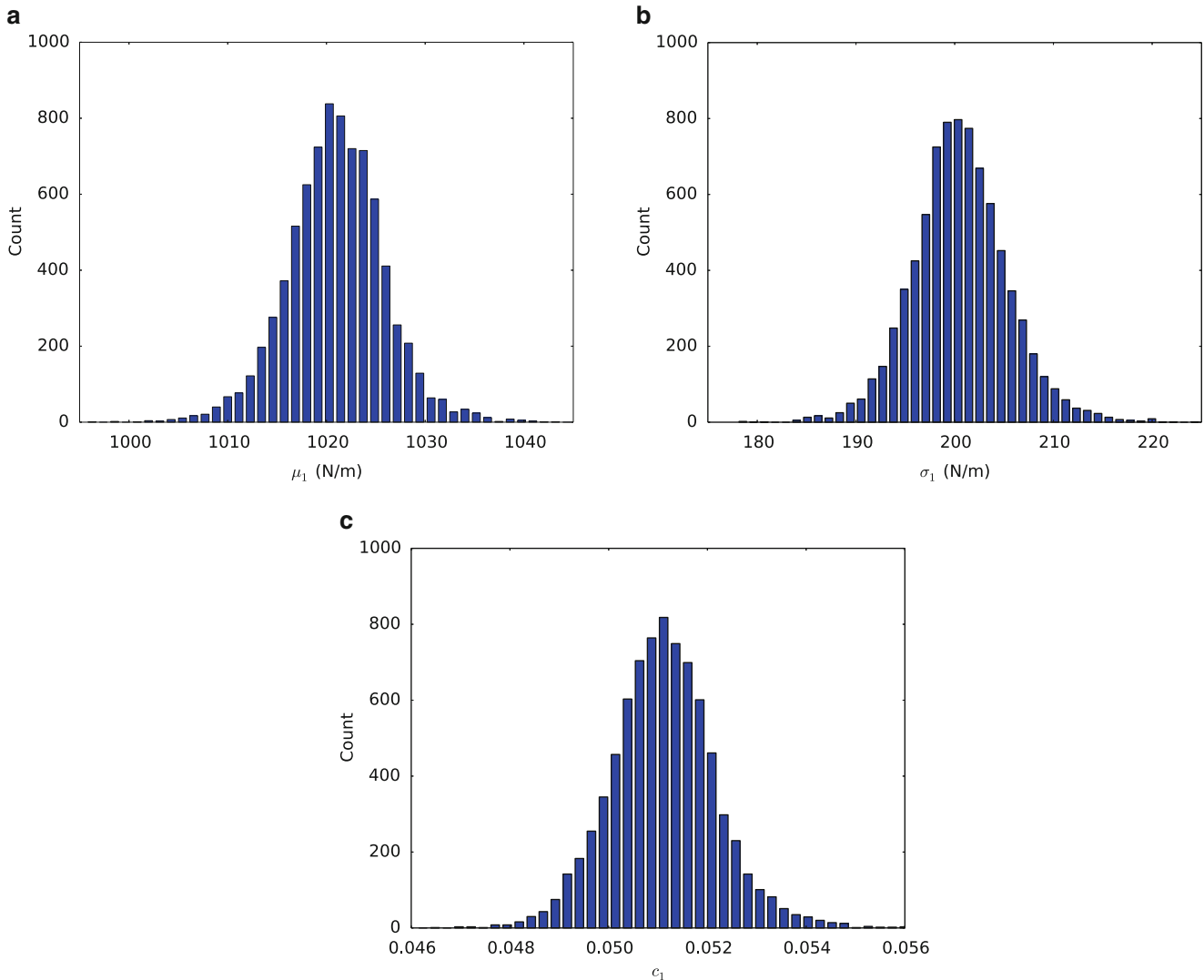
### 31.3.2 Inference Using the Two Layered Proposed Method

Since the likelihood is not a complex function, the metamodel is considered as follows:

$$Mm(K) = c_1 N(\mu_1, \sigma_1) \quad (31.10)$$

**Table 31.2** Ten points of the posterior

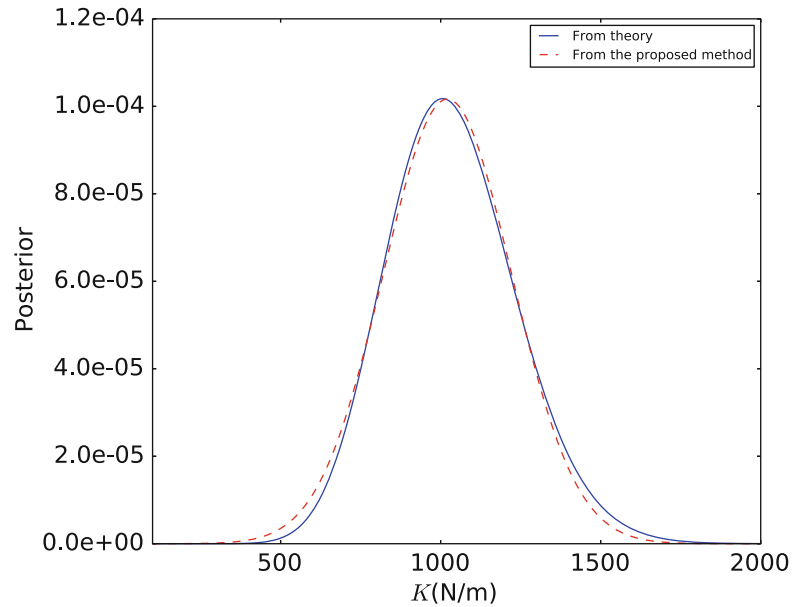
$K$	Posterior	$K$	Posterior
100	5.797e-15	1,100	9.166e-5
300	3.198e-9	1,300	3.976e-5
500	1.274e-6	1,500	8.723e-6
700	2.547e-5	1,700	1.105e-6
900	8.776e-5	1,900	8.886e-8

**Fig. 31.3** Inference about the metamodel parameters. (a)  $\mu$  of the metamodel. (b)  $\sigma$  of the metamodel. (c) Scale factor of the metamodel

where  $c_1$ ,  $\mu_1$ , and  $\sigma_1$  which are scale factor, mean and standard deviation of the metamodel respectively. A few points of the posterior, as are shown in Table 31.2, are selected to use as the data for generating the metamodel.

Bayesian inference is used to estimate the probabilities of  $c_1$ ,  $\mu_1$ , and  $\sigma_1$ . The prior for  $c_1$  was selected as a uniform distribution with the lower bound of 0.001 and the upper bound of 1.0. For  $\mu_1$ , a normal distribution with  $\mu = 800$  N/m and  $\sigma = 80$  was chosen as the prior. A normal distribution with  $\mu = 300$  N/m and  $\sigma = 100$  was selected for  $\sigma_1$ . MCMC was implemented to generate samples on the parameters of the metamodel. A total of 12,000 samples were obtained; 4,000 of them were considered burning samples and were discarded. The mean value for  $\mu_1$ ,  $\sigma_1$ , and  $c_1$  are obtained as 1,021, 201 N/m, and 0.051 respectively. The 95% HPD intervals for these parameters were obtained as [1,011, 1,031], [190, 210], and [0.049, 0.053] respectively. Figure 31.3 shows the histograms of samples obtained for these parameters.

**Fig. 31.4** Comparison of the posterior and the metamodel



### 31.3.3 Results

Figure 31.4 shows the results of the metamodel and the traditional methodology in the same figure. Results show that the metamodel does a good job describing the posterior. The example shows how this technique can reduce the computational cost in computationally expensive models. For the traditional method results shown in Fig. 31.2 the model had to be run 8000 times, but using the proposed technique the original model needs to be run only ten times. Then using the metamodel one can generate samples for the parameter of interest. This can be considered a great advantage in the case of a computationally expensive model. The 95 % HPD interval for  $K$  with the proposed approach is [627, 1,414] N/m which is similar to the 95 % HPD interval obtained from the original method (i.e. [642, 1,428]) N/m.

## 31.4 Conclusions

In this paper a new methodology was proposed to reduce the computational effort of Bayesian inference using complex models. The metamodel is used to approximate the posterior rather than the structural model itself. A SDOF problem was used to explore the capabilities of the technique. However, further research is necessary to explore the advantages and disadvantages of the method. The metamodel used in the paper was a combination of several normal distributions; however, it is possible to use other surrogate models. The fitting process is done in the second layer or step of the proposed technique. The results presented here show agreement between the traditional Bayesian inference technique and the method proposed here.

**Acknowledgements** This material is based upon work supported by the National Science Foundation under Grant No. CMMI-0846258.

## References

1. Zárate BA, Caicedo JM (2008) Finite element model updating: multiple alternatives. *Eng Struct* 30(12):3724–3730
2. Friswell M, Mottershead JE (1995) *Finite element model updating in structural dynamics*, vol 38. Springer, Berlin
3. Modak S, Kundra T, Nakra B (2002) Prediction of dynamic characteristics using updated finite element models. *J Sound Vib* 254(3):447–467
4. Rajan S (1995) Sizing, shape, and topology design optimization of trusses using genetic algorithm. *J Struct Eng* 121(10):1480–1487
5. Beck JL, Au S-K (2002) Bayesian updating of structural models and reliability using markov chain monte carlo simulation. *J Eng Mech* 128(4):380–391
6. Robert CP, Casella G (2004) *Monte Carlo statistical methods*, vol 319. Citeseer



7. El-Beltagy MA, Keane A (1999) Metalmodeling techniques for evolutionary optimization of computationally expensive problems: promises and limitations.
8. Meckesheimer M, Booker AJ, Barton RR, Simpson TW (2002) Computationally inexpensive metamodel assessment strategies. *AIAA J* 40(10):2053–2060
9. Madarshahian R, Caicedo JM, Zambrana DA (2014) Evaluation of a time reversal method with dynamic time warping matching function for human fall detection using structural vibrations. In: Atamturktur HS et al (eds) *Model validation and uncertainty quantification*, vol 3. Springer, New York, pp 171–176
10. Taguchi G, Yokoyama Y et al (1993) *Taguchi methods: design of experiments*, vol 4. American Supplier Institute, Dearborn
11. Owen AB (1992) Orthogonal arrays for computer experiments, integration and visualization. *Stat Sin* 2(2):439–452
12. Glynn PW, Iglehart DL (1989) Importance sampling for stochastic simulations. *Manag Sci* 35(11):1367–1392
13. Waggoner DF, Zha T (2003) A gibbs sampler for structural vector autoregressions. *J Econ Dyn Control* 28(2):349–366
14. Shan S, Wang GG (2010) Survey of modeling and optimization strategies to solve high-dimensional design problems with computationally-expensive black-box functions. *Struct Multidiscipl Optim* 41(2):219–241
15. Wang GG, Shan S (2007) Review of metamodeling techniques in support of engineering design optimization. *J Mech Des* 129(4):370–380
16. Sacks J, Welch WJ, Mitchell TJ, Wynn HP (1989) Design and analysis of computer experiments. *Stat Sci* 4:409–423
17. Cressie N (1988) Spatial prediction and ordinary kriging. *Math Geol* 20(4):405–421
18. Wang L, Beeson D, Akkaram S, Wiggs G (2005) Gaussian process meta-models for efficient probabilistic design in complex engineering design spaces. In: *ASME 2005 international design engineering technical conferences and computers and information in engineering conference*. American Society of Mechanical Engineers, New York, pp 785–798
19. Papadrakakis M, Lagaros ND, Tsompanakis Y (1998) Structural optimization using evolution strategies and neural networks. *Comput Meth Appl Mech Eng* 156(1):309–333
20. Jin R, Chen W, Simpson TW (2001) Comparative studies of metamodeling techniques under multiple modelling criteria. *Struct Multidiscipl Optim* 23(1):1–13
21. James F (2006) *Statistical methods in experimental physics*, vol 7. World Scientific, Singapore
22. Patil A, Huard D, Fonnesbeck CJ (2010) Pymc: Bayesian stochastic modelling in python. *J Stat Softw* 35(4):1

# Chapter 32

## Comparison of FRF Correlation Techniques

Timothy Marinone and Adam Moya

**Abstract** Mode shape correlation techniques have proven to be an excellent method for assessing the degree of similarity between a finite element model and a set of test data. Because mode shapes inherently contain spatial information on the mass and stiffness matrices of the model and are easily extracted from test data, this allows an overall similarity assessment as well as providing indications of localized areas of discrepancy. Although frequency response function (FRF) correlation contains the same information as used in mode shape correlation (both contain a collection of measurement points), FRF correlation has been found to be more difficult to use successfully. This difficulty is primarily because of the high sensitivity of frequency response functions to slight perturbations both in the boundary condition and in the excitation and response. As a result, the globally extracted mode shapes minimize the contamination due to testing perturbations, while frequency response functions maintain this sensitivity. This sensitivity makes it possible to measure similarity, or lack thereof, in so-called identical components or assemblies.

Sandia National Laboratories wishes to develop a quick testing process able to identify assembly errors in a complex structure with many joints while minimizing the structure's required downtime prior to its intended purpose. A frequency response function similarity approach was used where the structure was mounted on a test fixture and a limited number of responses were recorded with a single drive point. Because mode shape correlation techniques are widely used, the corresponding frequency response function correlation techniques have not been studied as much. For this paper, several different frequency response function correlation methods were assessed on a simplified structure to identify which technique(s) are best able to detect any assembly errors while being insensitive to other errors.

**Keywords** Modal testing • Correlation • Frequency response functions • Similarity

### Nomenclature

$\omega_{k,l}$	Specific (kth) Frequency at Degree of Freedom L
$H_1, H_2$	Frequency Response Function (1) or (2)
$A^H$	Complex Conjugate Transpose (Hermitian) of A
FRF	Frequency Response Function
CSF	Cross Signature Scale Factor
FRFSF	Frequency Response Function Scaling Factor
RMS	Root Mean Square
CSAC	Cross Signature Assurance Criterion

---

Sandia National Laboratories is a multi-program laboratory managed and operated by Sandia Corporation, a wholly owned subsidiary of Lockheed Martin Corporation, for the U.S. Department of Energy's National Nuclear Security Administration under contract DE-AC04-94AL85000.

T. Marinone (✉)

ATA Engineering, Inc., San Diego, CA, USA

e-mail: [tmarinon@ata-e.com](mailto:tmarinon@ata-e.com)

A. Moya

Experimental Mechanics, NDE, and Model Validation Department, Sandia National Laboratories, P.O. Box 5800 – MS 0557,

Albuquerque, NM 87185, USA

e-mail: [acmoya@sandia.gov](mailto:acmoya@sandia.gov)

## 32.1 Introduction

At Sandia National Laboratories, many of the structures tested are complex multibodies with many assembled joints. Sandia wants to define a quick testing process able to identify assembly errors while minimizing the downtime required on the unit. Similarity testing at Sandia has traditionally been performed on a vibration table where the unit is exposed to a low-level random input in all three principal directions; however, this is very time consuming and costly due to the parties and the hardware required. This testing is also less than ideal, as visual comparison of transfer functions leaves a lot of room for interpretation, as the most common metric used visually is peak response or resonant frequency. There is also a large variability in dynamic response introduced by the vibration table. For these reasons, Sandia chose modal testing as the test method for developing a unit-to-unit similarity metric. Unfortunately, the physical footprint of the assemblies often tested allows for only limited sets of internal instrumentation, making mode shape correlation difficult and time consuming. In comparison, a single FRF taken at a strategic external location gives an indicator of the test article's similarity to a previously tested unit. As a result, the engineer can perform a simple modal test with limited instrumentation to obtain useful FRFs, and these measurements can be used in the similarity metrics presented below instead of requiring a full experimental modal model.

Because structural dynamic correlation is commonly done using mode shapes, there has been significantly less research done on frequency response function correlation techniques. Allemang [1] provided a thorough overview of various correlation techniques, although most of the paper's focus is on the various mode shape correlation metrics. Pascual et al. [2] used both the frequency domain assurance criterion (FDAC) and frequency response scale factor (FRSF) to perform model updating. Heylen et al. [3] investigated multiple case studies using the frequency response assurance criterion (FRAC), although the majority of the paper focused on modal correlation metrics. Fotsch et al. [4] also examined the FDAC and FRAC while introducing a new tool called modal FRF assurance criterion (MFAC), which used a combination of mode shapes and FRFs to assess the correlation. Finally, Dascotte et al. [5] employed the cross signature assurance criterion (CSAC) and cross signature scale factor (CSF) to study sensitivity-based model updating.

Although there has been a lot of research done on the various FRF correlation techniques, very few case studies have been written where the different techniques are compared. Many of these correlation methods were developed for comparing experimental data to analytical or finite element analysis data for model correlation. The case study presented in this paper compares seven different metrics for discerning unit-to-unit variability and incorrect assembly using experimental modal data.

## 32.2 Theory

A summary of the different correlation techniques that were examined is provided below. Details of the mathematical development can be found in the respective references where appropriate.

### 32.2.1 *Technique 1: Frequency Peak Pick*

The easiest way to compare frequency response functions is by simply picking the frequency of the peak(s) on an FRF. This is traditionally how Sandia has compared the similarity of the two transfer functions; this technique is very visual and easy to understand. Because natural frequencies are characteristic of the structure, the discrepancy between the frequencies corresponding to the same peak on the FRFs of two different units can provide an initial assessment of the similarity. This technique has proven imprecise to use in the past due to a large dependence on engineer interpretation, usually of vibration data. While the boundary condition replicated in a free-free modal test is fairly repeatable, there are many unknowns in comparing vibration data between units. Typically, the auto spectrum of each response is compared, but this can be rather noisy due to the unknown force input. It has also been found that the more complicated the assembly, the more likely it is that the resonant peaks will not align. While this would typically indicate a different structure, Sandia is using a less rigorous definition of the word "similar" to include small shifts in modes that would lead to a large error using this metric while exhibiting similar measured dynamic responses between units.

### 32.2.2 *Technique 2: RMS Percent Error*

Rather than assessing the similarity at each frequency peak as described in technique 1, the overall similarity of the FRFs can be assessed. Using the RMS value of the FRF and comparing it to the RMS value of another measurement assesses the overall energy of the function. Although this allows slight perturbations between the functions to be minimized, the RMS calculation can yield the same RMS value for two visually different functions.

### 32.2.3 *Technique 3: $R^2$ Coefficient of the Imaginary Response*

Although transfer functions are normally viewed as an absolute magnitude, more information about the transfer function can often be obtained by converting the function amplitude into a complex number. By plotting the imaginary component of the response of the first FRF with respect to the imaginary component of the second FRF, a linear fit can be obtained. Based on the  $R^2$  term of this linear fit, the similarity of the measurements can be evaluated.

### 32.2.4 *Technique 4: Nyquist Comparison*

Another common way to view the transfer function is by plotting the real component of the FRF with respect to the imaginary part. Because damping heavily influences the real component of the FRF, the Nyquist comparison can indicate structural changes in the assembly or part. By averaging the maximum discrepancies between the real and imaginary legs of the Nyquist plots and the control assembly, this difference can be utilized for similarity quantification.

The next three techniques use a more rigorous calculation to obtain a correlation metric. All techniques use the assumed orthogonality of the FRFs to compute a ratio from 1.0 (identical) to 0.0 (no similarity). They also evaluate each FRF on a line-by-line basis in the frequency domain but are sensitive to different aspects of the FRF.

### 32.2.5 *Technique 5: Cross Signature Scale Factor (CSF)*

The CSF is used to evaluate discrepancies between amplitudes and is defined in Eq. 32.1. The CSAC (defined below) also ranges from 0 to 1 and is sensitive to changes in damping. Often the CSF is used with the CSAC in model correlation efforts.

$$CSF(\omega_k) = \frac{2 |H_1^H(\omega_k) H_2(\omega_k)|}{(H_1^H(\omega_k) H_1(\omega_k)) + (H_2^H(\omega_k) H_2(\omega_k))} \quad (32.1)$$

### 32.2.6 *Technique 6: Cross Signature Assurance Criterion (CSAC)*

The CSAC is used to evaluate discrepancies in the shape of the FRFs and is defined in Eq. 32.2. Similar to the traditional modal assurance criterion (MAC), the CSAC is adapted for the frequency domain. Since the position and number of resonant peaks mainly determine the shape of an FRF, the CSAC function is sensitive to changes in mass and stiffness.

$$CSAC(\omega_k) = \frac{|H_1^H(\omega_k) H_2(\omega_k)|^2}{(H_1^H(\omega_k) H_1(\omega_k)) * (H_2^H(\omega_k) H_2(\omega_k))} \quad (32.2)$$

### 32.2.7 Technique 7: Frequency Response Function Scaling Factor (FRFSF)

The FRFSF is used to evaluate discrepancies between amplitudes of the opposing FRFs and is defined in Eq. 32.3.

$$FRFSF = \frac{\sum_{j=1}^k \sum_{n=1}^L |H_1(\omega_{k,L})|}{\sum_{j=1}^k \sum_{n=1}^L |H_2(\omega_{k,L})|} \quad (32.3)$$

Because there are many different frequency response function correlation techniques, a case study was performed to evaluate the different techniques and determine which were the most useful for this particular application. These techniques will be narrowed down to the most useful and used on more complicated assemblies in the near future as more hardware becomes available to test.

### 32.3 Case Study: Vibration Fixture Plates with Attached Assembly

To assess the similarity metrics listed above, a mass mock assembly consisting of multiple components connected with bolted joints was used as a test article. The variability on which the similarity metrics were assessed was introduced by individually attaching multiple vibration test fixtures to the test article. The mass mock assembly attaches to each fixture via four 1/4-28 steel alloy bolts around the perimeter of the base. In addition to the evaluation of similarity metrics, this data also serves to check unit-to-unit variability on all of the vibration fixtures built by an outside entity, which are supposed to be identical and should lead to a duplicate response during environmental testing. The vibration fixtures were square titanium plates with special features cut to adapt to the mass mock test article. The mass mock was conical in nature and is represented as a general shape henceforth to protect proprietary information, as shown in Fig. 32.1. The experimental setup consisted of four assumed identical vibration fixtures with the mass mock assemblies sitting upon three foam pieces to represent a free-free boundary condition. The vibration fixture was instrumented with three PCB 356A03 triaxial accelerometers with a sensitivity of 10 mv/G and a PCB 288D01 impedance head with a sensitivity of 100 mv/lb and 100 mv/g attached to a 50 lb MB modal shaker. The modal shaker was oriented to input a 45-degree-skewed burst random force input in all three perpendicular axes between 20 and 2,000 Hz.

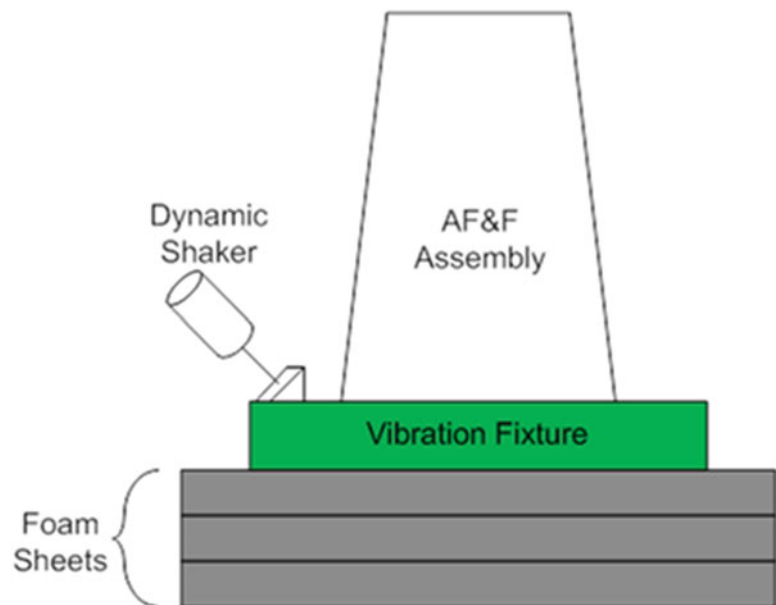


Fig. 32.1 Experimental test setup

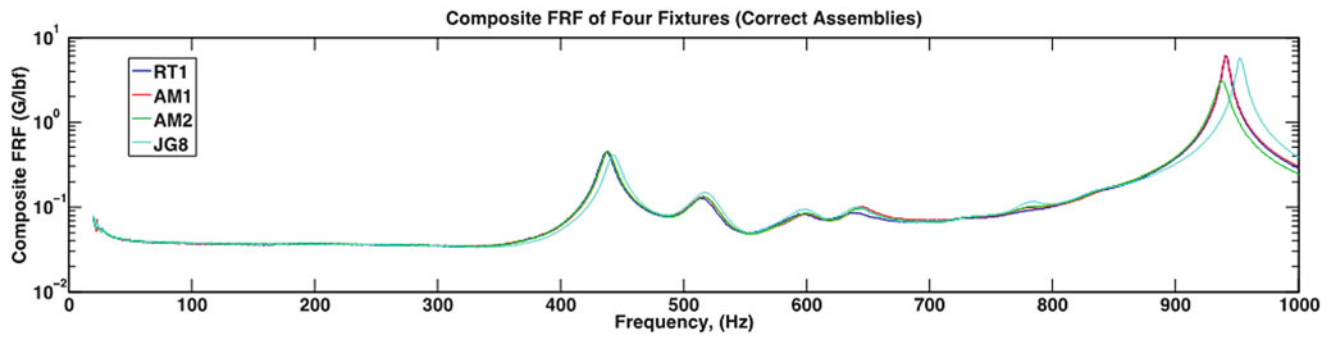


Fig. 32.2 Compiled FRF comparison of four fixtures correctly assembled

Four fixtures were tested, each machined to the same drawing and assumed identical. These fixtures are referred to as “RT1,” “AM1,” “AM2,” and “JG8” in the rest of the paper. The test setup was replicated for all cases so that the same shaker input, sensors, and boundary condition were maintained. Measurement nodes were measured precisely, although some instrumentation discrepancies are sure to exist due to user error.

For the purpose of evaluating the similarity of the fixtures, RT1 was used as the standard. Each fixture with its attached mass mock assembly was tested and compared to the standard fixture assembly. For the majority of the metrics described above, a compiled average FRF of all locations was used to filter out any unintended test assembly errors such as misaligned sensor placement or skewed shakers. This test setup was designed to provide the highest-quality data utilizing minimum instrumentation on the fixture and zero instrumentation on the unit, though ideally a larger number of accelerometers would be placed throughout the unit to capture modes that may not be picked up at the fixture locations. During testing, the burst random force input was averaged around 2.6 lbrms after a small nonlinearity test was run with varying force levels. At the frequency range and force levels tested, no nonlinearities were detected; however, an improved fixture with improved transmissibility could lead to different results.

The compiled FRFs in Fig. 32.2 compare the four fixtures correctly assembled to the mass mock assembly. While the results from the fixtures are generally similar, there is a mode around 940 Hz that contains a noticeable discrepancy. Although the fixtures are manufactured from the same drawing, they were made at different times and may have slightly different mass properties due to tolerances.

After this testing was completed, two different assembly errors were studied. The first consisted of torquing the set of four fasteners between the mass mock and fixture to an incorrect torque value (approximately one third of the specified value). The second assembly error consisted of properly installing the fasteners but removing one fastener from the set of four. These two assembly errors were conducted on all four fixtures, and the resulting data sets were then compared to the corresponding correctly assembled system. A comparison of these compiled FRFs is seen in Fig. 32.3 below. These plots highlight the discrepancy when the assembly is missing a bolt but does not obviously indicate when the bolt is incorrectly torqued. However, the goal of this paper is to find a metric that is sensitive to small changes in the structures dynamics – even as subtle as this incorrectly torqued bolt. Some of the metrics are presented in more detail below, and a detailed summary of the results of all metrics is given at the end of the paper.

### 32.3.1 Nyquist Comparison

Examining the Nyquist plots for the drive-point response on the correct and incorrect assemblies reveals some interesting discrepancies. As seen in Fig. 32.4 below, the diameter of the Nyquist plot at resonance (940 Hz mode) varies greatly depending on the assembly tested. Across all four fixtures, we see an increase in damping in the 940 Hz mode (characterized by a larger-diameter circle) when the bolt is incorrectly torqued and a decrease in damping (smaller-diameter circle) when the bolt is left out altogether. This metric thus has a large sensitivity to changes in damping and can be quantified and normalized for comparison as shown in the summary.

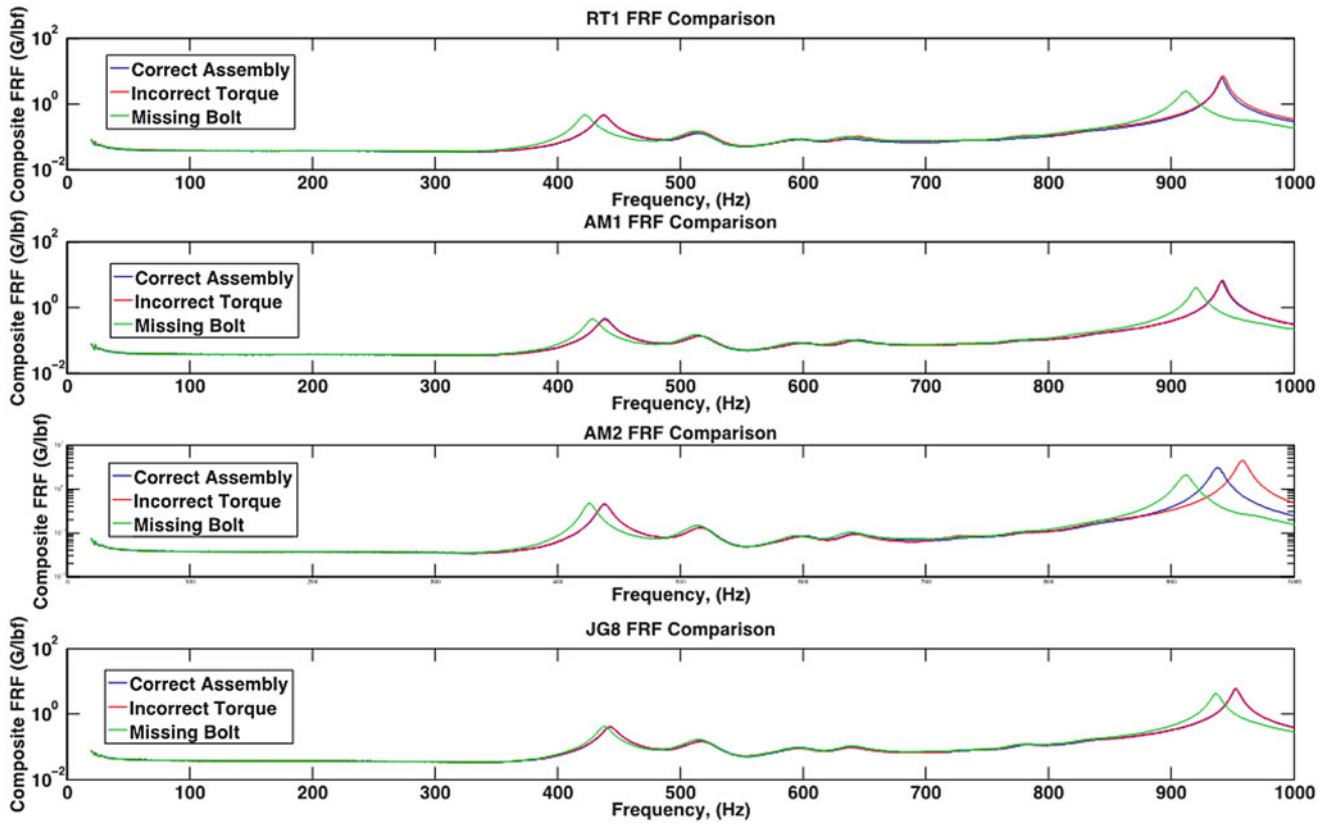


Fig. 32.3 Compiled FRF comparison of all four fixtures and assemblies

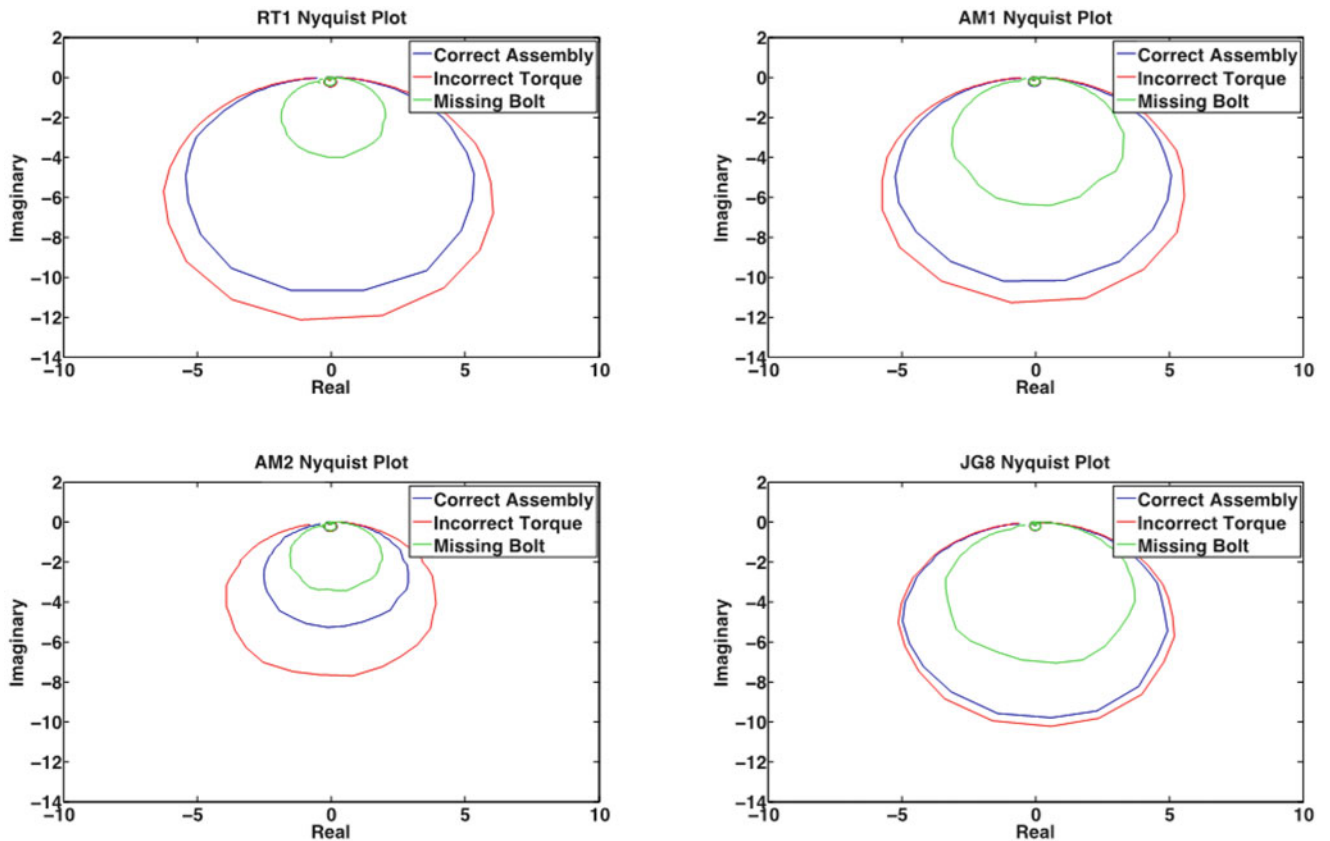
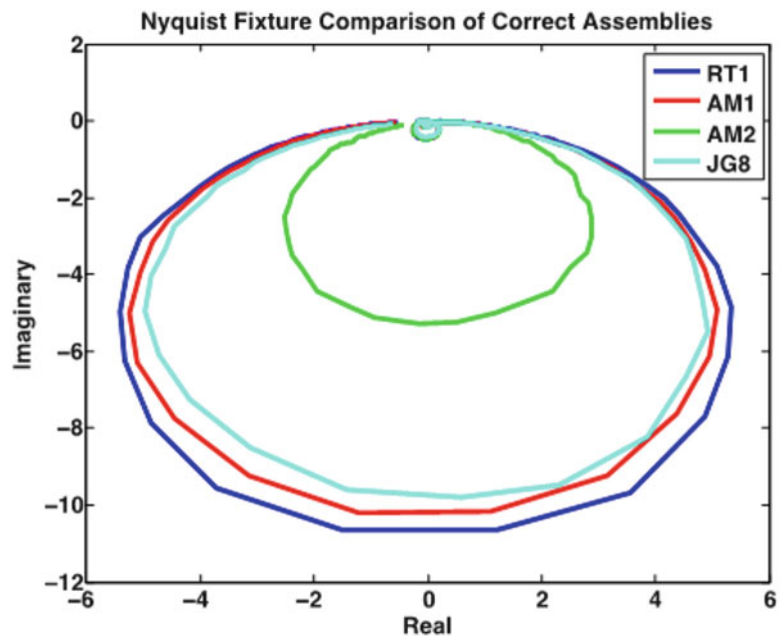


Fig. 32.4 Nyquist plot comparison of correct vs. incorrect assemblies

**Fig. 32.5** Nyquist plot comparison of all four correct assemblies



In a similar fashion, the correct assemblies of the fixture/mass mock components were compared to get a baseline measurement of the difference in the fixtures themselves. As seen in Fig. 32.5 below, this method shows a rather large variation between the “AM2” fixture and the other three fixtures.

### 32.3.2 $R^2$ Coefficient of the Imaginary Response

Another visual method of comparing similarity is by plotting the imaginary response of one assembly versus the other. For identical assemblies, the relationship would be linear with a slope and  $R^2$  value of 1. Although the results are tabulated in the following section, the plots shown below in Fig. 32.6 compare these linear relationships and explain this methodology in a visual format. Similar to the results seen in the Nyquist plots, the discrepancy due to a missing bolt is more pronounced than that from the incorrectly torqued fasteners.

While at first glance the linear relationship between the two assemblies appears to give a good representation of the unit’s assembly, the linear regression tends to be biased toward the largest mode while the lower modes are condensed near the origin. To ensure that the  $R^2$  value is a good representation of the comparison between correct and incorrect assemblies, the residuals from the linear regression are plotted against frequency in Fig. 32.7. In this figure, we see a very small deviation in the lower frequencies, giving confidence in the linear fit in the regime.

Figure 32.8 displays the imaginary responses for the correct assemblies and gives an insight into the differences in the fixture. This metric demonstrates a large difference between the “RT1” fixture and the “JG8” fixture; this is not surprising, as the “JG8” fixture is a few years old and has undergone wear and tear due to extensive vibration testing, while the other three fixtures are new and have had no time on the vibration table. Looking at the residual plot, we again gain confidence in the linear regression at lower frequencies. This also gives insight into the complexity of defining similarity, as the four units tested were manufactured to the same drawing and should exhibit little to no unit-to-unit variability, yet the metrics explored demonstrate a large unit-to-unit variability.

As seen in the plots, both the Nyquist and imaginary response comparison metrics were able to visually identify the incorrectly assembled test data sets. Furthermore, the metrics were more sensitive to the missing bolt assembly error than they were to the incorrect torque error. Any testing done in the future can use the results from these tests to help quickly identify assembly errors such as a missing bolt, but more testing is still needed to determine how sensitive these metrics may be to other anomalies such as bad welds, missing washers, or deformed material.



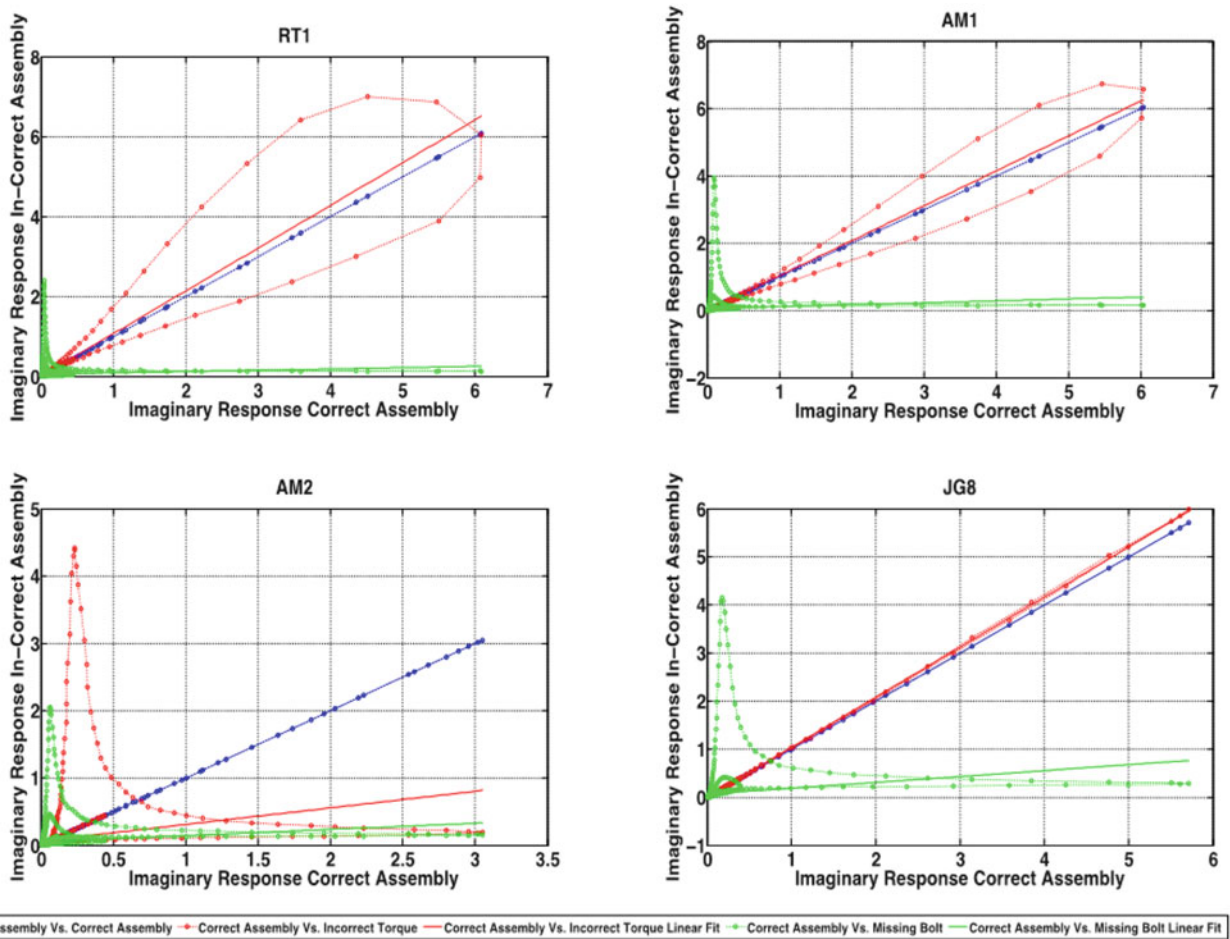


Fig. 32.6 Linear fit plots for all correct vs. incorrect assemblies

## 32.4 Evaluation of Metrics

All seven metrics were computed for each fixture/assembly combination for both assembly errors, and these are compared in Figs. 32.9 and 32.10 below with all metrics normalized to 1.0. Thus a metric of 1 would indicate that the two assemblies are perfectly identical, while a metric of 0 would indicate no similarity. For metrics where a percent error was calculated, the metric was normalized to 1 by taking 1 minus the error, thus a metric of 1 represents zero error. All metrics identified assembly errors well, except the peak picking metric, which is most often used as a visual metric. Most of the metrics were able to correctly indicate the missing bolt assembly error, but they did not perform as well in identifying the incorrectly torqued bolts. Because assembly errors may be caused by an incorrect torque, an ideal similarity metric would be sensitive to all assembly errors. For this case study, the Nyquist metric, RMS error, and  $R^2$  metric appear to be the metrics most sensitive to the torque assembly error; however, the RMS error appears to be less sensitive to shifts in frequency and does not capture unit-to-unit variability reliably.

Figure 32.10 displays the differences between all metrics when comparing the correct assemblies of the “AM1,” “AM2,” and “JG8” fixtures versus the “RT1” fixture as a reference. As expected from looking at the composite FRFs, RT1 vs AM1 shows a high degree of correlation across all metrics. In addition, both AM2 and JG8 are visually different from RT1, but not all of the metrics sufficiently capture this difference for both fixtures. Because only four fixtures were tested, additional fixtures would help identify the appropriate metrics to use for unit-to-unit variability.

For similarity testing to be useful, a threshold must be defined to indicate whether the two transfer functions are similar. This threshold value is difficult to define with the limited set of hardware, but averaging the similarity metric values gives some insight into what value might be acceptable for a given metric and assembly error. These early results indicate the need for various metrics to be used together to best identify any assembly errors or unit-to-unit variability. From the values shown

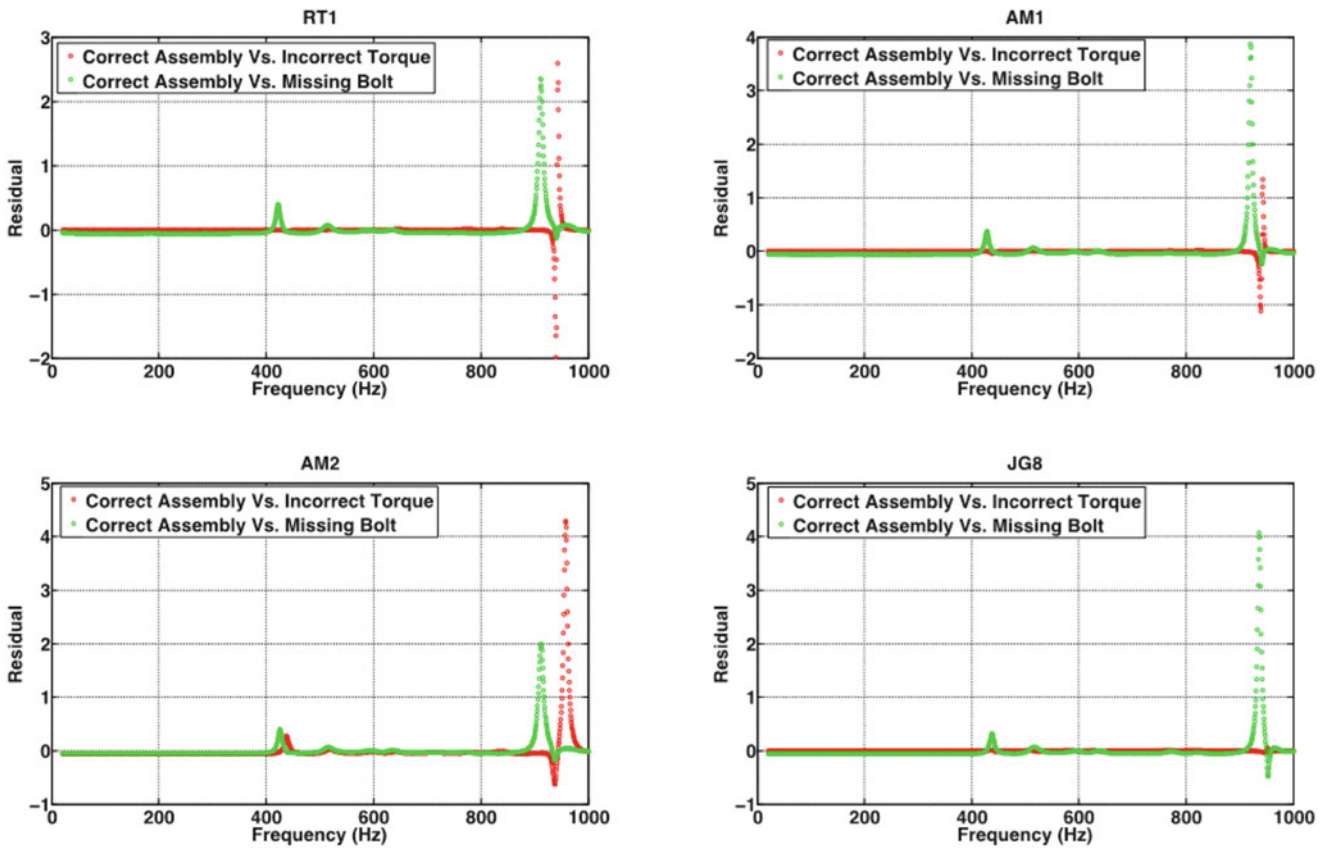


Fig. 32.7 Residuals vs. frequency for linear regression metric

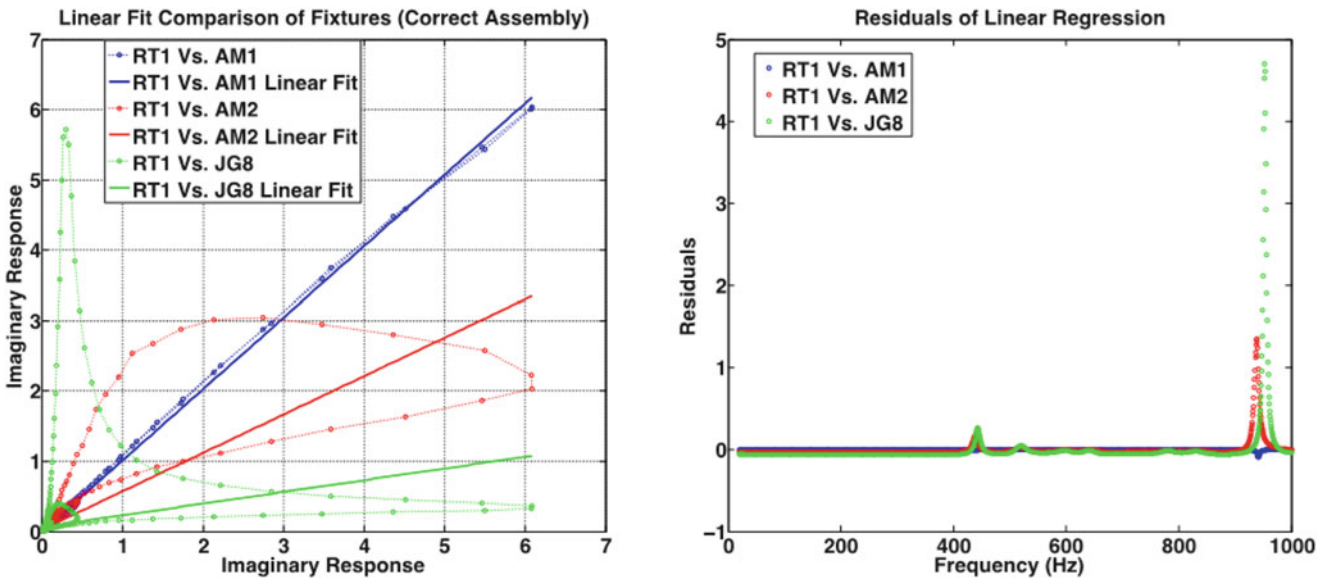


Fig. 32.8 Linear fit plot for fixture comparison

in Table 32.1, the FRFSF and peak-picking methods are not adequate metrics to measure similarity due to their high values for the incorrect assemblies. Considering the values for the three recommended metrics of Nyquist error, RMS error, and  $R^2$  error, it appears that an average similarity value above 0.9 would indicate a correct assembly. However, when evaluating unit-to-unit variability, this threshold may be much lower. More detailed testing will lead to an accurate threshold.

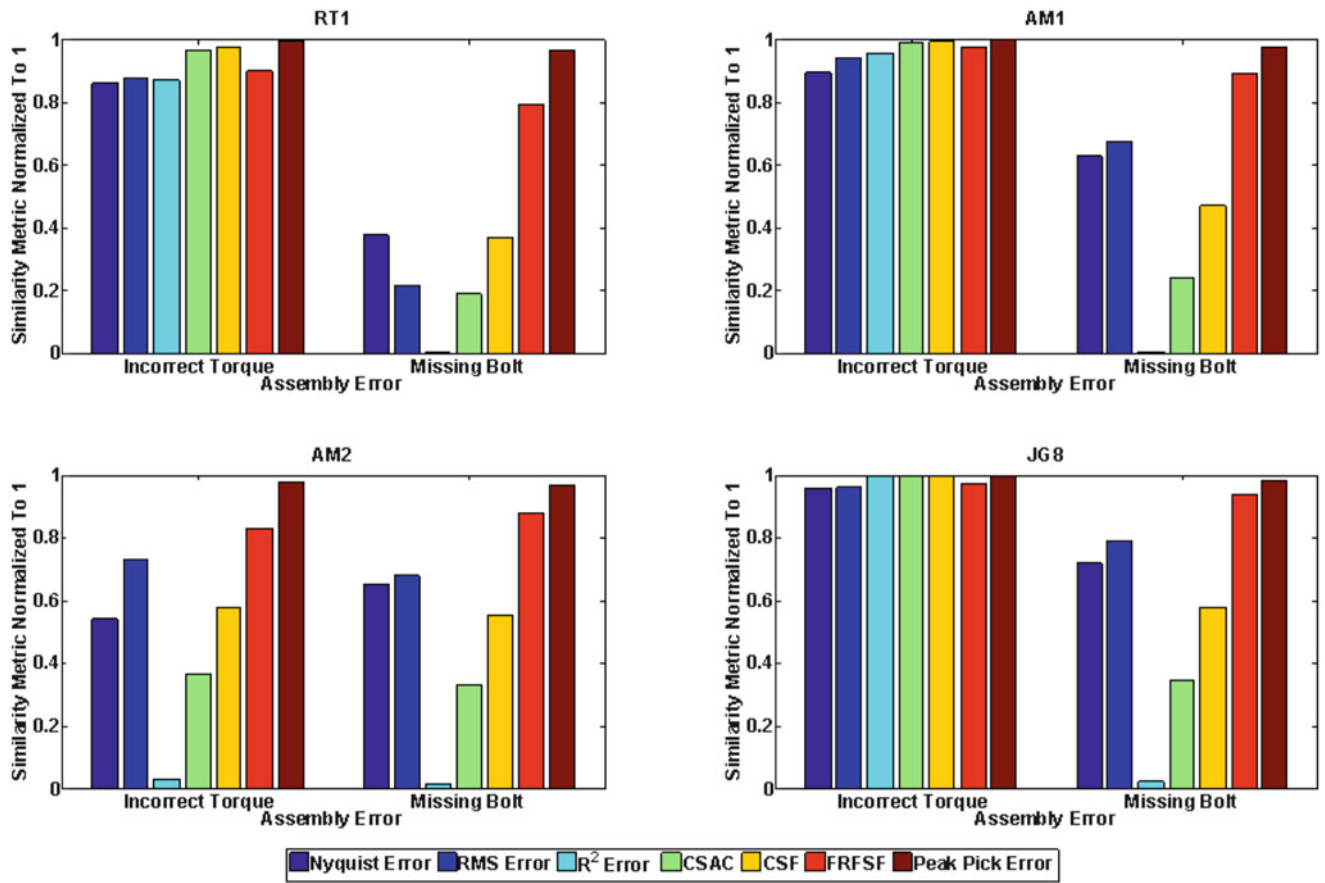


Fig. 32.9 Similarity metric comparison for incorrect assemblies normalized to one (1 = identical to correct assembly)

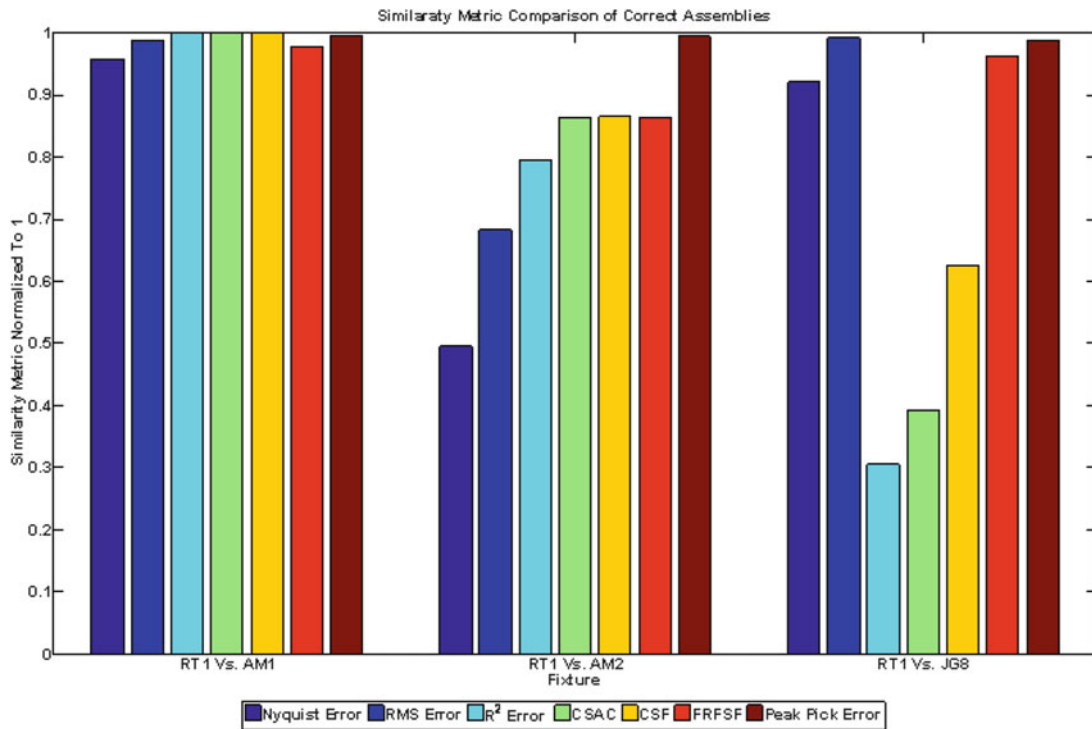


Fig. 32.10 Similarity metric comparison of fixtures for correct assemblies (1 = identical to RT1)

**Table 32.1** Average similarity comparing incorrect assemblies for all seven similarity metrics

	Nyquist error	RMS error	R <sup>2</sup> error	CSAC	CSF	FRFSF	Peak pick error
Incorrectly torqued average similarity	0.81	0.88	0.72	0.83	0.89	0.92	0.99
Missing bolt average similarity	0.59	0.59	0.01	0.28	0.49	0.88	0.97

## 32.5 Conclusion

Sandia National Laboratories chose to use similarity testing to quickly identify any assembly errors encountered during production of complex multibody assemblies. Because mode shapes could not be measured due to classification, radiological contamination, or concern with damaging the hardware, a single drive-point FRF measurement was combined with limited instrumentation on specialized test fixtures. In order to identify a metric that could be used to assess the similarity between assemblies, a study of various FRF correlation techniques was performed on a simplified test article under three different assembly configurations: correctly assembled, assembly-to-fixture bolts incorrectly torqued, and correctly torqued bolts with one removed. The three techniques chosen, Nyquist error, RMS error, and R<sup>2</sup> error, were found to provide the best assessment of the FRF and were used on the actual unit to help identify the presence of assembly errors.

## 32.6 Future Work

Further studies on similarity are underway at Sandia National Laboratories as additional hardware becomes available. These studies will provide some statistical confidence to verify that the metrics used are appropriate. This additional testing will also help identify the acceptable threshold for determining whether the two units are dynamically similar. The vibration test fixtures used in this work have contained unique and nonsymmetric geometry, creating some uncertainty in the results; similarity testing in the future would benefit from designing test fixtures with simplified geometry. Sandia is also planning to use these similarity tests on larger and more complicated structures for actual production use in the future.

Sandia also has interest in comparing environmental vibration data for similarity purposes. A large majority of the hardware being developed at Sandia undergoes vibration testing, and the definition of a similarity metric for response-only data could improve the ability to assess assembly on more units in production.

Sandia's primary goal with this work is to define a test procedure, metric, and threshold for assessing similarity between units being produced either on site or by an external contractor. This would allow similarity data to be acquired in a fast, reliable, and nonintrusive manner. The results in this paper show promise in this methodology, and future work will further refine this process, which can prove useful not only to Sandia Laboratories but to any industry where quality control is a concern.

## References

1. Allemang RJ (2003) The modal assurance criterion – twenty years of use and abuse. *Sound Vib Mag* August:14–20
2. Pascual R, Golinval J, Razeto M (1997) A frequency domain correlation technique for model correlation and updating. In: *Proceedings of the 15th international modal analysis conference*, pp 587–592
3. Heylen W, Avitabile P (1998) Correlation considerations – part 5 (degree of freedom correlation techniques). In: *Proceedings of the 16th international modal analysis conference*, pp 207–214
4. Fotsch D, Ewins DJ (2000) Applications of MAC in the frequency domain. In: *Proceedings of the 18th international modal analysis conference*, pp 1225–1231
5. Dascotte E, Strobbe J (1999) Updating finite element models using FRF correlation functions. In: *Proceedings of the 17th international modal analysis conference*

# Chapter 33

## Improved Estimation of Frequency Response Covariance

Daniel C. Kammer and Matthew Bonney

**Abstract** In high-consequence systems, critical decisions are made based on analytically predicted system response. In order to have confidence in the predictions, analytical models must be validated, and the effects of uncertainty on system response must be well understood. In systems with high modal density, modal based model validation is often problematic. It becomes more convenient to validate a model by directly using its response in the frequency domain. This then requires a corresponding frequency response based uncertainty quantification and propagation analysis. Covariance propagation is often used to propagate uncertainty and compute second order response statistics. However, linear covariance propagation applied to frequency response is inaccurate at resonances due to nonlinearity. A method is proposed that provides an improved estimate of the first two moments of frequency response uncertainty in the vicinity of resonances. It assumes that the uncertainty is small enough relative to damping such that an impedance based matrix inverse can be approximated using a finite number of terms. The method then propagates higher order moments of modal impedance uncertainty to approximate this inverse. The proposed approach can fit directly into a straightforward covariance propagation approach, and is applicable to substructured systems.

**Keywords** Uncertainty propagation • Covariance • Frequency response

### 33.1 Introduction

Critical decisions are made for high-consequence systems based on analytically predicted system response. For example, in the case of spacecraft, there must be a test-validated finite element model (FEM) that can be used to predict structural loads, response, performance, etc., prior to launch [1]. The model validation process includes tasks such as test/analysis correlation, analytical model updating, uncertainty quantification, and determination of predictive accuracy [2–4]. In spacecraft applications, finite element model validation has usually been performed in the modal domain. Test and analysis modal frequencies are compared directly, while mode shapes are compared using orthogonality and cross-orthogonality computations [5].

In order to have confidence in analytical predictions, the effects of uncertainty on system response must be well understood. Recently, quantification of model uncertainty and its propagation through large numerical simulations has been the focus of investigation [6–9]. While an engineer may design a single structure based on drawings, analysis, and experimental results, the reality is that the item produced is just one in an ensemble of structures due to variations and uncertainties in geometry, material parameters, construction, etc. The result is a random population of frequencies and mode shapes. If an analyst does not examine test-analysis correlation relative to uncertainty, very erroneous and dangerous decisions can be made regarding an analytical model's ability to make accurate predictions within both tested and untested regimes [10].

High-performance, precision space vehicles proposed by both the Air Force and NASA will require extremely low-level on-orbit vibration environments. Therefore, these space systems will require analytical models that are valid to a much higher than usual frequency range for accurate predictions. Within this higher frequency band, spacecraft become modally dense, and the corresponding vibration patterns have a short wavelength. Uncertainty then has an even larger influence on the structural response in modally dense systems. Vibrational modes become extremely sensitive to uncertainty, so the accepted modal-based methods of model correlation, such as cross-orthogonality, modal frequency comparisons, etc., simply

---

D.C. Kammer (✉) • M. Bonney

Department of Engineering Physics, University of Wisconsin-Madison, 1500 Engineering Dr., Madison, WI 53706, USA  
e-mail: [kammer@engr.wisc.edu](mailto:kammer@engr.wisc.edu)

do not work. An alternative, and possibly more desirable, approach would be to validate a model by directly using its response in the frequency domain. This would then require a corresponding frequency response based uncertainty quantification and propagation analysis.

A large number of researchers have investigated the effects of structural uncertainty on system response. For example, Mace and Shorter [11] and Hinke et al. [12] use linear perturbation methods to relate physical parameter uncertainties to uncertainty in modal parameters. The corresponding uncertainty in frequency response is then computed and the statistics determined through a Monte Carlo (MC) analysis. Hasselman and Chrostowski [13] use a covariance propagation approach to propagate modeling uncertainty into frequency response. This method avoids a MC analysis, however, it only produces the variance in the system response. In their applications, they also found that covariance propagation breaks down in the vicinity of system resonances and anti-resonances. Small resonant frequency shifts due to modeling uncertainties caused corresponding shifts in the peaks of the frequency response. In the case of isolated frequencies, small changes in frequencies produce large changes in frequency response. Therefore, the linear perturbation results that covariance propagation is based upon break down.

Kammer and Krattiger [14] expanded on the work done by Hasselman and Chrostowski by developing a systematic approach for propagating uncertainty using covariance propagation in substructured models. The uncertainty in the substructure is not restricted to any specific type, such as parameter uncertainty. It can be as general as uncertainty in the frequency response as determined by a series of substructure vibration tests. The approach is efficient, however, it is still inaccurate in predicting frequency response variance at resonances. This is due to the extreme nonlinear relation between uncertainty in frequency response and uncertainty in impedance at resonance. The objective of the research presented here is to improve upon the linear perturbation prediction for frequency response and its second order statistics in the vicinity of resonances.

### 33.2 Theory

In this presentation, it is assumed that any uncertainty of interest has already been propagated into the system level modal impedance matrix. For example, in the case of parameter uncertainty, the FEM physical impedance matrix at the  $i$ th frequency  $\omega_i$  can be expanded in a first order Taylor series about its nominal value in terms of the normalized design variables  $d_r$  using

$$Z_{Ri} = Z_i + \sum_{r=1}^{n_p} Z'_{ri} \Delta d_r \quad (33.1)$$

The nominal impedance is given by

$$Z_i = -\omega_i^2 M + i \omega_i C + K \quad (33.2)$$

in which  $M$ ,  $C$ , and  $K$  are the corresponding nominal mass, damping, and stiffness matrices, respectively. The normalized sensitivities,  $Z'_{ri}$ , can be easily computed in a commercial finite element code. Details for propagation of uncertainty at the substructure level into uncertainty at the system level can be found by Kammer and Krattiger [14]. In order to maintain accuracy, reduce numerical instability, and reduce the size of the computational problem, uncertainty propagation is performed in the modal space of the nominal FEM. A sufficient number of system modes,  $n_m$ , is computed to accurately represent the dynamics within the desired frequency band. This is usually 1.5–2.0 times the highest frequency of interest. It is assumed that the nominal mode set is rich enough such that it spans the uncertain system within the frequency range considered.

The expression in Eq. (33.1) can be transformed to modal coordinates, producing

$$z_{Ri} = z_i + \sum_{r=1}^{n_p} z'_{ri} \Delta d_r \quad (33.3)$$

where  $z_i = \phi^T Z_i \phi$ , is the nominal modal impedance matrix, etc. Let  $h_i$  be the nominal system modal displacement frequency response matrix at frequency  $\omega_i$ , then  $h_i = z_i^{-1}$  or

$$h_i z_i = I \quad (33.4)$$

Assuming modal damping, the modal frequency response matrix  $h_i$  is diagonal with the  $r$ th term given by

$$h_{irr} = [\omega_r^2 - \omega_i^2 + i2\zeta_r\omega_r\omega_i]^{-1} \quad (33.5)$$

in which  $\omega_r$  and  $\zeta_r$  are the natural frequency and damping coefficient for the  $r$ th system mode, respectively. If the nominal system is perturbed, Eq. (33.4) becomes

$$h_{Ri}z_{Ri} = (h_i + \Delta h_i)(z_i + \Delta z_i) = I \quad (33.6)$$

which can be expanded and rearranged to give

$$\Delta h_i = -h_{Ri} \Delta z_i h_i \quad (33.7)$$

This is the exact expression for the uncertainty, or change, in the frequency response for a given change, or uncertainty, in the impedance. Unfortunately, the corresponding perturbed modal frequency response  $h_{Ri}$  is not known. The usual covariance propagation approach is based on the first order approximation of Eq. (33.7) given by

$$\Delta h_i = -h_i \Delta z_i h_i \quad (33.8)$$

This approximation is accurate for small values of system uncertainty at frequencies that are removed from the resonances. As a resonance is approached, the relationship between the change in modal frequency response and the change in modal impedance becomes very nonlinear, and the linear approximation in Eq. (33.8) becomes poor.

As an alternative, Eq. (33.6) can be arranged to give the exact expression for uncertainty in frequency response in the form

$$\Delta h_i = -h_i \Delta z_i h_i [I + \Delta z_i h_i]^{-1} \quad (33.9)$$

The matrix inverse in Eq. (33.9) can be expanded in an infinite series to give

$$\Delta h_i = -h_i \Delta z_i h_i \left[ I - \Delta z_i h_i + \dots + (-1)^{k-1} (\Delta z_i h_i)^{k-1} + \dots \right] \quad (33.10)$$

If the spectral radius of matrix  $\Delta z_i h_i$  is less than 1.0, or equivalently, all the eigenvalues are within the unit circle, the series in Eq. (33.7) can be approximated by a finite number of terms. For example, in the case of uncertainty due to stiffness alone, the expression in Eq. (33.10) will converge for the  $r$ th isolated mode if the fractional uncertainty in the  $r$ th mode frequency due to the change in stiffness is less than the corresponding modal damping coefficient

$$\frac{\Delta \omega_r}{\omega_r} < \zeta_r \quad (33.11)$$

Defining the matrix

$$\Delta_{ik} = (\Delta z_i h_i)^{k-1} \Delta z_i \quad k = 1, \infty \quad (33.12)$$

the  $j$ th order approximation can be rewritten as

$$\Delta h_{ij} = h_i \left[ \sum_{k=1}^j (-1)^k \Delta_{ik} \right] h_i \quad (33.13)$$

Note that  $j = 1$  corresponds to the first order, or linear approximation used in straightforward covariance propagation. In terms of modal coordinates, the nominal physical frequency response matrix at the  $i$ th frequency is given by

$$H_i = \phi_s h_i \phi_a^T \quad (33.14)$$

in which  $\phi_s$  is the modal matrix row partitioned to  $n_s$  sensor locations, and  $\phi_a$  is the modal matrix row partitioned to  $n_a$  input locations. The  $j$ th approximation for the uncertainty in the physical frequency response matrix is then given by

$$\Delta H_{ij} = \phi_s h_i \left[ \sum_{k=1}^j (-1)^k \Delta_{ik} \right] h_i \phi_a^T \quad (33.15)$$

Uncertainty in velocity, or acceleration response can be determined by multiplying Eq. (33.15) by  $i\omega_i$  and  $-\omega_i^2$ , respectively. Equation (33.15) can be easily vectorized to give

$$p_j = H_X \left[ \sum_{k=1}^j (-1)^k q_k \right] \quad (33.16)$$

in which  $p_j = \text{vec}(\Delta H_{ij})$ ,  $q_j = \text{vec}(\Delta_{ij})$ , and  $H_X = (\phi_a h_i) \otimes (\phi_s h_i)$  represents a Kronecker product. Note that the subscript  $i$  has been dropped, recognizing the fact that computations are made at frequency each  $\omega_i$ . Based on Eq. (33.16), the  $j$ th approximation of the mean value of the frequency response uncertainty is then given by

$$E(p_j) = \bar{p}_j = H_X \left[ \sum_{k=1}^j (-1)^k \bar{q}_k \right] \quad (33.17)$$

The  $j$ th approximation for the frequency response correlation matrix can be computed using the expression

$$R_j = H_X \left[ \sum_{k=1}^j \sum_{l=1}^j (-1)^{k+l} \overline{q_k q_l^*} \right] H_X^* \quad (33.18)$$

in which  $*$  denotes a complex conjugate transpose. The associated covariance matrix is then given by

$$C_j = R_j - \bar{p}_j \bar{p}_j^* \quad (33.19)$$

An analogous procedure can be used to derive the associated relation matrix

$$S_j = E \left[ (p_j - \bar{p}_j) (p_j - \bar{p}_j)^T \right] \quad (33.20)$$

The covariance and relation matrices provide complete information regarding the second order statistics of the frequency response. However, it is more convenient to recover frequency response uncertainty directly in terms of magnitude and phase. It can be shown [15] that uncertainty in frequency response magnitude and phase for the  $lk$  input–output pair can be related to uncertainty in the corresponding real and imaginary parts using

$$\begin{Bmatrix} \Delta |H_{lk}| \\ \Delta \theta_{lk} \end{Bmatrix} = J_{lk} \begin{Bmatrix} \Delta (H_{lk})_R \\ \Delta (H_{lk})_I \end{Bmatrix} \quad (33.21)$$

where matrix  $J_{lk}$ , given by

$$J_{lk} = \begin{bmatrix} (H_{lk})_R / |H_{lk}| & (H_{lk})_I / |H_{lk}| \\ -(H_{lk})_I / |H_{lk}|^2 & (H_{lk})_R / |H_{lk}|^2 \end{bmatrix}$$

is evaluated using the nominal system model at frequency  $\omega_i$ , and subscripts  $R$  and  $I$  denote real and imaginary parts. Taking the expectation of the outer product produces

$$C_p = \begin{bmatrix} \overline{(\Delta |H_{lk}|)^2} & \overline{(\Delta |H_{lk}|)(\Delta \theta_{lk})} \\ \dots & \overline{(\Delta \theta_{lk})^2} \end{bmatrix} = J_{lk} \begin{bmatrix} \overline{(\Delta H_{lk})_R^2} & \overline{(\Delta H_{lk})_R (\Delta H_{lk})_I} \\ \dots & \overline{(\Delta H_{lk})_I^2} \end{bmatrix} J_{lk}^T = J_{lk} C_r J_{lk}^T \quad (33.22)$$



in which  $C_p$  and  $C_r$  are the covariance matrices for the polar and rectangular forms of the corresponding frequency response pair, respectively. The terms in  $C_r$  can be recovered from the frequency response covariance  $C_j$  and relation matrix  $S_j$  using the relationships

$$\begin{aligned}\overline{(\Delta H_{lk})_R^2} &= \frac{1}{2} \left[ (C_j)_{pp} + (S_j)_{Rpp} \right] \\ \overline{(\Delta H_{lk})_I^2} &= \frac{1}{2} \left[ (C_j)_{pp} - (S_j)_{Rpp} \right] \\ \overline{(\Delta H_{lk})_R (\Delta H_{lk})_I} &= \frac{1}{2} (S_j)_{Ipp}\end{aligned}\quad (33.23)$$

where subscript  $pp$  indicates the  $p$ th diagonal term in the corresponding matrices. The row and column indices  $l$  and  $k$  can be computed from  $p$  using  $l = p - \text{floor}(p/n_s) * n_s$ , and  $k = 1 + \text{floor}(p/n_s)$ , in which  $\text{floor}(x)$  is a function that rounds to the nearest integer towards minus infinity. Diagonal terms in  $C_p$  represent the mean-square values of the uncertainty in the frequency response magnitude and phase.

The vectors  $q_j$  first introduced in Eq. (33.16) contain products of  $j$  terms  $\Delta z_{ikl}$  from the modal impedance uncertainty matrix. In general, the mean values required in Eqs. (33.17, 33.18, 33.19, and 33.20) would have to be computed based upon knowledge of the finite element model inputs, combined with MC analysis. While this requires additional computations, it is considerably easier and less computationally intensive, to compute the statistics of the modal impedance matrix, than it is to directly apply MC to the frequency response. In addition, if it can be assumed that the model inputs are zero mean and jointly normally distributed, then many of the product mean values appearing in the previous equations are zero. For example

$$\bar{q}_k = 0 \quad k \text{ is odd}$$

and

$$Q_{lk}^* = \overline{q_l q_k^*} = 0 \quad Q_{lk} = \overline{q_l q_k^T} = 0 \quad l + k \text{ is odd}$$

Therefore, in the case of a second order improvement, the mean value of the vectorized uncertainty in the frequency response is

$$\bar{p}_2 = H_X [-\bar{q}_1 + \bar{q}_2] = H_X \bar{q}_2$$

The first order term, which corresponds to the usual covariance propagation, is zero. Using Eq. (33.18), the second order approximation of the correlation matrix  $R_2$  is given by

$$R_2 = H_X [Q_{11}^* - (Q_{12}^* + Q_{21}^*) + Q_{22}^*] H_X^* = H_X [Q_{11}^* + Q_{22}^*] H_X^*$$

Applying Isserlis' Gaussian moment theorem [16].

$$E(x_1 x_2 x_3 \cdots x_k) = \sum \prod E(x_i x_j)$$

the remaining product means can be expressed directly in terms of the quadratic entries within the covariance and relation matrices for the modal impedance uncertainty  $Q_{11}^* = \overline{q_1 q_1^*} = C_z$  and  $Q_{11} = \overline{q_1 q_1^T} = S_z$ , respectively. These two matrices are computed during the usual covariance propagation procedure, so no additional information is required for the proposed refined approximation approach. The notation  $\Sigma \Pi$  means summing over all distinct ways of partitioning  $x_1 x_2 x_3 \cdots x_k$  into pairs. For example, quartic expressions, such as  $\bar{q}_4$  or  $Q_{22}$ , will contain entries of the form  $\overline{x_1 x_2 x_3 x_4}$ , in which  $x_k$  is a zero mean, normally distributed term from within  $\Delta z_i$ . This quartic mean can then be written in terms of quadratic means in the form.

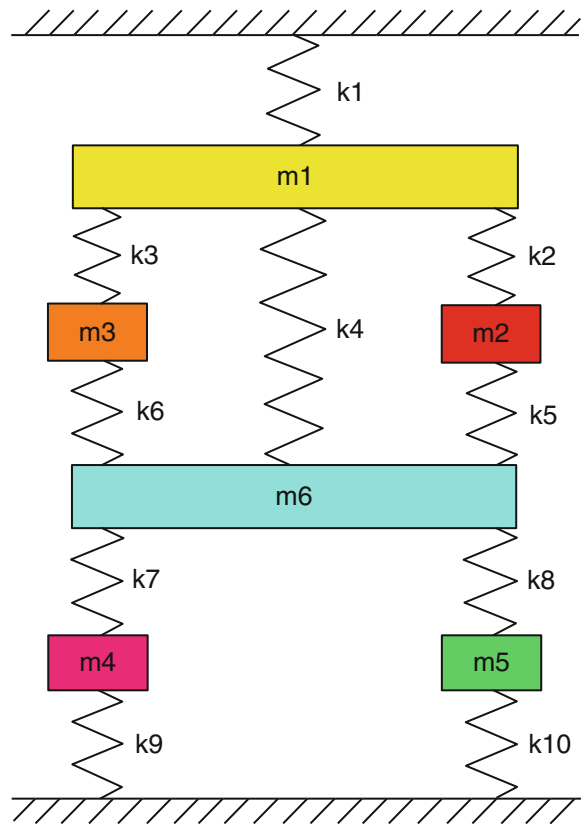
$$\overline{x_1 x_2 x_3 x_4} = \overline{x_1 x_2} \cdot \overline{x_3 x_4} + \overline{x_1 x_3} \cdot \overline{x_2 x_4} + \overline{x_1 x_4} \cdot \overline{x_2 x_3}$$

### 33.3 Numerical Example

The simple example shown in Fig. 33.1 was examined using the proposed approach. It contains ten uncertain springs. Table 33.1 lists the nominal system modal frequencies. A random representation of the system is generated by selecting each individual spring value from a normal probability distribution. Initially, the standard deviations of the distributions were restricted to 10 % of the nominal spring values. Three percent modal damping was used in the simulation, and the system was forced at mass 1.

Figure 33.2 shows the true value, the linear approximation ( $j = 1$ ), and the first three additional iterations ( $j = 2 - 4$ ) using Eq. (33.16) for the magnitude of the change in the drive point displacement frequency response for mass 1. It can be seen that the first additional iteration ( $j = 2$ ) provides a dramatic improvement over the linear approximation in regions removed from the resonances, and subsequent iterations further improve the results as the driving frequency gets closer to the resonances and anti-resonances. However, in the vicinity of the resonance at 7.39 Hz, the spectral radius of  $\Delta z_i h_i$  is close to 1.0, so convergence is very slow. Therefore, the coefficient of variation of the uncertainty was reduced to 5 %, and the modal damping was increased to 5 %.

The higher order approximation was then applied to compute the frequency response second order statistics for the new case of 5 % uncertainty and modal damping. Figure 33.3 shows the variance for the drive point frequency response. The usual covariance approximation is relatively accurate, however the sixth order approximation improves the prediction at the resonances. Figure 33.4 shows the corresponding term from the frequency response relation matrix. The sixth order approximation shows a significant improvement in predicting the mean square frequency response uncertainty. Figure 33.5

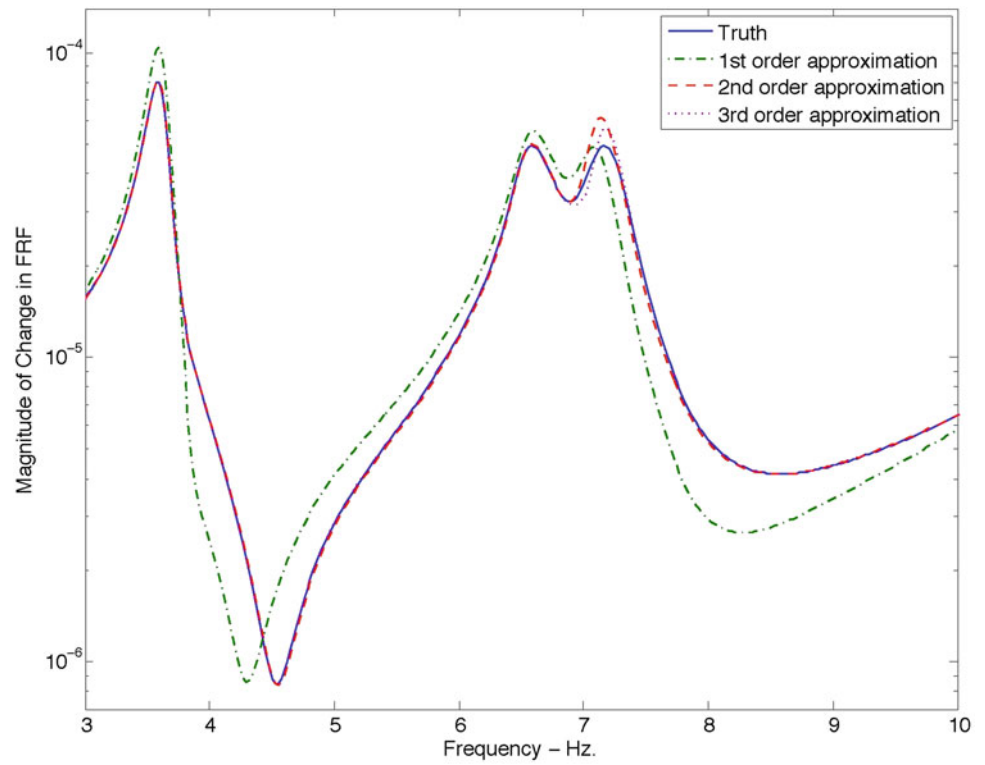


**Fig. 33.1** Simple concentrated mass and spring problem

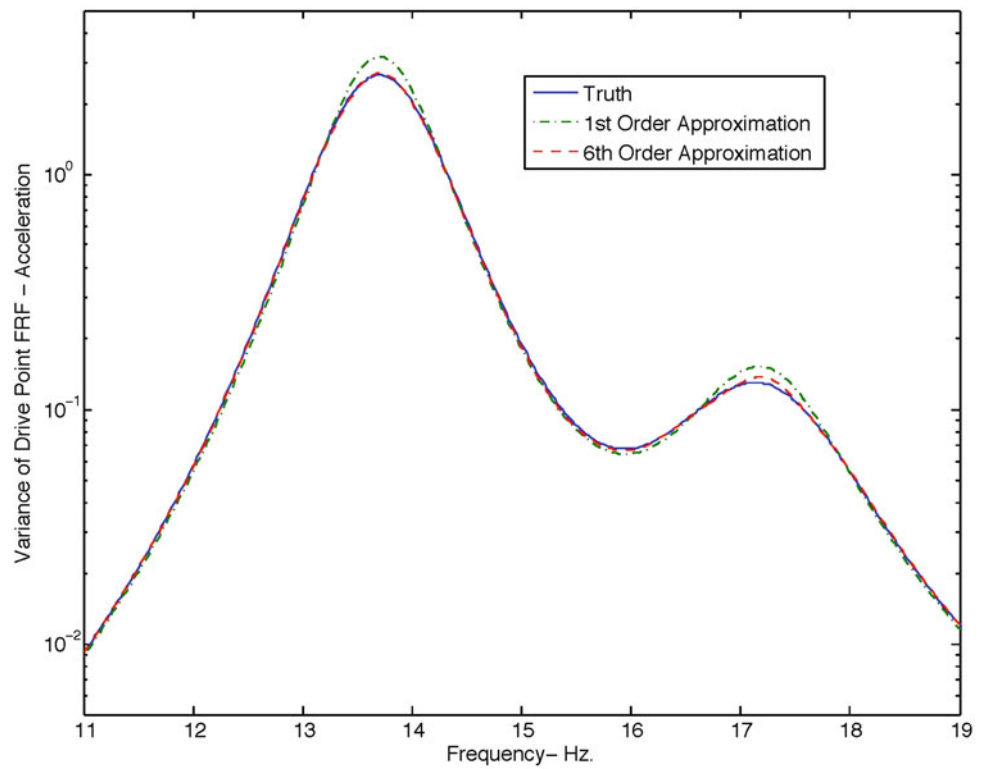
**Table 33.1** Natural frequencies of example system

Mode number	Frequency [Hz]
1	3.62
2	6.54
3	7.10
4	7.39
5	13.72
6	17.25

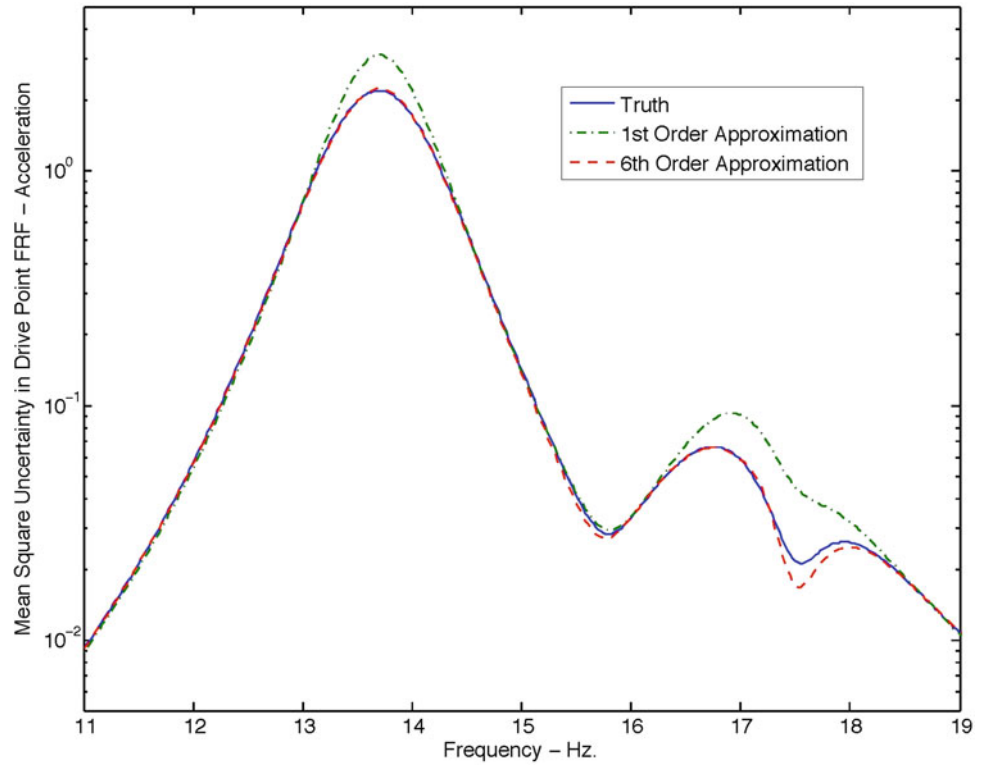
**Fig. 33.2** Uncertainty in drive point frequency response for mass 1



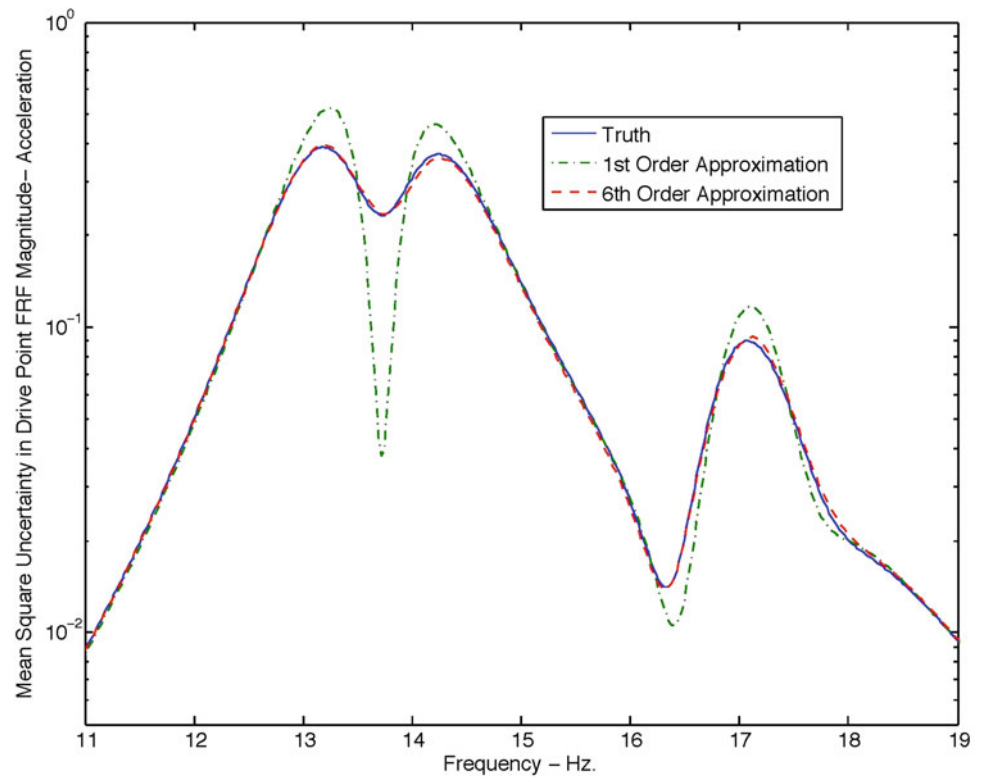
**Fig. 33.3** Drive point frequency response variance



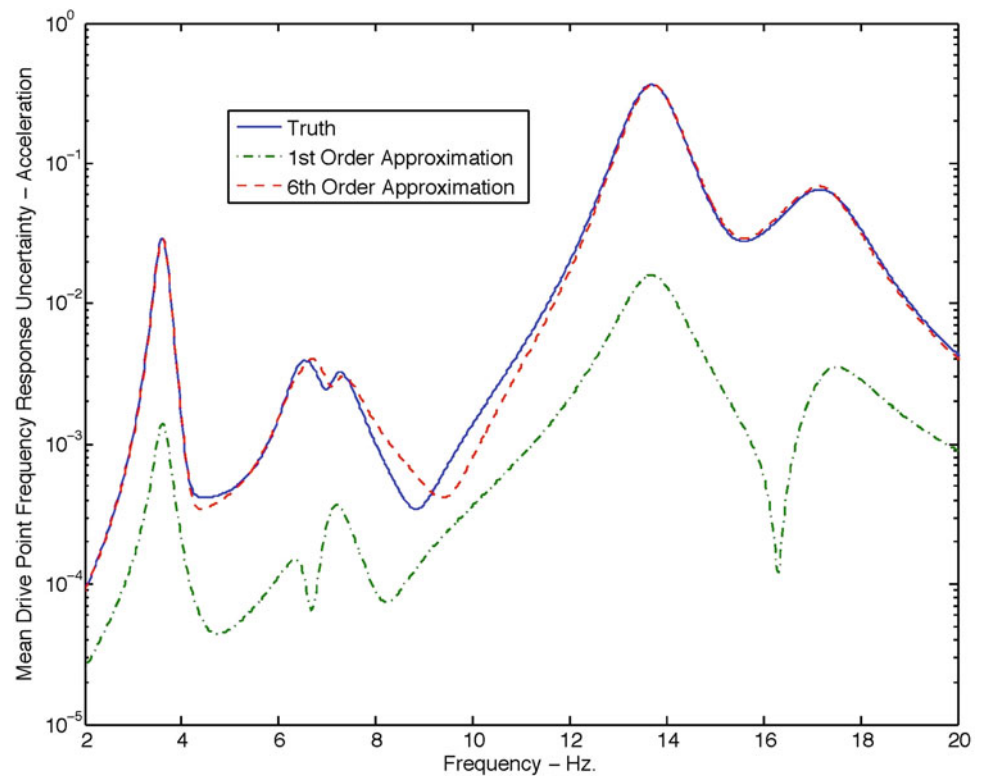
**Fig. 33.4** Drive point frequency response mean square uncertainty magnitude



**Fig. 33.5** Drive point frequency response mean square magnitude uncertainty



**Fig. 33.6** Drive point mean frequency response uncertainty magnitude



illustrates the uncertainty in the magnitude of the drive point frequency response. This result was recovered from the covariance and relation matrices using the linear perturbation approach outlined in the previous section. The sixth order approximation gives results that are clearly superior to the usual covariance propagation in the vicinity of the resonances. The results for phase uncertainty were just as accurate, and not shown here. The frequency response uncertainty mean can also be recovered using the proposed approach. Figure 33.6 shows that the sixth order approximation produces accurate results at the resonances. Note that the first order approximation should be nothing more than a computed zero.

### 33.4 Conclusion

It is well known that linear covariance propagation applied to frequency response is inaccurate at resonances due to nonlinearity. A method has been proposed that provides an improved estimate of the first two moments of frequency response uncertainty in the vicinity of a resonance. It assumes that the uncertainty is small enough relative to damping such that an impedance based matrix inverse can be approximated using a finite number of terms. The approach then propagates higher order moments of modal impedance uncertainty to approximate this inverse. If terms within the modal impedance uncertainty matrix are zero mean and jointly Gaussian, then the higher-order impedance moments can be computed using the modal impedance covariance and relation matrices that are produced by the usual linear covariance propagation formulation. The proposed approach can fit directly into a straightforward covariance propagation approach, and is applicable to substructured systems. The approach was applied to a simple example, and was shown to produce improved results. It is important to note that the higher-order approximation is only required in the vicinity of resonances, and anti-resonances. The usual frequency response covariance propagation approach works well at other frequencies. In cases where parameter uncertainty is large relative to the modal damping, a simple series acceleration approach was shown to greatly improve series convergence properties.

**Acknowledgement** This material is based on work supported by Sandia National Laboratories. Sandia is a multi-program laboratory operated by Sandia Corporation, a Lockheed Martin Company, for the United States Department of Energy's National Nuclear Security Administration.

## References

1. DOD (1999) Test requirements for launch, upper stage, and space vehicles, applications and guidelines, vol II. DOD Handbook-340A (USAF)
2. Hemez FM, Doebling SW, Anderson MC (2004) A brief tutorial on verification and validation. In: 22nd international modal analysis conference, Dearborn
3. ASME (2006) Guide for verification and validation in computational solid mechanics. ASME
4. Paez TL (2009) Introduction to model validation. In: 27th international modal analysis conference, Orlando
5. Hasselman TK, Coppelino RN, Zimmerman DC (2000) Criteria for modeling accuracy: a state-of-the-practice survey. In: 18th international modal analysis conference, San Antonio
6. Rebba R, Huang S, Liu Y, Mahadevan S (2006) Statistical validation of simulation models. *Int J Mater Prod Technol* 25(1):164–181
7. Hemez FM, Rutherford AC, Maupin RD (2006) Uncertainty analysis of test data shock responses. In: 24th international modal analysis conference, Saint Louis
8. Basseville M, Benveniste A (2006) Handling uncertainties in identification and model validation: a statistical approach. In: 24th international modal analysis conference, Saint Louis
9. Hasselman TK (2001) Quantification of uncertainty in structural dynamic models. *J Aerosp Eng* 14:158–165
10. Bergman E, Allen MS, Kammer DC, Mayes RL (2010) Probabilistic investigation of sensitivities of advanced test-analysis model correlation methods. *J Sound Vib* 329(13):2516–2531
11. Mace BR, Shorter PJ (2001) A local modal/perturbation for estimating frequency response statistics of built-up structures with uncertain properties. *J Sound Vib* 242:793–811
12. Hinke L, Dohnal F, Mace BR, Waters TP, Ferguson NS (2009) Component mode synthesis as a framework for uncertainty analysis. *J Sound Vib* 324:161–178
13. Hasselman TK, Chrowstowski JD (1994) Propagation of modeling uncertainty through structural dynamic models. In: 35th AIAA structures, structural dynamics, and materials conference, Hilton Head, pp 72–83
14. Kammer DC, Krattiger D (2013) Propagation of uncertainty in substructured spacecraft using frequency response. *AIAA J* 51(2):353–361
15. Schultz T, Sheplak M, Cattafesta LN (2007) Application of multivariate uncertainty analysis to frequency response function estimates. *J Sound Vib* 305:116–133
16. Michalowicz JV, Nichols JM, Bucholtz F, Olson CC (2009) An Isserlis' theorem for mixed Gaussian variables: application to the auto-bispectral density. *J Stat Phys* 136(1):89–102

# Chapter 34

## Cross Orthogonality Check for Structures with Closely Spaced Modes

Anders Skafte, Manuel L. Aenlle, and Rune Brincker

**Abstract** Structures with closely spaced modes can often be hard to correlate with numerical models due to the high sensitivity of the eigenvectors. Even the smallest change in either mass or stiffness can have a large influence on the eigenvectors, and makes it hard to fit a numerical model so its modal parameters matches those obtain from measurements. This paper introduces a robust method for calculating the cross orthogonality check for structures with closely spaced modes. The method utilizes the fact that a cluster of closely spaced eigenvectors from an experiment and from a well correlated numerical model will span the same subspace, although the experimental mode is badly correlated with its corresponding numerical mode. A new basis of numerical modes is created by redefining the closely spaced numerical modes as a linear combination of one another, based on their projection upon the experimental mode. This will enable a more robust calculation of the cross orthogonality check. The method is validated using simulation cases where the errors are evaluated using simulated responses for the different sets of modal parameters.

**Keywords** Closely spaced mode • Correlation • Cross orthogonality check • Mode shape sensitivity • Simulation

### 34.1 Introduction

The cross orthogonality check (XOR) is a method for measuring the correlation between an analytical model and experimental results, which basically consists of calculating the inner product of two sets of mode shapes over the mass matrix. When the two sets of mode shapes are perfectly correlated this yields the identity matrix, whereas any off diagonal elements can be seen as a coupling of modes. Thresholds for acceptable diagonal and off diagonal terms are often dictated by large agencies as NASA and ESA [1, 2], but will often be in the region of

$$\begin{aligned} XOR_{i,j} &\geq 0.9 \text{ for } i = j \\ XOR_{i,j} &\leq 0.1 \text{ for } i \neq j \end{aligned} \quad (34.1)$$

With XOR indicating the cross orthogonality matrix and  $i$  and  $j$  being row and column number.

Problems can arise when the test structure holds natural frequencies which are closely spaced. Then even the smallest discrepancy between the structure and the analytical model can result in large deviations of the mode shapes – which will cause large off-diagonal terms when calculating the XOR.

To overcome this problem it is suggested that clusters of closely spaced modes in the FE model are “rotated” so they align with the experimental mode shapes. This is done by individually projecting the FE mode shapes onto the cluster of closely spaced experimental modes, using this projecting as a linear combination and thereby rotating the modes in the subspace. When a structure has repeated poles the mode shapes will share the exact same subspace. For closely spaced modes this will only be an approximation. The aim of this paper is to show that in the case of closely spaced modes, the cluster of mode shapes can be rotated for a better correlation, without significantly changing the physics of the analytical model. The theory is tested on a simulation case using a three plate shell structure.

---

A. Skafte (✉) • R. Brincker  
Department of Engineering, Aarhus University, Aarhus, Denmark  
e-mail: ask@ase.au.dk

M.L. Aenlle  
Department of Construction and Manufacturing Engineering, University of Oviedo, Asturias, Spain

The topic of problems in correlation of models with closely spaced modes is well known. In [3] the author discusses the problems of non orthogonality arising from repeated poles. In [4] the authors argue that the correlation should be measured between clusters in the case of closely spaced modes and introduces the measure S2MAC. The sensitivities of mode shapes are discussed in [5] where the authors differ between “closely spaced modes” and “nearly repeated eigenvalues”.

## 34.2 Theory

### 34.2.1 Repeated Poles

To better understand the concept of rotating a cluster of closely spaced modes, we will start by taking a look at a system with repeated poles. Let the equations of motion for an undamped system be given by the eigenvalue problem

$$\mathbf{K} \mathbf{a} = \omega^2 \mathbf{M} \mathbf{a} \quad (34.2)$$

With  $\mathbf{a}$  being the experimental mode shape,  $\mathbf{M}$  and  $\mathbf{K}$  being the mass and stiffness matrices respectively, and  $\omega^2$  being the eigenvalue of the system. Using the orthogonality conditions Eq. 34.2 can be rewritten as

$$(\omega_i^2 - \omega_r^2) \mathbf{a}_i^T \mathbf{M} \mathbf{a}_r = 0 \quad (34.3)$$

With  $i$  and  $r$  representing mode numbers. When  $i = r$ , Eq. 34.3 is fulfilled for any linear combination of  $\mathbf{a}_i$  and  $\mathbf{a}_r$  [5]. This is illustrated in Fig. 34.1.

Here the mode shapes are illustrated as vectors. What is important here is not the individual direction of each mode, but rather that they always span the same subspace, and that any combination will fulfill Eq. 34.3. This also means that an FE model which perfectly matches the properties of the structure still can result in poor MAC-values [6] for the repeated modes. But the FE modes can be rotated to match those of the structure, without this having influence on the FE model.

### 34.2.2 Closely Spaced Modes

When a structure has two close modes, these will be highly sensitive to even small changes. This can be seen by observing the mode shape sensitivity equations [7].

$$\frac{\partial \mathbf{b}_i}{\partial u} = -\frac{1}{2m_i} \mathbf{b}_i^T \frac{\partial \mathbf{M}}{\partial u} \mathbf{b}_i \mathbf{b}_i + \sum_{r=1, r \neq i}^{N_m} \frac{1}{\omega_i^2 - \omega_r^2} \frac{1}{m_i} \mathbf{b}_r^T \left( -\lambda_i \frac{\partial \mathbf{M}}{\partial u} + \frac{\partial \mathbf{K}}{\partial u} \right) \mathbf{b}_i \mathbf{b}_r \quad (34.4)$$

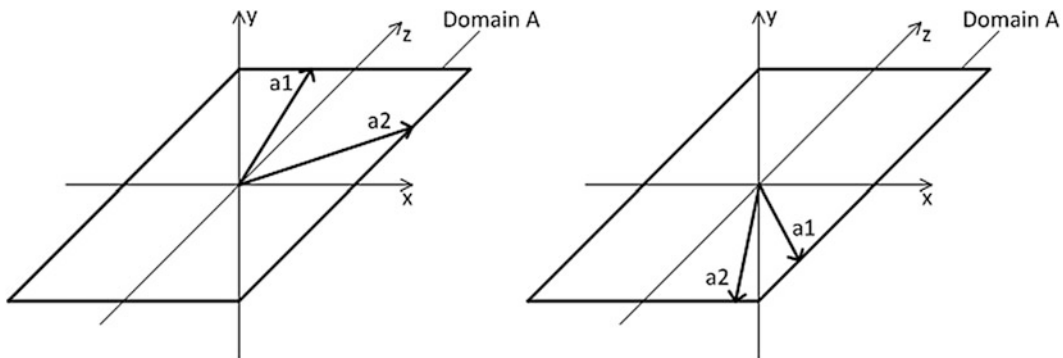
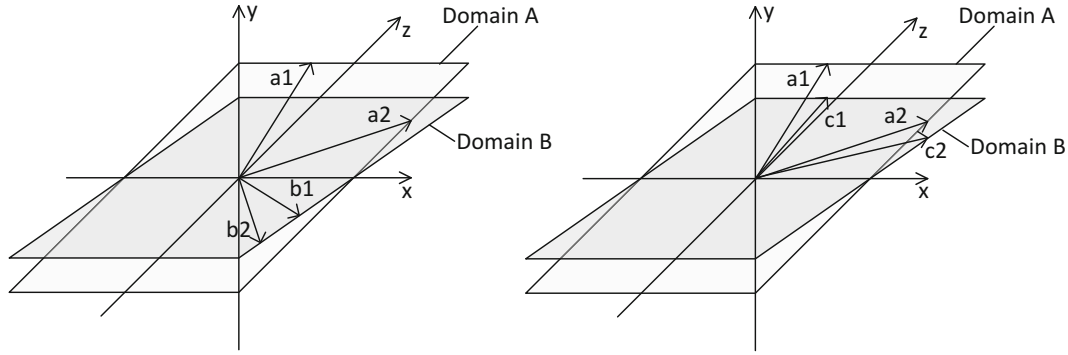


Fig. 34.1 Graphical illustration of two experimental mode shapes with repeated poles





**Fig. 34.2** Graphical illustration of two closely spaced modes

Here with  $\mathbf{b}$  being FE mode shapes,  $m_i$  the  $i$ 'th modal mass,  $N_m$  the total number of modes and  $u$  a parameter in which the model is perturbed. Here it is easily seen that when the factor  $\Delta\omega = \omega_i^2 - \omega_r^2$  goes towards zero, the change in mode shape will go towards infinity.

To illustrate the concept of closely spaced modes graphically, we will need to define two different domains:

- Domain A: Experimental mode shapes.
- Domain B: FE mode shapes.

The left of Fig. 34.2 illustrates the experimental mode shape in domain A, and the FE mode shapes in domain B. There will almost always be a difference between the experimental modes and FE modes which is illustrated by the difference between domain A and B (here plotted as two planes). Due to the high sensitivity the modes from A and B can be badly correlated.

The right of Fig. 34.2 again illustrates the experimental mode shapes, but here the FE mode shapes have been rotated by a linear transformation. The rotated mode shapes,  $c_1$  and  $c_2$ , will still belong to domain B. The mode shapes,  $b_1$  and  $b_2$ , will fulfill the condition

$$(\omega_i^2 - \omega_r^2) \mathbf{b}_i^T \mathbf{M}_{FE} \mathbf{b}_r = 0 \quad (34.5)$$

With  $\mathbf{M}_{FE}$  being the FE mass matrix.

But since we are dealing with closely spaced modes (and not repeated modes),  $c_1$  and  $c_2$ , will only be an approximate solution if substituted into Eq. 34.5. In other words we have to accept a small error in the analytical model in order to get a good correlation of the modes. The magnitude of this error is investigated later in the paper.

The vector describing the linear combination that rotate  $b_1, b_2$  onto  $c_1, c_2$  is found by projecting the modes from A onto B, here illustrated with the first and second mode shape

$$\mathbf{t}_1 = \mathbf{B}_{12}^\dagger \mathbf{a}_1 \quad (34.6)$$

With  $\mathbf{B}_{12}$  being the FE mode shape matrix holding the two first modes, and  $\dagger$  indicating the Moore-Penrose pseudo inverse.

Mode  $c_1$  can then be found by

$$\mathbf{c}_1 = \mathbf{B}_{12} \mathbf{t}_1 \quad (34.7)$$

### 34.2.3 Cross Orthogonality Check

The orthogonality conditions provide that the inner product of the mode shapes over the mass matrix gives the identity matrix.

$$\mathbf{B}^T \mathbf{M} \mathbf{B} = \mathbf{I} \quad (34.8)$$

With  $\mathbf{I}$  being the identity matrix.

The XOR is found by switching the transposed FE mode shape matrices in Eq. 34.8 with the experimental mode shapes.

$$XOR = A^T M B \tag{34.9}$$

Where the level of correlation is measured by evaluating the diagonal and off-diagonal elements in the XOR matrix, in comparison with certain threshold values, as for example given in Eq. 34.1. The FE model will almost always hold a much larger amount of DOF's than the experiment. This means that either the FE mass matrix has to be reduced or the experimental mode shapes must be expanded using techniques as Guyan, IRS, SEREP or Local Correspondence [8–11].

### 34.3 Numerical Study

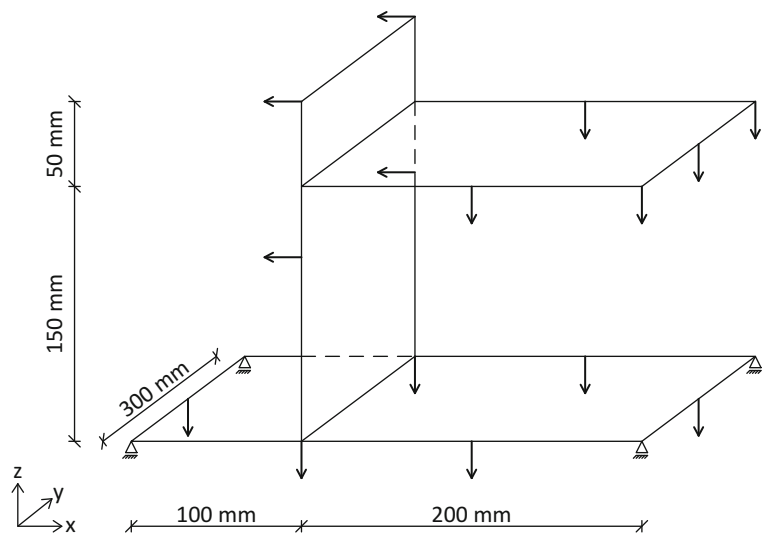
To verify the theory studies were made on two different FE model of a three plate steel structure, with pinned supports in the corners of the button plate. For both models the two horizontal plates have a thickness of 3 mm but the vertical plate was 1.6 mm in one model (Case 1) and 1.8 mm in the other (Case 2). This was done to make a model where mode 4 and 5 were a little separated and one where they were very close. Both models consist of a total of 377 nodes and 336 QUAD4 elements. The first five modes were used in the analysis, and 15 DOF's were chosen as *active* (Fig. 34.3).

Table 34.1 shows the first five natural frequencies of the reference case for both Case 1 and Case 2.

To create different sets of modal parameters small changes were made to 4 QUAD4 elements (Fig. 34.4). Here the density was changed by multiplying it with a scaling factor. In Case 1 the scaling factor was going from 1 to 2.5, with steps of 0.1, and in Case 2 from 1 to 1.3, with steps of 0.02. In both cases this gave 15 scenarios with density change (Model A), and 1 reference (Model B). For all of the 15 scenarios, the fourth and fifth mode shapes were rotated according to Eqs. 34.6 and 34.7 (Model C).

The XOR was calculated using Eq. 34.9 for all 15 scenarios. Comparisons were made on the difference between Model A and B, and Model A and C. For each scenario the largest error on both the diagonal and off-diagonal elements were evaluated. The results for Case 1 and 2 are presented in Figs. 34.5 and 34.6 respectively.

The left plot in Fig. 34.5 shows the diagonal value that has the largest distance to 1 as a function of the increased density in the four elements illustrated in Fig. 34.4. Here it is clear to see that the error in correlation between Model A and B drops considerably when the scale factor reaches 2. The error in correlation between Model A and C follows more a straight line. In this case the correlation for the diagonal elements stays within the threshold given in Eq. 34.1, for both “non-rotated” and “rotated” mode shapes. The effect of rotating the closely spaced modes becomes more significant when looking at the

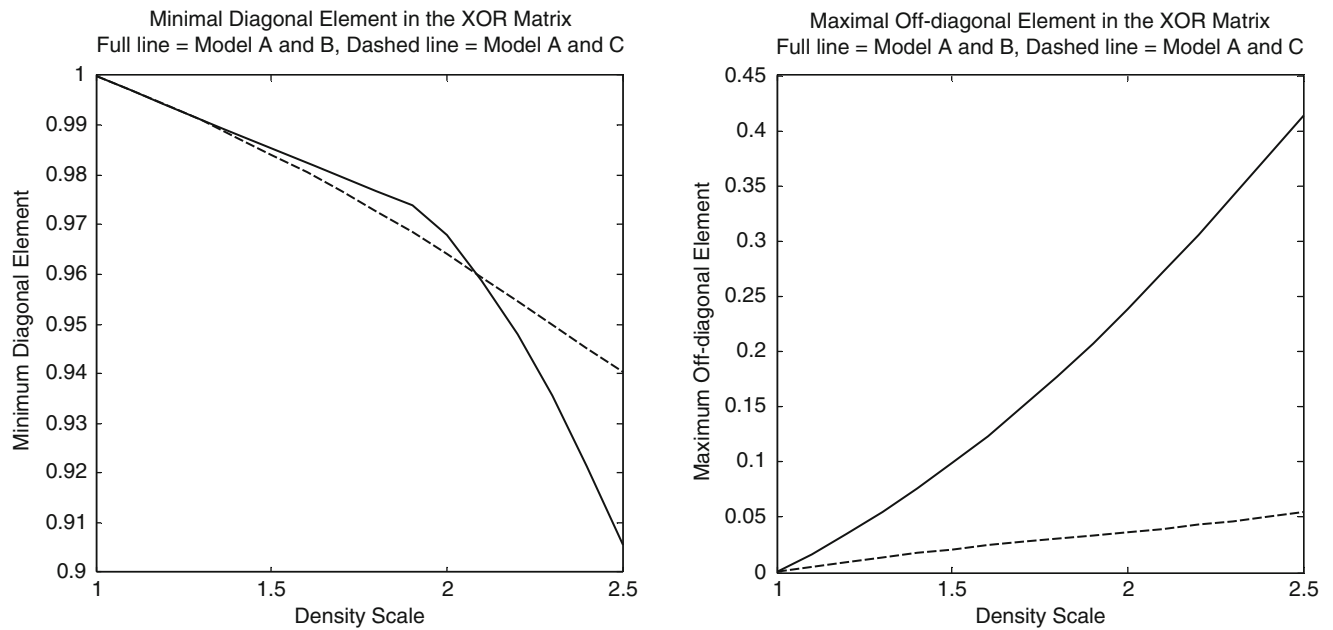
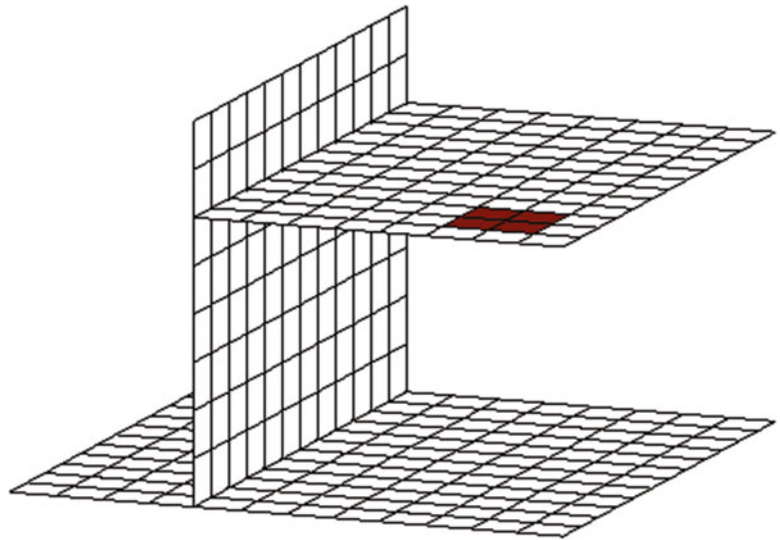


**Fig. 34.3** Illustration of the shell structure. *Arrows* indicate the “active” DOF’s

**Table 34.1** First five natural frequencies for the reference cases

Mode #	Mode 1	Mode 2	Mode 3	Mode 4	Mode 5
Frequencies, Case 1 [Hz]	3.368	7.570	11.846	16.476	16.967
Frequencies, Case 2 [Hz]	3.896	8.690	13.059	16.763	16.767

**Fig. 34.4** FE model of the structure. The *red area* indicates the elements where the density has been changed

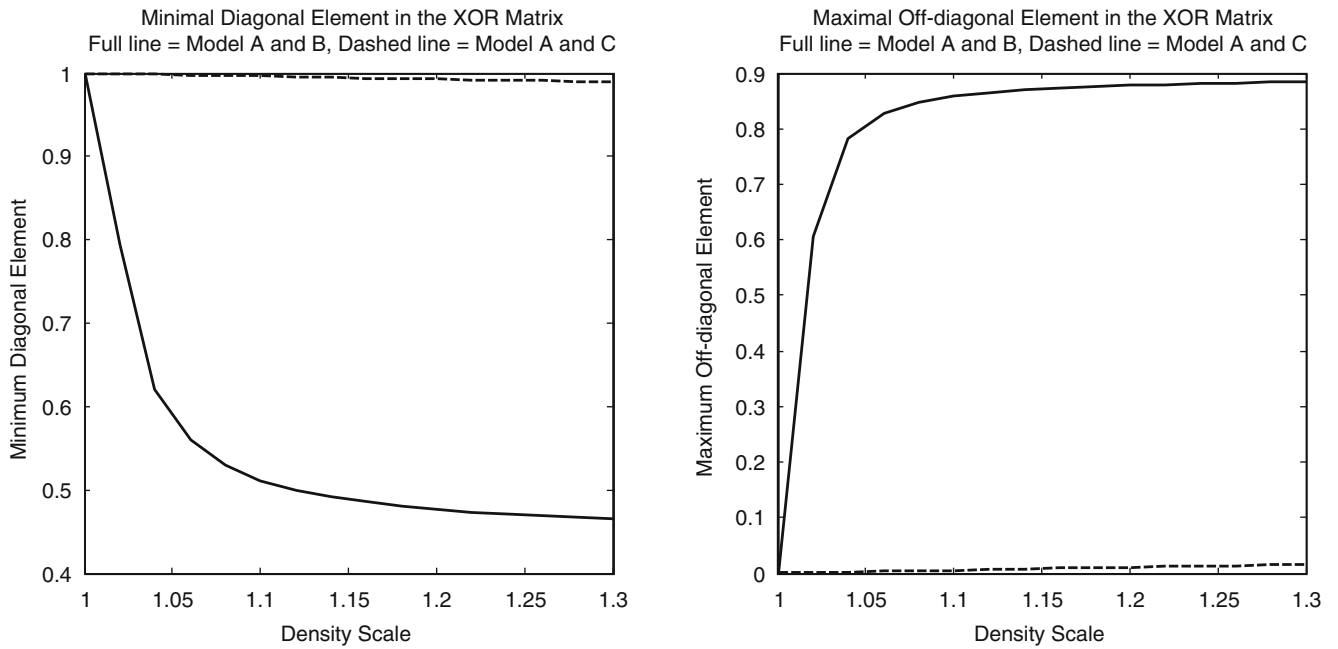


**Fig. 34.5** Result from Case 1. *Left*: Maximum error on the diagonal element as a function of the density scale factor. *Right*: Maximum error on the off-diagonal element as a function of the density scale factor

off-diagonal terms, which are illustrated in the right plot of Fig. 34.5. When looking at the correlation between Model A and B, the off-diagonal term will exceed the threshold when the scale factor reaches 1.5, where the off-diagonal term for the XOR matrix with Model A and C stays below the threshold for all 15 scenarios. The results from Case 2 are illustrated in Fig. 34.6, and show how extremely sensitive the modes become when the frequency distance gets really small. Here the thresholds from Eq. 34.1 are exceeded with the first scenario of density change, corresponding to a total mass change of 0.024 %. The correlation for the rotated mode shapes, however, shows good results for all scenarios.

Figures 34.5 and 34.6 show that certain correlation criteria can be achieved by rotating the closely spaced modes. But since mode 4 and 5 are not repeated modes, the physics of the FE model will change when going from Model B to Model C. What is left to answer is how big the magnitude of this change is. To investigate this, sets of responses were calculated in all 15 active DOF's using both the mode shapes from Model B and C. The simulated response for each channel was found as the inverse Fourier transformation of Eq. 34.10.

$$Y(\omega) = H(\omega) X(\omega) \quad (34.10)$$



**Fig. 34.6** Result from Case 2. *Left*: Maximum error on the diagonal element as a function of the density scale factor. *Right*: Maximum error on the off-diagonal element as a function of the density scale factor

Where  $\mathbf{Y}$  is the Fourier transformation of the response,  $\mathbf{H}$  is the frequency response matrix and  $\mathbf{X}$  is the Fourier transformation of the load. The damping was set to 0.2 % and the load was applied to the structure as Gaussian normal distributed.

The error between two coinciding channels from Model B and C, was calculated as

$$e_i = \frac{\sigma(y_{B,i} - y_{C,i})}{\sigma_{\bar{y}_B}} 100 \% \quad (34.11)$$

With  $\sigma$  symbolizing the standard deviation, and  $\sigma_{\bar{y}_B}$  being the mean value of the stand deviations of all the responses in Model B.

Further the angle between the subspaces was plotted as a measure for the linear dependency of the two subspaces.

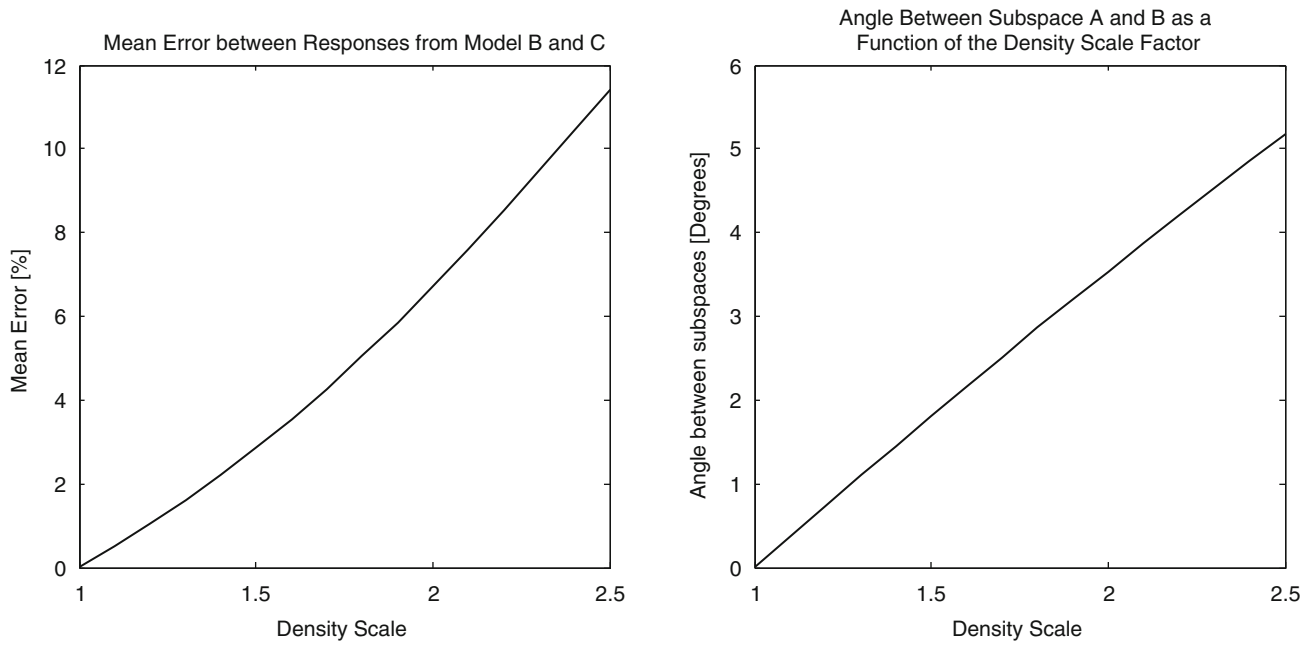
$$\theta = \min \left( \cos^{-1} \left( \frac{\mathbf{b}_i^T \mathbf{c}_i}{\|\mathbf{b}_i\| \|\mathbf{c}_i\|} \right) \right) \quad (34.12)$$

With  $\theta$  being the angle,  $\mathbf{b}_i$  and  $\mathbf{c}_i$  being the individual vectors of the subspace with closely spaced modes in B and C and  $\|\ \ \|$  symbolizing the length of the vector.

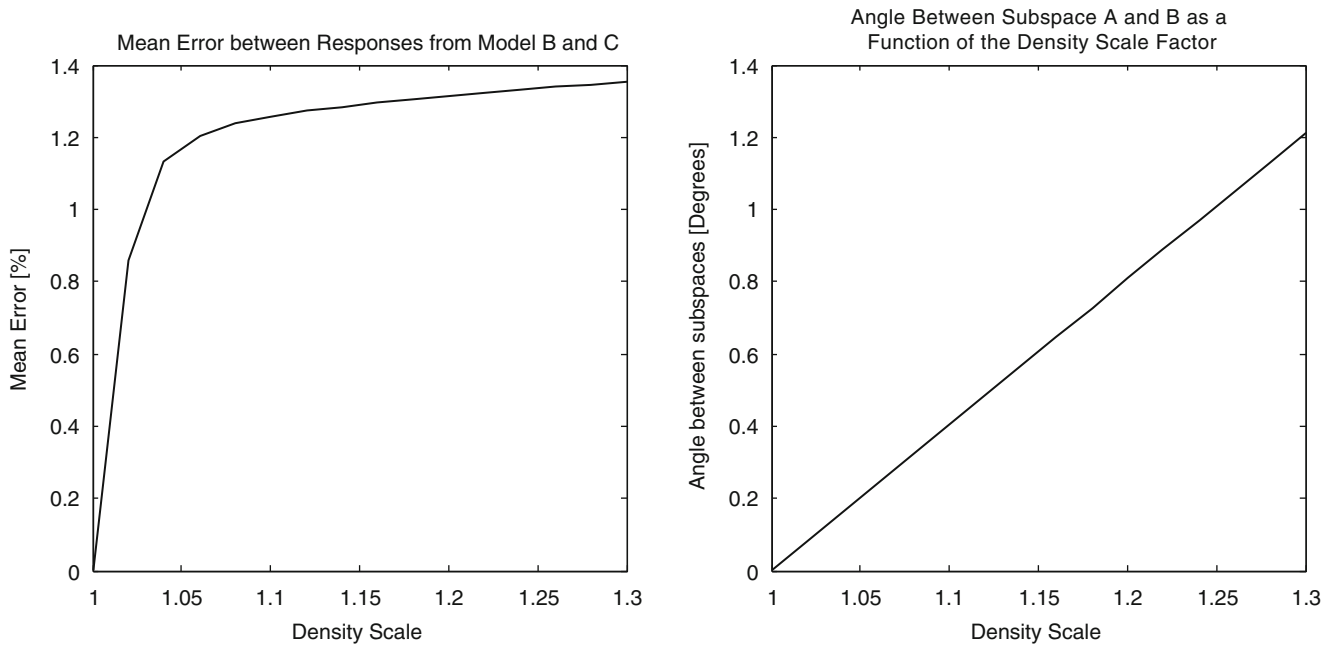
The results for Case 1 and 2 are presented in Figs. 34.7 and 34.8 respectively.

Figures 34.7 and 34.8 show the mean error of all the channels, for each of the 15 scenarios (left) and the angle between the subspaces A and B (right). For Case 1 Fig. 34.5 shows that the threshold for the off-diagonal error is exceeded when the scaling factor has a value of 1.5. This corresponds to a mean error of 1.8 % (Fig. 34.7, left) between the simulated responses of the “non-rotated” and “rotated” mode shapes. For Case 2 the thresholds for both diagonal and off-diagonal errors are exceeded as soon as the density is increased. But since the linear dependency between the subspaces is much stronger for this case, the errors calculated from the responses will be much smaller than for Case 1 (Fig. 34.8, left).

The results from both cases show that the methodology of rotating closely spaced modes can be used to obtain a better correlation – but only by accepting a small change in the properties of the FE model. How big a change that can be accepted will always depend on an engineering judgment.



**Fig. 34.7** Case 1: Error between simulated responses as a function of the scale factor (*left*). Angle between subspace A and B (*right*)



**Fig. 34.8** Case 2: Error between simulated responses as a function of the scale factor (*left*). Angle between subspace A and B (*right*)

### 34.4 Conclusion

In this paper a methodology for overcoming problems in correlating two structures with closely spaced modes is presented. The cross orthogonality check is used as correlation measure which often results in unreasonable diagonal and off-diagonal terms when dealing with closely spaced modes. In the paper it is suggested that the closely spaced modes are rotated by doing a linear combination, which is based on projecting the subset of finite element modes onto the given experimental modes.

The theory is validated using a numerical model of a shell structure, with focus on describing the error that's being introduced by rotating the mode shapes. The results show that the method can prove a valuable tool in achieving a certain correlation measure, but that the error introduced is highly dependent on the distance in frequency between the closely spaced modes.

## References

1. NASA (1996) Loads analyses of spacecraft and payloads, NASA-STD-5002. NASA, June 1996
2. ECSS-E-ST-32-11C (2008) Modal survey assessment – European Space Agency
3. Martin KF, Ghilain KH (1987) Non orthogonality arising from repeated roots. In: 5th international modal analysis conference, pp 1331–1337
4. D'Ambrogio W, Fregolent A (2003) Higher-order MAC for the correlation of close and multiple modes. *Mech Syst Signal Process* 17(3): 599–610
5. Brincker R, Aenlle ML (2015) Mode shape sensitivity of two closely spaced eigenvalues. *J Sound Vib* 334:377–387
6. Allemang RJ, Brown D (1982) A correlation coefficient for modal vector analysis. In: *Proceedings of IMAC I, SEM, Orlando*, pp 110–116
7. Heylen W, Lammens S, Sas P (1997) Modal analysis theory and testing. Katholieke Universiteit Leuven, Faculty of Eng., Dept. of Mech. Eng, Leuven
8. Guyan RJ (1965) Reduction of stiffness and mass matrices. *AIAA J* 3:380
9. O'Callahan (1989) A procedure for an Improved Reduced System (IRS) model. In: *Seventh international modal analysis conference, Las Vegas, February 1989*
10. O'Callahan JC, Avitabile PA, Riemer R (1989) System equivalent reduction expansion process (SEREP). In: *Seventh international modal analysis conference, Las Vegas, February 1989*
11. Brincker R, Skafte A, López-Aenlle M, Sestieri A, D'Ambrogio W, Canteli A (2014) A local correspondence principle for mode shapes in structural dynamics. *Mech Syst Signal Process* 45(1):91–104

# Chapter 35

## Modeling of an Instrumented Building Subjected to Different Ground Motions

Amaia Martinez and Carlos E. Ventura

**Abstract** The purpose of this paper is to compare the recorded response of an instrumented building in San Jose, California, with the response obtained from a finite element model of the building. Three ground motions from past earthquakes, one with significantly higher-amplitude than the other two, are used for the study. A detailed model of the building is created and calibrated using one of the lower-amplitude motions. It was demonstrated that the model closely simulates the building response under the other low-amplitude motion, while the results obtained using the larger motion did not match well with the recorded motions. For the higher-amplitude shaking, the building was more flexible as its fundamental period increased because of rocking effects. Hence, the model has to be updated by including soil-structure interaction effects using more flexible translational springs and adding vertical springs; resulting in a good match between measured and computed motions. As part of the study, the variation of the dynamic characteristics of the building obtained from a modal analysis of the recorded motions was investigated too. It can be concluded that a calibrated model based on only low level recorded motions may not be suitable to a higher level ground shaking.

**Keywords** Model updating • Soil-structure interaction • System identification • Instrumentation • Model calibration

### 35.1 Introduction

Recorded motions of instrumented buildings in seismic zones such as California help engineers understand their true behavior during earthquakes. The data recorded in several points of a building can be a useful source for calibrating its finite element models.

The purpose of this study is to investigate the dynamic response of a permanently instrumented ten-story commercial building in San Jose, California. The building was instrumented by the California Division of Mines and Geology – Strong Motion Instrumentation Program (CSMIP) in order to obtain strong motion and building response data during several events of significant ground motion episodes. On April 24th 1984, March 31st 1986 and 17th October 1989 the instruments installed in several locations of the building recorded valuable data during 1984 Morgan Hill, 1986 Mount Lewis and 1989 Loma Prieta earthquakes. The recorded motions have been used to calibrate and update a computer finite element model of the structure.

This study comprises the following parts: investigation of the building's structural system, modal identification using the strong motion data collected at the building, calibration and updating of a computer model of the building, and comparison of the response of the building model subjected to the three different ground motions.

This paper summarizes the important results obtained from this study.

### 35.2 Description of the Building and Instrumentation

#### 35.2.1 Description of the Building

The ten-story Great Western Saving building was built in 1964 and is located in San Jose, California. Its dimensions are 82 ft by 190 ft for its rectangular base (equal to typical floor dimensions) and 102 ft for the elevation. Story heights are typically

---

A. Martinez (✉) • C.E. Ventura  
Civil Engineering Department, University of British Columbia, 6250 Applied Science Lane, V6T 1Z4 Vancouver, BC, Canada  
e-mail: [amaiamar2@gmail.com](mailto:amaiamar2@gmail.com)

**Fig. 35.1** Ten story instrumented Great Western Saving building in San Jose, California (Adapted from CESMD)



**Table 35.1** Sensor number, location in the building and recorded direction of each accelerometer

Sensor number	Location		Measured direction
	Floor	Position	
1	Basement	South West	Vertical
2	Basement	South East	Vertical
3	Roof	South Center	Transversal (EW)
4	Roof	North Center	Transversal (EW)
5	Roof	South Center	Longitudinal (SN)
6	Fifth Floor	South Center	Transversal (EW)
7	Fifth Floor	In the middle	Transversal (EW)
8	Fifth Floor	North Center	Transversal (EW)
9	Fifth Floor	South Center	Longitudinal (SN)
10	Second Floor	South Center	Longitudinal (SN)
11	Basement	South Center	Transversal (EW)
12	Basement	North Center	Longitudinal (SN)
13	Basement	South Center	Longitudinal (SN)

12 ft, except from the ground floor and underground floor, which are 16 ft and 17 ft high respectively. The building is settled on a  $90' \times 194' \times 5'$  reinforced concrete spread footing. The geology of the site is mainly alluvium, but parameters of the soil profile were not available for this study.

The lateral force resisting systems of the structure consists of moment frames in the longitudinal direction (NS-direction) and two concrete shear walls in the transversal direction (EW-direction). The building includes two elevator cores in the middle of the base plan, stairs joined to the shear-walls in both sides and two interior openings. An exterior view of the building is presented in Fig. 35.1.

### 35.2.2 Instrumentation of the Building

The structure has 13 permanent force-balanced accelerometers which record accelerations at different locations of the building in different directions (vertical, longitudinal (SN) and transversal (EW)). Table 35.1 and Fig. 35.2 show the location of each sensor and the direction of the recorded data.



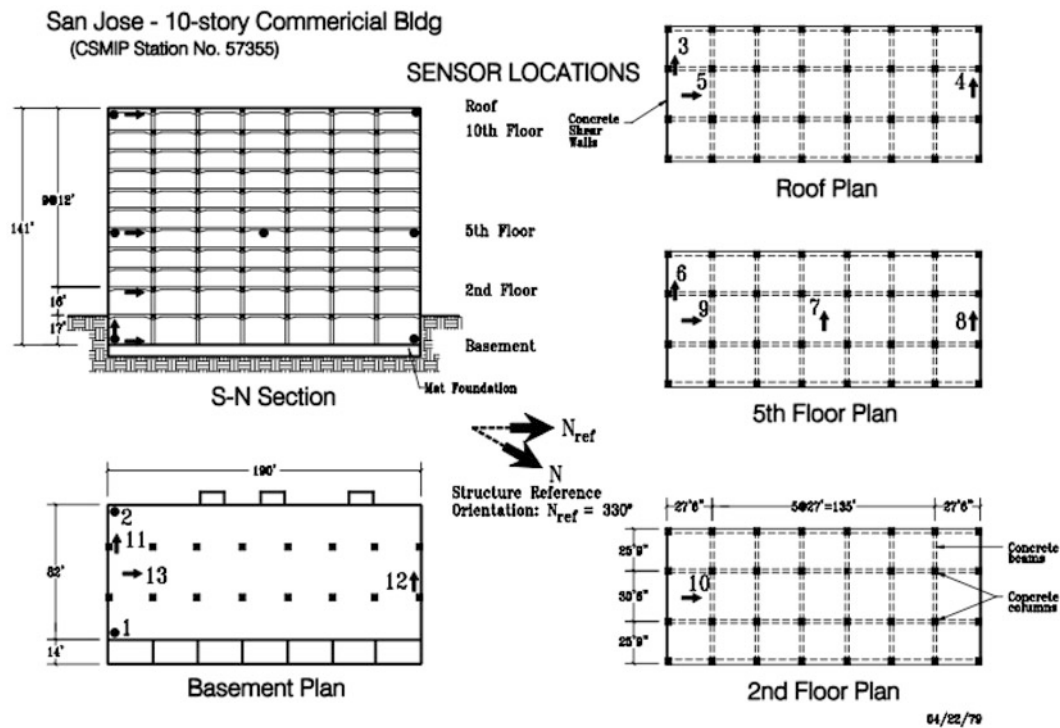


Fig. 35.2 Schematic map of instrumentation of the building (Adapted from CESMD)

### 35.3 Modeling of the Building and Its Calibration

#### 35.3.1 Finite Element Model Description

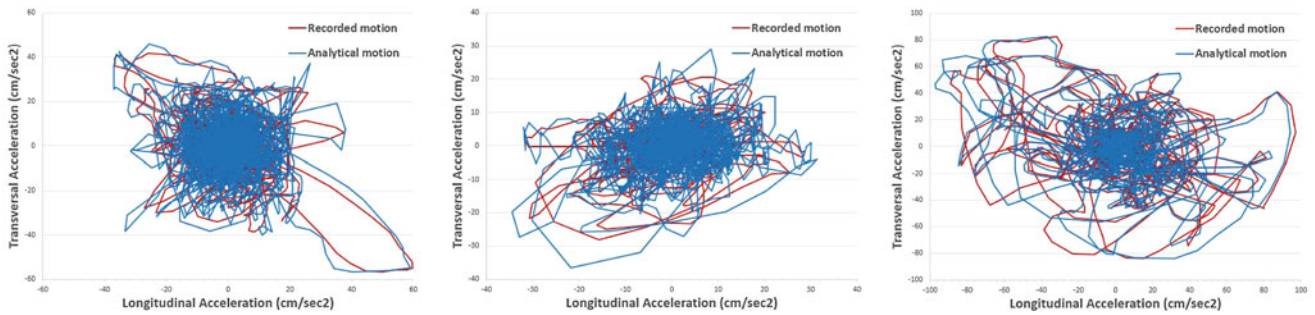
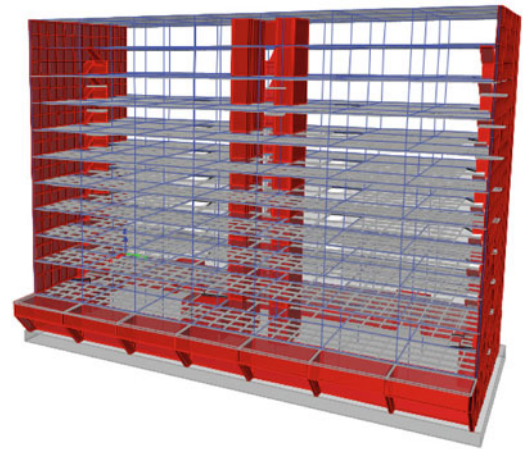
The design drawings of the building were used to develop a finite element model of the building using ETABS 2013 software. A linear elastic model of the structure supported by a flexible base was created. The base was designed as a series of springs of finite stiffness. The foundation springs were modeled using the soil and foundation information available using the parameters obtained from [1,2]. The model includes structural, as well as, non-structural elements. Gravity frames, lateral load resisting frames, shear walls, interior core walls, openings and stairs were modeled too. A three dimensional view of the ETABS model is shown in Fig. 35.3.

#### 35.3.2 Input Motions

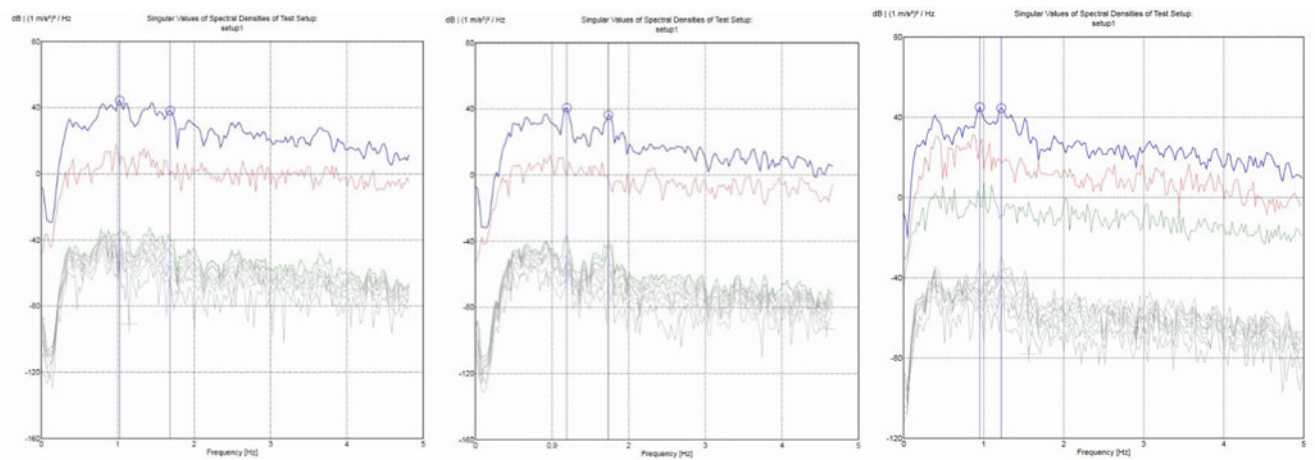
The recorded motions for all the sensors during Morgan Hill, Mount Lewis and Loma Prieta earthquakes were obtained from CESMD (Center for Engineering Strong-Motion Data). Free field data in the vicinity of the building for the same ground motions was not available. Consequently, the mean of the channels of the basement for each direction is calculated and used as input ground motion for the model. In case of a model with fix-based conditions the assumption of using the mean of these recorded motions at the basement of the building as inputs is justifiable. Nonetheless, soil-structure interaction was included in the model by adding translational springs to the foundation. The time history accelerations recorded at the basement are applied to the bases of these springs. Hence, the accelerations recorded at the channels of the basement of the model are different to the real recorded motions. The initial input error is computed for each of the earthquakes in longitudinal and transversal directions by comparing the recorded data to the obtained analytical data at the basement channels. In Fig. 35.4 the orbital horizontal acceleration of the real recorded data at the top of the foundation is compared to the orbital horizontal acceleration of the model at the same location for each of the earthquakes.

As it can be seen in this figure, the maximum input error recorded was 8 % for Mount Lewis earthquake in the longitudinal direction. Although for most of the cases the error is not that high, a future analysis should be performed to ensure that these initial errors are inside of the assumable error range.

**Fig. 35.3** 3D view of the ETABS model of the building



**Fig. 35.4** Orbital plots of horizontal input acceleration for Morgan Hill, Mount Lewis and Loma Prieta earthquakes



**Fig. 35.5** Spectral density in frequency domain for Morgan Hill, Mount Lewis and Loma Prieta earthquakes

### 35.3.3 Modal Identification

A modal analysis of the recorded motions for the three earthquakes was investigated using ARTEMIS® computer program. Figure 35.5 shows the obtained spectral densities in frequency domain for each of the ground motions. The frequencies for the first mode (longitudinal) and second mode (transversal) of the building were found (see Figs. 35.5 and 35.6).

The first natural frequency (longitudinal mode shape) for all the analyzed earthquakes was around 1 Hz. However, the second natural frequency, which represents the first transversal mode, for Loma Prieta earthquake was lower than for Morgan Hill and Mount Lewis. In other words, the natural period of the building is increased when higher intensity ground motion is applied. The results of this modal analysis were showing that the dynamic characteristics of the building were changed for the three ground motions, especially for Loma Prieta.

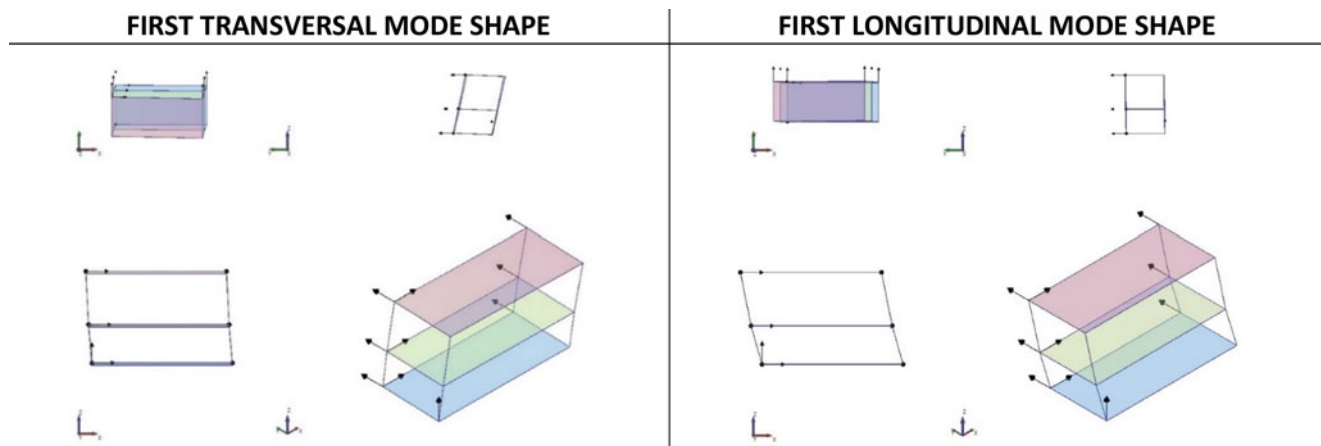


Fig. 35.6 Transversal and Longitudinal mode shapes of the building using Artemis

### 35.3.4 Calibration of the Model

The first calibration of the model was performed using Morgan Hill record. Structural properties and masses were modified manually until a “best match” between experimental and analytical results was obtained. The first and second natural frequencies, 1.06 and 1.66 Hz, for this calibrated ETABS model were similar to the ones obtained with Artemis. In addition, time history analysis results for acceleration, velocity and relative displacement were compared to the real recorded motions in all of the channels for this earthquake. The calibration of the model was considered acceptable once a good correlation coefficient between the experimental and analytical results was obtained (see time history results in Sect. 35.4.3, Fig. 35.9).

## 35.4 Model Validation and Discussion of the Results

### 35.4.1 Comparison Between the Ground Motions

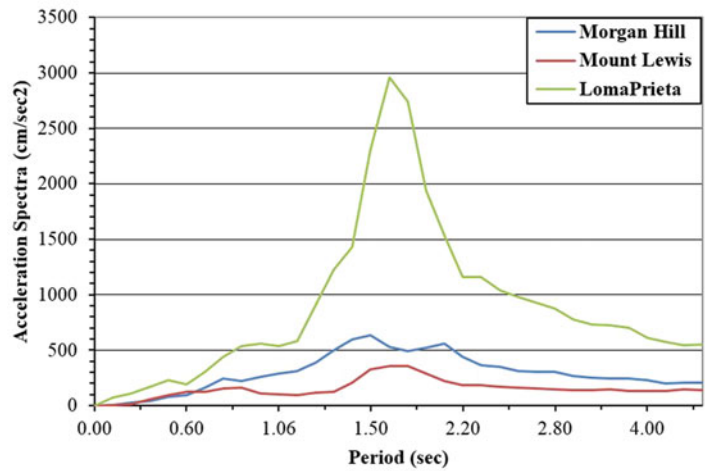
A comparison between the three earthquakes used for this study is shown in order to see the differences among them. The peak recorded accelerations at the basement of the building were 59.7 cm/sec<sup>2</sup> for Morgan Hill, 33.7 cm/sec<sup>2</sup> for Mount Lewis and 97.32 cm/sec<sup>2</sup> for Loma Prieta. The spectral acceleration with 5 % damping was also obtained and plotted for the three ground motions. Figure 35.7 shows that the spectral acceleration for Loma Prieta in the period range of the first modes of the building (around 0.74 and 1 s) is significantly higher than for the other two earthquakes. As an example, for the transversal first modal period of the building (0.74 s), the spectral acceleration ( $S_a$ ) for Loma Prieta is  $S_a = 360.22$  cm/sec<sup>2</sup>, followed by Morgan Hill  $S_a = 197.55$  cm/s and finally by Mount Lewis  $S_a = 133.95$  cm/s. Consequently, the demands in the building are considerably higher for the higher intensity earthquake than for the lower ones.

### 35.4.2 Model Validation

In order to validate the model, time history analysis for Mount Lewis and Loma Prieta, which present a lower and higher shaking than Morgan Hill respectively, were performed using the calibrated model. The same procedure used for Morgan Hill earthquake was followed. Accelerations, velocities and relative displacements of all the channels were compared to the recorded ones during Mount Lewis and Loma Prieta earthquake. Whereas the model was performing well for Mount Lewis (see time history results in Sect. 35.4.3, Fig. 35.10), the response of the model was not as good as expected for Loma Prieta. The results obtained for this last earthquake were not matching the experimental ones as desired.

The first and second natural frequencies, 1.06 and 1.66 Hz, for the first calibrated ETABS model were compared to the ones obtained through ARTEMIS modal analysis as shown in Fig. 35.5 and Table 35.2. While the first natural frequency completely matches for all the cases, the second natural frequency for Loma Prieta (1.22 Hz) is quite far from the one obtained from the model (1.66 Hz). Therefore, a new calibrated model was designed to capture better the response of the building under Loma Prieta earthquake.

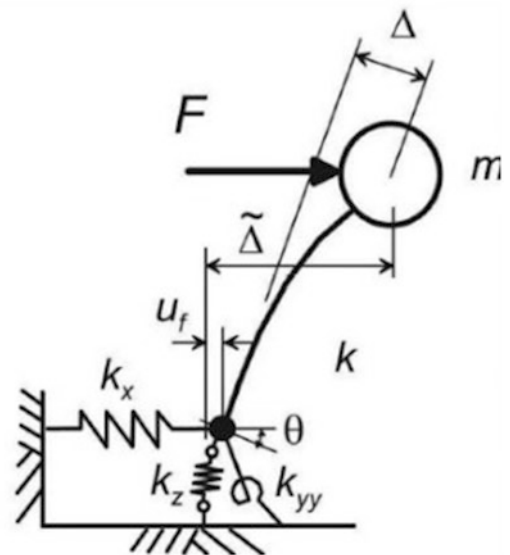
**Fig. 35.7** Acceleration Spectra with 5 % damping for Morgan Hill, Mount Lewis and Loma Prieta earthquakes



**Table 35.2** Longitudinal and transversal natural frequencies of the building for the modal analysis performed with ARTEMIS and for the finite element calibrated and updated models

Earthquake	Natural frequencies from Artemis		Natural frequencies from ETABS – first model		Natural frequencies from ETABS – updated model	
	1st long. $f_n$	1st trans. $f_n$	1st long. $f_n$	1st trans. $f_n$	1st long. $f_n$	1st trans. $f_n$
Morgan Hill	1.025	1.66	1.06	1.66	1.07	1.28
Mount Lewis	1.074	1.56				
Loma Prieta	0.95	1.22				

**Fig. 35.8** Schematic model of a simplified soil-structure interaction system [7]



None of the structural properties were changed in this new model except of the stiffness of the area spring. The transversal stiffness was reduced from 0.1 to 0.02 k/in/in. and vertical springs were added in order to allow the building to rock. These updates made the model to perform more flexible increasing the natural period of the building in the transversal direction. The modal analysis of this new model showed that the frequency for the first longitudinal mode shape was 1.07 Hz and for the first transversal mode shape 1.28 Hz, matching quite well the natural frequencies obtained from Artemis modal analysis for Loma Prieta. Table 35.2 compares the natural frequencies obtained with Artemis to the ones obtained for the finite element calibrated models.

In addition, time history analysis for this last higher intensity ground motion was performed using the new updated model, for which good match between the recorded motions and analytical results was obtained (see time history results in Sect. 35.4.3, Fig. 35.11).

The following simplified SDOF example (Fig. 35.8) helps to understand the increase on the period of the building due to soil-structure interaction. When lower stiffness are applied to the design of the spring foundation, the structure moves more

horizontally and rocks. The natural period increases with following formulation; where  $\tilde{T}$  is the natural period of the system,  $k$  the stiffness of the structure,  $k_x$  the translational stiffness,  $k_{yy}$  the rotational stiffness and  $m$  the mass of the structure.

$$\tilde{T}^2 = (2\pi)^2 m \left( \frac{1}{k} + \frac{1}{k_x} + \frac{h^2}{k_{yy}} \right) \quad (35.1)$$

Consequently, the importance of the proper design of the soil structure interaction in the model is fundamental to characterize the real response of the building. It also has to be noted that the intensity of shaking affects the soil-structure interaction, becoming softer and more important for stronger shaking (Loma Prieta case) than for lower shaking (Mount Lewis and Morgan Hill cases).

### 35.4.3 Time History Analysis Results

The first calibrated model was used to perform a time history analysis of the structure for Morgan Hill and Mount Lewis earthquakes, while the second updated model was used for the Loma Prieta earthquake. The input motions were the mean of the recorded accelerations at the base of the structure in each direction (as explained in Sect. 35.2). The comparison between the absolute acceleration, velocity and relative displacement time histories for the recorded motions and the analytical motions resulted in a good match for all the channels. The models captured the peaks, frequencies and values of the time histories quite accurately. The correlation coefficient (C.C.) between the experimental and analytical data was also calculated. The average of the C.C. values is 85 % with a minimum of 73 %, which indicates a good correlation for practical purpose.

The relative displacements were obtained by subtracting the displacement at the basement to the total displacement of each channel. Therefore, the relative displacements account for the displacements due to the rocking and bending of the structure.

Figures 35.9, 35.10 and 35.11 show the comparison of the time histories of acceleration, velocity and relative displacement for two channels at the roof of the building, channel 5 (longitudinal) and 4 (transversal).

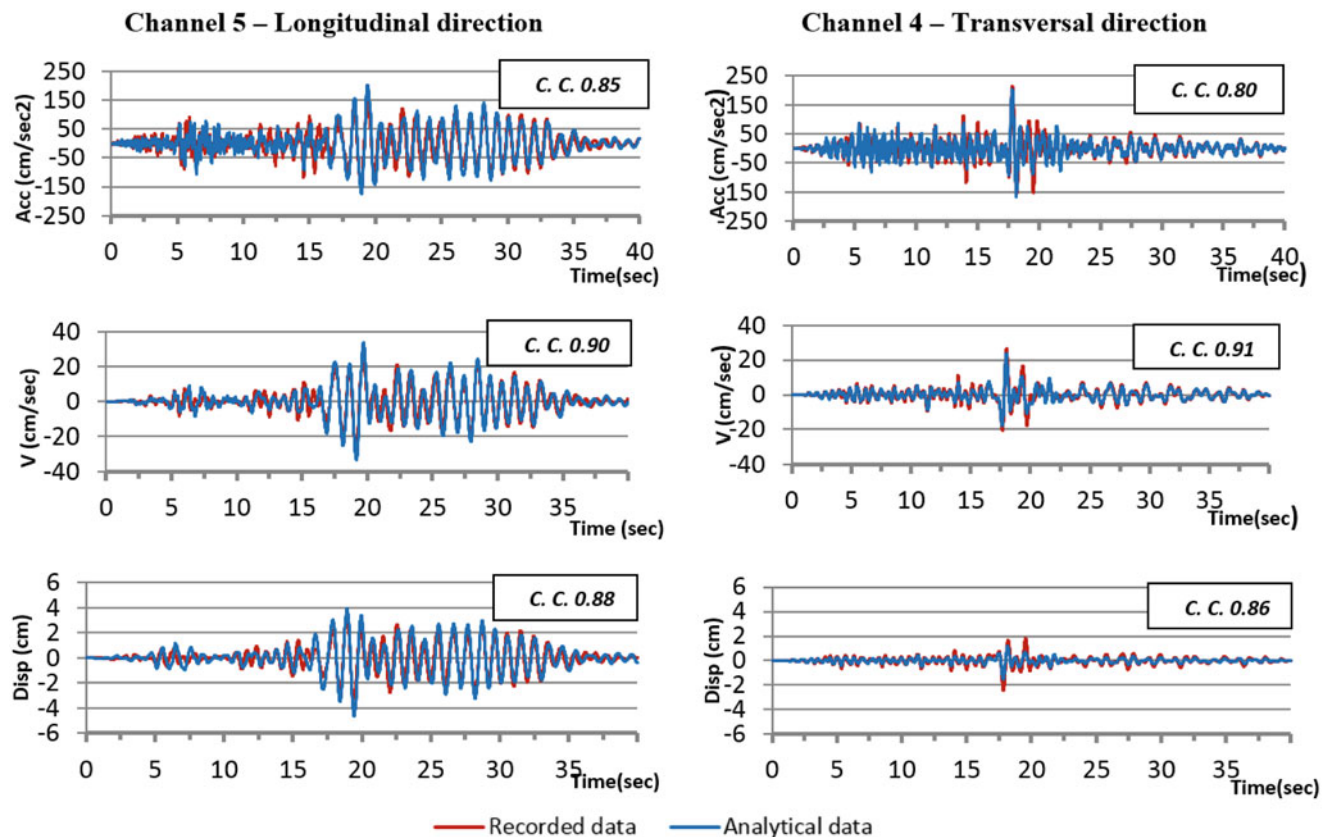


Fig. 35.9 Recorded and analytical acceleration, velocity and relative displacement time histories at Channels 5 and 4 for Morgan Hill earthquake

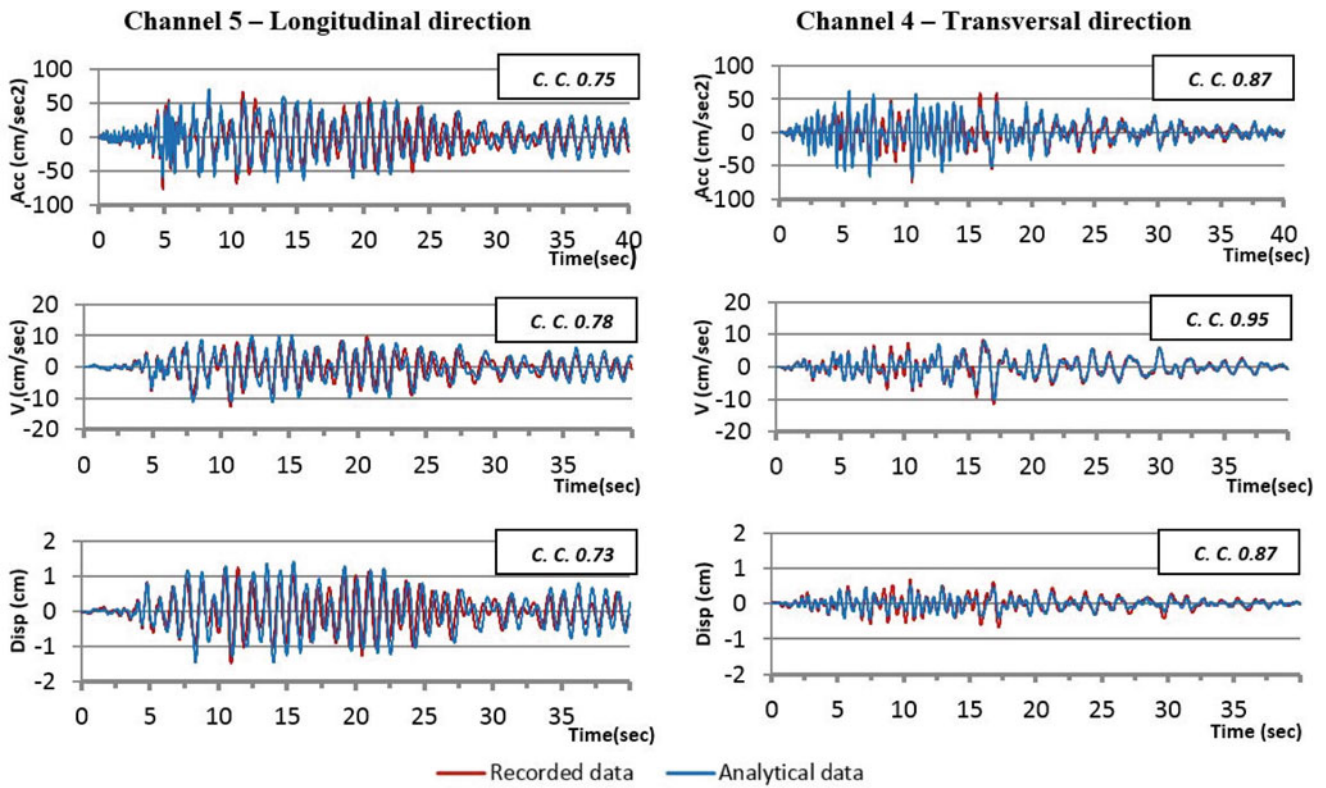


Fig. 35.10 Recorded and analytical acceleration, velocity and relative displacement time histories at Channels 5 and 4 for Mount Lewis earthquake

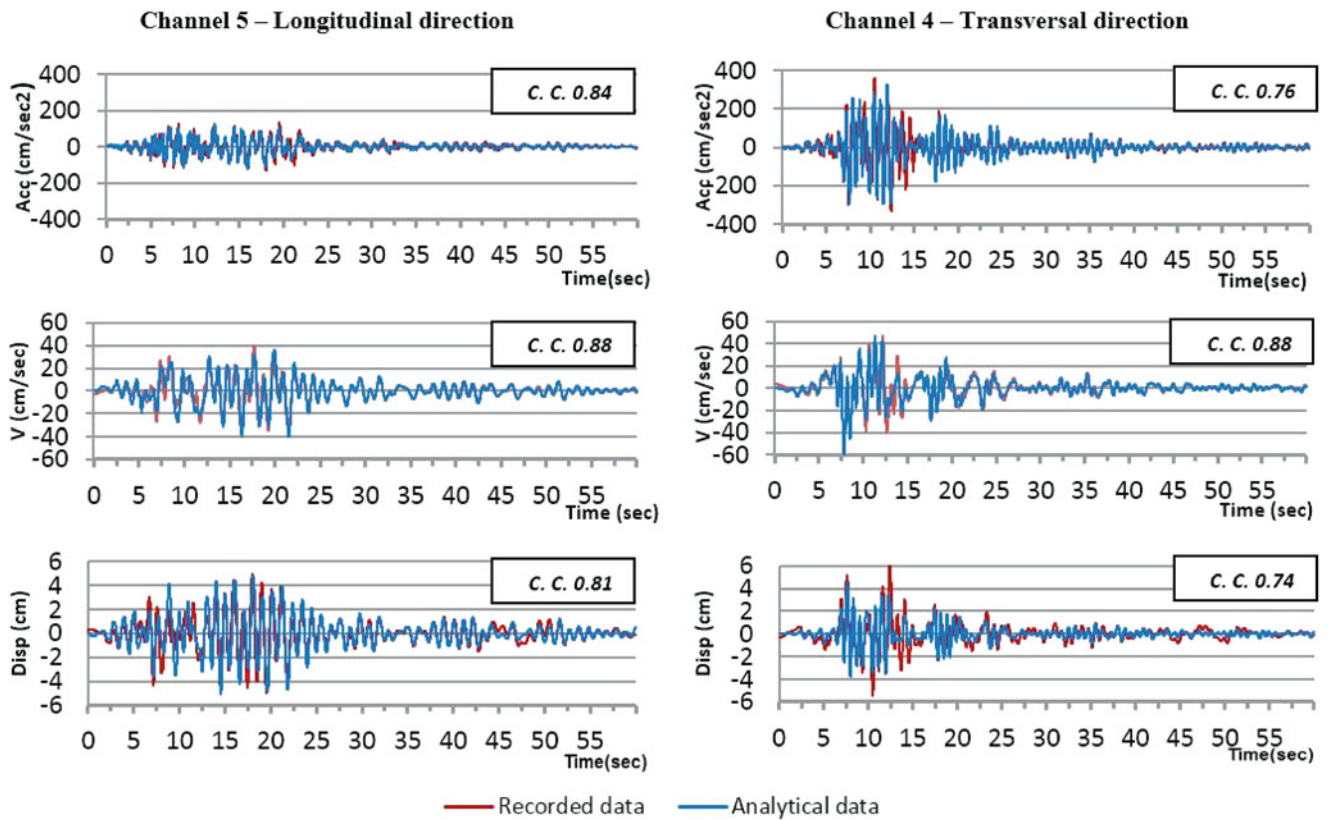


Fig. 35.11 Recorded and analytical acceleration, velocity and relative displacement time histories at Channels 5 and 4 for Loma Prieta earthquake

## 35.5 Conclusion

The strong-motion records of a ten story commercial building in San Jose, California, obtained during the 1984 Morgan Hill earthquake were used to calibrate a computer model of the building. The recorded motions at the basement of the building were used as input motions at the base of the springs. Suitability of this assumption will need to be analyzed in further studies. The same model was subjected to 1986 Mount Lewis earthquake with a good match between the measured data and analytical results. Nevertheless, the results did not match as good as expected for Loma Prieta earthquake, which presents a significant stronger shaking than the other two.

The results from a modal identification were used to demonstrate the importance of soil-structure interaction in this building. The fundamental period in the transversal direction of the structure increased for Loma Prieta earthquake due to the rocking effects.

Softer translational stiffness and vertical springs were added to base area spring of the finite element model in order to capture the transversal response of the building better. For the updated model, the time history results matched the recorded measured during the Loma Prieta earthquake at different locations of the building. This study proves that the effects of soil-structure interaction becomes more important when the building is subjected to the higher intensity ground motion.

In conclusion, a calibrated model based on low level recorded motions may not be suitable to predict the response of certain types of buildings to a higher level of ground shaking. In some cases, soil-structure interaction effects become more important and they cannot be neglected. Modeling a building without considering these effects may not be enough to capture properly the behavior of the building under different ground motions.

## References

1. Gazetas G (1983) Analysis of machine foundation vibration: state of the art. *Soil Dyn Earthq Eng* 2(1):2–42
2. Kramer SL (1996) *Geotechnical earthquake engineering*. EERC, Report no 97/01, Prentice Hall
3. Stewart JP, Stewart AF (1997) Analysis of soil-structure interaction effects on building response earthquake strong motion recordings at 58 sites. EERC, Report no 97/01
4. Chopra A (2001) *Dynamics of structures, theory & applications to earthquake engineering*, 3rd edn. 2007, Prentice Hall, Englewood Cliffs, Upper Saddle River
5. Murty CVR, Goswami R, Vijayanarayanan AR, Mehta VV (2001) *Some concepts in earthquake behaviour of buildings*. Gujarat State Disaster Management Authority, Prentice Hall, Chennai, India
6. Wilson EL (2002) *Three-dimensional static and dynamic analysis of structures: a physical approach with emphasis on earthquake engineering*, 3rd edn. Computer and Structures Inc, Berkley, California, USA
7. Ventura CE (2013) C4-II- advanced course in earthquake engineering and seismicity. SEABC Coursenotes, Vancouver

# Chapter 36

## Calibration and Cross-Validation of a Car Component Model Using Repeated Testing

Karl-Johan Larsson, Snævar Leó Grétarsson, Majid K. Vakilzadeh, and Thomas Abrahamsson

**Abstract** Repeated testing has been made both in the sense of testing multiple test pieces of the same type and in the sense of repeated tests on the same test piece by 13 testers at different occasions. Between the individual tests, the test subject has been dismantled from the test stand and the sensors have been re-calibrated. Statistical evaluation of these tests gives information about the spread that can be expected in modal tests. The SIMO test data and data statistics are used for traditional validation and cross-validation of a finite element model of the car component under test. Planning of the sensor layout has been made prior to testing with the use of the nominal finite element model. A model calibration is made prior to the model validation. The finite element model size is over 20,000 degrees-of-freedom and involves two calibration parameters. The work has been made as part of a structural dynamics model validation Master's course. An open-source Matlab application has been used for calibration, validation and cross-validation.

**Keywords** FEM calibration • FEM cross validation • Repeated testing • Monte Carlo cross validation • Vibration testing

### 36.1 Introduction

Finite Element (FE) modelling is commonly used in industry to simulate and evaluate component and product behaviour with respect to different load cases. Compared to prototype testing, FE analysis and simulation quickly becomes an effective tool when evaluating the effects of changes in material parameters, geometry and varying load cases. However, real world products will always exhibit a spread in properties. This spread stems from a variety of sources, such as material variation, production process variability and imperfections in the assembly of components. To create FE models that account for these differences requires data of the about the spread, in terms of characteristic properties of the population. Modal analysis can be used to quantify the spread in dynamical properties [1], which are the properties of interest in this paper. When data about the spread has been gathered from experiments, a sufficiently detailed FE model can be calibrated to reproduce the observed behaviour with acceptable accuracy. Here sufficiently detailed depends greatly on the physical properties affecting the behaviour observed during experiment. Unfortunately, the process of gathering data from experiment might also be subject to variability.

The background to this paper is a Masters course; Structural Dynamics Model Validation, given at the department of Applied Mechanics, Chalmers, where 13 students have performed vibrational experiments, in order to gather data to be used in the calibration of a FE model of the tested product; the windscreen of a popular car model that is being produced today.

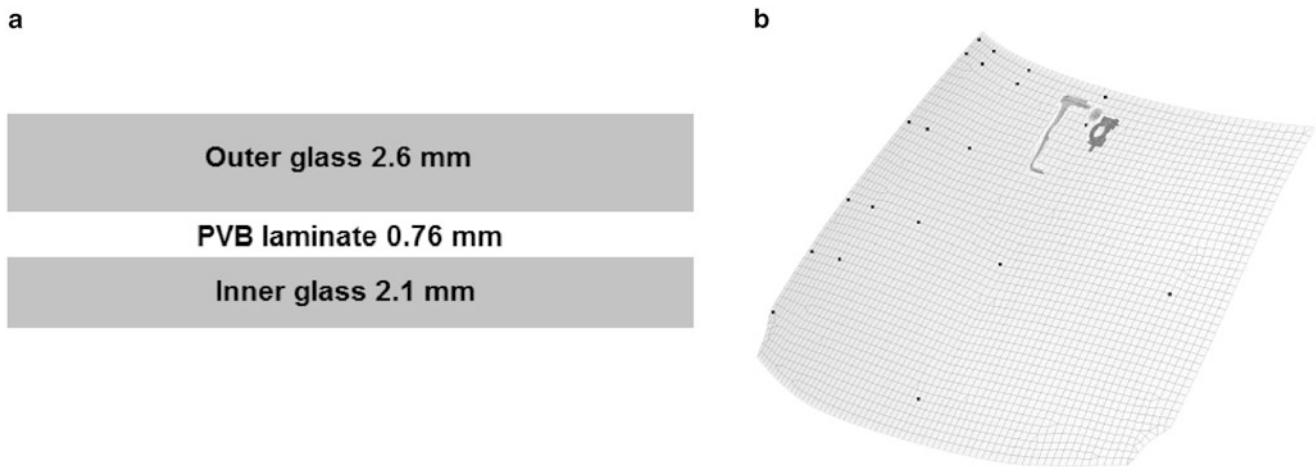
### 36.2 The Windscreens and Nominal FE Model

Three windscreens for a common car model that is mass produced today (2014) was obtained from the car manufacturer, together with a FE model with nominal values set for the parameters. The windscreen consists of one inner and one outer glass layer with a thinner layer of PVB polymeric material between the glass layers, see Fig. 36.1a. The windscreens also have plastic components for attaching a rear-view mirror and other equipment glued to the inner side. These components are also present in the FE model. The FE model is a Nastran model with 23,136 degrees of freedom. The windscreens are modelled with plate elements (QUAD4), with assigned isotropic laminate properties (PCOMP). The plastic components are

---

K.-J. Larsson • S. L. Grétarsson • M.K. Vakilzadeh • T. Abrahamsson (✉)  
Department of Applied Mechanics, Chalmers University of Technology, 41296 Göteborg, Sweden  
e-mail: [karlars@student.chalmers.se](mailto:karlars@student.chalmers.se); [snvar@student.chalmers.se](mailto:snvar@student.chalmers.se); [thomas.abrahamsson@chalmers.se](mailto:thomas.abrahamsson@chalmers.se)





**Fig. 36.1** Laminate layup and FE-mode. (a) Section cut of the windscreen showing the thickness properties. (b) Isometric view of the provided FE model. The *black marks* are FE nodes corresponding to sensor placements during testing

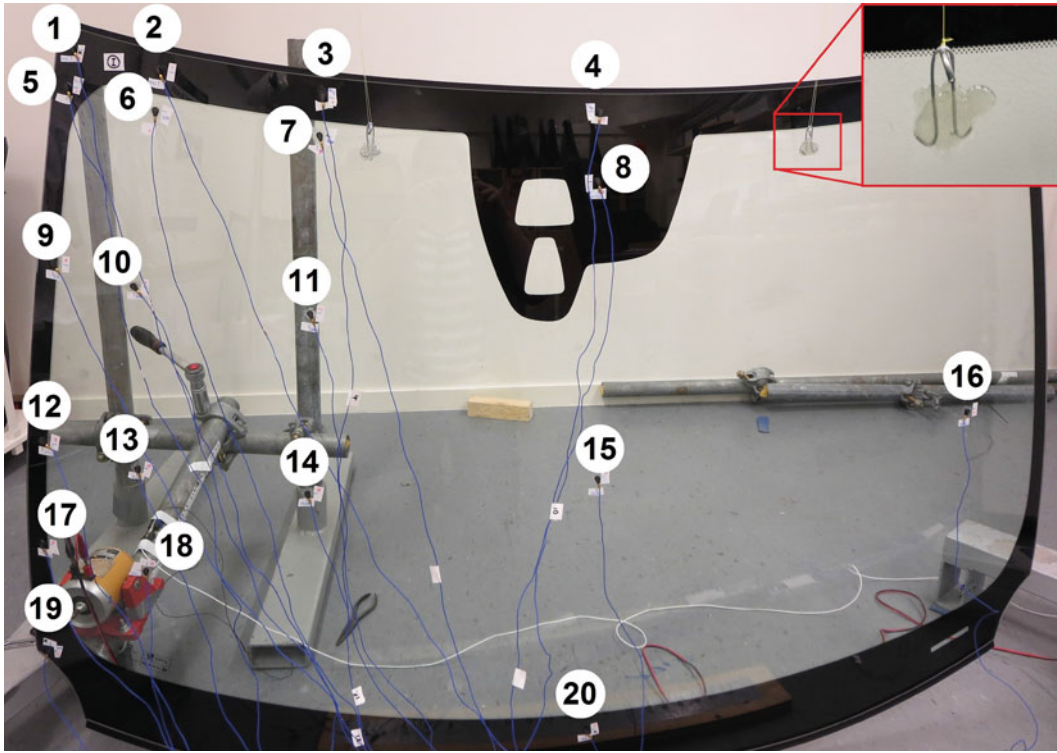
modelled with solid tetrahedral elements (CTETRA) and connected to the windscreen trough rigid elements. The rubber seals are added as concentrated masses on grid points (CONM2). A pretest sensor placement planning was made, to a 20 sensor layout, using the method of effective independence for sensor placement [2], using the nominal FE model.

### 36.3 Vibration Testing Procedure

Test were performed on three seemingly identical windscreens numbered I, II and III. The vibration tests were performed by the 13 students participating in the course. Between tests, the test subject was dismounted from the test stand and all sensors were removed and re-calibrated. Since every student had to place their sensors at marked, predefined locations, a small variation of the sensor positions between tests is expected. Each student hung their assigned windscreen in two thin and very elastic light-weight cords, connected to clips glued to the windscreen (see insert in Fig. 36.2), which gave close to a free-free boundary condition. Light-weight accelerometers of IEPE (Integrated Electronics Piezo Electric) type were used (PCB 352C55, 0.5 gramme) and placed at the 20 defined locations, see Fig. 36.2, using synthetic bees wax. The mass added by the test equipments was neglected in the FE modelling. The shaker was located at the opposite side of an accelerometer at the lower left corner of the windscreen, see Fig. 36.2. The shaker connects to the windscreen through a force transducer (Brüel & Kjær type 8,203 with an Brüel & Kjær charge-to-IEPE unit). A force transducer/accelerometer pair with accelerometer 19 was used to obtain a close approximation to the direct accelerance. The input signal to the shaker was a constant amplitude stepped sine ranging from 15 to 300 Hz. The data collected during the experiment are the 20 Frequency Response Functions (FRFs) of the 20 accelerometers (accelerometer output/force input) in the single-input configuration.

#### 36.3.1 Inspection of Test Data

The data gathered from all tests were inspected. In Fig. 36.3 typical results from measurements on windscreen I are shown, where a total of six tests were performed. The data from test number three (I.T3) deviated from the others in the high frequency range which is demonstrated by the peak response at around 280 Hz for accelerometers 1, 12 and 18. The data from this test were considered as outliers and were omitted. For comparison between windscreens I, II and III, the FRF from accelerometer 20 are also plotted for all tests in Figs. 36.3, 36.4, and 36.5. Two test were performed on windscreen II and typical results are seen in Fig. 36.4. Since only two test were performed, a general behaviour is hard to determine. However, the two data sets exhibit similar behaviour over the frequency range in the test and both were kept for comparison. For windscreen III one test shows a dissimilar behaviour in the higher frequency range for multiple accelerometers, see Fig. 36.5 (III.T2) and the data from this were also considered as being outliers and were omitted from the study. All other test data were used in the procedure presented.



**Fig. 36.2** The test setup. Locations of all 20 accelerometers are shown. Shaker location is seen at *bottom left* behind accelerometer 19. Insert of *top right* show chord attachment

### 36.3.2 System Identification from Test Data

To obtain modal properties from test data, system identifications were performed in Matlab using the System Identification toolbox to obtain state space models of the tested windscreens. A linear identification method, N4SID, based on a state space subspace method, further explained by McKelvey et al. in [3] and Van Overschee and De Moor in [4], was used. The system identifications were made using the same system identification parameter setting, resulting in state space models of the same order for all windscreens in all tests.

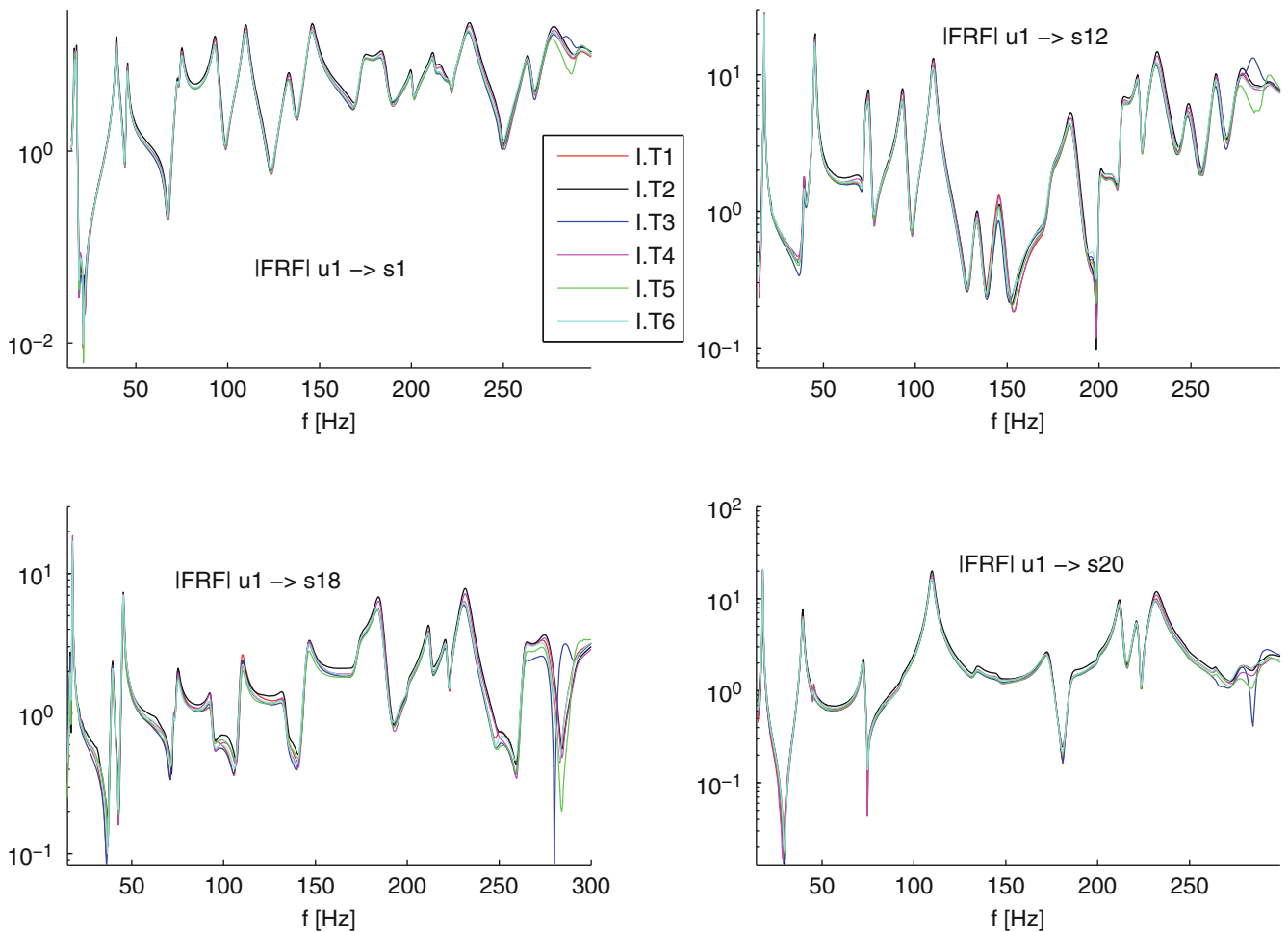
## 36.4 Calibration and Validation Procedure

The 15 FRFs from every state space model that best approximates the measured FRFs from the test are used as reference to represent the windscreen during the calibration procedure. One exception from this rule is that the direct accelerance is always included in this set of the 15 of the reference. This leaves five measured FRFs outside the calibration procedure, and they are used for a hold-out validation after the calibration. The calibration procedure makes use of FRF damping Equalization and is described in detail in the paper by Abrahamsson and Kammer [5]. In short the Levenberg-Marquardt method is used to minimize the deviation metric  $Q$  as

$$Q(\mathbf{p}) = \frac{\delta^H(\mathbf{p})\delta(\mathbf{p})}{N} \quad (36.1)$$

in which the deviation vector  $\delta(\mathbf{p})$  that depend on the model parameter set  $\mathbf{p}$  is defined as

$$\delta(\mathbf{p}) = \log_{10} \text{vect}(\mathbf{H}^A(\mathbf{p})) - \log_{10} \text{vect}(\mathbf{H}^X) \quad (36.2)$$



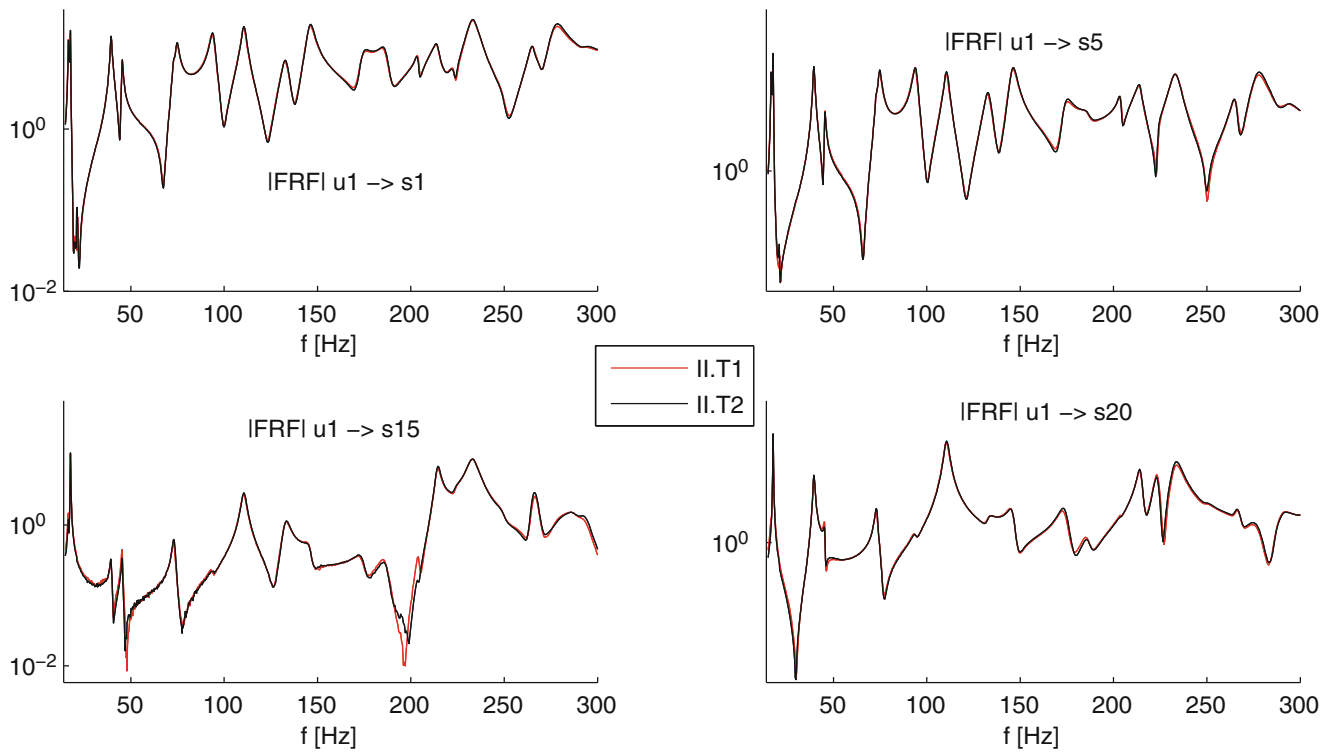
**Fig. 36.3** Typical measured FRFs from six measurements on windscreen I.  $u_1$  denotes force input,  $s_{XX}$  denotes accelerometer number  $XX$  of the SIMO test and  $T_i$  denotes the  $i$ th test

where superscripts  $A$  and  $X$  denote transfer functions,  $\mathbf{H}$ , from analytical (FE) model and experimental (state space model identified from test data) respectively. The vectorizing operation  $\text{vect}$  makes all FRF elements of the  $n_y \times n_u$  transfer function, at all  $n_f$  discrete frequencies used for evaluation, into a  $n_y n_u n_f \times 1$  column vector. The number of data points  $N$  is thus

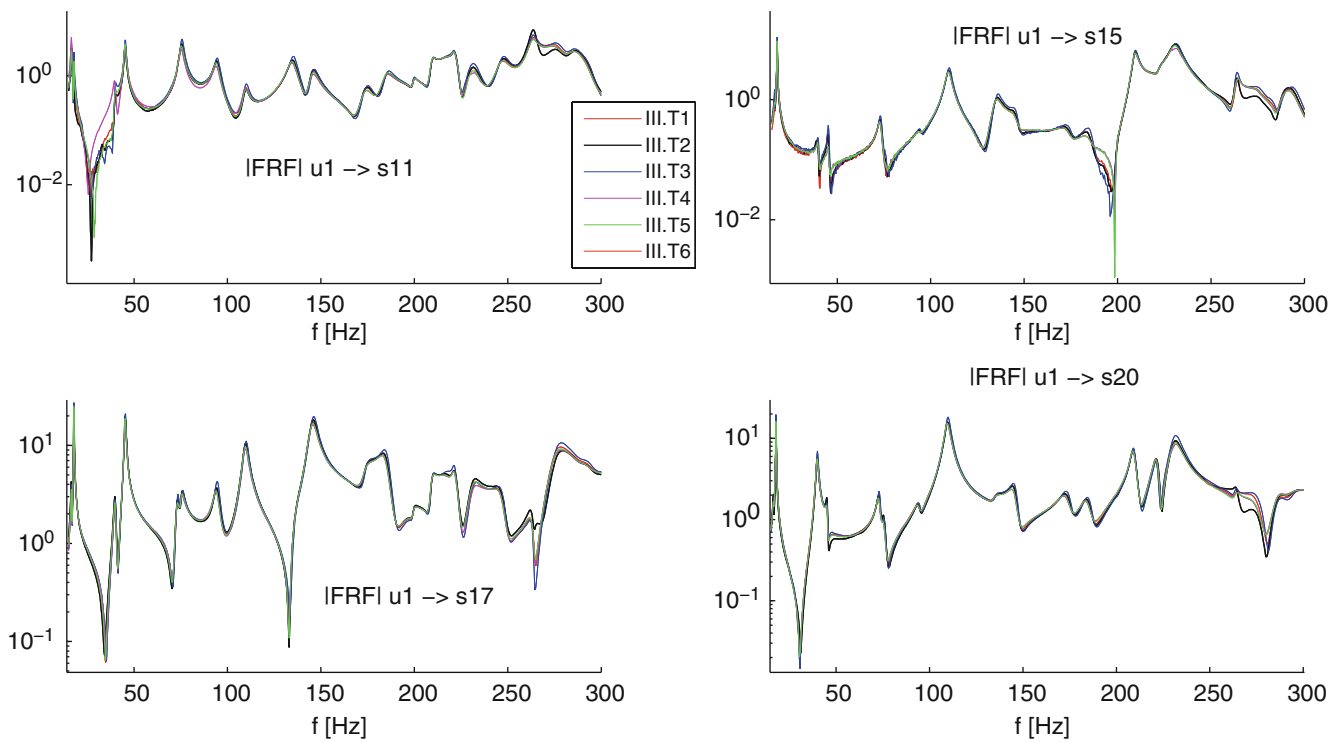
$$N = n_y n_u n_f \quad (36.3)$$

A gradient based minimization procedure is applied to find the minimum of the deviation metric. Since it is no guarantee that it will converge to the global minimum when starting from the nominal parameter set, the likelihood of reaching a global minimum is increased by applying random starts for the minimizer. In this, a Latin Hypercube sampling is used to generate 100 random realizations of the parameters to evaluate the metric. In the Latin Hyper cube sampling, the parameters are assigned a uniform probability distribution ranging between  $\pm 20\%$  of the nominal value. The random parameter sets resulting in the five lowest values of the metric were also used as starting points for the minimizer. All calibration procedures were performed in Matlab using an open-source Matlab app, FEMcali.<sup>1</sup>

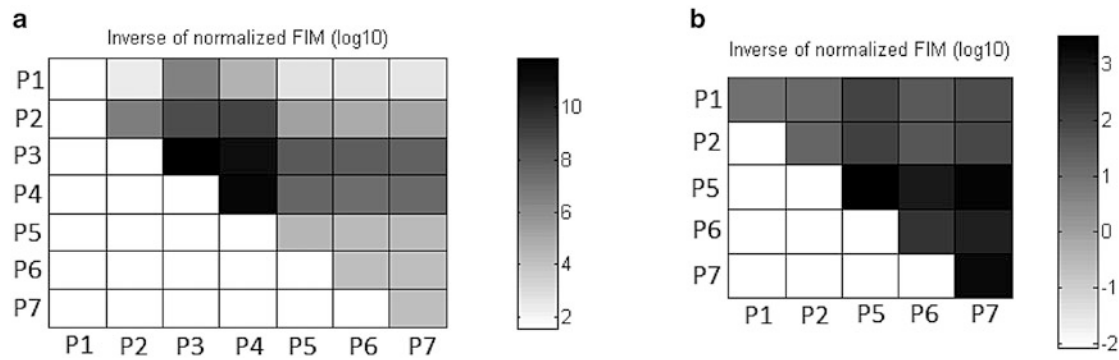
<sup>1</sup>This app can be downloaded from: <http://www.mathworks.se/matlabcentral/fileexchange/44317-femcali>.



**Fig. 36.4** Typical measured FRFs from two measurements on windscreen II



**Fig. 36.5** Typical measured FRFs from six measurements on windscreen III



**Fig. 36.6** The inverse of the Fisher Information Matrix calculated during pre calibration at nominal parameter settings. Upper diagonal is only shown due to symmetry. (a) The inverse FIM calculated for the initial parameter set. (b) The inverse FIM after omitting P3 and P4. Note significant drop of order

### 36.4.1 Parametrization of the FE Model

The parameter set used in the calibration is:  $\mathbf{p} = \{E_{glass}, \rho_{glass}\}$ , with nominal values  $E_0 = 7$  [GPa] and  $\rho_0 = 2,500$  [kg/m<sup>3</sup>]. A pre calibration investigation of an initial set including the Youngs modulus and density of the PVB polymer,  $E_{PVB} = 1$  [GPa],  $\rho_{PVB} = 1,100$  [kg/m<sup>3</sup>] and nominal thicknesses of the different lamina layers, see Fig. 36.1a, was made. Both  $E_{PVB}$  and  $\rho_{PVB}$  are small compared to the corresponding properties of the glass. This in combination with the small thickness of the PVB layer (0.76 out of a total thickness of 5.46 mm) makes the identifiability of these parameters poor, as confirmed by the inverse Fisher Information Matrix (FIM), see Fig. 36.6a (parameters P3 and P4). Omitting these and looking at remaining parameters in the FIM, shows that the thickness parameters for the inner and outer layer of the glass also show poor identifiability, see Fig. 36.6b (parameters P5 and P7). As a final stage the thickness of the PVB polymer layer (P5 in FIM figures) was omitted from the parameter set. This was done because changes to the thickness of the PVB layer significantly impacts the bending stiffness of the windscreen as do the Youngs modulus of the glass. The influence on mass caused by this parameter can easily be compensated for by changing the density of the glass. Thus keeping the PVB thickness for the calibration procedure causes an unwanted behaviour since it enables large variations of parameters for small changes of the metric,  $Q$ .

### 36.4.2 Validation of Calibrated Model

Two types of validation is used. First, classic validation (sometimes called a hold-out validation) where the calibrated model output is compared to the five FRFs from test data that were not used during calibration. This results in a percentage representing the decrease (or increase if the calibration was unsuccessful) in the deviation metric for the calibrated model, compared to the deviation of the model using the nominal parameters. Secondly, a Monte Carlo cross-validation (MCCV) is used, with 20 starts from the calibrated parameter set and a validation fraction of 50% of the total amount of data. During MCCV, the validation fraction of test data is randomly removed during every start, and the calibration procedure starts from the calibrated setting and calibrates against the remaining set of data. By this procedure the validity of the calibrated parameters can be investigated. If the MCCV mean values of calibration parameters is close to the calibrated parameter setting, confidence about the accuracy of the calibrated parameters can be gained. However, if the MCCV parameter statistics does not point to the calibrated parameter set, it is likely that noise and uncertainties in the measurements have resulted in a parameter setting that can not be trusted to be precise estimates.

## 36.5 Measured Eigenfrequencies

From the identified state space models the mean of measured eigenfrequencies have been calculated. The mean and coefficient of variation (C.o.V.) of the tests for each windscreen, along with the overall mean and range between highest and lowest measured eigenfrequency, are shown in Table 36.1. Table 36.1 shows that the spread in measured eigenfrequencies

**Table 36.1** Eigenfrequency statistics of the first 20 modes, for all tests on the three windscreens

Mode	Windscreen I		Windscreen II		Windscreen III		All windscreens	
	$\mu$ [Hz]	C.o.V $\times 10^2$	$\mu$ [Hz]	C.o.V $\times 10^2$	$\mu$ [Hz]	C.o.V $\times 10^2$	$\mu_{All}$ [Hz]	Range[Hz]
1	16.61	0.30	16.62	0.13	16.53	0.18	16.58	0.14
2	17.77	0.09	17.70	0.07	17.84	0.03	17.78	0.16
3	39.44	0.06	39.51	0.03	39.86	0.19	39.60	0.56
4	45.33	0.10	45.35	0.03	45.28	0.13	45.32	0.15
5	72.54	0.11	73.09	0.10	73.08	0.20	72.84	0.85
6	74.78	0.09	74.57	0.10	75.46	0.22	74.99	1.18
7	93.24	0.11	93.96	0.14	94.34	0.28	93.77	1.61
8	109.74	0.09	110.51	0.11	109.62	0.18	109.84	1.12
9	133.38	0.12	132.76	0.10	134.95	0.26	133.84	2.79
10	145.64	0.10	145.94	0.09	145.58	0.18	145.67	0.65
11	173.23	0.12	173.90	0.13	173.78	0.25	173.55	1.44
12	184.88	0.12	186.40	0.11	184.86	0.21	185.15	2.00
13	200.25	0.02	203.94	0.06	199.55	0.06	200.67	4.65
14	212.06	0.05	214.32	0.03	209.25	0.05	211.45	5.22
15	215.64	0.12	214.60	0.09	217.96	0.25	216.29	4.26
16	221.66	0.01	223.50	0.03	221.73	0.03	222.02	1.91
17	231.31	0.13	233.18	0.00	231.02	0.10	231.55	2.31
18	248.33	0.08	249.71	0.04	246.91	0.12	248.06	3.10
19	263.76	0.07	265.51	0.05	263.56	0.09	264.00	2.33
20	264.13	0.06	267.77	0.03	264.25	0.08	264.84	3.93

Here  $\mu$  denotes the mean, C.o.V denotes coefficient of variance and Range is the total range of the identified eigenfrequencies for all windscreens

is very small, in particular for the lowest five modes. Moving up in the frequency range we see that the range between the highest and the lowest measured frequency becomes larger. The range is especially large for the last three modes. The C.o.V is consistently low.

## 36.6 Calibration and Validation Results

Calibration results for all tests on all windscreens are shown in Table 36.2 along with the results of the Monte Carlo cross validation. Looking at Table 36.2 we see a good agreement between most of the calibrated parameters and their mean values. The calibrated stiffness and mass parameters from test 2 on windscreen I were significantly lower than the other results. In fact it is the only one that results in a calibrated value for  $E_{glass}$  that is lower than the nominal value. This result is supported by the cross validation results for the test as well. Although test 2 for windscreen I could not be considered as an significant outlier before calibration, the calibrated parameters clearly are. A further inspection of the FRFs of test 2 on windscreen I reveals an overall offset to larger response. The reason for this is yet unknown. Omitting the parameters of test 2 on windscreen I gives the quotient to the calibrated to nominal parameters as

$$\bar{P}_E^* = 1.0447, \quad \bar{P}_\rho^* = 1.0840$$

which, gives us the mean of calibrated parameters as

$$\bar{E}_{calibrated} = 7.3126 [GPa], \quad \bar{\rho}_{calibrated} = 2,710 [kg/m^3]$$

Table 36.3 shows the validation results for the tests in Table 36.2. The calibration and validation metric reduction quantifies the decrease of the deviation metric when evaluated before and after calibration. Monte Carlo metric is the mean and C.o.V of the deviation criterion  $Q$  at the calibrated setting after the 20 Monte Carlo evaluations. The smaller values for both Calibration and Validation metric reduction seen for windscreen III tests reveals that the FE model at nominal parameter settings most closely resembles windscreen III. However, the MCCV mean value for the deviation metric shows that the FE model becomes calibrated to better resemble the measurements of windscreens I and II as well.

**Table 36.2** Calibration results for all tests on all windscreens

Test	$P_E^*$	Cross validation		$P_{\rho}^*$	Cross validation	
		$\mu_{P_E^*}$	$C.o.V_{P_E^*} \times 10^2$		$\mu_{P_{\rho}^*}$	$C.o.V_{P_{\rho}^*} \times 10^2$
I.T1	1.0463	1.0316	0.7560	1.0932	1.0758	0.8190
I.T2	0.9799	0.9654	0.5330	1.0153	0.9962	0.5640
I.T3	1.0526	1.0386	0.5030	1.0968	1.0793	0.5460
I.T4	1.0550	1.0558	0.6660	1.1023	1.1014	0.7780
I.T5	1.0380	1.0175	0.4540	1.0862	1.0636	0.5010
II.T1	1.0437	1.0469	0.6060	1.0826	1.0840	0.6730
II.T2	1.0619	1.0711	0.7240	1.1050	1.1149	0.7900
III.T1	1.0380	1.0387	0.5150	1.0728	1.0739	0.5350
III.T2	1.0403	1.0483	1.0220	1.0744	1.0838	1.0600
III.T3	1.0329	1.0395	0.7360	1.0577	1.0649	0.8070
III.T4	1.0379	1.0420	0.5240	1.0691	1.0736	0.5690
Mean:	1.0388			1.0778		

$P_E^*$  and  $P_{\rho}^*$  are the calibrated parameters divided by the nominal parameters,  $P_E^* = E_{\text{calibrated}}/E_0$  and  $P_{\rho}^* = \rho_{\text{calibrated}}/\rho_0$

**Table 36.3** Validation results for all tests on all windscreens

Test	Calibration metric		Validation metric reduction [%]	Monte Carlo metric	
	nominal	reduction [%]		Mean	C.o.V $\times 10^2$
I.T1	0.4662	25.0846	8.9180	0.3729	1.3050
I.T2	0.4396	22.3054	7.1732	0.3715	2.0600
I.T3	0.4357	24.4811	10.0028	0.3594	1.6890
I.T4	0.4254	25.1620	11.3020	0.3494	1.7400
I.T5	0.4868	26.1638	11.3020	0.3860	1.5800
II.T1	0.4314	17.7980	5.9857	0.3671	1.3730
II.T2	0.4874	24.9819	9.6275	0.3943	2.1850
III.T1	0.3897	19.6693	2.2119	0.3254	1.6500
III.T2	0.3422	16.8200	-0.6030	0.2920	1.7950
III.T3	0.3715	15.3728	0.1368	0.3247	1.9750
III.T4	0.3603	19.1389	2.3348	0.3014	2.0940

## 36.7 Evaluation of Calibrated Model

The eigenfrequencies of the nominal and calibrated FE model in relation to the mean eigenfrequencies of all windscreens as presented in Sect. 36.5, Table 36.1 is compared. Further, the correlation between mode shapes of the calibrated FE model and the windscreens is quantified by the Modal Assurance Criterion (MAC), followed by a comparison of frequency response functions of the nominal and calibrated FE model and the mean response of all tests.

### 36.7.1 Comparison of Eigenfrequencies

Table 36.4 shows the eigenfrequencies of the first 20 modes for the nominal FE model, the calibrated FE model and mean values of the measure eigenfrequencies. It shows that all eigenfrequencies have been lowered for the calibrated model, and 14 eigenfrequencies out of the first 20 are more accurately predicted after the calibration.

### 36.7.2 MAC Correlation

From the test data, a single state space model for each windscreen was created by evaluating the average FRFs from each windscreen and performing system identification. This enables calculating modal data from a mean model of each windscreen. MAC correlation between the calibrated FE model and windscreens I, II and III can be seen in Fig. 36.7a, b,

**Table 36.4** Comparison between the eigenfrequencies of the FE model with the mean calibration parameters and the mean eigenfrequencies of the test data, subscripts nom and cal denote nominal and calibrated parameters, [Hz]

Mode	1	2	3	4	5	6	7	8	9	10
FE <sub>nom</sub>	17.12	18.78	40.12	45.51	72.73	75.65	94.81	110.42	138.45	146.49
FE <sub>cal</sub>	16.86	17.90	39.54	44.92	71.66	74.49	93.39	108.78	136.36	144.33
Test, $\mu_{All}$	16.58	17.78	39.60	45.32	72.84	74.99	93.77	109.84	133.84	145.67
Mode	11	12	13	14	15	16	17	18	19	20
FE <sub>nom</sub>	176.47	188.98	206.77	209.23	222.60	230.56	236.73	255.35	258.37	275.92
FE <sub>cal</sub>	173.89	186.12	203.78	206.08	219.20	227.14	233.21	251.65	254.39	271.85
Test, $\mu_{All}$	173.55	185.15	200.67	211.45	216.29	222.02	231.55	248.06	264.00	264.84

c respectively. The MAC correlation between the different windscreens are shown in Fig. 36.7d–f. The mode shapes of the calibrated FE-model match the test data very well for 15 modes for all three windscreens. However, only the first 12 of the 15 are found on the main diagonal of the frequency ordered MAC matrix. Figure 36.7e shows very strong correlation between test data of windscreens I and III for all modes but the highest frequency mode. The MAC correlations between windscreens I and II as well as II and III are also strong, although modes 19 and 20 seem to be shifted between the two windscreens.

### 36.7.3 Frequency Response Functions FE Model Before and After Calibration

State space models of the calibrated and nominal FE models were assigned the mean modal damping, calculated from the modal damping of all test data. FRFs from accelerometer positions 1 and 12 represents typical results. The behaviour in the frequency range 15–150 Hz can be seen in Fig. 36.8 and the responses in the range of 150–300 Hz in Fig. 36.8.

Figure 36.8 shows that the FRFs of the calibrated model is better aligned with the mean value for measured FRFs up to 100 Hz. Between 100 and 150 Hz no significant improvement have been obtained. In Fig. 36.9 the FRFs are shown for the higher frequency range. Between 150 and 180 Hz, the calibrated model have moved towards the mean value. From 180 Hz and upwards the range of measured eigenfrequencies in tests, as listed in Table 36.1, increases and the mean value gives no clear trend. Thus, the fit improvement of the of the calibrated model in this area is not obviously significant.

## 36.8 Conclusions and Discussion

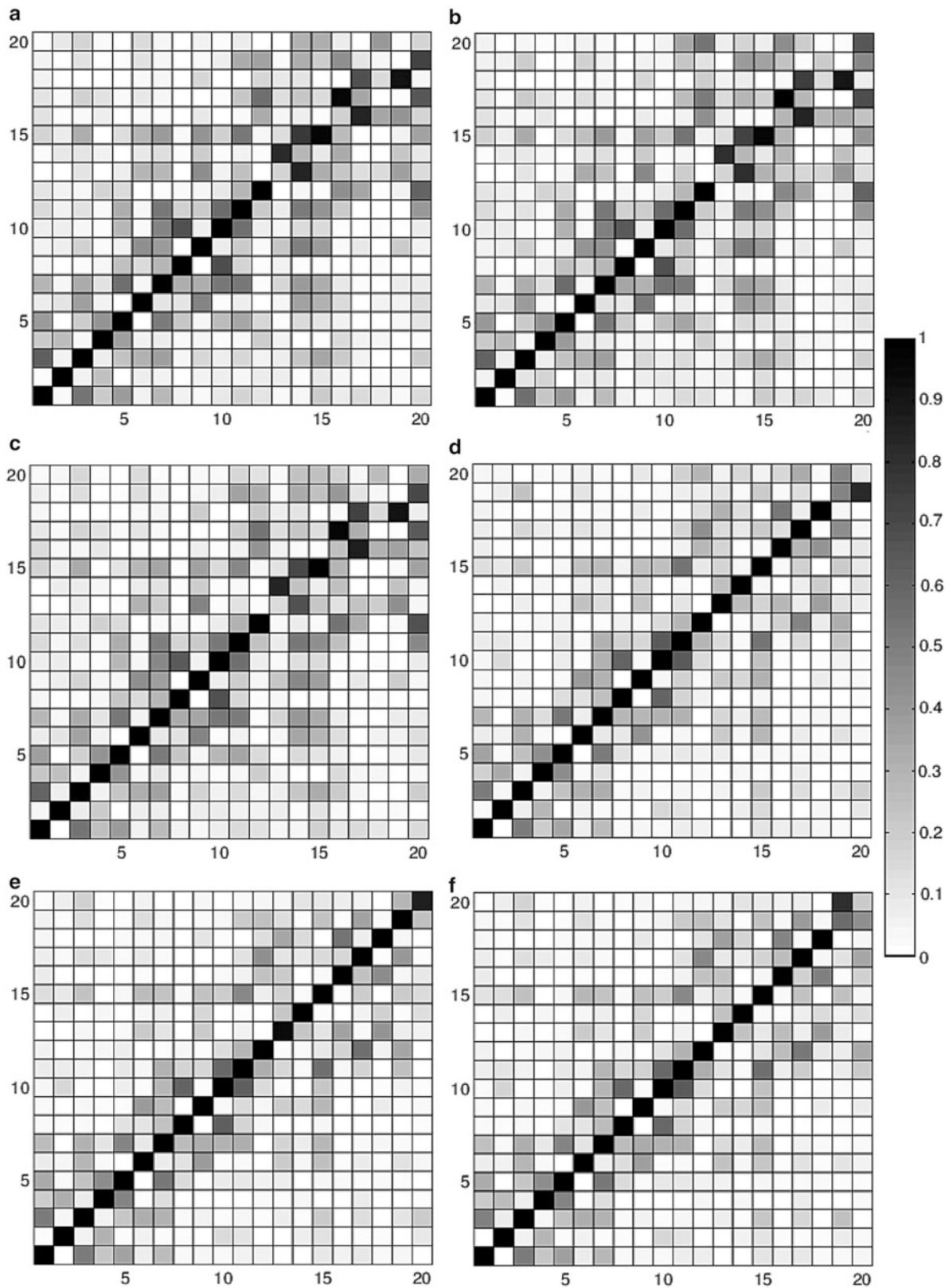
Tests were made on three car windscreens. A post-test screening was made on test data. Inspection of test data showed two outliers that were omitted prior to calibration. The modal results, having omitted these outliers, showed little spread in measured eigenfrequencies, both between different tests and different test pieces, although the variance increased in the higher frequency spectrum.

The calibration process successfully reduced the deviation metric for all tests and statistics gave the mean for  $Q$  between 0.3 and 0.4 for all of them. All calibrations, except for one, converged to stiffness and mass parameter settings higher than nominal. The exception was omitted when creating the mean calibrated parameters, and mean state space models of windscreens. Comparison of eigenfrequencies before and after calibration with the mean test data showed improvement for 14 of the first 20 modes. The MAC calculated for the mean models show very good mode shape correlation between the three windscreens, and all correlate very well with the first 12 modes of the calibrated FE model. It can be concluded that repeated testing allowed for identification of outliers that would not have been detected in a single test. After calibration another set of test data led to deviations in the calibrated parameters. This deviation was also supported by the statistics from the Monte Carlo cross-validation, which shows that the test data has an overall deviation. The remainder of the parameter sets from windscreen I clearly marks these parameters as outliers, and they could be excluded when establishing the mean calibrated parameters for all windscreens.

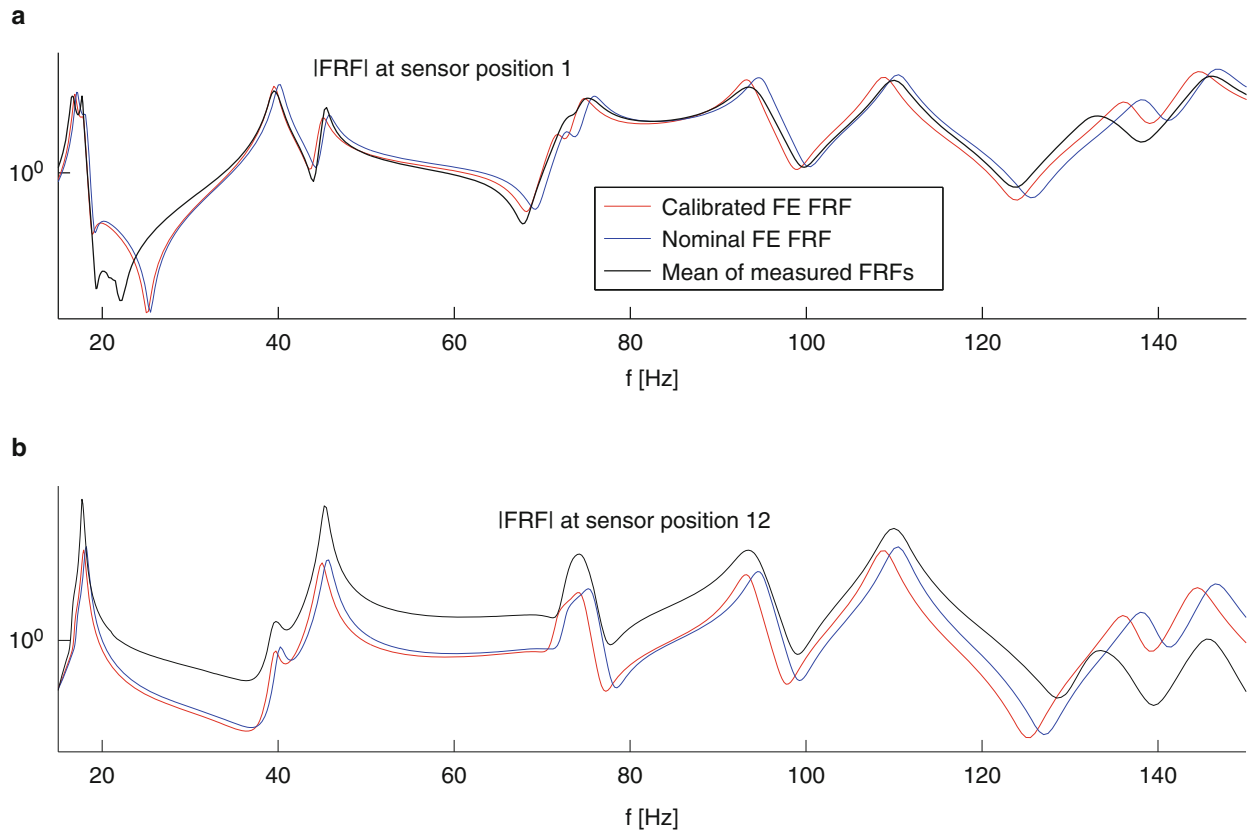
The results show that the calibrated FE model predicts the behavior of the windscreens well, especially in the lower half of the tested frequency range, i.e. up to 150 Hz.

**Acknowledgements** We acknowledge the Volvo Car Corporation for donating the windscreens needed for testing.

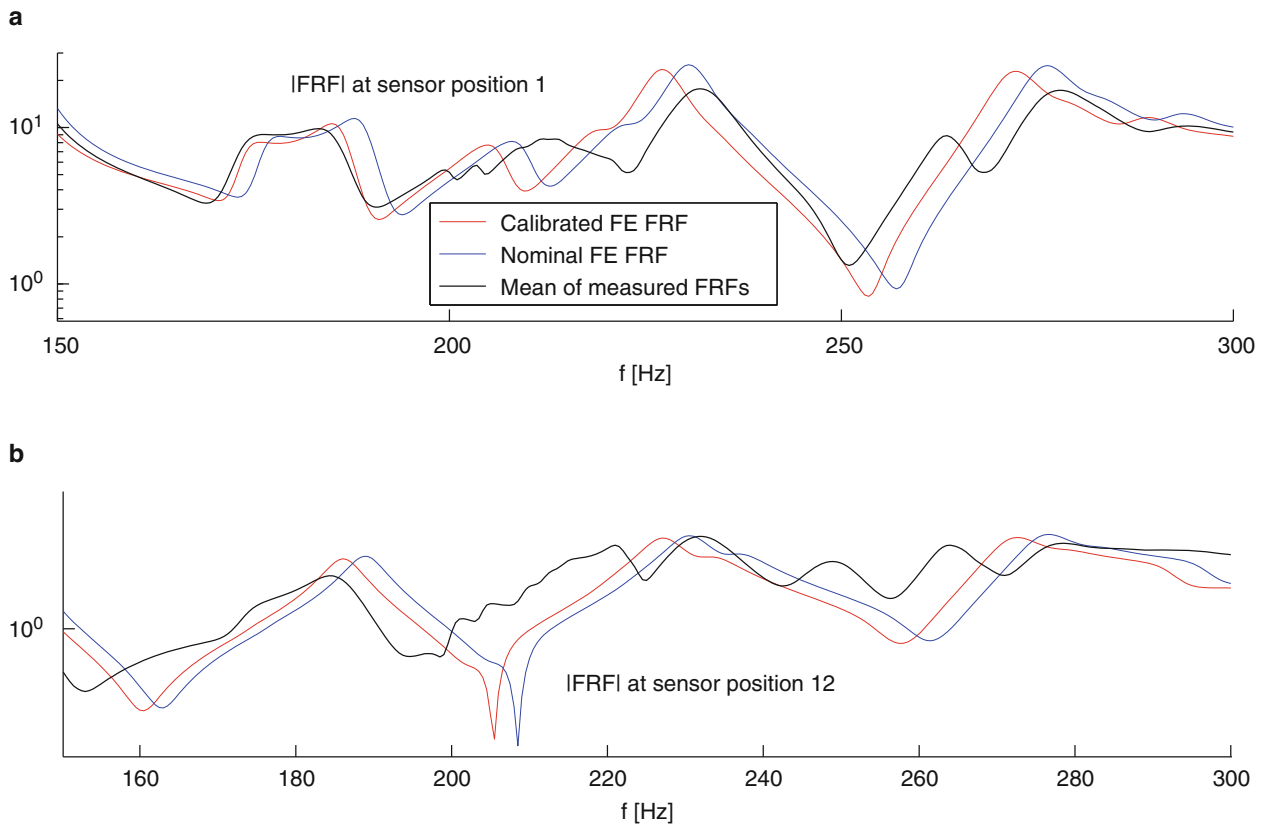




**Fig. 36.7** MAC plots showing the correlations between calibrated FE model and mean test data for all three windscreens as well as correlation between test data of different windscreens. (a), (b) and (c) show correlation between calibrated FE model and mean test data from windscreens I, II and III respectively, (d) shows correlation between mean test data of I and II, (e) between I and III and (f) between II and III



**Fig. 36.8** Representative FRFs of nominal and calibrated FE Models, and the mean of FRFs measured in tests, from 15 to 150 Hz



**Fig. 36.9** Representative FRFs of nominal and calibrated FE Models, and the mean of FRFs measured in tests, from 150 to 300 Hz

## References

1. Friswell MI, Mottershead JE (1995) Finite element model updating in structural dynamics. Kluwer Academic, Dordrecht
2. Kammer DC (2005) Sensor set expansion for modal vibration testing. *Mech Syst Signal Process* 14:700–713
3. McKelvey T, Akcay H, Ljung L (1996) Subspace-based multivariable system identification from frequency response data. *IEEE Trans Autom Control* 41(7):960–979
4. Van Overschee P, De Moor B (1994) N4SID: subspace algorithms for the identification of combined deterministic-stochastic systems. *Automatica*. Special Issue on Stat Signal Process Control 30(1):75–93
5. Abrahamsson TJS, Kammer HC (2014) FEM calibration with FRF damping equalization. In: 32nd IMAC conference, Orlando

# Chapter 37

## Structural Dynamics Model Calibration and Validation of a Rectangular Steel Plate Structure

Hasan G. Pasha, Karan Kohli, Randall J. Allemang, Allyn W. Phillips, and David L. Brown

**Abstract** To characterize the dynamics of a structure accurately and to minimize uncertainties, it is important to perform modal testing in various configurations. However, performing such rigorous testing of structures can be a resource intensive process. In addition, simulating certain conditions may not be possible in the lab. Developing a calibrated and a validated model that can predict the dynamic response of a structure accurately can be a key to address this issue. In this paper, a model calibration and validation case study performed on a rectangular steel plate structure is presented. The geometric and material properties used in the model were updated to calibrate the model. The accuracy of the calibrated model was confirmed by performing a validation process involving perturbed mass and constrained boundary condition FE modal analysis and modal testing. The validation criteria were achieved using the calibrated model and thus proved that the model could reliably predict the dynamic response of the structure.

**Keywords** Model verification • Model calibration • Model validation • Modal correlation • Model updating • Perturbed boundary conditions • Constrained boundary condition testing

### Notation

Symbol	Description
$\gamma$	Mass per unit area of a plate ( $\text{kg}/\text{m}^2$ )
$\rho$	Density of the material ( $\text{kg}/\text{m}^3$ )
$\nu$	Poisson ratio
$b$	Width of the plate (m)
$f_{ij}$	Modal frequency (Hz)
$h$	Thickness of the plate (m)
$i$	Mode index, number of half waves in mode shape along horizontal direction
$j$	Mode index, number of half waves in mode shape along vertical direction
$l$	Length of the plate (m)
$D$	Flexural rigidity ( $\text{N} \cdot \text{m}^2$ )
$E$	Young's modulus (Pa)
CMIF	Complex Mode Indicator Function
FEA	Finite Element Analysis
MRIT	Multi-reference Impact Testing

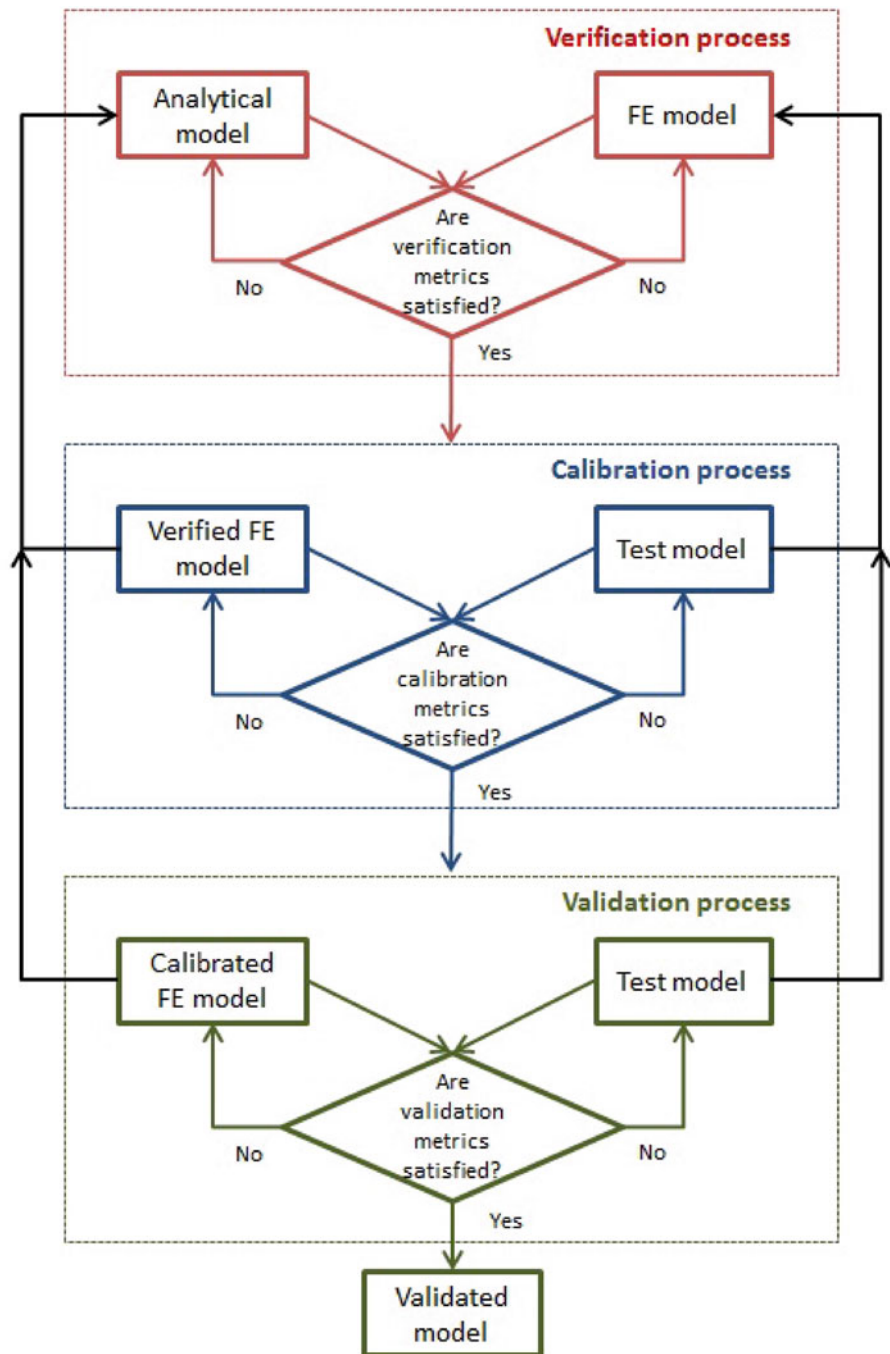
### 37.1 Introduction

Testing a structure to determine its dynamic characteristics is both time consuming and expensive. This situation has made it necessary to develop analytical/mathematical models that can predict the response of system in real time without performing actual tests. Such models need to undergo verification, calibration and validation with actual test data before they can be relied upon to extrapolate results for future studies. In this context, *verification* and *validation* (V&V) are defined as below:

---

H.G. Pasha (✉) • K. Kohli • R.J. Allemang • A.W. Phillips • D.L. Brown  
University of Cincinnati – Structural Dynamics Research Lab (UC-SDRL), Cincinnati, OH, USA  
e-mail: [pashahg@mail.uc.edu](mailto:pashahg@mail.uc.edu)

**Fig. 37.1** Verification, calibration and validation processes



**Verification:** refers to process of determining that a model implementation accurately represents the developer’s conceptual description of the model and the solution to the model [1]. Frequently, the verification portion of the process answers the question “*Are the model equations correctly implemented?*”

**Validation:** refers to the process of determining the degree to which a model is an accurate representation of the real world system from the perspective of the intended uses of the model [1]. Frequently, the validation process answers the question “*Are the correct model equations implemented?*”

In this paper, a FE model of the plate structure was developed to determine its dynamic characteristics (modal frequencies and mode shapes). A step by step approach was taken to verify, calibrate and validate the results generated by the model in different test configurations (Fig. 37.1).

## 37.2 Verification

### 37.2.1 Analytical Modeling and Formulation

Ideally, a plate is considered a two-dimensional layer of elastic material made up of a sheet that lies in a plane. A plate as a structure possesses bending rigidity due to its thickness and elasticity. As a result, when the plate vibrates, it deforms primarily by flexing perpendicular to its own plane.

The following assumptions were made while performing the analytical formulation of the rectangular plate structure [9]:

- The plate is composed of homogeneous, linear, elastic, isotropic material
- The plate is flat and has constant thickness
- The plate is thin, with a thickness of less than 1/10 of the minimum lateral plate dimension
- The in-plane load on the plate is zero and it deforms through flexural deformation
- The deformation is small in comparison with the thickness of the plate. There is no deformation at normal to the mid surface or nodal lines. In addition, the rotary and shear deformations are ignored.
- In the case of free vibration, total transverse deformation is defined as the sum of all modal deformations such that

$$z = \sum_i \sum_j A_{ij} \tilde{z}_{ij} \sin(2\pi f_{ij}t + \phi_{ij}) \quad (37.1)$$

where  $\tilde{z}_{ij}$  is the mode shape of the mode (i, j),  $A_{ij}$  is the modal amplitude and  $\phi_{ij}$  is the phase. The modal frequency of the plate is defined as  $f_{ij} = \frac{\lambda_{ij}^2}{2\pi l^2} \sqrt{\frac{Eh^3}{12\gamma(1-\nu^2)}}$ , where  $\lambda_{ij}$  is a dimensionless parameter, which is generally a function of the mode indices (i, j). Flexural rigidity of plate is defined as  $D = \frac{Eh^3}{12\gamma(1-\nu^2)}$ .

### 37.2.2 Verification

*Verification* is the process of comparing different analytical models to be certain that the analysis results are correct [1, 2]. In this case, a FE model is compared to the analytical, closed form results for a rectangular plate. An analytical rectangular plate model, with aspect ratio of 1.5 was developed, such that the first mode is a torsion mode roughly at 40 Hz and the second mode is a bending mode roughly at 44 Hz. Closed form expressions [9] were used to develop an analytical model (Figs. 37.2 and 37.3).

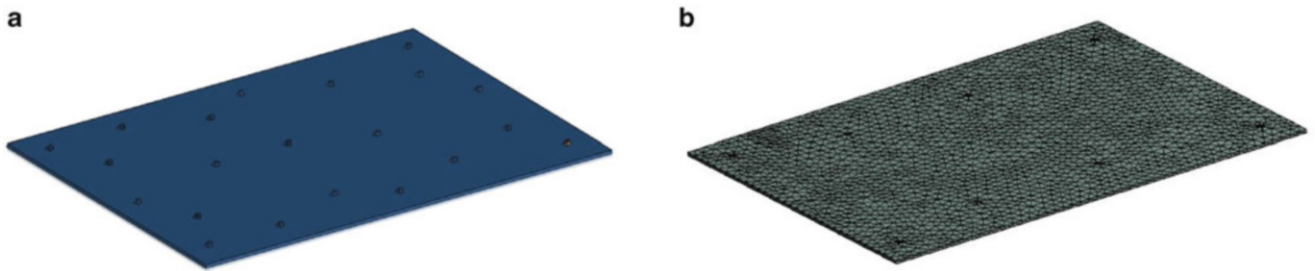
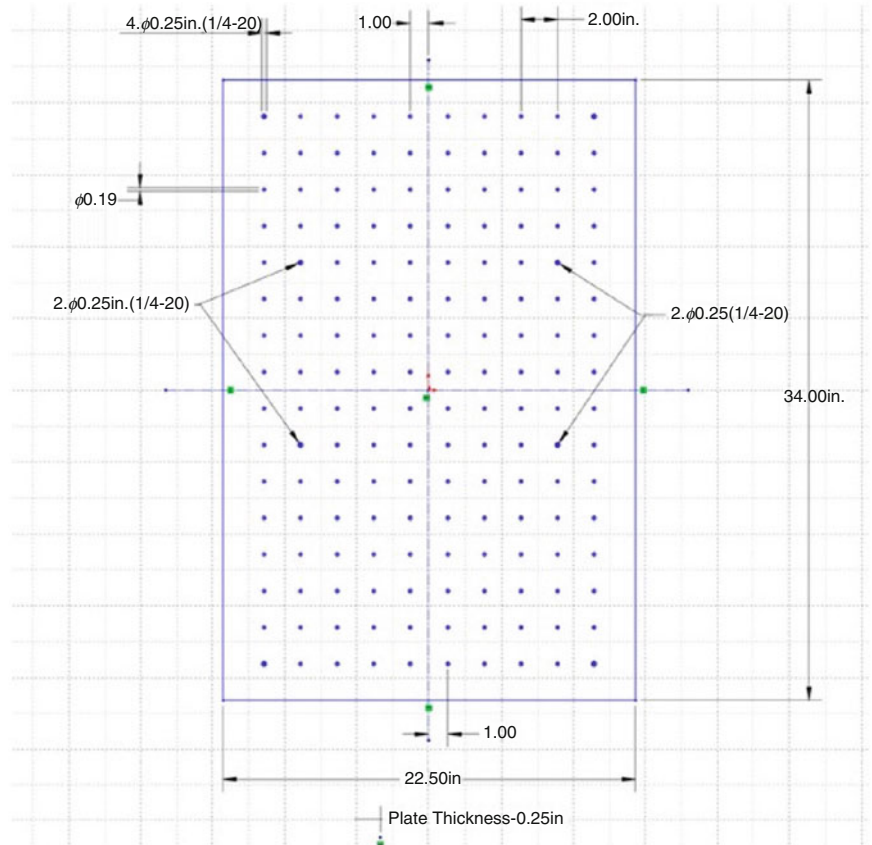
A comparable rectangular plate FE model was developed using the dimensions and material properties chosen for the analytical closed form model of the plate. Analytical modal analysis was performed on the plate FE model. The modal frequencies and mode shapes for the first six deformation modes were retrieved and compared with the analytical model prediction.

The modes were in the expected sequence and the relative difference in modal frequencies was less than 2%. This verified the FE model (Table 37.1).

## 37.3 Calibration

*Calibration* of a model involves comparing the analytical results to equivalent experimental results. Calibration in this case involves correlating the modal parameters obtained from an analytical modal analysis of the rectangular plate FE model and impact testing of the fabricated rectangular plate structure. The details of the various activities performed in the calibration process are explained in the subsequent sections.

**Fig. 37.2** 2-D drawing showing plate dimensions



**Fig. 37.3** Rectangular plate model. (a) CAD model. (b) Mesh

**Table 37.1** Preliminary verification of the FE model—modal frequency comparison

Mode #	Description	Modal frequency (Hz)		Rel. diff. (%)
		Analytical	FE	
1	First torsion	41.55	41.34	0.51
2	First X bending	44.59	43.95	1.46
3	Second torsion	96.3	95.12	1.24
4	First Y bending	103.8	102.99	0.79
5	Second X bending	121	119.16	1.54
6	Anti symmetric X bending	139.3	137.39	1.39

### 37.3.1 Analytical Modal Analysis

Analytical modal analysis was performed in ANSYS® Workbench 14.5. The default material model for steel in the ANSYS® material library was chosen. The modal frequencies and mode shapes were extracted in the frequency range 0–250 Hz.

### 37.3.2 Experimental Modal Analysis

The plate structure was tested using the multi-reference impact testing (MRIT) technique with 21 accelerometers mounted on the rectangular plate at locations identified in Fig. 37.4. For simulating the free-free boundary condition, the plate was initially suspended using shock cords. However, the support system was dynamically coupled with the third mode of the rectangular plate (second torsion mode) and it acted as a vibration absorber. Subsequently, the plate was supported on racquet balls, as shown in Fig. 37.5. Though the racquet ball supports offered a lesser frequency separation ratio between the rigid body modes and the first elastic mode (compared to the shock cords), they were well isolated from the test structure [11].

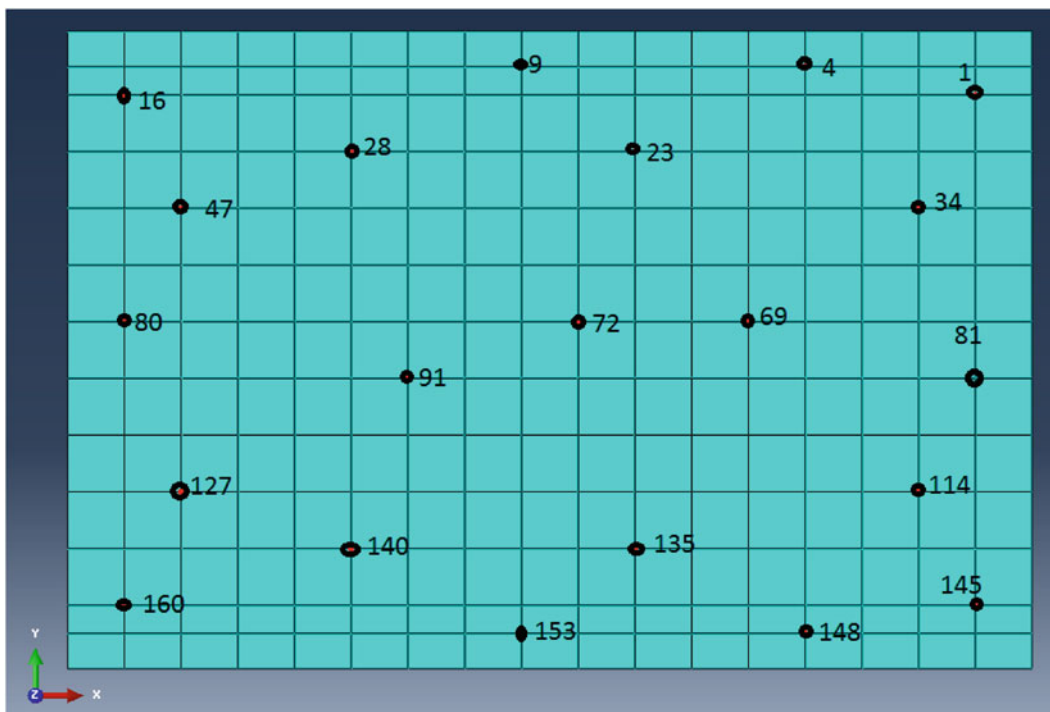


Fig. 37.4 Rectangular plate—reference locations

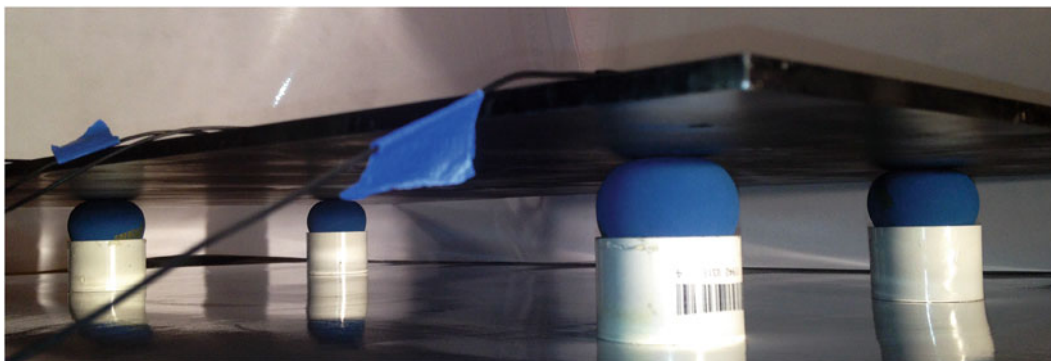
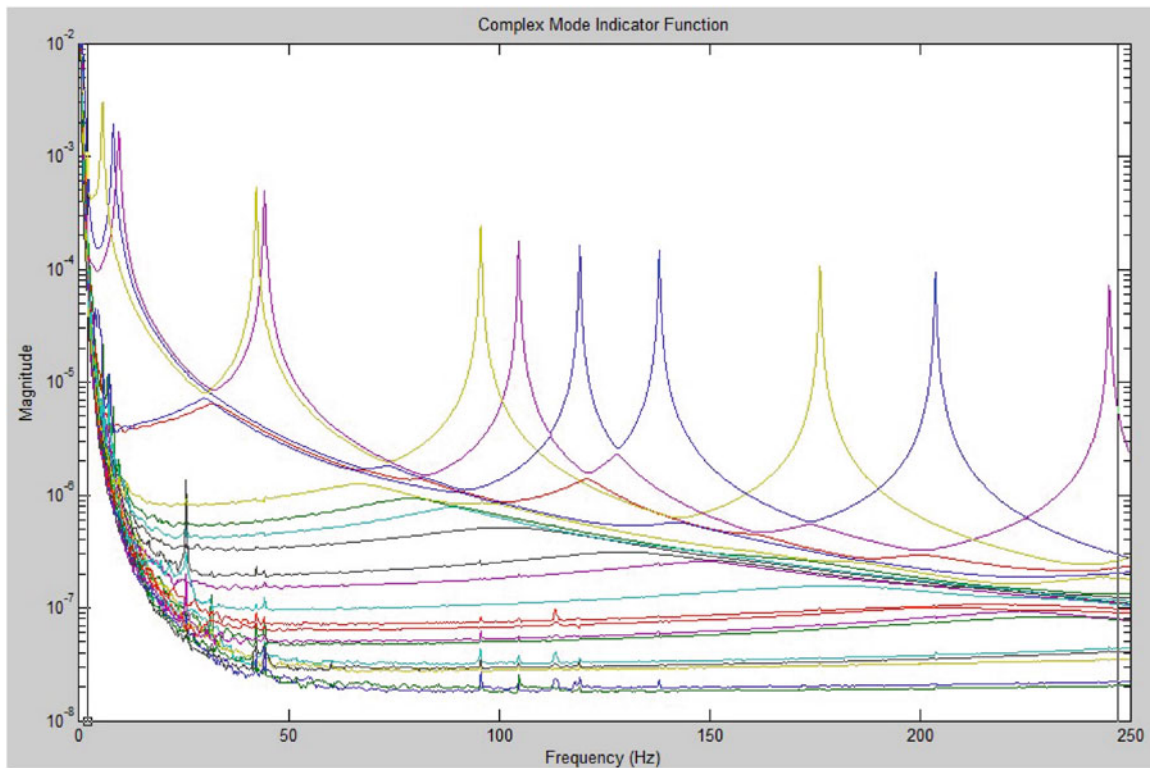


Fig. 37.5 Rectangular plate—support system





**Fig. 37.6** Complex mode indicator function

On processing the measured data, nine deformation modes in the 0–250 Hz frequency range were identified, as evident from the CMIF plot shown in Fig. 37.6. The first torsion and the first bending mode were at 42.16 Hz and 44.16 Hz respectively. The mode shapes are shown in Fig. 37.7.

### 37.3.3 Modal Correlation

The relative difference between the modal frequencies obtained from FE modal analysis and impact testing is  $>2\text{--}3\%$ . The sequence of the modes was established to be in the same order for both cases by viewing the mode shape animations.

### 37.3.4 Model Calibration

From the correlation of the modal parameters from the preliminary analytical modal analysis and impact testing, it was identified that there were various sources of uncertainty. On the modeling side, the sources of uncertainty were geometric and material properties of the steel plate. In addition, the soft supports had not been modeled. On the testing side, the support system, location of supports, sensor calibration, impact hammer tip and signal processing parameters were considered to be the sources of uncertainty. The relative difference in modal frequencies was desired to be less than 2% and was set as the *calibration criteria* or *calibration metric*.

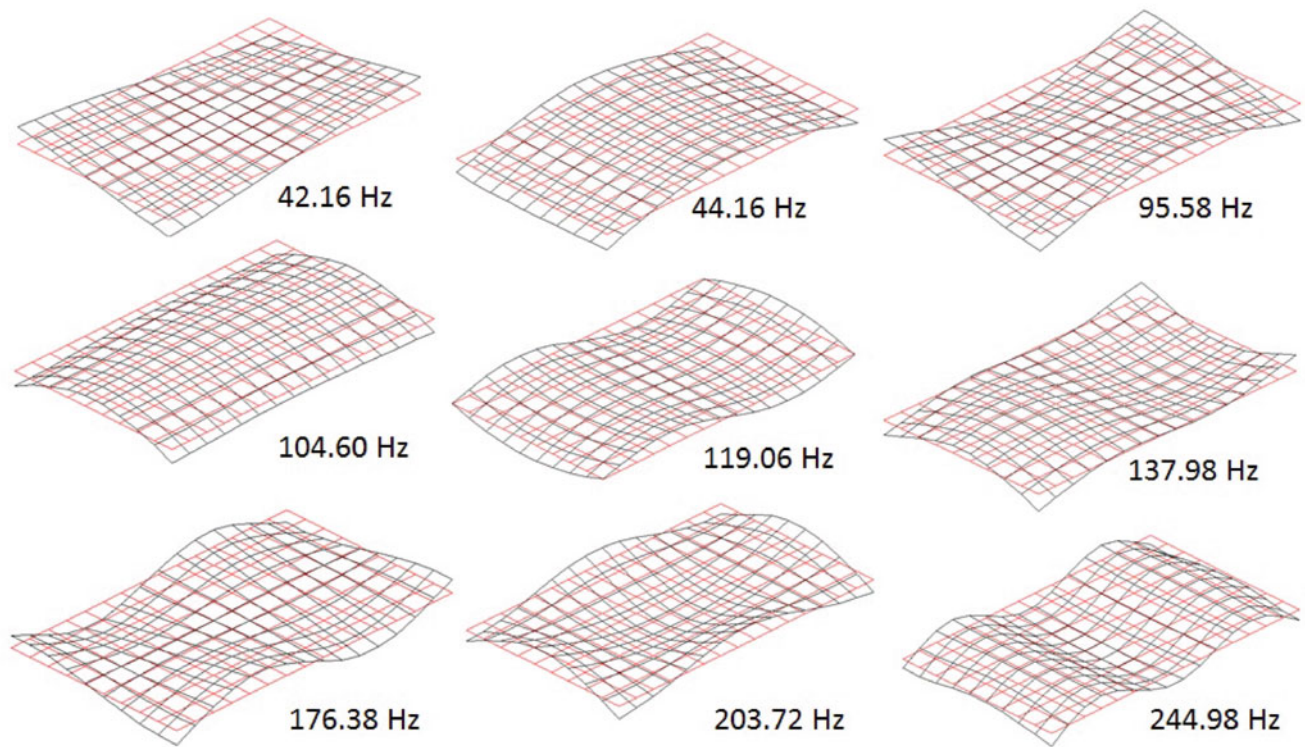


Fig. 37.7 Experimental mode shapes

#### 37.3.4.1 Model Updating

**Geometric properties:** It was established that the plate thickness, originally intended to be 0.25 in. was not constant. The plate was weighed (52.5 lb<sub>m</sub>) and the thickness of the plate model was adjusted (0.243 in.) to match the measured weight of the plate.

**Material model:** The relative difference for the third mode (second torsion mode) was reasonably high compared to other modes. A parametric study, in which the effect of varying the Young's modulus, mass density and Poisson ratio on the modal frequencies, was studied. For the calibrated model, the material properties were established as: Young's modulus  $E = 2.05 \times 10^{11}$  Pa ( $2.9734 \times 10^7$  psi), mass density  $\rho = 7,850$  kg/m<sup>3</sup> ( $0.2836$  lb/in<sup>3</sup>) and Poisson ratio  $\nu = 0.29$ .

**Modeling support system:** Four racquet balls were used to support the plate during impact testing. These racquet balls act as springs and their stiffness value was estimated to be roughly 40 lb<sub>f</sub>/in. At locations corresponding to the supports, linear springs were added in the FE model. This reduced the relative difference for the modal frequencies further.

#### 37.3.4.2 Testing Related Changes

**Support system:** Free-free boundary conditions are relatively easier to achieve compared to other boundary conditions such as a fixed boundary condition. Support systems add stiffness and can also interact with the test structure. Certain precautions need to be followed while selecting support systems [11].

Initially, shock chords were used to support the structure. However, it was observed that the shock chord supports dynamically interacted with the third deformation mode (second torsion mode), and acted as a vibration absorber. As a result, a racquet ball support system, that was reasonably isolated from the test structure, was selected.

**Sensor calibration:** The sensors (accelerometers and impact hammer load cells) need to be calibrated before data is acquired. Sensors generally tend to have variability in the sensitivity in the order of 2–5 %, which when not accounted for could skew the measurement magnitudes (but would have no effect on the calibration metric involving modal frequencies).

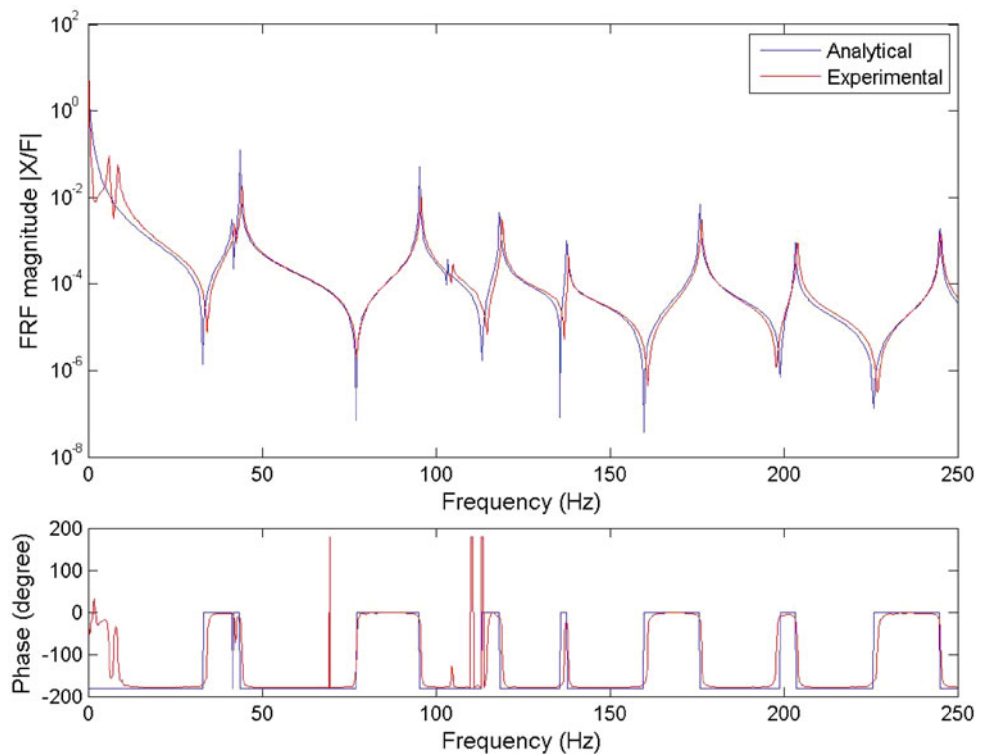
**Impact hammer tip:** The impact hammer tip should be selected such that the modes in the required frequency range are adequately excited without exciting higher frequency modes. When the focus is to acquire data in lower frequency range, using a harder tip would possibly cause overloads on the data acquisition channels associated with sensors near the impact location. As a result, an appropriate hammer tip should be selected. A soft hammer tip was selected as the plate structure was lightly damped.

**Signal processing parameters:** The rectangular plate is a very lightly damped structure. It was noted that after every impact, it took over 16 s for the response to die out. After selecting the frequency bandwidth, the frequency resolution should be chosen such that the response at all the reference locations is completely observed in the captured time segment. If this condition is not met, it would result in leakage errors. If desired, the force-exponential windows can be applied to condition the signal to avoid leakage and measurement noise. The number of ensembles acquired per average also affects the ability to obtain good quality data and minimize measurement noise. In this test, data was acquired in the 0–100 Hz and 0–250 Hz frequency ranges. The frequency resolution ( $\Delta F$ ) was chosen for each case such that each ensemble was observed for 16 s. The force-exponential window was chosen, with a cutoff value of 10 % for the force window and an end value for exponential window as 20 %.

### 37.3.4.3 Modal Correlation after Calibrating the FE Model

Modal correlation was performed after updating the FE model and incorporating the changes identified for the test setup. The relative difference for modal frequencies reduced to a value less than 2 %.

FRFs from the FE model were synthesized at a few locations corresponding to the driving-points in the impact test. The measured FRFs were compared with the corresponding synthesized FRFs as a further calibration metric that involves damping and sensor calibration issues. A plot comparing the measured FRF with the synthesized FRF for a driving-point is shown in Fig. 37.8. It is apparent from the comparison that the peaks of the synthesized FRF are sharp as damping was not prescribed in the FE model. However, the peaks of the measured FRF are damped. In reality the modes do not have the amount of damping that is evident in the FRF comparison plot as the rectangular plate is a lightly damped structure. The damped peaks in the measured FRF are a result of the artificial damping introduced by the force-exponential window that was used to eliminate leakage while performing the impact testing.



**Fig. 37.8** Comparison of a driving-point FRF

**Table 37.2** Correlation of modal frequencies for free-free case with no perturbed mass and updated FE models

$h = 6.17 \text{ mm (0.243")}$ ,  $E = 2.05 \times 10^{11} \text{ Pa (2.9734} \times 10^7 \text{ psi)}$   
 FE model I:  $\rho = 7,810 \text{ kg/m}^3 \text{ (0.2821 lb/in}^3)$ ,  $m = 23.8 \text{ kg (52.44 lb)}$   
 FE model II:  $\rho = 7,850 \text{ kg/m}^3 \text{ (0.2836 lb/in}^3)$ ,  $m = 23.9 \text{ kg (52.69 lb)}$

Mode	Modal frequency (Hz)			Rel. diff. (%)	
	Experimental	FE model I	FE model II	FE model I	FE model II
First torsion	42.16	41.33	41.34	2	1.98
First X bending	44.16	43.71	43.65	1.02	1.16
Second torsion	95.58	95.04	95.12	0.57	0.48
First Y bending	104.6	103.1	102.99	1.45	1.56
Second X bending	119.06	118.19	118.16	0.74	0.76
Anti sym. X bending	137.98	137.38	137.39	0.44	0.43
Third torsion	176.38	175.52	175.81	0.49	0.32
X and Y bending	203.72	202.86	203.25	0.42	0.23
Third X bending	244.98	243.65	244.1	0.54	0.36

The results of modal correlation are presented in Table 37.2. The calibration criteria, a relative difference for modal frequencies less than 2% was met and a calibrated rectangular plate FE model was obtained.

## 37.4 Validation

*Validation* is the process of determining the correctness of a model in its description of the reference system under a set of test conditions [1, 2]. For validating the calibrated rectangular plate FE model and thereby establishing the robustness of the model, it was decided to analyze and to perform testing for the following two cases:

1. Perturbed mass analytical modal analysis and testing
2. Constrained boundary analytical modal analysis and testing

The relative difference in modal frequencies was chosen as the *validation criteria* or the *validation metric*. For the perturbed mass case, the validation criteria was set to less than 2% relative difference in modal frequencies.

Constraining specific points is possible theoretically in a FE model; however, it is impractical to achieve while testing. In addition, modeling real boundary conditions is involved. As a result it was decided to set the validation criteria less than 5% relative difference for modal frequencies for the constrained boundary condition case.

### 37.4.1 Perturbed Mass Modal Analysis

Two separate cases were studied by attaching two cylindrical masses, 1 lb 1.5 oz and 2 lb 1.5 oz each, to the calibrated plate FE model. The perturbation masses were also attached to the fabricated plate structure and impact testing was conducted. The results obtained from the modal analysis and impact testing were correlated. The correlated results for 1 lb 1.5 oz and 2 lb 1.5 oz perturbed mass cases are listed in Tables 37.3 and 37.4 respectively. It is evident that the validation criteria, relative difference for modal frequencies less than 2%, was met.

### 37.4.2 Constrained Boundary Condition Modal Analysis

The plate was clamped to ground at two locations near one of the edges using steel spacers, which in turn were grounded to a huge isolated mass. The test setup is shown in Fig. 37.9. Impact testing was performed on the clamped plate.

**Table 37.3** Correlation of modal frequencies for free-free case with perturbed mass of 0.496 kg (1 lb 1.5 oz) and updated FE models)

$h = 6.17 \text{ mm (0.243")}$ ,  $E = 2.05 \times 10^{11} \text{ Pa (2.9734} \times 10^7 \text{ psi)}$   
 FE model I:  $\rho = 7,810 \text{ kg/m}^3 \text{ (0.2821 lb/in}^3\text{)}$ ,  $m = 23.8 \text{ kg (52.44 lb)}$   
 FE model II:  $\rho = 7,850 \text{ kg/m}^3 \text{ (0.2836 lb/in}^3\text{)}$ ,  $m = 23.9 \text{ kg (52.69 lb)}$

Mode	Modal frequency (Hz)			Rel. diff. (%)	
	Experimental	FE model I	FE model II	FE model I	FE model II
First torsion	38.95	38.4	38	1.43	1.06
First X bending	42.42	42.15	41.84	0.63	0.76
Second torsion	89.53	89.73	88.86	0.23	0.98
First Y bending	99.96	98.93	97.79	1.04	1.17
Second X bending	117.39	117.09	116.11	0.26	0.84
Anti sym. X bending	128.95	128.94	127.56	0.31	1.08
Third torsion	167.56	168.34	166.33	0.46	1.21
X and Y bending	197.19	198.36	196.76	0.59	0.81
Third X bending	235.5	237.82	233.8	0.98	0.71

**Table 37.4** Correlation of modal frequencies for free-free case with perturbed mass of 0.95 kg (2 lb 1.5 oz) and updated FE models,

$h = 6.17 \text{ mm (0.243")}$ ,  $E = 2.05 \times 10^{11} \text{ Pa (2.9734} \times 10^7 \text{ psi)}$   
 FE model I:  $\rho = 7,810 \text{ kg/m}^3 \text{ (0.2821 lb/in}^3\text{)}$ ,  $m = 23.8 \text{ kg (52.44 lb)}$   
 FE model II:  $\rho = 7,850 \text{ kg/m}^3 \text{ (0.2836 lb/in}^3\text{)}$ ,  $m = 23.9 \text{ kg (52.69 lb)}$

Mode	Modal frequency (Hz)			Rel. diff. (%)	
	Experimental	FE model I	FE model II	FE model I	FE model II
First torsion	36.86	36.47	36.17	1.07	1.92
First X bending	41.22	41.09	40.82	0.33	0.97
Second torsion	86.62	86.92	86.28	0.34	0.39
First Y bending	96.26	95.49	94.5	0.8	1.86
Second X bending	115.98	115.85	114.99	0.11	0.86
Anti sym. X bending	125.37	125.29	124.39	0.26	0.79
Third torsion	163.3	164.29	162.74	0.6	0.34
X and Y bending	195.1	196.22	195.05	0.57	0.23
Third X bending	229.84	231.37	230.8	0.67	0.42

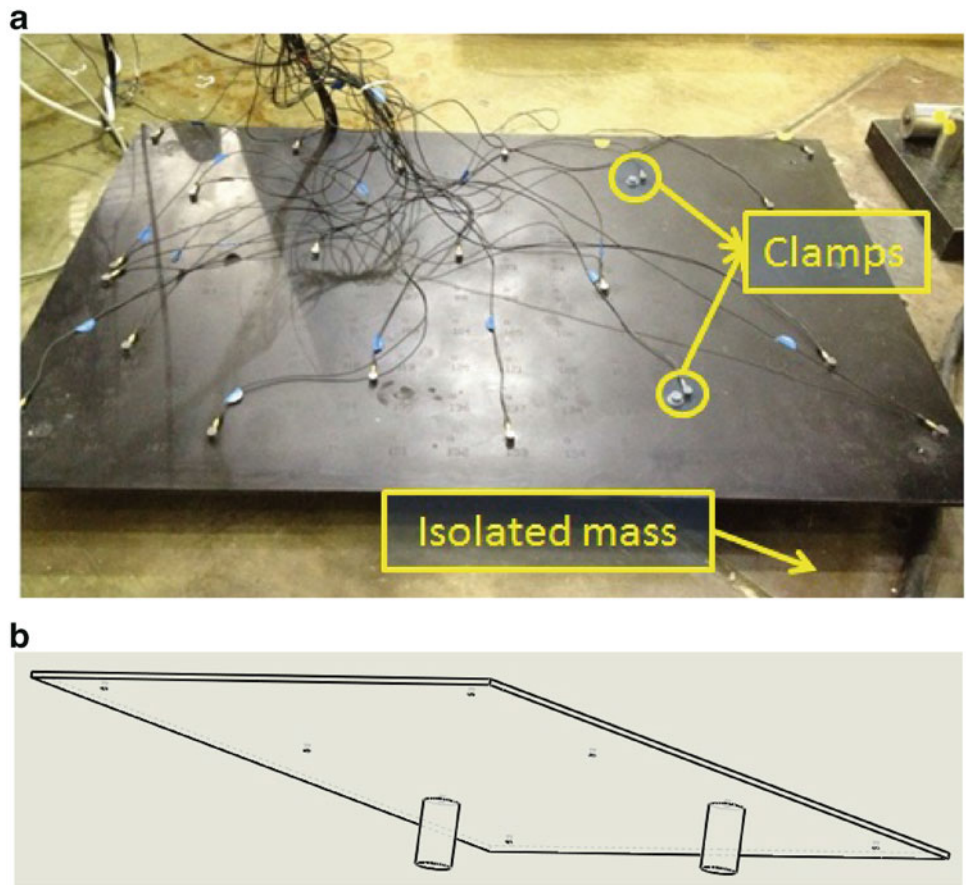
Subsequently, the FE model was analyzed after applying constraints in vertical direction at the location corresponding to the clamping points. The modal frequencies for the constrained boundary analysis and modal testing are listed in Table 37.5.

The larger relative difference for this case was expected, and can be attributed to the uncertainties involved in modeling the boundary constraints used in the test. While it is aimed to constrain only the vertical direction translation of the plate at two points, it is practically not possible to achieve this boundary condition. The support system constrains the motion of the plate at a small but finite patch near the clamping location. The boundary condition of the constrained plate test setup is difficult to incorporate in a FE model. As the FE model is not a true representation of the test setup, the relative difference for this case is higher. However, the validation criteria was met for the constrained boundary condition case as well.

## 37.5 Conclusions

- Testing is expensive and resource intensive. Therefore, it is necessary to develop a well calibrated and validated FE model to assist in predicting system response.
- This paper presents an example of model calibration and validation of the FE model of a rectangular steel plate based on correlation with experimental results.

**Fig. 37.9** Rectangular plate with constraints. (a) Test setup; (b) supports and clamping location



**Table 37.5** Comparison of modal frequencies for constrained boundary condition case

Mode #	Description	Modal frequency (Hz)		Rel. diff. (%)
		FE	Experimental	
1	Pseudo-pitch	10.76	11.02	2.42
2	First X bending	33.34	34.1	2.28
3	Second torsion	53.99	52.71	2.37
4	First Y bending	82.14	83.56	1.75
5	Second X bending	94.92	91.75	3.34
6	Anti symmetric X bending	114.7	118.59	3.39
7	Third torsion	124.4	128.43	3.24
8	X and Y bending	151.9	154.53	1.73
9	Third X bending	205.4	208.28	1.4

- A plate structure was fabricated and tested to estimate its dynamic properties. A FE model of the plate was developed to perform modal correlation and validation.
- The results obtained from both the model and the test showed some differences in modal frequencies due to uncertainties in geometric parameters, the material model and boundary conditions.
- Once corrections to material model and geometric parameters were applied, the FE model was calibrated. An improved support system was used for testing. Subsequently, a good agreement between FE and modal testing results was achieved. The relative error was reduced to 1–2 %, which met the validation criteria.
- Both FE model and modal testing results had similar modal frequencies obtained in the frequency range of 0–250 Hz. The first nine elastic modes showed good agreement in determining torsion, bending or combination of both torsion and bending modes.
- The robustness of the validated model was checked by comparing the results predicted by the FE model with the results of perturbed mass and constrained boundary testing.

## References

1. AIAA (1998) Guide for the verification and validation of computational fluid dynamics simulations. AIAA G-077-1-1998
2. ASME (2006) Guide for verification and validation in computational solid mechanics. ASME V&V 10-2006
3. Oberkampf WL, Roy CJ (2010) Verification and validation in scientific computing. Cambridge University Press, Cambridge
4. Allemang RJ (2010) Validation of the “digital twin” of a reusable, hot structure, hypersonic vehicle. In: US Air Force Summer Faculty Fellowship Program
5. Paez TL (2009) Introduction to model validation. In: Proceedings of the 27th IMAC, SEM, Orlando
6. Hirsch C (2002) Verification and validation for modeling and simulation in computational science and engineering applications. In: Foundations for verification and validation in the 21st century workshop. Johns Hopkins University/Applied Physics Laboratory, 22–23 October 2002
7. Trucano TG, Swiler LP, Igusa T, Oberkampf WL, Pilch M (2006), Calibration, validation, and sensitivity analysis: What’s what, reliability engineering and system safety 91:1331–1357
8. Mariappan D (2009) Simulation and experimental validation of automotive components. In: Proceedings of the 27th IMAC, SEM, Orlando
9. Blevins RD (1979) Formulas for natural frequency and mode shape, Butterworth-Heinemann, USA, pp 252–253
10. Schwarz BJ, Richardson MH (1999) Experimental modal analysis. In: CSI reliability week, Orlando, October 1999
11. Pasha HG, Allemang RJ, Brown DL, Phillips AW, Kohli K (2014) Support systems for developing system models. In: Proceedings of the international modal analysis conference (IMAC) XXXII – a conference and exposition on structural dynamics

# Chapter 38

## Human Activity Recognition Using Multinomial Logistic Regression

Ramin Madarshahian and Juan M. Caicedo

**Abstract** Activity monitoring is one of the predominant concerns of the elderly living at home. For example, serious complications or even death can be avoided if the elder is helped shortly after a serious fall. Several methods have been proposed to recognize human activity. Most of them can be categorized in three general groups: (1) vision-based methods; (2) wearable sensors; and (3) vibration-based methods. Despite the advantages of vision-based methods and wearable sensors, privacy concerns in the first type, and compliance challenges in the second group motivate the health care industry to pay attention to other types of environmental monitoring techniques such as vibration-based methods. Vibration-based methods use accelerometers placed at the floor of the patient's dwelling. These methods are appealing because accelerometers are not expensive and installation is easy. The classification of events is critical in vibration-based methods. This paper proposes a classification algorithm using Multinomial Logistic Regression (MLR). A data set of different human activities is experimentally obtained. Some signals are used to train the classification algorithm while the remaining records are used to test the proposed technique. The signal "peak" and a "proposed time index" are used for classification. Principal component analysis is used to reduce the number of parameters considered for MLR given that each event was captured by four sensors. The main advantage of this classification algorithm is its probabilistic nature. Results show that in most cases, the event was correctly identified by the group having the highest probability. However, other signal characteristics should be explored to improve the performance of the proposed technique.

**Keywords** Human activity monitoring • Floor vibration • Classification • Multinomial logistic regression (MLR) • Fall detection

### 38.1 Introduction

Improvements in medical science and public health have had a considerable impact on life expectancy. Longer lifespans are more common now in comparison to previous decades [1]. An increase in life expectancy has resulted in an increase in the population of the age group defined as elderly. As the population ages, diseases that affect human activities like Alzheimer's, and Parkinson's are more predominant [2]. Falls are considered to be one of the most important causes of serious injury in the elderly, specially when the individual suffers from Alzheimer's or Parkinson's. Different studies show that "long lie", defined as remaining on the ground for more than one hour without conscious control, is the reason for a high mortality rate followed by a fall. Since the medical outcome of a fall is largely correlated with the rescue time, eliminating the time between fall occurrence and medical care becomes very important [3].

Telecare systems that automatically communicate with a medical center or a family member at the time of a fall have been proposed and implemented in the last decade. Three general monitoring systems are commonly used for this goal: (1) vision-based systems; (2) wearable sensors; and (3) vibration-based systems [4]. Vision-based and wearable systems have been used for several years and many different algorithms have been proposed for the identification of a fall. However, vision systems have privacy concerns and wearable sensors have compliance challenges, especially in patients with dementia. For more information about pros and cons of these systems see [5–8].

Fall detection through floor vibration is considered to be a very new approach in comparison to aforementioned methods. These methods do not require the elderly or patients to wear anything and therefore has no compliance issues. Also people do not feel "watched", which is an advantage when compared with vision based systems. From a cost perspective, accelerometers are not very expensive in comparison to cameras or wearable sensors. Alwan et al. showed that vibrations

---

R. Madarshahian (✉) • J.M. Caicedo  
University of South Carolina, 300 Main St., Columbia, SC 29208, USA  
e-mail: [mdrshhn@email.sc.edu](mailto:mdrshhn@email.sc.edu); [caicedo@cec.sc.edu](mailto:caicedo@cec.sc.edu)



induced by human activities have a specific pattern and this signature is different from those made by objects [9, 10]. In some studies, sound has been used in addition to floor vibration to gain a better classification of the events [11, 12]. The project “eHome”, with the objective of prolonging elders’ independent life, used floor mounted accelerometers to collect signals when a fall happened [13]. The current body of research shows that acceleration signals of interest can be detected by setting a trigger, however more research is needed to classify these signals and identify only those of interest [14]. Madarshahian et al. [15] studied the use of Dynamic Time Warping (DTW) and demonstrated that type of excitation played an important role in the methodology.

In this work, a probabilistic algorithm that takes signal characteristics as input is used for classification. The methodology consists of two steps, (1) Principal Component Analysis (PCA), and (2) Multinomial Logistic Regression (MLR). A set of experimental data was collected to study how to classify human induced and other type of floor vibrations, such as objects being dropped. The dataset was created by dropping two different objects at two heights, and by having three individuals jump. Signal characteristics such as amplitude and duration were calculated for each signal. Four sensors were used for data collection, therefore signal parameter of data collected with one sensor could be highly correlated with those from other sensors for a specific event. Therefore PCA, which is recommended for high correlated variables, is implemented to reduce the number of signal characteristics to consider. Then, the variables obtained from PCA are used in the MLR to estimate the probability of an occurred event belonging to a particular class.

The paper is organized as follows. First, the dataset is described, then the implementation of PCA and MLR is discussed. Finally, the algorithm is tested and evaluated using the experimental dataset. A confusion matrix is used to determine the capabilities of the classifier. Finally, the results are discussed.

## 38.2 Experimental Setup

The dataset used in this study contains seven classes of events as shown in Table 38.1. The first two classes contain signals of a bag of K’nex of 0.45 kg of mass dropped on the floor from two different heights. The first class was dropped from a height of 2.10 m while the second class was dropped from 1.42 m. Classes 3 and 4 are similar to the first two classes using a 0.56 kg basketball. The last three classes are jumps of three different people at the same location that the ball and bag had been dropped. The mass of each person was of 80, 85, and 55 kg for classes 5, 6 and 7 respectively.

The experiments took place at a second floor of a steel structure with concrete slabs. Each of the events was recorded by four PCB 333B50 accelerometers at distances of 3.15, 3.80, 2.60 and 1.15 m respectively. The accelerometers were connected to a NI CompactDAQ with a NI9234 module. Each record was collected at 1651.7 Hz for 2 s.

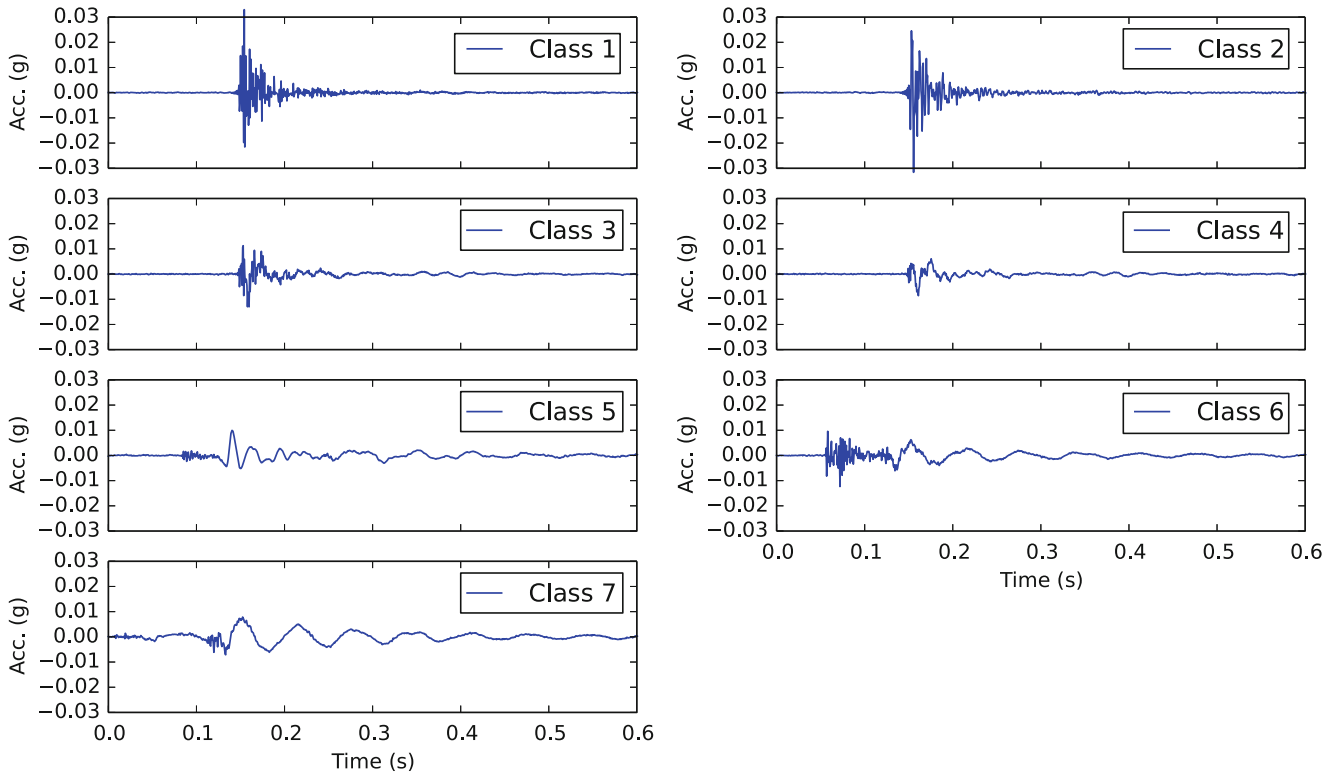
A total of 120 events were recorded for each class. Twenty records are used for training the algorithm and the remaining 100 are used for testing purposes. Figure 38.1 shows typical signals for each class and Fig. 38.2 shows a typical record for class 4 (ball low) as collected by all four sensors.

## 38.3 Methodology

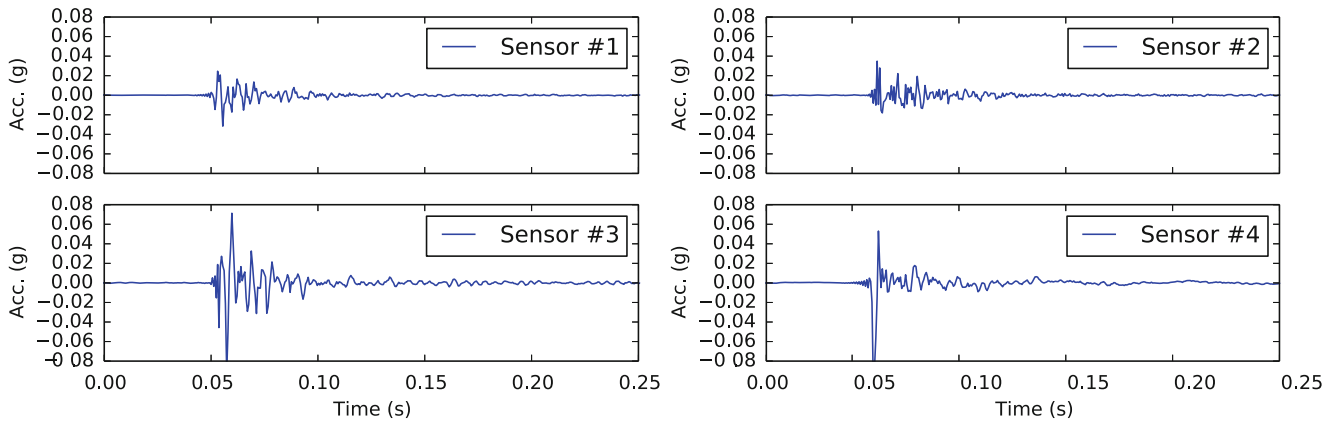
The signal parameters used for analysis are introduced in the first part of this section. The second part is a general overview of Principal Component Analysis (PCA) and Multinomial Logistic Regression (MLR). Lastly, the classification algorithm is discussed.

**Table 38.1** Classes used in the dataset

Events		
Class	Description	Abbreviation
1	Bag of Knex dropped from a height of 2.10 m	baghigh
2	Bag of Knex dropped from a height of 1.42 m	baglow
3	Basketball dropped from a height of 2.10 m	ballhigh
4	Basketball dropped from a height of 1.42 m	balllow
5	Jump records of a person with mass of 80 kg	djump
6	Jump records of a person with mass of 85 kg	jjump
7	Jump records of a person with mass of 55 kg	wjump



**Fig. 38.1** Typical signals for different classes



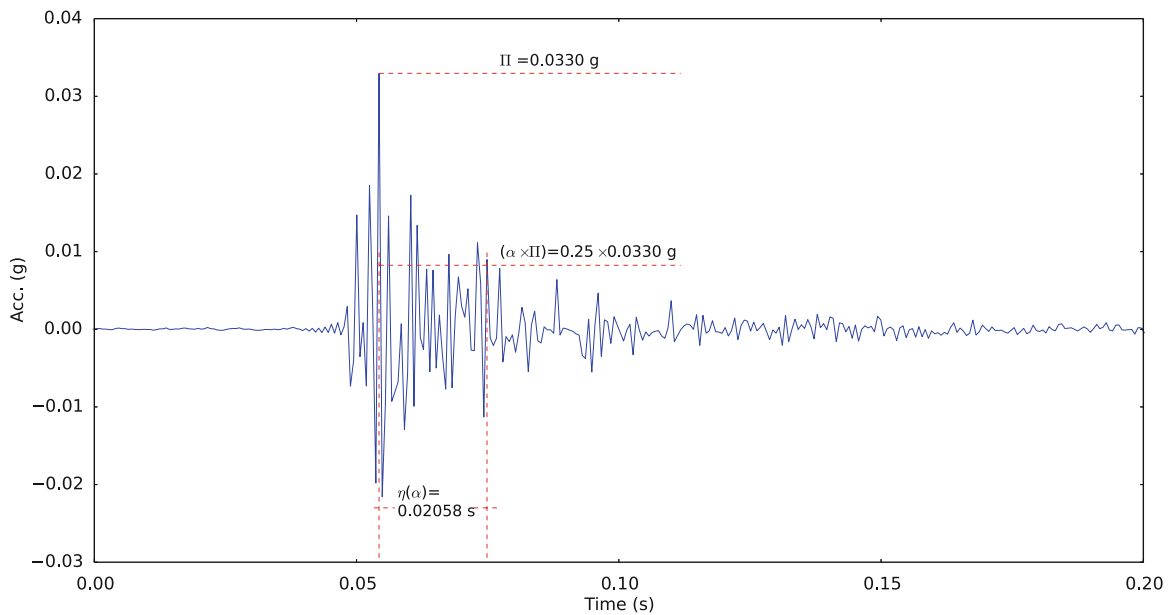
**Fig. 38.2** Typical signals for class 4 (balllow) as recorded by all four sensors

### 38.3.1 Signal Characterization

An acceleration signal can be described by a set of parameters such as its peak, duration, statistical moments, rise and fall time, range, energy, etc. [16, 17]. Any of these parameters can be used as input variables to classification algorithms. In this particular paper we focus on the use of the Peak of the signal, and propose a new parameter called the Proposed Time Index (PTI). The Peak of the signal is defined by the equation:

$$\Pi = \max_{i=1}^{i=n} |s_i| \quad (38.1)$$

where  $\Pi$  stands for the Peak,  $s_i$  is the  $i$ th sample, and  $n$  is total numbers of samples of the acceleration signal. The symbol  $||$  indicates absolute value.



**Fig. 38.3** Calculation of  $\eta$  based on  $\alpha$

PTI is a parameter that allows us to measure the shape of the acceleration signal. PTI is defined by the equation:

$$PTI = \int_{\alpha=0}^{\alpha=1} \eta(\alpha) d\alpha \quad (38.2)$$

where  $\alpha$  is a ratio between zero and one.  $\eta(\alpha)$  is the fall time and it is defined as the time between the peak of the signal and the time of the last sample that is above  $\alpha$  times of the peak, and  $\alpha$  is a number between zero and one [18]. Figure 38.3 has a graphical representation of  $\eta(\alpha)$

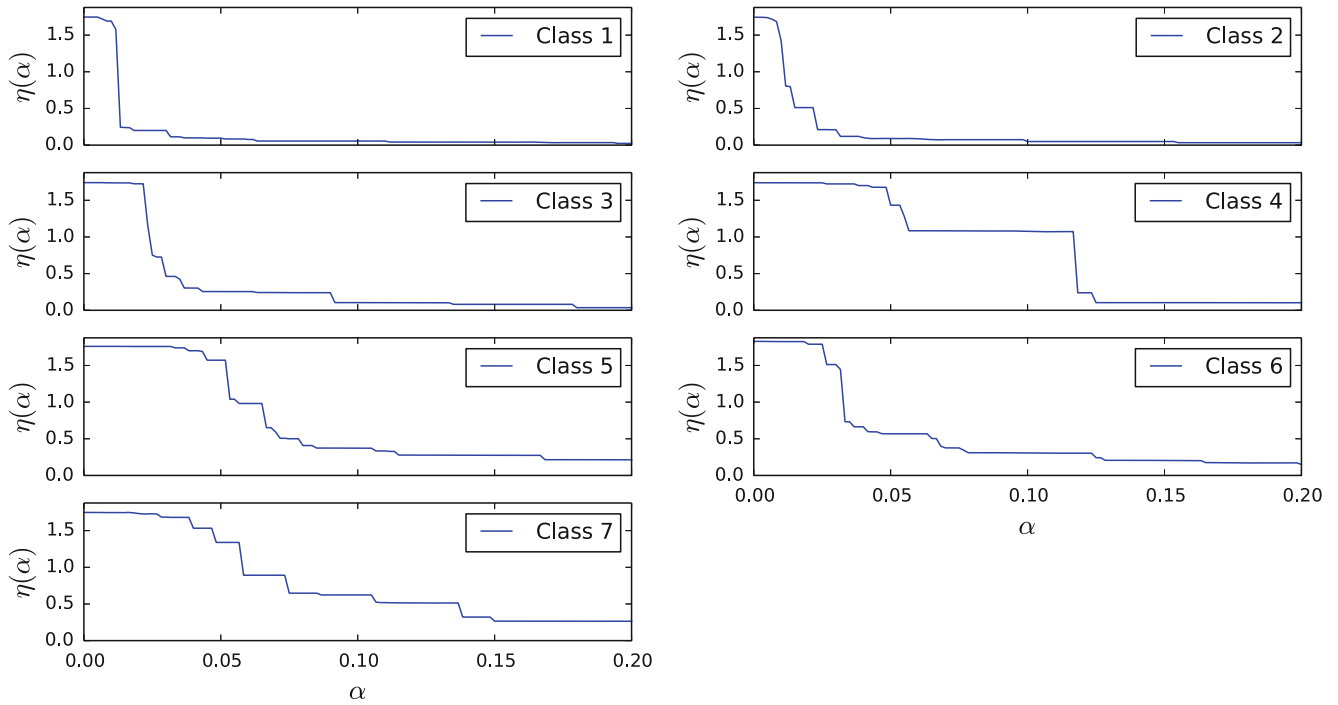
Figure 38.4 shows the fall time profiles of the signals in Fig. 38.1. PTI is the area under these profiles.

### 38.3.2 Principal Component Analysis (PCA)

The parameters used in this paper (Peak and PTI) are calculated for each of the four sensors. It is possible that some of these parameters will be correlated because they are generated by a single event. The Principal Component Analysis (PCA) is a well known eigenvector-based multivariate analysis tool to reduce the number of parameters to consider in the analysis. The main goal of this orthogonal linear transformation is to describe the variability in a large set of correlated parameters by a fewer uncorrelated variables. The new variables, or principal components, are a linear combination of the initial parameters. The principal components are usually sorted based on their contribution to the original set of parameters. Principal components with a small contribution can be omitted to reduce the computational cost involved with the data analysis. Although the first component has the most contribution, the second or even higher components are important for pattern recognition and classification problems [19]. For example, it has been shown that higher components are beneficial in classifying metals, performing kinetic modeling of food quality, and study of the changes in gene expression [20–22]. The parameters used in this paper (Peak and PTI) have different units. These parameters are scaled by their mean as recommended to improve the performance of PCA [19].

### 38.3.3 Multinomial Logistic Regression (MLR)

Multinomial Logistic Regression is a probabilistic classification method used for categorical outcomes [23–26]. The method estimates the probability to a discrete random variable by providing a mapping between the parameters of the acceleration



**Fig. 38.4** Typical fall time profiles

signal (explanatory variables) and the probability of the event belonging to a specific class [27]. This is performed by calculating the logarithmic of the odds ratio between classes, allowing to map an explanatory variable with domain  $[-\infty, +\infty]$  to a probability (i.e.  $[0,1]$ ). MLR does not require normality or linearity which makes its implementation robust [28]. The general form of MLR is shown in Eq. (38.3):

$$P(Y = c|X = x) = \frac{e^{\beta_0^{(c)} + x \cdot \beta^{(c)}}}{\sum_c e^{\beta_0^{(c)} + x \cdot \beta^{(c)}}} \quad (38.3)$$

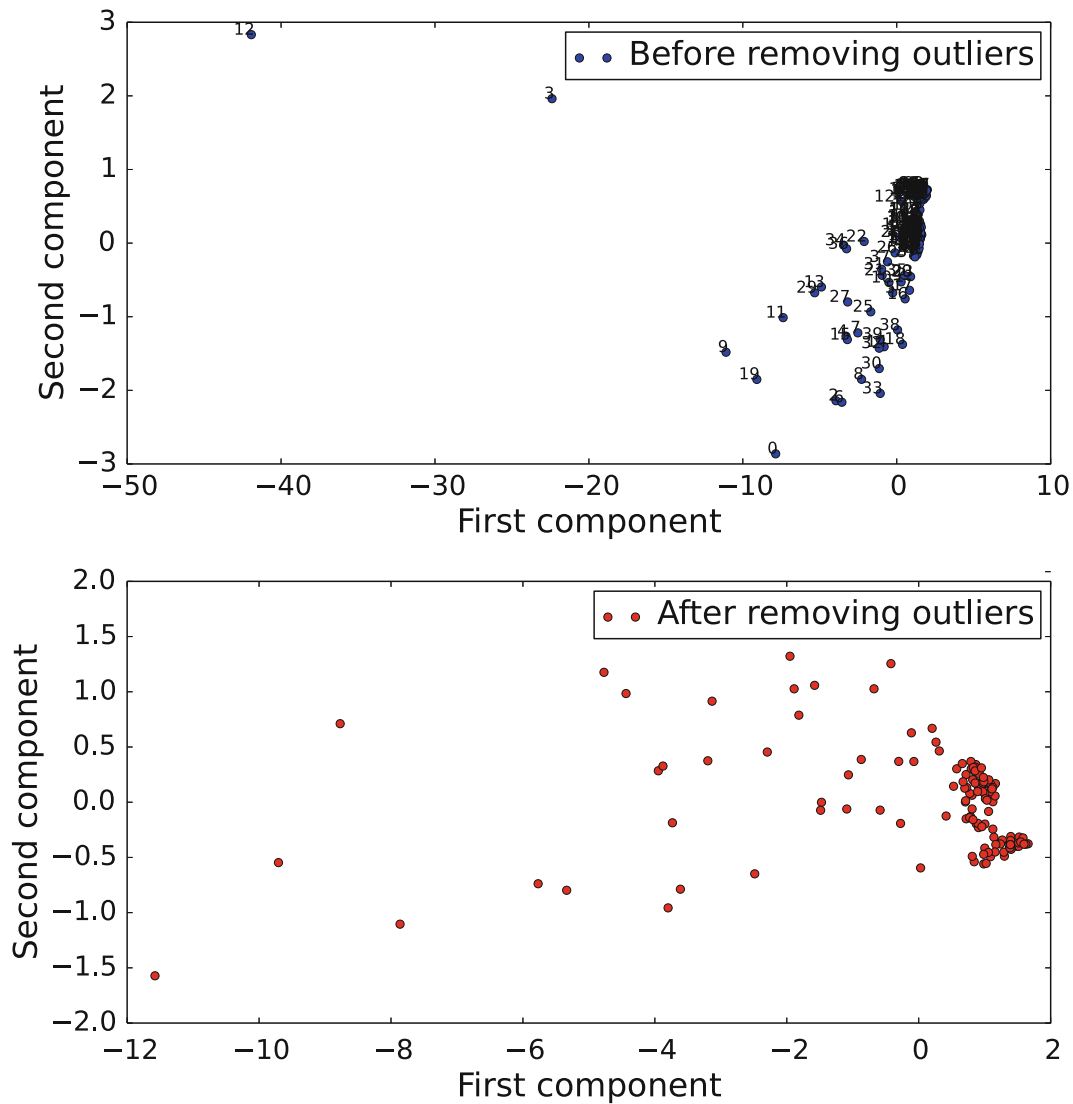
$P(Y = c|X = x)$  is the probability of the response variable  $Y$  belonging to class  $c$  given the observation  $x$ .  $\beta_0^{(c)}$ , and  $\beta^{(c)}$  are the logistic regression parameters for each class. These parameters are first estimated with the 20 records available to train the algorithm.

### 38.3.4 Training the MLR Model

The training dataset used in this problem contains twenty events for each of the seven classes considered. Each event was recorded by four sensors for a total of 560 signals. First, the signal characteristics (Peak and PTI) are calculated for each signal. PCA is used to reduce the number of parameters to be considered by MLR and detect outliers. Outliers are identified visually after plotting the first two principal components of each event. Principal components are re-calculated after outliers are removed. The first two components were found to be the most significant in the analysis and are the only parameters used to build the MLR model. The python scikit-learn python package is used for calculations [29].

### 38.3.5 Testing the Proposed Algorithm

One hundred events per class are available for testing for a total of 2,800 signals. The signal characteristics and principal components are calculated for each event. The MLR model developed with the training data is used for classification.



**Fig. 38.5** First two components for case 1 with and without outliers

A confusion or error matrix is used to determine the performance of the algorithm [30]. Each column of the matrix shows the classes as classified by the algorithm, while each row shows the actual class. A perfect classification corresponds to a diagonal matrix with the number of events for each class in the appropriate locations.

## 38.4 Results

The proposed methodology is used in three different cases. In the first case only the signal Peak is used for the analysis. In the second case only PTI, and the last case uses both Peak and PTI. The type of variable used for the analysis in cases 1 and 2 have the same units (Peak and PTI respectively). Therefore, scaling the parameters is not required to apply the PCA. The third case requires scaling the parameters by the mean because the values of Peak and PTI have different units. The parameters are scaled in all cases to provide consistency in the application of the technique. The mean for the Peaks and PTI was calculated as 0.0338 g and 0.174 s respectively.

Four values for the Peak are calculated for each event in case 1. This is, one from the data collected by each sensor. Figure 38.5 shows the first two principal components for the 140 signals considered for training. The top figure shows the first and second components before removing outliers. Outliers are selected visually as events 3 and 12. The same outliers

**Table 38.2** MLR summary for case 1

MLR summary			
Class ↓	$\beta_0$	$\beta_1$	$\beta_2$
Class 1	-3.177	-0.880	1.955
Class 2	-1.992	-0.294	0.930
Class 3	-7.020	5.004	9.022
Class 4	-10.937	8.782	10.771
Class 5	-5.111	1.530	-7.476
Class 6	-1.992	0.429	0.015
Class 7	-5.947	1.783	-8.857

were identified for case 3 and no outliers were found for case 2. The bottom figure shows the principal components after the analysis is repeated without these events. The variances of the first two components in case 1 are calculated as 94.8% and 4.2% of the total variance respectively. Similar percentages were found for case 2. However, for the case 3 share of the first component from total variance was reduced to 74.2%, and share of the second component was increased to 19.4%. The MLR model is obtained using these two components only. Table 38.2 shows the coefficient of the MLR model for case 1.

The methodology is tested with 100 additional events from each class. Signals are first scaled and transformed to the principal components found during the training process. Then, the events were classified using the previously obtained MLR model. Figure 38.6 shows the classes (areas) and testing data (circle) mapped in the domain of the first two principal components. Circles that have a different darkness than the area where they are placed were not classified correctly.

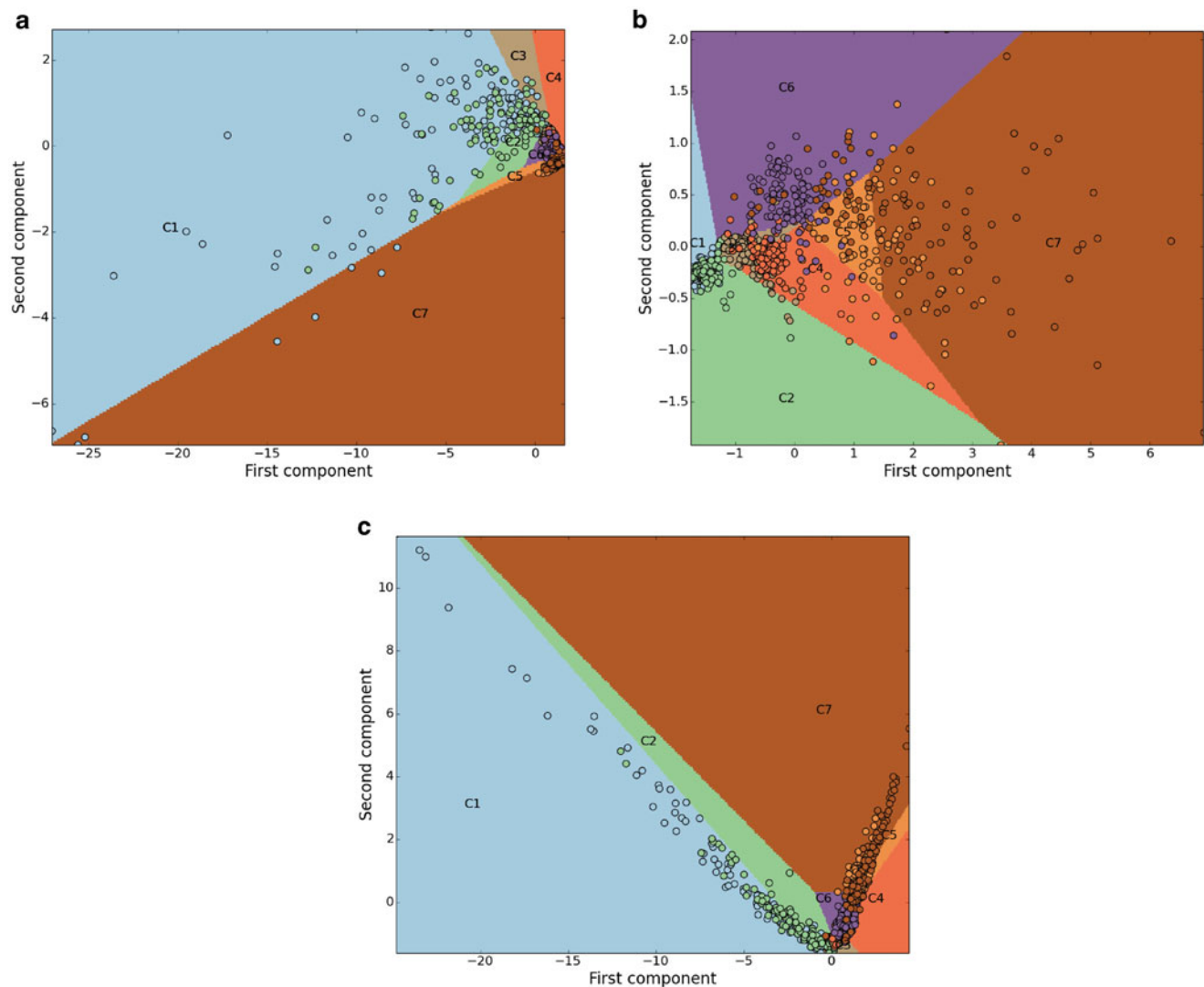
The algorithm provides the probability of an event belonging to a particular class. This helps make an informed decision on the classification process. It is possible to include in the analysis a minimum percentage of probability required to classify an event. Events that have a probability smaller than this minimum for all classes can be considered as class unknown. In addition, one could combine classes to get a better estimation on the type of object striking the floor. For example, the basketball is used for events that belong to classes 3 and 4. The only difference between these classes is the amplitude of the impact.

It is possible to make a better classification of the type of object (e.g. ball vs bag) than classifying the type of object and amplitude of impact. The probability of the event being produced by the basketball can be calculated by adding the results of classes 3 and 4. Table 38.3 shows the results of two events as an example. The actual class of both events is Class 1. Event 1 was correctly classified and Event 2 was incorrectly classified. Notice that the maximum probability of Event 2 is only 35% and it could be considered as unclassified if a minimum probability is specified. However, we can say with a good degree of certainty that both samples were produced by the basketball because the summation of the probabilities for class 1 and 2 (62.9%) are much higher than the probability of any other classes.

Confusion matrices can be used to explore the performance of classification algorithms. Table 38.4 shows the confusion matrices for all cases. The top part of the table contains the results for case 1. Sixty nine out of the 100 events used in class 1 were classified correctly. Eleven of them are classified as class 2. Both classes 1 and 2 used the bag of K'nex. Therefore, a total of 80% of the events identified the type of object correctly when the bag was used. Only 7 of the events were classified as a jump. The worst performance for case 1 was for events in class 2. Only 27% of the events were classified correctly when considering the type of object and the amplitude of the force. This percentage increases to 84% when only the type of object is classified. In addition, only 3 of the 100 events were classified as a jump. The algorithm did a good job classifying jumps of two out of the three people used in case 1. The third person (class 6) was not correctly identified as a jump 30% of the time. It is possible that the Peak of this person jumping is similar to that created with a the basketball (class 4).

The results of case 2 are arguably better than the results of case 1 when considering the type of object striking the floor. The classification of events belonging to class 6 is much improved, indicating that the shape of the signal, expressed in terms of the PTI could have an effect on the classification of the signals. Similarly, the percentage of bag events (classes 1 and 2) that are correctly classified improved.

In case 3 both the Peak and the PTI are considered. After removing the outliers, the two principal components represent 74% and 19% of the total variance. Considering both variables (Peak and PTI) increases the share of the second component. Figure 38.6c shows that the distribution of the testing data on the principal components plane is different than with the previous cases. The results on the confusion matrix for case 3 (Table 38.4) are good for bag and basketball events. However, over 50% of the events for class 6 are not classified as a jump. This is similar to the results of case 1.



**Fig. 38.6** Logistic regression results on principal components. (a) case 1; (b) case 2; (c) case 3

**Table 38.3** Probabilities correspond to two events of testing data

Event ↓	Probability						
	Class 1	Class 2	Class 3	Class 4	Class 5	Class 6	Class 7
1 (correctly classified)	0.602	0.356	0.001	0.000	0.000	0.040	0.000
2 (incorrectly classified)	0.274	0.355	0.186	0.005	0.000	0.179	0.000

## 38.5 Conclusion and Future Work

This paper proposes a methodology to classify floor vibration signals depending on the source of the excitation. The possible applications of the technique are in human activity recognition such as identifying human falls. The methodology uses Principal Component Analysis and a Multinomial Logistic Regression for classification. A large dataset of experimental data was used to test the proposed method, including floor vibrations induced by a basketball, people jumping and a bag of plastic pieces (K'nex). Two levels of excitation were studied for each source type.

Only two principal components were required to describe the multi-dimensional data set independent on the case considered. When the Peak was the only variable used for the MLR (case 1) events created by the bag were more scattered in the in the principal component plane. Jump events (classes 5 to 7) were more scattered in the principal component plane for case 2 (PTI). Finally, the test events formed “v” shape in the principal component plane when both Peak and PTI are used (case 3). The variance of the second component was higher when both Peak and PTI were used.

**Table 38.4** Confusion matrices for all cases

Case 1							
	Classified						
Actual ↓	Class 1	Class 2	Class 3	Class 4	Class 5	Class 6	Class 7
Class 1	69	11	13	0	0	0	7
Class 2	56	27	14	0	0	3	0
Class 3	0	0	53	36	0	11	0
Class 4	0	0	7	88	0	5	0
Class 5	0	0	0	0	43	2	55
Class 6	0	0	3	27	0	70	0
Class 7	0	1	0	5	21	0	73

Case 2							
	Classified						
Actual ↓	Class 1	Class 2	Class 3	Class 4	Class 5	Class 6	Class 7
Class 1	78	18	4	0	0	0	0
Class 2	54	40	6	0	0	0	0
Class 3	0	5	58	31	0	6	0
Class 4	0	0	24	68	0	8	0
Class 5	0	3	1	10	44	8	34
Class 6	0	0	3	9	6	82	0
Class 7	0	0	0	0	18	24	58

Case 3							
	Classified						
Actual ↓	Class 1	Class 2	Class 3	Class 4	Class 5	Class 6	Class 7
Class 1	75	21	4	0	0	0	0
Class 2	55	37	8	0	0	0	0
Class 3	0	2	63	17	0	18	0
Class 4	0	0	14	83	1	2	0
Class 5	0	0	0	8	39	3	50
Class 6	0	0	3	50	1	44	2
Class 7	0	1	1	8	21	9	60

Confusion matrices to classify the type of the source of the vibrations and the amplitude were developed. These matrices show a slight advantage when only PTI was used. These results indicate that the shape of the acceleration record is an important parameter to be considered. In general, the proposed algorithm had a modest performance when asked to classify the type and amplitude of excitation. The methodology is more effective at identifying the type of object striking the floor only.

Other signal characteristics such as energy, range and duration should be evaluated in the future. In addition, a “layered” process should be studied where the type of object used to induce vibrations is identified first. Subsequent analysis can be done to estimate the intensity of the impact.

**Acknowledgements** This work was partially supported by a SPARC Graduate Fellowship from the Office of the Vice President for Research at the University of South Carolina. Partial support was provided by the Alzheimer’s association. The authors would like to thank Diego Arocha, Wesley Harvey and Jennifer Yu for their help collecting the experimental data used for this work.

## References

1. Arias E (2014) United States life tables, 2009. In: National vital statistics reports: from the Centers for Disease Control and Prevention, National Center for Health Statistics, National Vital Statistics System, vol 62, no 7, pp 1–63
2. Salarian A, Russmann H, Vingerhoets FJ, Burkhard PR, Aminian K (2007) Ambulatory monitoring of physical activities in patients with parkinson’s disease. *IEEE Trans Biomed Eng* 54(12):2296–2299
3. Reece AC, Simpson JM (1996) Preparing older people to cope after a fall. *Physiotherapy* 82(4):227–235
4. Mubashir M, Shao L, Seed L (2013) A survey on fall detection: principles and approaches. *Neurocomputing* 100:144–152



5. Chen J, Kwong K, Chang D, Luk J, Bajcsy R (2006) Wearable sensors for reliable fall detection. In: 27th annual international conference of the engineering in medicine and biology society, 2005 (IEEE-EMBS 2005). IEEE, New York, pp 3551–3554
6. Patel S, Park H, Bonato P, Chan L, Rodgers M (2012) A review of wearable sensors and systems with application in rehabilitation. *J Neuroeng Rehabil* 9(1):21
7. Williams A, Ganesan D, Hanson A (2007) Aging in place: fall detection and localization in a distributed smart camera network. In: Proceedings of the 15th international conference on Multimedia. ACM, New York, pp 892–901
8. Fleck S, Straßer W (2008) Smart camera based monitoring system and its application to assisted living. *Proc IEEE* 96(10):1698–1714
9. Alwan M, Rajendran PJ, Kell S, Mack D, Dalal S, Wolfe M, Felder R (2006) A smart and passive floor-vibration based fall detector for elderly. In: 2nd Information and communication technologies, 2006 (ICTTA'06), vol 1. IEEE, New York, pp 1003–1007
10. Rajendran P, Corcoran A, Kinoshia B, Alwan M (2008) Falls, fall prevention, and fall detection technologies. In: *Eldercare technology for clinical practitioners*. Springer, New York, pp 187–202
11. Litvak D, Zigel Y, Gannot I (2008) Fall detection of elderly through floor vibrations and sound. In: 30th annual international conference of the IEEE engineering in medicine and biology society, 2008 (EMBS 2008). IEEE, New York, pp 4632–4635
12. Zigel Y, Litvak D, Gannot I (2009) A method for automatic fall detection of elderly people using floor vibrations and sound—proof of concept on human mimicking doll falls. *IEEE Trans Biomed Eng* 56(12):2858–2867
13. Werner F, Diermaier J, Schmid S, Panek P (2011) Fall detection with distributed floor-mounted accelerometers: an overview of the development and evaluation of a fall detection system within the project ehome. In: 2011 5th international conference on pervasive computing technologies for healthcare (PervasiveHealth). IEEE, New York, pp 354–361
14. Davis BT, Caicedo JM, Langevin S, Hirth V (2011) Use of wireless smart sensors for detecting human falls through structural vibrations. In: *Civil engineering topics*, vol 4. Springer, New York, pp 383–389
15. Madarshahian R, Caicedo JM, Zambrana DA (2014) Evaluation of a time reversal method with dynamic time warping matching function for human fall detection using structural vibrations. In: *Model validation and uncertainty quantification*, vol 3. Springer, New York, pp 171–176
16. Nise NS (2007) *Control systems engineering (with CD)*. Wiley, New York
17. Soliman SS, Hsue S-Z (1992) Signal classification using statistical moments. *IEEE Trans Commun* 40(5):908–916
18. Khatak H, Raj B (2002) *Corrosion of austenitic stainless steels: mechanism, mitigation and monitoring*. Elsevier, Amsterdam
19. Everitt BS (2006) *An R and S-PLUS® companion to multivariate analysis*. Springer, London
20. Passos EDA, Alves JC, dos Santos IS, Alves JDPH, Garcia CAB, Spinola Costa AC (2010) Assessment of trace metals contamination in estuarine sediments using a sequential extraction technique and principal component analysis. *Microchem J* 96(1):50–57
21. Saavedra J, Córdova A, Gálvez L, Quezada C, Navarro R (2013) Principal component analysis as an exploration tool for kinetic modeling of food quality: a case study of a dried apple cluster snack. *J Food Eng* 119(2):229–235
22. Park H-J, Oh JH, Yoon S, Rana S (2008) Time dependent gene expression changes in the liver of mice treated with benzene. *Biomark Insights* 3:191
23. Peng CYJ, Lee KL, Ingersoll GM (2002) An introduction to logistic regression analysis and reporting. *J Educ Res* 96(1):3–14
24. Muriithi DK, Njoroge GG, Njoroge E, Mark O (2013) Classification of higher education loans using multinomial logistic regression model. *J Math Sci Adv Appl* 22:1–17
25. Pal M (2012) Multinomial logistic regression-based feature selection for hyperspectral data. *Int J Appl Earth Obs Geoinf* 14(1):214–220
26. Silva A, Gaspar P, de Brito J (2014) Durability of current renderings: a probabilistic analysis. *Autom Constr* 44:92–102
27. Lyman O, Longnecker M (1988) *An introduction to statistical methods and data analysis*. PWS-Kent, Boston
28. Starkweather J, Moske AK (2011) Multinomial logistic regression. Consulted page at September 10th: [http://www.unt.edu/rss/class/Jon/Benchmarks/MLR\\_JDS\\_Aug2011.pdf](http://www.unt.edu/rss/class/Jon/Benchmarks/MLR_JDS_Aug2011.pdf)
29. Pedregosa F, Varoquaux G, Gramfort A, Michel V, Thirion B, Grisel O, Blondel M, Prettenhofer P, Weiss R, Dubourg V, Vanderplas J, Passos A, Cournapeau D, Brucher M, Perrot M, Duchesnay E (2011) Scikit-learn. *J Mach Learn Res* 12:2825–2830
30. Parker J (2001) Rank and response combination from confusion matrix data. *Inf Fusion* 2(2):113–120